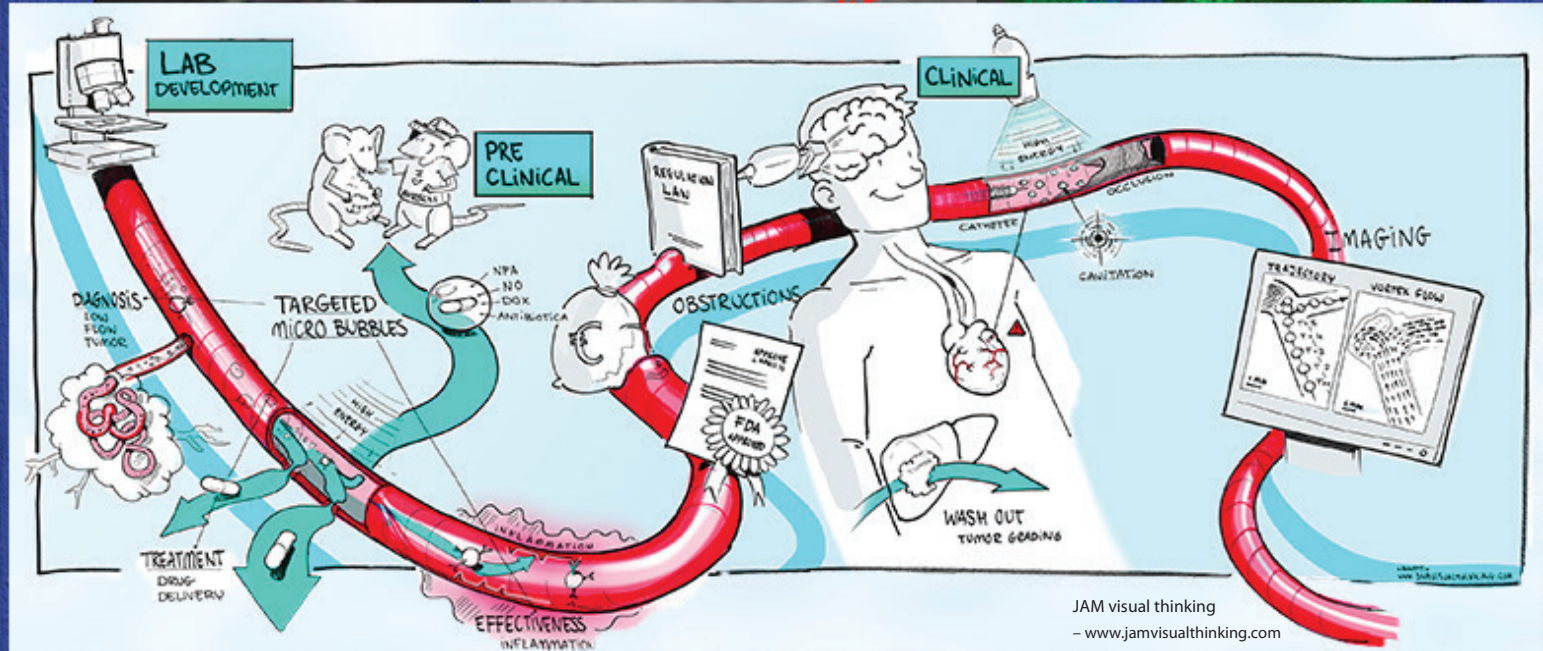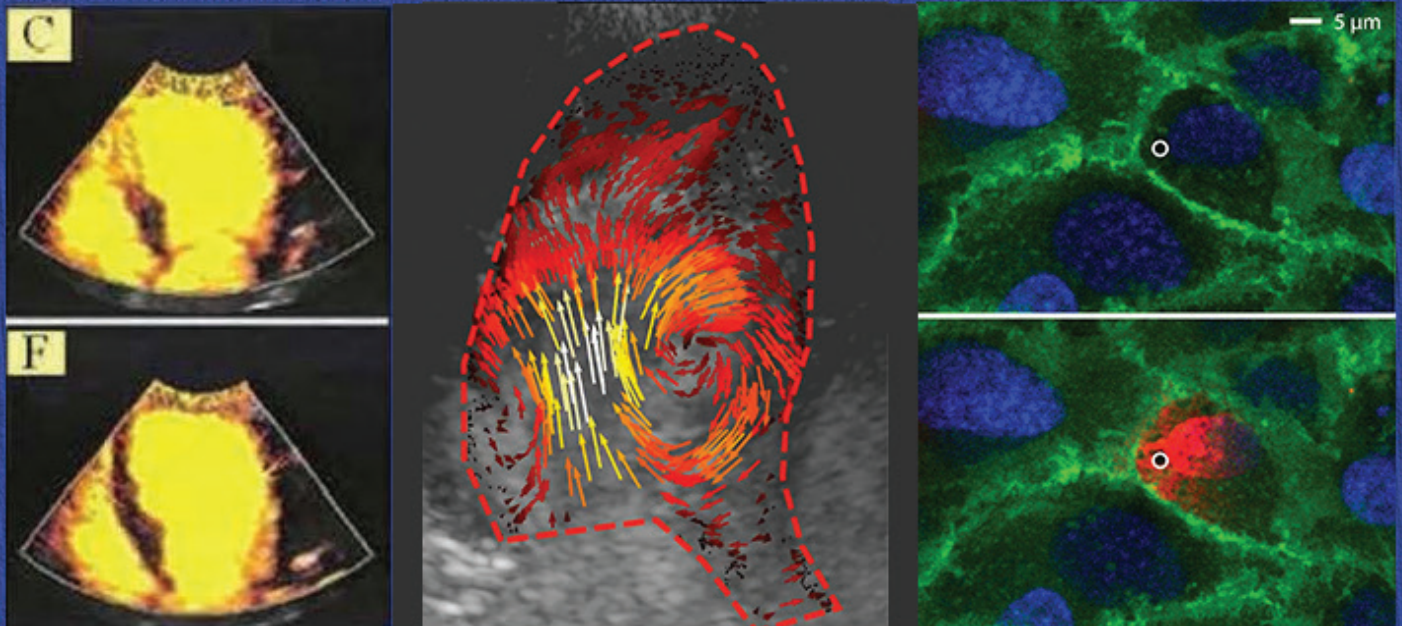# The 28th European Symposium on Ultrasound Contrast Imaging
- An ICUS-Endorsed Conference -

Abstract book

19-20 January 2023, Rotterdam, the Netherlands

Organised by Rik Vos, Klazina Kooiman, Annemien van den Bosch, Folkert ten Cate and Nico de Jong

Erasmus MC Rotterdam

Dinner

Thursday January 19th, 2023

Time: starting at 18:30 hrs

Address: Societeit aan de Maas

Veerdam 1, 3016 DD Rotterdam

Only 10 minutes walking distance from Mainport Hotel

THE 28TH EUROPEAN SYMPOSIUM ON ULTRASOUND CONTRAST IMAGING
January 19-20, 2023

28th ESUCI Rotterdam Bubble Conference Program

<u>WEDNESDAY, 18 January 2023</u>

13.00   PhD defense (Erasmus MC) Gonzalo Collado Lara: Radiotherapy Dosimetry with Ultrasound Contrast Agents
Location: Prof. Andries Querido zaal, Erasmus MC, Rotterdam
17.30 – 19.30   Welcome Drinks at the conference location: Mainport Hotel, Leuvehaven 77, Rotterdam
Registration

<u>THURSDAY, 19 January 2023</u>

Oral program

FRIDAY, 20 January 2023

07.30 – 08.00 Registration

07.30 – 09.00   PARALLEL SHORT ORAL SESSION I (poster room 1) and SESSION II (poster room 2); walk-in breakfast provided

Oral program

15.45   ANNOUNCEMENT OF THE WINNERS OF THE COMPETITION AND POSTER PRIZES

FAREWELL DRINKS

THE 28TH EUROPEAN SYMPOSIUM ON ULTRASOUND CONTRAST IMAGING
January 19-20, 2023

Poster sessions Thursday 19 January 2023

Organised by: Rik Vos, Klazina Kooiman, Annemien van den Bosch, Folkert ten Cate, Nico de Jong

Scientific board: Mike Averkiou, Mark Borden, Paolo Colonna, Olivier Couture, Beat Kaufmann, Eleanor Stride

THE 28TH EUROPEAN SYMPOSIUM ON ULTRASOUND CONTRAST IMAGING
January 19-20, 2023

Erasmus MC · Erasmus · THORAX CENTRUM

<u>FRIDAY, 20 January 2023</u>

07.30 – 08.00 Registration

Parallel short oral and poster sessions Friday 20 January 2023

Organised by: Rik Vos, Klazina Kooiman, Annemien van den Bosch, Folkert ten Cate, Nico de Jong

Scientific board: Mike Averkiou, Mark Borden, Paolo Colonna, Olivier Couture, Beat Kaufmann, Eleanor Stride

Erasmus MC · Erasmus · THORAX CENTRUM

THE 28TH EUROPEAN SYMPOSIUM ON ULTRASOUND CONTRAST IMAGING
January 19-20, 2023

Organised by: Rik Vos, Klazina Kooiman, Annemien van den Bosch, Folkert ten Cate, Nico de Jong

Scientific board: Mike Averkiou, Mark Borden, Paolo Colonna, Olivier Couture, Beat Kaufmann, Eleanor Stride

The use of contrast-enhanced ultrasound in pregnant women

Dirk-André Clevert [1]

[1]Department of Radiology, University of Munich-Grosshadern Campus, Munich, Germany
Corresponding author: Dirk.Clevert@med.uni-muenchen.de

Introduction

Ultrasound is an essential imaging tool for evaluating physiological and pathologic fetal or maternal conditions during pregnancy. Published data is limited concerning the application of CEUS during pregnancy. For assessing uteroplacental blood flow, caesarean scar pregnancy and invasive placenta percreta CEUS has already been safely applied. CT and MRI scans during pregnancy must be thoroughly evaluated due to harmful ionizing radiation and cerebral Gadolinium deposition, respectively. The aim of the present retrospective monocenter study is to assess the diagnostic performance and safety of CEUS during pregnancy to assess hepatic, renal and vascular lesions of unknown entity.

Methods

28 pregnant patients were included in this study on which CEUS was performed between 2005 - 2021. The applied contrast agent was a second-generation pool agent (SonoVue®, Bracco, Milan, Italy). CEUS examinations were performed and interpreted by a single radiologist with experience since 2000 (EFSUMB Level 3).

Table 1. Case 1]

Caae 1t		
25-year old female, 24 weeks pregnant, rectal bleeding	Native B-mode: hyperechoic 4,2 cm lesion in liver segment VI.	CEUS: early arterial contrast uptake and portal-venous wash-out.

The abstracts will be shown online when accepted and when the program has been compiled, as PDF document and/or in HTML, so colours are kept. Graphics prepared as native formats in Word using overlays (WMF, MEX) may not convert well. Please flatten the image, insert as PNG/high-resolution JPG, or insert a screen dump from the original native format (method: enlarge the native Word image drastically, select the image, cut the image, then paste as Picture (U), then reduce the size again; this ensures a good resolution).

Results

CEUS was safely performed on all included pregnant women without occurrence of adverse fetal or maternal events. In the context of this present work, CEUS helped to safely differentiate hepatic metastases, focal nodular hyperplasia, atypical hemangioma, hepatic arteriovenous malformation, cystic echinococcosis and vascular and renal lesions. One intervention was done under contrast enhanced ultrasound guided. In two patients CEUS determined immediate therapy.

Conclusions

Although not clinically approved in obstetrics so far, CEUS is a safe imaging modality which in addition to B-mode and Color Doppler ultrasonography may be applied during pregnancy for further medical indications and provide helpful information [1-3].
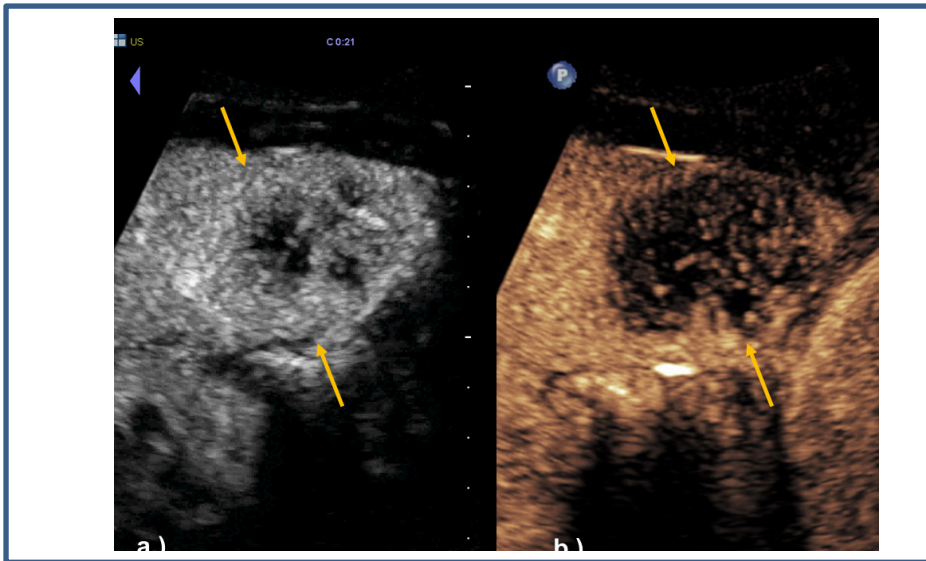
Figure 1. Unclear liver lesion with a wash out in the portal venous phase. The final diagnosis was liver mets from rectal cancer.

References

[1]. Schwarze V, Marschner C, Negrão de Figueiredo G, Rübenthaler J, Clevert DA Single-Center Study: Evaluating the Diagnostic Performance and Safety of Contrast-Enhanced Ultrasound (CEUS) in Pregnant Women to Assess Hepatic Lesions.Ultraschall Med. 2020 Feb;41(1):29-35]

[2]. Geyer T, Rübenthaler J, Froelich MF, Sabel L, Marschner C, Schwarze V, Clevert DA. Contrast-Enhanced Ultrasound for Assessing Abdominal Conditions in Pregnancy.Medicina (Kaunas). 2020 Dec 8;56(12):675

[3] Schwarze V, Froelich MF, Marschner C, Knösel T, Rübenthaler J, Clevert DA. Safe and pivotal approaches using contrast-enhanced ultrasound for the diagnostic workup of non-obstetric conditions during pregnancy, a single-center experience. Arch Gynecol Obstet. 2021 Jan;303(1):103-112

Spatiotemporal analysis of ultrasound contrast-enhanced breast lesions for aiding the differentiation of malignant or benign

Chuan Chen[1] , Simona Turco[1], Panagiotis Kapetas[2], Ritse Mann[3], Hessel Wijkstra[1], Chris de Korte[3], Massimo Mischi[1]

[1] *Eindhoven University of Technology, 5612 AZ, Eindhoven, Netherlands*
[2] *Medical University of Vienna, Spitalgasse 23, 1090 Wien, Vienna, Austria*
[3] *Radboud University Medical Center, Geert Grooteplein Zuid 10, 6525 GA Nijmegen, Netherlands*
Corresponding author: c.chen3@tue.nl

Introduction

Breast cancer is a major threat to women's health [1]. Currently, ultrasound (US) serves as one of the standard imaging modalities in diagnosing breast lesions. However, US is limited to the assessment of morphological information and produces large numbers of false-positives, leading to unnecessary biopsies [2]. Prior studies have shown the potential of contrast-enhanced ultrasound (CEUS) in improving the differentiation between benign and malignant breast lesions [3]. By administrating an ultrasound-contrast-agent (UCA) into the bloodstream, CEUS is able to visualize the altered tumor microvasculature characteristics as a result of angiogenesis [4]. Previous analyses of CEUS in breast cancer were mostly qualitative and based on the evaluation of a time-intensity curve (TIC) measured from a whole region of interest (ROI). In this study, quantitative spatiotemporal analysis of breast CEUS is proposed by assessment of the TIC similarity between neighboring pixels. Four spatiotemporal similarity parameters were estimated and evaluated for their ability to classify benign and malignant lesions in the breast.

Methods

This study included 120 patients (one breast lesion per patient) who were evaluated at the medical university of Vienna. Histopathological analysis of biopsy samples from each lesion was regarded as the ground truth. Prior to biopsy, after intravenous injection of 4.8-mL UCA, a 90-s CEUS sequence was acquired by an S2000 US scanner (Siemens Healthineer, DE). An ROI was manually delineated on the enhanced area of each lesion. Based on the visual evaluation of CEUS loops and quantitative metrics, the degree of enhancement in each lesion was categorized into four grades: hyper-enhanced lesions as grade 1, partly-enhanced lesion as grade 2, lowly-enhanced lesions as grade 3, and hypo-enhanced lesions as grade 4. Only lesions of grades 1 and 2 were selected for the follow-up analysis. In the delineated ROI of each lesion, only the areas of adequate contrast enhancement were included in the spatiotemporal analysis.

Spatiotemporal features in each ROI were estimated over a moving kernel by comparing the TIC in the central pixel (central TIC) with those (periphery TICs) in its ring-shaped periphery (inner radius: 0.5, outer radius: 1 mm), as shown in **Figure 1(a)**. Four spatiotemporal parameters were estimated to quantify the similarity between the central TIC and periphery TICs: mutual information (I) [4], conditional entropy (H),

Table 1 Comparison of diagnostic performance of spatiotemporal parameters					
	Parameter	Sensitivity (95% CI)	Specificity (95% CI)	AUC	P value
Lesions of grade 1 (45/120)	Correlation coefficient (r)	89.3% (72.5 96.9)	64.7% (40.5 86.7)	0.743	0.010
	Spectral coherence (ρ)	67.9% (48.3 82.7)	82.3% (57.3 100)	0.724	0.015
	Mutual information (I)	85.7% (68.2 96.4)	94.4% (68.8 100)	0.893	<0.001
	Conditional entropy (H)	78.6% (60.8 92.9)	88.2% (41.7 100)	0.874	<0.001
Grouped lesions of grade 1 or 2 (64/120)	Correlation coefficient (r)	80.5% (66.7 90.5)	66.5% (37.8 75.0)	0.704	0.008
	Spectralcoherence (ρ)	63.4% (48.2 76.3)	75.9% (53.0 91.7)	0.670	0.034
	Mutual information (I)	90.2% (79.6 97.5)	82.6% (61.2 94.5)	0.848	<0.001
	Conditional entropy (H)	78.1% (62.6 89.7)	78.3% (56.0 90.0)	0.817	<0.001

correlation coefficient (r), and spectral coherence (ρ) [5]. The pixel-level parameter values were assembled as benign and malignant sets. The difference between the two sets was assessed by statistic D and the p-value based on Kolmogorov–Smirnov test. For each lesion, the mean values of these parameters were also calculated to compare their classification performances by receiver operating characteristic (ROC) curve analysis.

Results

Of the 120 lesions, 58 were benign and 62 were malignant based on the biopsy result. For the enhancement grading, 39.6% of benign lesions (n = 23) and 66.2 % of malignant lesions (n = 41) were graded as hyper-enhanced (grade 1) or partly-enhanced (grade 2). The applied spatiotemporal analysis can produce parametric maps that can be used for further quantitative analysis (See **Figure 1(b)**). The ROC curves of four parameters for differentiating benign and malignant lesions are presented in **Figure 3**. The results on the diagnostic performance and lesion-level parameter differences are summarized in **Table 1**. The diagnostic accuracies of I and H were higher than those of r and ρ. For all perfused lesions, the diagnostic performance of I was superior to the other three parameters (AUC = 0.89 in patients of grade 1, AUC = 0.85 in patients of grade 1 or 2).

Conclusions

In this study, four spatiotemporal parameters were extracted from the analysis of TICs measured by CEUS in biopsy-proven breast lesions after the intravascular injection of an UCA bolus. The parameter statistics shows a significant difference between benign and malignant breast lesions. Compared to benign lesions, pixel-based TICs evidence less similarity in malignant lesions. This result can possibly be explained by the higher microvascular heterogeneity in malignant lesions due to angiogenesis [6]. Mutual information, which measures the shared information between TICs, presents the best differentiation and classification performance. To conclude, our preliminary results support the potential of applying spatiotemporal analysis of CEUS recordings for accurate diagnosis of breast cancer.
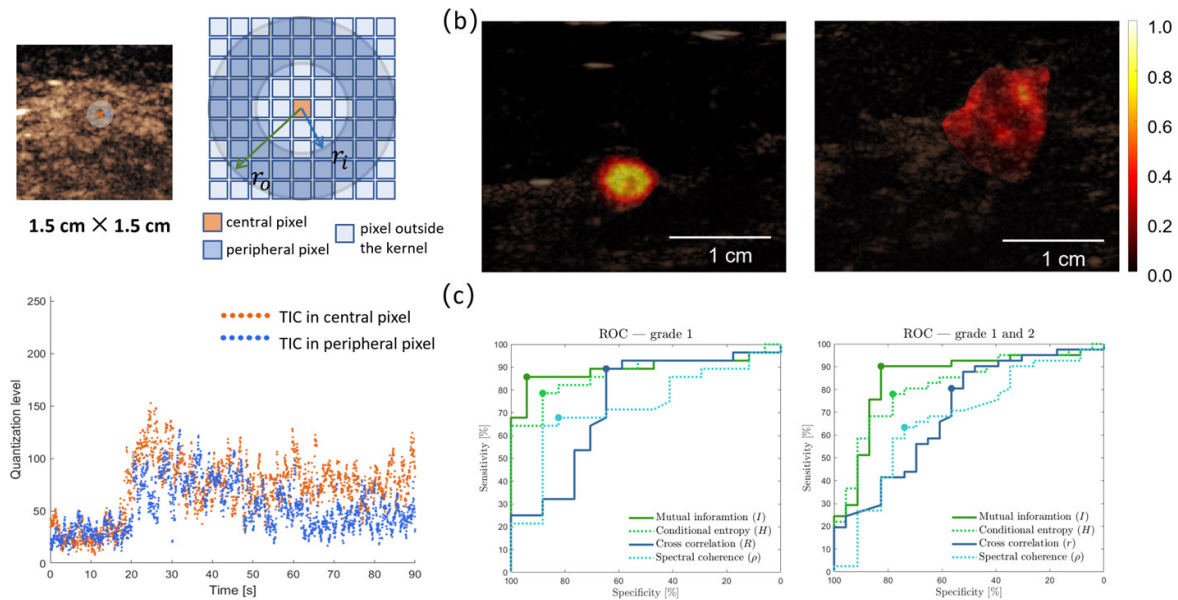
Figure 1. (a) illusrates the design of the kernel used for assessing the TIC similarity. On the top-left panel, a ring-shape kernel is placed around the central pixel with the arrangement as shown on the top-right panel. The bottom panel presents the TICs in the central pixel and a peripheral pixel. (b) present example images of overlayed map of mutual information (I) in one benign lesion (left) and one malignant Ulesion (right). (c) presents the receiver operating charactersitic (ROC) curves of the four parameters in lesions of grade 1 (A) and lesions of grade 1 or 2 (B). The optimal operating points that are closest to the left-upper corner are marked by large dots.

References
[1] F. Bray, J. Ferlay, I. Soerjomataram, R. L. Siegel, L. A. Torre, A. Jemal, Global cancer statistics 2018: GLOBOCAN estimates of incidence and mortality worldwide for 36 cancers in 185 countries, CA: a cancer journal for clinicians, vol. 68, no. 6, pp. 394-424, 2018.
[2] R. L. Siegel, K. D. Miller, A. Jemal, Cancer Statistics, 2017, 2020.
[3] Y. X. Zhao, S. Liu, Y. B. Hu, et al. Diagnostic and prognostic values of contrast-enhanced ultrasound in breast cancer: a retrospective study, OncoTargets and therapy, vol. 10, pp. 1123, 2017.
[4] S. G. Schalk, L. Demi, N. Bouhouch, et al. Contrast-enhanced ultrasound angiogenesis imaging by mutual information analysis for prostate cancer localization, IEEE Transactions on Biomedical Engineering, vol. 64, no. 3, pp. 661-670, 2016.
[5] M. Mischi, M. P. Kuenen, H. Wijkstra, Angiogenesis imaging by spatiotemporal analysis of ultrasound contrast agent dispersion kinetics, IEEE transactions on ultrasonics, ferroelectrics, and frequency control, vol. 59, no. 4, pp. 621-629, 2012.
[6] S. C. Lee, H. Tchelepi, N. Khadem, et al. Imaging of Benign and Malignant Breast Lesions Using Contrast-Enhanced Ultrasound: A Pictorial Essay, Ultrasound Quarterly, vol. 38, no. 1, pp. 2-12, 2022

Using a deep-learning model and lymphosonography to differentiate benign and malignant sentinel lymph nodes in patients with breast cancer

Priscilla Machado[1], Aylin Tahmasebi[1], Samuel Fallon[2], Ji-Bin Liu[1], Basak E. Dogan[3], Laurence Needleman[1], Melissa Lazar[4], Alliric I. Willis[4], Kristin Brill[4], Susanna Nazarian[4], Adam Berger[4], Flemming Forsberg[1]

[1]Department of Radiology, Thomas Jefferson University, Philadelphia, PA, 19107, USA
[2]Sidney Kimmel Medical College, Thomas Jefferson University, Philadelphia, PA, USA
[3]Department of Radiology, University of Texas, Southwestern Medical Center, Dallas, TX, USA
[4]Department of Surgery, Thomas Jefferson University, Philadelphia, PA, USA

Introduction

Mapping the lymphatic chain is clinically important to predict long-term outcomes for patients with breast cancer and currently is obtained after the injection of blue dye and/or a radioactive tracer followed by surgical excision [1-3]. The current approaches for detection of sentinel lymph nodes (SLNs) have shown wide variability in accuracy ranging from 76% to 97% [3, 4].

The use of contrast-enhanced ultrasound (CEUS) to detect lymphatic channels (LCs) and SLNs after subcutaneous injections of a microbubble-based ultrasound contrast agent (termed "lymphosonography") has been proposed as an alternative [5-7]. Moreover, our group studied the safety of lymphosonography in healthy volunteers and showed that the only adverse events observed were minor, local and completely resolved without any intervention [8].

The development of artificial intelligence techniques to serve as a second reader and help with clinical decision making for detecting SLN axillary breast cancer metastasis has been studied with promising results [9, 10]. One of these techniques is Google AutoML Vision (Google, Mountain View, CA, USA), which is a supervised learning platform where an algorithm is trained to recognize patterns from pre-labeled data. The advantages of this deep learning (DL) model include cloud computing (reduces required computational hardware) and transfer learning (reduces data requirement for training). Hence, the objective of this study was to use a DL model to differentiate benign and malignant SLNs using grayscale and CEUS images that were acquired in patients with breast cancer prior to their standard of care surgical excision of SLNs with pathology providing the final diagnosis. Results from the DL model were compared to radiologists' assessments of the grayscale and CEUS images.

Materials and Methods

In this prospective**,** clinical study, women scheduled for breast cancer surgery with SLN excision were enrolled between March of 2017 and January of 2022 and provided written informed consent to participate. The study was approved by the University's Institutional Review Board as well as the United States Food and Drug administration (IND no. 124,465). The full protocol and statistical analysis plan are available at *https://clinicaltrials.gov/ct2/show/NCT02652923* (trial registration number: NCT02652923).

Subjects had their lymphosonography examination on the day of surgery prior to the radioactive tracer and blue dye injections, the wire localization (when applicable) and the surgery itself. The ultrasound examination consisted of grayscale imaging to locate and measure the tumor. Then the contrast agent Sonazoid (GE Healthcare, Oslo, Norway), a reticuloendothelial system (RES) specific agent [7, 8, 11], was subcutaneously injected around the tumor area at the 12,-3,-6,-and 9 o'clock positions (0.25 mL per position, total of 1 mL). Dual imaging grayscale and CEUS was performed (i.e., lymphosonography) to identify the number, and location of the SLNs (Figure 1) using Cadence Pulse Sequencing (CPS) on an S3000 HELX scanner (Siemens Healthineers, Issaquah, WA, USA) with a high frequency, broad bandwidth (4 – 9 MHz) linear array probe. Imaging parameters e.g., focal zone, scanning depth and time-gain compensation (TGC) were adjusted on an individual basis to optimize visualization of the target region. No compounding or other image processing techniques were applied. After their surgical excision the *ex vivo* SLN specimens

were classified as positive or negative for presence of blue dye, radioactive tracer and Sonazoid [12] and sent to pathology to determine the presence or absence of metastatic involvement (the reference standard).

We used a deep learning (DL) model to differentiate benign and malignant SLNs using separated dual imaging grayscale and CEUS images of SLNs with pathology providing the final diagnosis. Results were compared to 3 radiologists' assessments of the same images. Google AutoML was used for model designation and image classification. The performance metrics for this model were precision (PPV) and recall (sensitivity) that were reported for the validation of the model as area under precision/recall curve (AuPRC). The 1656 uploaded images were divided into 80% for training (validation) and 20% for testing. The majority of the SLNs were benign, which created an unbalanced data set. Therefore, data analysis was carried out for two groups each with 2 subgroups (grayscale and CEUS). Group 1 consisted of images from 217 SLNs (183 benign and 34 malignant), with 1,357 benign and 302 malignant images uploaded (B-mode as well as CEUS images). Group 2 was designed to have the same number of benign and malignant SLNs (34 each); the benign SLNs in this group were randomly selected from the totality of benign SLNs. Hence, group 2 consisted of 272 images with 136 benign and 136 malignant images (B-mode and CEUS). All statistical comparisons were performed using Prism 9.3.1 (GraphPad Software, San Diego, CA, USA) with p-values less than 0.05 indicating statistical significance.
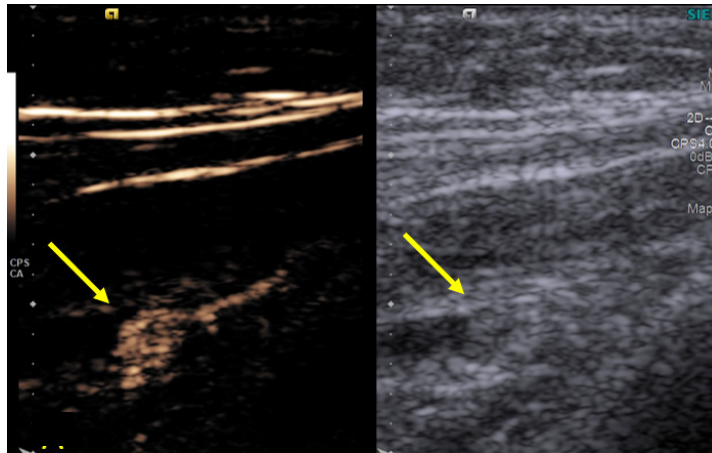
Figure 1: Example of dual-imaging CEUS and B-mode of an SLN (arrows) with metastatic deposits in a 53 year old woman diagnosed with an invasive ductal carcinoma (measuring 1.1 cm).

Results

Eighty-six (86) women enrolled in the study and 79 had their CEUS examination and underwent the surgical procedure completing the study. The mean age of the 79 subjects was 61 years (range: 27-84 years), and the mean tumor size at the time of diagnosis was 1.8 cm (range: 0.3-9.7 cm). A total of 252 SLNs were surgically excised from the 79 subjects (average: 3.2 SLNs/subject) and sent to pathology to determine the final diagnosis. Thirty-four (34) SLNs excised from 18 subjects (average 1.9 SLNs/subject) were determined to have metastatic disease by pathology (13.5%).

The CEUS examination done prior to the surgical procedure using lymphosonography identified 217 SLNs (average: 2.7 SLNs/subject). All SLNs identified had their location and measurements recorded, and dual B-mode and CEUS images were acquired for all SLNs, which does mean that the grayscale images acquired were not optimal for a detailed anatomical characterization of the SLNs. Nonetheless, these were the images available and used for the DL model and the radiologists' reads. No adverse events occurred in any subject.

The DL model validation results showed an AuPRC of 0.84 for grayscale and an AuPRC of 0.91 for CEUS in group 1, while group 2 achieved AuPRCs of 0.91 and 0.87 for grayscale and CEUS, respectively. The DL model testing results for group 1 and group 2 as well as the readers' data were analyzed to determine sensitivity/specificity/PPV/NPV/accuracy and are summarized in Table 1. The readers' results were compared to the DL model results and showed statistically significant differences amongst all groups and subgroups (p ≤ 0047)

Table 1: *Comparison of the DL model outcomes and radiologists' assessments.*

			Sensitivity (%)	Specificity (%)	PPV (%)	NPV (%)	Accuracy (%)
Group 1	Grayscale	DL model	4	96	17	85	82
		Radiologist	44	71	23	88	68
	CEUS	DL model	0	95	0	84	80
		Radiologist	39	70	21	87	65
Group 2	Grayscale	DL model	100	40	65	100	71
		Radiologist	14	57	30	29	36
	CEUS	DL model	71	77	77	71	74
		Radiologist	14	71	47	45	43

Conclusions

The DL model showed improved diagnostic performance with a more balanced dataset for both grayscale and CEUS. Radiologist's performance remained the same for both datasets using both B-mode and CEUS.

References
[1] Emerson DK, Limmer KK, Hall DJ, Han S-H, Eckelman WC, Kane CJ, et al. A receptor-targeted fluorescent radiopharmaceutical for multireporter sentinel lymph node imaging. *Radiology* 2012; 265(1):186-193.
[2] Tokin CA, Cope FO, Metz WL, Blue MS, Potter BM, Abbruzzese BC, et al. The efficacy of Tilmanocept in sentinel lymph mode mapping and identification in breast cancer patients: a comparative review and meta-analysis of the 99mTc-labeled nanocolloid human serum albumin standard of care. *Clin Exp Metastasis* 2012; 29(7):681-686.
[3] Veronesi U, Paganelli G, Viale G, Luini A, Zurrida S, Galimberti V, et al. A randomized comparison of sentinel-node biopsy with routine axillary dissection in breast cancer. *N Engl J Med* 2003;349(6):546-553.
[4] Camp ER, Cendan JC, Feezor R, Lind DS. The hottest sentinel lymph node is not always the positive node. *Am Surg* 2004; 70(6):475-478.
[5] Omoto K, Matsunaga H, Take N, Hozumi Y, Takehara M, Omoto Y, et al. Sentinel node detection method using contrast-enhanced ultrasonography with sonazoid in breast cancer: preliminary clinical study. *Ultrasound Med Biol* 2009; 35(8):1249-1256.
[6] Sever AR, Mills P, Jones SE, Cox K, Weeks J, Fish D, et al. Preoperative sentinel node identification with ultrasound using microbubbles in patients with breast cancer. *AJR Am J Roentgenol* 2011; 196(2):251-256.
[7] Machado P, Liu JB, Needleman L, Lazar M, Willis AI, Brill K, Nazarian S, Berger AC, Forsberg F. Sentinel lymph node identification in breast cancer patients using lymphosonography. *Ultrasound Med Biol* 2022. In press.
[8] Machado P, Stanczak M, Liu JB, Moore JN, Eisenbrey JR, Needleman L, et al. Subdermal ultrasound contrast agent injection for sentinel lymph node identification: an analysis of safety and contrast agent dose in healthy volunteers. *J Ultrasound Med* 2018; 37(7):1611-1620.
[9] Tahmasebi A, Qu E, Sevrukov A, Liu J-B, Wang S, Lyshchik A, et al. Assessment of Axillary lymph nodes for metastasis on ultrasound using artificial intelligence. *Ultrason Imag.* 2021; 43(6):329-336.
[10] Lee Y-W, Huang C-S, Shih C-C, Chang R-F. Axillary lymph node metastasis status prediction of early-stage breast cancer using convolutional neural networks. *Comput Biol Med* 2021; 130:104-106.
[11] Sontum PC. Physicochemical characteristics of Sonazoid, a new contrast agent for ultrasound imaging. *Ultrasound Med. Biol.*, 2008; 34:824-833.
[12] Forsberg F, Piccoli CW, Liu JB, Rawool NM, Merton DA, Mitchell D, Goldberg BB. Hepatic tumor detection: MR imaging and conventional US versus pulse-inversion harmonic US of NC100100 during its reticuloendothelial system-specific phase. *Radiology* 2002; 222:824–829.

Ionoacoustics and Contrast agents: status and perspectives

Julie Lascaud[1] and Katia Parodi[1]

[1]*Department of Medical Physics, Faculty of Physics, Ludwig-Maximilians-Universität München (LMU Munich), Garching b. München, Germany*
Corresponding author: Katia.Parodi@lmu.de

Introduction

Ion therapy is a still emerging external beam radiotherapy modality which exploits the advantageous physical and biological properties of swift ion interactions in matter in order to offer a better targeting of a biologically effective radiation dose to the tumour, with improved sparing of surrounding normal tissue compared to the widely adopted X-rays. However, full clinical exploitation of these advantages is still hindered by remaining uncertainties in the knowledge of the exact location in tissue of the so called Bragg peak, indicating the characteristic maximum of ion dose deposition in depth. Hence, techniques enabling in vivo visualization or at least localization of the Bragg peak position in real time, ideally co-registered to the underlying anatomy, are subject of ongoing intense research efforts. To this end, a topic which is regaining considerable attention is the sensing of thermoacoustic emissions induced by the dose deposition of pulsed ion beams (ionoacoustics), which are becoming increasingly available due to current trends of technological developments for therapeutic ion beam production. However, a major limitation is the typical low ionoacoustics signal amplitude (with pressures in the order of mPa) and frequency (in the order of 10-100 kHz). In this context, agents able to improve signal detectability (in terms of amplitude and/or frequency enhancement) and correlation with underlying anatomical ultrasound images would be highly beneficial.

Methods

We started experimental and computational investigations addressing the co-registration needs between ionoacoustics and ultrasound imaging, along with the possible role of candidate contrast agents for supporting ionoacoustic range verification and dose reconstruction in proton and carbon ion therapy. While the experiments were so far only performed at a research accelerator providing pre-clinical proton beams of variable MHz pulsing structure, the simulations took into account realistic beam delivery from modern clinical synchrocyclotron (protons) and synchrotron (protons and carbon ions) accelerators.

Results and discussion

Experiments with pre-clinical proton beams stopped in a target filled with different contrast agent mixtures indicated an intriguing increase of up to 200% of the ionoacoustic signal emission in the MHz frequency range by combining microbubbles and India ink. Additional simulation studies for materials typically employed as radiation sensitizers or finding applications in photodynamic therapy show promise to enable ionoacoustic applicability also at MHz-modulated beams from synchrotron accelerators, besides offering possibilities for an improved co-registration of the ionoacoustic signal to the underlying anatomy. However, a deeper understanding of the mechanisms responsible for the initial observations, along with experimental confirmation and characterization of an even broader range of candidate materials in dedicated phantoms of increasing complexity is warranted.

Conclusions

Although still in its infancy, ionoacoustics could offer a cost-effective method for in vivo monitoring of ion beam treatment for favourable tumour indications and depending on the underlying accelerator technology. Suitable contrast agents could support this application by overcoming current challenges due to the low signal amplitude/frequency, along with improved co-registration to underlying anatomy and possible pre-treatment ultrasound images for tumour localization. However, further research is required to enable a possible future translation of the first initial promising results to pre-clinical or clinical applications.

Ultrasound-based proton range verification with superheated nanodroplets

Gonzalo Collado-Lara[1], Sophie V. Heymans[1,2,3], Bram Carlier[4,5], Yosra Toumia[6], Marta Rovituso[7], Martin Verweij[8], Gaio Paradossi[6], Edmond Sterpin[4], Uwe Himmelreich[5], Verya Daeichin[8], Koen Van Den Abeele[2], Hendrik J. Vos[1], Jan D'Hooge[3], Nico de Jong[1,8]

[1]*Department of Biomedical Engineering, Erasmus Medical Center, Rotterdam, the Netherlands*
[2]*Department of Physics, KU Leuven Campus Kulak, Kortrijk, Belgium*
[3]*Department of Cardiovascular Sciences, KU Leuven, Leuven, Belgium*
[4] *Department of Oncology, KU Leuven, Leuven, Belgium*
[5]*Department of Imaging & Pathology, KU Leuven, Leuven, Belgium*
[6]*Department of Chemical Sciences and Technology, University of Rome Tor Vergata, Italy*
[7]*HollandPTC, Delft, the Netherlands*
[8]*Department of Medical Imaging, TU Delft, Delft, the Netherlands*
Corresponding author: g.colladolara@erasmusmc.nl

Introduction

Proton therapy is an emerging alternative to conventional radiotherapy [1]. Protons, in contrast to photons, stop completely within the patient. Furthermore, their stopping depth (i.e. proton range) can be tuned. These two principles allow to target most of the radiation dose to the tumor, sparing surrounding healthy organs, and consequently decreasing the probability of undesired secondary effects. However, in practice, the proton range is influenced by multiple uncertainty sources. To account for these uncertainties, the irradiated volume is enlarged with substantial safety margins, which inconveniently increase the dose to healthy tissues [2]. An *in vivo* measurement of the proton range is desirable, in order to mitigate the aforementioned uncertainties and minimize the safety margins, thus optimizing the treatment [3].

Here, we discuss the potential of superheated nanodroplets in combination with ultrasound imaging for proton range verification. Superheated liquids were first used to detect high energy particles by Glaser in the 1950s with the bubble chamber (Fig. 1A), which granted him a Nobel prize [4]. In these bulky devices, charged particles transferred their energy into a reservoir of superheated liquid, producing a trail of bubbles along the particle track, owing to the phase change of the liquid. The concept was later downscaled by Apfel with the superheated detector (Fig. 1B) [5]. These portable devices contained emulsions of submillimetric superheated droplets, which vaporized upon interaction with high-energy particles. Following the downscaling trend, the *Amphora* project (a consortium of European universities, institutes and a start-up company, funded by the European Union Horizon 2020 scheme to develop a radiotherapy dosimetry platform based on contrast enhanced ultrasound) investigated the use of submicron phase-change contrast agents, or superheated nanodroplets, to measure the distribution of protons during proton beam irradiation. The vaporization response when exposed to proton beams was confirmed in gel phantoms [6], showing a temperature-dependent relationship between the vaporization region and the proton range [7]. Importantly, the phase change of these droplets is easily detectable with an ultrasound imaging device (Fig. 1C). Thus, these injectable droplets have the potential to accumulate in the tumor region, and their phase change could be detected non-invasively, providing critical information about the *in vivo* proton range.

Methods

In a series of studies as subpart of the *Amphora* project, we addressed the viability of the aforementioned concept in well-controlled *in vitro* experiments irradiated in the Holland Proton Therapy Center facilities (HollandPTC, Delft, the Netherlands), using perfluorobutane nanodroplets enclosed with a polyvinyl alcohol shell (PVA-PFB NDs) [8] dispersed in a gel phantom. First, we proposed two online acoustic methods, one active [9] and one passive [10] that exploited the principles of Ultrasound Localization Microscopy [11] to detect and localize the droplet vaporizations. Then, we studied the sensitivity of the

droplets to protons at different temperatures, i.e. degrees of superheat, and compared it to the thermal spike theory developed for the bubble chamber and validated for superheated detectors [12]. Furthermore, we assessed the relation between the spatial distribution of droplet vaporizations and the spatial distribution of protons. We also proposed a method to enhance the sensitivity of these droplets to protons by modulating their degree of superheat using an acoustic field, hence reducing the energy required to vaporize the droplet during the rarefactional phase of an ultrasound wave [13]. Besides, we assessed the number of vaporizations for a given droplet concentration, droplet size, and number of protons. The number of vaporizations was combined with Monte Carlo simulations to predict the range verification precision as a function of the droplet concentration. Finally, in order to prove the feasibility of this concept in physiological conditions, a preliminary *in vivo* experiment was performed as part of the *Amphora* project in a Sprague-Dawley rat, approved by the KU Leuven animal ethics committee . The rat liver was aimed at with two different proton beam energies at the Centre de Resources du Cyclotron (UCLouvain, Louvain la Neuve, Belgium), in order to assess the feasibility of detecting beam range shifts, and simultaneously imaged with ultrasound.

Results

Both acoustic localization methods, i.e. active and passive, provided an excellent precision measuring the vaporization distribution. The vaporization distribution changed after increasing the phantom temperature, owing to the detection of particles with a lower energy transfer [7]. At room and physiological temperatures, without acoustic aid, PVA-PFB NDs were not directly sensitive to protons, but to secondary products of protons undergoing nuclear reactions. Only at higher temperatures did they become directly sensitive to protons. In both cases, the vaporization distributions were related to the proton stopping distribution, allowing us to extract the proton range. The proton range determined from the vaporization profiles was in sub-millimetric agreement when compared with an independent measurement using an ionization chamber. The measured temperature thresholds were in relative good agreement with the thermal spike theory. Furthermore, we observed that acoustic waves could enable direct sensitivity to protons at physiological temperatures using a low $MI = 0.3$.

Experimentally, the number of vaporizations was proportional to the fraction of PFB volume in the irradiation target. When combined with Monte Carlo simulations, we predicted a necessary PFB concentration in homogeneous conditions between 0.03-0.3 (μL liquid PFB)/(L blood), assuming a direct sensitivity of the droplets to protons. These droplet concentration values may serve as a guideline when assessing the biocompatibility of superheated nanodroplets in future experiments. Finally, the preliminary *in vivo* measurements showed that the phase-change of PVA-PFB NDs was also triggered under physiological conditions. Furthermore, vaporizations at increased body depths were observed when the rat was irradiated with the highest beam energy, agreeing with an increased beam range.

Conclusions

The long standing concept of using superheated liquids to detect high-energy particles was successfully downscaled to submicron phase-change agents, originally used in contrast-enhanced ultrasound. The *in vitro* measurements suggest that the distribution of vaporizations relate to the proton range with an excellent precision. Furthermore, the preliminary *in vivo* proof-of-concept suggests feasibility of clinical translation.

These results open the door to the development of a novel technique for *in vivo* proton range verification, relying on the clinical approval of phase-change agents.
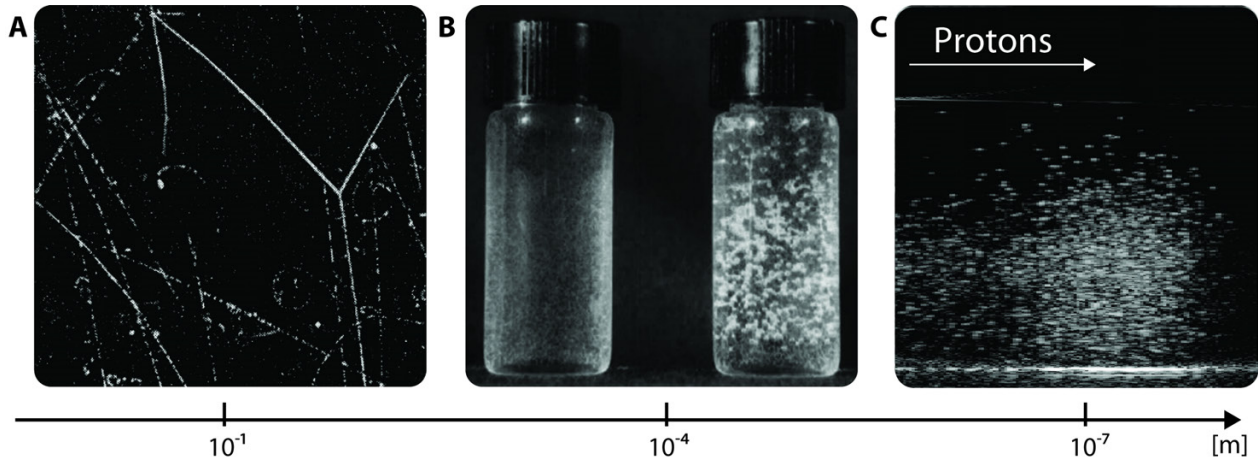
Figure 1. A Bubble chamber: Bubble tracks formed in the bulk of a superheated liquid owing to single charged particles (image from [14]). **B** Superheated drop detector: Emulsion of large superheated droplets before (left) and after (right) irradiation. Bubbles formed upon irradiation (image from [15]). **C** Superheated nanodroplets: A suspension of droplets in a gel was irradiated with protons and imaged using ultrasound. Vaporizations were observed, which related to the stopping distribution of protons.

References

[1]. Paganetti H, ed. *Proton therapy physics*. CRC press, 2018.

[2]. Paganetti H, "Range uncertainties in proton therapy and the role of Monte Carlo simulations." *Physics in Medicine & Biology* 57.11 (2012): R99.

[3]. Parodi K, Polf JC "In vivo range verification in particle therapy." *Medical physics* 45.11 (2018): e1036-e1050.

[4]. Glaser DA, "Bubble chamber tracks of penetrating cosmic-ray particles." *Physical Review* 91.3 (1953): 762.

[5]. Apfel RE, "The superheated drop detector." *Nuclear instruments and Methods* 162.1-3 (1979): 603-608.

[6]. Carlier B, et al. "Proton range verification with ultrasound imaging using injectable radiation sensitive nanodroplets: a feasibility study." Physics in Medicine & Biology 65.6 (2020): 065013.

[7]. Heymans SV, et al. "Modulating ultrasound contrast generation from injectable nanodroplets for proton range verification by varying the degree of superheat." *Medical Physics* 48.4 (2021): 1983-1995.

[8]. Toumia Y, et al. "Ultrasound-assisted investigation of photon triggered vaporization of poly (vinylalcohol) phase-change nanodroplets: A preliminary concept study with dosimetry perspective." *Physica Medica* 89 (2021): 232-242.

[9]. Collado-Lara G, et al. "Spatiotemporal distribution of nanodroplet vaporization in a proton beam using real-time ultrasound imaging for range verification." *Ultrasound in Medicine & Biology* 48.1 (2022): 149-156.

[10]. Heymans SV, et al. "Passive Ultrasound Localization Microscopy of nanodroplet vaporizations during proton irradiation." *IEEE open journal of ultrasonics, ferroelectrics, and frequency control* 2 (2022): 203-219.

[11]. Desailly Y, et al. "Sono-activated ultrasound localization microscopy." *Applied Physics Letters* 103.17 (2013): 174107.

[12]. Seitz F, "On the theory of the bubble chamber." *The physics of fluids* 1.1 (1958): 2-13.

[13]. Heymans SV, et al. "Acoustic modulation enables proton detection with nanodroplets at body temperature." *IEEE Transactions on Ultrasonics, Ferroelectrics, and Frequency Control* 69.6 (2022): 2028-2038.

[14]. Agnew L, et al. "p̄ − p Elastic and Charge Exchange Scattering at About 120 Mev." *Physical Review* 110.4 (1958): 994.

[15]. D'Errico F, "Radiation dosimetry and spectrometry with superheated emulsions." *Nuclear Instruments and Methods in Physics Research Section B: Beam Interactions with Materials and Atoms* 184.1-2 (2001): 229-254.

Ischemia/Reperfusion (I/R) injury increased accumulation of perfluoropropane droplets in the microvasculature

Cheng Chen[1], _Shouqiang Li_[2], _Ping Zeng_[2], _Terry Matsunaga_[3], _John J. Pacella_[1], _E. Carr Everbach_[4], _John Lof_[2], _Feng Xie_[2], _Thomas Porter_[2], _Flordeliza S. Villanueva_[1], _Xucai Chen_[1*]

[1]_Center for Ultrasound Molecular Imaging and Therapeutics, University of Pittsburgh, Pittsburgh, PA, USA_
[2]_Division of Cardiovascular Medicine, University of Nebraska Medical Center, Omaha, NE, USA_
[3]_Department of Biomedical Engineering and Department of Medical Imaging, University of Arizona, Tucson, AZ, USA_
[4]_Swarthmore College, Swarthmore, PA, USA_
Corresponding author: chenxx2@upmc.edu

Introduction

Perfluoropropane droplets (**PD**) are nanometer-sized particles and their unique properties could significantly enhance their cardiovascular diagnostic and therapeutic potential [1]. PDs can be formulated from commercially available contrast agents or home-made microbubbles. The preferential retention of PDs in diseased microvascular beds can be detected by ultrasound imaging techniques post acoustic activation, and offer an opportunity for the detection of such processes like scar formation. We used a rat cremaster muscle model to simulate a microvascular environment that can be imaged. We hypothesized that in the presence of ischemia/reperfusion (**I/R**), retention of intraveneuously injected PDs could be enhanced.

Methods

Using an established intravital microscopy model of rat cremaster microcirculation [2], we determined the retention and subsequent acoustic activation behavior of PDs. Perfluoropropane microbubbles (**PMB**) were formulated by dissolution of 1,2-dipalmitoyl-sn-glycero-3-phosphatidylcholine (DPPC), 1,2-dipalmitoyl-sn-glycero-3-hosphatidylethanolaminepolyethyleneglycol-5000 (DPPE-PEG-5000), and 1,2-dipaalmitoyl-sn-glycerol-3-phosphatidic acid (DPPA) in a molar ratio of 82:10:8 in an excipient liquid comprised of propylene glycol, glycerol, and normal saline (1:1:8, v:v:v). After adding 1.5 mL of the resulting solution to a 2 mL vial, the solution was degassed on a vacuum manifold followed by purging with perfluoropropane (Fluoromed, Round Rock, Tx). PMBs were formed by shaking the vial on a dental amalgamator for 45 sec. The PMBs were diluted in normal saline (1:1$ v:v) and loaded into a 10 mL syringe and cooling in an isopropyl alcohol bath (-10°C) for three minutes. The cooled PMB suspension was then pressurized by clamping the syringe with a rubber stopper in a clamp which applied a controlled pressure for 3 min. The condensed PMBs went through phase change and became PDs. PMBs were fluorescently labeled with a commercially available lipophilic fluorophore, 1,1'dioctyldecyl 3,3,3',3'tetramethylindocarbocyanine (**DiI**).

Intravital fluorescence microscopy (Olympus BX51, Olympus America, Inc., Center Valley, PA) was performed on the exposed rat cremaster muscle. All protocols were approved by the Institutional Animal Care and Use Committee at the University of Pittsburgh. The rat cremaster muscle was exteriorized through a scrotal incision and secured to a translucent pedestal. The blood flow to the cremaster tissue was interrupted for 10 min with a ligature around the cremasteric artery proximal to the muscle body to mimic ischemia, followed by a 20 min reperfusion to cause reperfusion injury. A 200 μL intravenous injection of DiI-PD was administered following I/R. At 2 min post injection, the cremaster muscle was imaged with a fundamental non-linear imaging system (CPS mode;Simens Acuson 512) at 7 MHz (with the 15L7 probe) or 1.5 MHz. (with the 3V2c probe) for 10 frames (MI 1.1, time triggered with 500 ms interframe interval). For each animal, 10 random fluorescence images were captured. Images were analyzed using MATLAB 2020a (MathWorks, Natick, MA) and ImageJ. Normal cremaster muscle was used as a control. The fluorescence images were transformed into a matrix to represent the relative brightness, and a threshold was

determined based on all the images taken for one animal. All the pixels above threshold were considered 'intensity area' and quantified for each image.

Results

All the rats were randomized in to four groups: low frequency control ($n = 8$), high frequency control ($n = 7$), low frequence I/R ($n = 8$), and high frequency I/R ($n = 7$). Retention and acoustic activation of intravenously injected PDs were observed in the microvasculature in the creamaster tissue (Figure 1). Increased retained PD were observed in the I/R group compared with control group with both low frequency and high frequency activation ($p < 0.05$). There was a trend, though not statistically different, toward more intensity area with high frequency activation compared with low frequency activation in the I/R groups.

Conclusions

Some perfluoropropane droplets were retained within the microvasculature after intravenous administration and were acoustically activated with imaging pulses. The increased droplet retention in ischemia/reperfusion model may allow ultrasound imaging techniques to be developed for myocardial scar detection.
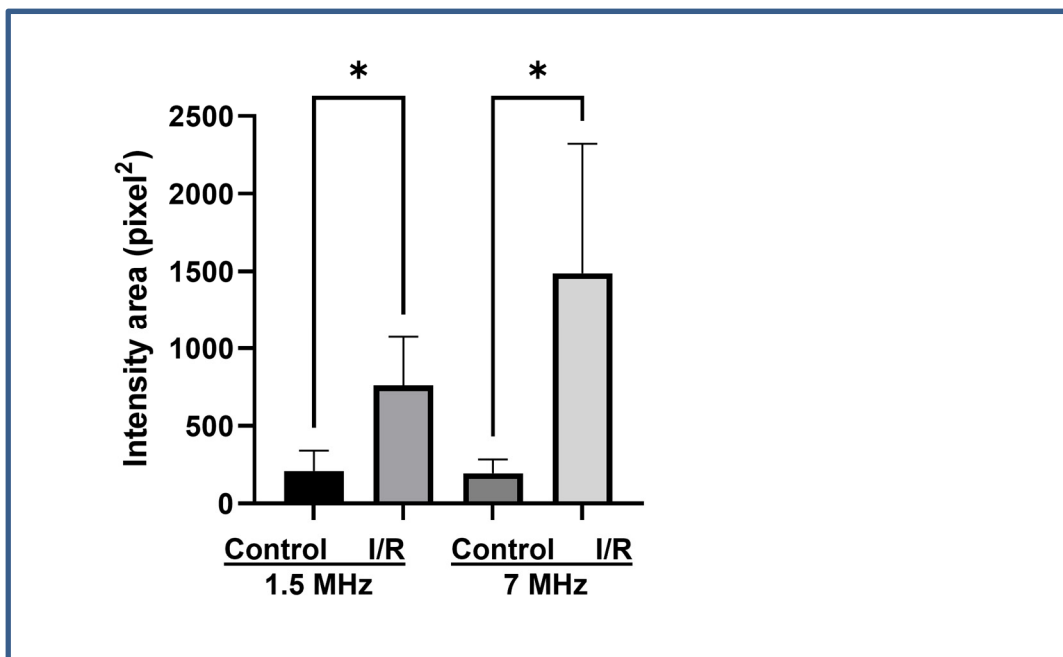
Figure 1. Retention of perfluoropropane droplets in the microvesculature in rat creamaster muscule. More droplets were retained and activated with by clinical ultrasound in the ischemia/reperfusion group compared with control group in both ultrasound settings (multiple comparison was performed using ANOVA followed by Kruskal-Wallis test, *$p < 0.05$).

References

[1]. Zeng P, Chen C, Lof J, Stolze E, Li S, Chen X *et al*. Acoustic Detection of Retained Perfluoropropane Droplets Within the Developing Myocardial Infarct Zone. *Ultrasound in Medicine & Biology* 2022; 48: 2322-2334.

[2]. Leng X, Wang J, Carson A, Chen X, Fu H, Ottoboni S *et al*. Ultrasound detection of myocardial ischemic memory using an e-selectin targeting Peptide amenable to human application. *Mol Imaging* 2014; 16: 1-9.

Xenon microbubbles for cerebroprotection in a porcine model of intracerebral hemorrhage

Seth Thomas[1], Maxime Lafond[2], Virginie Désestret[3], Samantha Ford[1], Robert T. Kleven[4], Joanne Tetens-Woodring[5], Christy K. Holland[1,4]

[1]*Department of Internal Medicine, Division of Cardiovascular Health, University of Cincinnati, Cincinnati, Ohio, USA*
[2]*LabTAU, INSERM, Centre Léon Bérard, Université Lyon 1, Univ Lyon, F-69003, LYON, France*
[3]*Institut MeLiS, Equipe Synaptopathies et Autoanticorps (SynatAc), INSERM U1314 / CNRS 5284, Lyon, France*
[4]*Department of Biomedical Engineering, University of Cincinnati, Cincinnati, Ohio, USA*
[5]*Laboratory Animal Medical Services, University of Cincinnati, Cincinnati, OH, USA*

Corresponding author: Christy.Holland@uc.edu

Introduction

Intracerebral hemorrhage (ICH) has a 46% one year survival rate, with fewer than a third of patients recovering to achieve independent function [1]. Treatment for ICH is limited to supportive care and surgical intervention to reduce hematoma size. Therapeutic intervention to protect the penumbra surrounding an ICH could improve outcomes in hemorrhagic stroke. Targeted delivery of Xenon, (Xe) a noble gas with antiproteolytic properties, using ultrasound sensitive microbubbles is under development for treatment of ICH [2-10]. Our objective is to determine if ultrasound-triggered release of Xe from microbubbles (MB) in the cerebral circulation significantly reduces cell death in brain tissue surrounding ICH.

Methods

Air and octafluoropropane-loaded and Xe and OFP-loaded microbubbles (Air-OFP-MB or Xe-OFP-MB, respectively) were created using either air or Xenon mixed in a 9:1 ratio with OFP [7]. A juvenile porcine model of ICH was adapted based on the model developed by Wagner *et al.* [11] (Fig. 1). ICH was created in 10 juvenile pigs (20.5 ± 0.5 kg) according to a protocol approved by the University of Cincinnati Institutional Animal Care and Use Committee, in compliance with the National Research Council's Guide for the Care and Use of Laboratory Animals [12] and the ARRIVE guidelines [13]. After establishing arterial access and exposing the cranium, a 3 mL aliquot of autologous arterial blood was infused over 10 min.
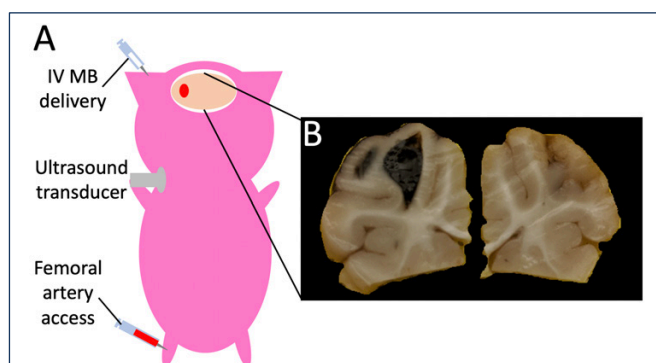
Figure 1. A: Schematic of porcine ICH with autologous arterial blood and intravenous (ear) infusion of either Air-OFP-MB (sham treatment) or Xe-OFP-MB (Xe treatment). B: Perfusion fixed brain tissue with intracerebral hematoma.
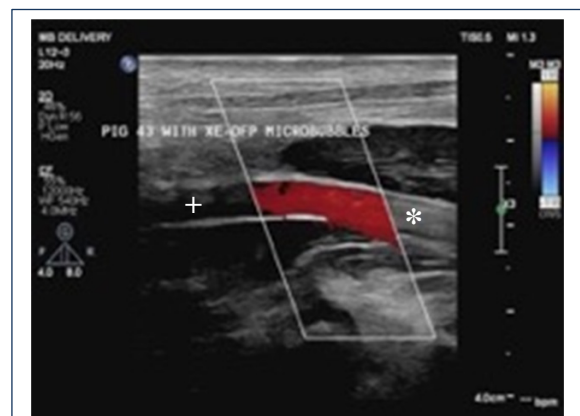
Figure 2. B-Mode ultrasound confirmed destruction of MB by color Doppler. Blood flow in the common carotid artery (CCA) is from right to left in the image. *: MB seen in lumen of proximal CCA. +: MB destruction evident in distal CCA.

into right frontal white matter of each pig through a cranial burr hole. The hematoma allowed to retract for two hours. Thereafter, a total volume of 0.738 mL/kg of either Air-OFP-MB (sham treatment) or Xe-OFP-MB at a Xe concentration of 146 μL Xe/mL (48 μmol Xe/kg treatment) was infused through an ear vein over 1 hr. The total dose was 2.14 mL Xe in a 14.75 mL solution of Xe-OFP-MB. Throughout the infusion the right proximal carotid artery was continuously insonated with duplex color Doppler ultrasound (Philips Epic 7G, 12-5 12-3 linear array, MI = 1.3) to induce microbubble destruction and liberation of the encapsulated gas into the bloodstream (Fig. 2). To formalin perfusion fix the brain immediately post mortem, the internal carotid arteries were dissected and cannulized bilaterally with 20 G catheters and secured with sutures. Heparinized saline (2 U/mL) was perfused through the brain with a peristaltic pump, followed by 1.8 liters of 10% formalin at a rate of 0.2 mL/min under a necropsy fume hood. The brain was removed and placed in 10% formalin for 72 to 96 hours. Following fixation, the brain was sectioned into 5 mm thick slices and stained with either hematoxylin and eosin (H&E) or immunofluorescent terminal deoxynucleotidyl transferase dUTP nick end labeling (TUNEL) stain, cross stained with the nuclear stain 4′,6-diamidino-2-phenylindole (DAPI) and imaged with an Axiovert 100 TV inverted microscope (Fig. 3). Images were reviewed by a neuropathologist (VD) blinded to the treatment arm to avoid artifacts and processed with custom MATLAB code to determine the density of TUNEL positive cells within the first 1 mm of the penumbra surrounding intracerebral clots of both the sham (n=5) and Xe treated (n = 5) groups. The average density of apoptic cells was also determined in the contralateral lobe as a negative control (Fig. 5). To determine the statistical difference between the sham and Xe treated pigs (n=5 each), a repeated measures ANOVA method was carried out in R (version 4.2.1, R Foundation for Statistical Computing, Vienna, Austria). A p-value ≤ 0.05 was considered significant.

Results

Microbubble destruction during the infusion was achieved, as observed by the lack of echogenicity in the carotid artery distal to the color Doppler window (Fig. 2). The perfusion fixation protocol adequately preserved the histological architecture surrounding the hematoma (Fig. 3). The infusion of autologous arterial blood in the frontal subcortical white matter of young swine reproduced acute ICH triggered by vascular rupture due to hypertension or bleeding of arterioveinous malformations. As observed in human acute ICH, the hematoma was surrounded by a zone of compressed ischemic tissue. Vascular leakage in the penumbra caused cerebral edema and vascular congestion and both features were observed on H&E. Immunofluorescent TUNEL and DAPI stains demonstrated specificity for apoptotic cells in the penumbra surrounding the intracerebral hemorrhage (Fig. 3). Both treatment groups exhibited a decrease in apoptotic cell density as a function of distance from the hematoma (Fig. 4). The rate of decrease in cell death density for the Xe-OFP-MB treatment group was faster than the air-OFP-MB treatment group (Fig. 4). The
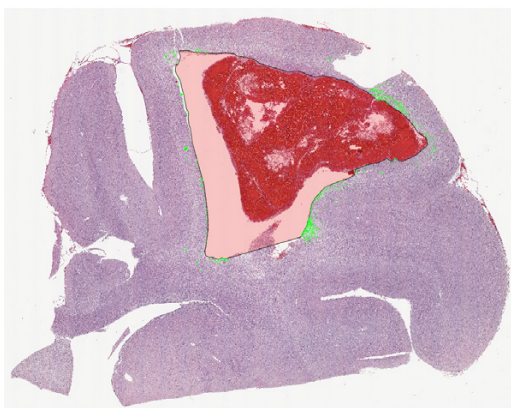
Figure 3. A: Composite H&E and TUNEL (green) stained histology of porcine brain with a hematoma surrounded by penumbra of damaged tissue.
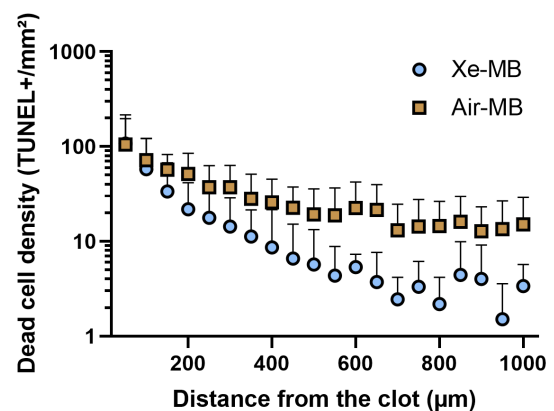
Figure 4. Apoptotic cell death density as a function of distance from the thrombus in the penumbra N=5 for sham and N=5 for Xe-OFP-MB treatments.

difference between the sham and Xe treatment groups was statistically significant ($p<0.001$). TUNEL positive cell density was an order of magnitude higher in Air-OFP-MB treated brains than Xe-OFP-MB treated brains at a distance of 1 mm from the hematoma. At this same distance, the density of cell death of Xe-treated brains was similar to control (contralateral side). The euthanasia, decapitation, and formalin fixation protocol yielded only a scant amount of apoptosis in the lobe without an intracerebral hematoma, two orders of magnitude less than than in the penumbra adjacent to the hematoma (Figs. 4 and 5). Interestingly, Xe-OFP-MB treatment also reduced the cell death density on the contralateral side (Fig. 5).

Figure 5. Apoptotic cell death density on contralateral side (without hematoma). N=5 for sham and N=5 for Xe-OFP-MB treatments.

Conclusions

The porcine ICH model exhibited histopathological features like that of human ICH in young patients. Sucessful delivery of Xe to the brain was achieved via destruction of Xe-OFP-MB under ultrasound guidance in the common carotid artery with a commercially available system. Ultrasound-triggered Xe delivery at a total dose of 48 µmol/kg over a 1-hour infusion produced over an order of magnitude decrease in apoptotic cell burden 1 mm from the hematoma. This pre-clinical ICH model demonstrates initial proof-of-concept and efficacy of Xe-OFP-MB for cerebroprotection.

Acknowledgements

References

[1] M. T. C. Poon, A. F. Fonville, and R. A. S. Salman, "Long-term prognosis after intracerebral haemorrhage: systematic review and meta-analysis," *Journal of Neurology Neurosurgery and Psychiatry,* vol. 85, no. 6, pp. 660-667, Jun, 2014.

[2] H. N. David, F. Leveille, L. Chazalviel *et al.*, "Reduction of ischemic brain damage by nitrous oxide and xenon," *Journal of Cerebral Blood Flow and Metabolism,* vol. 23, no. 10, pp. 1168-1173, Oct, 2003.

[3] J. H. Abraini, H. N. David, O. Nicole *et al.*, "Neuroprotection by nitrous oxide and xenon and its relation to minimum alveolar concentration," *Anesthesiology,* vol. 101, no. 1, pp. 260-261, Jul, 2004.

[4] H. N. David, F. Leveille, L. Chazalviel *et al.*, "Reduction of ischemic brain damage by nitrous oxide and xenon.," *Behavioural Pharmacology,* vol. 17, no. 5-6, pp. 547-547, Sep, 2006.

[5] H. N. David, B. Haelewyn, J. J. Risso *et al.*, "Xenon is an inhibitor of tissue-plasminogen activator: adverse and beneficial effects in a rat model of thromboembolic stroke," *Journal of Cerebral Blood Flow and Metabolism,* vol. 30, no. 4, pp. 718-728, Apr, 2010.

[6] G. L. Britton, H. Kim, P. H. Kee *et al.*, "In Vivo Therapeutic Gas Delivery for Neuroprotection With Echogenic Liposomes," *Circulation,* vol. 122, no. 16, pp. 1578-1587, Oct 19, 2010.

[7] H. Shekhar, A. Palaniappan, T. Peng *et al.*, "Characterization and Imaging of Lipid-Shelled Microbubbles for Ultrasound-Triggered Release of Xenon," *Neurotherapeutics,* vol. 16, no. 3, pp. 878-890, Jul, 2019.

[8] C. K. Holland, J. L. Raymond, and J. T. Sutton, *Bioactive gas-encapsulated echogenic liposomes and methods for treating cardiovascular disease*, USA 10,500,227, December 10, 2019.

[9] C. K. Holland, H. Shekhar, and A. Palaniappan, *Gas-encapsulated acoustically responsive stabilized microbubbles and methods for treating cardiovascular disease*, 10,456,483, July 23, 2019.

[10] C. K. Holland, H. Shekhar, and A. Palaniappan, *Gas-encapsulated acoustically responsive stabilized microbubbles and methods for treating cardiovascular disease*, 11,007,284, May 18, 2021.

[11] K. R. Wagner, G. H. Xi, Y. Hua *et al.*, "Lobar intracerebral hemorrhage model in pigs - Rapid edema development in perihematomal white matter," *Stroke,* vol. 27, no. 3, pp. 490-497, Mar, 1996.
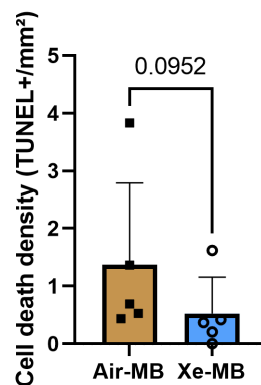
[12] N. R. Council, *Guide for the Care and Use of Laboratory Animals*, 8th ed., Washington D.C.: The National Academies Press, 2011.

[13] N. P. du Sert, V. Hurst, A. Ahluwalia *et al.*, "The ARRIVE guidelines 2.0: Updated guidelines for reporting animal research," *Plos Biology,* vol. 18, no. 7, Jul, 2020.

Ultrasound enhanced drug delivery in brain: review of clinical progress

Kullervo Hynynen[1,2]

[1]Sunnybrook Research Institute, Toronto, Ontario, Canada
[2]Medical Biophysics, University of Toronto, Toronto, Ontario, Canada
Corresponding author: khynynen@sri.utoronto.ca

Introduction

Blood-brain-barrier (BBB) prevents over 98% of potentially therapeutic molecules from entering the brain[1]. Focused ultrasound in combination of microbubbles has been explored over twenty years for enhancing the BBB permeability for therapy delivery in selected locations of the brain[2]. Since the first trasnkull demostration of the BBB permeability enhancement in a human patient in 2015[3] there have been a numnber of feasibility studies continuing to demonstrate the safety and lately effecasy of the approach. In this talk our resent clinical experinece will be reviewed.

Methods

In our clinical studies we used InSightec 4000 system that has 1024 ultrasound transducers forming a 30 cm hemisphere placed around the shaved patient's head. On the day of the procedure, a Cosman-Roberts-Wells (CRW) stereotactic frame was fixed to the patient's head under local anaesthetic. The CRW frame was coupled to the helmet transducer array. A rubber membrane was placed around the patient's head and sealed to the opening of the helmet, allowing degassed water to provide acoustic coupling. A 3-Tesla MRI system was used to obtain MRI scans of the head for targeting and BBB permeability measurments. Definity microbubbles were infused via a saline bag gravity drip at a rate of 0.8 µl/kg/min. The ultrasound exposures consisted of 10 ms bursts repeated once every second (1% duty cycle), for a total duration of 2 minutes. During the 2 min sonication up to 32 points could be secuentially sonicated on an arbitarily shaped grid. Eight cavitation receivers installed within the hemispherical helmet surface were used to detect bubble scattered signals during the sonications. Both narrow-band (115±5 kHz) and broad-band (115±40 kHz, 150±30 kHz) spectral integrations around the subharmonic frequency were calculated in real-time. The mean of the cavitation signals across all spots in a grid and all receivers was used to modulate the applied power level in a feedback control loop. A cavitation emissions-based feedback controller was employed to modulate the acoustic power automatically according to prescribed target cavitation dose levels. BBB opening was measured by Gadolinium (Gd)-enhanced T1-weighted MR imaging, and the presence of micro-hemorrhage induced by the exposures was assessed via T2*-weighted MR imaging[4, 5].

Results

Our studies evaluating the feasibility of therapy delivery have shown that upto 400% increase in targeted antiboby theraputics can be achieved in brain tumours[6]. Our follow up studies with Parkinson's patients demonstrated the feasibility that the overactivity of sonicated putamen was down regulated by Cerezyme delivery. There was also an early observation of potential funtional benefit[5]. However, the enhancemnet was not uinform with the method used for the sonications[4]. In a separate study the safety of sonicating multiple locations in the brains of nine Alzheimer's patients was demonstrated without therpeutic delivery in multiple treatments. The BBB permeability of the bilateral hippocampi, anterior cingulate cortex, and precuneus was transiently increased without grade 3 or higher adverse events. Participants did not experience worsening trajectory of cognitive decline (ADAS-cog11, MMSE) (Meng et al., Brain, accepted)

Conclusions

BBB modulation using focused ultrasound continues to show feasibility and safety in the clinical testing. There appears to bo be emerging evidence of potential therapeutic effect in the first clinical studies

delivering therapeutics into the brain. Similarly, the BBB modulation appears to enhance the release of cell-free DNA to the bloosd stream thus potentially allowing molecular diagnosis from blood samples[7].

References

[1]. W. M. Pardridge, "Targeting neurotherapeutic agents through the blood-brain barrier," *Arch. Neurol,* vol. 59, no. 1, pp. 35-40, 1/2002 2002. [Online]. Available: http://www.ncbi.nlm.nih.gov/pubmed/11790228.

[2]. K. Hynynen, N. McDannold, N. Vykhodtseva, and F. A. Jolesz, "Noninvasive MR imaging-guided focal opening of the blood-brain barrier in rabbits," *Radiology,* vol. 220, no. 3, pp. 640-646, 9/2001 2001. [Online]. Available: http://www.ncbi.nlm.nih.gov/pubmed/11526261.

[3]. T. Mainprize *et al.*, "Blood-Brain Barrier Opening in Primary Brain Tumors with Non-invasive MR-Guided Focused Ultrasound: A Clinical Safety and Feasibility Study," *Sci. Rep,* vol. 9, no. 1, pp. 321-36340, 1/23/2019 2019.

[4]. Y. Huang *et al.*, "Cavitation Feedback Control of Focused Ultrasound Blood-Brain Barrier Opening for Drug Delivery in Patients with Parkinson's Disease," (in eng), *Pharmaceutics,* vol. 14, no. 12, Nov 26 2022, doi: 10.3390/pharmaceutics14122607.

[5]. Y. Meng *et al.*, "Putaminal Recombinant Glucocerebrosidase Delivery with Magnetic Resonance-Guided Focused Ultrasound in Parkinson's Disease: A Phase I Study," (in eng), *Mov Disord,* vol. 37, no. 10, pp. 2134-2139, Oct 2022, doi: 10.1002/mds.29190.

[6]. Y. Meng *et al.*, "MR-guided focused ultrasound enhances delivery of trastuzumab to Her2-positive brain metastases," *Sci Transl Med,* vol. 13, no. 615, p. eabj4011, Oct 13 2021, doi: 10.1126/scitranslmed.abj4011.

[7]. Y. Meng *et al.*, "MR-guided focused ultrasound liquid biopsy enriches circulating biomarkers in patients with brain tumors," (in eng), *Neuro Oncol,* Mar 10 2021, doi: 10.1093/neuonc/noab057.

Ultrasound-triggered microbubble destruction augmentation of tumor radioembolization

John R. Eisenbrey[1], Flemming Forsberg[1], Corinne E. Wessner[1], Lauren J. Delaney[1], Kristen Bradigan[1], Andrej Lyshchik[1], Patrick O'Kane[1], Ji-Bin Liu[1], Jesse Civan[2], Kevin Anton[1], Stephen Topper[1] , Colette M. Shaw[1]

[1]Department of Radiology, Thomas Jefferson University, Philadelphia, PA, USA
[2]Department of Medicine, Division of Hepatology, Thomas Jefferson University, Philadelphia, PA, USA

Introduction

Hepatocellular carcinoma (HCC) is the third leading cause of cancer mortality worldwide and the single fastest growing cause of cancer mortality in the United States [1]. Despite the decrease in hepatitis C-associated HCC, the overall incidence of HCC is likely to continue to rise due to increases in non-alcoholic steatohepatitis [1]. Transarterial embolization is recommended for the 15-25% of HCC patients who present with Barcelona Liver Clinic (BCLC) Stage B or more advanced disease [2, 3]. Within the umbrella of embolic therapies, transarterial radioembolization (TARE) with Yttrium-90 (Y90) is gaining in popularity as a treatment option in this patient population. It relies on catheter-directed delivery of radioactive microspheres, consisting of 20- to 60-µm glass beads containing Y90 into the tumor arterial blood supply, providing a localized and sustained release of radiation. Y90 undergoes pure beta emissions as it decays to stable Zirconium-90 with a half-life of 64 hours and average energy emission of 0.94 MeV. Consequently, although delivered dosages are high (110-150 Gy), radiation exposure to malignant tissue is highly dependent on source location, which contributes to the less than ideal response rates [4-6].

Contrast-enhanced ultrasound (CEUS) uses gas microbubbles, encapsulated by an outer protein or lipid shell for stability, to improve visualization of blood flow with nonlinear ultrasound imaging modes. At higher acoustic pressures (albeit well within United States Food and Drug Administration (FDA) limits) the microbubbles undergo destruction via gas diffusion and inertial cavitation, which produces numerous bioeffects [7]. Among these bioeffects, microbubble cavitation (generally induced at mechanical indexes (MI) > 0.2) can sensitize solid tumors to radiation, as first described by Czarnota and colleagues [8]. This synergistic response was found to be dependent on ceramide production, which acts as an apoptotic signaling molecule in endothelial cells and can reduce the radiation dosages required to permanently disrupt the tumor vasculature [9]. Later mechanistic studies demonstrated that this tumor sensitization from microbubble cavitation arises from mechanical insult to endothelial cells within the tumor vasculature, which in turn results in both activation of the acid sphingomyelinase-ceramide pathway [10] and upregulation of uridylyltransferase glycosyltransferase 8, accelerating the transfer of galactose to ceramide [11]. Our group replicated this phenomenon in an orthotopic model of human HCC, showing a 170% reduction in tumor growth and roughly a 320% improvement in animal survival when ultrasound-triggered microbubble destruction (UTMD) was combined with radiotherapy [12]. Consequently, the goal of this work is to investigate the safety and therapeutic benefits of combining radioembolization and UTMD in patients with HCC.

Methods

This protocol (NCT#03199274) was approved by the Institutional Review Board of Thomas Jefferson University and performed under FDA IND #126,768. Eligible patients had HCC scheduled for sub-lobar radioembolization (130-150 Gy) of a previously untreated tumor < 6 cm in diameter using TheraSpheres (Boston Scientific, Marlblorough, MA USA). Following confirmation of eligibility, patients provided informed consent before being randomized to groups receiving standard of care TARE or TARE combined with 3 UTMD sessions.

Patients assigned to the control arm received standard of care TARE while patients randomized to the experimental arm of the study underwent TARE with 3 UTMD sessions: at 1-4 hours post radioembolization and at approximately 1 and 2 weeks post treatment. Ultrasound imaging was performed using a commercially available S3000 HELX or Sequoia scanner with a 6C1 probe and flash-replenishment nonlinear imaging package (Siemens Healthineers, Issaquah, WA) by a sonographer with more than 5 years of clinical and research experience in CEUS.

Five ml of activated Optison (GE Healthcare, Princeton, NJ) was suspended in 50 ml of saline and infused through an 18- to 22-gauge angiocatheter placed in a peripheral arm vein at a rate of 120 ml/h. After confirmation of contrast-enhancement within the mass, a series of UTMD-replenishment sequences was initiated. Patients were asked to temporarily halt respiration while a 4-second UTMD sequence (MI = 1.13 at 1.5 MHz, transmitting 2.3 μs pulses at a pulse repetition frequency of 100 Hz) was transmitted, followed by nonlinear imaging of contrast replenishment at lower intensity using Cadence Pulse Sequencing (MI = 0.06) for 10 seconds. This sequence was first repeated 3-5 times at the tumor midline to evaluate tumor vascularity changes over time. Following these acquisitions, the sequence was modified for the remainder of the contrast infusion (~10 min) to consist of sweeps through the entire tumor volume during the 4-second UTMD pulse sequences (approximately 25 UTMD sequences).

For safety assessment, vital signs including temperature, heart rate, and blood pressure were obtained for all patients pre- and post-UTMD. Adverse events were monitored electronically and through patient communication. Additionally, liver function testing was performed for all patients approximately one month post treatment and changes compared across groups. For therapeutic efficacy, two board-certified radiologists with over 15 years of experience in body imaging blinded to the treatment arm assignment evaluated the patient's contrast-enhanced MRI pre-embolization and 4-6 months after radioembolization and provided a consensus treatment response assessment using the modified response evaluation criteria in solid tumors (mRECIST) system. Additionally, patients were electronically monitored for time to required next treatment and 1 year survival.

Results

To date, 83 subjects have been enrolled in this ongoing clinical trial, and safety and interim efficacy results were recently published [13]. No statistical differences have been observed in physiologic signs pre- and post-UTMD in the control group ($p > 0.09$). Nine adverse events (grade I-II) have been observed in experimental arm to date, and all were deemed by the medical monitor to be unrelated to Optison infusion and consistent with the adverse event rate in the control arm. No radiopharmaceutical activity has been detected outside of the liver in any patient and no evidence of pulmonary fibrosis, radiation pneumonitis, or gastroduodenal injury associated with Y90 repositioning has been observed. Similarly, no differences in changes in liver function (bilirubin, AST, ALT, creatinine, hemoglobin, and albumin) have been observed between the experimental and control arms ($p > 0.08$).

Evaluation of mRECIST is ongoing with data collection completed on the first 45 patients. These data are summarized in Figure 1 and show a statistically significant improvement in tumor response when UTMD is combined with radioembolization ($p = 0.007$). Importantly, more than 50% of patients in the experimental arm have shown a complete response to therapy and only 2 patients have shown stable disease on follow up. Similarly, patients receiving UTMD in combination with radioembolization have shown improvements in time to required next treatment and one year survival, although these differences are not currently statistically significant ($p > 0.07$). Subject enrollment and monitoring continues, with trial accrual expected to be completed in late 2023.

Conclusions

The addition of UTMD in patients undergoing radioembolization of HCC is safe and appears to improve tumoral response and clinical outcomes. While enrollment and data analysis are ongoing, this work supports the hypothesis that microbubble cavitation alters radiotherapeutic response in solid tumors.
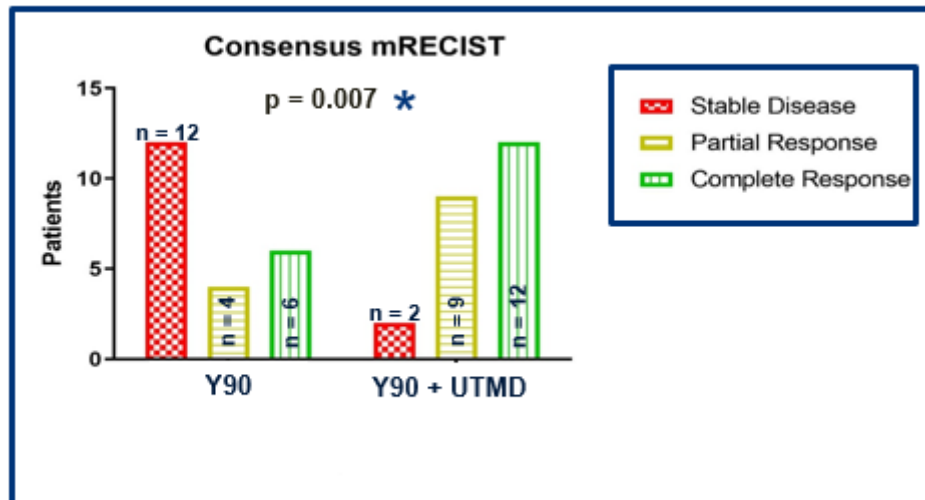
Figure 1: Summary of mRECIST consensus reads of tumors receiving transarterial radioembolization (TARE) alone, or TARE combined with ultrasound-triggered microbubble destruction (UTMD).

References

[1]. McGlynn et al. Epidemiology of Hepatocellular Carcinoma. Hepatology 2021 73(S1)

[2]. Ahmed O, Liu L, Gayed A, et al. The changing face of hepatocellular carcinoma: forecasting prevalence of nonalcoholic steatohepatitis and hepatitis C cirrhosis. J Clin Exp Hepatol. 2019; 9(1):50-55.

[3]. Bruix J, Sherman M. Management of hepatocellular carcinoma: an update. Hepatology 2011; 52:1020-2.

[4]. Saraswat VA, Pander G, Shetty S. Treatment algorithms for managing hepatocellular carcinoma. J Clin Exp Hepatol 2014; S3:80-9.

[5]. Andreana L, Isgro G, Marelli L, et al. Treatment of hepatocellular carcinoma (HCC) by intra-arterial infusion of radio-emitter compounds: trans-arterial radio-embolisation of HCC. Cancer Treat Rev 2012; 38:641-9.

[6]. Paul SB, Sharma H. Role of Transcatheter Intra-arterial Therapies for Hepatocellular Carcinoma. J Clin Exp Hepatol 2014; S3:112-121.

[7]. Kirchner T, Marquardt S, Werncke T, et al. Comparison of health-related quality of life after transarterial chemoembolization and transarterial radioembolization in patients with unresectable hepatocellular carcinoma. Abdom Radiol (NY) 2019; 44(4):1554-1561.

[8]. Lyshchik A (Editor). Fundamentals of CEUS. Elsevier. Manitoba, Canada. 2019.

[9]. Czarnota GJ, Karshafian R, Burns PN, et al. Tumor radiation response enhancement by acoustical stimulation of the vasculature. Proc Natl Acad Sci U S A 2012; 109(30):E2033-41.

[10]. Nofiele JT, Karshafian R, Furukawa M, et al. Ultrasound-activated microbubble cancer therapy: ceramide production leading to enhanced radiation effects in vitro. Technol Cancer Res Treat 2013; 12(1):53-60.

[11]. El Kaffas A, Al-Mahrouki A, Hashim A, et al. Role of acid sphingomyelinase and ceramide in mechano-acoustic enhancement of tumor radiation responses. J Natl Cancer Inst 2018; 110(9): 1009-1018.

[12]. Al-Mahrouki A, Giles A, Hashim A, et al. Microbubble-based enhancement of radiation effect: role of cell membrane ceramide metabolism. PLos One 2017; 12(7):e0181951.

[13]. Daecher A, Stanczak M, Liu JB, et al. Localized microbubble cavitation-based antivascular therapy for improving HCC treatment response to radiotherapy. Cancer Lett 2017; 411:100-105.

[14]. Eisenbrey JR, Forsberg F, Wessner CE, et al. US-triggered Microbubble Destruction for Augmenting Hepatocellular Carcinoma Response to Transarterial Radioembolization: A Randomized Pilot Clinical Trial. Radiology. 2021 Feb;298(2):450-457.

Ongoing Sonothromboysis Trials in Acute ST Segment Elevation Myocardial Infarction

Thomas Porter[1]

[1]*Division of Cardiovascular Medicine, University of Nebraska Medical Center, Omaha, NE, USA*
Corresponding author: trporteri@unmc.edu

Persistent microvascular obstruction (MVO) after recanalization of the epicardial vessel (PCI) in acute ST segment elevation myocardial infarction (STEMI) has been well-described1, with several potential pathophysiologic characteristics 2. The presence of MVO, even after angiographically successful epicardial recanalization in acute STEMI, predicts lack of recovery of left ventricular function, higher risk for heart failure, higher need for implantable devices, and increased mortality.3,4 Although angiographic and electrocardiographic criteria exist for persistent MVO, they underestimate the extent of MVO when compared with cardiac magnetic resonance imaging2 or myocardial contrast echocardiography in the current early interventional era4. MVO has been detected in up to 60% of STEMIs involving the left anterior descending artery despite achieving TIMI 3 angiographic flow4. Pharmacologic or interventional therapies to prevent MVO following emergent epicardial recanalization in acute myocardial infarction have had limited success in reducing reperfusion injury and subsequent scar formation in clinical trials. Therefore, with current standard of care we still witness situations where large amounts of myocardium fail to recover function following emergent PCI in ST segment elevation myocardial infarction (STEMI). This may even apply to non-ST segment elevation myocardial infarction as well. Although there has been limited success in reducing MVO with high intensity statins and beta blockers in the pre and post PCI time period, significant microvascular perfusion abnormalities are still present 4.

For over 20 years, we have been demonstrating the potential for ultrasound induced microbubble cavitation (sonothrombolysis) to dissolve both large vessel thrombi and microthrombi. Although initial work in this area was with non-imaging transducers and long pulse durations, we have observed that guided high MI impulses from a commercially approved diagnostic transducer combined with a continuous infusion of commercially available microbubbles successfully, and safely, restores microvascular flow in pre-clinical large animal models of acute STEMI5. Moreover, in pure models of MVO created by arterial embolization of <200 micron thrombotic debri, applied diagnostic ultrasound high MI impulses appeared to restore microvascular flow via both a nitric oxide and microthrombus dissolution effect6. The first clinical trials have demonstrated the safety and efficacy for diagnostic high MI impulses to improve both epicardial and microvascular thrombus dissolution in acute STEMI7-10. Ongoing studies are now determining what role pre-PCI sonothrombolysis has in acute coronary syndromes when compared to post PCI only sonothrombolysis. The REDUCE trial recently reinforced the findings of the MRUSMI trial in demonstrating the ability of sonothrombolysis applied just prior to, and following, emergent PCI to reduce myocardial infarct size in increase the amount of salvaged myocardium11. In 2023 additional trials will be completed that will demonstrate the efficacy of post PCI sonothrombolysis only in reducing ultimate myocardial infarct size in left anterior descending STEMI. Investigators are also now exploring the role of sonothrombolysis in non STEMI (HUBBLE trial).

References

[1]. Niccoli G, Scalone G, Lerman A, Crea F. Coronary microvascular obstruction in acute myocardial infarction. Eur Heart J. 2016;37:1024-33. doi: 10.1093/eurheartj/ehv484.

[2]. Symons R, Pontone G, Schwitter J, Francone M, Iglesias JF, Barison A, Zalewski J, de Luca L, Degrauwe S, Claus P, et al. Long-term incremental prognostic value of cardiovascular magnetic resonance after ST-segment elevation myocardial infarction. A study of the Collaborative Registry on CMR in STEMI. JACC Cardiovasc Imaging. 2018;11:813-25. doi: 10.1016/j.jcmg.2017.05.023.

[3]. Aggarwal S, Xie F, High R, Pavlides G, Porter TR. Prevalence and predictive value of microvascular flow abnormalities after successful contemporary percutaneous coronary intervention in acute ST segment elevation myocardial infarction. J Am Soc Echocardiogr. 2018;31:674-82. doi: 10.1016/j.echo.2018.01.009.

[4]. Xie F, Qian L, Goldsweig A, Xu D, Porter TR. Event-free survival following successful percutaneous intervention in acute myocardial infarction depends on microvascular perfusion. Circ Cardiovasc Imaging 2020;13:e010091.doi:10.1161/circimaging.119.010091.

[5]. Wu J, Xie F, Lof J, Sayyed S, Porter TR. Utilization of modified diagnostic ultrasound and microbubbles to reduce myocardial infarct size. *Heart* 2015;101:1468-74.

[6]. Porter TR, Radio S, Lof J, Everbach C, Powers JE, Vignon F, Shi WT, Xie F. Diagnostic ultrasound high mechanical index impulses restore microvascular flow in peripheral arterial thromboembolism Ultrasound Med Biol 2016;42:1531-40

[7]. Slikkerveer J, Kleijn SA, Appelman Y, Porter TR, Veen G, van Rossum AC, Kamp O. Ultrasound enhanced prehospital thrombolysis using microbubbles infusion in patients with acute ST elevation myocardial infarction: pilot of the Sonolysis study. *Ultrasound Med Biol* 2012;38:247-52.

[8]. Mathias W, Jr., Tsutsui JM, Tavares BG, Xie F, Aguiar MO, Garcia DR, Oliveira MT, Jr., Soeiro A, Nicolau JC, Lemos PAN, Rochitte CE, Ramires JA, Kalil RF, Porter TR. Diagnostic Ultrasound Impulses Improve Microvascular Flow in Patients With STEMI Receiving Intravenous Microbubbles. *J Am Coll Cardiol* 2016;67:2506-15.

[9]. *Roos* ST, Juffermans LJM, van Royen N, van Rossum AC, Xie F, Appelman Y, Porter TR, Kamp O. Unexpected high incidence of coronary vasoconstriction in the reduction of microvascular injury using sonolysis (ROMIUS) trial. Ultrasound Med Biol 2016; 42:1919-1928

[10]. Mathias W Jr, Tsutsui JM, Tavares BG, Fava AM, Aguiar MOD, Borges BC, Oliveira MT Jr, Soeiro A, Nicolau JC, Ribeiro HB, Chiang HP, Sbano JCN, Morad A, Goldsweig A, Rochitte CE, Lopes BBC, Ramirez JAF, Kalil Filho R, Porter TR; MRUSMI Investigators. Sonothrombolysis in ST-segment elevation myocardial infarction treated with primary percutaneous coronary intervention. J Am Coll Cardiol. 2019 Jun 11;73(22):2832-2842.

[11]. Jeyaprakash P, Pathan F, Madan K, Khor L, Sivapathan S, Yu C, Madronio C, Porter T, Hallani H, Ozawa K, Loh H, Robledol K, Mansberg R, Nguyen D, Negishi K. The effect of sonothrombolysis on infarct size and myocardial salvage in ST elevation myocardial infarction: A pilot RCT. J Am Soc Echocardiogr 2022; 35:e2(Abstract).

.

The profound and unique path of the sole microbubble

Couture, Olivier

CNRS, Sorbonne Université, INSERM, Paris, France
Corresponding author: olivier.couture@sorbonne-universite.fr

Microbubble lives and emits waves at vastly different scales. As they were conceived to flow within the smallest capillaries without causing embolism, their size is restrained to the micrometric scale. However, we image them with ultrasound wavelengths that are hundreds of time larger, chosen to penetrate deep within tissue by avoiding frequency-dependent attenuation. Despite their size, individual microbubbles have been known to be visible deep within tissue with ultrasound imaging.

Since 2010, the role of microbubble as a bridge between the micrometric and the submillimetric scale has been exploited for super-resolution ultrasound imaging [Couture et al. 2018, Christensen-Jeffries

Figure 1: Rat brain imaging with ultrasound localization microscopy (V.Hingot in Couture et al. 2018)

et al. 2020]. On an imaging point-of-view, the microbubble can be seen as an analogy to optical fluorescent markers, which themselves allowed the super-resolution microscopy revolution [Betzig et al. 2006].

The introduction of ultrasound localization microscopy (ULM) has allowed a significant gain in resolution, up to a factor of 10 [Errico et al. 2020]. The rapid development of this technique, along with other super-resolution approaches [Bar-Zion et al. 2018, Ilovitsch et al. 2018], have led to many preclinical and clinical studies on various organs, such as the brain [Demené et al. 2021, Renaudin et al. 2022], kidney [Foiret et al. 2017], liver [Huang et al.2021], lymph nodes and various diseases such as cancer [Lin et al. 2017], Alzheimer's' disease [Lowerison et al. 2022], stroke [Hingot and Brodin et al. 2020]. The ULM community now collects the strength of many laboratory worldwide and open-science approaches can extend its use even more rapidly [Heiles and Chavignon, 2022].

Figure 2: Transcranial 3D ULM of the rat brain with a multiplexed matrix probe (Chavignon et al. 2021)

In the last few years, we chose to concentrate our efforts toward stroke emergency imaging, which remains a vast medical challenge today. Stroke impacts our world massively with 6 million deaths per year and leading to a large share of acquired handicap. Stroke treatment is very time-sensitive, actions being required within the first few hours following onset. However, the necessary distinction between ischemic and hemorrhagic stroke still requires access to MRI and CT, elongating treatment time.

We proposed to use ULM as an emergency neuroimaging tool. However, several hurdles needed to be surpassed. ULM had to become volumetric for a single acquisition to yield a 3D vision of the brain, to allow quantification and alleviate user-dependency [Heiles et al. 2019, Heiles et al.
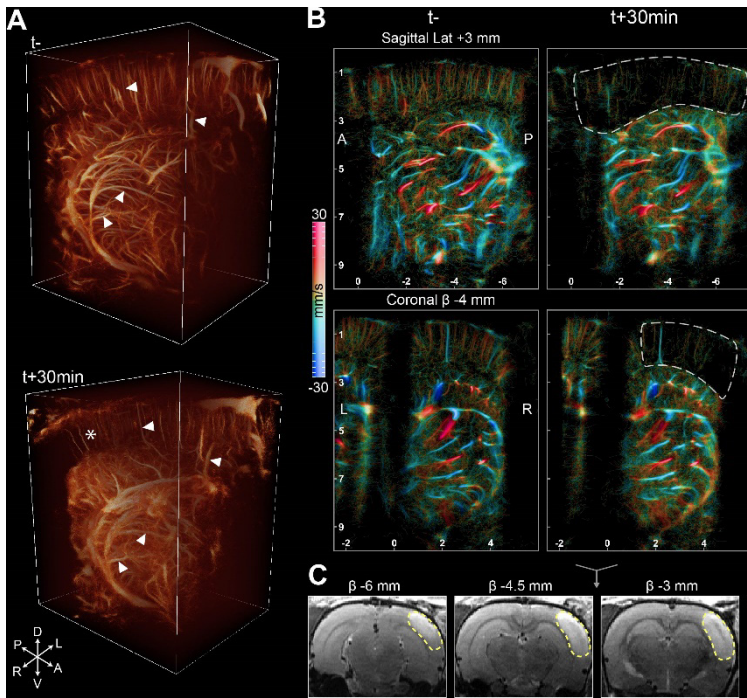
Figure 3: 3D ULM of an ischemic stroke model (Chavignon et al. 2022)

2022]. Moreover, ULM had to become transcranial to guarantee its non-invasiveness. Additionally, ULM had to be portable to preserve one of the main advantages of ultrasound imaging [Chavignon et al. 2021]. Also, new biomarkers of stroke had to be defined based on this new type of microcirculation imaging [Chavignon et al. 2022]. Finally, these different components needed to be combined and demonstrated in small models, then larger models (see A.Coudert presentation) before human studies. This presentation will summarize the path that we have taken toward ULM stroke imaging.

As the technology now enters the realm of industrialization, it is necessary to reflect upon newly discovered fundamental aspects of ULM. Observing the path of individual microbubbles can yield more information than just pretty pictures or even diagnostically-useful pretty pictures. Indeed, a single microbubble can be seen as a probe of its immediate environment, as it was demonstrated many times in-vitro. Its micrometric path and ultrasonic response can teach us about its immediate surrounding, much like the tip of an atomic force microscope, but deep within living tissue.

As an example of this sensing ULM (sULM), we could observe peculiar behavior of individual microbubbles in the cortex of the human kidney. It could highlight the functional units of this organ that would otherwise only be observed through invasive imaging techniques. The use of 3D ULM would alleviate the issues with planar projection and even allow to study the precise ultrasonic response of individual bubbles. In the future, we believe that the fundamental work displayed at this conference will find a direct application in understanding the physical behavior of single microbubbles in the human body and help comprehend the physiology of circulation at its smallest scale.
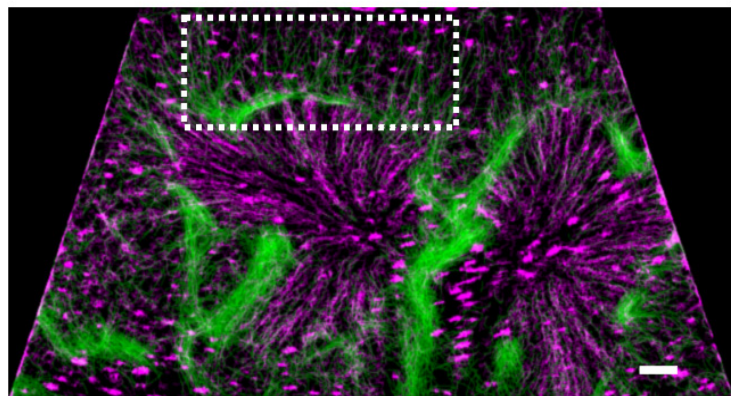
Figure 4: Human kidney ULM using a clinical scanner displaying specific microbubble behavior (Denis and Bodard, in review, 2022). See presentation by Louise Denis

High-frame-rate contrast-enhanced ultrasound porcine myocardial perfusion imaging with higher-order singular value decomposition

Geraldi Wahyulaksana[1], Luxi Wei[1], Maaike te Lintel Hekkert[2], Daniel J. Bowen[3], Jason Voorneveld[1], Antonius F.W. van der Steen[1,4], Hendrik J. Vos[1,4]

[1]*Biomedical Engineering, Dept Experimental Cardiology, Erasmus MC University Medical Center Rotterdam, Rotterdam, the Netherlands*
[2]*Thoraxcenter, Dept Experimental Cardiology, Erasmus MC University Medical Center Rotterdam, Rotterdam, the Netherlands*
[3] *Dept Cardiology, Erasmus MC University Medical Center Rotterdam, Rotterdam, the Netherlands*
[4]*Medical Imaging, Faculty of Applied Sciences, Delft University of Technology, Delft, the Netherlands*
Corresponding author: g.wahyulaksana@erasmusmc.nl

Introduction

Contrast-enhanced ultrasound (CEUS) is a promising bedside diagnosis tool for myocardial perfusion imaging that has the potential for improving the diagnosis and treatment of patients with ischemic heart disease. Despite the use of ultrasound contrast agents, obtaining accurate and reliable images of the perfusion in the myocardium with CEUS is still a challenge. Some of the most common problems are: artefacts from attenuation; shadowing and clutter from the lungs or ribs; and strong clutter signal originating from tissue, which have the effect of concealing the microbubble signal [1], [2].

Several contrast-specific pulsing schemes that exploit the nonlinear properties of microbubbles have been developed to improve contrast detection. The most widely used CEUS sequences include: amplitude modulation (AM); pulse inversion (PI); and their combination (AMPI). These CEUS sequences work by transmitting a series of complementary pulses which are then summed linearly to suppress the linear tissue reflections, while retaining the non-linear contrast signal. However, non-linear propogation of the ultrasound wave (through tissue or microbubble clouds) and tissue motion, can cause leakage of unwanted tissue clutter into the CEUS signal. Both problems are severely detrimental in myocardial perfusion imaging [2]. Post-processing solutions, namely spectral clutter filters, or singular value decomposition (SVD) clutter filters, are also not effective because the tissue and perfusion signal are highly coherent and as the contrast is moving with the tissue

In this study, we propose to improve microbubble detection of AM and AMPI by implementing higher-order singular value decomposition (HOSVD) to combine the received echoes instead of conventionally summing them. We are using an *in vivo* porcine model to investigate the efficacy of our proposed method to detect myocardial perfusion.

Methods

The female Yorkshire x Norwegian Landrace porcine experiments (n=10) followed European Union and institutional guidelines for the care and use of laboratory animals, with CCD approval AVD1010020172411 (SP2100125). They were first sedated, put under full anesthesia, and vented mechanically. Vital signs were monitored. A diluted (30x) Definity® solution (Lantheus Medical Imaging Inc., MA, USA) was continously infused through the jugular vein at 1.5 ml/min. The acquisitions were performed in both closed-chest and open-chest procedures.

RF acquisitions were performed with a phased array transducer (64-element P7-4, Philips ATL, Bothell, WA), connected to a Vantage 256 system (Verasonics Inc., Redmond, WA). An acquisition consisted of 1s of high-frame rate (HFR) recordings, a high mechanical index "FLASH" microbubble destruction sequence, followed by 4s of HFRrecordings. The HFR transmission sequence consisted of 3 overlaping synthetic transmit apertures (21 elements each) [3], with a pulse repetition frequency of 4.5 kHz and center frequency

of 5.2 MHz. Channel data were beamformed offline using the Ultrasound Toolbox [4] in Matlab (2022A, the Mathworks, Natick, 2022) on a 0.5 λ resolution grid and further processed.

We implemented HOSVD on a beamformed IQ image series, arranged as a 3rd order tensor with spatial, temporal, and pulsing sequence as the input dimensions. Analogous to the regular 2D SVD, the filtering process is performed by suppressing eigenvectors that contain clutter and noise. We developed automatic thresholding algorithms to select the ranks for each set of eigenvectors to remove operator dependencies and improve reproducibility.

 Results

The example of power Doppler images (ensemble length of 20 frames), of closed-chest acquisition are shown in Figure 1 and open-chest in Figure 2. We could identify more myocardial perfusion signal (pre-FLASH destruction) after HOSVD processing (Fig. 1c), compared to the conventional AM processing (Fig. 1a). The images post-FLASH destruction sequence (Fig. 1 b and d) show less signal traces inside the myocardium and suggest that the detected signal on pre-FLASH images originate from microbubbles rather than tissue residuals. We also observed the myocardial perfusion signal replenishment on the subsequent heartbeats. The open-chest HOSVD-processed images (Fig. 2 c and d) show more microbubble signal and less motion artefacts compared with the conventionally process AMPI images (Fig. 2 a and b).

Closed-chest parasternal short-axis view
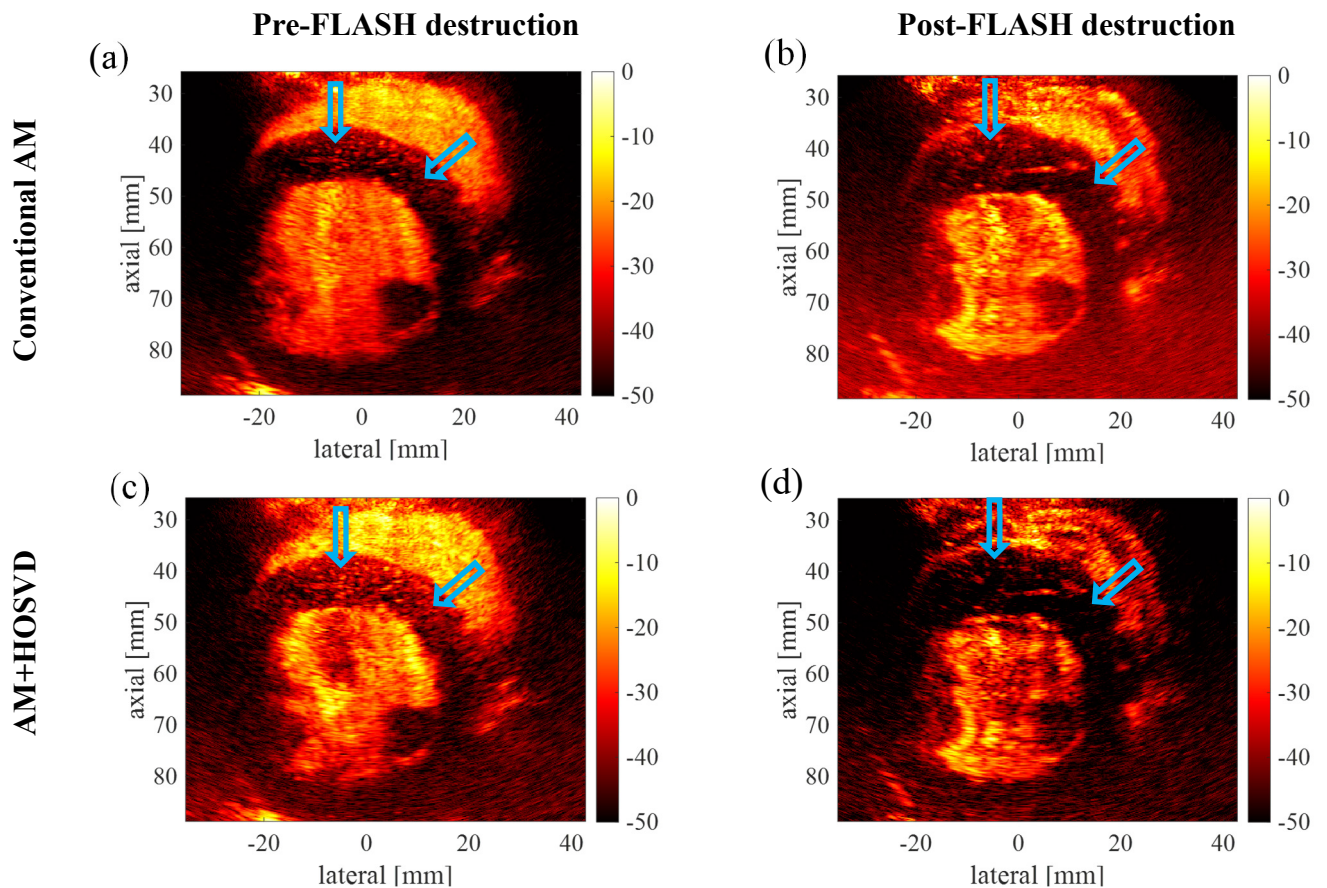
Figure 1. Comparison between closed-chest parasternal short axis AM images, processed conventionally and HOSVD. The images processed with conventional AM (a) and (b) can be compared with the HOSVD-processed image (c) and (d). The myocardium of interventricular septum (cyan arrows) contains more microbubble signal before the FLASH destruction sequence.

Open-chest apical view (pre-FLASH)

Slow moving tissue   **Fast moving tissue**
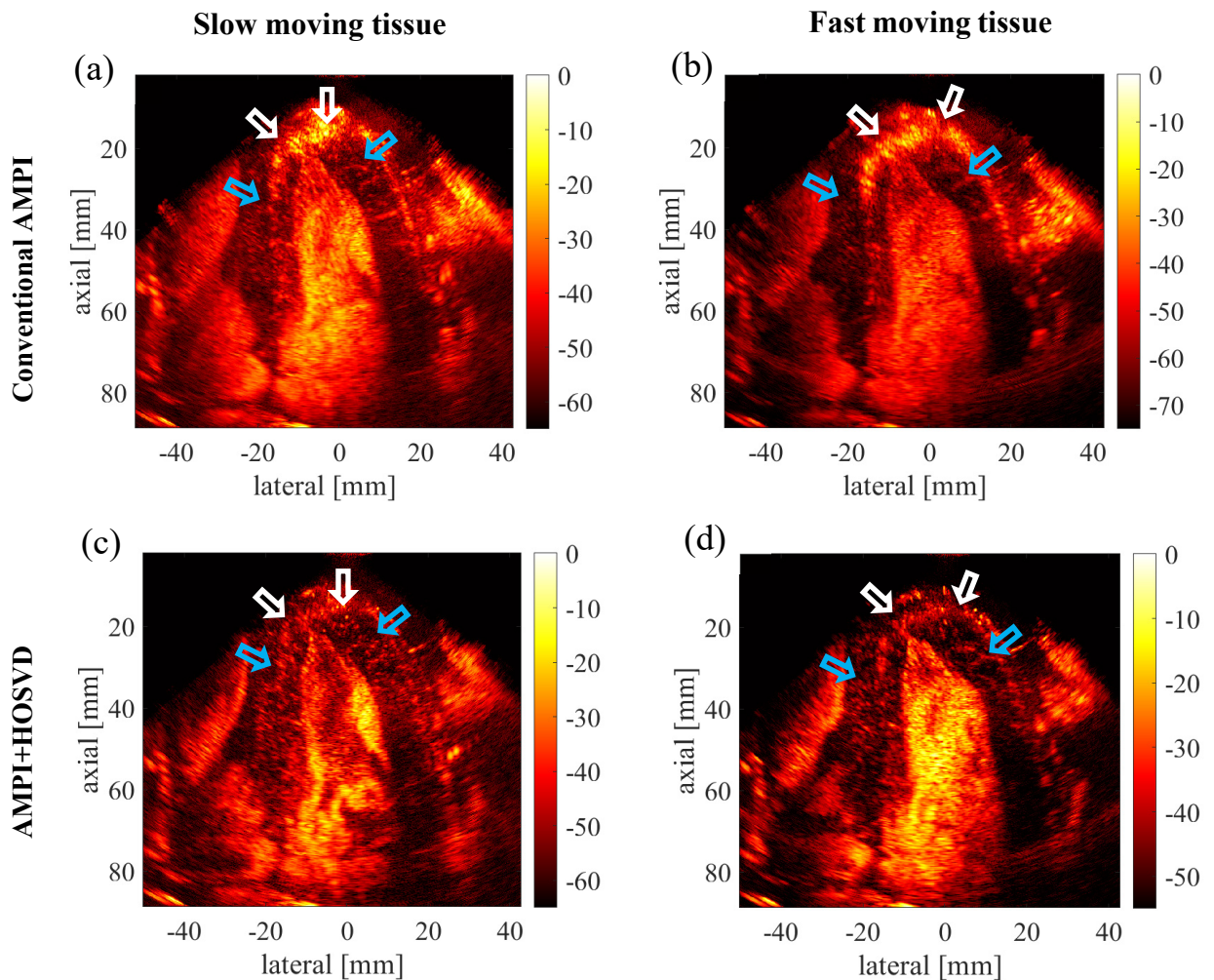
Figure 2. Comparison between open-chest apical four-chamber AMPI images, processed conventionally and HOSVD. The images processed with conventional AMPI (a) and (b) can be compared with the HOSVD-processed image (c) and (d). The tissue motion artefacts (white arrows) are more suppressed with HOSVD and more microbubble signal can be detected in the myocardium (cyan arrows).

Conclusions

We proposed HOSVD as a method to process multi-pulse contrast schemes and performed *in vivo* evaluation with porcine heart model. The results showed that it can improve contrast detection for myocardial perfusion imaging compared to conventionally processing (summation) the contrast pulsing schemes.

References

[1] M. Dewey *et al.*, "Clinical quantitative cardiac imaging for the assessment of myocardial ischaemia," *Nat. Rev. Cardiol.*, vol. 17, no. 7, pp. 427–450, 2020, doi: 10.1038/s41569-020-0341-8.

[2] M. A. Averkiou, M. F. Bruce, J. E. Powers, P. S. Sheeran, and P. N. Burns, "Imaging Methods for Ultrasound Contrast Agents," *Ultrasound Med. Biol.*, vol. 46, pp. 498–517, 2020, doi: 10.1016/j.ultrasmedbio.2019.11.004.

[3] C. Papadacci, M. Pernot, M. Couade, M. Fink, and M. Tanter, "High-contrast ultrafast imaging of the heart," *IEEE Trans. Ultrason. Ferroelectr. Freq. Control*, vol. 61, no. 2, pp. 288–301, 2014, doi: 10.1109/TUFFC.2014.6722614.

[4] A. Rodriguez-Molares *et al.*, "The UltraSound ToolBox," Oct. 2017, doi: 10.1109/ULTSYM.2017.8092389.

Transcranial 3D Ultrasound Localization Microscopy in sheep brain

Antoine Coudert[1], Louise Denis[1], Arthur Chavignon[1], Cyrille Orset[2], Denis Vivien[2,3], Olivier Couture[1],

[1]Sorbonne Université, CNRS, INSERM, Laboratoire d'Imagerie Biomedicale, Paris, France,
[2]Normandie Univ, UNICAEN, INSERM U1237, Etablissement Français du Sang, Physiopathology and Imaging of Neurological Disorders (PhIND), GIP Cyceron, Institut Blood and Brain @Caen-Normandie (BB@C), Caen, France,
[3]CHU Caen, Department of clinical research, Caen-Normandie University Hospital, Avenue de la côte de Nacre, Caen, France.

Introduction

Ultrasound Localization Microscopy (ULM) has been used to map the microvasculature in-vivo in several organs, mostly in 2-dimensions [1]–[5]. However, 2D imaging has several drawbacks: appropriate plane selection is difficult, flow quantification and motion correction remain heavily biased, and acquisition time for a full volume is detrimental. 3D ULM addresses most of these issues and could reduce user dependency on ultrasound imaging [6].

Recent works in small animals show that Transcranial 3D ULM could be invaluable for the rapid diagnosis of stroke [8]. However, 3D ULM has not been performed on humans or large animals where the skull is thicker. In this study, we propose to image the microvascular system of a sheep's brain with 3D ULM based on diverging waves. Such a sheep model was selected due to its skull bone thickness equivalent to the human temporal bone. Furthermore, we performed a new cylindrical multiplexing approach to characterize microbubbles in 3D and compared ULM results with MRI.

Methods

The study was performed following the agreement of the ethics committee. A matrix probe (32 x 32, pitch 0.5 mm, 1.5 MHz, Vermon) connected to a Vantage 256 (Verasonics) with a 4-to-1 multiplexer was placed on the shaved head of an 18month anesthetized sheep. The placement was helped by a ZTE MRI, which highlights the skull and then confirmed by a real-time 2D power-doppler sequence. For 3D imaging, we exploited a combination of three cylindrical waves in full-emission mode, in which all elements emit, and two spherical waves in synthetic emission. A bolus of 1.75ml of Sonovue contrast agent (Bracco) was injected through the marginal vein every minute during the first 7 minutes. A total of 112k volumes were acquired at 208.8 Hz volume rate and reconstructed by delay-and-sum beamforming. After mean temporal filtering, microbubbles were localized by radial symmetry and tracked. The resulting ULM volume was compared with 3D Time-of-Fly MRI.

Results

3D ULM allows visualization of vessels within the sheep brain in a 2cmx2cmx5cm area. (Fig1.A-D). According to MRI, the matrix probe was placed over an area where the skull thickness was 2.5±0.5 mm. (Fig1.B). ULM could be superimposed with MRI. ULM highlight both the middle cerebral artery (MCA) and the circle of Willis (Fig1.D). Small vessels invisible to MRI also appear on 3D ULM (Fig1.D-E squares). However, some vessels seem to be shifted with MRI (Fig1.D arrow), and others are divided in two (Fig1.D-E ellipses).

Conclusions

In this study, we succeed in perfoming 3D transcranial ULM in sheep. However, the area remains limited, partly due to the restricted zone with skull planarity and poor SNR on matrix arrays. Future studies will attempt to improve SNR with the correction of cranial aberrations. Following improvements in these aspects, a 3D ULM system could be exploited to image large volume of the adult human brain through the temporal window and potentially provide stroke diagnosis with a portable system.
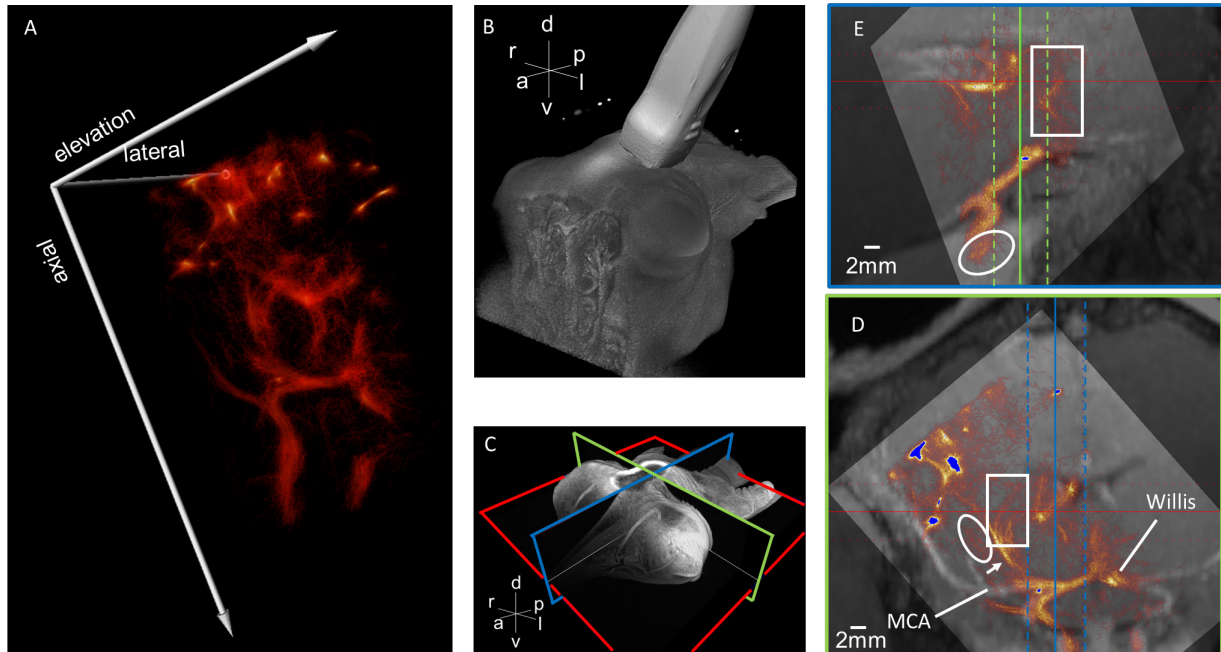
Figure 1: A. 3D rendering of ULM density. B. Illustration on MRI of Probe positioning. C. Illustration of plan slice localization on MRI. D-E. ULM density projection (colored) superposed on TOF MRI (white) for two slices 7mm thick: D. left-right and E. anterior-posterior. Squares highlight vessels not present in MRI but existing in ULM. Ellipses highlight vessels that seem to be divided in two. The arrow shows the shifting between ULM and MRI. Middle Cerebral Artery (MCA); Circle of Willis (Willis)

References

[1]. K. Christensen-Jeffries et al., « Super-resolution Ultrasound Imaging », Ultrasound Med. Biol., vol. 46, no 4, Art. no 4, avr. 2020, doi: 10.1016/j.ultrasmedbio.2019.11.013.

[2]. S. B. Andersen et al., « Evaluation of 2D super-resolution ultrasound imaging of the rat renal vasculature using ex vivo micro-computed tomography », Sci. Rep., vol. 11, no 1, p. 24335, déc. 2021, doi: 10.1038/s41598-021-03726-6.

[3]. Q. Chen, H. Song, J. Yu, et K. Kim, « Current Development and Applications of Super-Resolution Ultrasound Imaging », Sensors, vol. 21, no 7, p. 2417, avr. 2021, doi: 10.3390/s21072417.

[4]. V. Hingot et al., « Early Ultrafast Ultrasound Imaging of Cerebral Perfusion correlates with Ischemic Stroke outcomes and responses to treatment in Mice », Theranostics, vol. 10, no 17, Art. no 17, 2020, doi: 10.7150/thno.44233.

[5]. B. Heiles et al., « Volumetric ultrasound localization microscopy of the whole brain microvasculature », sept. 2021. doi: 10.1101/2021.09.17.460797.

[6]. B. Heiles et al., « Ultrafast 3D Ultrasound Localization Microscopy Using a 32 $\times$ 32 Matrix Array », IEEE Trans. Med. Imaging, vol. 38, no 9, p. 2005-2015, sept. 2019, doi: 10.1109/TMI.2018.2890358.

[7]. A. Chavignon, B. Heiles, V. Hingot, C. Orset, D. Vivien, et O. Couture, « 3D Transcranial Ultrasound Localization Microscopy in the Rat Brain With a Multiplexed Matrix Probe », IEEE Trans. Biomed. Eng., vol. 69, no 7, p. 2132-2142, juill. 2022, doi: 10.1109/TBME.2021.3137265.

Super-resolution imaging of myocardial microvasculature on an *ex vivo* pig model

Biao Huang[1], Konstantinos Ntagiantas[1,2], Kai Riemer[1], Matthieu Toulemonde[1], Justin Perkins[3], Jipeng Yan[1], Rasheda A Chowdhury[2], Meng-Xing Tang[1]

[1]*Department of Bioengineering, Imperial College London, London, London, United Kingdom*
[2]*National Heart and Lung Institute, Imperial College London, London, United Kingdom*
[3]*Department of Clinical Science and Services, The Royal Veterinary College, Hertfordshire, United Kingdom*
Corresponding author: mengxing.tang@imperial.ac.uk

Introduction

Coronary microvasculature plays an important role in controlling blood supplements for the myocardium. In a recent clinical trial, only 37.6% of patients, who were pre-diagnosed positive by non-invasive testing, were confirmed to have obstructive coronary artery diseases after using invasive imaging approaches[1]. This result suggested that circulatory disorder may exist in myocardial microvasculature, however current non-invasive imaging modalities are not able to effectively image microvasculatures.

Benefiting from high frame rate contrast-enhanced ultrasound (CEUS) imaging and super-resolution ultrasound (SRUS) imaging (also known as ultrasound localisation micriscopy or ULM), we visualised myocardial microvessels through localising and tracking of microbubbles (MBs) trajectories in a Langendorff *ex vivo* porcine heart.

Methods

A Langendorff apparatus was constructed for the *ex vivo* experiment to keep the porcine heart alive outside the body[2]. A GE M5ScD phased array probe (center frequency 2.4MHz) and a Verasonics system (Vantage 256, Kirkland, WA, USA) were used for data acquisition. A focused wave was first transmitted to destroy the MBs in the left ventricular myocardium followed by diverging waves to acquire image data for 5 seconds after MB destruction. The imaging depth was set to 11 cm in the study. 6 compounding angles with an amplitude modulation sequence were used in image acquisition to extract the nonlinear signal from MBs. The frame rate in the acquisition was 305Hz. SonoVue microbubbles (Bracco, Milan, Italy) were infused into the heart at the infusion rate of 5 ml/min.

To reduce artefacts and improve the signal-to-noise ratio, a two-stages spline-based nonrigid motion correction algorithm[3], [4] and a temporal smoothing algorithm were used. To visualise the myocardial microvasculature, we localised and paired MBs from the images using an SRUS processing framework proposed in [5] where a Kalman motion model and MB image features were used for tracking.

Results

The result from the *ex vivo* parasternal short-axis view is presented in Figure 1. The contrast-enhanced image and B-mode image from the acquisition are shown in Figures 1a and 1b. Figure 1c presented the zoomed-in maximum intensity projection image in the region of interest. Figure 1d presents a super-resolution density map of the microvasculature. The corresponding flow angle map is shown in Figure 1e. The angle map presents the microvasculature flow direction from the epicardium to the myocardium.

Conclusions

This study shows the feasibility of SRUS in cardiac myocardial microvasculature imaging in an *ex vivo* porcine heart using a clinical low-frequency phased array probe. Future work will involve the vessel occlusion model with the *ex vivo* heart and translate this to human imaging.
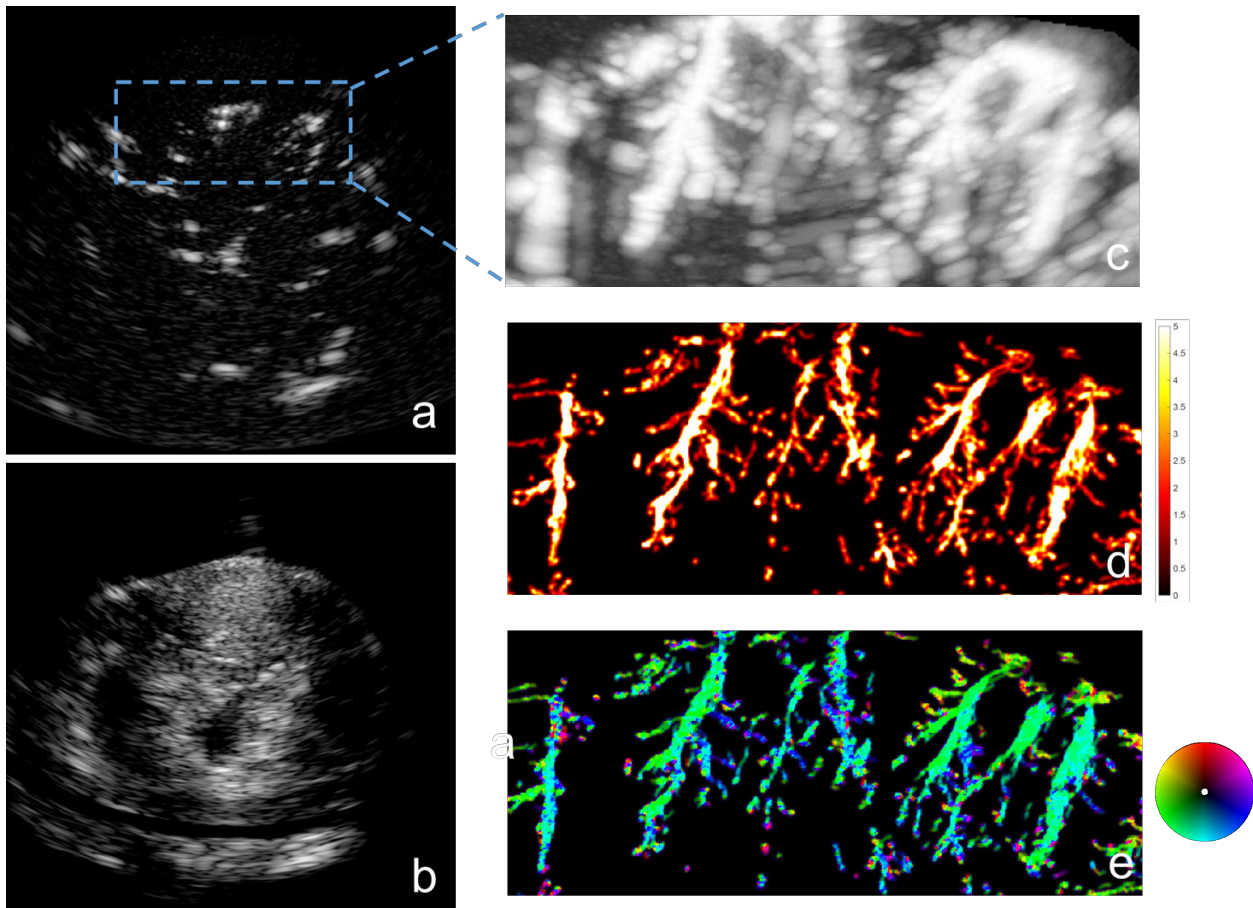
Figure 1. Super-resolution result of myocardial microvasculature in *ex vivo* porcine heart. a) Parasternal short axis contrast-enhanced image of the *ex vivo* porcine heart. b) The corresponding Bmode image. c) The maximum intensity projection image of the region of intest. d) The super resolution myocardial microvasvulature. e) The flow angle map of the myocardial microvasculature.

Acknowledgements

References

[1] M. R. Patel *et al.*, "Low Diagnostic Yield of Elective Coronary Angiography," *N Engl J Med*, vol. 362, no. 10, pp. 886–895, Mar. 2010, doi: 10.1056/NEJMoa0907272.

[2] J. Brook *et al.*, "Development of a pro-arrhythmic ex vivo intact human and porcine model: cardiac electrophysiological changes associated with cellular uncoupling," *Pflugers Arch - Eur J Physiol*, vol. 472, no. 10, pp. 1435–1446, Oct. 2020, doi: 10.1007/s00424-020-02446-6.

[3] D. Rueckert, L. I. Sonoda, C. Hayes, D. L. G. Hill, M. O. Leach, and D. J. Hawkes, "Nonrigid registration using free-form deformations: application to breast MR images," *IEEE Trans. Med. Imaging*, vol. 18, no. 8, pp. 712–721, Aug. 1999, doi: 10.1109/42.796284.

[4] S. Harput *et al.*, "Two-Stage Motion Correction for Super-Resolution Ultrasound Imaging in Human Lower Limb," *IEEE Trans. Ultrason., Ferroelect., Freq. Contr.*, vol. 65, no. 5, pp. 803–814, May 2018, doi: 10.1109/TUFFC.2018.2824846.

[5] J. Yan, T. Zhang, J. Broughton-Venner, P. Huang, and M.-X. Tang, "Super-Resolution Ultrasound Through Sparsity-Based Deconvolution and Multi-Feature Tracking," *IEEE Trans. Med. Imaging*, pp. 1–1, 2022, doi: 10.1109/TMI.2022.3152396.

Tracking Macrophages with Ultrasound for Cancer Diagnosis

Ashley Alva[1], Chulyong Kim[2], Hohyun Lee[2], Costas Arvanitis [2, 3, 4]

[1]*Electrical and Computer Engineering, Georgia Institute of Technology, Atlanta, Georgia, United States*
[2]*Mechanical Engineering, Georgia Institute of Technology, Atlanta, Georgia, United States*
[3]*Biomedical Engineering, Georgia Institute of Technology, Atlanta, Georgia, United States*
[4]*Emory University, Atlanta, Georgia, United States*
Corresponding author: aalva3@gatech.edu

Introduction

Macrophages play a key role amongst the immune cells in host defense. These cells are distributed throughout the host's body and maintain homeostasis by getting rid of pathogens and cell debris through phagocytosis. They are also involved in various complex processes ranging from angiogenesis to erythropoiesis and have the capacity to infiltrate in disease environments like in the case of cancer and atherosclerosis [1]. Hence imaging macrophages and their trafficking patterns (density, flux rates, etc.) could provide important prognostic and diagnostic markers of human disease. While attempts at imaging immune cells including macrophages have been done in the past, current methods are limited in one or more of the following: depth of penetration, spatial resolution, and sensitivity [2]. We hypothesize that labelling macrophages with microbubble contrast agents could render them visible to ultrasound and potentially overcome these limitations to enable imaging of macrophage trafficking at high resolution and sensitivity deep into tissues.

Methods

To test our hypothesis, first we assessed our ability to label macrophages with microbubbles (MB) through phagocytosis. Next, we established the exposure window for imaging the labeled macrophages by assessing their echogenicity and viability (*in vitro*). Then, within this exposure window, we assessed our ability to image these "echogenic" macrophages in a tissue mimicking gelatin phantom, using an 18 MHz transducer (Vermon) connected to a programmable ultrasound scanner (Verasonics Vantage). We also assessed different image acquisition techniques, including compounded B-mode (7 tilted plane waves varying from -3º to +3º), pulse inversion (PI), amplitude modulation (AM) and a combination of the latter two (AMPI) to determine which technique led to the best contrast to noise ratio (CNR). Subsequently, we determined whether the "echogenic" macrophages retained their functionality and maintained a chemotactic movement towards tumor cells by employing transwell inserts in the presence or absence of 4T1 breast tumor cells. Finally, we tested our ability to image them *in vivo* in BALB/c mice with heterotopic 4T1 breast tumors in the upper flank following intratumoral injection.

Results

We verified using optical microscopy that 80% of the macrophages were labeled with MB following 4 hours of co-incubation and that the labeling did not affect their migratory capacity through the transwell membrane as compared to controls (unlabeled macrophages). We found that at exposures at or below 0.1 MI (Mechanical Index) the MB-labeled macrophages emitted strong harmonic emissions (i.e., evidence of highly nonlinear behavior) without adversely impacting cell viability. However for exposures above 0.1 MI, cell death increased by $27.4 \pm 9.26\%$ (P<0.0001). At this MI, wideband emissions were clearly visible in the acoustic emissions' power spectrum, indicating the onset of MB collapse (inertial cavitation). At these MIs, we also confirmed using high frame rate microscopy, that MBs collapsed within the cells. For the exposures employed (MI: 0.02 – 1) , the cell viability in the controls (unlabeled macrophages) did not change significantly ($1.1 \pm 0.89\%$, P=n.s.). Together these data suggest that for MI of 0.02 - 0.1, the MB-labeled macrophages retain both high viability and echogenicity (i.e., associated with stable MB oscillation). Using these settings (MI =0.02) in the experiments with the tissue mimicking gelatin phantom, we observed a 40 fold increase in CNR when we imaged the echogenic macrophages with compounded B-mode, as compared

to unlabeled macrophages. The CNR was further increased by 4-fold when using AMPI. Lastly, we confirmed that the engineered echogenic macrophages could clearly be imaged *in vivo* (7-fold increase in CNR as compared to unlabeled macrophages) following intratumoral injection in subcutaneous tumors.

Conclusions

In this study, we showed that macrophages can be labeled with MB, identified exposure settings where they can retain high echogenicity and viability without affecting their functionality (*in vitro*) and confirmed that they can produce a strong image contrast *in vivo*. Together, these data support the notion that engineered echogenic macrophages can be a viable ultrasound imaging contrast agent. Moving forward, we will assess their ability to infiltrate in tumors following intravenous administration, evaluate their trafficking patterns (density, flux rates) and determine whether this information can provide prognostic and diagnostic information (i.e., cancer biomarkers).

References

[1] M. D. Park, A. Silvin, F. Ginhoux, and M. Merad, "Macrophages in health and disease," *Cell*, vol. 185, no. 23, pp. 4259–4279, Nov. 2022, doi: 10.1016/j.cell.2022.10.007.

[2] M. F. Kircher, S. S. Gambhir, and J. Grimm, "Noninvasive cell-tracking methods," *Nat Rev Clin Oncol*, vol. 8, no. 11, pp. 677–688, Nov. 2011, doi: 10.1038/nrclinonc.2011.141.

Microfluidic lipid-coated monodisperse microbubble formation

Tim Segers

BIOS / Lab on a Chip Group, Max Planck Center Twente for Complex Fluid Dynamics, MESA+ Institute of Nanotechnology, University of Twente, Enschede, The Netherlands
t.j.segers@utwente.nl

Lipid-coated microbubbles driven by ultrasound are fascinating objects rich in nonlinear dynamics [1]. Their intricate ultrasound-driven response is governed by bubble size, viscoelastic coating properties, and ultrasound driving parameters through resonance. Diagnostic and therapeutic applications of bubbles and ultrasound critically rely on bubble dynamics. Therefore, control over microbubble size and coating properties is considered as a promising avenue to enable emerging applications of bubbles and ultrasound such as non-invasive blood pressure sensing, molecular imaging, and controlled and monitorable blood-brain barrier permeabilization [2]. Microfluidics allows the controlled formation of microbubbles by flow-focusing. In a flow-focusing device, a gas thread is focused between a liquid co-flow through an orifice where it destabilizes and pinches off to release monodisperse bubbles. In this talk, I will summarize the current understanding of microfluidic bubble formation following the lifetime of a bubble. The challenges posed by stable monodisperse microbubble formation have brought understanding of lipid adsorption, lipid-coated bubble coalescence, and bubble stabilization through mechanical shell compression via partial diffusive bubble dissolution [3,4]. This understanding now allows the formation of highly stable size-controlled bubble suspensions [5,6], which are an invaluable tool to gain understanding of, e.g., mechanical shell properties [7], ultrasound-imaging sensitivity [8], and cavitation bioeffects. Finally, current challenges in controlled bubble formation for high-precision ultrasound sensing will be discussed.

References

[1]. Versluis, M.; Stride, E.; Lajoinie, G.; Dollet, B.; Segers, T. Ultrasound contrast agent modeling: a review. *Ultrasound Med. Biol.* 382 **2020**, *46*, 2117–2144.

[2]. Frinking, P.; Segers, T.; Luan, Y.; Tranquart, F. Three decades of ultrasound contrast agents: a review of the past, present and 384 future improvements. *Ultrasound Med. Biol.* **2020**, *46*, 892–908.

[3]. Segers, T.; de Rond, L.; de Jong, N.; Borden, M.; Versluis, M. Stability of monodisperse phospholipid-coated microbubbles formed 386 by flow-focusing at high production rates. *Langmuir* **2016**, *32*, 3937–3944. 387

[4]. Segers, T.; Lohse, D.; Versluis, M.; Frinking, P. Universal equations for the coalescence probability and long-term size stability of 388 phospholipid-coated monodisperse microbubbles formed by flow-focusing. *Langmuir* **2017**, *33*, 10329–10339. 389

[5]. Segers, T.; Lassus, A.; Bussat, P.; Gaud, E.; Frinking, P. Improved coalescence stability of monodisperse phospholipid-coated 390 microbubbles formed by flow-focusing at elevated temperatures. *Lab. Chip* **2019**, *19*, 158–167. 391

[6]. Segers, T.; Gaud, E.; Casqueiro, G.; Lassus, A.; Versluis, M.; Frinking, P. Foam-free monodisperse lipid-coated ultrasound contrast 392 agent synthesis by flow-focusing through multi-gas-component microbubble stabilization. *Appl. Phys. Lett.* **2020**, *116*, 173701.

[7]. Segers, T.; Gaud, E.; Versluis, M.; Frinking, P. High-precision acoustic measurements of the non-linear dilatational elasticity of 437 phospholipid coated monodisperse microbubbles. *Soft Matter* **2018**, *14*, 9550.

[8]. Helbert, A.; Gaud, E.; Segers, T.; Botteron, C.; Frinking, P.; Jeannot, V. Monodisperse versus polydisperse ultrasound contrast 391 agents: In vivo sensitivity and safety in rat and pig. *Ultrasound Med. Biol.* **2020**, *46*, 3339–3352.

What's in a name? Micro v. Nanobubbles in Ultrasound Imaging and Therapy

Mihir Sheth[1], Caed Knight[1], Qiang Wu[1], Alexandra Vasilyeva[1], Si Cheng Ma[1], Veerle Brans[1], Luca Bau[1], Nicholas Ovenden[2], Eleanor Stride[1]

[1]*Institute of Biomedical Engineering, University of Oxford, Oxford, UK*
[2]*Department of Mathematics, University College London, London, UK*
Corresponding author: eleanor.stride@eng.ox.ac.uk

Introduction

Microbubbles (1-10 μm in diameter) were initially developed as contrast agents for use in ultrasonic imaging due to their echogenicity and have subsequently been investigated in a range of therapeutic applications. Drawbacks of microbubbles include their relatively short circulation half-lives and inability to extravasate. Consequently, various sub-micrometre particles have been investigated in both diagnostic and therapeutic applications. Gas "nano" bubbles with diameters <1 μm have been widely explored and reported as being able to extravasate whilst remaining visible to conventional ultrasound imaging[1,2]. "Nano"bubbles have also been reported as effective agents for numerous therapeutic applications, e.g., for blood brain barrier permeabilisation, drug delivery and mechanical ablation. These results are surprising as theory suggests that sub-micrometre particles should not be able to exhibit comparable performance under the same ultrasound exposure conditions as microbubbles as either diagnostic or therapeutic agents. There is considerable variability, however, in the definition of "nano"bubbles in published studies and a wide range of techniques used to determine their size and concentration[3,4].

We investigated the following hypotheses to explain the observed acoustic responses from "nano"bubble suspensions: (i) the presence of pre-existing microbubbles as proposed by Myers et al. (2022)[3] (ii) coalescence resulting in the formation of microbubbles over time (iii) changes in the characteristic acoustic impedance of "nano"bubble suspensions at high bubble concentrations (iv) nonlinear propagation through high concentration bubble suspensions and/or (v) inconsistencies between expected and actual bubble size distributions and concentrations arising from challenges associated with measuring highly polydisperse bubble suspensions.

Methods

The acoustic responses of bubbles with diameters from 100nm to 10μm were modelled using a Rayleigh-Plesset type equation via both numerical and analytical solutions and these data were used to predict the attenuation and speed of sound in a bubble suspension[5]. Experimentally, several formulations of microbubbles (MB) and "nano"bubbles (NB) were fabricated[2,6]. These were then characterized with multiple methods: sub-micrometre bubble size was measured using Dynamic Light Scattering (DLS) on a ZetaSizer (Malvern, UK) and Transmission Electron Microscopy (TEM FEI Tecnai T12) using uranyl acetate staining. Micrometre and sub-micrometre bubble size and concentration were measured by Coulter Counter (Multisizer), light microscopy using a 40x objective (Leica, UK), or Nanoparticle Tracking Analysis using both Videodrop (Myriade, France) and Nanosight NT 300 (Malvern, UK) systems. Bubble suspensions were also imaged in both B-mode and contrast mode using a clinical ultrasound system with a 5-12MHz diagnostic ultrasound imaging probe (Philips L12-5A), and bubble oscillations were captured using high-speed imaging at 1 million frames per second (Shimadzu HPVx2) when driven at 0.5 MHz with peak negative pressures up to 1 MPa.

Results

Experimentally, there were considerable differences in the measured size distributions recorded from the different instruments. For NB, the modal diameter measured by the ZetaSizer was 200nm, by the Videodrop it was 235nm whilst the Nanosight reported 100nm. TEM indicated a range of sizes from 10s to 100s of nanometres, but it was not possible to obtain a sufficient number of images to generate a statistically meaningful size distribution. There was better agreement in the concentration measurements from the Videodrop and the Nanosight for the NB (1.94×10^{12} particles/ml and 8×10^{12} particles/ml respectively). None of these methods indicated the presence of any bubbles larger than 1 μm. Much better agreement was obtained for MB diameter measurements between the Multisizer and light microscopy than between the DLS, Nanosight and Videodrop, but neither is suitable for detecting bubbles smaller than ~500nm. These results are supportive of hypotheses (i) and (v) consistent with Myers et al (2022)[3].

Bubble stability was measured by recording the size distribution and concentration over time. The size and concentration of NBs were found to decrease by 18.5% and 19% respectively across 3 days when stored at 4°C (Figure 1) but there was no evidence of rapid coalescence at either 20°C or 37°C when measurements were taken over 20 minutes in the Videodrop and NTA systems. Preliminary theoretical modelling of coalescence probability supported these findings, suggesting that hypothesis (ii) is not valid.

As expected, theoretical modelling predicted a substantial difference in scattering and attenuation coefficients between MB and NB for both linear and nonlinear propagation, with measurable scattering only being predicted at very high bubble concentrations for bubbles smaller than 400nm or frequencies above 15MHz. These results were in good agreement with the experimental ultrasound measurements. Negligible image contrast was observed under either B-mode or contrast imaging from NB suspensions, suggesting that neither hypothesis (iii) and (iv) was correct (Figure 2). Similarly, negligible bubble activity was observed under high-speed imaging from NB suspensions under exposure conditions associated with therapeutic applications and under which inertial cavitation was observed with MB.

Conclusions

The results of this study support the findings of Myers et al. that it is very difficult to accurately size a highly polydisperse bubble suspension and therefore difficult to produce bubble suspensions containing only bubbles of a particular size range without repeated filtration and/or centrifugation. There was no evidence to support the hypotheses of NB coaelscence or nonlinear effects at high NB concentrations being responsible for reported acoustic responses in either diagnostic or therapeutic applications. Whilst NB may offer advantages in terms of circulation time, extravasation and/or cellular fusion, higher pressure amplitudes and/or frequencies will be required to elicit an acoustic response and this may have important implications for bioeffects. The limitations of available bubble sizing methods need to be carefully considered in experimental design to avoid misinterpretation of results and to avoid errors in dose estimation. There is also a pressing need for a consensus on nomenclature for MB and NB as the latter currently encompass bubbles from 100-800nm, but this may correspond to a wide range of different bubble dynamics depending on the ultrasound exposure parameters.
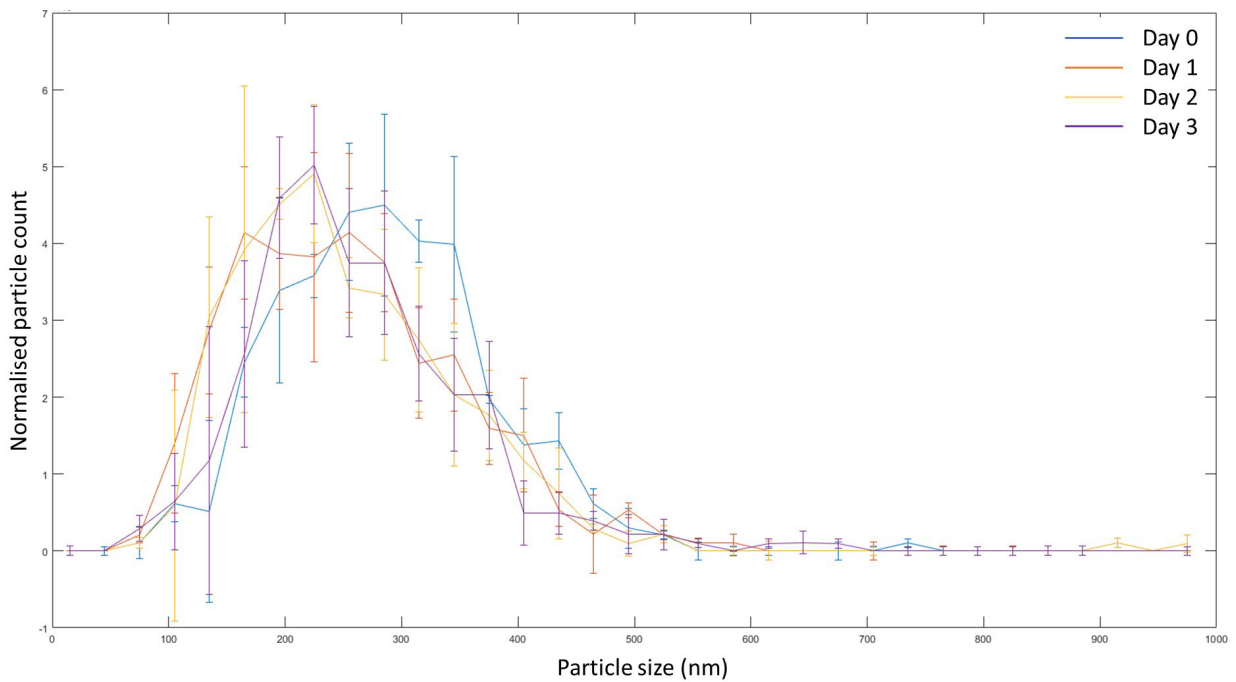
Figure 1. Size distribution of "nano"bubbles across multiple days (n=3, error bars represent standard deviation). There is a decrease in size and a more defined peak as the sample gets older but no evidence of substantial coalescence.
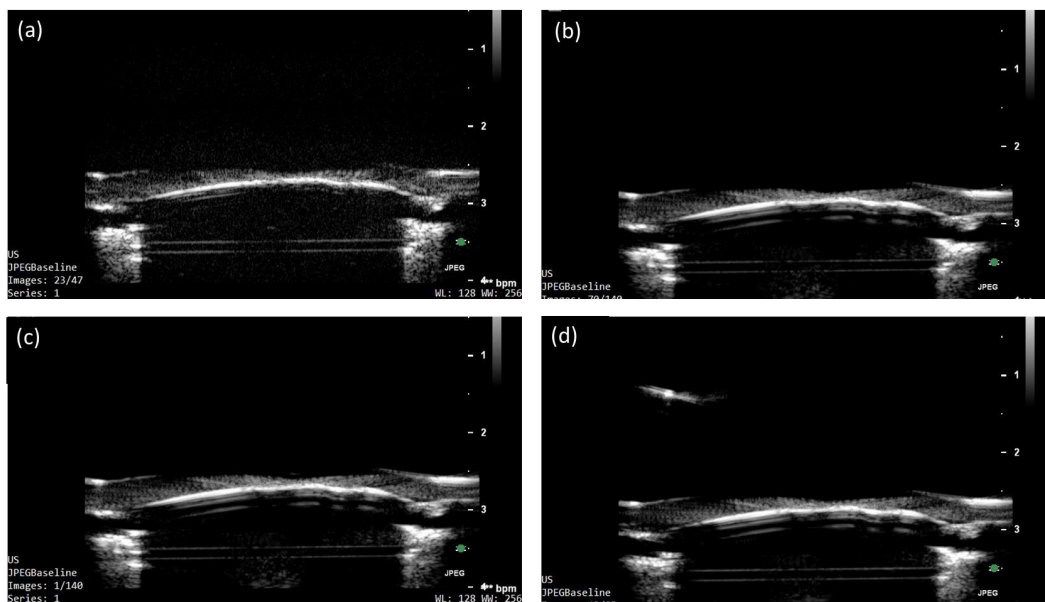
Figure 2. Images showing negligible detection of Contrast and B-Mode Ultrasound responses of water and "nano"bubbles in a tissue mimicking phantom. (a) and (b) show Contrast and B-Mode Ultrasound response of Milli-Q filtered water respectively. (c) and (d) shows Contrast and B-Mode Ultrasound response of NB suspensions respectively.

References

[1]. Owen J, Logan K, Nesbitt H, et al. Orally administered oxygen nanobubbles enhance tumor response to sonodynamic therapy. Nano Select. 2022;3(2):394-401.

[2]. Owen J, McEwan C, Nesbitt H, et al. Reducing Tumour Hypoxia via Oral Administration of Oxygen Nanobubbles. PLoS One. 2016;11(12):e0168088.

[3]. Myers JZ, Navarro-Becerra JA, Borden MA. Nanobubbles are Non-Echogenic for Fundamental-Mode Contrast-Enhanced Ultrasound Imaging. Bioconjug Chem. 2022;33(6):1106-1113.

[4]. de Leon A, Perera R, Hernandez C, et al. Contrast enhanced ultrasound imaging by nature-inspired ultrastable echogenic nanobubbles. Nanoscale. 2019;11(33):15647-15658.

[5]. Ovenden NC, O'Brien JP, Stride E. Ultrasound propagation through dilute polydisperse microbubble suspensions. J Acoust Soc Am. 2017;142(3):1236.

[6]. Browning RJ, Aron M, Booth A, et al. Spectral Imaging for Microbubble Characterization. Langmuir. 2020;36(2):609-617.

Viscosity measurements and rheology modelling of phospholipid-coated microbubbles

Marco Cattaneo, Outi Supponen

Institute of Fluid Dynamics, ETH Zürich, Zürich, Switzerland
Corresponding author: mcattaneo@ethz.ch

Introduction

Understanding the shell rheology of ultrasound contrast agent microbubbles is vital for anticipating their bioeffects in the clinical practice. Pioneering studies using sophisticated acoustic techniques first, and optical techniques later have made enormous progress in this direction [1-5], allowing for development of shell models able to adequately reproduce the nonlinear behavior of the bubble [6-7]. However, the puzzling radius dependecy of shell viscosity [4,5,9-11] demands further rheological investigation. In this study, we use ultra-high speed microscopy imaging and optical trapping to investigate individual microbubble response to ultrasonic driving across a range of bubble sizes. The shell dilatational viscosity is inferred from the maximum radial expansion of the bubble. The results suggest that the dependency of the shell viscosity on the bubble resting radius found in previous works may be an artifact of the experimental methodology used. We hypothesise that the large, one order of magnitude variance in bubble viscosity reflects the arbitrariness of the size and distribution of phospholipid domains among bubbles.

Methods

A custom-designed 3D-printed test chamber with optically and acoustically transparent windows on top and bottom (LDPE, acoustic impedance $z = 1.79$) is suspended in a water bath (T $\approx$ 22 ℃) filled with deionised water, and positionally-controlled by a motorised 3D microtranslation stage. Lipid-coated (DPPC and DPPE-PEG5K at a molar ration 9:1) gas (C_4F_{10}) microbubbles manufactured in-house ($2 - 4$ μm) are injected at a very low dilution ratio in the test chamber and let adhere to the top window by flotation. Single bubbles are optically trapped and moved away from the top window of the test chamber by $\sim$50 μm using a custom-built holographic optical tweezers setup (Verdi G10, Coherent, as trapping laser; PLUTO-2.1 VIS-096, HOLOEYE Photonics, as spatial light modulator) in order to avoid wall interferences. The microbubbles are sonicated (20-cycle sinusoidal pulse at 1.5 MHz and with 40 kPa of peak negative pressure) with a focused ultrasound transducer (PA1612, Precision Acoustics) connected to a manual 3D microtranslation stage for alignment. The ultrasound transducer is positioned with an angle of 30° with respect to the horizontal plane to minimise acoustic reflections. The bubble dynamics is recorded using a custom-built microscope equipped with a f = 2 mm water-immersion microscope objective (CFI Plan 100XC W, Nikon) and a f = 400 mm tube lens (TL400-A, Thorlabs) for a total magnification of 200X. The optical trap is deactivated during the recording by using a microsecond-fast optical shutter based on an acousto-optic modulator (AOTF.NC-VIS/TN, AA Opto Electronic). A calibrated needle hydrophone (0.2 mm, Precision Acoustics) is used to measure the acoustic pressure inside the test chamber and to align the acoustic focal point with the optical field. Recordings at 10 million frames per second are performed using an ultra-high-speed camera (HPV-X2, Shimadzu), allowing for a continuous visualization over 25.6 μs with a 160 nm-pixel resolution. Backlight illumination is provided by two Xenon strobe lamps used sequentially and focused on the sample through a custom-built condenser. Radius-time curves are extracted from the recordings using a feature extraction image processing algorithm.

Results

In Figure 1, the optically-measured maximum radial expansion of single bubbles as a function of the bubble resting radius (red dots) is compared with the computed one (black lines) using the Marmottant model [8] and shell dilatational viscosity values of $\kappa_s = 1 \cdot 10^{-9}$ kg/s and $4 \cdot 10^{-8}$ kg/s. The good agreement between the measured and the modelled maximum bubble expansion suggests the following: i)

the bubble radial expansion shows a great variability that can be explained by a large variance in the shell dilatational viscosity; ii) the fitting shell viscosity is independent from the bubble resting radius.

These results are in contrast with previous studies that have reported a smaller scatter in shell viscosity and a significant dependency of the shell viscosity on the bubble resting radius [4,5,9-11]. The latter behaviour is believed to be unphysical, nevertheless it has thus far never been either explained or proven as such. In light of the results presented above, we believe that it may be an artifact caused by the microbubble spectroscopy method employed in those studies.
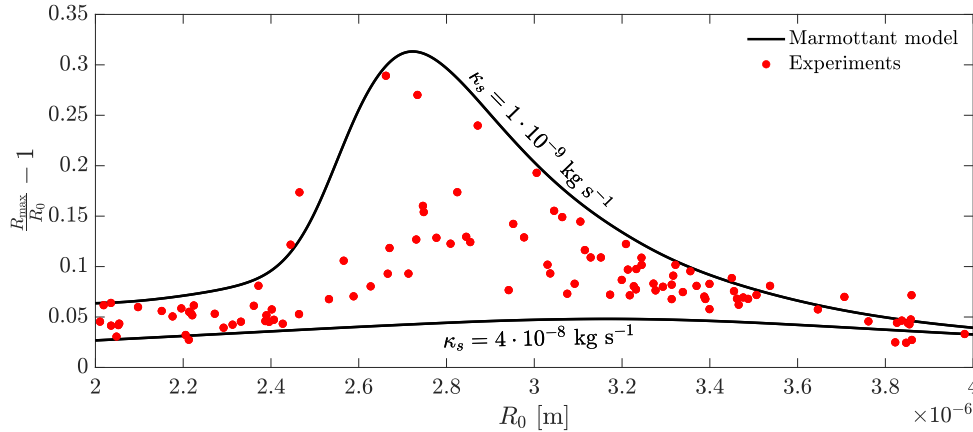
Figure 1: Comparison of optically measured (red dots) and computed (black lines) maximum radial expansion, normalised to R_0, as a function of the bubble resting radius.

The microbubble spectroscopy method was first proposed by [4] and enables to estimate the shell viscosity from the half-power bandwidth of the microbubble frequency response function considering the microbubble as a damped linear oscillator. The microbubble frequency response function can be reconstructed by scanning through a range of driving frequencies [4,5,9,10] or directly acquired using impulsive driving [11]. It can be shown that if the experimental half-power spectral widths are affected by a systematic over-estimation error Δf_{err}, the estimated shell viscosities are impacted by an amount:

$$\kappa_{s,\text{err}} \approx \frac{\pi}{2} \rho R_0^3 \Delta f_{\text{err}}.$$

It is clear that the cubic dependency of such error on the resting bubble radius has major consequences on the shell viscosity estimation, which results in even small systematic errors on the spectral width yielding significant variations in the shell viscosity across a range of bubble sizes. Figure 2(a) shows how an error $\Delta f_{\text{err}} = 200$ kHz inflates the shell viscosity estimate, gives rise to a strong dependency on the initial radius and shrinks the shell viscosity variance. The bandwidth over-estimation can be caused by different factors: large frequency steps when scanning through frequencies, short observation time of the bubble dynamics, nonlinear bubble dynamics, etc. Figure 2(b) shows the departure of the shell viscosity estimates from the true values when using the experimental parameters employed by [2] (scan frequency interval $\Delta f_{\text{scan}} > 50$ kHz, observation time $T_{\text{obs}} \approx 4.2$ μs, peak negative pressure $P_a = 40$ kPa).

Phospholipid monolayers can generate close-zero surface tension values at gas-water interface by forming a two-dimensional polydomain liquid crystal with different tailgroup orientations. The variability in shell viscosity can be rooted in the arbitrariness of the size and distribution of such phospholipid domains on the bubble interface. The edge of the domains, where phospholipids with different tailgroups interact with each other, can be considered as defects of the bubble shell. A larger amount of defects results in more frequent interactions between phospholipids with different tailgroups orientations which, in turn, could yield a higher shell viscosity [12].

Conclusions

This experimental study utilising ultra-high speed microscopy imaging and optical trapping reveals no dependency of the shell dilatational viscosity on the bubble resting radius. These results are in contrast with

previous studies using bubble spectroscopy which have instead reported such a dependency. We believe that this trend is caused by an over-estimation of the half-power spectral bandwidth that inflates the estimates of the shell viscosity proportionally to the cube of the microbubble resting radius. Our experimental results also reveal a large variability in the shell viscosity that may lead to unexpectedly strong bubble oscillations and, by extension, violent bioeffects. We hypothesise that this variability reflects the arbitrariness of the size and distribution of phospholipid domains among bubbles.
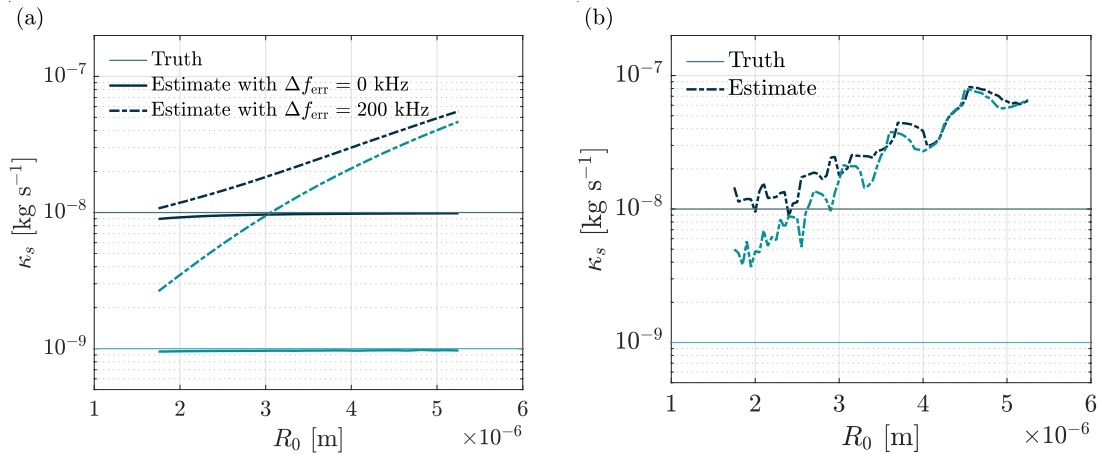
Figure 2: (a) Effect of a systematic error in the spectral width on the estimation of the shell viscosity over a range of bubble sizes. (b) Shell viscosity estimate employing the experimental parameters used in [2].

Acknowledgments

References

[1]. de Jong N, Hoff L, Skotland T, Bom N, Absorption and scatter of encapsulated gas filled microspheres: Theoretical considerations and some measurements, Ultrasonics 30 (2) 95–103, 1992.

[2]. Gorce J-M, Arditi M, Schneider M, Influence of bubble size distribution on the echogenicity of ultrasound contrast agents: A study of sonovue(TM), Investigative Radiology, 35 (11) 661–671, 2000.

[3]. Morgan K, Allen J S, Dayton P A, Chomas J E, Klibanov A L, Ferrara K W, Experimental and theoretical evaluation of microbubble behavior: effect of transmitted phase and bubble size, IEEE Transactions on Ultrasonics, Ferroelectrics, and Frequency Control, 47 (6) 1494–1509, 2000.

[4]. van Der Meer S, Dollet B, Voormolen M, Chin C, Bouakaz A, De Jong N, Versluis M, Lohse D, Microbubble spectroscopy of ultra-sound contrast agents, Journal of the Acoustical Society of America, 121 (1), 2007.

[5]. Lum J, Stobbe D, Borden M, Murray T, Photoacoustic technique to measure temperature effects on microbubble viscoelastic properties, Applied Physics Letters 112 (11), 2018.

[6]. Church C, The effects of an elastic solid surface layer on the radial pulsations of gas bubbles, Journal of the Acoustical Society of America, 97 (3) 1510–15, 1995.

[7]. Chatterjee D, Sarkar K, A Newtonian rheological model for the interface of microbubble contrast agents, Ultrasound in Medicine and Biology, 29 (12) 1749–1, 2003.

[8]. Marmottant P, Van Der Meer S, Emmer M, Versluis M, De Jong N, Hilgenfeldt S, Lohse D, A model for large amplitude oscillations of coated bubbles accounting for buckling and rupture, Journal of the Acoustical Society of America, 118 (6) 3499–3505, 2005.

[9]. Luan Y, Faez T, Gelderblom E, Skachkov I, Geers B, Lentacker I, van der Steen T, Versluis M, de Jong N, Acoustical Properties of Individual Liposome-Loaded Microbubbles, Ultrasound in Medicine and Biology, 38 (12), 2174–2185, 2012.

[10].   van Rooij T, Luan Y, Renaud G, van der Steen A, Versluis M, de Jong N, Kooiman K, Non-linear Response and Viscoelastic Properties of Lipid-Coated Microbubbles: DSPC versus DPPC, Ultrasound in Medicine and Biology, 41 (5) 432–1445, 2015.

[11].   Daeichin V, Inzunza-Ibarra M, Lum J, Borden M, Murray T, Photoacoustic Impulse Response of Lipid-Coated Ultrasound Contrast Agents, IEEE Transactions on Ultrasonics, Ferroelectrics, and Frequency Control, 68 (6) 2311–2314, 2021.

[12].   Hermans E, Vermant J, Interfacial shear rheology of DPPC underphysiologically relevant conditions, Soft Matter, 10 (1) 175–186, 2014.

The initial size of a monodisperse microbubble plays a large role in pore and tunnel formation in endothelial cells

Yuchen Wang[1], Hongchen Li[1], Bram Meijlink[1], Robert Beurskens[1], Antonius F. W. van der Steen[1,2], Benjamin R. G. Johnson[3], Klazina Kooiman[1]

[1] *Department of Biomedical Engineering, Thoraxcenter, Erasmus MC, Rotterdam, the Netherlands*
[2] *Section of Medical Imaging, Department of Imaging Physics, Delft University of Technology, 2628 CD Delft, the Netherlands*
[3] *Molecular and Nanoscale Physics Group, School of Physics and Astronomy, University of Leeds, Leeds LS2 9JT, United Kingdom*
Corresponding author: y.wang@erasmusmc.nl

Introduction

Endothelial cells lining the blood vessel wall form a biological barrier that prevents numerous drugs from being efficiently delivered to extravascular targets. To overcome this challenge, phospholipid-coated microbubbles (MBs) combined with ultrasound can locally enhance drug delivery. Drugs can be delivered by oscillating MBs through for example cell membrane permeation, tunnel formation, cell-cell contact opening and endocytosis [1, 2]. However, the different MB sizes in polydisperse MBs contribute to different drug delivery outcomes [2]. We aimed to study the single endothelial cell-MB interactions using monodisperse MBs with radius ranging from 1.25 to 3 μm, focusing on pore and tunnel formation.

Methods

Monodisperse MBs with a C_4F_{10} gas core were coated with a lipid mixture containing DSPC and DSPE-PEG5000 mixed at 9:1 molar ratio. Lipid dye DiD was added to fluorescently label the MBs coating before production. The monodisperse MBs were produced in a flow-focusing device using the microfluidic platform Horizon [3]. Different microbubble sizes were obtained by adjusting the flow rate and gas pressure. Coulter Counter was used to measure the MBs size distribution.

Human Umbilical Vein Endothelial Cells (HUVECs) were grown to confluency in a CLINIcell. Fluorescent dyes were added to stain the HUVECs for live confocal microscopy imaging. The cell membranes were stained with CellMask Green, Hoechst was added to stain cell nuclei, and propidium Iodide (PI) was added to detect sonoporation events. A final concentration of 3.75×10^4 MBs/ml of microbubbles was added. The CLINIcell was then inverted and immersed in a 37 °C water bath. A Z-stack was first performed to visualize the microbubble-cell morphology in 3D. Subsequently, a time-lapse confocal imaging started ~30s before ultrasound (2 MHz, 200 kPa PNP, single 10-cycle burst) and continued for 3.5 min after US. During insonification, the MB dynamic was recorded with an ultra-high-speed camera (Shimadzu HPV-X2) at 10 Mfps. After the time-lapse imaging, another Z-stack was acquired. Using a customized MATLAB script, the MB excursion amplitudes ($R_{max} - R_0$) and excursion ratio ($R_{max} - R_{min}/R_0$) (R=radius) were determined from the obtained radius-time curves of the oscillating MBs.

Results

Typical examples of cellular responses are presented in Fig. 1, containing selected frames of confocal microscopy time-lapse imaging and the radius-time curve of the oscillating MB. Fig. 1A is a typical example of PI uptake and resealing pore. After ultrasound, the PI signal was detected and membrane perforation was identified. The perforation area increased to maximum during the first ~17s and gradually resealed after 30s, which was also comfirmed by the Z-stack imaging. In Fig. 1B a typical example of PI uptake and non-resealing pore is shown. After ultrasound, the pore was created next to the microbubble and remained open throughout the rest of the recording. The final Z-stack imaging shows that the basal membrane was still present, suggesting that only the apical membrane was perforated. Fig. 1C is a typical example of PI uptake

with a tunnel formation. After ultrasound insonification, a pore was created on the cell membrane that did not reseal throughout the recording. Different from the example shown in Fig. 1B, the Z-stack imaging shows that both the apical and basal membrane had been perforated, which resulted into a transcellular perforation.
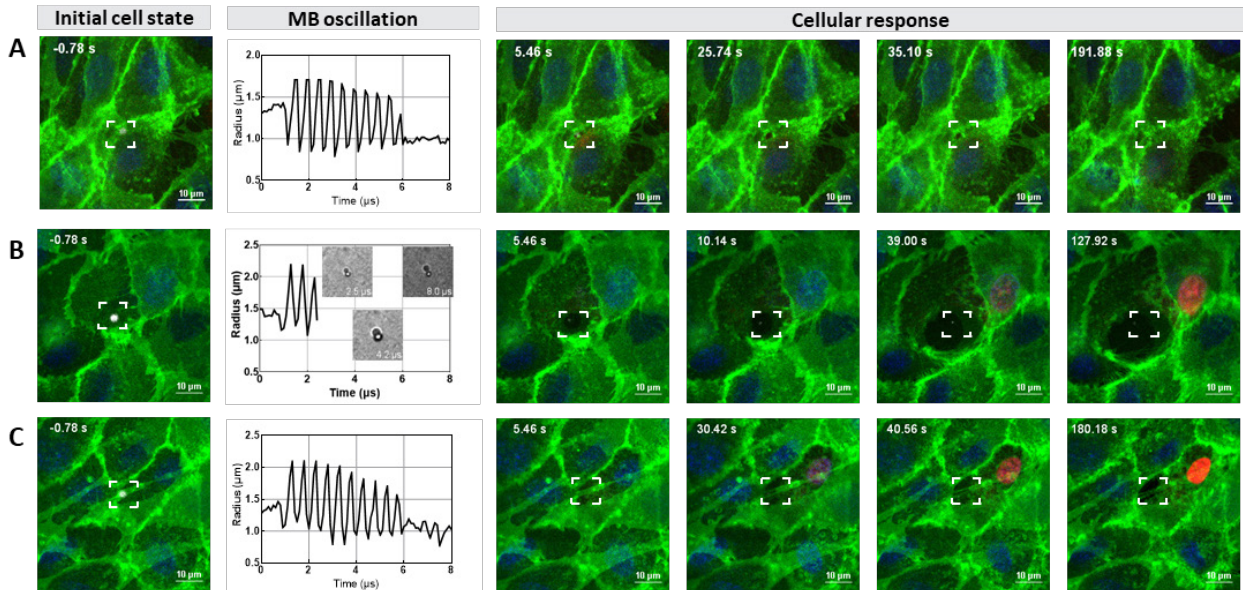
Figure 1. Typical examples of microbubble mediated-drug delivery by pores and tunnels. A) PI uptake and a resealing pore. B) PI uptake and a non-resealing pore. C) PI uptake and distinguishable membrane perforation identified as a tunnel. For every example the images from left to right show: initial cell state before ultrasound; the microbubble radius-time curve obtained from the ultra-high-speed imaging during ultrasound; four selected frames of confocal microscopy time-lapse imaging after ultrasound

Fig. 2A shows the occurrence of four distinct cellular responses for monodisperse MBs of different sizes: no PI uptake, PI uptake with a resealing pore, PI uptake with a non-resealing pore, and PI uptake with tunnel formation. The 1.25 µm MBs resulted in the highest occurrence rate (46.6%) of PI uptake and tunnel formation, while the 1.5 µm MBs induced PI uptake and resealing pore (50%) more often compared to the other MBs sizes. Note that the 3 µm MBs only had a 4.2% occurrence of PI uptake and tunnel formation, while the 3.5 µm MBs induced no cellular response.

The excursion amplitude as a function of the initial microbubble radius is plotted for each cellular responses (Fig. 2B). Insonifying these microbubbles resulted in excursion amplitudes ranging from 0.1 µm to 1.1 µm. Note that for some microbubbles with similar initial radius, their excursion amplitudes varied, and therefore induced different cellular responses. As plotted in Fig. 2C, the microbubble excursion can also be quantified by the ratio of the excursion amplitude to the initial radius ($R_{max} - R_{min}/R_0$). The excursion ratio ranged from 0.14 to 0.82 and seems to separate the tunnel formation data points from other cellular responses.
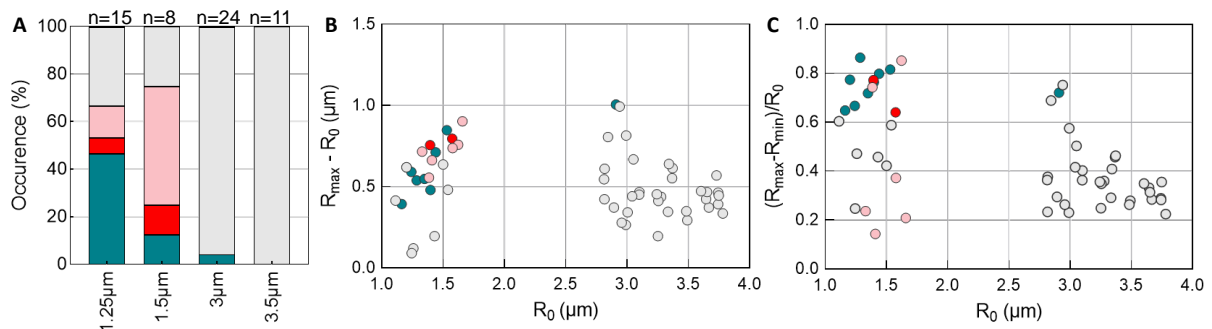
Figure 2. Cellular responses upon microbubble oscillation: no PI uptake (gray), PI uptake with resealing pore (pink), PI uptake with non-resealing pore (red) and PI uptake with tunnel formation (dark green). A) Occurrence of PI uptake and cellular responses at different monodisperse microbubble populations with

initial microbubble size in radius B) Microbubble excursion amplitude (R_{max} - R_{min}) as a function of the initial microbubble radius for each cellular response. C) Microbubble excursion (R_{max} - R_{min}/R_0) as a function of the initial microbubble radius for each cellular response.

Conclusions

Evaluating the morphology of the cell membrane revealed that monodisperse microbubble oscillation either caused pore formation with perforation of the apical membrane only, or tunnel formation with perforation of both the apical and basal membrane. Furthermore, we found that (R_{max} - R_{min}/R_0) correlated better with the occurrence of PI uptake and cellular responses than (R_{max} - R_0) for monodisperse microbubbles. This is different from polydisperse microbubbles since there was no significat difference between (R_{max} - R_{min}/R_0) and (R_{max} - R_0) for predicting the drug delivery outcome [4]. These observations show the differences in cellular response depending on the initial MB sizes and underlines the importance of using the appropriate monodisperse MB size for future applications of microbubble-mediated drug delivery.

References

[1]. Kooiman, K., S. Roovers, S.A.G. Langeveld, R.T. Kleven, H. Dewitte, M.A. O'Reilly, J.M. Escoffre, A. Bouakaz, M.D. Verweij, K. Hynynen, I. Lentacker, E. Stride, and C.K. Holland, Ultrasound-Responsive Cavitation Nuclei for Therapy and Drug Delivery. Ultrasound Med Biol, 2020. 46(6): p. 1296-1325.

[2]. Beekers, I., S.A.G. Langeveld, B. Meijlink, A.F.W. van der Steen, N. de Jong, M.D. Verweij, and K. Kooiman, Internalization of targeted microbubbles by endothelial cells and drug delivery by pores and tunnels. J Control Release, 2022. 347: p. 460-475.

[3]. Abou-Saleh, R.H., F.J. Armistead, D.V.B. Batchelor, B.R.G. Johnson, S.A. Peyman, and S.D. Evans, Horizon: Microfluidic platform for the production of therapeutic microbubbles and nanobubbles. Review of Scientific Instruments, 2021. 92(7): p. 074105.

[4]. Beekers, I., M. Vegter, K.R. Lattwein, F. Mastik, R. Beurskens, A.F.W. Van Der Steen, N. De Jong, M.D. Verweij, and K. Kooiman, Opening of endothelial cell–cell contacts due to sonoporation. Journal of Controlled Release, 2020. 322: p. 426-438.

Investigation of Cardioprotective Efficacy of Nitrofatty Acid Microbubbles (NFABs) in Rat Myocardial Ischemia Reperfusion Injury Model

Muhammad Wahab Amjad[1], **Soheb Anwar Mohammed[1], MarcoFazzari[2], Xucai Chen[1], Bruce A. Freeman[2], Terry O. Matsunaga[3], John J. Pacella*[1]**

[1]*Center for Ultrasound Molecular Imaging and Therapeutics, Heart and Vascular Medicine Institute, University of Pittsburgh, Pittsburgh, PA, USA*
[2]*Department of Pharmacology and Chemical Biology, School of Medicine, University of Pittsburgh, Pittsburgh, PA, USA*
[3]*Department of Biomedical Engineering and Department of Medical Imaging, University of Arizona, Tucson, AZ, USA*
Corresponding author: pacellajj@upmc.edu

Introduction/ Background

In 2019, 17.9 million people died from cardiovascular diseases; 85% of which were due to acute myocardial infarction (MI) [1]. Post-MI congestive heart failure is increasing due to microvascular obstruction (MVO). MVO is the blockage of the microcirculation by thrombi and tends to occur after coronary stenting for acute MI, resulting in hypoperfusion. Current therapeutic strategies for MVO are not consistently effective. Hence, we have been developing ultrasound (US)-targeted microbubble cavitation (UTMC) as a potential treatment for MVO. In its current form, UTMC only mechanically restores the blood flow in the obstructed vessels by disintegrating the microtrombi; it does not address the accompanying harmful oxidative stress and inflammation. Nitro-fatty acids (NFA) pleiotropically modulate cell signaling and inflammatory cell responses, resulting in antioxidant, anti-inflammatory and cytoprotective actions [2]. All these responses are relevant to the prevention and treatment of MVO. In our prior study, we developed US-guided NFA-loaded microbubbles (NFABs) to treat ischemia-reperfusion (IR) in rat hindlimb model. We demonstrated that NFABs UTMC resulted in the greatest improvement in perfusion and the greatest reduction in proinflammatory cytokine gene expression, demonstrating the promise of this technique. Herein, we apply this theraptuetic strategy to treat IR in the rat myocardial model.

Methods

We developed rat cardiac ischemia reperfusion injury model. Briefly, rats were anesthetized, intubated, and kept on ventilator. Baseline echocardiography (short axis) was taken (Vevo 2100) and left anterior descending (LAD) coronary artery was ligated. During ligation, echocardiography was recorded. The LAD ligation was released at 30 min, allowing for reperfusion. NFABs were infused intravenously for 15 min in the presence of rapid short US pulses generated by a transducer positioned over the chest covering the heart. Post-treatment echocardiography was recorded at 1.5 h, followed by euthanization of rats and collection of tissues and blood. Left ventricular fractional shortening (%) was calculated from the echocardiography data. Cardiac tissue concentration of NFA was determined using liquid chromatography-mass spectrometry (LCMS).

Results

Left ventricular fractional shortening (%) at baseline, during LAD ligation and post-treatment were calculated for all the groups in rat myocardial ischemia reperfusion injury study. NFABs+UTMC outperformed free NFA and other groups. The increase in the fractional shortening post-treatment was highest in NFAB+UTMC group (Figure 1).
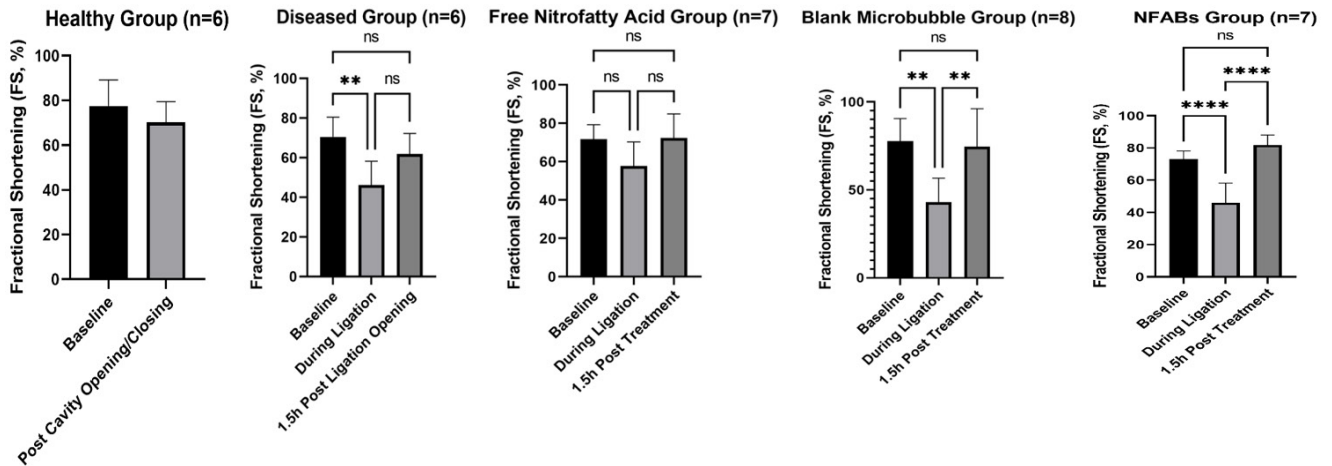
Figure 1. Fractional Shortening (%) changes among different groups during LAD ligation and post-treatment in myocardial ischemia reperfusion injury model.

NFABs+UTMC exhibited targeted myocardial NFA delivery in rats. The concentration of NFA in the heart was significantly higher than in the left gastrocnemius muscle of rats. In free NFA group, the concentration of NFA in heart was significantly lower than that exhibited by NFABs (Figure 2).
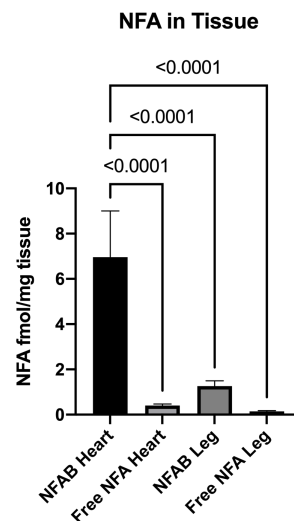
Figure 2. Focal tissue concentration of NFA.

Conclusions

Initial findings from rat myocardial ischemia reperfusion injury study are promising. NFABs exhibited promising efficacy in improving fractional shortening post IR and in targeted delivery of NFA to heart. Studies assessing ejection fraction, myocardial area at risk, histopathology, inflammatory burden, oxidative stress and cytoprotective biomarkers are underway.

References
[1]. World Health Organization, Cardiovascular diseases (CVDs) key facts, (2021).

[2]. N.K. Khoo, L. Li, S.R. Salvatore, F.J. Schopfer, B.A. Freeman, Electrophilic fatty acid nitroalkenes regulate Nrf2 and NF-κB signaling: A medicinal chemistry investigation of structure-function relationships, Sci Rep. 8 (2018) 2295.

Investigation of the ultrasound-mediated toxicity mechanisms of various sonosensitive drugs

Kritika Singh[1,2], Alexandra Vasilyeva[1], Michael Gray[1], Eleanor Stride[1]

[1]_Institute of Biomedical Engineering, Department of Engineering Science, University of Oxford, Oxford, UK_
[2]_Laboratory of Cellular Oncology, Center for Cancer Research, NCI, Bethesda, MD, USA._
Corresponding author: Eleanor.stride@eng.ox.ac.uk

Introduction

Cancer is the second leading cause of death and, in 2018, resulted in 18 million cases and 9.6 million deaths worldwide. According to the World Health Organization, 70% of deaths from cancer occur in low- and middle- income countries (LMICs) where health systems are already overburdened and not as prepared to manage the increasing cancer cases[1]. For this and many other reasons, there is a pressing need to develop novel platforms for cancer therapeutics that are efficient, reduce side effects for patients, and are minimally invasive. One such platform is photodynamic therapy (PDT) where light is used as an external stimulus to activate drugs at a target location. However, PDT's clinical applications are limited due to poor light penetration in tissue. Multiple studies have shown that ultrasound with or without cavitation nuclei (microbubbles) can also be used to activate photodynamic drugs, however the mechanism of this activation remains unclear. Ultrasound has the additional advantage of having a well-known safety profile and has been shown to promote drug extravasation. Despite these clear advantages, ultrasound-mediated drug activation, or sonodynamic therapy (SDT), has yet to be adopted clinically and there are few phase II+ clinical trials. A key reason for this is the lack of understanding of a consolidated mechanism to explain "sonosensitive" drug activation[2].

The majority of PDT drugs generate reactive oxygen species (ROS) when actived by light and many studies have reported ROS production when the same drugs are exposed to ultrasound, with or without microbubbles. Multiple questions remain, however, regarding the mechanism of ROS generation, the types of ROS produced, and whether the quantities are sufficient to promote cell killing[3]. The high levels of reported cell kill in both in vitro and in vivo experiments are particularly surprising given the short range of action of ROS. Answering these questions is unfortunately not straightforward due to the multiple types of ROS generated, the effect of ultrasound on chemical ROS sensors (e.g. singlet oxygen sensor green (SOSG) undergoes self-activation when exposed to ultrasound[4,5]), and the very wide variety of ultrasound parameters and setups used in different studies.[6] Moreover, ultrasound can produce a wide variety of effects in tissue such as heating, enhanced extravasation of drugs[7,8] and cell permeabilization (sonoporation)[9]. The vast majority of studies on SDT neglect the potential role of sonoporation in mediating cell death. Here, however, we hypothesise that intracellular drug uptake may contribute to the toxicity of SDT and potentially explain the high levels of cell kill observed for comparatively low concentrations of ROS.

Methods

A schematic of the ultrasound exposure chamber used in this study[10] is shown in Fig.1 and comprises a water bath containing a 1 MHz focused ultrasound transducer (Imasonic 8233 A101, Imasonic SAS, France) and 7.5 MHz passive cavitation detector (7.5MHz center frequency, Olympus V320, Olympus, UK) into which a cell culture chamber can be immersed. The 1 MHz transducer was driven by a waveform generator (Agilent 33250A, Agilent Technologies, USA; amplifier ENI300, Electronic Navigation Industries, USA) and a power amplifier (generator Agilent 33250A, Agilent Technologies, USA; amplifier ENI A300, Electronic Navigation Industries, USA, or 1140LA, Electronics & Innovation, Ltd., USA). The output of the amplifier was monitored with a high voltage probe connected to an oscilloscope (Teledyne LeCroy, USA). A 2 MHz high-pass filter (2 MHz, Allen Avionics, Inc., USA, or 1.8 MHz, ThorLabs, USA) was also used to remove the drive frequency from the PCD signal which was then preamplified 5x (SR445A, SRS, Sunnyvale, USA) and recorded using a second oscilloscope (TiePie HS3 or HS5 depending on experiment, TiePie engineering, The Netherlands). The final ultrasound parameters used were 250 kPa pk-

----

pk spatial average over the cell dish surface, 30% duty cycle, 10Hz PRF, for 30 seconds. Multiple cell lines were tested including A549s, HeLas, CT26, and GFP-VE (ATCC). SDT drugs tested included Rose Bengal, IR780 iodide, ICG, and IR700. The concentrations of drug tested were kept at 5uM and the concentration of microbubbles were kept constant at 8 x 10^6 MBs/ml (DPBC-PEG40S PFB MBs). To determine whether sonoporation had an effect on drug action, the time at which the drug was administered was varied. In one group it was added during ultrasound exposure, in a second it was added immediately after ultrasound exposure, in a third it was added 20-40 min after ultrasound exposure, and in the fourth no drug was added. Cell death was detected by the absense of Calcein AM signal. Samples were imaged on a Nikon fluorescence microscope and images were analzyed in Fiji.
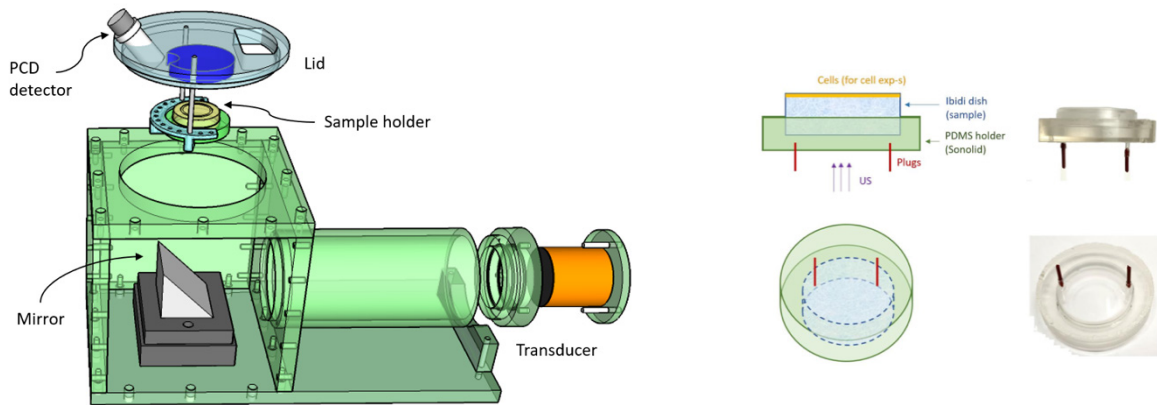
Figure 1. Schematic of the system for acoustic transfection (SAT) setup used for the ultrasound exposures for these experiments. Sample holders for the 35mm ibidi dishes for cultured cells are shown on the right.
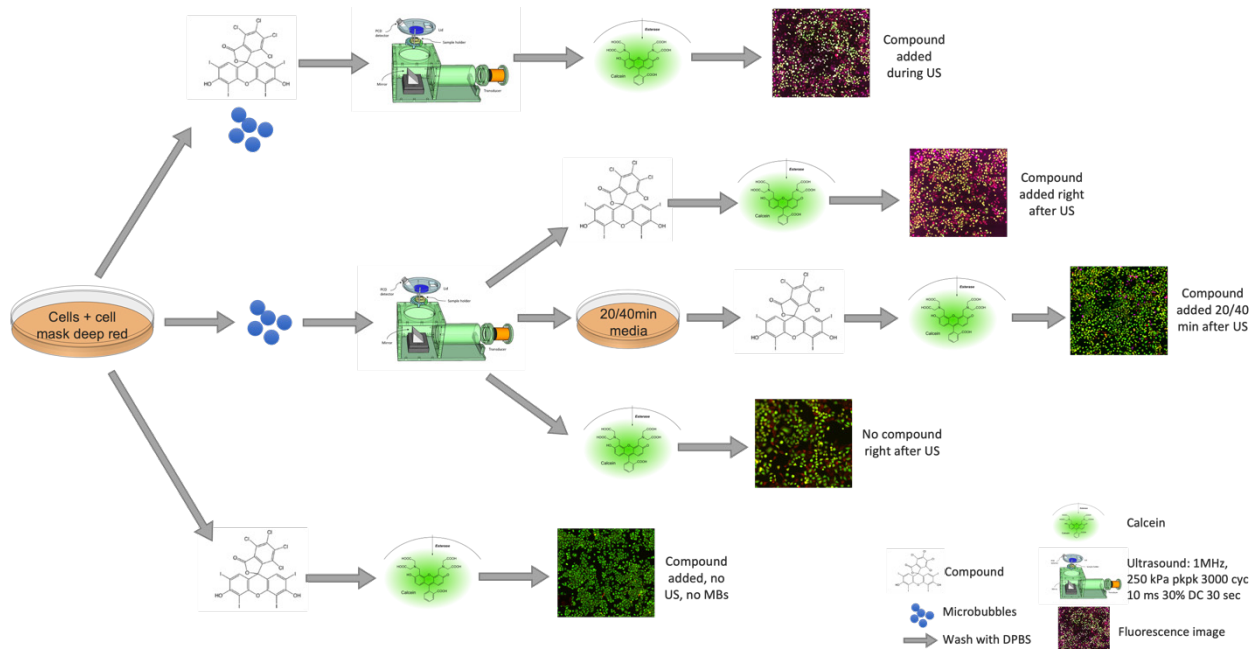
Figure 2. Schematic of assay flow. Groups presented are compound added during ultrasound, compound added right after ultrasound, compound added 20/40 minutes after ultrasound, compound added with no ultrasound exposure, and no compound (cavitation control) after ultrasound.

Results

Consistent with previous studies, the data demonstrate that sonoporation is ultrasound parameter, cavitation nuclei presence, and cell line dependent. Contrary to previous reports, however, drug uptake and cell killing were observed in the group which had drug added immediately after ultrasound exposure. This was not observed when cells were allowed to recover post ultrasound exposure. These findings were consistent across the cell types however the extent of killing was different based on the different cell types. Figure 3 shows some fluorescence microscopy images of the findings. It is important to note, that the highest cell death was seen in the ultrasound + MB + drug group however, there was still considerable killing in the drug administered post ultrasound group.
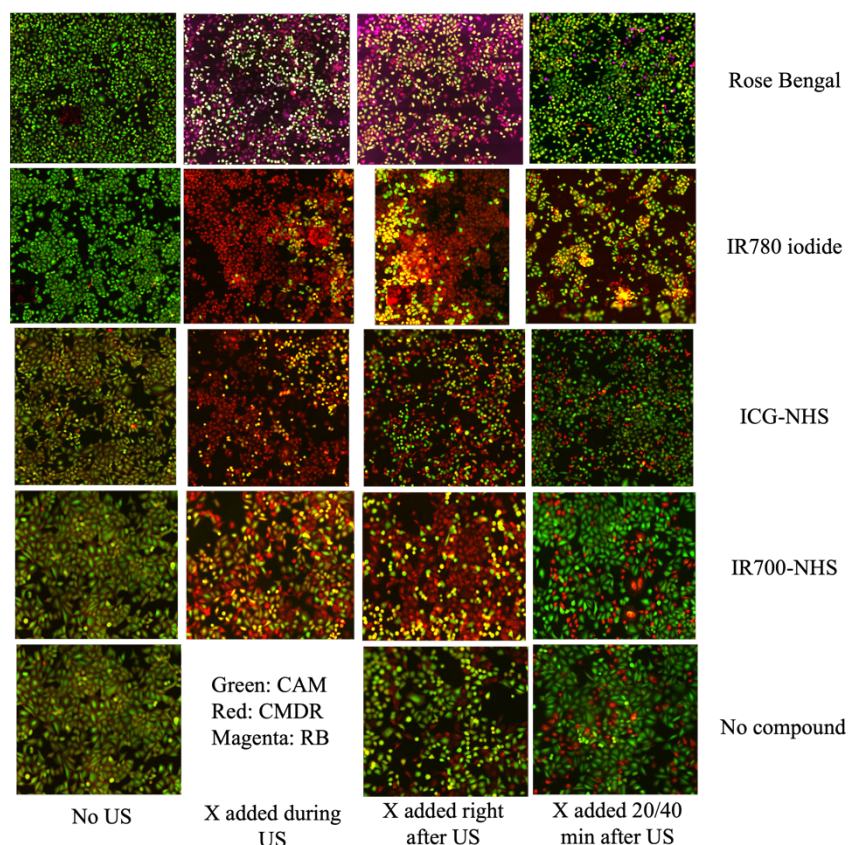
Figure 3. Rose Bengal, IR780 iodide, IR700-NHS, and ICG-NHS added without ultrasound, during ultrasound, immediately after ultrasound, and 20/40 minutes after ultrasound. Red is cell mask red (membrane), green is calcein AM (indicating cells is alive), lack of green (indicates cell is dead), magenta is Rose Bengal.

Conclusions

The results of this study support the hypothesis that intracellular uptake via sonoporation plays an important role in SDT-induced cell death. Further work is needed to quantify the relative contributions of drug activation and the intrinsic "dark" toxicity of SDT drugs in the intracelluar environment.

References

[1]. World Health Organization. (2018). *Cancer, 2018.* Retrieved from https://www.who.int/news-room/fact-sheets/detail/cancer

[2]. Zhang Y, Zhang X, Yang H, Yu L, Xu Y, Sharma A, Yin P, Li X, Kim JS, Sun Y. Advanced biotechnology-assisted precise sonodynamic therapy. Chem Soc Rev. 2021 Oct 18;50(20):11227-11248. doi: 10.1039/d1cs00403d. PMID: 34661214.

[3]. Beguin, E. *et al.* Direct Evidence of Multibubble Sonoluminescence Using Therapeutic Ultrasound and Microbubbles. *ACS Appl. Mater. Interfaces* **11**, 19913–19919 (2019).

[4]. Koh, E. & Fluhr, R. Singlet oxygen detection in biological systems: Uses and limitations. *Plant Signal. Behav.* **11**, 1–5 (2016).

[5]. Li, E. *et al.* The Abnormal Physicochemical Phenomena of Singlet Oxygen Sensor Green in Water in the Presence of Ultrasound. *ChemistrySelect* **6**, 6631–6635 (2021).

[6]. Barati, A. H., Mokhtari-Dizaji, M., Mozdarani, H., Bathaie, Z. & Hassan, Z. M. Effect of exposure parameters on cavitation induced by low-level dual-frequency ultrasound. *Ultrason. Sonochem.* **14**, 783–789 (2007).

[7]. Arvanitis, C. D., Bazan-Peregrino, M., Rifai, B., Seymour, L. W. & Coussios, C. C. Cavitation-Enhanced Extravasation for Drug Delivery. *Ultrasound Med. Biol.* (2011) doi:10.1016/j.ultrasmedbio.2011.08.004.

[8]. Hu, Y., Wan, J. M. F. & Yu, A. C. H. Membrane Perforation and Recovery Dynamics in Microbubble-Mediated Sonoporation. *Ultrasound Med. Biol.* **39**, 2393–2405 (2013).

[9]. Pepe, J., Rincón, M. & Wu, J. Experimental comparison of sonoporation and electroporation in cell transfection applications. *Acoust. Res. Lett. Online* **5**, 62–67 (2004).

[10]. Gray M, Vasilyeva AV, Brans V, Stride E. Studying Cavitation Enhanced Therapy. J Vis Exp. 2021 Apr 9;(170). doi: 10.3791/61989. PMID: 33900296.

Ultrasound-targeted microbubble cavitation delivers microRNA to tumor cells and the tumor microenvironment: Direct visualization using miRNAscope assay

Cheng Chen[1], Nikhil S Chari[2], Thiruganesh Ramasamy[1], Xucai Chen[1], Wei Lu[3], Khaja B Khan[3], Lorena I Gomez[3], Luisa M Solis[3], Stephen Y Lai[2], Flordeliza S. Villanueva[1]*

[1]Center for Ultrasound Molecular Imaging and Therapeutics, University of Pittsburgh, Pittsburgh, PA, USA
[2]Department of Head and Neck Surgery, The University of Texas MD Anderson Cancer Center, Houston, TX, USA
[3]Department of Translational Molecular Pathology, The University of Texas MD Anderson Cancer Center, Houston, TX, USA
Corresponding author: villanuevafs@upmc.edu

Introduction

Ultrasound targeted microbubble cavitation (**UTMC**) has been investigated for site-specific, image-guided drug and gene delivery. This approach utilizes gas-filled ultrasound contrast agents, or microbubbles, which carry the therapeutic (e.g. nucleic acid), and which oscillate in an ultrasound field. The ensuing cavitation causes sonoporation and endothelial hyperpermeability, facilitating endocytosis-independent uptake of the payload into the insonified cells. While it has been shown that UTMC can deliver therapeutic oligonucleotide payloads with functional results such as inhibition of tumor growth or ventricular hypertrophy [1-3], it has not been proven that the payloads concentrate in the extravascular space of the target site. Here, we used a novel *in situ* hybridization approach (miRNAscope) to demonstrate that UTMC delivery of the complementary strand of miR-27a, miRNA-27a*, a microRNA which is pro-apoptotic in tumors [4, 5], causes miRNA-27a* accumulation in tumor cells and the tumor microenvironment.

Methods

1,2-distearoyl-sn-glycero-3-phosphocholine (18:0 PC, DSPC), 1,2-distearoyl-sn-glycero-3-ethylphosphocholine (chloride salt) (18:0 EPC, DSEPC), and 1,2-disteraroyl-sn-glycero-3-phospho-(1'-rac-glycerol) (sodium salt) (18:0 PG, DSPG) were purchased from Avanti Polar lipids (Birmingham, AL). Polyethylene glycol-40 (PEG-40) stearate was purchased from Sigma-Aldrich (St. Louis, MO). DSPC, DSEPC, DSPG, and PEG-40 were mixed with a mass fraction of 100:45:1:4.5 in chloroform and dried with argon gas. The dried lipid film was then hydrated using isotonic saline and sonicated using a bath Ultrasonic Cleaner (VWR, Model 75D, NY) until the lipids were evenly dispersed as 4× lipid stock solution. To prepare miR-loaded microbubbles, 200 μL of 4× lipid stock solution was diluted with saline to 800 μL in a glass vial, and 10 μg of miR-27a* or negative control miR was added and sealed. The headspace of the vial was filled with perfluorobutane gas (FluoroMed, LP, Round Rock, TX), and the glass vial was vortexed for 45 s using a dental amalgamator. The microbubbles were washed with 0.5 mL saline twice. The microbubbles carried miR-27a* (**miR-27a*-MB**) or negative control miR (**CON-miR-MB**) via charge-charge interaction.

We studied 8-week old immunocompetent C3H/HeJ female mice (Jackson laboratory, Bar Harbor, ME) with SCCVII xenograft tumors who received either 10 μg i.v. miR-27a* only, or MBs loaded with 10 μg miR-27a* (or control-miR) in conjunction with UTMC. On treatment day, mice were anesthetized, and a catheter was placed in the internal jugular vein for microbubble infusion as described previously [6]. UTMC treatment was performed as follows: microbubbles (1×10^9 microbubbles formulated with 10 μg miR-27a* or control miRNA) were infused into the jugular vein over 15 min. Therapeutic ultrasound was delivered using a single-element immersion transducer (A303S-SU, 12.7 mm in diameter, Olympus NDT, Center Valley, PA), driven by an arbitrary function generator (AFG3252, Tektronix, Beavertona, OR) connected to a gated radio frequency power amplifier (250A250AM8, Amplifier Research, Souderton,

PA). The therapy transducer was oriented directly over the tumor, tilted slighted toward the tail of the animal to avoid ultrasound delivery to the abdomen. Ultrasound was delivered at 1 MHz transmit frequency, 0.70 MPa peak negative pressure (spatial peak temporal peak), 100 µs pulse duration, repeated 5 times every 1 ms, followed by a 2-sec waiting period to allow microbubble reperfusion into the treatment area. The successful destruction and replenishment of microbubbles in the treatment area was confirmed by simultaneous contrast-specific ultrasound perfusion imaging with a clinical ultrasound imaging system (Sequoia 512, Siemens, Mountain View, CA, USA) in CPS mode at low mechanical index (0.2).

One group of mice (n=14) was euthanized 48 hours after UTMC treatment and tumor tissue was collected for immunoblot quantification of miR-27a* target protein expression. Another group of mice (n=4) was euthanized 45 minutes after UTMC treatment, tumor tissue was paraffin-embedded, and processed using miRNAscope and HALO image analysis.

Results

At 48 hours following treatment, protein expression of direct miR-27a* targets (EGFR, AKT, mTOR, NUP62 and ΔNP63α) was significantly less after miR-27a*-MB + UTMC vs i.v. miR-27a* or Con-miR-MB + UTMC. Further, whereas i.v. miR-27a* did not decrease tumor expression of these proteins vs. non-treated tumors, miR-27a*-MB + UTMC significantly reduced tumor expression of EGFR, NUP62 and ΔNP63α by 50-75%, and trended to reduce expression of AKT and MTOR, compared to non-treated tumors. **Figure 1** is a processed miRNAscope image showing that when delivered by UTMC, miR-27a* was localized diffusely, both within tumor cells and in the tumor microenvironment.

Conclusions

This is the first demonstration of the specific spatial and cellular distribution of oligonucleotide delivery by UTMC, proving that the changes in target protein expression after UTMC + miR-27a*-MB are associated with true extravascular delivery of miR-27a*. These findings may account for the observation that UTMC-mediated delivery of miR-27a* is superior to intravenous delivery of equivalent dose miR-27a* for downregulating target genes known to be involved in tumor proliferation, invasion, and metastasis. These data substantiate the utility of UTMC for non-invasive delivery of oligonucleotide payloads to extravascular target sites.
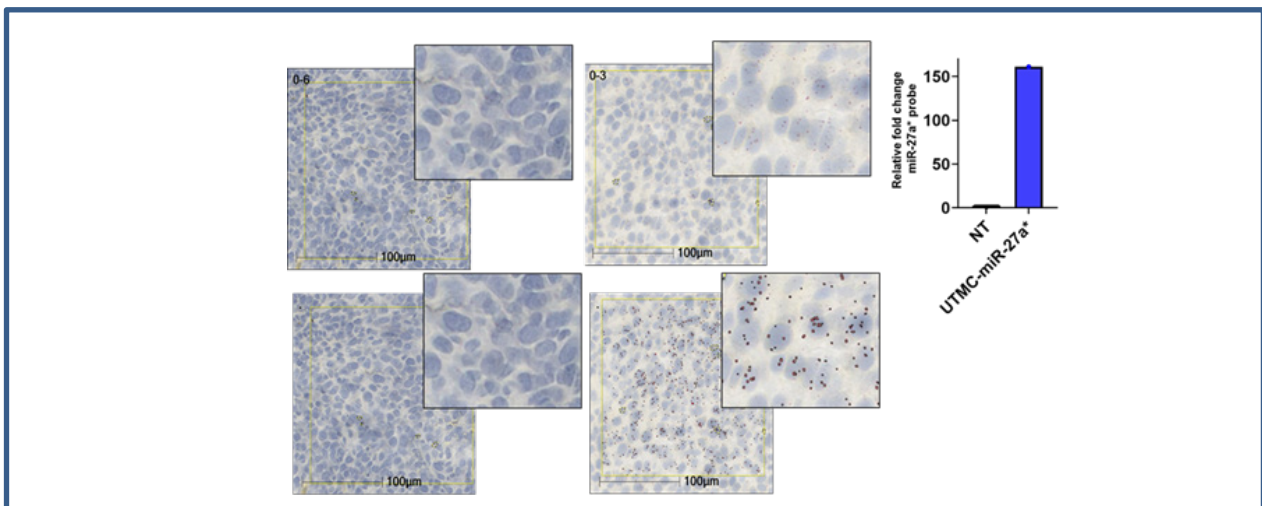
Figure 1. miRNAscope assay identifies increased miR-27a* delivery in mice treated with UTMC-miR-27a* (*Right panels*) **compared to No Treatment** (NT; *Left panels*). Insets are magnifications. Upper panels are raw images. Lower panels are digital analysis of mark-ups obtained using HALO software to quantify miRNA-27a* signal (brown) in cells. Graph:-fold increase in UTMC-miR-27a* *vs* NT.

References

[1]. Kopechek JA, McTiernan CF, Chen X, Zhu J, Mburu M, Feroze R *et al*. Ultrasound and microbubble-targeted delivery of a microRNA inhibitor to the heart suppresses cardiac hypertrophy and preserves cardiac function. *Theranostics* 2019; 9: 7088.

[2]. Kopechek JA, Carson AR, McTiernan CF, Chen X, Hasjim B, Lavery L *et al*. Ultrasound Targeted Microbubble Destruction-Mediated Delivery of a Transcription Factor Decoy Inhibits STAT3 Signaling and Tumor Growth. *Theranostics* 2015; 5: 1378-1387.

[3]. Ramasamy T, Chen X, Qin B, Johnson DE, Grandis JR, Villanueva FS. STAT3 decoy oligonucleotide-carrying microbubbles with pulsed ultrasound for enhanced therapeutic effect in head and neck tumors. *PLoS One* 2020; 15: e0242264.

[4]. Chari NS, Ivan C, Le X, Li J, Mijiti A, Patel AA *et al*. Disruption of TP63-miR-27a* Feedback Loop by Mutant TP53 in Head and Neck Cancer. *JNCI: Journal of the National Cancer Institute* 2019; 112: 266-277.

[5]. Wu X, Bhayani MK, Dodge CT, Nicoloso MS, Chen Y, Yan X *et al*. Coordinated targeting of the EGFR signaling axis by microRNA-27a*. *Oncotarget* 2013; 4: 1388-1398.

MRI Guided Focused Ultrasound Drug Delivery to DIPG Tumors in a Mouse Model

Payton Martinez[1], Genna Nault[2], Jenna Steiner[2], Natalie Serkova[2], Adam Green[3], Mark Borden[1,4]

[1]*Biomedical Engineering, University of Colorado – Boulder, Boulder, USA*
[2]*Animal Imaging, University of Colorado – Anschutz, Aurora, USA*
[3]*Pediartic Oncology, University of Colorado – Anschutz, Aurora, USA*
[4]*Mechanical Engineering, University of Colorado – Boulder, Boulder, USA*
Corresponding author: mark.borden@colorado.edu

Introduction

Diffuse midline glioma, specifically pontine and H3 K27M-altered, is the most common and unfortunately the deadliest brainstem tumor in children [1]. Current clinical treatment methods only involve palliative radiotherapy that does not significantly improve survival beyond its poor mean survival of 9 months [2]. These tumors remain difficult to treat with chemotherapy as they maintain an intact blood brain barrier (BBB). Although a technique using focused ultrasound (FUS) and microbubbles (MBs) has been shown to disrupt the blood brain barrier (BBBD) allowing larger chemotherapeutics to enter the parenchyma [3]. Panobinostat is one of the chemotherapeutics that has difficulty crossing the BBB although it has promising effects in vitro [4]. Therefore, in this study we hypothesized that using FUS we could disrupt the BBB allowing a higher concentration of Panobinostat to enter the tumor region and provide a therapeutic effect.

Methods

Mice were injected with BT-245 (patient biopsied DIPG cell line) orthotopically into the pons, 1 mm laterally to the right hemisphere. Initial set of mice (n = 12) had two weeks of growth then MR images were taken and used to guide FUS targeting to the center of the tumor location. In house microbubbles were size isolated to 3 ± 0.5 um and half of the mice (n = 6) were injected via tail vein at 25 µl/kg. Right before (10-20 seconds) sonication was started with parameters as follows: center frequency: 1.515 MHz, peak negative pressure: 0.77 MPa, pulse length: 1 ms, pulse repetition frequency: 1 Hz. Sonication lasted for 3 minutes, and passive cavitation data was collected and analyzed as previously described [5]. Directly after FUS Panobinostat (LBH-589) was given (10 mg/kg) intraperitonially (IP) and MR images were taken to determine extent of BBBD. After 1.5 hours mouse serum and brains were extracted and split at the midbrain and cerebellum. All three samples were sent in for liquid chromatography tandem mass spectrometry and mass spectrometry to determine concentration of Panobinostat at each location.

The second set of mice (n = 20) were treated weekly for three weeks. Half of which were treated with both FUS and Panobinostat with the same parameters to the first set, the other half was only given Panobinostat. After 3 weeks no treatment was done on either set. MR images were taken, and body weight was examined weekly prior to treatment and after treatment period ended to evaluate extent of BBBD and tumor progression.

Results

We have demonstrated that FUS-mediated BBBD can successfully deliver Panobinostat (LBH-589) to the pons with DMG tumors over 3-fold (Fig.1a) while only slightly increasing the concentration of the forebrain 51% (Fig. 1b). Passive cavitation detection during treatments showed ideal harmonic cavitation throughout the 3 minutes while not having any significant broadband cavitation (Fig. 2). The combination of both Panobinostat and FUS showed major decreases in tumor growth by ~71% by the end of the treatment weeks when compared to Panobinostat without FUS (Fig. 3a). A significant survival benefit was also demonstrated when treated with both Panobinostat and FUS improving the mean survival from 21 to 31.5 days (Fig. 3b).

Conclusions

Our study demonstrates that FUS-mediated BBBD can increase the delivery of Panobinostat (LBH-589) to an orthotopic DMG tumor (BT-245). The increased concentration exclusively at the tumor site was shown to significantly decrease tumor growth (~71%) and significantly increase survival (50%). Therefore, we see a strong indication that this methodology can be used to improve the treatment of DMGs in patients.
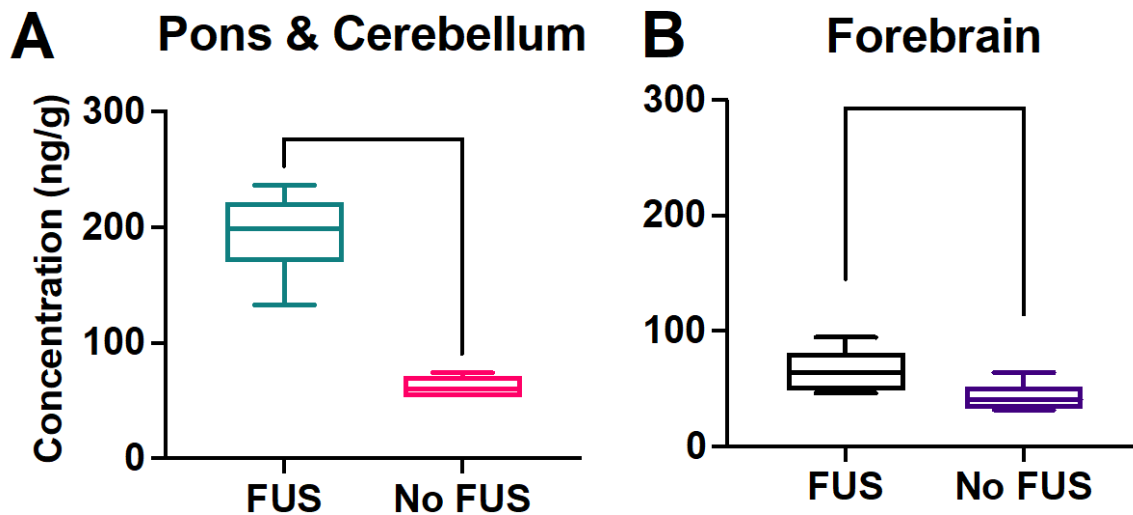
Figure 1. Concentration of Panobinostat found in the pons and cerebellum (A) and forebrain (B) 1.5 hours after FUS-mediated BBBD occurred (if applicable) and Panobinostat was injected IP. Analysis was done using mass spectrometry. Wiskers illistrate 10-90 percentile. Significance testing was done using student's t test (n=6). * indicates $P < 0.05$; **** indicates $P < 0.0001$.
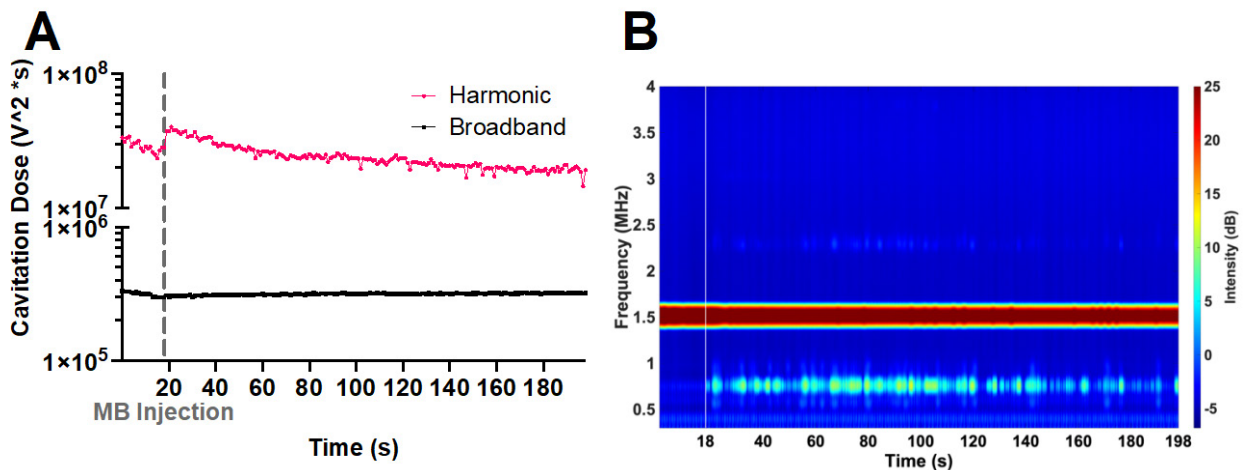
Figure 2. Passive cavitation dectection during 3 minute treatments. A) Illistrates the harmonic and broadband cavitation dose (HCD and BCD respectively) found during each 10 ms pulse. Gray dotted line at 18 seconds represents the point where all microbubbles were injected. B) Spectrogram of total treatment. Non sonication time between pulses were removed. White line at 18 seconds represent the time at which microbubbles were injected.
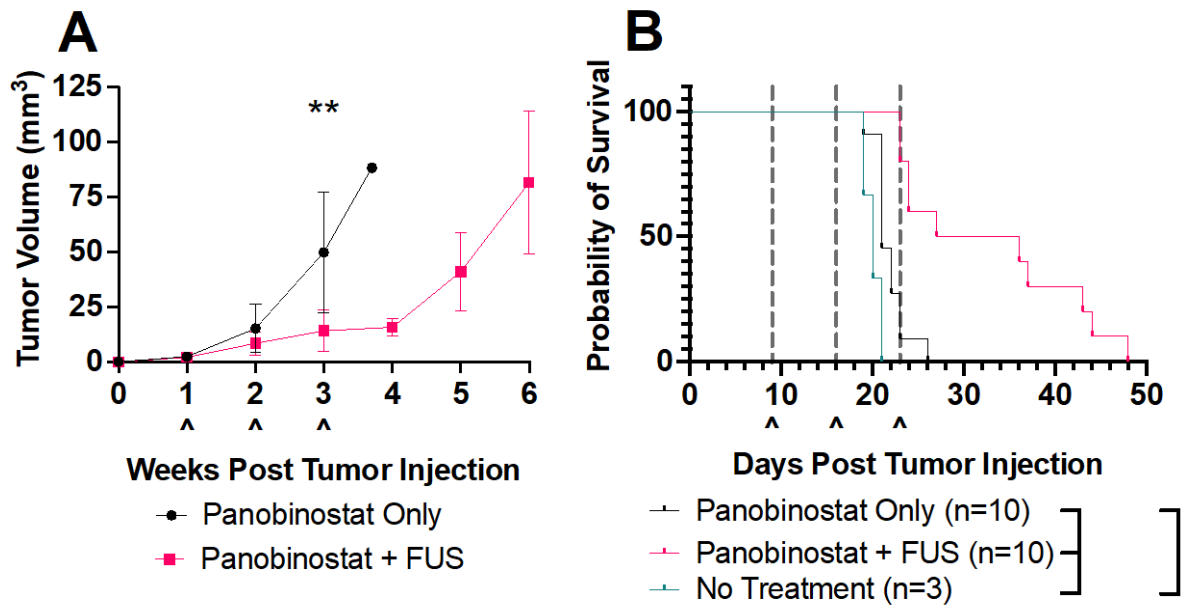
Figure 3. Longitutional analysis of tumor volume using MR images obtained weekly (A) and surivival (B). Dotted gray lines on both plots represent the treatment days. Signifcance testing was done using student's t test for A, and Mantel-Cox test (n=10) for B, where *, **, *** indicates P <0.05, 0.01, and 0.001 respectively.

References

[1]. Veldhuijzen van Zanten, Sophie EM, et al. "A twenty-year review of diagnosing and treating children with diffuse intrinsic pontine glioma in The Netherlands." Expert review of anticancer therapy 15.2 (2015): 157-164.

[2]. Packer, Roger J., et al. "Outcome of children with brain stem gliomas after treatment with 7800 cGy of hyperfractionated radiotherapy. A childrens cancer group phase 1/11 trial." Cancer 74.6 (1994): 1827-1834.

[3]. Woodworth, Graeme F., et al. "Emerging insights into barriers to effective brain tumor therapeutics." Frontiers in oncology 4 (2014): 126.

[4]. Grasso, Catherine S., et al. "Functionally defined therapeutic targets in diffuse intrinsic pontine glioma." Nature medicine 21.6 (2015): 555-559.

[5]. Martinez, Payton, Nick Bottenus, and Mark Borden. "Cavitation Characterization of Size-Isolated Microbubbles in a Vessel Phantom Using Focused Ultrasound." Pharmaceutics 14.9 (2022): 1925.

CEeDD: Clinical Translation of Cavitation-Enhanced Oncological Drug Delivery from Sonosensitive Particles Guided by Passive Acoustic Mapping

Jeffrey Rubasingham[1], Christian Coviello[2], Cliff Rowe[2], Paul Lyon[3], Calum Crake[2], Paul Boulos[2], Massimo Massiero[2], Laura Spiers[1,4], Prateek Katti[1], Christophoros Mannaris[1], Daniel McAleese[4], David Thompson[4], James Kwan[1], Michael Gray[1], Robert Carlisle[1], Fergus Gleeson[3], Rachel Kerr[4], Constantin Coussios[1]

[1]Institute of Biomedical Engineering, University of Oxford, Oxford, UK
[2]OxSonics Therapeutics, Oxford, UK
[3]Department of Radiology, Oxford University Hospitals NHS Foundation Trust, Oxford, UK
[4]Department of Oncology, University of Oxford, Oxford, United Kingdom,
Corresponding author: constantin.coussios@eng.ox.ac.uk

Introduction

SonoTran Particles (SPs) are gas-stabilizing solid cavitation nucleation agents, developed specifically to enable ultrasound-enhanced drug delivery and distribution of unmodified therapeutics into solid tumours [1]. Following nearly a decade of research and development across the University of Oxford and OxSonics Therapeutics to achieve pre-clinical proof-of-concept [1,4,5], scale-up to GMP, and pre-clinical demonstration of safety and efficacy in small and large animal models [6,7], they have entered a first-in-human clinical trial (CEeDD) funded by the National Institute for Health Research (NIHR201655)]. Recruitment and assessment of all 9 patients in the safety cohort was recently completed.

Methods

SPs are cup-shaped monodisperse particles of typical diameter 480nm that stabilize a single gas inclusion on the order of 200 nm [1]. Upon excitation to 0.5 MHz focused ultrasound, they preferentially generate broadband acoustic emissions and sustained microstreaming [2], the presence and location of which can be mapped in real time at depth within the body using passsive acoustic mapping (PAM) enhanced by optimal beamforming [3].

Ahead of the clinical trial, a range of studies were conducted in tumour-bearing mice to quantify the safety and feasibility of PAM-guided cavitation-enhanced drug delivery with macromolecular therapeutics ranging from antibodies [2,5] and antibody-drug conjugates [7] to oncolytic viruses [3]. This was followed by extensive toxicological, pharmacokinetic and biocompatibility GLP studies to confirm SSP safety over the range of doses anticipated in patients. Lastly, the full SonoTran Platform developed by OxSonics Therapeutics, which includes both an ultrasound engine capable of real-time treatment delivery, guidance and monitoring, and the sterilzed SPs for intravenous administration, underwent extensive testing in a large animal (pig) model to demonstrate safety and effectiviness at human-relevant treatment depths [6].

The first phase of the CEeDD clinical trial consisted of an early feasibility cohort with the primary end point of safety and tolerability of SonoTran Particles, and of the feasibility of delivering the SonoTran Platform to patients with mCRC. This cohort consists of a 3+3 (n=9) dose escalation design with doses ranging from 200-600mg of particles. The secondary objective is to assess the capability of the SonoTran platform to induce detectable and reproducible inertial cavitation activity in the target tumour during the intervention, as determined by real-time PAM.

Results

Pre-clinical studies in tumour-bearing mice demonstrated that the use of SPs in combination with 0.5 MHz ultrasound using derated peak rarefactional pressures in the range 1-2.9 MPa and duty cycles in the range 0.5-5% result in 3-10x increases in the delivery of antibody-based therapeutics, accompanied by noteable improvements in tumour coverage away from blood vessels.

In the safety cohort of the CEeDD clinical study, all 9 patients successfully received the SonoTran intervention, safely reaching the highest SP dose level.

Conclusions

Pre-clinical evidence and early clinical evidence of PAM-guided cavitation-enhanced drug delivery suggests that the intervention is feasible, safe, and has the potential to improve unmodifed therapeutic delivery and distribution in solid tumours.

Figure 1. Photograph of the treatment of the first patient in the CEeDD trial. Following intravenous administration of the SonoTran Particles, an mCRC tumour in the liver is targeted using the hand-held ultrasound probe, with the display evidencing real-time Passive Acoustic Mapping of cavitation activity overlaid onto a B-mode image of the target tumour.

References

[1]. Kwan JJ, Myers R, Coviello CM, Graham SM, Shah AR, Stride E, Carlisle RC, Coussios CC. Ultrasound-propelled nanocups for drug delivery. Small. 2015;11(39):5305-14.

[2]. Kwan, J., S. Graham, R. Myers, R. Carlisle, E. Stride and C. Coussios (2015). "Ultrasound-induced inertial cavitation from gas-stabilizing nanoparticles." Physical Review E 92(2): 023019.

[3]. Coviello C, Kozick R, Choi J, Gyöngy M, Jensen C, Smith PP, Coussios CC. Passive acoustic mapping utilizing optimal beamforming in ultrasound therapy monitoring. The Journal of the Acoustical Society of America. 2015;137(5):2573-85.

[4]. Myers, R., C. Coviello, P. Erbs, J. Foloppe, C. Rowe, J. Kwan, C. Crake, S. Finn, E. Jackson, J.-M. Balloul, C. Story, C. Coussios and R. Carlisle (2016). "Polymeric Cups for Cavitation-mediated Delivery of Oncolytic Vaccinia Virus." Molecular Therapy 24(9): 1627-1633.

[5]. Grundy, M., L. Bau, C. Hill, C. Paverd, C. Mannaris, J. Kwan, C. Crake, C. Coviello, C. Coussios and R. Carlisle (2020). "Improved therapeutic antibody delivery to xenograft tumors using cavitation nucleated by gas-entrapping nanoparticles." Nanomedicine 16(1): 37-50.

[6]. Masiero M, Boulos P, Crake C, Rowe C, Coviello CM. Ultrasound-induced cavitation and passive acoustic mapping: SonoTran platform performance and short-term safety in a large-animal model. Ultrasound in Medicine & Biology. 2022.

[7] Masiero M, Vojtasova E, Boulos P, Zammarchi F, van Berkel P, Crake C, Coviello C, Rowe C. Ultrasound-induced cavitation enhances therapeutic efficacy of AXL-targeting ADC leading to improved survival in a human xenograft model of renal cancer. European Journal of Cancer. 2022;174:S101-S2.

Tumor perfusion quantification with parametric processing of contrast-enhanced ultrasound

Connor D. Krolak[1], Marissa R. Shumaker[1], Alicia Clark[1], Manjiri Dighe[2], Michalakis A. Averkiou[1]

[1]*Department of Bioengineering, University of Washington, Seattle, USA*
[2]*Department of Radiology, University of Washington, Seattle, USA*
Corresponding author: maverk@uw.edu

Introduction

Tumor vasculature is incredibly complex and may be described as a dense web of abnormal vessels that continuously remodel either due to tumor angiogenesis or response to therapy [1]. Contrast-enhanced ultrasound (CEUS) is ideally positioned to evaluate tumor vasculature due to the blood pool nature of its contrast agent (inert gas microbubbles 1-10μm) and its unique traits of high temporal resolution, ease of use, and being safe and well tolerated [2-4]. Recent efforts on super-resolution approaches with CEUS have provided qualitative vascular tumor information beyond the limits of diffraction and with unsurpassed detail in animals and humans. Furthermore, accurately quantifying tumor blood flow and perfusion during the progression or regression of tumor angiogenesis will provide clinicians with the necessary metrics for characterization and surveillance of tumors, essential for improving patient outcomes. Various approaches for quantification of tumor perfusion with CEUS have been pursued but have not seen success in terms of clinical translation. Major limitations include lesion segmentation and tracking, tissue motion, access to linearized data and the development of a robust analysis software package. We have developed a comprehensive approach consisting of a scanning protocol to limit bubble destruction, use of an articulated arm to register and control motion, and an image processing algorithm utilizing parametric processing in order to quantitatively evaluate the wash-in and washout of the transit of a bolus in the tumor vasculature. Parametric images of the rise time and the degree of washout generated from the CEUS image loops provide robust and reproducible metrics to quantitatively assess tumor vascularity.

Methods

Scanning Protocol

To develop our approach, CEUS data was collected from 29 confirmed hepatocellular carcinoma (HCC) lesions. Lesions were located in conventional B-mode ultrasound with a Philips EPIQ C5-1 transducer (Philips Medical Systems, Bothell, WA), which was then spatially fixed with an articulated arm. The articulated arm is critical for reduction of sonographer and patient motion, and accuracy of lesion tracking during breathing motion. A 1.2 mL bolus of Lumason contrast agent followed by a 5 mL saline flush was delivered intravenously, and a 5-minute image video loop was collected while scanning the liver with a contrast specific mode (amplitude modulation). For preservation of contrast, scanning was performed continuously for the first 90 seconds, and only for 15 seconds at the 2, 3, 4, and 5-minute mark. The probe was then adjusted to a different image plane on the same tumor and the process above was repeated up to four times to allow for the assessment of reproducibility.

Respiratory Gating and Motion Compensation

Analysis of HCC image loops, extracted as native DICOM data, was performed in a MATLAB tool titled *qDicomUW* operating on linearized data (the tool removes the logarithmic compression) acquired via a proprietary data transformation script from Philips (Philips Medical Systems, Bothell, WA). The loops from the 5-minute scan were stitched together and an automatic respiratory gating (ARG) algorithm was incorporated to eliminate out-of-plane respiratory motion relative to a user selected key frame. To further reduce the effects of motion and improve perfusion quantification accuracy, a motion compensation

algorithm utilizing two-dimensional normalized cross-correlation on the fundamental image of the respiratory gated frames was used.

Quantitative Parametric Processing

For the parametric imaging processing, a 9x9 pixel region of interest (ROI) was marched across the contrast image, and a time intensity curve (TIC) was generated from the ARG and motion compensated loop. The ROI was translated by 3 pixels horizontally first and then vertically to cover the entire image. To quantify the wash-in and washout dynamics for the tumor, rise time (RT) and degree of washout (DW) calculations were extracted from each TIC. RT was determined by the elapsed time from when contrast first arrived in the ROI to its peak intensity (Fig 1). DW is defined as,

$$DW(t) = \frac{I(\max)}{I(t)} \ where \ t = 2' or\ 5', \qquad\qquad (1)$$

where $I(t)$ is the mean intensity at time t (Fig. 1). Parametric images for RT and DW(2) and DW(5) at 2' and 5' respectively, were generated for all injections (2 examples are shown in Fig 2), compressing temporal and intensity-based information from 5-minute scans into single images. User defined ROIs were then drawn around the lesion and liver parenchyma, and automatically co-registered in all images (fundamental and parametric) allowing for robust ROI selection. Mean and standard deviation values were calculated for each parametric image (RT, DW(2), and DW(5)) within these ROI. The mean values were averaged across injections observing the same lesion and inter-injection variability was assessed.

Results

Examples of perfusion quantification after the parametric processing are shown in Fig. 2. To assess reproducibility of RT, DW(2) and DW(5), the coefficient of variation (COV) was calculated between injections on the same patient and then averaged across all lesions. The average COV of RT was 11.4% for the tumor and 10.8% for the surrounding parenchyma. For DW(2), the average COV was 29.4% for the tumor and 24.4% for the parenchyma; and similarly for DW(5) was 27.7% for the tumor and 28.0% for the parenchyma. To contextualize these metrics, COV of bolus CEUS perfusion parameters in an in-vitro setup were found to be approximately 8% for RT and 50% for amplitude-based metrics like peak intensity and area under the curve [3]. Higher variability was anticipated for DW as it is an amplitude-based metric and injections captured different planes of the heterogenous lesion, but still is able to quantify the characteristic washout for the entire tumor that is challenging to assess qualitatively.
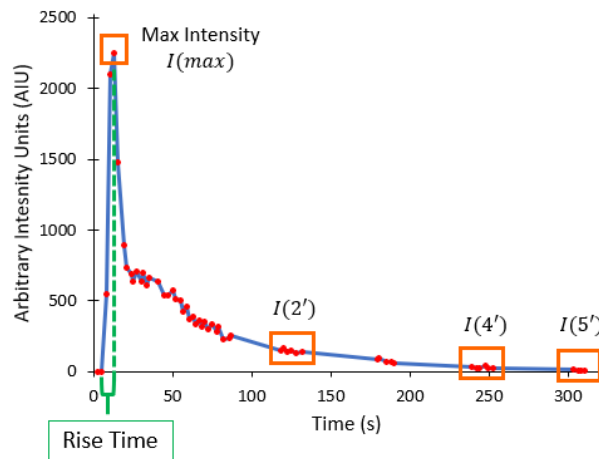
Figure 1. An example time intensity curve demonstrating the calculation of the rise time (RT) and the intensity values used in the degree of washout (DW) calculation.
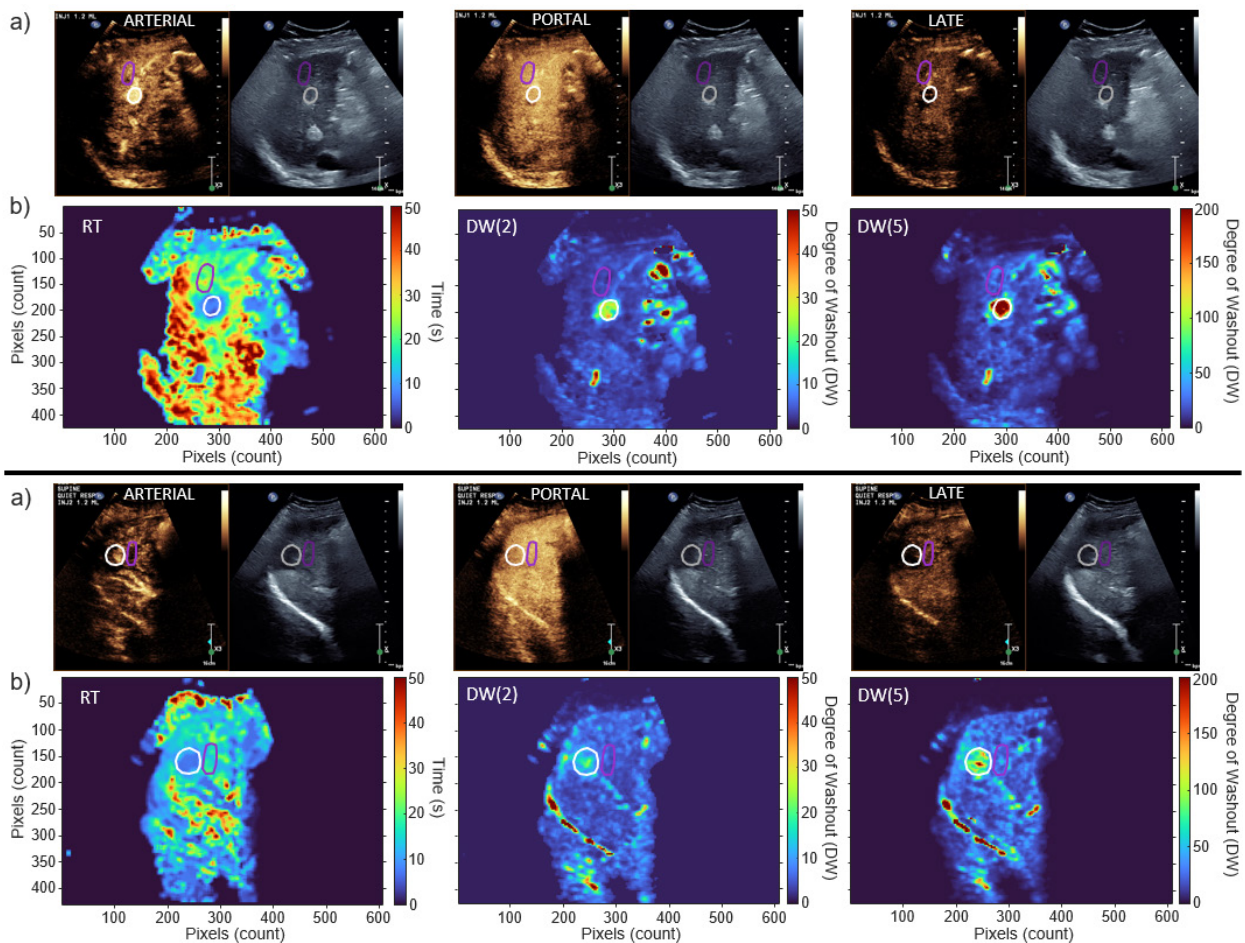
Figure 2. CEUS and parametric images for two patients. In row a) from left to right, CEUS images for the arterial, portal, and late phase. In row b) from left to right, parametric images of rise time (RT), and degree of washout $DW(2)$ and $DW(5)$. The tumor and liver regions of interest are white and purple respectively.

Conclusions

We have developed a robust and reproducible scanning protocol and analysis software for the quantitative assessment of tumor vascularity from CEUS loops. Through parametric processing of RT and DW, we can produce detailed and quantifiable images compiling information from minutes of CEUS data to reduce bias of ROI selection, reliably quantify perfusion dynamics, and provide important metrics to clinicians for evaluating tumor response to therapy. We have tested the ability of our tool on patient data to demonstrate its capability to improve and expand the current clinical utility of CEUS by providing quantifiable metrics of tumor perfusion despite the immense challenges of motion with a 2D scan and bubble longevity that limit new technologies such as super-resolution. This method is ideally positioned to evaluate tumor blood flow for patients undergoing therapies that alter the tumor vasculature.

References

[1]. Carmeliet, P. and R.K. Jain, Principles and mechanisms of vessel normalization for cancer and other angiogenic diseases. Nature Reviews Drug Discovery, 2011. 10(6): p. 417-427.

[2]. Averkiou MA, Bruce MF, Powers JE, Sheeran PS, Burns PN. Imaging Methods for Ultrasound Contrast Agents. Ultrasound in Medicine & Biology. 2020;46(3):498-517.

[3]. Averkiou MA, Juang EK, Gallagher MK, Cuevas MA, Wilson SR, Barr RG, Carson PL. Evaluation of the Reproducibility of Bolus Transit Quantification With Contrast-Enhanced Ultrasound Across Multiple Scanners and Analysis Software Packages—A Quantitative Imaging Biomarker Alliance Study. Investigative Radiology. 2020;55(10):643-56.

[4]. Wilson SR, Burns PN, Kono Y. Contrast-Enhanced Ultrasound of Focal Liver Masses: A Success Story. Ultrasound in Medicine & Biology. 2020;46(5):1059-70.

Sensing Ultrasound Localization Microscopy reveals glomeruli in living rats and humans

Authors: <u>Louise Denis</u>[1], Sylvain Bodard[1,2,3*], Vincent Hingot[1], Arthur Chavignon[1], Gilles Renault[4], Franck Lager[4], Abderrahmane Aissani[1], Olivier Hélénon[1,3], Jean-Michel Correas[1,2,3], Olivier Couture[1,]*
* These authors contributed equally to this work

1 Sorbonne Université, CNRS, INSERM Laboratoire d'Imagerie Biomédicale, F-75006, Paris, France
2 AP-HP, Hôpital Necker Enfants Malades, Service d'Imagerie Adulte, F-75015, Paris, France
3 Université de Paris Cité, F-75006, Paris, France
4 Université de Paris, Institut Cochin, INSERM, CNRS, F-75014 PARIS, France
Corresponding author: louise.denis@sorbonne-universite.fr

Introduction

Ultrasound Localization Microscopy (ULM) is a recent technique that uses contrast agents [1] and allows vascular mapping with up to 10-fold higher resolution than conventional echography [2]. Its principle is to localize injected and isolated microbubbles in order to follow their movement to the microvascular structure [3]. Although arteriolis and venules are easily detected and tracked by ULM, a lack of sensitivity has so far prevented us from observing finer microvessels [4].

In this study, the application of ULM to subpopulations of microbubbles separated by their speed allowed us to highlight a particular behavior of microbubbles in the renal cortical part, and more precisely in the glomeruli. Using the microbubble's own behavior, we can get information about its environment; we called this technique "sensing ULM" (sULM).

Methods

Ultrasound sequences, using Sonovue injection, were acquired on 15 rats' kidneys, and 14 human allografts ; respectively with a Verasonics 256 in rats (probe L22-14v, 15MHz, frame rate 500Hz), and with Contrast Enhanced Ultrasound Sequences of the Canon Applio i800 in humans (probe i8cX1, 3MHz, frame rate 14-64Hz). We performed a double sULM : one for fast microbubbles thanks to a spatiotemporal or a high pass filter ; and one for slow microbubbles using slow sULM parameters (adding a low SVD cutoff for rats). Classical steps were used during both : localization [5], tracking [6], and accumulation. A micro-CT was performed in 6 rats post-mortem in order to compare sULM with a gold standard [7]. 5 patients and 2 rats are presented in this study.

Results

sULM combined density map, i.e. fast tracks in blue and slow tracks in red (Figure 1a), highlighted specific spinning microbubbles in the rat's kidney's cortex (Figure 1b). Micro CT comparison confirmed that these shapes are glomeruli (Figure 1c, 1d).

Thanks to sULM, these spinning behaviors were also observed in humans kidneys' cortex with fast tracks in blue and slow ones in red (Figure 2a). Zoomed in the cortex area (Figure 2b) and on specific cortex's tracks (Figure 2c, 2d) highlight these movements of microbubbles flowing up, spinning around itself, and flowing back down: just as the afferent artery, the glomerulus and then the efferent artery.

Conclusions

In this study, we observed and tracked microbubbles flowing in the glomerular architecture in 5 living humans and in 2 rats. We used post-mortem micro-tomography for side-by-side comparison in 6 rats: one rat is shown here and analyses of the others are in progress.

The observation of glomeruli by sULM is a discovery that would allow the diagnosis of a number of chronic kidney disease [9]. Further studies are needed to prove that sULM is feasible in native kidney, first; and to study if sULM could allow a diagnosis on diseased ones then. 3D will also be needed to correct out-of-plane movements and to have precise characterization of microbubbles' behaviour in all planes.

Although much progress is still needed, we believe that this new modality brings imaging capabilities closer to the functional units of organs, which is one of the keys to understanding most diseases.

References
[1] C. Baracchini *et al.*, « Safety and Tolerability of SonoVue® in Patients with Large Artery Anterior Circulation Acute Stroke: Safety and Tolerability of SonoVue® in Acute Stroke », *J Neuroimaging*, vol. 27, nᵒ 4, p. 409-413, juill. 2017, doi: 10.1111/jon.12416.
[2] C. Errico *et al.*, « Ultrafast ultrasound localization microscopy for deep super-resolution vascular imaging », *Nature*, vol. 527, nᵒ 7579, p. 499-502, nov. 2015, doi: 10.1038/nature16066.
[3] O. Couture, V. Hingot, B. Heiles, P. Muleki-Seya, et M. Tanter, « Ultrasound Localization Microscopy and Super-Resolution: A State of the Art », *IEEE Trans. Ultrason., Ferroelect., Freq. Contr.*, vol. 65, nᵒ 8, Art. nᵒ 8, août 2018, doi: 10.1109/TUFFC.2018.2850811.
[4] Y. Desailly, A.-M. Tissier, J.-M. Correas, F. Wintzenrieth, M. Tanter, et O. Couture, « Contrast enhanced ultrasound by real-time spatiotemporal filtering of ultrafast images », *Physics in Medicine and Biology*, vol. 62, nᵒ 1, Art. nᵒ 1, janv. 2017, doi: 10.1088/1361-6560/62/1/31.
[5] B. Heiles, Chavignon, Arthur, V. Hingot, Lopez, Pauline, Teston, Eliott, et O. Couture, « Open Platform for Ultrasound Localization Microscopy: performance assessment of localization algorithms », *Nature Biomedical Engineering*, vol. 6, nᵒ 5, p. 605-616, 2022.
[6] J.-Y. Tinevez, « simpletracker - A simple particle tracking algorithm for MATLAB that can deal with gaps. » 13 octobre 2021. Consulté le: 11 janvier 2022. [En ligne]. Disponible sur: https://github.com/tinevez/simpletracker
[7] P. Blery *et al.*, « Vascular imaging with contrast agent in hard and soft tissues using microcomputed-tomography », *Journal of Microscopy*, vol. 262, nᵒ 1, p. 40-49, avr. 2016, doi: 10.1111/jmi.12339.
[8] S. E. Shelton *et al.*, « Quantification of microvascular tortuosity during tumor evolution using acoustic angiography », *Ultrasound in medicine & biology*, vol. 41, nᵒ 7, p. 1896-1904, 2015.
[9] G. Kanzaki, N. Tsuboi, A. Shimizu, et T. Yokoo, « Human nephron number, hypertension, and renal pathology », *Anat Rec (Hoboken)*, vol. 303, nᵒ 10, Art. nᵒ 10, oct. 2020, doi: 10.1002/ar.24302.

Figures
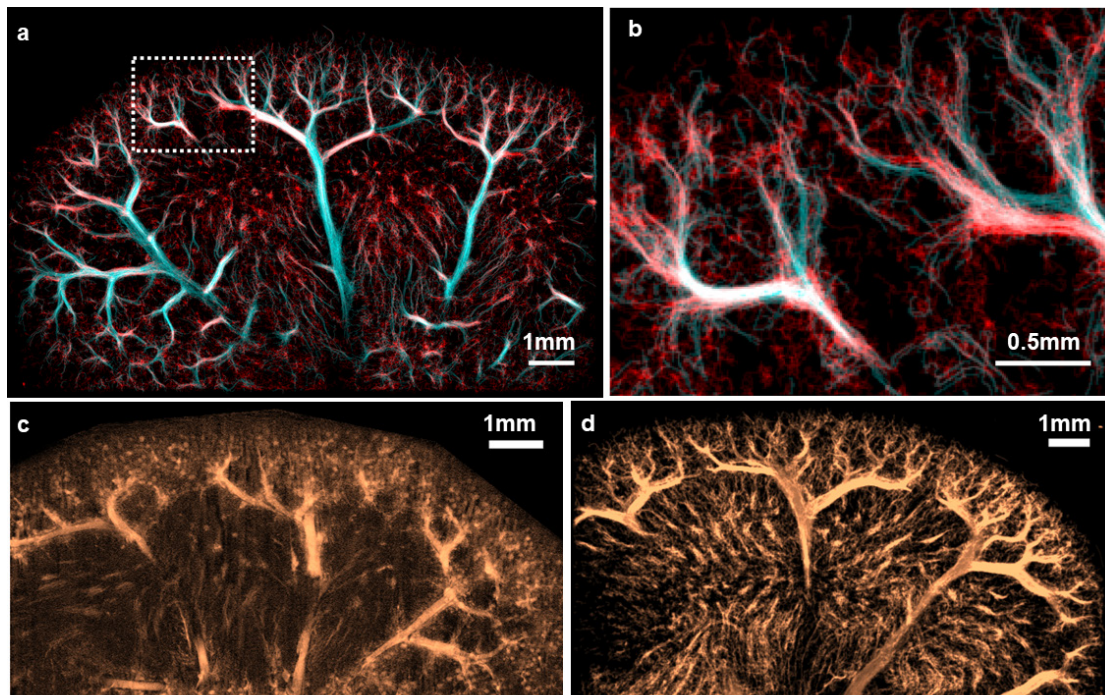
Figure 1. Glomerular structures were observed in one rat kidney cortex by sULM, and microCT confirmed that these are glomeruli.
a. sULM density map in rat 14 in the longitudinal plane with superimposed slow-tracking (red) and fast-tracking (blue).
b. Zoom in the cortex area.
c. Micro CT was manually registered in rat 7 on the same longitudinal plane as sULM (d).
d. sULM density map in rat number 7 on the same longitudinal plane as micro CT (c).
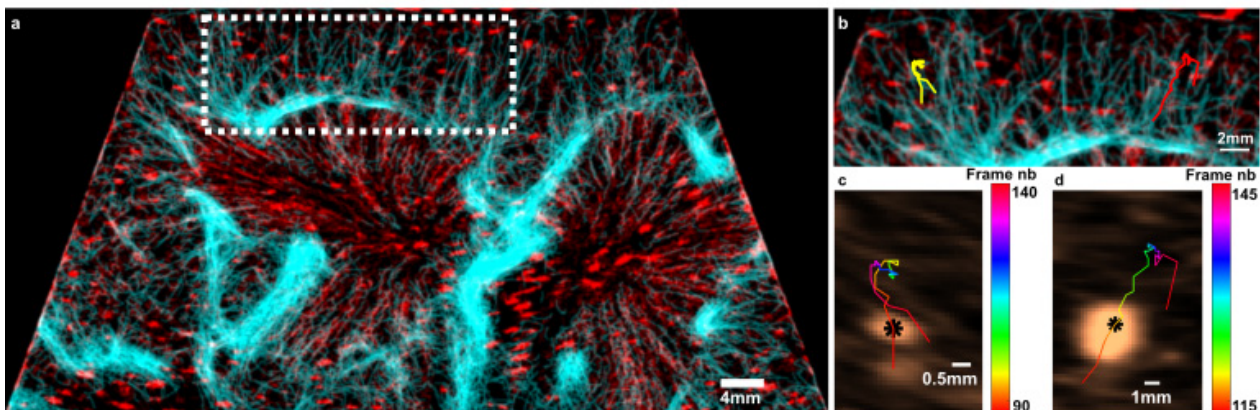
Figure 2. Similar glomerular structures can be observed in the human kidney cortex by sULM.
a. sULM density map in humans with superimposed slow-tracking (red) and fast-tracking (blue).
b. Zoom in the cortex area. Yellow (left) and red (right) tracks are zoomed-in in c and d.
c. Zoom of yellow glomerular behavior highlighted in b.
d. Zoom of red glomerular behavior highlighted in b.

Ultrafast Contrast-Enhanced Ultrasound Velocimetry in the Abdominal Aorta Before and After Endovascular Aneurysm Repair: Preliminary Results

Majorie van Helvert[1,2,3], Erik Groot Jebbink[1,2], Guillaume Lajoinie[3], Jason Voorneveld[4], Johan G. Bosch[4], Michel Versluis[3], Michel M.P.J. Reijnen[1,2]

[1]*Multi-Modality Medical Imaging Group, TechMed Centre, University of Twente, Enschede, The Netherlands*
[2]*Dept. of Vascular Surgery, Rijnstate Hospital, Arnhem, The Netherlands*
[3]*Physics of Fluids group, TechMed Centre, University of Twente, Enschede, The Netherlands*
[4]*Dept. of Biomedical Engineering, Thorax Center, Erasmus MC, Rotterdam, The Netherlands*
Corresponding author: m.vanhelvert@utwente.nl

Introduction

Abdominal aortic aneurysm (AAA) is a common vascular pathology with high risk of mortality in case of rupture[1]. Local hemodynamics are suspected to play a key role in the pathogenesis of an AAA, as it is related to aneurysmal growth, intraluminal thrombus formation and rupture risk[2]. Nowadays, endovascular aneurysm repair (EVAR) is the preferred treatment in patients with a suitable anatomy. However, EVAR is associated with higher long-term reintervention rates of up to 26%[1]. The placement of a stent graft may alter local hemodynamics and introduce unfavorable flow conditions that could lead to complications, and indications for reintervention, such as limb occlusion and renal dysfunction[3,4].

Prior to treatment, visualization and quantification of local blood flow patterns could provide insight into the underlying mechanisms of aneurysm growth. After treatment, such quantification could reveal unfavorable flow conditions. However, accurate in vivo blood flow quantification is a great challenge, especially in the abdominal aorta owing to its depth and to blood flow velocities exceeding 1 m/s. High-frame-rate contrast-enhanced ultrasound (HFR CEUS) combined with particle image velocimetry (echoPIV), enables 2D quantification of local hemodynamics in the aorto-iliac tract[5,6]. Here, we investigate the applicability of echoPIV in AAA patients before and after EVAR.

Methods

Blood flow was imaged in two patients – in an ongoing clinical trial (n = 10) – diagnosed with an infrarenal AAA that were treated with EVAR. Both US and reference 4D phase contrast (PC) MRI measurements were performed within eight weeks prior to treatment and eight weeks after treatment. First, B-mode imaging and Pulsed-wave (PW) Doppler measurements were performed in the lowest renal artery, the infrarenal neck, the aneurysmal sac, and both common iliac arteries with a clinical US scanner (Hitachi ARIETTA 850; FUJIFILM Healthcare Corporation). Second, at the same locations HFR CEUS data were acquired with a curved array transducer (GE C1-6-D; GE Healthcare) connected to a fully programmable US system (Vantage 256; Verasonics). Images were captured after a 0.75 mL bolus injection of SonoVue microbubbles (Bracco Imaging) using a 3-angled diverging wave scheme at a PRF of 6000 Hz – effective imaging rate of 2000 Hz – and a center frequency of 2.2 MHz. PIV analysis was performed using a four-iteration grid refinement approach, with a final interrogation window of 2.8 x 2.8 mm^2 and 75% overlap (final vector grid spacing of 0.7 x 0.7 mm). Correlation averaging of 10 frames was applied for smoothing purposes[7]. As a reference, 4D PC MRI data were collected with a 3T MR scanner (Ingenia; Philips Healthcare) using a 4D Qflow sequence including retrospective ECG gating and respiratory motion compensation. Data were acquired in a volume ranging from the suprarenal aorta down to the external iliac arteries with a reconstructed isotropic voxel size of 1.25 mm at 28 timepoints during the cardiac cycle. The velocity encoding range (venc) was set per scan.

Results

On first qualitative inspection the outcomes of the first patient show good agreement in measured velocities between echoPIV, PW Doppler and PC MRI in the aneurysmal neck. Preoperatively, it was found that both echoPIV and PC MRI had difficulties with blood flow quantification in the aneurysmal sac where very low to almost stagnant blood flow is present during diastole. During systole echoPIV revealed complex flow patterns and recirculation zones at the proximal edge of the aneurysmal sac. Postoperatively, it was found that both echoPIV and MRI were able to quantify blood flow inside the stent graft. As an example, blood flow velocity outcomes obtained of the right iliac artery after EVAR are given in Figure 1. The echoPIV data shows a recirculation zone at the distal edge of the limb (panel B). The PC MRI data shows regions with relatively high velocities (panel C). Stent graft related artefacts were marginal. In-depth analysis of the PC MRI data as well as detailed comparison of spatiotemporal blood flow velocity profiles and complex flow phenomena between echoPIV and PC MRI is ongoing.
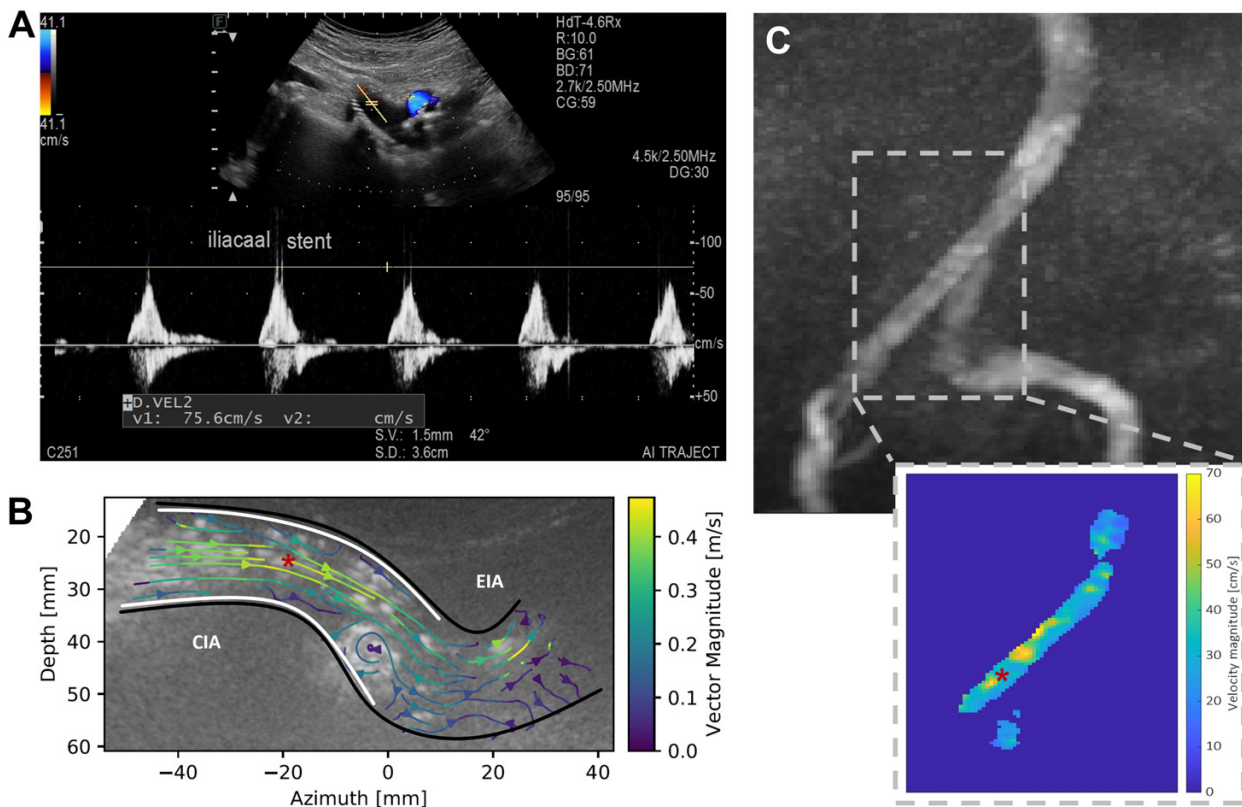
Figure 1. (A) Pulsed-wave Doppler, **(B)** echoPIV and **(C)** 4D phase contrast MRI systolic velocity outcomes of the right common iliac artery after endovascular treatment. The black and white lines in panel B indicate the estimated vessel outline and location of the stent, respectively. The red asterisk in panel B and C indicates the approximate sampling location for the pulsed-wave Doppler measurement. CIA; common iliac artery, EIA; external iliac artery.

Conclusions

Preliminary results indicate good agreement between measured velocities with echoPIV and corresponding PC MRI data of an AAA patient before and after EVAR. Furthermore, echoPIV was able to capture complex flow phenomena such as recirculation zones. If and to what extent these phenomena are confirmed by PC MRI data is the topic of future analysis.

References

[1]. Patel R, Sweeting MJ, Powell JT, Greenhalgh RM. Endovascular versus open repair of abdominal aortic aneurysm in 15-years' follow-up of the UK endovascular aneurysm repair trial 1 (EVAR trial 1): a randomised controlled trial. Lancet. 2016;388(10058):2366–74.

[2]. Lasheras JC. The biomechanics of arterial aneurysms. Annu Rev Fluid Mech. 2007;39:293–319.

[3]. Boersen JT, Groot Jebbink E, Versluis M, Slump CH, Ku DN, de Vries JPPM, et al. Flow and wall shear stress characterization after endovascular aneurysm repair and endovascular aneurysm sealing in an infrarenal aneurysm model. J Vasc Surg. 2017;66(6):1844–53.

[4]. van de Velde L, Donselaar EJ, Groot Jebbink E, Boersen JT, Lajoinie GPR, de Vries JPPM, et al. Partial renal coverage in endovascular aneurysm repair causes unfavorable renal flow patterns in an infrarenal aneurysm model. J Vasc Surg. 2018;67(5):1585–94.

[5]. Engelhard S, Voorneveld J, Vos HJ, Westenberg JJM, Gijsen FJH, Taimr P, et al. High-frame-rate contrast-enhanced US particle image velocimetry in the abdominal aorta: First human results. Radiology. 2018;289(1):119–25.

[6]. Engelhard S, van Helvert M, Voorneveld J, Bosch JG, Lajoinie GPR, Versluis M, et al. US Velocimetry in Participants with Aortoiliac Occlusive Disease. Radiology. 2021;(9):210454.

[7]. Willert C. Adaptive PIV processing based on ensemble correlation. 14Th Int Symp Appl Laser … [Internet]. 2008;7–10.

Fast 3D Nonlinear Sound-Sheet Imaging of Endogenous, Protein-based, and Synthetic Contrast Agents

B. Heiles[1], A. Kuliesh[1], D. Terwiel[1], R. Waasdorp[1], B. M. Park[1], D. Maresca[1,]*

[1]Department of Imaging Physics, Delft University of Technology, Delft, The Netherlands
[*]Corresponding author:d.maresca@tudelft.nl

Introduction

Lipid-shelled gas-filled microbubbles are intravascular synthetic ultrasound contrast agents that enable ultrasound imaging beyond the diffraction limit [1], leading to *in vivo* atlases of the vasculature down to the microscale with an approach called ultrasound localization microscopy [2–4]. In 3D, the mapping of large portions of organs is now possible [5], but challenges remain when it comes to mapping entire organs [6] due to data and high electronic channel count management. Row Column Addressed (RCA) arrays have emerged as a technical solution to these problems, offering large fields of view and reduced channel counts, but they suffer from lower contrast and a reduced ability to focus ultrasound waves [7]. This poses challenges for contrast-enhanced imaging with RCA probes.

In 2014, the discovery of genetically encoded acoustic biomolecules known as gas vesicles (GVs) enabled fundamental advances in molecular ultrasound such as imaging of gene expression [9], enzyme activity [10], or tumor hypoxia [11]. To date, amplitude modulation sequences based on cross-propagating plane waves (xAM) provide the most sensitive and specific ultrasound images of GVs [12]. However, because xAM imaging is performed line-by-line using a relatively large sliding sub-aperture, it is intrinsically limited in framerate and field of view [13]. The development of a dedicated RCA mode dedicated to faster, wide-field, and volumetric GV detection would represent a major advance.

Here, we introduce a new imaging method called 3D Sound Sheet Imaging (SSI) implemented on RCA probes and capable of detecting both synthetic (microbubbles) and protein-based (GVs) ultrasound contrast agents with high specificity. SSI relies on the interaction of two intersecting planar excitations of long thin line elements. Cross-propagation occurs at their intersection and generates a sound sheet perpendicular to the active surface of the probe. The position, thickness, and depth of this non-diffracting beam can be changed to deliver 2D or 3D imaging with isotropic resolution across a volume of 1.2 cm^3. We implemented SSI using a 15 MHz RCA probe (Imasonic, France) and demonstrate its potential by imaging genetically encoded GVs, synthetic microbubbles, but also red blood cells in the rat brain.

Methods

(N)SSI sequence. A custom-built 15 MHz 128+128 elements RCA probe was driven using a 256-channel programmable ultrafast ultrasound scanner (Verasonics, USA) (**Figure 1a**). Rows (and alternatively columns) were used to transmit simultaneous cross-propagating plane waves from two contiguous half-apertures $D_{Ap/2}$ at angles α and $-\alpha$. The two transmitted plane waves span the whole elevation width of the RCA probe and intersect along a 2D plane, referred to as the sound-sheet (**Figure 1b**). A double amplitude planar wave-front is generated at the plane waves intersection and propagates across the sound-sheet plane at a supersonic velocity $\frac{c_0}{\cos(\alpha)}$ [12]. Image reconstruction of the echoes received by the columns of the RCA probe relies on delay-and-sum beamforming [14] with the assumption that backscattering only arises from the sound-sheet plane (**Figure 1c**). The receive volume spans the entire transducer field of view. A large volume can be captured by sweeping this transmission along the rows of the array.

For the non-linear mode, the same sub-apertures were used for two additional transmits, each firing independently this time, and eliciting half-amplitude linear backscattering from the medium. The amplitude-modulated signal was obtained by subtracting the two single amplitudes to the double amplitude received RFs (**Figure 1d**).

Figure 1. a) Dimensions and architecture of the Row-Column array probe. b) Two cross-propagating plane waves are used to create a sound-sheet with doubled amplitude in one direction. c) The Receive volume contains all the volume of view of the probe while the transmit focusing is restored by the sound-sheet. Sub-wavelength orthogonal scan allows to perform 3D imaging. d) Thanks to the higher amplitude at the cross-propagation plane, an amplitude modulation scheme can also be implemented with the transmit TX2 and TX3 only using half of the sub-aperture of the first transmit.

GV phantom. Anabaena flos aquae GVs were cultured and transferred to sterile separating funnels. Buoyant cells were separated from the growth media through natural flotation, and GVs were harvested after 48h of hypertonic lysis. A cycle of centrifugation and resuspension allows to purify the GVs further. A stock of wild-type GVs (wtGVs) was stripped of their GvpC protein layer with a 6-M urea solution to obtain GVs that scatter higher harmonics (hGVs). These two GV variants were either stored in phosphate buffered saline (PBS) or clustered to end up with 4 different imaging samples: wtGVs, aggregated wtGVs (wtGVs+), hGVs and aggregated hGVs (hGVs+). A 2% agar phantom comprising 2 mm in diameter wells was casted using custom-printed molds and imprints. Wells were filled with agar (control) or agar mixed with one of the 4 different GV variants prepared. The final GV concentration was measured optically at OD2.5 ($285\ pM$).

Results

The RCA probe was placed over the GV phantom filled with 5 different samples, agar and the 2 GV variants (**Figure 2a**). We first display in **figure 2a** one sound-sheet at a fixed position in the coronal and sagittal direction. We can successfully observe the contrast increase in both of the GV-containing wells. Then, we performed NSSI scanning of the GV phantom at a pressure eliciting nonlinear scattering of hGVs (300-600 kPa range). At each sub-aperture position, 13 sound-sheets were transmitted with angles spanning 9° to 21° to increase SNR via angular compounding. The two wells filled with hGVs were detected by the 3D NSSI mode whereas echoes arising from the linear GV variants are extinguished as well as the artifacts below the wells. All images were log-compressed and are displayed with a 100 dB range and 70 dB range for the volume.
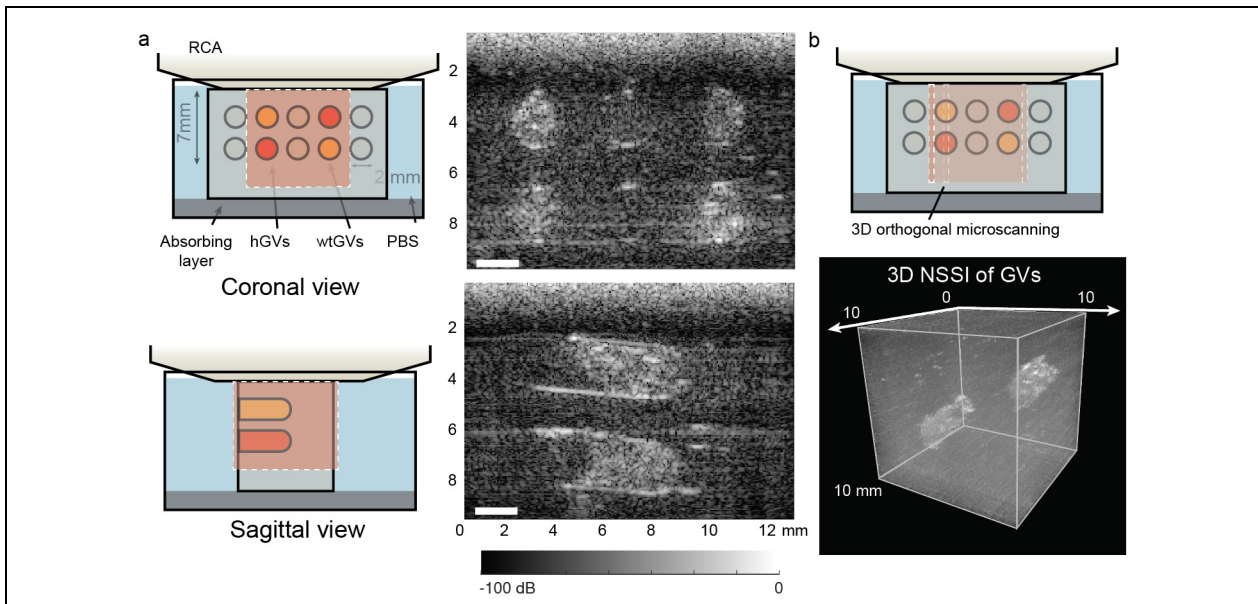
Figure 2. a) Linear Sound-Sheet imaging of well containing harmonic and wild-type GVs in Sagittal and Coronal views. b) Non-Linear Sound-Sheet imaging allows 3D imaging of harmonic GVs with orthogonal microscanning.

The Non-Linear Sound-Sheet imaging sequence was also used to image microbubbles (Micromarker® Fujifilm, Bracco). NSSI delivers filter-free imaging of microbubbles and we could successfully image the flow using non-linear Power Doppler (**figure 3 a**).

Finally, we used the RCA probe to image the vasculature of a rat brain. After craniotomy, the probe was placed over the anesthetized animal and a coronal scan spanning $300\ \mu m$ was acquired at 1000 Hz for 0.5 s (**figure 3b**). Singular Value Decomposition filtering was applied to retain only blood signal in the different sound-sheets. A Maximum Intensity Projection is displayed in **figure 3c** and spans a thickness of $300\ \mu m$, comparable to what would be obtained at the focal point with a 2D probe transmitting through a lens at 15 MHz. A brighter band is present on the left images which is an artifact from the probe. All images are acquired without microbubles.
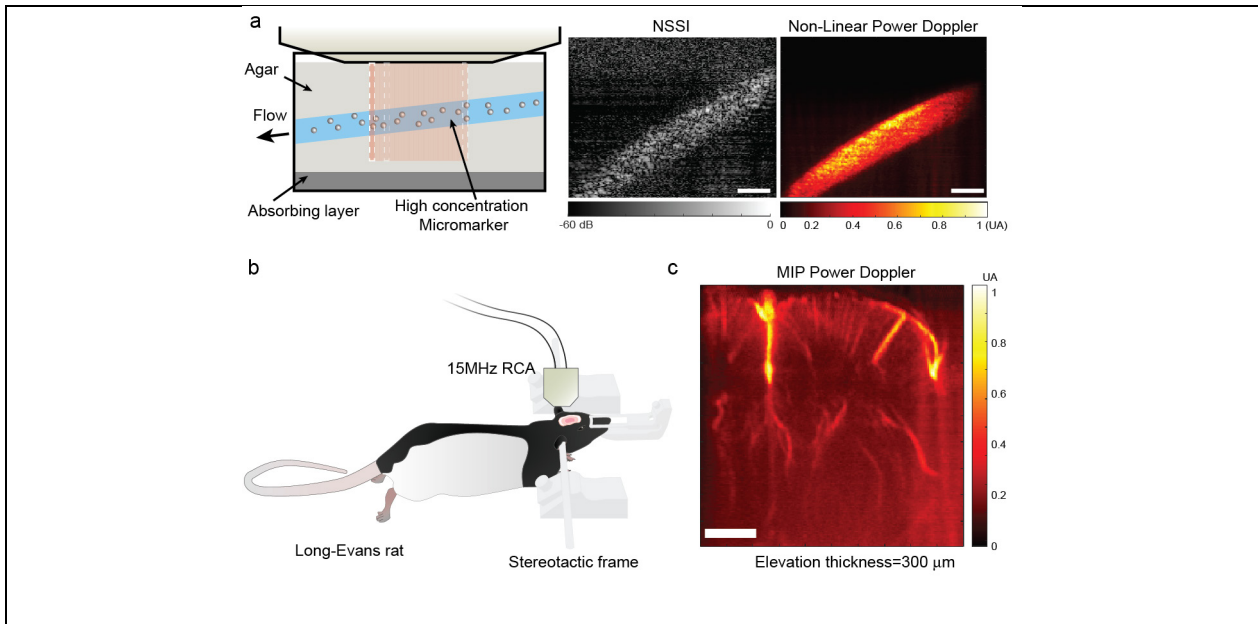
Figure 3. a) Non-linear Sound Sheet Imaging of high concentration microbubbles (Micromarker ® Fujifilm, Bracco) and associated Power Doppler Imaging. b) In vivo SSI microscanning of an anesthetized Long-Evans rat brain. The animal is maintained in a stereotactic frame and the probe is place over the brain with acoustic gel. c) Maximum Intensity Projection of a Power Doppler image in the sagittal direction over a $300\ \mu m$ thick elevation plane. Scale bar is 2 mm.

Conclusions

We introduce fast 3D nonlinear sound-sheet imaging (NSSI), a contrast-enhanced ultrasound imaging method dedicated to RCA probes and capable of detecting synthetic and protein-based contrast agents with high specificity. We successfully imaged linear and non linear GVs. NSSI achieves kHz framerates in the sound-sheet plane and volume rates of up to 300 Hz, which is on par with 4D fUS imaging [8]. Sound-sheet imaging also enabled microscanning of the rodent cerebral vasculature using high-frame Power Doppler. In the near future, (N)SSI will enable time-resolved ultrasound imaging of biological events in their native spatial arrangements. By combining RCA probes and ultrafast imaging, NSSI solves the xAM limitations in terms of field-of-view and imaging speed, allowing to produce high resolution imaging of contrast agents and of the vasculature.

References

[1]. Couture O, Besson B, Montaldo G, Fink M, Tanter M. Microbubble ultrasound super-localization imaging (MUSLI). In: 2011 IEEE International Ultrasonics Symposium [Internet]. Orlando, FL, USA: IEEE; 2011 [cited 2020 Feb 20]. p. 1285–7. Available from: http://ieeexplore.ieee.org/document/6293576/

[2]. Errico C, Pierre J, Pezet S, Desailly Y, Lenkei Z, Couture O, et al. Ultrafast ultrasound localization microscopy for deep super-resolution vascular imaging. Nature. 2015 Nov;527(7579):499–502.

[3]. Siepmann M, Schmitz G, Bzyl J, Palmowski M, Kiessling F. Imaging tumor vascularity by tracing single microbubbles. In: 2011 IEEE International Ultrasonics Symposium [Internet]. Orlando, FL, USA: IEEE; 2011 [cited 2020 Feb 20]. p. 1906–9. Available from: http://ieeexplore.ieee.org/document/6293297/

[4]. Demené C, Robin J, Dizeux A, Heiles B, Pernot M, Tanter M, et al. Deep Transcranial Adaptive Ultrasound Localization Microscopy of the Human Brain Vascularization. Nature Biomedical Engineering. 2021;(5):219–28.

[5]. Heiles B, Rabut C, Hingot V, Rahal L, Lopez P, Pernot M, et al. Volumetric ultrafast Ultrasound Localization Microscopy in vivo. In Kobe, Japan; 2018.

[6]. Heiles B, Chavignon A, Bergel A, Hingot V, Serroune H, Maresca D, et al. Volumetric ultrasound localization microscopy of the whole rat brain microvasculature. IEEE Open Journal of Ultrasonics, Ferroelectrics, and Frequency Control. 2022;1–1.

[7]. Jensen JA, Schou M, Jorgensen LT, Tomov BG, Stuart MB, Traberg MS, et al. Anatomic and Functional Imaging using Row-Column Arrays. IEEE Trans Ultrason, Ferroelect, Freq Contr. 2022;1–1.

[8]. Daeichin V, Bosch JG, Needles A, Foster FS, van der Steen A, de Jong N. Subharmonic, Non-linear Fundamental and Ultraharmonic Imaging of Microbubble Contrast at High Frequencies. Ultrasound in Medicine & Biology. 2015 Feb;41(2):486–97.

[9]. Farhadi A, Sigmund F, Westmeyer GG, Shapiro MG. Genetically encodable materials for non-invasive biological imaging. Nat Mater. 2021 May;20(5):585–92.

[10]. Lakshmanan A, Jin Z, Nety SP, Sawyer DP, Lee-Gosselin A, Malounda D, et al. Acoustic biosensors for ultrasound imaging of enzyme activity. Nat Chem Biol. 2020 Sep;16(9):988–96.

[11]. Hurt RC, Buss MT, Duan M, Wong K, You MY, Sawyer DP, et al. Genomically Mined Acoustic Reporter Genes Enable In Vivo Monitoring of Tumors and Tumor-Homing Bacteria [Internet]. Bioengineering; 2021 Apr [cited 2021 Nov 19]. Available from: http://biorxiv.org/lookup/doi/10.1101/2021.04.26.441537

[12]. Maresca D, Sawyer DP, Renaud G, Lee-Gosselin A, Shapiro MG. Nonlinear X-Wave Ultrasound Imaging of Acoustic Biomolecules. Phys Rev X. 2018 Oct 4;8(4):041002.

[13]. Rabut C, Wu D, Ling B, Jin Z, Malounda D, Shapiro MG. Ultrafast amplitude modulation for molecular and hemodynamic ultrasound imaging. Appl Phys Lett. 2021 Jun 14;118(24):244102.

[14]. Rasmussen MF, Christiansen TL, Thomsen EV, Jensen JA. 3-D imaging using row-column-addressed arrays with integrated apodization - part i: apodization design and line element beamforming. IEEE Trans Ultrason, Ferroelect, Freq Contr. 2015 May;62(5):947–58.

In-vivo high frame rate contrast-enhanced volumetric vasculature imaging using a sparse array

Luxi Wei[1], Geraldi Wahyulaksana[1], Maaike te Lintel Hekkert[2], Robert Beurskens[1], Enrico Boni[3], Alessandro Ramalli[3], Emile Noothout[4], Piero Tortoli[3], Antonius F.W. van der Steen[1,4], Nico de Jong[1,4], Martin Verweij[1,4], Hendrik J. Vos[1,4]

[1]*Biomedical Engineering, Erasmus MC, Rotterdam, the Netherlands.* [2]*Experimental Cardiology, Erasmus MC, Rotterdam, the Netherlands.*[3]*Department of Information Engineering, University of Florence, Italy.* [4]*Medical Imaging, TU Delft, the Netherlands. Corresponding author: l.wei@erasmusmc.nl*

Introduction

Sparse arrays enable high frame rate volumetric imaging with relatively low hardware requirements. They are especially suited for microbubble imaging because of their inherently low transmit sensitivity: low transmit pressures avoid bubble disruption, while the scattered signal is high due to bubble resonance. For vascular imaging using microbubbles, our group has previously designed and manufactured sparse arrays in a spiral layout [1]. An earlier prototype of this probe was used for high frame rate volumetric microbubble imaging a tissue-mimicking phantom and chicken embryos [2]. The phantom provided uniform tissue-like scattering, while the chicken embryo provided physiological blood flow in a low-scattering structure. The next step is vascular imaging in a more complex *in vivo* environment. In this study, we demonstrate the feasibility of transcutaneous volumetric imaging of a porcine-kidney model and show 3D power and color Doppler results.

Methods

A Yorkshire x Norwegian Landrace pig (35 kg) was anesthetized and placed on Pentobarbital (15 mg/kg/h). The animal experiments followed European Union and institutional guidelines for the care and use of laboratory animals, with CCD approval AVD10010020172411 (SP2100125). A diluted (30x) Definity® solution (Lantheus Medical Imaging Inc., MA, USA) was infused through the jugular vein at a 6 mL/min flow rate. Volumetric imaging of the left kidney was performed using our home-built sparse spiral array centered at 5 MHz [1] driven by a Vantage 256 system (Verasonics Inc., Redmond, WA). A scan sequence based on the transmission of 5 steered diverging waves [2] was used. A 5 kHz pulse repetition frequency enabled 1 kHz frame rate (post-angular compounding). The acquisition was 2-seconds-long and the collected raw radio-frequency data was beamformed offline (USTB [3]). The singular-value-decomposition (SVD) filter was used on the beamformed and angle compounded data to remove tissue signals. The filtered data was then used to calculate power and color Doppler volumetric images. To remove breathing motion, rigid motion correction [4] was performed using the power Doppler time series and applied to both power and color Doppler results.

Results

A branch of the kidney artery tree was imaged. After clutter filtering and power Doppler filtering, the 3D structure can be seen in Fig.1a. Smaller vessels in the renal cortex are visible in power Doppler maximum intensity projections (b) as well as in volume (c). Accumulation in time allowed the visualization of complete vessels (b). Application of volume-wide color Doppler processing (d) allowed the distinction of flow directions in small vessels. In the renal cortex, parallel vessels could be seen with microbubbles flowing in opposite directions (d, black arrows).

Conclusions

This work demonstrates in-vivo transcutaneous volumetric microbubble imaging in a complex organ using a sparse spiral array. The array, which was developed in house by our group and collaborators, enables high frame rate imaging at reduced channel counts, thus providing the high correlation in both space and time to remove tissue signals with SVD.
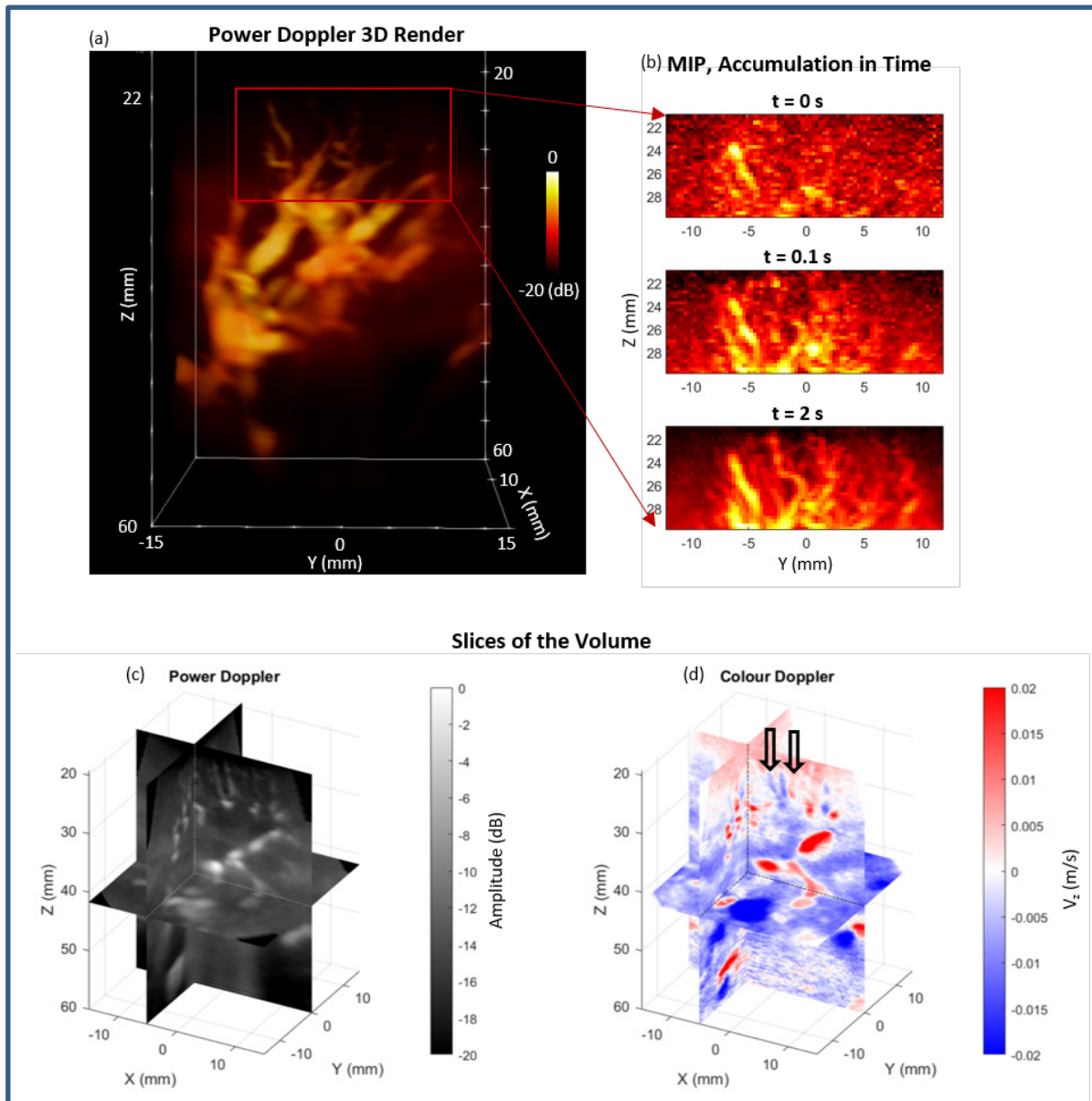
Figure 1. (a) 3D render of the average power Doppler of the entire acquisition (2 s). (b) Small vessels with few bubbles at any given time become clearer as the power Doppler frames were accumulated and displayed as maximum intensity projections (MIP). (c,d) Slices through the volumes after power (c) and colour (d) Doppler processing. Smaller vessels are clearer in power Doppler, while colour Doppler gives information on the direction of flow. Parallel vessels flowing in opposite directions can be seen in (d, black arrows).

References

[1]. L. Wei et al., "Sparse 2-dimensional PZT-on-PCB arrays with density tapering," IEEE Trans Ultrason Ferroelectr Freq Control, Oct. 2022.

[2]. L. Wei et al., "High frame rate volumetric imaging of microbubbles using a sparse array and spatial coherence beamforming," IEEE Trans Ultrason Ferroelectr Freq Control, Oct. 2021.

[3]. A. Rodriguez-Molares et al., "The ultrasound toolbox," in Proc. IEEE Ultrason. Symp., Sep. 2017.

[4]. E. A. Pnevmatikakis and A. Giovannucci, "NoRMCorre: An online algorithm for piecewise rigid motion correction of calcium imaging data," J Neurosci Methods, vol. 291, pp. 83–94, Nov. 2017.

Detecting tumors in acoustic angiography: a deep learning approach

Thomas M. Kierski[1], Kathlyne Jayne B. Bautista[1], Isabel G. Newsome[1], Paul A. Dayton

[1]*Joint Department of Biomedical Engineering, The University of North Carolina, Chapel Hill, NC, USA*
Corresponding author: kathlyne@live.unc.edu

Introduction

Acoustic angiography images microvasculture in 3-D at high resolution and high contrast-to-tissue ratio. Given the high specificity and senstivity, quantitative metrics of vascular tortuosity and density of tumors can be derived from these images to inform cancer diagnostics [1]. However, the current image analysis pipeline suffers from time-consuming vessel segmentation and high inter-operator variability [2], which significantly limits the translation of this technique towards the clinic. Alternatively, deep learning can be used to automate the classification task [3] in an end-to-end manner without reliance on hand-crafted metrics of vascular morphology. Here, we demonstrate the feasibility of classifying healthy tissue and tumors in *in-vivo* acoustic angiography images using deep convolutional neural networks (CNNs).

Methods

We obtained 3-D acoustic angiography images of both healthy and tumor-associated tissue in Fischer-344 rats using a dual-freuency (Tx = 4 MHz, Rx = 30 MHz) wobbler transducer with $n = 195$ images (97 tumors, 98 controls). We evaluated 5 CNN architectures: (1) EfficientNet-B0-3D, (2) EfficientNet-B0, (3) EfficientNet-B1, (4) DenseNet-121, and (5) ResNet-18. We then compared the performance of the various architectures in a nested k-fold cross validation study where the number of inner and outer folds were each set to 5. We also utilized Grad-CAM to measure network attention on test images.

Results

The 3-D CNN (EfficientNet-B0-3D) produced the highest average test accuracy across the 5 outer folds compared to the 2-D CNNs (Fig. 1a), as expected given that the 3-D representation of images are maintained during training whereas 2-D maximum projections are used to train the 2-D models. Nonetheless, the 2-D CNNs still demonstrated high accuracies between 78.2 and 88.8% and remain feasible candidates in cases where computationally intensive training of 3-D architectures may be limited. Additionally, as a qualitative metric of the model performance, saliency maps (Fig. 1b) highlight regions of high vascular tortuosity and density as areas that largely contributed to the correct classification of tumors, which agrees with clinical understanding of tumor vasculature.

Conclusions

This work demonstrates the feasibility of CNNs for accurate classification of *in-vivo* tumors from healthy tissue. We attained an average accuracy of $92.8 \pm 3.4\%$ for the 3-D CNN and $88.8 \pm 4.6\%$ for the best performing 2-D CNN, calculated on the outer folds. Furthermore, qualitative assessment of the models' classification indicates general agreement with known clinical markers of tumor-associated vasculature. Future application of this methodology include detection of spontaneously developing tumors and prediction of tumor treatment response.
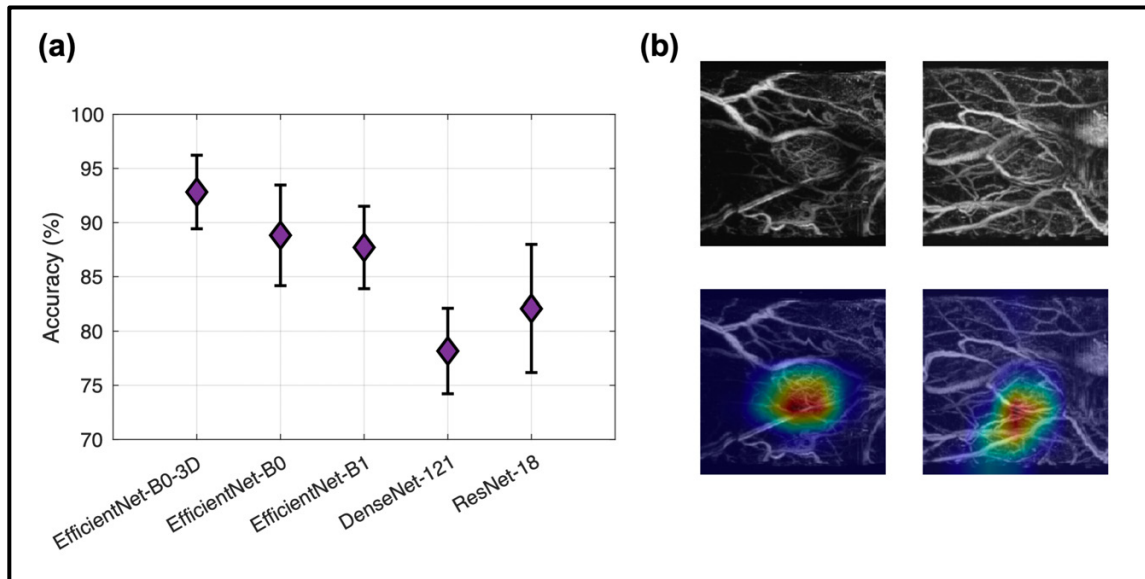
Figure 1. (a) The accuracies of each CNN evaluated. (b) Representative Grad-CAM saliency maps from EfficientNet-B0 of correctly identified tumor images, where "hot" areas represent regions of importance for the model's classification.

References

[1]. Shelton SE, Lee YZ, Lee M, et al, Quantification of Microvascular Tortuosity during Tumor Evolution Using Acoustic Angiography, Ultrasound in Medicine & Biology, 41(7):1896-1904, 2015.

[2]. Rao SR, Shelton SE, Dayton PA, The "Fingerprint" of Cancer Extends Beyond Solid Tumor Boundaries: Assessment With a Novel Ultrasound Imaging Approach, IEEE Transactions on Biomedical Engineering, 63(5):1082-1086, 2016.

[3]. Li H, Weng J, Shi Y, et al, An improved deep learning approach for detection of thyroid papillary cancer in ultrasound images, Sci Rep, 8(1):6600, 2018.

Shell characterization of single microbubbles using a novel stress-strain analysis

Charlotte Nawijn[1], Sander Spiekhout[2], Jason Voorneveld[2], Hans Bosch[2],
Michel Versluis[1], Tim Segers[3], and Guillaume Lajoinie[1]

[1]*Physics of Fluids Group, Technical Medical (TechMed) Center, University of Twente, The Netherlands*
[2]*Department of Biomedical Engineering, Thorax Center, Erasmus MC University Medical Center, Rotterdam, the Netherlands*
[3]*BIOS Lab-on-a-Chip group, Max-Planck Center Twente for Complex Fluid Dynamics, MESA+ Institute for Nanotechnology, University of Twente, The Netherlands*
Corresponding author: c.l.nawijn@utwente.nl

Introduction

Microbubbles are of great interest for ultrasound imaging, where they are used as contrast agents, as well as for ultrasound therapy, in drug and gene delivery applications. In both cases, a full characterization of the response of microbubbles to ultrasound is crucial to fully exploit the nonlinear features of these bubbles. Besides the intrinsic bubble dynamics nonlinearities, these nonlinearities also depend on the nonlinear viscoelastic shell beahvior, especially at low driving amplitudes [1]. While acoustic attenuation measurements can be used to characterize bubble populations at low acoustic pressure, these need to be performed on a microbubble suspension, and thus high-precision characterization is only possible by using monodisperse bubbles [2, 3]. In contrast, single microbubbles can be characterized using ultra-high-speed optical imaging [3], but this requires relatively large oscillation amplitudes, and measurements in the free-field pose great difficulties.

Here we propose a novel method to characterize the viscoelastic shell properties of single microbubbles in an acoustical camera setup [4, 5]. Detailed knowledge of the acoustic driving pressure and frequency combined with a precise measure of the resulting strain, and strain rate of the bubble interface allows us to derive the elastic and viscous properties of single microbubbles. Not only does this technique allow the study of single bubble dynamics, but it also opens new possibilities to unravel the dissipation mechanisms within the interface as a function of strain and strain rate.

Methods

The elastic and viscous pressure contributions (which we call function f) are the result of a pressure balance resulting from inertia, thermodynamic behavior of the gas inside the bubble, sound re-radiation, atmospheric pressure, and the incident acoustic pressure, which we extract by rewriting the Keller-Miksis bubble dynamics equation [1]:

$$f = P_{elas} + P_{visc} = -\rho_L \left(R \frac{d^2 R}{dt^2} + \frac{3}{2} \frac{dR}{dt} \right) + \left(P_0 + \frac{2\sigma(R_0)}{R_0} \right) \left(\frac{R_0}{R} \right)^{3\kappa} \left(1 - \frac{3\kappa}{c_L} \frac{dR}{dt} \right) - P_0 - P_{ac}, \quad (1)$$

with $R = R(t)$ the bubble radius, R_0 the initial radius, $\sigma(R_0)$ the initial surface tension at rest, ρ_L the density of the medium, κ the polytropic exponent of the gas, c_L the speed of sound in the medium, P_0 the atmospheric pressure, and P_{ac} the incident acoustic pressure. The elastic and viscous contribution are commonly modeled as [1]:

$$\frac{2\sigma(R)}{R} + \frac{4}{R} \frac{dR}{dt} \left(\mu_L + \frac{\kappa_s}{R} \right), \quad (2)$$

with $\sigma(R_0)$ the radius-dependent surface tension, μ_L the viscosity of the medium, and κ_s the shell viscosity. Through nondimensionalization of Eq. 1, the viscous and elastic pressure contributions can be written as a function of the radial strain $(R(t) - R_0)/R_0$, and its time derivatives. The elastic contribution, and thereby the effective surface tension, is independent of the strain rate and can thus be determined from the nondimensionalized function $\tilde{f}$ at zero strain rate. The remainder of the shell contributions is due to the

viscosity of the shell and of the medium. Note that this approach does not require any a priori knowledge on the material constitutive laws of the monolayer shell.

The viscoelastic contribution of the shell of a single microbubble as a function of the radius and bubble wall velocity is determined by ramping-up the incident acoustic pressure, while measuring radial strain and strain rate, using the 'acoustical camera' setup as described in [4, 5], see Fig. 1A. Briefly, this setup consists of a tank filled with a microbubble suspension, in which an ultrasound transducer provides the acoustic field that drives the radial oscillations of the microbubbles at a frequency of 1.6 MHz. The wave is programmed to increase in amplitude from 0 to 38 kPa in a time span of 100 µs, before it is ramped-down to 0 kPa over another 100 µs. Simultaneously, two high-frequency transducers (25 MHz frequency) are used to probe the bubble oscillations: the first transmits ultrasound with an amplitude of 500 kPa for 245 µs, arriving 35 µs before the low-frequency pulse, while the second receives the amplitude-modulated wave scattered by the bubble. The radial strain time trace is then recovered using amplitude demodulation [5].
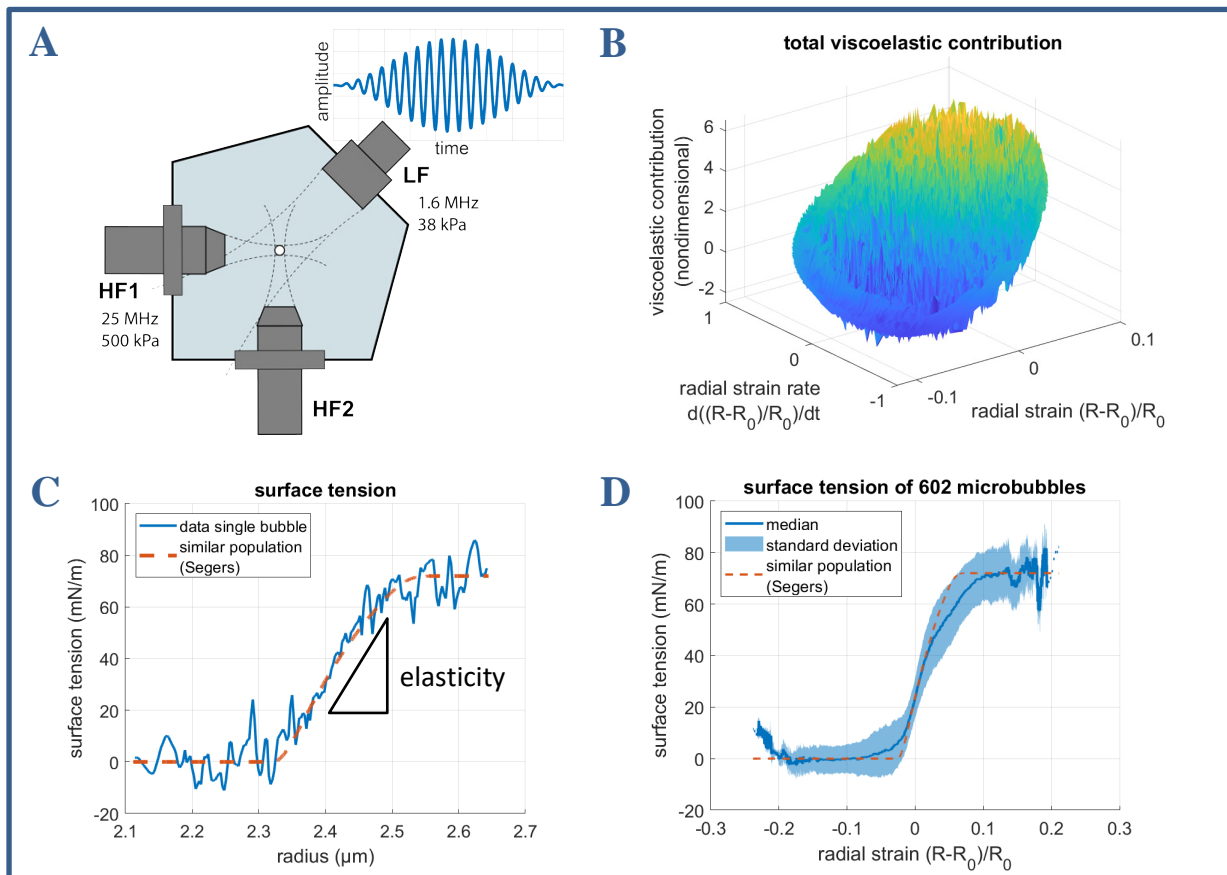
Figure 1. A) Schematic of the acoustical camera setup, with low-frequency (LF) and high-frequency (HF) transducers [5]. B) The viscoelastic pressure contribution of a single microbubble as a function of strain and strain rate. C) The strain-dependent surface tension as determined from the viscoelastic pressure contribution in 1B. The orange dashed line shows a measured surface tension curve of DPPC-based bubbles of the same size by Segers et al. [3]. D) The combined surface tension curves of all bubbles analyzed in this work. The solid blue line indicates the median, and the shaded region the standard deviation. The orange dashed line again shows the measured surface tension curve by Segers et al. [3].

To validate this novel characterization approach, we use lipid-shelled (DSPC mixed with DPPE-PEG5000, 9:1 molar ratio) monodisperse C_4F_{10}-filled microbubbles, made in-house using a flow-focusing device at 55°C and using a gas mixture of 13 v% C_4F_{10} in CO_2, as described in [6, 7]. The bubbles had a radius of 2.6 ± 0.27 µm. The surface tension as a function of bubble radius is recovered by applying an error minimization routine that enforces a zero surface tension when the bubble is fully compressed, and a surface tension equal to that of water when the bubble shell is fully ruptured, in line with the Marmottant

shell-buckling model [8]. From the error minimization we can extract three physical parameters: the initial radius R_0 (within the narrow size distribution), the initial surface tension $\sigma(R_0)$, and the phase of the incident acoustic pressure wave relative to the bubble's radial response (within the limits of experimental uncertainty).

Results

The total viscoelastic pressure contribution f as a function of the strain and strain rate of a single microbubble is shown in Fig. 1B. Starting at a zero strain and near zero strain rate, the hyperplane is travelled in successively larger spirals as the driving pressure increases. A typical surface tension curve extracted for a single bubble is shown Fig. 1C. The orange dashed line depicts the surface tension curve measured experimentally for a monodisperse bubble suspension (DPPC:DPPE-PEG5k, 9:1 molar ratio) with the same mean size [3]. Good agreement is found between the surface tension resulting from our stress-strain analysis with error minimization, and the curves measured previously on an entire population of bubbles.

The surface tension curves from 602 bubbles as a function of strain are shown in Fig. 1D, where the median is indicated by the solid blue line, and the standard deviation by the shaded region. From the waist of the curve at zero strain we can determine the distribution of the initial surface tension: $\sigma(R_0) = 26 \pm 8.4$ mN/m. The slope of the curve corresponds to the shell elasticity (0.54 N/m) measured via acoustic characterization of a bubble population at low acoustic pressure amplitudes (<5 kPa) and is in good agreement with previous measurements on monodisperse bubble populations (0.5 N/m) [3]. The size distribution determined through error minimization ($R_0 = 2.3 \pm 0.28$ μm) also agrees well with Coulter Counter measurements of the bubble suspension.

Conclusions

The combined viscoelastic pressure contribution of lipid-shelled microbubbles is determined from the radial strain of single microbubbles recorded by an acoustical camera. The elastic contribution, obtained at zero strain rate, provides the surface tension as a function of the bubble radius. The surface tension is in good agreement with earlier measurements on a monodisperse bubble population, for small radial amplitude oscillations. The stress-strain analysis and error minimization also provide statistics on the size and the initial surface tension of single microbubbles. Future work will investigate the dependence of the viscous contribution of the shell on the strain and strain rate.

References

[1]. M. Versluis, E. Stride, G. Lajoinie, B. Dollet, and T. Segers, "Ultrasound Contrast Agent Modeling: A Review", Ultrasound in Medicine & Biology, 46.9: 2117-2144, 2020.

[2]. M. A. Parrales, J. M. Fernandez, M. Perez-Saborid, J. A. Kopechek, and T. M. Porter, "Acoustic characterization of monodisperse lipid-coated microbubbles: Relationship between size and shell viscoelastic properties", The Journal of the Acoustical Society of America, 136.3: 1077-1084, 2014.

[3]. T. Segers, E. Gaud, M. Versluis, and P. Frinking, "High-precision acoustic measurements of the nonlinear dilatational elasticity of phospholipid coated monodisperse microbubbles", Soft Matter, 14.47: 9550-9561, 2018.

[4]. G. Renaud, J. G. Bosch, A. F. W. Van Der Steen, and N. De Jong, "Low-Amplitude Non-linear Volume Vibrations of Single Microbubbles Measured with an 'Acoustical Camera'", Ultrasound in Medicine & Biology, 40.6: 1282–1295, 2014.

[5]. S. Spiekhout et al., "Observations of monodisperse microbubble resonance by an 'Acoustical Camera'", presented at the 26th European Symposium on Ultrasound Contrast Imaging, 2021.

[6]. T. Segers, A. Lassus, P. Bussat, E. Gaud, and P. Frinking, "Improved coalescence stability of monodisperse phospholipid-coated microbubbles formed by flow-focusing at elevated temperatures," Lab on a Chip, 19.1: 158-167, 2019.

[7]. T. Segers, E. Gaud, G. Casqueiro, A. Lassus, M. Versluis, and P. Frinking, "Foam-free monodisperse lipid-coated ultrasound contrast agent synthesis by flow-focusing through multi-gas-component microbubble stabilization", Applied Physics Letters, 116.17: 173701, 2020.

[8]. P. Marmottant, S. van der Meer, M. Emmer, M. Versluis, N. de Jong, S. Hilgenfeldt and D. Lohse, "A model for large amplitude oscillations of coated bubbles accounting for buckling and rupture", The Journal of the Acoustical Society of America, 118.6: 3499-3505, 2005.

Predicting the Spontaneous Vaporisation of Nanodroplets

**Luca Bau[1], Qiang Wu[1], Cameron A.B. Smith[2], Kai Reimer[3], Mengxing Tang[3], Nicholas Ovenden[4], Eleanor Stride[1]**

[1]_Institute of Biomedical Engineering, University of Oxford, Oxford, UK_
[2]_Division of Chemistry and Chemical Engineering, California Institute of Technology, Pasadena, USA_
[3]_Department of Bioengineering, Imperial College London, London, UK_
[4]_Department of Mathematics, University College London, London, UK_
Corresponding author: luca.bau@eng.ox.ac.uk; eleanor.stride@eng.ox.ac.uk; n.ovenden@ucl.ac.uk

Introduction

Superheated perfluorocarbon droplets have been widely explored as agents for ultrasound imaging and therapy [1] and in other applications such as radiation dosimetry [2]. Submicron, or nano-, droplets offer a number of potential advantages over microbubble agents, e.g. longer circulation half-lives, higher surface area to volume ratio and the ability to perfuse the microvasculature more easily. A key challenge in the use of nanodroplets, however, is the need to avoid spontaneous vaporisation whilst keeping the energy required for acoustic activation within the range of pressures that can be used safely in humans. This is especially important for imaging applications. Perfluoropropane (C_3F_8) microbubbles can be condensed to form liquid nanodroplets [3] that offer a good trade-off between thermal stability and acoustic vaporisation threshold. Anecdotal reports, however, suggest that C_3F_8 droplets can spontaneously vaporise, and may therefore pose a potential safety risk, especially in the presence of concurrent coalescence. The aim of this study was to build on recent theoretical models of droplet vaporisation [4] and investigate the probability of vaporisation as a function of temperature and interfacial tension.

Methods

The spontaneous vaporisation of a droplet of radius r_D at temperature T is modelled as a Poisson process with rate

$$\lambda(r_D, T) = J(r_D, T) \cdot \frac{4}{3} \pi \, r_D^3$$

where $J(r_D, T)$ is the volumetric nucleation rate. The half-life of a droplet is then

$$t_{1/2}(r_D, T) = \frac{\ln 2}{\lambda(r_D, T)}$$

while the volume fraction of vaporised droplets as a function of time is

$$\chi(t; T) = \frac{\int_0^t \int_0^\infty \frac{4}{3} \pi \, r_D^3 \, PSD(r_D) \, \lambda(r_D, T) \exp[-\lambda(r_D, T)\tau] \, dr_D \, d\tau}{\int_0^\infty \frac{4}{3} \pi \, r_D^3 \, PSD(r_D) dr_D}$$

where $PSD(r_D)$ is the normalised droplet size distribution.

Classical nucleation theory (CNT) predicts a non-zero work of formation at the spinodal, which results in the underestimation of nucleation rates [5]. In order to make the CNT result for the nucleation rate consistent with the vanishing work of formation at the spinodal, we apply a correction factor $F(r_D, T)$ to the surface tension [6].

The corrected nucleation rate is

$$J(r_D, T) = \frac{N_A}{v_L(T)} \sqrt{\frac{2F(r_D,T)\sigma_{CNT}(T)}{\pi m}} \exp\left[-\frac{F(r_D,T)^3 W_{CNT}^*(r_D,T)}{kT}\right]$$

where

$$W_{CNT}^*(r_D, T) = \frac{16}{3}\pi \frac{\sigma_{CNT}(T)^3}{[p_G(r_D,T) - p_L(r_D)]^2}$$

is the reversible work of formation of a critical nucleus, N_A is Avogadro's number, $v_L(T)$ is the molar volume of the superheated liquid, $\sigma_{CNT}(T)$ is the surface tension at a flat interface, m is the molecular mass, k is Boltzmann's constant, $p_G(r_D, T)$ is the pressure inside the critical nucleus and $p_L(r_D)$ is the pressure of the superheated liquid. The correction factor, which is equal to one at the binodal, where CNT is expected to hold exactly, and zero at the spinodal, is [6]

$$F(r_D,T) = \left[1 - A\, x(r_D,T) + \left(A - 1 - \frac{A^3}{108}\right)x(r_D,T)^2 - \frac{A^2}{6}x(r_D,T)^2\, \ln x\,(r_D,T) + \frac{A^3}{108}\,x(r_D,T)^3\right]^{1/3}$$

where $x(r_D, T)$ is a nondimensional degree of superheat defined as $x(r_D, T) = \frac{p_G(r_D,T)-p_L(r_D)}{p_{G,S}(T)-p_S(T)}$

where $p_{G,S}(T)$ is the pressure inside the critical nucleus at the spinodal, and $p_S(T)$ the spinodal pressure. The parameter $A \simeq 0.1481118$ is determined by fitting $F(x)^3$ to $W_{DFT}^*(x)/W_{CNT}^*(x)$, where $W_{DFT}^*(x)$ is the work of formation determined by density functional theory (DFT) for a Lennard-Jones fluid, using literature data [7]–[9].

The pressure of the superheated liquid is calculated using the Young-Laplace equation

$$p_L(r_D) = p_{ext} + \frac{2\sigma_D}{r_D}$$

where p_{ext} is the external pressure and σ_D the interfacial tension of the droplet-water interface. The pressure inside the critical nucleus is calculated using the Kelvin equation

$$p_G(r_D, T) = p_{sat}(T)\, \exp\left[-\frac{v_L(T)}{RT}\left(p_{sat}(T) - p_L(r_D)\right)\right]$$

where $p_{sat}(T)$ is the vapour pressure at a flat interface and R is the gas constant. The pressure $p_{G,S}(T)$ inside the critical nucleus at the spinodal is calculated by replacing $p_L(r_D)$ with $p_S(T)$ in the expression for $p_G(r_D, T)$ above. Vapour pressure, molar volume and spinodal pressure are predicted using a volume-translated Peng-Robinson equation of state [10], [11]. The temperature-dependent $\sigma_{CNT}(T)$ was predicted using the model described in [12].

The droplets used in the serum stability experiments were manufactured by emulsification of 100 µl of liquid perfluorobutane in 4 ml of 16:3:1 phosphate buffered saline/propylene glycol/glycerol containing 1,2-distearoyl-sn-glycero-3-phosphocholine and 1,2-distearoyl-sn-glycero-3-phosphoethanol-amine-N-

[methoxy(polyethylene glycol)-2000] in a 9:1 molar ratio at a final concentration of 4 mg/ml, using a probe sonicator (Q125, QSonica, USA) at 50% power for 3 minutes (20 kHz, 33% duty cycle) at –5 °C. The droplets were then purified by three cycles of centrifugation at 11,000g for 6 min and resuspension in the same volume of phosphate buffered saline. A final concentration of 10^9 droplets/ml were stained with Laurdan (50 µM), incubated in 10% fetal bovine serum and imaged at 5 min intervals in a Zeiss 780 confocal microscope (355 nm excitation laser, BP 450/50 emission filter, C-Apochromat 63x/1.2 objective).

Results

The exact value of the interfacial tension of droplets obtained from the condensation of phospholipid-shelled microbubbles is not known, and could in fact be substantially lower than the equilibrium interfacial tension of 25 mN/m [13] because of monolayer compression. We investigated a range of interfacial tensions σ_D between 0 and 25 mN/m, and found that half-lives of a few seconds to minutes at 37 °C are predicted for submicron C_3F_8 droplets for values of the interfacial tension lower than about 10 mN/m (figure 1a). These results are in contrast with Mountford's model [4], which predicts long-term stability across the entire range of interfacial tensions (figure 1b).
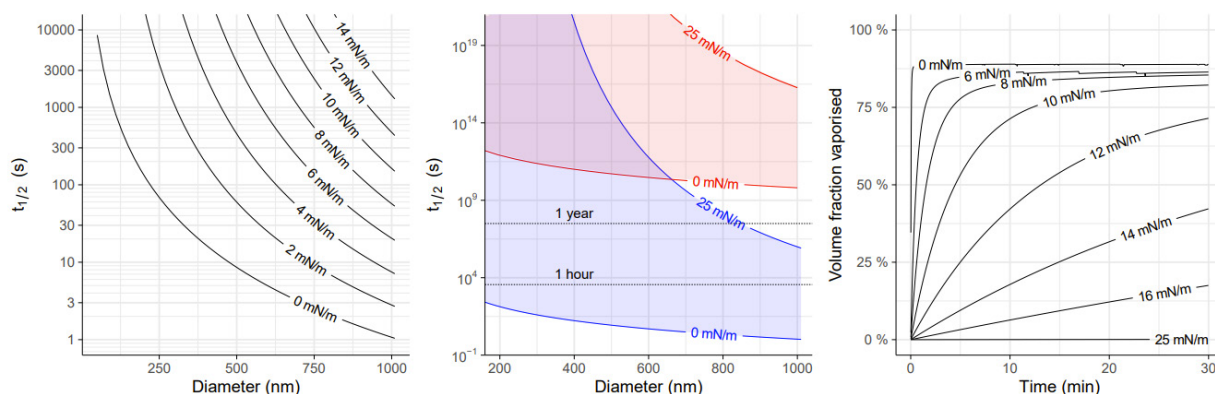
Figure 1. a) Predicted half-life of C_3F_8 droplets at 37 °C as a function of diameter and droplet-water interfacial tension; b) Range of half-lives predicted by our model (blue) and [4] (red) at 37 °C for droplet-water interfacial tensions between 0 and 25 mN/m; c) Time evolution of the volume fraction of vaporised droplets at 37 °C for a starting population with lognormal size distribution (median diameter 400 nm, coefficient of variation 50%).

We also modelled the time evolution of the volume fraction of vaporised droplets at 37 °C starting from a polydisperse size distribution of median diameter 400 nm modelled as lognormal with coefficient of variation 50%. A substantial fraction of the total droplet volume, reaching and even exceeding 50%, can be vaporised within typical *in vitro* and *in vivo* experimental time scales in a physically plausible range of interfacial tensions (figure 1c). It is important to note that our predictions do not take into account the possibility of heterogeneous nucleation, which would further increase the vaporisation rate.
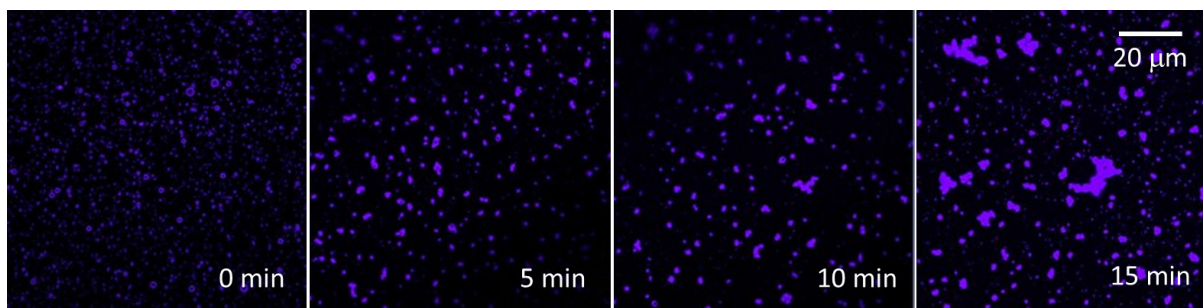
Figure 2. Time course confocal microscopy images of Laurdan-stained perfluorobutane droplets in fetal bovine serum at 37 °C.

During our experimental investigations of droplets stability, we also observed accelerated vaporisation of perfluorobutane droplets in fetal bovine serum compared to phosphate buffered saline (PBS) at 37 °C. Confocal microscopy of fluorescently labelled droplets revealed the formation of large aggregates within 15 minutes of incubation, which, if followed by coalescence, would be a possible explanation for the observed vaporisation behaviour. (figure 2).

Conclusions

Acoustically activatable nanodroplets show great potential but there are challenges for their clinical translation, especially in diagnostic applications. Anecdotal observations of spontaneous vaporisation of C_3F_8 droplets have remained unexplained so far. In this study, however, we find that the rate of spontaneous vaporisation at 37 °C can be substantially higher than previously predicted. A model has been derived which predicts the half-life of a population of C_3F_8 droplets and the corresponding increase of the vaporised volume fraction over time, showing the potential for vaporisation to proceed to a significant degree within an experimentally relevant time scale. We have also shown accelerated aggregation of perfluorobutane droplets in fetal bovine serum, which could explain their increased vaporisation rate when compared to PBS. Further work is needed to develop the model to include heterogenous nucleation and predict acoustic activation thresholds. The inherent instability of low boiling point perfluorocarbon droplets should be taken into account in preclinical work and, most importantly, in clinical translation.

References

[1] O. D. Kripfgans, J. B. Fowlkes, D. L. Miller, O. P. Eldevik, and P. L. Carson, 'Acoustic droplet vaporization for therapeutic and diagnostic applications', *Ultrasound in Medicine & Biology*, vol. 26, no. 7, pp. 1177–1189, Sep. 2000, doi: 10.1016/S0301-5629(00)00262-3.

[2] R. E. Apfel, 'The superheated drop detector', *Nuclear Instruments and Methods*, vol. 162, no. 1–3, pp. 603–608, Jun. 1979, doi: 10.1016/0029-554X(79)90735-3.

[3] P. S. Sheeran, S. Luois, P. A. Dayton, and T. O. Matsunaga, 'Formulation and Acoustic Studies of a New Phase-Shift Agent for Diagnostic and Therapeutic Ultrasound', *Langmuir*, vol. 27, no. 17, pp. 10412–10420, Sep. 2011, doi: 10.1021/la2013705.

[4] P. A. Mountford and M. A. Borden, 'On the thermodynamics and kinetics of superheated fluorocarbon phase-change agents', *Advances in Colloid and Interface Science*, vol. 237, pp. 15–27, Nov. 2016, doi: 10.1016/j.cis.2016.08.007.

[5] P. G. Debenedetti, *Metastable liquids: concepts and principles*. Princeton University Press, 1996.

[6] D. Kashchiev, 'Nucleation work, surface tension, and Gibbs–Tolman length for nucleus of any size', *The Journal of Chemical Physics*, vol. 153, no. 12, p. 124509, Sep. 2020, doi: 10.1063/5.0021337.

[7] V. K. Shen and P. G. Debenedetti, 'A kinetic theory of homogeneous bubble nucleation', *The Journal of Chemical Physics*, vol. 118, no. 2, pp. 768–783, Jan. 2003, doi: 10.1063/1.1526836.

[8] I. Kusaka, 'On the scaling behavior of the free energetics of nucleation', *The Journal of Chemical Physics*, vol. 118, no. 12, pp. 5510–5515, Mar. 2003, doi: 10.1063/1.1555843.

[9] K. Koga and X. C. Zeng, 'Thermodynamic expansion of nucleation free-energy barrier and size of critical nucleus near the vapor-liquid coexistence', *The Journal of Chemical Physics*, vol. 110, no. 7, pp. 3466–3471, Feb. 1999, doi: 10.1063/1.478214.

[10] A. M. Abudour, S. A. Mohammad, R. L. Robinson, and K. A. M. Gasem, 'Volume-translated Peng–Robinson equation of state for saturated and single-phase liquid densities', *Fluid Phase Equilibria*, vol. 335, pp. 74–87, Dec. 2012, doi: 10.1016/j.fluid.2012.08.013.

[11] J. Wisniak and K. Galon, 'Supersaturation, the Spinodal, and Their Prediction Using Equations of State', *Physics and Chemistry of Liquids*, vol. 38, no. 6, pp. 643–661, Nov. 2000, doi: 10.1080/00319100008030312.

[12] I. Cachadiña, A. Mulero, and J. Tian, 'Surface Tension of Refrigerants—Selection of Data and Recommended Correlations', *Journal of Physical and Chemical Reference Data*, vol. 44, no. 2, p. 023104, Jun. 2015, doi: 10.1063/1.4921749.

[13] K. Ullmann, L. Poggemann, H. Nirschl, and G. Leneweit, 'Adsorption process for phospholipids of different chain lengths at a fluorocarbon/water interface studied by Du Noüy ring and spinning drop', vol. 298, pp. 407–417, 2020, doi: 10.1007/s00396-020-04618-3.

Time-resolved acoustic vaporization of droplet aggregates

Anunay Prasanna[1], Samuele Fiorini[1], <u>Gazendra Shakya</u>[1], Outi Supponen[1]

[1]*Institute of Fluid Dynamics, Department of Mechanical and Process Engineering, ETH Zurich, Zurich, Switzerland*
Corresponding author: gshakya@ethz.ch

Introduction

Acoustic droplet vaporization (ADV) is a phase change phenomenon where a volatile liquid droplet undergoes a phase transition into a gaseous bubble when exposed to a pressure field above a certain threshold. After the initial observations of ADV of perfluoropentane droplets by Kripfgans et. al.[1], this phenomenon has been used in many biomedical applications using fluorocarbons as the vaporizing species, owing to their high vapor pressure [1, 2, 3]. However, heavier fluorocarbons that are stable against dissolution are difficult to vaporize and require higher acoustic intensities [1, 4, 5, 6]. Droplet aggregations have been proposed as a potential solution to lower the thresholds required for ADV [4, 7]. Nevertheless, an understanding of the underlying physics behind the acoustic vaporization of such droplet aggregations and an explanation to the reduced threshold are still missing. Here, we aim at filling this knowledge gap by temporally resolving the vaporization process of droplet aggregations using ultra-high-speed video-microscopy. Although sub-micron droplets are more suited for biomedical applications, here we use larger micron-sized droplets to facilitate their optical characterization.

Methods

Perfluoropentane (C_5F_{12}) droplets of 3-10 μm in radius were fabricated using a flow-focusing microfluidic device. Lipid solution with a mixture of 1,2-distearoyl-sn-glycero-3-phosphocholine, 1,2-distearoyl-sn-glycero-3-phosphoethanolamine-n-[polyethylene glycol]-2000 (Na salt) and a biotinylated lipid, 1,2-distearoyl-sn-glycero-3-phosphoethanolamine-N-[biotinyl(methoxy polyethylene glycol)-2000] (90:5:5 molar ratio, 10 mg/ml) was used as the surfactant to generate the droplets. Droplet aggregations were formed by taking advantage of the streptavidin-biotin binding scheme. Briefly, droplets were washed with PBS to get rid of extra lipids and 400 μl of the droplets were mixed in with 10 ml of 0.2-0.5 mg/ml streptavidin solution and left overnight to facilitate streptavidin-biotin binding and form aggregates. The droplet aggregates were placed in an optically and acoustically transparent chamber. The droplets were kept in a superheated state by placing the chamber in a temperature-controlled water bath. A custom-built microscope with a total magnification of 200X, attached to a commercial ultra-high-speed camera (Shimadzu HPV-X2) was used to record the images at 10 Mfps. A 5-MHz high-intensity focused ultrasound (HIFU) transducer was used to initiate droplet vaporization.

Results

We show that stable droplet aggregations could be generated using streptavidin-biotin binding complex. Although aggregations with different number of droplets were generated, for simplicity, this work mainly focuses on 2-droplet aggregations. We observed a slight reduction in the vaporization threshold when comparing vaporizations of 2-droplet aggregations to single droplet vaporizations. This assessment was performed in two ways: by comparing i) the radius of the smallest droplet in the aggregation, and ii) the effective radius of the combined droplet aggregation. Figure 1 shows typical visualization of the vaporization of a 2-droplet aggregation.

Interestingly, we also observed some differences in the location of the vapor nucleation site for different orientations of the droplet pair with respect to the incoming ultrasound. Additionally, in droplet-pairs containing droplets of different sizes, even though the larger droplet typically vaporizes first, the location of the larger droplet with respect to the incoming ultrasound affected the vaporization behavior of the smaller
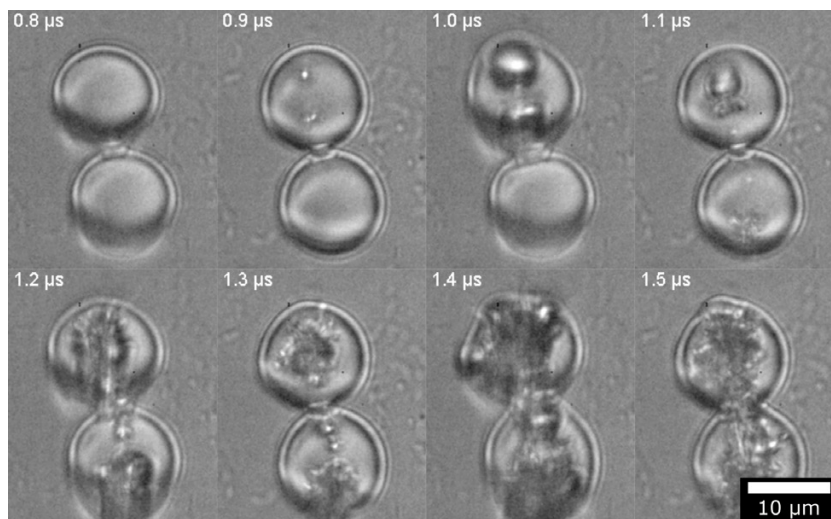
Figure 1: Series of images showing the nucleation of vapor embryo and subsequent growth of vapor bubble in a droplet pair undergoing ADV. The droplet pair is under 5 MHz acoustic field, traveling from bottom to top, in all the images. Time t = 0 corresponds to the time when the ultrasound was turned on.

droplet. We hypothesize that these curious observations of ADV in droplet aggregates arise, at least partly, from complex acoustic lensing effects in these droplets, which enhances the pressure amplification inside the droplets [8].

Finally, after the generation of the vapor bubble inside the droplet, in some cases, entrainment of the droplet fluid also created micro-jets. These micro-jets could be sufficiently strong to significantly contribute to the mechanical effects of ADV to its surroundings, with implications in the sonoporation of neighboring cells such as those forming the blood vessel walls. Future work will focus on numerical studies of acoustic lensing in droplet aggregates, physical mechanisms underlying ADV of droplet aggregates, evaluation of the final bubble formation from droplet aggregates, and scaling down the sizes of droplets for a more biologically relevant investigation.

Conclusions

With the increasing use of ADV for various biomedical applications, better physical understanding of the dynamics of ADV is desirable. In our work, we use ultra-high-speed microscopy to shed light on these mechanisms for ADV of droplet aggregations. We show that droplet aggregations could be a viable method to reduce the acoustic intensities required to initiate ADV. Our time-resolved video microscopy also unveils a possibly interesting correlation between the first vapor nucleation site and the orientation of the droplet pair to the incoming ultrasound, as well as the relative size and location of the droplets in the aggregate.

References

[1]. O. D. Kripfgans, J. B. Fowlkes, D. L. Miller, O. P. Eldevik, and P. L. Carson, "Acoustic droplet vaporization for therapeutic and diagnostic applications," Ultrasound in Medicine & Biology, vol. 26, no. 7, pp. 1177–1189, Sep. 2000, doi: 10.1016/S0301-5629(00)00262-3.

[2]. E. Vlaisavljevich et al., "Effects of Ultrasound Frequency on Nanodroplet-Mediated Histotripsy," Ultrasound in Medicine & Biology, vol. 41, no. 8, pp. 2135–2147, Aug. 2015, doi: 10.1016/j.ultrasmedbio.2015.04.007.

[3]. M. A. Borden, G. Shakya, A. Upadhyay, and K.-H. Song, "Acoustic Nanodrops for Biomedical Applications," Curr Opin Colloid Interface Sci, vol. 50, p. 101383, Dec. 2020, doi: 10.1016/j.cocis.2020.08.008.

[4]. S. Guo et al., "Lowering of acoustic droplet vaporization threshold via aggregation," Appl. Phys. Lett., vol. 111, no. 25, p. 254102, Dec. 2017, doi: 10.1063/1.5005957.

[5]. P. S. Sheeran, S. H. Luois, L. B. Mullin, T. O. Matsunaga, and P. A. Dayton, "Design of ultrasonically-activatable nanoparticles using low boiling point perfluorocarbons," Biomaterials, vol. 33, no. 11, pp. 3262–3269, Apr. 2012, doi: 10.1016/j.biomaterials.2012.01.021.

[6]. A. M. Vezeridis et al., "Fluorous-phase iron oxide nanoparticles as enhancers of acoustic droplet vaporization of perfluorocarbons with supra-physiologic boiling point," Journal of Controlled Release, vol. 302, pp. 54–62, May 2019, doi: 10.1016/j.jconrel.2019.03.013.

[7]. S. Guo et al., "Manipulation of Nanodroplets via a Nonuniform Focused Acoustic Vortex," Phys. Rev. Applied, vol. 13, no. 3, p. 034009, Mar. 2020, doi: 10.1103/PhysRevApplied.13.034009.

[8]. O. Shpak, M. Verweij, N. de Jong, M. Versluis, "Droplets, Bubbles and Ultrasound Interactions", Adv Exp Med Biol. 2016;880:157-74. doi: 10.1007/978-3-319-22536-4{$_$}9. PMID: 26486337.

Buckling and propulsion of monodisperse lipid coated microbubbles

G. Chabouh[1], B. van Elburg[2], M. Versluis[2], T. Segers[3], C. Quilliet[1], G. Coupier[1]

[1]CNRS, Laboratoire Interdisciplinare de PHYsique (Liphy), Grenoble, France.
[2]Physics of Fluids group, Technical Medical (TechMed) Center, University of Twente, Enschede, The Netherlands.
[3]Bios/Lab-on-a-chip Group, Max Planck Center Twente for Complex Fluid Dynamics, MESA+ Institute of Nanotechnology, University of Twente, Enschede, The Netherlands.
Corresponding author: georges.chabouh@sorbonne-universite.fr

Introduction

Collapse of lipidic ultrasound contrast agents under high-frequency compressive load has historically been interpreted as the vanishing of surface tension [1]. By contrast, buckling of elastic shells is known to occur when costly compressible stress is released through bending. Through quasi-static compression experiments on lipidic monodisperse microbubbles, we analyze the buckling events in the framework of classical elastic buckling theory and deduce the mechanical characteristics of these shells [2]. They are then compared to that obtained through acoustic characterization [3]. Finally, we evidence a non-zero displacement of about one-third the microbubble radius/cycle upon a complete cycle of deflation and re-inflation.

Methods

The monodisperse microbubbles suspensions were produced in a flow-focusing device described in detail in [3]. These microbubbles react to an ultrasound pulse by oscillating at a characteristic resonance frequency that depends on the stiffness that will be called dynamic stiffness χ_d in what follows in order to underline that it may differ from the stiffness obtained in a quasi-static situation. The dynamic stiffness was obtained by fitting a theoretical linear oscillator model to measured attenuation spectra [3]. Monodisperse microbubbles of dynamic stiffness ranging from 0.6 to 4.5 N/m were considered as well as the commerical contrast agent SonoVue/Lumason® (Bracco Spa, Milan, Italy) to validate the generecity of our result with our homemade shells.

Shells were gently poured in degased water and placed in a Falcon microfluidic reservoir of 15 ml (Fisher Scientific, USA) connected to an Elveflow® pressure controller (Elvesys®, France) and to a flow-through cuvette (Aireka Scientific® Co., Ltd) using PTFE tubings. The chamber is made from quartz with a square cross section (12.5mm x 12.5mm). It is placed under an inverted microscope (Olympus®, model IX70), which was twisted 90 degrees through three stabilizing aluminium legs (See **Fig. 1a**). This configuration allows to have an observation axis z perpendicular to gravity axis y. After injection in the chamber, the microbubbles float upward due to buoyancy.

The other end of the observation chamber is connected 1) to a valve which is left open to inject the UCAs into the chamber by a gentle increase of the pressure in the reservoir (of order 30 mPa above atmospheric pressure), and closed to allow for pressurization of the chamber in order to compress the shells and 2) to a pressure sensor (MPS1, Elvesys®, France). Following the instruction of the manufacturer, the sensor was first calibrated by connecting it directly to the outlet of the pressure controller. This sensor was placed at the same altitude as the objective of the microscope and allowed us to measure the ambient pressure around the shells, while checking potential time delay in the response of the whole device regarding imposed pressure variation.

In order to correlate shell shape evolution with values of external pressure, both pressure sensor and fast camera (Miro 310®, Vision Research) are triggered through the Elveflow interface. Movies are taken at a rate of 100 frame/s. An automated stage (MS-2000, ASI®, USA) is used to select a microshell prior to the recording.
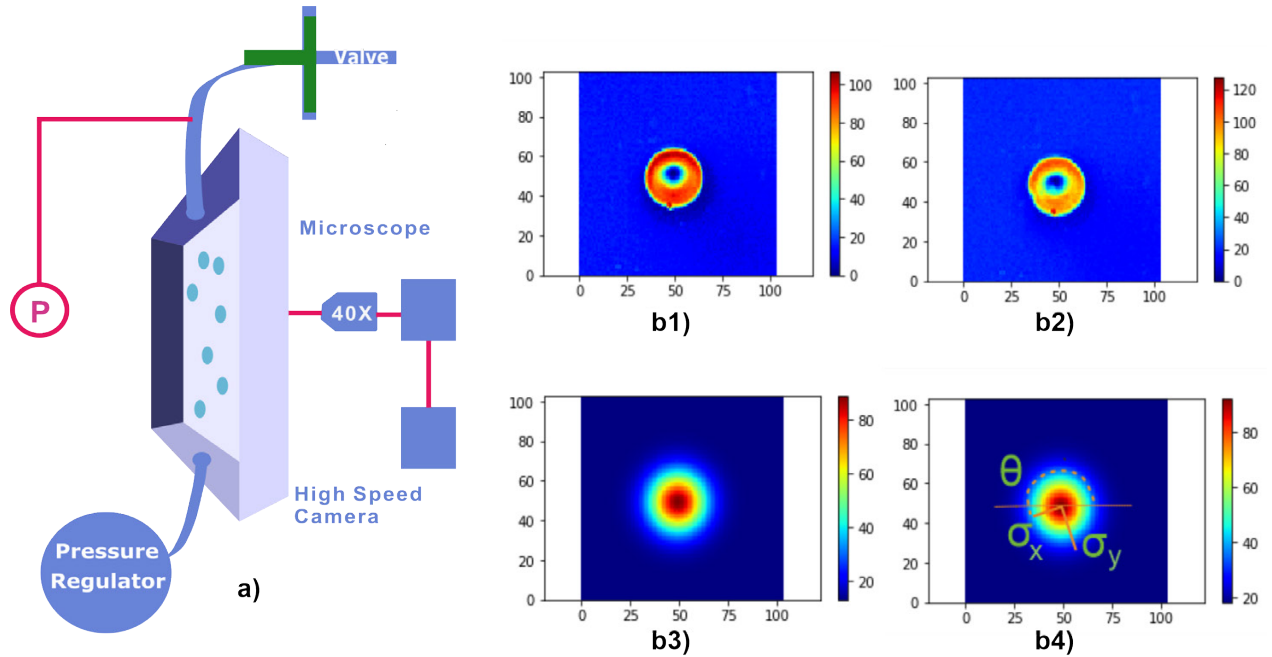
Figure 1. a) Experimental set-up for buckling experiments, b) Light intensity distribution of b1) raw image in 'spherical shape, b2) raw image in 'buckled' shape, b3) fitted image in 'spherical' shape and b4) fitted image in 'buckled' shape.

Experiments were conducted at room temperature (around 25 degrees) and the concentration of shells (10^5 shells/mL) is such that interactions between shells can be considered negligible.

To track the UCAs and get their shape at each time step, we developed a tracking algorithm with sub-micron resolution. The intensity profile of a non-spherical shell is complex and depends on the angle of the shell relatively to the optical axis. Being interested essentially in the detection of non-spherical deformation events, we approximate it by a two-dimensional (2D) elliptical Gaussian distribution with a tilt angle θ as seen in **Fig. 1b**.

Results

We first considered slow variations of pressure, which varied from the atmospheric pressure $\boldsymbol{P_{atm}} = \boldsymbol{101.1}$ kPa to a maximum value $\boldsymbol{P_{max}}$ and back to $\boldsymbol{P_{atm}}$ within 40 s. We systematically observed that when the maximum pressure $\boldsymbol{P_{max}}$ was set to be slightly above a given value $\boldsymbol{P_b}$ shells would loose their spherical symmetry at threshold $\boldsymbol{P_b}$ and collapse into a bowl-like shape which had most of the time a three-fold symmetry, as can be seen on **Fig. 2a.** This deformation was reversible and could be repeated several times through slow pressure cycles between $\boldsymbol{P_{atm}}$ and $\boldsymbol{P_{max}}$ with no apparent damage. These points are clear signatures of an elastic behaviour, since shapes of shells driven only by surface tension effects would be non-specific when surface tension vanishes. Threshold $\boldsymbol{P_b}$ is determined from the rapid change of the shell size **h (Fig. 2b)** and will be called "buckling pressure". Elastic moduli were estimated by fitting the measured linear decay of the aspect ratio as function of the pressure to the buckling theoretical model derived in this work. They are in close agreement with the ones measured acoustically except the shell with $\boldsymbol{\chi_d} = 4.5$ N/m, where surface tension based model fails to describe the measured buckling pressures **(Fig. 2c).**

Finally, displacements perpendicular to gravity were measured for SonoVue® microbubbles as well as for the homemade monodisperse microbbubles. To detect precisely the gravity direction, which may be potentially biased by microstreams due to leakage or material deformation, we mixed the UCA suspension with 5 µm average diameter hollow glass beads. These shells did not buckle when an overpressure was applied and could be used as reference particles to detect the main advection direction *y*.

The overlaid boxplot in **Fig. 2d** summarizes all the swimming experiments on SonoVue microbubbles for two different frequencies $f = 1$ Hz and $f = 2$ Hz and for the homemade microbubbles for only one

frequency $f = 1$ Hz. In all experiments, reference beads with a similar density (which do not buckle) were added as a control. A statistical significance in the net displacement of microbubbles is shown through a Student T-test (exact $p_{val} < 0.001$). Homemade microbubbles show higher net displacement compared to SonoVue which it can be understood by their higher elastic moduli.
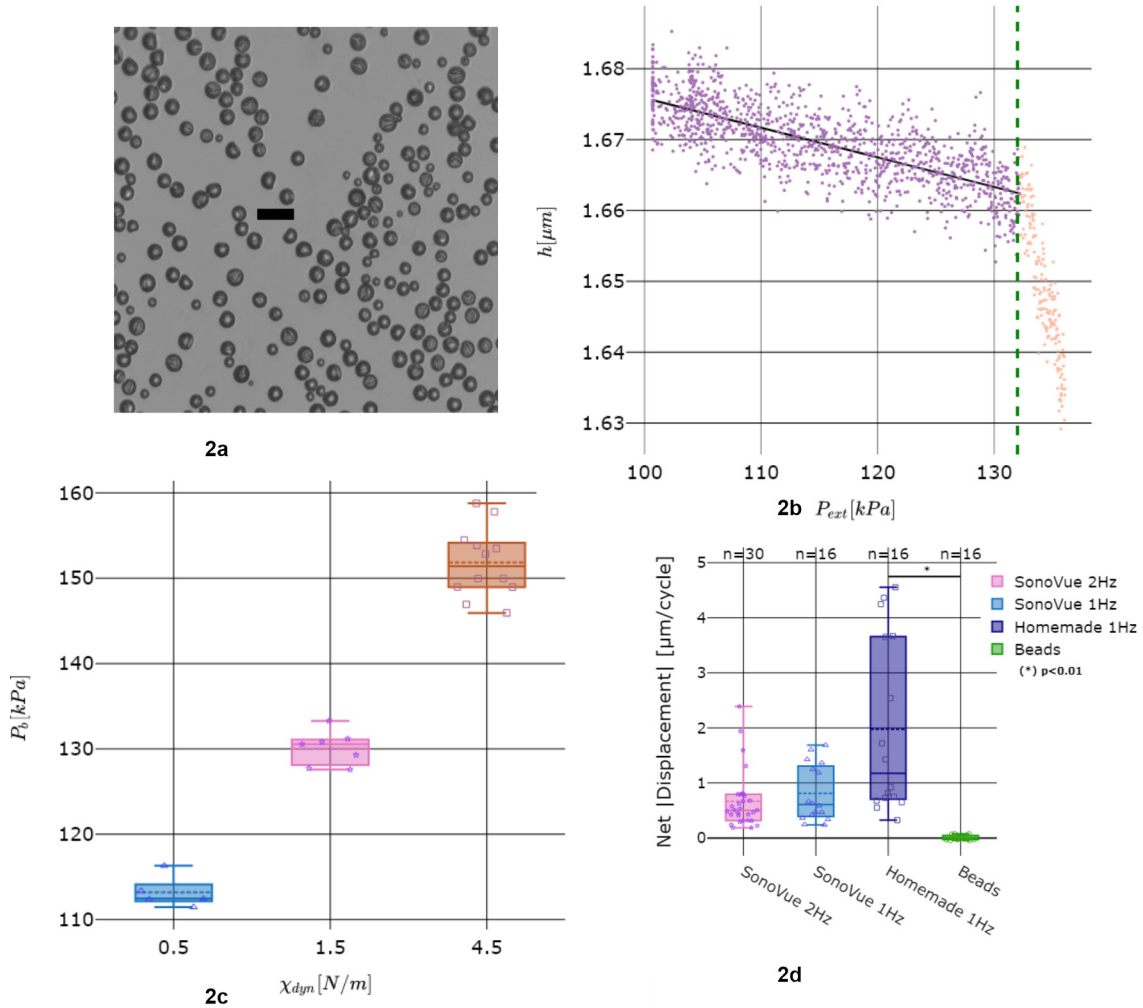
Figure 2 a) Zoology of shapes of UCAs after buckling. The 3-fold geometry is dominant. The scale bar represents 6 μm. b) Variation of the shell size *h* with the applied pressure P_{ext}, for a shell with $\chi_d = 1.5$ N/m. The spherical part (where *h* is equal to the shell radius *R*, purple dots) is linear and the corresponding fit is indicated by the solid line. The buckling P_b corresponds to the change of slope, when the height *h* of the shell decreases more abruptly (indicated with the dashed line). c) Buckling pressures P_b for three considered shells. d) The absolute net displacement of SonoVue microbubbles (two different frequencies), homemade microbubbles and the control (glass beads). Each symbol represents net displacement averaged on at least 8 cycles. The overlaid boxplots show the median, interquartile range, mean, and the minimum to maximum values. Statistical significance indicated with * Student T-test $p_{val} < 0.001$.

.

Conclusions

Our results highlight the difficulty in assessing a coherent view of the mechanical properties of lipidic microshells that would be relevant for all frequencies and amplitudes of loads, including triggering of buckling, or buckling-like, events.

Surface tension based models intrinsically assume that the shell is always overpressurized, while buckling processes require, in the elastic shell framework, the inner pressure to be lower than the outer pressure. Here, we explained the buckling process under quasi-static load in the framework of elastic theory, and showed that the overall elastic response in the spherical deformation under quasi-static load is similar to that obtained under pulsed, high amplitude, excitation, using a surface tension based model. However, we showed that coherence with known buckling thresholds and the typology of deformation with a small number of folds in our case, can only be explained by considering that vanishing surface tension is not the key to understand non-spherical deformations. Rather, an elastic contribution that includes an effective characteristic lengthscale that would emerge from the transverse anisotropy of the shell, is required to account for the observed phenomena.

On the other hand, we showed that this buckling mechanism can be a type of propulsion for microbubbles. Though, the direction is controlled in the shell reference frame and can be an answer to the problem of directivity accounted in the acoustic radiation force technique used in ultrasound molecular imaging and drug delivery.

References

[1]. P. Marmottant, S. van der Meer, M. Emmer, M. Versluis, N. de Jong, S. Hilgenfeldt and D. Lohse. A model for large amplitude oscillations of coated bubbles accounting for buckling and rupture. JASA 118(6), p.3499-3505, (2005).

[2]. G. Chabouh, B. van Elburg, M. Versluis, T. Segers, C. Quilliet and G. Coupier. Buckling of lipidic ultrasound contrast agents under quasi-static load. Phil. Trans. Royal Society A, 2022 (accepted).

[3]. T. Segers, E. Gaud, M. Versluis and P. Frinking. High precision acoustic measurements of the nonlinear dilatational elasticity of phospholipid coated monodisperse microbubbles. Soft Matter 14(14), p. 9550-9561, (2018).

Evaluation of microbubble control performance using electric fields

Arisa Murakami[1], Toshihiko Sugiura[2]

[1]_Integrated design engineering/Graduate school of Keio university, Yokohama, Japan_
[2]_Mechanical Engineering, Keio university, Yokohama, Japan_

Introduction

Microbubbles (MBs) with diameters ranging from 1 to 100 μm have been studied for various applications, including cleaning and medicine. In this study, we focused on drug delivery systems (DDS), one of the medical applications, and proposed and evaluated a method using electric fields for precise motion control of MBs, which is indispensable for realizing DDS. Currently, ultrasound is the most common method to apply a control force to MBs, and it can capture MBs as a standing wave. On the other hand, the method using an electric field can apply an attractive force due to Coulomb force to MBs, and is expected to enable more precise control than trapping. In the experiments of this study, the velocity change of MBs with changing voltage was measured, and the same trend as in the previous study [1] was confirmed. However, under an electric field, forces due to electro-osmosis flow in the liquid inside the container and convection flow due to hydrogen generation at the electrodes also act on the MBs, but the effects of these forces have not been fully investigated. In this study, the possibility of motion control of MBs using an electric field was investigated, including these effects.

Methods

In order for the Coulomb force to act on MB, the bubble surface must be charged. Therefore, we first positively charged the MB surface using a cationic surfactant as shown in Fig.1. An electric field was generated by a DC stabilized power supply to the MBs thus generated, and the MBs were observed to be attracted by the Coulomb force. The area captured was the central 1.7 mm x 2.1 mm region indicated by the red frame in Fig. 2. Here, there is one point to consider regarding the experimental system in Fig. 2. The results measured with this experimental system include not only the velocity due to the Coulomb force intentionally generated in this case, but also other external forces. Therefore, in this study, we considered two external forces other than the Coulomb force.

The first is the effect of convection on hydrogen generation. In this study, the electrodes were installed in water, so hydrogen was generated on the anode side, generating a flow as shown in Fig.3. To suppress this effect, a plate was inserted on the anode side and the experiment was conducted again. The second is the effect of electro-osmosis flow, as shown in the image in Fig.4. When an electric field is applied to a liquid containing ions, the liquid has a flow velocity due to the bias in the ion distribution caused by the electric charge on the tank wall. In the case of this study, because the wall surface is positively charged, the liquid near the wall surface has a distribution containing many negative ions, and the liquid near the wall surface flows in the direction of the blue arrow and in the center in the direction of the red arrow. Since it is difficult to suppress the electro-osmotic flow experimentally at this time, numerical estimates were made using the Navier-Stokes equation and the Poisson-Boltzmann equation.
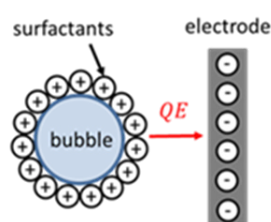
Figure 1. Image of microbubble control using Coulomb force.
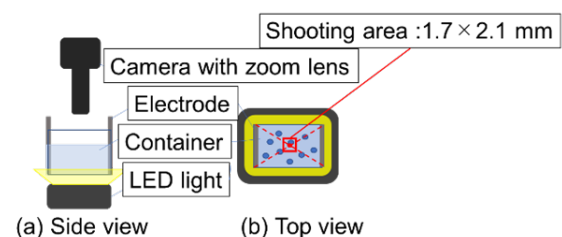
Figure 2. Experimental setup.
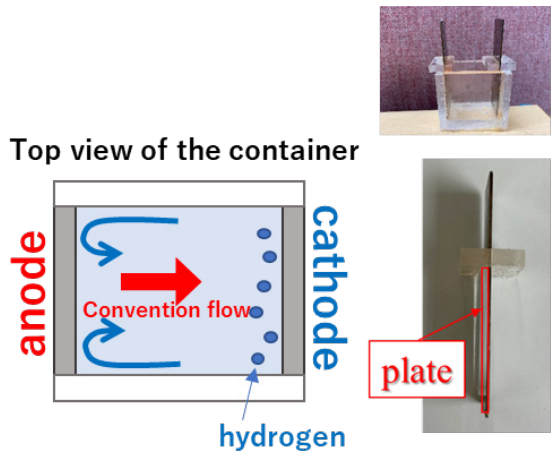
Figure 3. Image of convention flow and picture of plate.
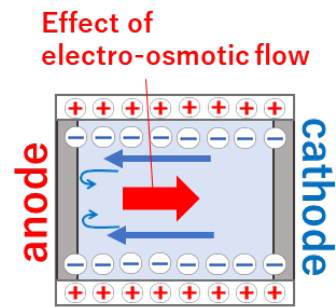
Figure 4. Electro-osmotic flow (Top view).

Results

Fig. 5 shows the average velocity of MB with and without plates shown in Fig.3 at 40V. Comparing the solid and dashed lines, the velocity indicated by the dashed line is suppressed to 56% of the solid line at the same voltage, indicating that the effect of convection associated with hydrogen generation is well suppressed by the plate insertion. However, this convection itself does not have a significant enough effect to change the velocity scale. Fig.6 shows the relationship between the voltage and the average velocity of the MBs. It can be seen that the average velocity increases with the voltage. This suggests the possibility of motion control of MBs by changing the electric field strength. Fig.7 shows the velocity of the electro-osmotic flow evaluated theoretically. It is significantly small relative to the Coulomb force, as seen in Fig.6.

Conclusions

The evaluation of the control performance of microbubbles using an electric field showed that the effect of other external forces on the intentionally generated Coulomb force was small, and it is expected that motion of MBs can be controlled by an electric field even taking these external forces into account.
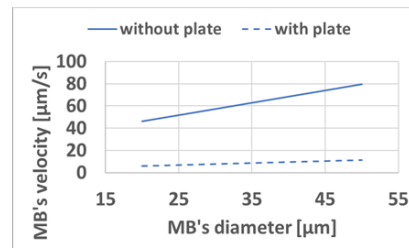
Figure 5. Experimental result showing convection effect under 40V.
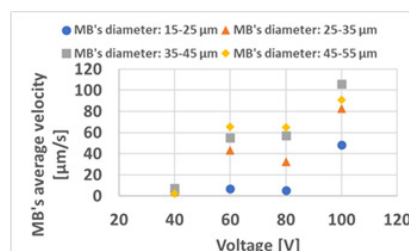
Figure 6. Experimental result showing dependence of MB's velocity on voltage.
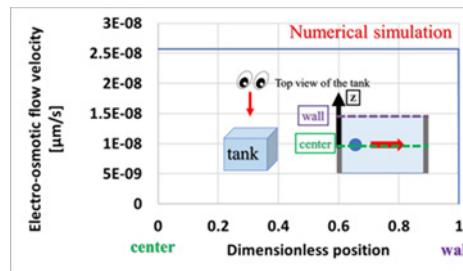
Figure 7. Velocity of the electro-osmotic flow evaluated theoretically.

References

[1]. Yokoi S,Yoshioka S,Velocity measurement of microbubbles driven by electric field in horizontal direction, Journal of the Japanese Society for Experimental Mechanics, Vol.20: 109-114, 2020.

In-vitro investigation of the impact of monodisperse microbubble size on contrast-enhanced ultrasound super-localization imaging

<u>P.Chen[1]</u>, A. Pollet[2], S. Turco[1], M. de Vargas[3] , L. te Winkel[3] , W. van Hoeve[3], J. den Toonder[3], H. Wijkstra[1] , M. Mischi[1]

[1]Department of Electrical Engineering, Eindhoven University of Technology, Eindhoven, Netherlands
[2] Department of Mechanical Engineering and Institute for Complex Molecular Systems, Eindhoven University of Technology, Eindhoven, Netherlands
[3]Solstice Pharmaceuticals, Enschede, Netherlands
Corresponding author: p.chen1@tue.nl

Introduction

Microvascular imaging plays a major role in medical diagnostics. Contrast-enhanced ultrasound (CEUS) imaging provides real-time analysis of the vasculature with the help of injected ultrasound contrast agent (UCA) microbubbles. Recently, based on CEUS imaging, super-localization methods have shown promise for the assessment of fine microvascular networks by localizing and tracking microbubbles, achieving resolutions beyond the diffraction limit [1-3].

In most super-localization applications, the injected UCA microbubbles are polydisperse with a relatively wide size distribution, leading to a wide range of resonance frequencies. However, most clinical ultrasound probes operate at a relatively narrow frequency bandwidth with respect to the resonance frequency range of UCAs, which results in only a small fraction of the microbubbles being efficiently excited at their resonance frequency. Moreover, a center frequency of around 3.5 MHz is usually used in clinical scanning due to the dominant resonance frequency of the typical microbubble population [4]. The employment of this low frequency does hamper high spatial resolution of the obtained ultrasound images.

In recent years, monodisperse microbubbles have been proposed, aiming at improving the insonating efficiency of UCAs and the signal-to-noise ratio of CEUS imaging by matching the ultrasound transmit frequency and the UCA microbubble resonance frequency [5, 6]. Monodisperse microbubbles have a narrow size distribution, which thus helps improve the insonating efficiency when transmitting at a certain frequency. Moreover, the resonance frequency of monodisperse microbubbles is usually tunable by controlling the microbubble size; therefore, fabricating monodisperse microbubbles with smaller size, which results in a higher resonance frequency, and insonating them at their resonance frequency may be beneficial for enhancing CEUS imaging quality. Based on the properties of monodisperse microbubbles, we hypothesize that CEUS imaging and its corresponding super-localization imaging can be optimized by jointly tuning the ultrasound transmit settings and the monodisperse microbubble sizes.

In this work, the impact of monodisperse microbubble size on CEUS imaging quality and the efficacy of super-localization imaging was investigated in an *in-vitro* setting by jointly tuning different frequencies, acoustic pressures, and monodisperse microbubble sizes.

Methods

First of all, a dedicated microfluidics device provided by Solstice Pharmaceuticals (Solstice Pharmaceuticals, Enschede, Netherlands) was employed to fabricate the monodisperse microbubbles. The size distribution indicated by the median bubble diameter of the microbubble solution was then measured using a Coulter Counter (MultiSizer 4e, Beckman Coulter, Brea, CA). The resonance frequency of the fabricated monodisperse microbubbles was also quantified using an attenuation approach [6, 7]. In this way, SP1 monodisperse microbubbles (Solstice) having dominant size of 3.7, 3.3, 2.9, 2.7, and 2.6 μm, corresponding respectively to resonance frequencies of 3.43, 4.09, 4.58, 5.08, and 5.42 MHz were prepared. All the monodisperse microbubbles were diluted at a concentration of 1.6×10^6 bubbles/mL.

In this *in-vitro* investigation, a sugar-printed dual-bifurcation microvasculature phantom made of polyacrylamide (PAA) material, and enclosed in a polymethylpentene (TPX) case for ensuring reliable perfusion was perfused with UCA microbubbles [8]. The channel diameter in the phantom varies from 330 to 650 μm through the subsequent bifurcations. The diluted monodisperse microbubbles were infused into the phantom using a syringe pump (Fusion 200, Chemyx, Stafford, USA) at a flow rate of 0.08 mL/min. The flow through the phantom was acquired by CEUS imaging in a contrast-specific mode, combining the pulse inversion technique and a band-pass filter centered at twice the transmit frequency, using a Verasonics Vantage 256 system (Verasonics Inc., USA) equipped with an L12-3 probe. For each microbubble size, we transmitted frequencies varying from 3.0 to 6.0 MHz with 0.5-MHz steps while imaging. At each frequency, we applied four acoustic pressures corresponding to mechanical index (MI) of 0.1, 0.13, 0.2, and 0.3, separately. All the obtained CEUS loops were then post-processed to generate the super-localization map using a typical Gaussian-centroid localization approach [1].

Results

In Figure 1, an example of CEUS maximum intensity projection (MIP) and corresponding super-localization maps is demonstrated. These maps correspond to the five different microbubble sizes combined with transmit frequency at their own resonance frequency and MI = 0.13. Finer channel structure in the super-localization maps can be observed compared to that in the MIP maps. Figure 2 shows the CEUS MIP example of the microbubbles insonated using their resonance frequency and using off-resonance frequency when the same MI of 0.13 was applied. Shaper channel structure in the MIP maps can be obtained when using a higher transmit frequency, which evidences a better spatial resolution. However, we also observed degraded CEUS enhancement when using small microbubbles (e.g. 2.6 and 2.7 μm) combined with high transmit frequencies (e.g. 5.5 and 6.0 MHz), which may be attributed to the high frequency-associated acoustic attenuation, the limited bandwidth of the probe, as well as weak backscattered signal intensity caused by small scattering cross-section of the microbubbles.
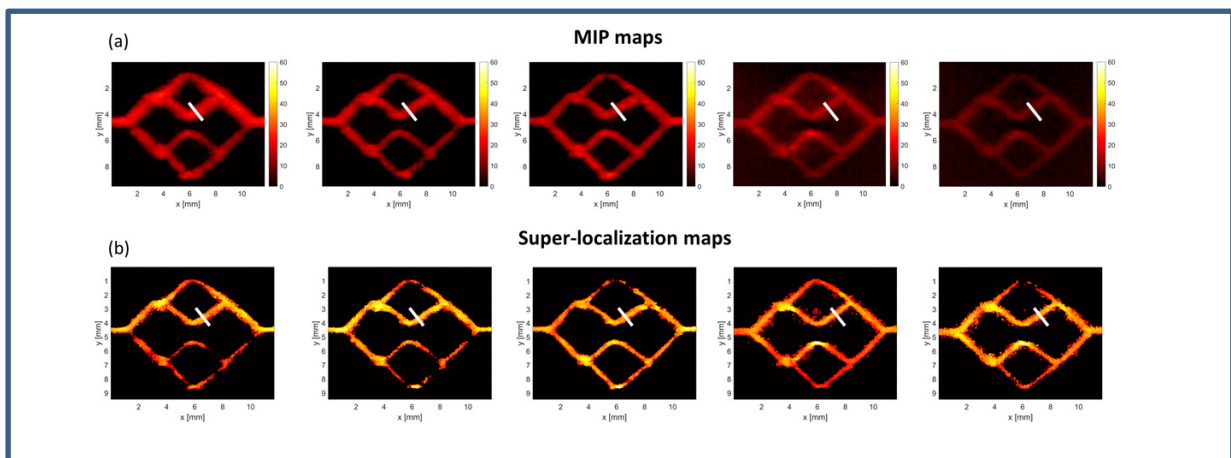
Figure 1. The five pairs of maps refer to the five different microbubble sizes combined with transmit frequencies at their own resonance frequency (3.5, 4.0, 4.5, 5.0, and 5.5 MHz) and an MI of 0.13. The line in each map is used to extract the pixel intensity profile.

Metrics including the generalized contrast-to-noise (gCNR) ratio of the CEUS acquisitions, full-width half-maximum (FWHM) of the pixel intensity profile extracted across a flow channel as shown in Figure 1, and the number of localization events, were employed to further quantify the CEUS imaging quality and super-localization performance. From the quantification results, an interesting phenomenon was observed. For the effectively resonated monodisperse microbubbles, the best MI choice shifted from a high MI range of 0.13-0.2 to a low MI range of 0.1-0.13 when the transmit frequency increased, as evidenced by the high gCNR values. This could be explained by a change in the elastic regime of monodisperse microbubbles [5]. Moreover, the overall FWHM values in the MIP maps are higher than those in the super-localization maps,

evidencing the importance of super-localization techniques in microvascular imaging. However, by observing the FWHM results of super-localization maps, the changes of FWHM values with the variation of transmit frequency does not show a clear trend associating higher transmit frequency with higher resolution. This could be ascribed to variations in the localization efficiency. High-frequency imaging allows the isolation of two neighboring microbubbles that may not be distinguished in a low-frequency imaging setting. Hence, more microbubbles can be localized and accumulated to form the super-localization maps, contributing to a more complete reconstruction of the microvascular architecture while possibly leading to larger channel diameters. The results on the number of localization events support this hypothesis. Therefore, this also leads to the contradictory deduction that higher FWHM values in the super-localization maps at higher frequencies are not necessarily associated with a worse spatial resolution, but may on the contrary reflect better super-localization performance.
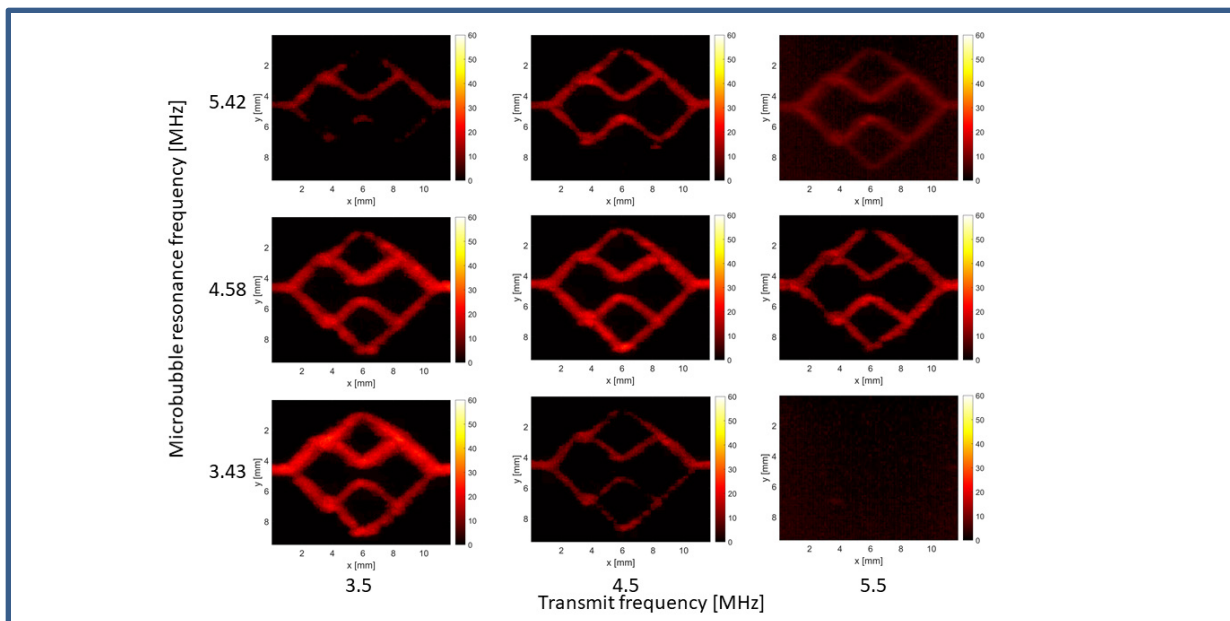
Figure 2. MIP maps showing microbubbles insonated at their resonance frequency and using off-resonance frequency when the same MI of 0.13 was applied.

Conclusions

In this study, the impact of the monodisperse microbubble size on CEUS imaging quality and the performance of super-localization imaging was investigated using five different monodisperse microbubble sizes, combined with seven different transmit frequencies and four MI values. In general, improved CEUS imaging quality and better super-localization performance can be achieved by jointly optimizing the transmit frequency and pressure for monodisperse microbubbles with smaller sizes. Yet, the weaker backscatter of smaller microbubbles must also be considered.

References

[1]. C. Errico et al., "Ultrafast ultrasound localization microscopy for deep super-resolution vascular imaging," Nature, vol. 527, no. 7579, pp. 499–502, 2015, doi: 10.1038/nature16066.

[2]. R. J. G. Van Sloun et al., "Super-Resolution Ultrasound Localization Microscopy through Deep Learning," IEEE Trans. Med. Imaging, vol. 40, no. 3, pp. 829–839, Mar. 2021, doi: 10.1109/TMI.2020.3037790.

[3]. K. Christensen-Jeffries et al., "Super-resolution Ultrasound Imaging," Ultrasound Med. Biol., vol. 46, no. 4, pp. 865–891, 2020, doi: 10.1016/j.ultrasmedbio.2019.11.013.

[4]. N. de Jong, M. Emmer, A. van Wamel, and M. Versluis, "Ultrasonic characterization of ultrasound contrast agents," Med. Biol. Eng. Comput., vol. 47, no. 8, p. 861, 2009, doi: 10.1007/S11517-009-0497-1.

[5]. T. Segers, P. Kruizinga, M. P. Kok, G. Lajoinie, N. de Jong, and M. Versluis, "Monodisperse Versus Polydisperse Ultrasound Contrast Agents: Non-Linear Response, Sensitivity, and Deep Tissue Imaging Potential," Ultrasound Med. Biol., vol. 44, no. 7, pp. 1482–1492, 2018, doi: 10.1016/j.ultrasmedbio.2018.03.019.

[6]. W. van Hoeve et al., "Improved Sensitivity of Ultrasound-Based Subharmonic Aided Pressure Estimation Using Monodisperse Microbubbles," J. Ultrasound Med., pp. 1–9, 2021, doi: 10.1002/jum.15861.

[7]. N. de Jong, L. Hoff, T. Skotland, and N. Bom, "Absorption and scatter of encapsulated gas filled microspheres: Theoretical considerations and some measurements," Ultrasonics, vol. 30, no. 2, pp. 95–103, Mar. 1992, doi: 10.1016/0041-624X(92)90041-J.

[8]. P. Chen et al., "Acoustic characterization of tissue-mimicking materials for ultrasound perfusion imaging research," Ultrasound Med. Biol., vol. 48, no. 1, pp. 124–142, Jan. 2022, doi: 10.1016/J.ULTRASMEDBIO.2021.09.004.

Rheology of viscoelastic materials using ultrasound contrast agents

A. Rezaei[1], K. Dijs[1], J. Snoeijer[1], D. Fernández Rivas[2], M. Versluis[1], and G. Lajoinie[1]

[1]*Physics of Fluids (POF) group, Technical Medical (TechMed) Center,*
University of Twente, Enschede, The Netherlands
[2] *Mesoscale Chemical Systems Group,*
University of Twente, Enschede, The Netherlands
Corresponding author: m.versluis@utwente.nl

Introduction

The dynamics of ultrasound contrast agents (UCA) is affected by both their stabilizing shell (typically phospolipids) and the viscoelastic properties of the surrounding medium. Both the shell elasticity and the medium elasticity increase the resonance frequency, while the viscosity of both the shell and the medium increase the damping [1]. In addition, mechanical properties of medium are a function of strain rate [2]. However, the elasticity and the viscosity of medium experienced by the bubbles in the MHz range cannot be directly estimated from to standard rheological measurements typically performed at low strain rate. Here, we use monodisperse microbubbles driven at MHz frequencies to measure the viscoelastic properties of polyacrylamide hydrogels using ultra-high speed imaging. The aim of the present study is to devise more physically accurate models to simulate the fully nonlinear oscillations of contrast agents in viscoelastic tissue.

Methods

Ultra-high-speed imaging (Shimadzu HPV-X2) at a frame rate of 10 Mfps was used to record the nonlinear response of acoustically driven phospholipid-coated microbubbles in polyacrylamide (PAM) hydrogels with different stiffness, see Fig. 1a. The ultrasoud wave was generated using a programmable arbitrary waveform generator (8026, Tabor Electronics Ltd., Tel Hanan, Israel) fed into a high-power RF amplifier (Vectawave VBA100-200 10kHz-100MHz 200W). The microbubbles were insonified by a focused ultrasound transducer (C305 SU, Olympus). The transducer was calibrated to ensure that the pressure at the focus remains constant at different insonifying frequencies. A PAM hydrogel was chosen as tissue surrogate since it is easy to vary its stiffness by tuning the ratio between acrylamide and water and because it is optically transparent. In terms of acoustic transparency, PAM hydrogels are very close to human tissue. The details of PAM samples preparation are explained in reference [3]. The microbubbles were produced using the flow focusing technique in a custom-built setup [4]. The concentration of microbubbles was adjusted to minimize their interaction during insonification. Thus, the concentration of the original bubble container (obtained by Multisizer 3 Coulter Counter, Beckman Coulter) was used to calculate the optimum dilution amount in the acrylamide solusion. We adjusted this dilution to ensure the bubbles were, statistically, more than 200 μm away from each other.

The radius-time curve of the oscillating microbubbles was extracted from the high-speed recordings using a custom written edge detection MATLAB script. The resonance curves were then computed using fast fourier transform (fft function in MATLAB) and compared with the simulated resonance curves using a root mean square error (RMSE) minimization routine. For simulations, the Rayleigh-Plesset equation was modified to account for the C_4F_{10} gas in the bubble, stabilizing shell surface tension [5], and the elastic (G) and viscous (μ) properties of the medium [6].

(a)   (b)
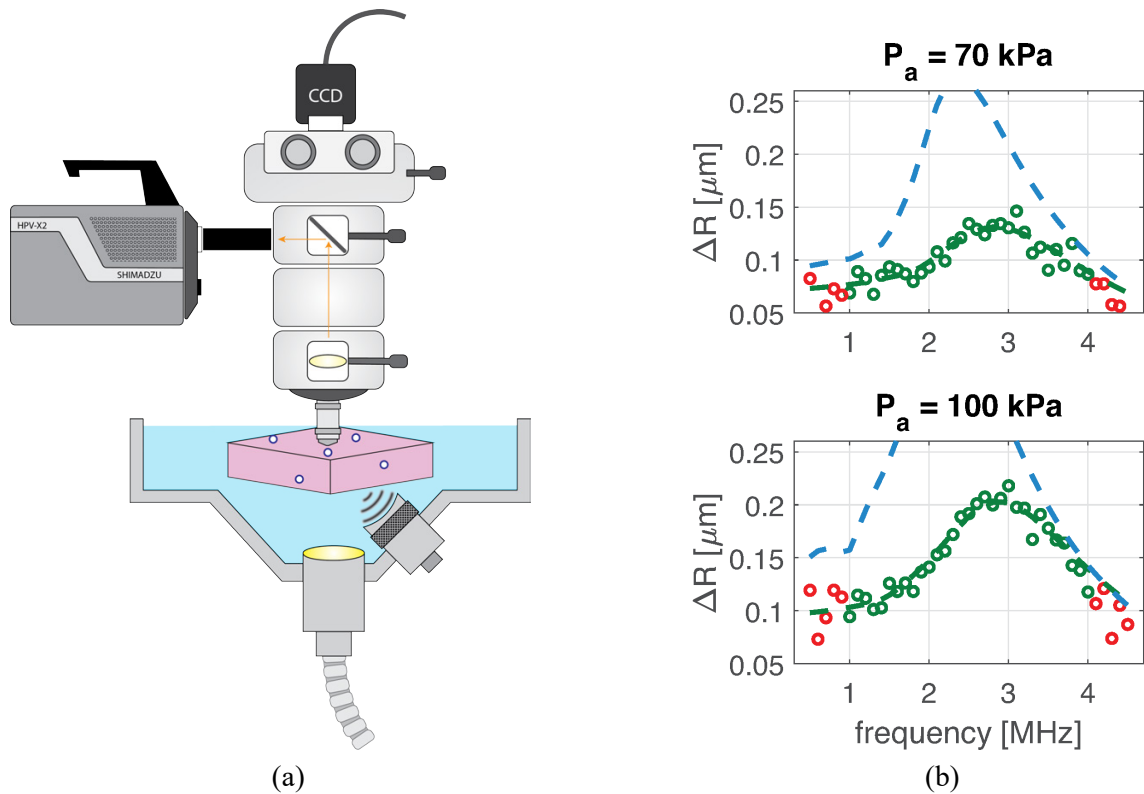
Figure 1 (a) Schematic of the optical characterization setup: The microscope and the ultrasound transducer are confocal, and the SHIMADZU HPV-X2 ultra-high-speed camera records the bubble cavitation at 10 Mf/S. (b) The best fit from the root mean square error (RMSE) minimization, MB excursion curves as a function of frequency for two pressures for the data set of a MB with $R0 \approx 1.70$ μm in a soft hydrogel. The circles correspond to optical measurements; the red circles were not considered in determining the error minimization; the green circles were included. The green dashed line is the error minimization simulation, and the blue dashed line represents the same MB (with shell) in water, with μ = 2 mP as, accounting for thermal damping.

Results

We observe that the resonance frequency of the microbubbles increases proportionally with the stiffness of the surrounding medium. However, the amplitude of oscillation is strongly reduced and the full width at half maximum of the resonance curves is increased which indicates higher damping that originates the added viscosity of the medium, see Fig.1b.

We show the difference between the storage and loss modulus (G' and G'' respectively) of hydrogels at low (Hz) and high (MHz) strain rates in Figure 2. These graphs indicate that the microbubbles experience higher stiffness at the MHz strain rate. Namely, $G' = 150$ kPa is measured with rheometer (Anton Paar MCR 502), while microbubble senses $G' = 300$ kPa. Interestingly, the rheology of the PAM hydrogels differ strongly from that of water for low strain rates, but becomes very comparable in the MHz frequency range.
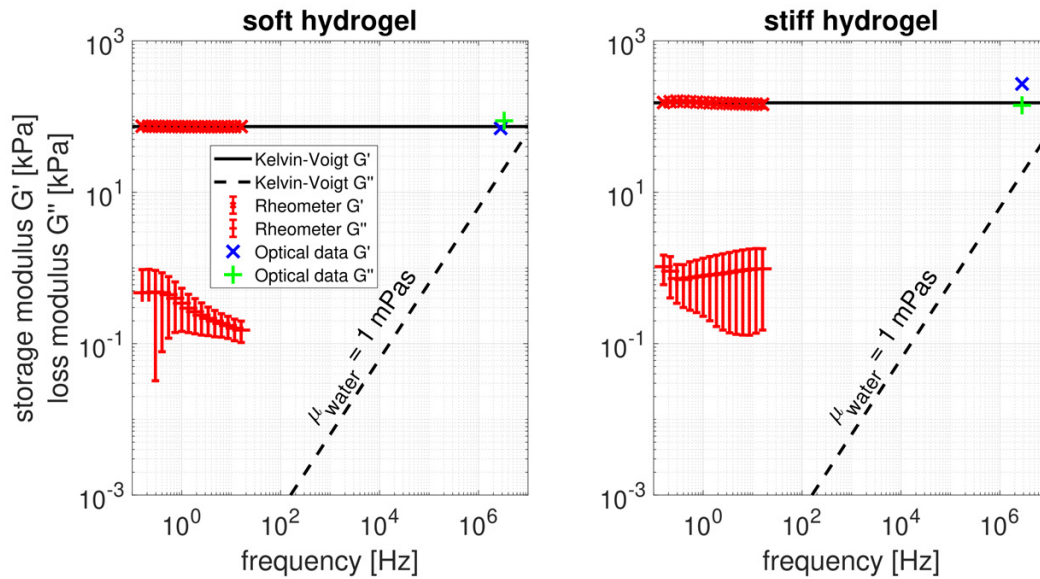
Figure 2 Rheological measurements (red) and the Kelvin-Voigt model (black). Data points retrieved by optical characterization are added in blue and green. Note that the error bars represent one standard deviation. The error bars for G′ are small (≈ 3 kPa) and not visible due to the logarithmic scale. Additionally, two lower bounds of the error bars in the soft gel experiment are not shown as they reach into a negative G″, not depicted on logarithmic scale.

The values of G and μ for the softer and stiffer PAM hydrogel measurements as a function of transmitted acoustic pressure are shown in Fig. 3. The error bars represent best fit parameters. It should be noted that there is an uncertainty in finding the edges of the bubble due to high microscope magnification and light diffraction limit. Therefore, a sensitivity analysis is performed with +5% and -5% of the initial radius. These are shown by the red and blue dashed lines in Fig. 3.
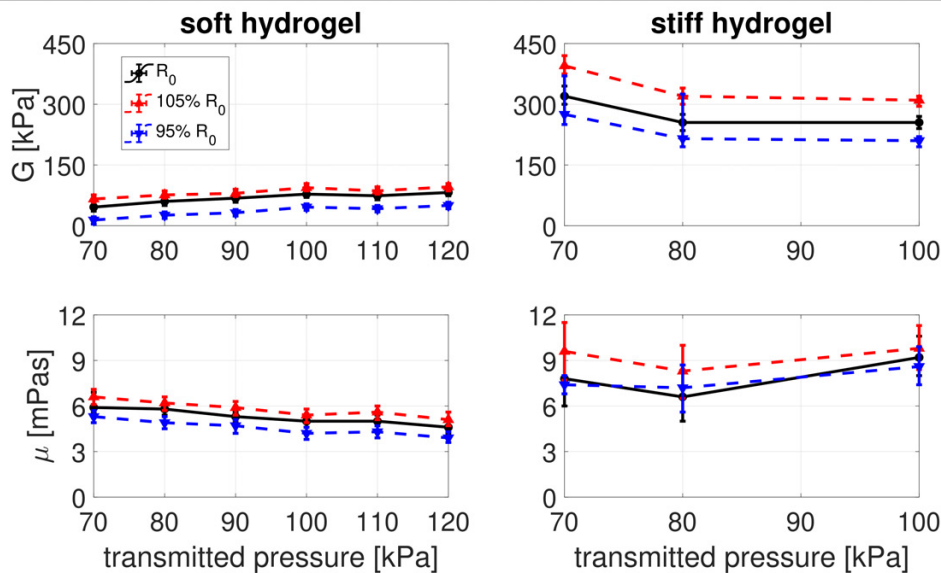
Figure 3 The shear modulus and the viscosity of polyacrylamide hydrogel as a function of transmitted acoustic pressure for two different stiffnesses. Soft and stiff hydrohels contain 6.4% and 16% acrylamide respectively.

Microbubbles have shown their potential to be a good tool for rheological measurements at such a high frequency (MHz). Previously Jamburidze et al. performed experiments in the kHz regime using largebubbles in agarose gel [2]. In this article, we have gone one step further by considering the interplay between the phospholipid shell and the viscoelastic medium in the US medical imaging frequency range. This will provide more insights into optimizing ultrasound parameters and UCA properties for therapeutic applications.

Conclusions

Our experiments show that the viscoelastic properties of the surrounding medium modify the resonance frequency of the microbubbles. This change allowed us to extract rheological properties of the hydrogel, such as shear modulus and viscosity, at a high strain rate ($> 10^6$/s). Conversely, the strain rate applied by the contrast agent microbubbles modifies the rheological properties of the medium. This study can helps us to better understand the interaction between UCAs and cells for ultrasound-mediated drug delivery with bubbles. We investigated the linear deformation of the medium in this study. However, there is still a gap in our knowledge of yield stress and the effect of high amplitude strain on the medium, which will be the future direction of our research.

References

[1]. Segers, Tim, et al. "High-precision acoustic measurements of the nonlinear dilatational elasticity of phospholipid coated monodisperse microbubbles." Soft matter 14.47 (2018): 9550-9561.

[2]. Jamburidze, Akaki, et al. "High-frequency linear rheology of hydrogels probed by ultrasound-driven microbubble dynamics." *Soft Matter* 13.21 (2017): 3946-3953.

[3]. Negussie, Ayele H., et al. "Thermochromic tissue-mimicking phantom for optimisation of thermal tumour ablation." International Journal of Hyperthermia 32.3 (2016): 239-243.

[4]. Benjamin van Elburg, Gonzalo Collado-Lara, Gert-Wim Bruggert, Tim Segers, Michel Versluis, and Guillaume Lajoinie, Feedback-controlled microbubble generator producing one million monodisperse bubbles per second, Review of Scientific Instruments 92, 035110 (2021)

[5]. Marmottant, Philippe, et al. "A model for large amplitude oscillations of coated bubbles accounting for buckling and rupture." The Journal of the Acoustical Society of America 118.6 (2005): 3499-3505.

[6]. Dollet, Benjamin, Philippe Marmottant, and Valeria Garbin. "Bubble dynamics in soft and biological matter." Annual Review of Fluid Mechanics 51 (2019): 331-355.

Shape oscillation of a phospholipid-coated microbubble induced by ultrasound

Hongchen Li[1], _Yuchen Wang[1]_, _Ruisheng Su[2]_, _Antonius F. W. van der Steen[1]_, _Martin D. Verweij[1,3]_, _Nico de Jong[1,3]_, _Klazina Kooiman[1]_

[1]_Department of Biomedical Engineering, Erasmus MC, Rotterdam, the Netherlands_
[2]_Department of Radiology & Nuclear Medicine, Erasmus MC, Rotterdam, the Netherlands_
[3]_Section of Medical Imaging, Department of Imaging Physics, Delft University of Technology, Delft, the Netherlands_
Corresponding author: h.li@erasmusmc.nl

Introduction

Microbubble-assisted biomedical imaging and therapy show increasing importance due to the noninvasive and cost-effective theranostics properties that ultrasound contrast agents possess. The dynamic responses of microbubbles to ultrasound, such as size changes and shape oscillations, are crucial for contrast agent design [1], harmonic imaging [2], and the interaction between microbubbles and tissues and/or bacteria [3]. Existing shape oscillation studies mostly considered uncoated air bubbles with a size of more than 10 µm in radius insonified with kHz ultrasound [4-5], which is far from clinical applications. This limits the translation of microbubble dynamics to enhance ultrasound imaging quality and/or microbubble-mediated drug delivery efficiency. Therefore, this study aimed to investigate the shape oscillation characteristics and relationship between different surface modes and oscillation amplitude of phospholipid-coated microbubbles (3 to 10 µm in radius) both experimentally and analytically.

Methods

An ultra-high-speed camera (Shimadzu HPV-X2) was air-coupled to a custom-built upright Eclipse Ni-E microscope (Nikon Instruments, the Netherlands) at 100× magnification with a frame rate of 5 Mfps, in order to record microbubble shape oscillation upon insonification. DSPC-based lipid-coated microbubbles with a C_4F_{10} gas core were made by a microfluidic flow-focusing device (Horizon [6]). Through adjusting the flow rate and gas pressure, different microbubble sizes ranging from 3 to 10 µm in radius were obtained. Microbubbles were placed in an IbiTreat polymer µ-slide (0.2 mm channel height; IBIDI GMBH) in a concentration of 1×10^5/ml at room temperature. A single-element transducer (used at 1 MHz) was placed underneath the microchannel at a 45° angle to insonify the microbubbles. The experimental setup is schematically illustrated in Fig. 1a.
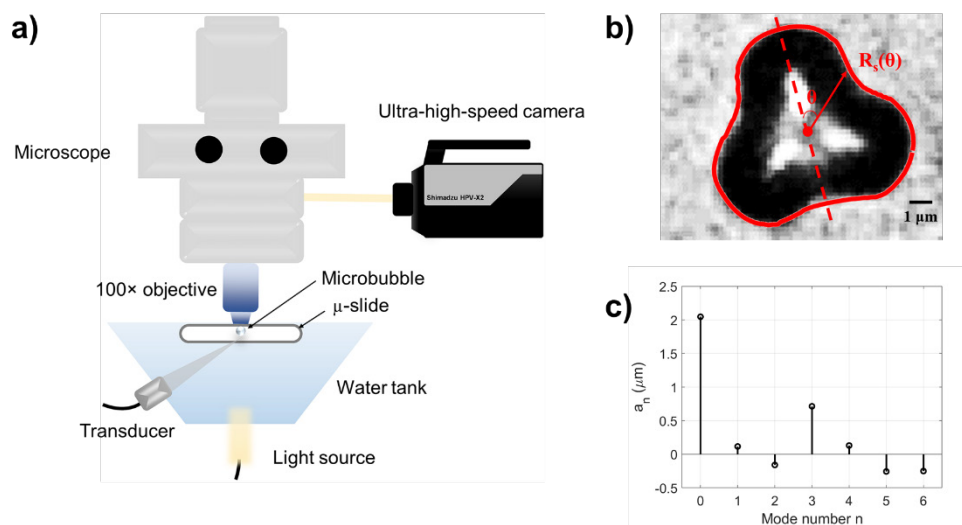
Figure 1. (a) Schematic representation of the experimental setup (not drawn to scale). (b) Definition of the microbubble contour $R_s(\theta)$ at one snapshot of an ultra-high-speed recording. (c) The associated mode decomposition of the microbubble in Fig. 1b having an initial size of $R_0 = 4.21$ µm.

After acquiring the microbubble oscillation recordings, the centroid, area, and the microbubble contour $(R_s(\theta))$ were tracked by image processing based on gray value distribution using MATLAB (see one example in Fig. 1b). Assuming axial symmetry, a proper expansion of $R_s(\theta)$ as a Legendre polynomial (Eq. 1), leads to the computation of the modal coefficients a_n (Eq. 2) by projecting R_s on the P_n polynomial basis [7]. Limited by the optical resolution and considering simplification, surface modes above seven were disregarded.

$$R_s(\theta) = \sum_{n=0}^{6} a_n P_n(cos\theta), \tag{1}$$

$$a_n = \frac{2n+1}{2} \int_{-1}^{1} R_s P_n(x)dx \quad with \quad x = cos\theta. \tag{2}$$

Each a_n corresponds to the oscillation amplitude at the nth-order surface mode. Fig. 1c shows the modal decomposition of the microbubble contour shown in Fig. 1b, which highlights the predominance of the third surface mode.

To predict the onset of shape oscillation of the phospholipid-coated microbubble, firstly, a simplified shape-stability analytical model [8] was applied (Eqs.3-8), where the unstable mode can be predicted due to parametric instability. Compared to conventional models, this model contains a rotational correction which helps to achieve better prediction. Secondly, due to the surface tension variation of the encapsulated microbubble compared to an uncoated air bubble, we propose an equivalent surface tension σ_e (Eq. 9) based on the Marmottant model [9], by calculating an average surface tension that the microbubble experienced.

$$C_t = \sqrt{(\alpha_1 - 1)^2 + 4(\alpha_2 + \alpha_{2rot})^2/X^2 + Y^2}, \tag{3}$$

where

$$X = 2n + 1 - 1.5\alpha_1 + 2(\alpha_2 + \alpha_{2rot})^2, \tag{4}$$

$$Y = \alpha_3 + \alpha_{3rot}, \tag{5}$$

$$\alpha_1 = 4(n-1)(n+1)(n+2)\frac{\sigma}{\rho\omega_d^2 R_0^3}, \tag{6}$$

$$\alpha_2 = 2(n+1)(n+2)\frac{\mu}{\rho\omega_d R_0^2}, \qquad \alpha_{2rot} = 2n(n+2)\frac{\mu}{\rho\omega_d R_0^2}, \tag{7}$$

$$\alpha_3 = -12n(n+1)\frac{\mu}{\rho\omega_d R_0^2}, \qquad \alpha_{3rot} = -12n\frac{\mu}{\rho\omega_d R_0^2}, \tag{8}$$

$$\sigma_e = \int_{R_{min}}^{R_{max}} \sigma \, dR/(R_{max} - R_{min}), \; where \; \sigma = \begin{cases} 0 & R \le R_{buckling} \\ \chi(R^2/R_{buckling}^2 - 1) & R_{buckling} \le R \le R_{rupture} \\ \sigma_{water} & R \ge R_{rupture} \end{cases} \tag{9}$$

C_t is the relative amplitude of microbubble oscillation, which in this work it expressed as excursion rate, equal to $(R_{max} - R_0)/R_0$, where R_{max} represents the maximum radius of the microbubble before it turns to shape oscillation and R_0 denotes the initial radius of the microbubble. The elastic modulus χ of microbubble's shell is taken from Langeveld et. al [10] where a similar microbubble formulation was used.

Results

Typical examples of the recorded microbubble shape oscillation are shown in Fig. 2a for microbubbles of radii 4.4 μm, 4.5 μm, 4.5 μm, 5.3 μm, 6.5 μm, and 9.3 μm, revealing the onset and evolution of the surface modes n $= 2, 3, 4, 5, 6$ respectively. It should be noted that these shape oscillations appeared after certain cycles of spherical oscillation, and gradually shifted to a specific order of the surface mode. The combined analysis of the predominant surface mode (Eqs. 1-2) and experimental data (21 points) of microbubbles' shape oscillation are plotted in Fig. 2b using different markers. It shows that surface mode is sensitive to the initial microbubble size at the applied ultrasound frequency (1 MHz): the larger the microbubble, the higher the order of the surface mode it can generate.

By solving Eqs. 3-9, the analytical prediction of different surface modes at different amplitude thresholds is shown in lines with different colors in Fig. 2b, which separates shape-stable (below the line, grey area) and shape-unstable regions (above the line). The shape-unstable region means the microbubble preferably turns to a certain mode of shape oscillation which is indicated by the corresponding colors. Compared to larger sized uncoated air bubbles [4], the phospholipid-coated microbubbles below 10 μm in radius shows a more mixed trend of different surface modes, which possibly causes a more complicated tuning of a particular oscillation regime that is in demand. In general, the results of the analytical model agree well with the experimental dataset.
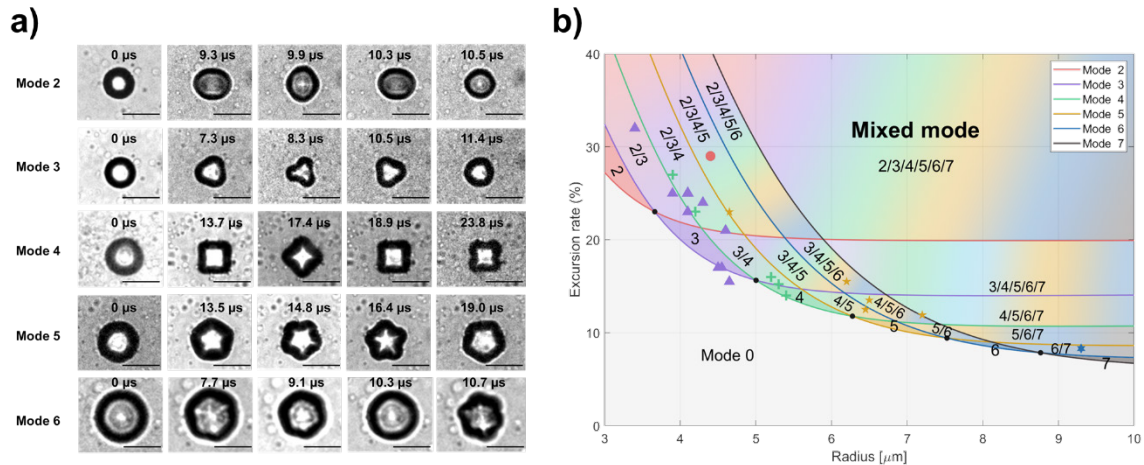
Figure 2. (a) Selected frames of different surface modes observed from various recordings of microbubble oscillation (Scale bar = 10 μm). (b) Excursion rate-radius diagram showing the different surface modes of the microbubbles in the established regimes. Mode 0 represents spherical oscillation. The background colors correspond to the analytical solution: red, mode 2; purple, mode 3; green, mode 4; yellow, mode 5; blue, mode 6; black, mode 7. The combination of different colors means a mix of possible surface modes. Experimental data points are illustrated as ●, mode 2; ▲, mode 3; +, mode 4; ★, mode 5; ✶, mode 6.

Conclusions

In this study, we could monitor the shape oscillation of phospholipid-coated microbubbles ranging from 3 to 10 μm in radius with surface modes n=2 to n=6, by ultra-high-speed microscopic imaging. The shape-stability analytical model integrated with equivalent surface tension agrees well with our experimental findings. Thereby, it enables us to predict different regimes of encapsulated microbubble shape oscillation above the oscillating amplitude threshold. With these findings, we are able to gain additional information and control of microbubble oscillation upon ultrasound, which could lead the way to more efficient and tailored microbubble-assisted ultrasound imaging and therapy.

References
[1]. E. Stride, T. Segers, G. Lajoinie, S. Cherkaoui, T. Bettinger, M. Versluis, M. Borden. Microbubble Agents: New Directions. Ultrasound Med Biol, 46 (2020) 1326-1343.
[2]. M.A. Averkiou, M.F. Bruce, J.E. Powers, P.S. Sheeran, P.N. Burns. Imaging Methods for Ultrasound Contrast Agents. Ultrasound Med Biol, 46 (2020) 498-517.
[3]. K. Kooiman, S. Roovers, S.A.G. Langeveld, R.T. Kleven, H. Dewitte, M.A. O'Reilly, J.M. Escoffre, A. Bouakaz, M.D. Verweij, K. Hynynen, I. Lentacker, E. Stride, C.K. Holland. Ultrasound-Responsive Cavitation Nuclei for Therapy and Drug Delivery. Ultrasound Med Biol, 46 (2020) 1296-1325.
[4]. M. Versluis, D.E. Goertz, P. Palanchon, I.L. Heitman, S.M. van der Meer, B. Dollet, N. de Jong, D. Lohse. Microbubble shape oscillations excited through ultrasonic parametric driving. Phys Rev E Stat Nonlin Soft Matter Phys, 82 (2010) 026321.
[5]. Q.X. Wang, W.K. Liu, C. Corbett, W.R. Smith. Microbubble dynamics in a viscous compressible liquid subject to ultrasound. Physics of Fluids, 34 (2022).

[6]. R.H. Abou-Saleh, F.J. Armistead, D.V.B. Batchelor, B.R.G. Johnson, S.A. Peyman, S.D. Evans. Horizon: Microfluidic platform for the production of therapeutic microbubbles and nanobubbles. Rev Sci Instrum, 92 (2021) 074105.

[7]. M. Guedra, C. Inserra, C. Mauger, B. Gilles. Experimental evidence of nonlinear mode coupling between spherical and nonspherical oscillations of microbubbles. Phys Rev E, 94 (2016) 053115.

[8]. K. Murakami, R. Gaudron, E. Johnsen. Shape stability of a gas bubble in a soft solid. Ultrason Sonochem, 67 (2020) 105170.

[9]. P. Marmottant, S. van der Meer, M. Emmer, M. Versluis, N. de Jong, S. Hilgenfeldt, D. Lohse. A model for large amplitude oscillations of coated bubbles accounting for buckling and rupture. Journal of the Acoustical Society of America, 118 (2005) 3499-3505.

[10]. S.A.G. Langeveld, I. Beekers, G. Collado-Lara, A.F.W. van der Steen, N. de Jong, K. Kooiman. The Impact of Lipid Handling and Phase Distribution on the Acoustic Behavior of Microbubbles. Pharmaceutics, 13 (2021).

Simulating the dual-frequency imaging response of microbubbles at clinically relevant depths

Kathlyne Jayne B. Bautista[1], *Isabel G. Newsome[1]*, *Gianmarco F. Pinton[1]*, *Paul A. Dayton[1]*

[1]*Joint Department of Biomedical Engineering, The University of North Carolina, Chapel Hill, NC, USA*
Corresponding author: kathlyne@live.unc.edu

Introduction

Acoustic angiography is a dual-frequency, contrast-enhanced imaging approach that transmits at a low frequency (f_0) and receives at high frequencies ($>3f_0$) to isolate microbubble signal within the vasculature from surrounding tissue. This superharmonic technique generates high-resolution microvasculature images with resolution on the order of 100 μm with promising application towards evaluating diseases that affect microvascular morphology, such as cancer [1]. Due to bandwidth limitations of current piezoelectric technology, dual-frequency imaging typically requires separate transmit and receive elements. Here, we determine the optimal transmit-receive combinations *in silico* that maximize microbubble signal relative to tissue at clinically relevant depths.

Methods

The simulations were implemented in MATLAB R2020b (Mathworks, Inc. Natick, MA, USA). To model the propagation of transmit waveforms, we applied a modified angular spectrum approach that uses a flux-conservative Rusanov method to solve nonlinearity. Frequency-dependent models of tissue attenuation were also considered. The response of polydisperse microbubbles were calculated using the Marmottant equation [2], which provides a widely accepted model of nonlinear microbubble behaviors that are important for superharmonic imaging [3]. Given the polydisperse distribution, we computed the bulk scattered pressure from the microbubbles using a size integration technique [4]. Finally, we calculated the contrast-to-tissue ratio (CTR), assuming a mostly linearly attenuated tissue signal propagating back to the transducer, to evaluate the overall imaging response. To evaluate the accuracy of the simulations, we compared the *in silico* calculations of CTR with *in vitro* measurements acquired in a cellulose microvessel embedded in a tissue-mimicking gel-graphite phantom.

Results

The *in vitro* experimental results (Fig. 1) show general agreement with the CTR trends generated from the simulations for a subset of parameters at 20 mm depth. Both show increasing CTR with increasing transmit pressure that appears to reach a saturation level at higher pressures. Furthermore, the trends indicate that transmitting above a threshold pressure (>625 kPa) is necessary to generate sufficient superharmonic signals. For a 1-MHz transmit, both the experimental and simulation results show a maximum CTR with a 10-MHz receive at the highest pressure. However, 2-MHz simulations results show more variable results, likely due to the limitations of the Marmottant solver. The simulation results also restate the importance of lower transmit frequencies for imaging deeper targets. At focal depths ≥60 mm, minimal CTR (<3dB) is observed when transmitting ≥2 MHz, regardless of receive frequency.

Conclusions

We have developed a custom tool for simulating the superharmonic response of polydisperse microbubbles to evaluate imaging response, in terms of CTR, as a function of transmit and receive frequency, transmit pressure, and focal depth. With trends that follow *in vitro* results, the simulations can serve as guidelines for the future development of dual-frequency transducers. Further optimization, especially in the computationally intensive solving of the Marmottant equation, can improve the robustness and accuracy of the simulations.
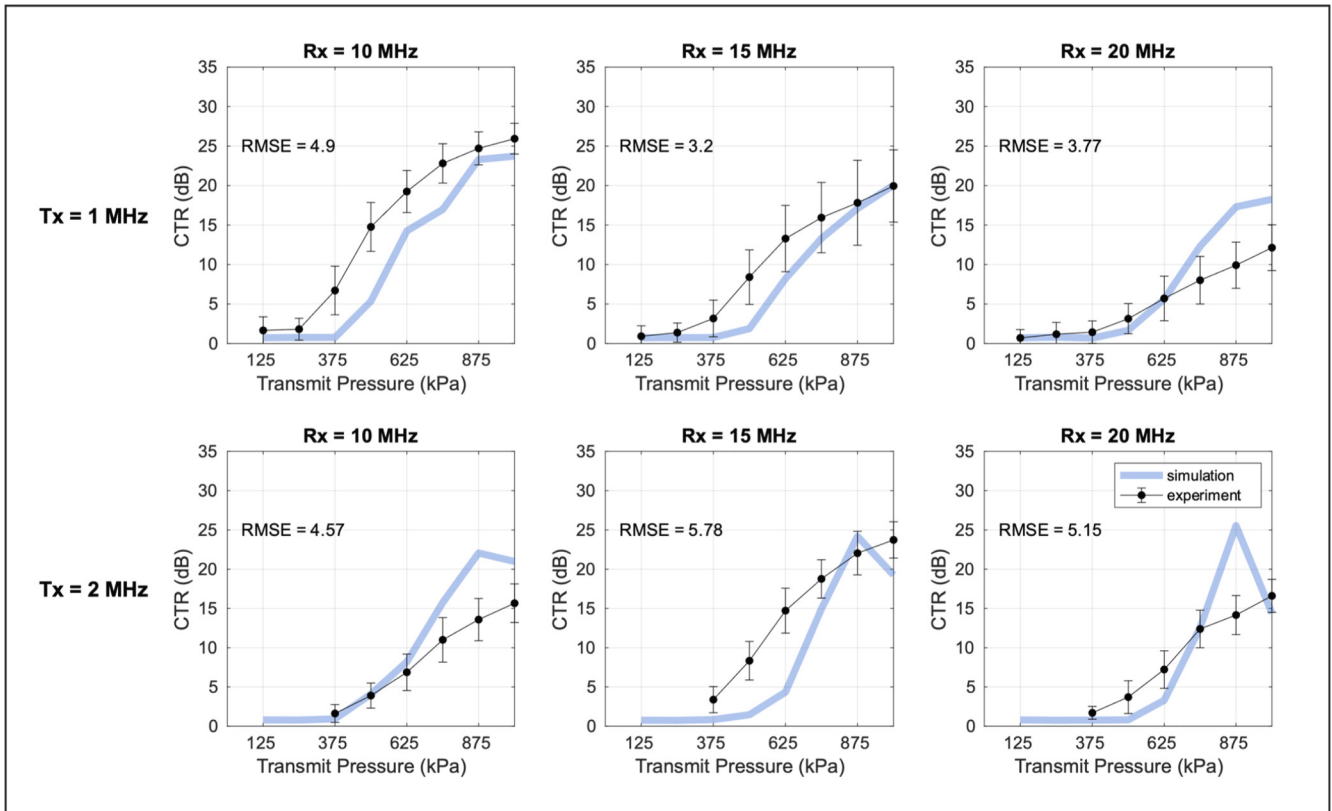
Figure 1. Comparison of experimental results with simulated calculations of CTR at 20 mm depth.

References

[1]. Shelton SE, Lee YZ, Lee M, et al, Quantification of Microvascular Tortuosity during Tumor Evolution Using Acoustic Angiography, Ultrasound in Medicine & Biology, 41(7):1896-1904, 2014.

[2]. Marmottant P, van der Meer S, Emmer M, et al, A model for large amplitude oscillations of coated bubbles accounting for buckling and rupture. The Journal of the Acoustical Society of America, 118(6):3499-3505, 2005.

[3]. King DA, O'Brien WD, Comparison between maximum radial expansion of ultrasound contrast agents and experimental postexcitation signal results, The Journal of the Acoustical Society of America, 129(1):114-121, 2011.

[4]. Zheng H, Barker A, Shandas R, Predicting backscatter characteristics from micron- and submicron-scale ultrasound contrast agents using a size-integration technique, IEEE Transactions on Ultrasonics, Ferroelectrics, and Frequency Control, 53(3):639-644, 2006.

Optical Validation of Normalized Singular Spectrum Area Measurement by Observing Adherent Microbubble Small Displacements

Yi Huang[1], Yanjun Xie[1], Alexander L. Klibanov[1,2], John A. Hossack[1]

[1]*Department of Biomedical Engineering, University of Virginia, Charlottesville, USA*
[2]*Division of Cardiovascular Medicine, University of Virginia, Charlottesville, USA*
Corresponding author: jh7fj@virginia.edu

Introduction

Targeted ultrasound contrast agents, comprising gas-filled microbubbles (MBs) conjugated with molecule specific ligands, are used to image physiological processes at the molecular level by targeting to the molecular markers associated with the disease of interest [1]. Ultrasound molecular imaging (USMI) relies on the separation and differentiation of ultrasound signals resulting from non-adherent MBs (indicating absence of selected molecular marker) and adherent MBs (indicating presence of selected marker). Prior studies from our laboratory, both *in vitro* and *in vivo*, have demonstrated that the normalized singular spectrum area (NSSA) measurement provides effective and fast differentiation of adherent MB signals (intermediate NSSA value) with respect to both non-adherent MB signals (high-NSSA value) and static background tissue signals (low NSSA value) [2], [3]. In this study, we tested our hypothesis that the intermediate NSSA values of adherent MBs are due to their small motions along the vessel wall by observing adherent MBs dynamics optically. The speed of adherent and non-adherent MBs measured from the optical validation was used in a numerical simulation and the NSSA values of simulated signals were in good agreement with our previous work.

Methods

NSSA measurement is based on the spatiotemporal property derived from the sigular value decomposition (SVD) of the interframe signals from an ensemble of ultrasound data [3]. Briefly speaking, the highly dimensional signal from non-adherent MBs has energy dispersed across multiple singular values, leading to a high NSSA value. Conversely, the low dimensional signal from static tissue has energy predominantly in the first eigenvalue resulting in a low NSSA value.

MBs were prepared using previously described methods [4]. We prepared two kinds of MBs for the optical validation: the cationic MBs to enhance the adherence and normal lipid-coated MBs as control. We assumed that cationic MBs would have similar dynamics to molecular targeted MBs, wobbling or having small displacements before they become completely static. On the other hand, control MBs move with a higher speed and never become adherent. Optical visualization was provided using an inverted microscope (IX71, Olympus, Japan), a fiber optic illuminator (NOVAFLEX Fiber Optic Illuminator, World Precision Instruments, USA) as the light source, and a digital single-lens reflex camera (EOS Rebel T3i, Canon, Japan) to record images at a frame rate of 18Hz. An ibidi μ-slide I Luer (ibidi GmBH, Martinsried, Germany) was fixed on the stage above the microscope and the objective lens (40X ELWD Objective, Nikon, Japan) was focused at the bottom of the channel. Connection tubing were connected into the adapters of the ibidi slide and diluted MB solution at a concentration of 5×10^5 mL^{-1} was injected through the tubing using a syringe pump (PHD 2000, Harvard Apparatus, USA). The injection flow rate was set to be 0.03 mL/min. The recorded images were exported and the measurement was completed in MATLAB (MathWorks, USA).

For the numercial simulation, we used single scatter points with high signal intensity located in the vessel region represent the MBs, and the random scatterers outside the vessel region were considered as the background static tissues. The displacements of MBs in the simulation were set to match the optical measurement results. The non-adherent MBs were distributed randomly throughout the lumen of simulated vessel and were set to move in lateral dimension at 40 μm/s. To simulate the adherent MBs and their small

displacement, we located them in a specific region on the bottom wall and they were set to move slowly at 10 μm/s.

Results

For cationic MBs, we selected 8 MBs that exhibited small displacements in the microscope field of view (FOV). Similarly, we also followed the movement of 8 control MBs under the microscope. The mean movement speed of MBs adherent to the bottom was 9.77 ± 2.40 μm/s while the mean movement speed of non-adherent MBs was 40.70 ± 9.03 μm/s. The Welch's T-test was used for statistical analysis and we found that the movement speed of adherent MBs was significantly different from the non-adherent MBs ($P < 0.001$).

The NSSA values of the simulated signals matched our previous results. The non-adherent MB flow showed a high NSSA value (mean NSSA value = 2.23), the static tissue showed a low NSSA value (mean NSSA value = 1.02), and the adherent MB on the vessel wall exhibited a intermediate NSSA value (mean NSSA value = 1.42).

Conclusions

In this optical validation study, we observed the small displacements of MBs adherent to a solid surface. The movement speed of these adherent MBs was significantly lower than the non-adherent MBs moving with the flow ($P < 0.001$). The NSSA measurements from the simulation are consistent with our hypothesis that the small displacements of adherent MBs result in intermediate NSSA values that can be used to differentiate signals from both moving non-adherent MBs and static background tissue.
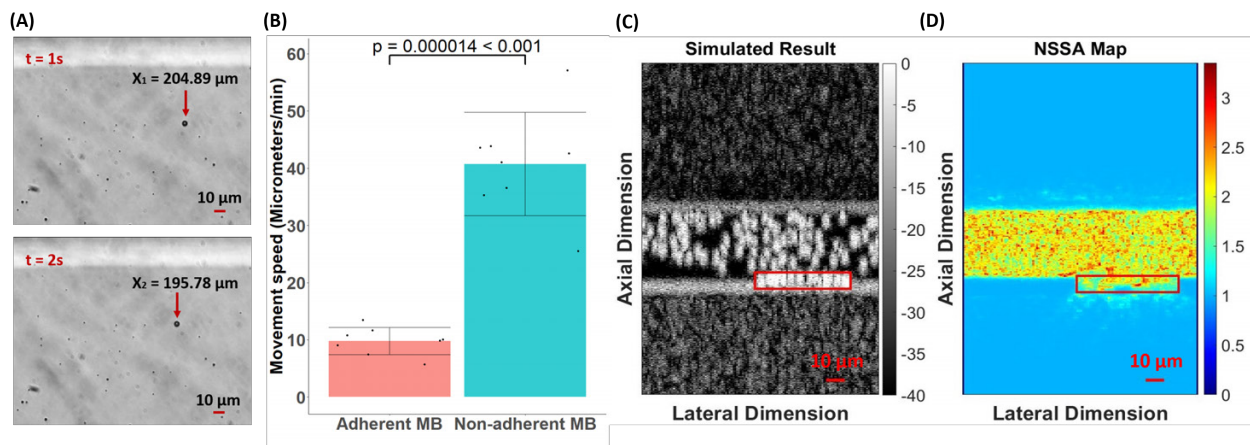
Figure 1. (A) The small displacement of adherent MB measured under the microscope. Above: X coordinate of the MB at t=1s; Below: X coordinate of the MB at t=2s. (B) The Welch's T-test revealed that the movement speed of adherent MBs was significantly lower than the non-adherent MBs ($P < 0.001$). (C) The simulated adherent and non-adherent MB ultrasound images in the vessel region. Red solid lines indicated the locations of adherent MBs. (D) The NSSA mapping of the simulated image, the adherent MBs showed an intermediate NSSA value compared to the non-adherent MBs and static background.

References

[1] S. Wang, J. A. Hossack, and A. L. Klibanov, "Targeting of microbubbles: contrast agents for ultrasound molecular imaging," *J. Drug Target.*, vol. 26, no. 5–6, pp. 420–434, May 2018, doi: 10.1080/1061186X.2017.1419362.

[2] E. B. Herbst, S. Unnikrishnan, A. L. Klibanov, F. W. Mauldin, and J. A. Hossack, "Validation of Normalized Singular Spectrum Area as a Classifier for Molecularly Targeted Microbubble Adherence," *Ultrasound Med. Biol.*, vol. 45, no. 9, pp. 2493–2501, Sep. 2019, doi: 10.1016/j.ultrasmedbio.2019.05.026.

[3] F. W. Mauldin, D. Lin, and J. A. Hossack, "The Singular Value Filter: A General Filter Design Strategy for PCA-Based Signal Separation in Medical Ultrasound Imaging," *IEEE Trans. Med. Imaging*, vol. 30, no. 11, pp. 1951–1964, Nov. 2011, doi: 10.1109/TMI.2011.2160075.

[4] A. L. Klibanov *et al.*, "Targeting and ultrasound imaging of microbubble-based contrast agents," *Magn. Reson. Mater. Phys. Biol. Med.*, vol. 8, no. 3, pp. 177–184, Aug. 1999, doi: 10.1007/BF02594596.

3D super-resolution ultrasound imaging of deep cardiac microvasculature in an *ex vivo* porcine heart

Kai Riemer[1], Konstantinos Ntagiantas[1,2], Biao Huang[1], Matthieu Toulemonde[1], Jipeng Yan[1], Justin Perkins[3], Christopher Dunsby[4], Rasheda A Chowdhury[2], Meng-Xing Tang[1]

[1]*ULIS, Department of Bioengineering, Imperial College London, London, United Kingdom*
[2]*National Heart and Lung Institute, Imperial College London, United Kingdom*
[3]*Royal Veterinary College, University of London, London, United Kingdom*
[4]*Department of Physics, Imperial College London, London, United Kingdom*
Corresponding author: mengxing.tang@imperial.ac.uk

Introduction

The ability of ultrasound localization microscopy (ULM) to visualize the microcirculation beyond the diffraction limit and its sensitivity to physiologic parameters has made ULM a very valuable tool in clinical research. ULM has been demonstrated to measure parameters such as vascular tortoisity and blood flow with unprecedented detail and accuracy. A limitation of 2D ULM is out of plane flow, complex threedimensional vasculature and motion. This limits the ability of ULM to measure myocardial microvasculature structures. Recently, 3D coronary ULM has been demonstrated *ex vivo* in a small laboratory models of a rat's heart [1]. Here, we present our preliminary results on the feasability of deep 3D ULM with a matrix array in a large porcine model with realistic motion [2] to narrow the translational gap between research and meaningful clinical applications.

Methods

A large animal Langendorff experimental apparatus was combined with a high frame rate tilted plane wave imaging scheme to investigate the potential of 3D ULM in a contracting *ex vivo* porcine heart. Imaging was performed with a Verasonics Vantage 256 research ultrasound system and a Vermon multiplexed 8 MHz 1024-Matrix array probe. In transmission 1024 and in reception a random pattern of 256 elements were used. The transmit frequency was 8 MHz, with a frame rate of 200 fps and 5 angles yielding a range of 15° degrees. The total number of frames was 960 corresponding to 4.8 s with an imaging depth of 60 mm. SonoVue microbubble contrast agent (Bracco, Milan, Italy) was infused at a rate of 5 ml/min. All experiments complied with the Animals (Scientific Procedures) Act 1986 and were approved by the Animal Welfare and Ethical Review Body of the Royal Veterinary College. For motion correction Matlab function *imregdemons* was used. Data was clutter filtered using Singular Value Decomposition and a purpose written 3D ULM algorithm will be used to generate super-resolution maps of the microvasculature [3].

Results

Figure 1 shows the B-Mode result from the *ex vivo* short (a, b) and long-axis (c, d) view. Figure 1 (a, c) each illustrates a maximum intensity projection of a single volume along each axis and Figure 1 (b, d) shows the maximum intensity projection of all 960 frames along each axis. The coronary artery, left ventricular myocardial wall and left ventricular lumen are clearly distinguishable from each other. With ULM the microvasculature flow direction mainly from epicardium to endocardium can be visualized. Towards the chamber and with depth the microvascular density appears to decrease.

Conclusions

Our preliminary results illustrate the feasability to performf 3D super-resolution ultrasound imaging of deep cardiac microvasculature in an *ex vivo* porcine heart which will foster the translation of 3D ULM to the clinical application.
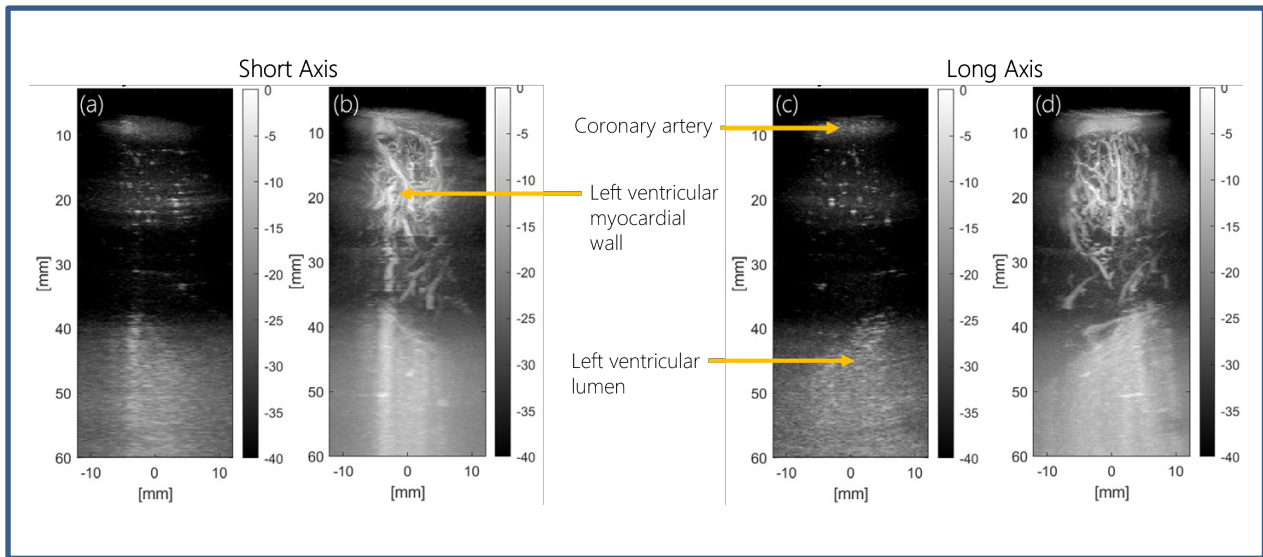
Figure 1. 3D imaging of deep cardiac microvasculature in an *ex vivo* porcine heart. (a, b) short and (c, d) long-axis view. (a, c) each illustrates a maximum intensity projection of a single volume along each axis and (b, d) show the maximum intensity projection of all 960 frames along each axis.

Acknowledgement

References

[1]. Demeulenaere et al., Coronary Flow Assessment Using 3-Dimensional Ultrafast Ultrasound Localization Microscopy, JACC Cadriovascular Imaging, 2022

[2]. Brook et al., Development of a pro-arrhythmic ex vivo intact human and porcine model: cardiac electrophysiological changes associated with cellular uncoupling, Integrative Physiology. 2020

[3]. Yan et al., Super-Resolution Ultrasound Through Sparsity-Based Deconvolution and Multi-Feature Tracking; Transactions on Medical Imaging

Does Mixing Iodinated Contrast Media and Microbubble-based Contrast Agent Have an Effect on Subharmonic Signals?

Cara Esposito[1], Kenneth Tzan[1,2], Priscilla Machado[1], Flemming Forsberg[1] and Jaydev K. Dave[1]

[1]Department of Radiology, Thomas Jefferson University, Philadelphia, PA 19107, USA
[2]Sidney Kimmel Medical College, Thomas Jefferson University, Philadelphia, PA 19107, USA

Corresponding author: cme009@jefferson.edu

Introduction

Subharmonic aided pressure estimation (SHAPE) is a technique that utilizes subharmonic signals from microbubble-based contrast agents for pressure estimation [1-4]. Validation of the SHAPE technique in cardiology relies on synchronous measurements of intra-cardiac pressures using contrast microbubbles and a pressure catheter (as the reference standard). During cardiac catheterization procedures, iodinated contrast is used for catheter guidance and placement and for visualizing vascular patency. Therefore, during data acquisition for validation studies of the SHAPE technique, both ultrasound contrast microbubbles and iodinated contrast are present simultaneously within the vasculature. The effect of iodinated contrast on the subharmonic signals from contrast microbubbles has not been reported. This study aims to elucidate the effects of iodinated contrast (Visipaque, GE Healthcare, Chicago, IL, USA) on subharmonic signal amplitude from contrast microbubbles (Definity, Lantheus Medical Imaging, Inc., N Billerica, MA, USA).

Methods

In an acrylic water-tank, lined with 25.5 mm of Sorbothane (McMaster-Carr, Atlanta, GA, USA) and gum rubber of thickness 9.5 mm (McMaster-Carr) to eliminate effects from standing waves, 0.06 mL of Definity and varied amounts of Visipaque (0.14, 0.85, and 1.70 mL) were added to 425 mL of deionized water. Ultrasound scanning was then performed with an SonixTablet scanner (BK Medical Systems; Peabody, MA, USA) using previously determined optimized parameters for Definity ($f_{transmit}$ = 3.0 MHz; chirp down) [5] . The order of injecting Definity and Visipaque was randomized in order to decipher the impact Visipaque has on the subharmonic signals from Definity microbubbles. Subharmonic data was acquired at 16 incident acoustic outputs (IAO; n=3). The subharmonic signal amplitude exhibits a sigmoidal relationship with incident acoustic power characterized by occurrence, growth and saturation stages, and the subharmonic signal in the growth stage is used for SHAPE applications [6]. Therefore, from all the 16 IAOs, data from the growth stage corresponding to 9 incident acoustic outputs (301 kPa$_{peak-to-peak}$ - 900 kPa$_{peak-to-peak}$) were analyzed for each trial. Unpaired t-tests with Bonferroni corrections were utilized to determine if the changes in subharmonic amplitude for different experimental considered were significant.

Results

Across the different IAOs analyzed, the variation in subharmonic signal at baseline (deionized water only) ranged from 2.2 to 3.2 dB with a mean value of 2.8 dB. Over the same range of IAOs, change in the subharmonic signal relative to baseline was 1.4 ± 0.9 dB with 0.14 mL Visipaque, 0.5 ± 0.3 dB with 0.85 mL Visipaque and 16.9 ± 1.4 dB with 0.06 mL Definity microbubbles. The change in subharmonic signal amplitude after mixing Visipaque and Definity contrast agents are provided in Table 1.

Table 1: Results from the mixture of Definity and Visipaque

Experimental condition	Change in subharmonic signal amplitude (dB) compared to baseline		
	Mean ± Standard deviation	Minimum	Maximum
Baseline + Visipaque (0.14 mL) + Definity	19.8 ± 1.2	17.9	21.3
Baseline + Visipaque (0.85 mL) + Definity	17.7 ± 2.0	13.7	19.6
Baseline + Definity + Visipaque (1.70 mL)	15.0 ± 0.8	13.6	16.3

When Definity microbubbles were added to a mixture of deionized water and 0.14 or 0.85 mL Visipaque, the enhancement in the subharmonic signal amplitude from Defnity microbubbles was 2.8 ± 1.3 dB ($p < 0.001$) and 0.7 ± 1.2 dB ($p = 0.09$), respectively, relative to enhancement due to Definity microbubbles and deionized water. When 1.70 mL Visipaque was added to a mixture of deionized water and Definity microbubbles, the subharmonic signal amplitude dropped by 1.9 ± 0.7 dB ($p < 0.001$), relative to enhancement due to Definity microbubbles.

Conclusions

Changes were noted due to the presence of Visipaque in the subharmonic signals from Definity microbubbles. The magnitude of changes in the growth stage subharmonic signal amplitude (relative to enhancement of Definity microbubbles) ranged from 0.2 to 4.2 dB across different IAOs and experimental conditions considered in this study, with mean values of 0.7, 1.9 and 2.8 dB, which are unilkely to impact *in vivo* SHAPE meassurements.

References
[1]. J. Dave *et al.*, "Noninvasive Intracardiac Pressure Measurements Using Subharmonic Aided Pressure Estimation: Proof Of Concept In Humans," *Ultrasound in Medicine and Biology,* vol. 43, no. 11, pp. 2718-2724, 2017.
[2]. J. K. Dave *et al.*, "Noninvasive LV Pressure Estimation Using Subharmonic Emissions From Microbubbles," *JACC. Cardiovascular imaging,* vol. 5, no. 1, pp. 87-92, 2012.
[3]. J. K. Dave *et al.*, "Subharmonic microbubble emissions for noninvasively tracking right ventricular pressures," *American journal of physiology. Heart and circulatory physiology,* vol. 302, no. 13, pp. 126-132, 2012.
[4]. V. G. Halldorsdottir *et al.*, "Subharmonic Contrast Microbubble Signals for Noninvasive Pressure Estimation under Static and Dynamic Flow Conditions," *Ultrasonic Imaging,* vol. 33, no. 3, pp. 153-164, 2011/07/01 2011.
[5]. C. Esposito, K. Dickie, F. Forsberg, and J. K. Dave, "Developing an Interface and Investigating Optimal Parameters for Real-Time Intra-Cardiac Subharmonic Aided Pressure Estimation," *IEEE Transactions on Ultrasonics, Ferroelectrics, and Frequency Control,* pp. 579-585, 2020.
[6]. W. Shi, F. Forsberg, J. Raichlen, L. Needleman, and B. Goldberg, "Pressure dependence of subharmonic signals from contrast microbubbles," *Ultrasound in Medicine & Biology,* vol. 25, no. 2, pp. 275-283, 1999.

Quantifying the effect of acoustic parameters on cavitation activity from infused Definity® through the EkoSonic™ catheter

Daniel Suarez Escudero[1], _Kevin J. Haworth[1,2]_, _Curtis Genstler[3]_, _Christy K. Holland[1,2]_

[1]_Department of Internal Medicine, Division of Cardiovascular Health and Disease, University of Cincinnati, Cincinnati, OH, USA_
[2]_Department of Biomedical Engineering, University of Cincinnati, Cincinnati, OH, USA_
[3]_Boston Scientific, Maple Grove, MN, USA_
Corresponding author: suarezdl@ucmail.uc.edu

Introduction

Cavitation-enhanced delivery of therapeutic agents is under development for a number of medical applications, including sonothrombolysis. The objective of this study was to ascertain the amount of cavitation activity that could be sustained for 30 minutes by Definity® (Lantheus, Billerica, MA, USA) infused through the EkoSonic™ Endovascular Catheter System (Boston Scientific, Arden Hills, MN, USA) employing 3 different insonation protocols in an _in vitro_ phantom mimicking porcine venous flow. Inertial and stable cavitation activity was quantified using passive cavitation imaging. The cavitation energy was quantified over the duration of each pulse in order to determine the temporal cavitation behavior for each of the insonation protocols.

Methods

An _in vitro_ flow phantom mimicking flow in the common femoral vein circulated 0.9% saline at 37 ℃ (180 mL/min ± 10 mL/min). The EkoSonic™ Endovascular System was positioned in a latex tube (9.5 mm-inner diameter latex tubing with a 1.6-mm wall thickness). The L11-5v transducer array (Verasonics, Kirkland, WA, USA) was aligned over the first active proximal transducer with a transverse view using micro-positioners (MTS25-Z8, Thorlabs, Newton, NJ, USA) based on radio-frequency passive acquisitions emitted by the EkoSonic™ System. Room temperature (22 ± 1 ℃) Definity® was activated per the manufacturer's instructions, and diluted in 13.7 mL 0.9% saline. The Definity® dilution was infused at a rate of 28.6 ml/h over 30 min.

The EkoSonic™ transducers were driven at a 2.25 MHz center frequency using three different insonation protocols. The first protocol was a 3 ms pulse duration, 50 Hz pulse repetition frequency (PRF), and 18 W electrical drive pulse power. The second protocol employed a 15 ms pulse duration, a 10 Hz PRF, and 18 W electrical drive pulse power. The third protocol, shown in Table 1, sequenced four different schemes of acoustic parameters every 5 seconds, which approximated the insonation protocol of the FDA-cleared EkoSonic™ system. A total of four 30-minute runs were acquired for each insonation protocol.

Passive cavitation data and B-Mode images were acquired with a Vantage 256 US scanner (Verasonics). The data was post-processed using custom MATLAB code (R2018b, The MathWorks Inc., Natick, MA, USA). Data was acquired during the entire pulse duration and the acquisition was triggered at the beginning of each EkoSonic™ pulse. The acquired passive data was divided into 288 µs segments to minimize spectral leakage [2]. Inharmonic and ultraharmonic bands, representing inertial and stable cavitation, respectively, were independently beamformed in the Fourier domain [2] within the bandwidth of the array. The discretized cavitation energy and point spread function deconvolution were computed according to the signal processing described by Lafond et al. [1] and Suarez et al. [3]. The processed received pulses were averaged to obtain cavitation energy during the pulses duration over 30 min. Cavitation data from 10 min. 0.9% saline infusions served as a baseline and were subtracted from the Definity® runs. Next, the obtained cavitation energy during the pulses duration was averaged between runs. Finally, the cavitation dose was computed as the product of the treatment time, the PRF, and the integral of the average cavitation energy

during the pulses for each run. Statistical significance was determined using One-Way ANOVA with Tukey's multiple comparison correction.

Table 1. Acoustic parameters for the third insonation protocol. The order of schemes was 1, 2, 3, 4, 3, 2.

Scheme #	Pulse duration [ms]	PRF [Hz]	Electrical drive pulse power [W]
Scheme 1	4.0	27	47
Scheme 2	6.9	21	30
Scheme 3	5.0	27	15
Scheme 4	8.0	21	9

Results

Cavitation was sustained for the entire 30 min. infusion using the three insonation protocols. The total cavitation energy over the pulse duration for the first and second protocols are shown in Fig. 1. The peak inertial cavitation energy occured at the beginning of the pulse and subsequently decreased an order of magnitude. The stable cavitation energy initially increased and reached a maximum after ~1 ms and subsequently decreased to a level higher than the sustained inertial cavitation energy. This behavior was similar for all the pulsing schemes used in the third protocol, independent of the pulse duration, PRF, or electrical drive pulse power.
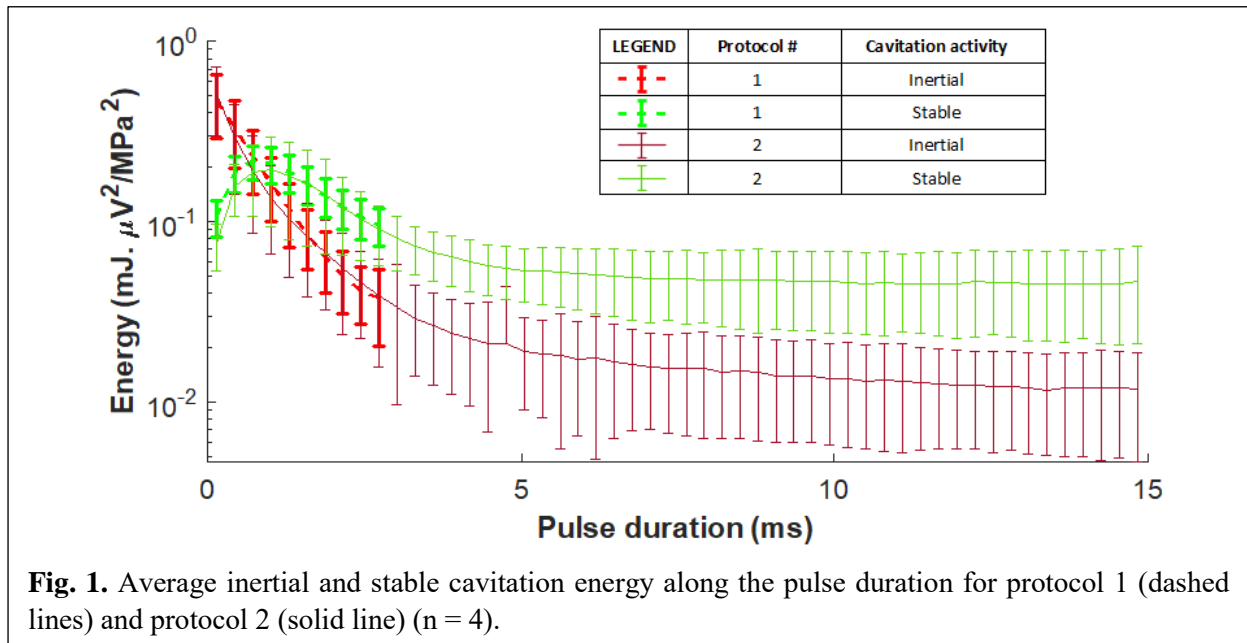
Fig. 1. Average inertial and stable cavitation energy along the pulse duration for protocol 1 (dashed lines) and protocol 2 (solid line) (n = 4).

The cavitation dose for the three insonation protocols is shown in Fig. 2a and for the four separate schemes in the third insonation protocol in Fig. 2b. In Fig. 2a, when comparing insonation protocols 1 and 2, the inertial cavitation dose decreased significantly from ~42 to ~11 mJ μV^2 s / MPa^2 (p<0.05) when the PRF decreased by a factor of 5 and the pulse duration increased by the same factor (the duty cycle was preserved). The same observation applied for the stable cavitation dose that decreased significantly from ~41 to ~18 mJ μV^2 s / MPa^2 (p<0.05). In Fig. 2b, when the electrical drive pulse power increased in schemes 1, 2 and 3, the inertial cavitation dose increased significantly (p<0.05) and when the electrical drive pulse power increased in schemes 1, 2, 3 and 4 the stable cavitation doses increased significantly (p<0.05). The predominance of stable cavitation or inertial cavitation varied according to insonation scheme.

Fig. 2. a) Inertial and stable cavitation dose for the three insonation protocols (n = 4). b) Inertial and stable cavitation dose along the pulse duration for four schemes of the insonation protocol 3 (n = 4).
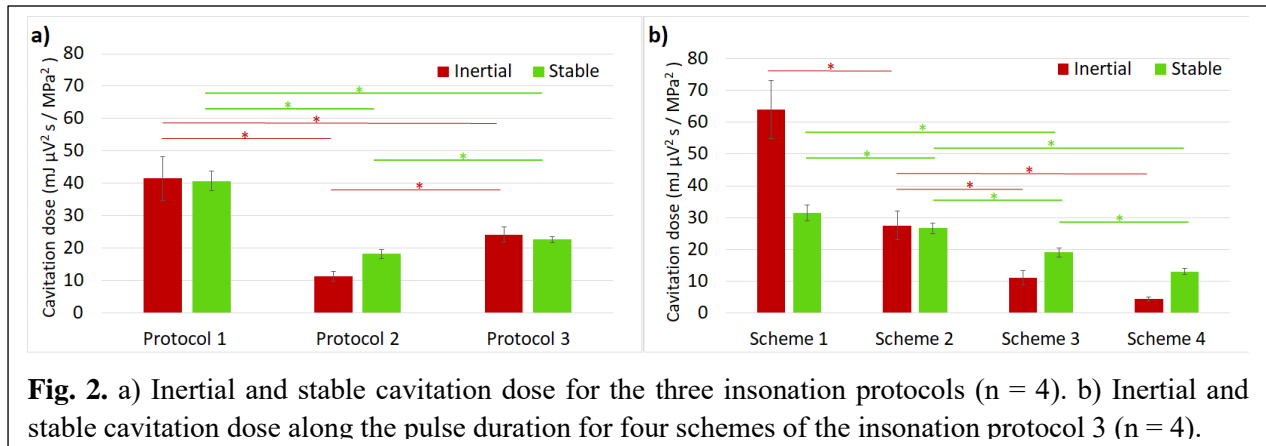
Conclusions

PCI was used to quantify and compare inertial and stable cavitation activity promoted by three insonation protocols employed with the EkoSonic™ Endovascular System. Specific bubble dynamics were studied by processing the cavitation activity along the pulse duration. Some schemes exhibited a maximum in inertial cavitation dose and other schemes suppressed the inertial cavitation dose and enhanced the stable cavitation dose. Thus depending on the type of cavitation desired to promote or suppress a particular bioeffect, a particular pulsing scheme could be employed. Our future goal will be to correlate inertial and stable cavitation dose with sonothrombolytic efficacy in a model of human deep vein thrombosis using Definity® infused through the EkoSonic™ catheter.

References

[1]. Lafond, M. et al. Cavitation Emissions Nucleated by Definity Infused through an EkoSonic Catheter in a Flow Phantom. Ultrasound in medicine & biology 47, 693-709 (2021)

[2]. Haworth, K. J. Et al. Quantitative Frequency-Domain Passive Cavitation Imaging. T-UFFC 64, 177-191 (2017)

[3]. Suarez Escudero, D. et al. Corrigendum to "Cavitation emissions nucleated by Definity infused through an Ekosonic catheter in a flow phantom". Ultrasound in Medicine & Biology (Submitted, 2022)

Biocompatibility of Cellulose Nanofiber-Coated Perfluoropentane Droplets

Ksenia Loskutova[1], Mar Torras[1], Ying Zhao[2], Anna J. Svagan[3], Dmitry Grishenkov[1]

[1]_Department of Biomedical Engineering and Health Systems, KTH Royal Institute of Technology, Stockholm, Sweden_
[2]_Department of Laboratory Medicine, Karolinska Institute, Stockholm, Sweden_
[3]_Department of Fibre and Polymer Technology, KTH Royal Institute of Technology, Stockholm, Sweden_
Corresponding author: ksenial@kth.se

Introduction

The cellulose nanofiber(CNF)-shelled perfluoropentane (PFP) droplets were the subject of the evaluation in this work. CNF-shelled PFP droplets Mechanical and acoustic properties were studied previously and reported elsewhere [1-4], however more insights into the biological effects of these droplets are needed to translate previous in vitro tests into in vivo applications as drug carriers in ultrasound-mediated drug delivery.

The aim of this work is to investigate the effect of CNF-shelled PFP droplets on cell viability of 4T1 cells, a murine breast cancer cell line. Cells were exposed to different concentrations of droplets with or without the addition of paclitaxel, i.e. a hydrophobic cancer drug.

Methods

Droplets were produced by mixing 0.35 wt% CNF-in-water suspension with PFP using Ultra-Turrax and a 25 N - 8 G Dispersing Tool. The volume size distribution and concentration of droplets was estimated using optical microscopy (Eclipse Ni-E, Nikon Corporation, Japan).

4T1 cells were cultivated in RPMI-1640 cell medium supplemented with 10% fetal bovine serum and 1% penicillin-streptomycin at 5% CO_2 and 37°C. For cell viability mesurements, 5,000 cells were seeded per well in a 96-well plate. Seven test groups were evaluated: 24 droplets per well, 48 droplets per well, 72 droplets per well, 24 droplets and 50 nM paclitaxel per well, 48 droplets and 50 nM paclitaxel per well, 72 droplets and 50 nM paclitaxel per well, and 50 nM paclitaxel only per well. A control group and a group exposed to DMSO only was studied in addition to the test groups. An 3-[4,5-dimethylthiazol-2yl]-2,5-diphenyltetrazolium bromide (MTT) assay was used to determine the cell viability in each well after 48 hours of exposure.

Student t-tests and ANOVA-tests were performed to evaluate whether there was statistically significant differences between groups. Results were considered as statistically significant if the p-value was smaller than 5%.

Results.

The average diameter and concentration of CNF-shelled PFP droplets was 14.4 ± 5.3 μm and 3.50 ± 0.64 million droplets/mL, respectively.

50 nM of paclitaxel decreased the cell viability of 4T1 cells to 62% compared to the control group, as presented in Figure 1c. However, the CNF-shelled PFP droplets did not influence the cell viability of 4T1 cells at any concentration compared to the control. In addition, when studying cells which were exposed to both CNF-shelled PFP droplets and paclitaxel (see Figure 1c) there was no further decrease in cell viability observed beyond the effect of only paclitaxel. These results indicate that the droplets do not impact the cell viability at the concentrations used.

Conclusions

CNF-shelled PFP droplets showed no impact on cell viability of 4T1 cells, which shows that these droplets have the potential to be applied as drug carriers in clinical ultrasound-mediated therapy.
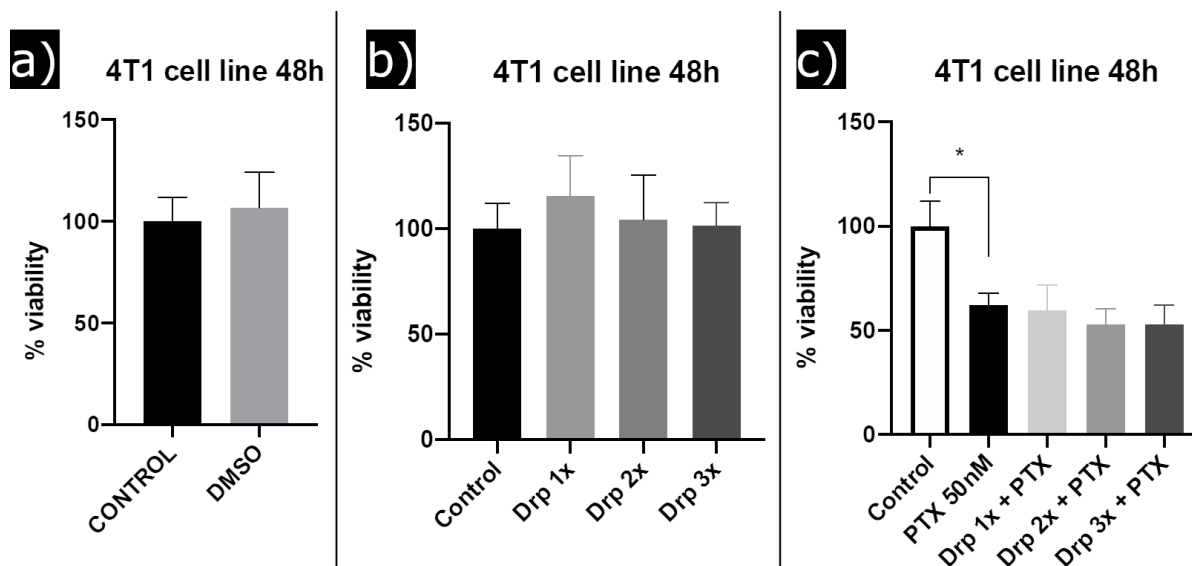
Figure 1. Cell viability of 4T1 cells when studying the effect of a) DMSO; b) presence of droplets (where 1x, 2x and 3x are equal to 24, 48 and 72 droplets per well, respectively); and c) combination of droplets and paclitaxel in each well.

Acknowledgements

References

[1]. Ghorbani M, Olofsson K, Benjamins J-W, Loskutova K, Paulraj T, Wiklund M, Grishenkov D, Svagan A J, Unravelling the Acoustic and Thermal Responses of Perfluorocarbon Liquid Droplets Stabilized with Cellulose Nanofibers, Langmuir 35(40): 13090-13099, 2019.

[2]. Song X, Loskutova K, Chen H, Shen G, Grishenkov D, Deriving acoustic properties for perfluoropentane droplets with viscoelastic cellulose nanofiber shell via numerical simulations, The Journal of the Acoustical Society of America 150(3): 1750-1761, 2021.

[3]. Loskutova K, Nimander D, Gouwy I, Chen H, Ghorbani M, Svagan A J, Grishenkov D, A Study on the Acoustic Response of Pickering Perfluoropentane Droplets in Different Media, ACS Omega 6(8): 5670-5678, 2019.

[4]. Loskutova K, Olofsson K, Hammarström B, Wiklund M, Svagan A J, Grishenkov D, Measuring the Compressibility of Cellulose Nanofiber-Stabilized Microdroplets Using Acoustophoresis, Micromachines 12(12): 1465, 2021.

Targeted local hyperthermia with local and systemic injections of ultrasound contrast agents during HIFU

Lance H. De Koninck[1], Eric K. Juang[1], Kaleb S. Vuong[1], Aswin Gnanaskandan[2], Michalakis A. Averkiou[1]

[1]*Department of Bioengineering, University of Washington, Seattle, USA*
[2]*Department of Mechanical & Materials Engineering, Worcester Polytechnic Institute, Worcester, USA*
Corresponding author: maverk@uw.edu

Introduction

High-intensity focused ultrasound (HIFU) is used for targeted thermal ablation but is limited by the acoustic energy needed to overcome anatomical constraints. An increase in the acoustic energy input may lead to complications such as unwanted heat deposition outside the focus or intended target, potentially leading to burns in the skin and subcutaneous fat. Bubble-enhanced heating (BEH), administration of ultrasound contrast agent microbubbles during HIFU, can mitigate this challenge as microbubble cavitation enhances the conversion of acoustic energy into thermal and mechanical energy and lowers the requirement for acoustic energy input to generate thermal lesions in tissue. BEH for thermal ablation has been studied previously both in vitro and in vivo with limited success and mostly overshadowed by safety concerns and procedural difficulties. We believe that BEH may be ideally suited for local targeted *mild hyperthermia* (5-10 ℃) in drug enhancement applications such as chemotherapeutics for liver cancer. We previously studied BEH in tissue-mimicking phantoms with diluted microbubbles and observed that nonlinear attenuation of pre-focal microbubbles modified the HIFU pressure field due to excess attenuation and acoustic shadowing. Directly delivering microbubbles to the target area via local injection might be a solution to this issue. The goal of this work was to study BEH (using HIFU and commercial UCA microbubbles) in ex vivo non-perfused and machine-perfused porcine liver under diagnostic ultrasound guidance. Microbubble delivery with systemic and local injections of microbubbles was considered. Thermocouple measurements provided information of the thermal lesions formed with varying acoustic intensities/pressures and were compared with theoretical simulations. A thermal lesion enhancement (greater temperature elevation and/or larger thermal lesions) with contrast microbubbles was observed at all pressures (0.63-3.75 MPa).

Methods

The experimental setup consisted of a porcine liver partially submerged in a container filled with blood mimicking fluid. Two models of porcine liver were prepared in this study: (a) machine perfused porcine liver (MPL) [1] and (b) non-perfused liver procured by dissecting the MPL. Each liver model was insonified from above using a single element focused transducer (H116; Sonic Concepts) coupled to the liver using a 4-cm long coupling cone and monitored in real-time using a C5-1 curved array transducer connected to a Philips iU-22 scanner (Philips Healthcare, Bothell, WA, USA). HIFU was delivered as a 30 second treatment at 0.9 MHz, 372000 cycles, 82% duty cycle, and at estimated non-derated (water) focal acoustic pressures of 0.63, 1.25, 2.50, and 3.75 MPa. Temperature measurements were recorded with a needle thermocouple positioned under image guidance at the focus of the HIFU transducer. The transducer was translated for off axis measurements. Microbubbles were introduced to the liver via local injections at the HIFU focus or systemic injections delivered simultaneously to the portal vein and hepatic artery. Local injection of microbubbles used 0.05 mL of Sonazoid (estimated concentration: 2×10^8 microbubbles/mL) while systemic injections used 0.3 mL of Sonazoid in both the portal vein and the hepatic artery. The presence and location of the injected microbubbles was confirmed with the C5-1 imaging probe while scanning in contrast mode, i.e., amplitude modulation at 1.7 MHz and at a low mechanical index (0.05) to avoid bubble destruction.

Temperature elevation in the absence of microbubbles for both tissue types was modeled using the Pennes' bioheat transfer equation. We added a term in the bioheat equation to account for heat convection due to blood perfusion.

Results

Temperature elevation measurements in non-perfused ex vivo liver tissue are shown in Figure 1. In Fig. 1a we show the temperature elevation at the focus over time at 1.25 MPa focal pressure. Without microbubbles, the temperature elevation is in good agreement with simulation. When microbubbles are injected, we see two prominent features in the temperature profile: an initial rapid temperature rise within the first second of HIFU activation, and a significant difference in peak temperature compared to HIFU-only treatments. The influence of injected microbubbles is further summarized in Fig. 1b which shows the peak measured focal temperature elevation (at 40 s total time according to Fig. 1a) at all considered focal pressures. A temperature gain is observed at all pressures. At higher pressures (2.50, 3.75 MPa), cavitation of residual air micro pockets in the liver tissue was confirmed with imaging during the procedure even when no microbubbles were injected. The cavitation of native bubbles also increases temperature elevation and at 3.75 MPa there is little difference between using and not using microbubbles. The off-axis peak temperature measurements (Fig. 1c) provide further evidence of the beneficial action of the introduced microbubbles at all pressures, where temperature elevation was always greater when microbubbles were injected. Another time point of interest was 35 s after the HIFU was turned off (at 75 s total time according to Fig. 1a) to investigate the cooling of the medium and is shown in Fig. 1d. The temperature elevation was greater at this time point across all focal pressures when microbubbles were injected in the tissue (the green line is above the blue line). Given the increased retention of heat for all focal pressures with microbubbles in Fig. 1d, we deduce that larger thermal lesions are formed when microbubbles are added.
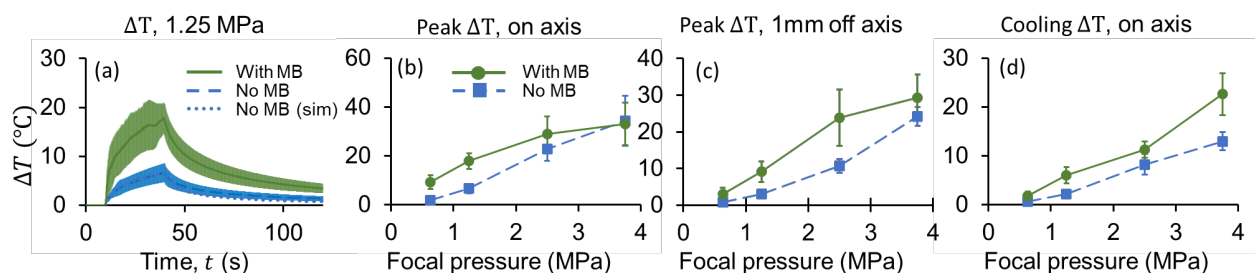
Figure 1. (a) Measured temperature elevation with and without microbubbles on axis at 1.25 MPa focal pressure. Measured temperature elevation with and without microbubbles as a function of acoustic pressure after 30 s of heating on axis (b), 1 mm radially off axis (c), and 35 s after heating on axis (d). Shaded region and error bars indicate one standard deviation.

In Figure 2, we show the temperature elevation in a perfused liver with and without microbubbles supplied either systemically (injected into the main feeding vessels) or locally (injected directly at the focus under image guidance) at pressures 1.25 (Fig. 2a) and 2.50 MPa (Fig. 2b). The presence of perfusion demonstrates the effect of heat convection due to blood flow, with lower peak temperatures in the MPL model (Fig. 2) compared to their corresponding pressures in non-perfused tissue (Fig. 1b). We also observe that the local injections result in markedly higher temperatures as seen previously with the non-perfused liver. Systemic injections showed little to no thermal lesion enhancement at any pressure, with similar temperature elevation and cooling rates to the cases without microbubbles. More importantly, local injections produce a significant thermal lesion enhancement at pressures of 1.25 MPa and higher. At 2.50 MPa the temperature elevation reaches a plateau due to excessive cavitation. In addition, a slower rate of cooling that resists the enhanced convective effects of perfusion is further proof of thermal lesion enhancement at higher pressures with microbubbles.

Conclusions

We demonstrated that adding contrast agent microbubbles during HIFU leads to thermal lesion enhancement compared to HIFU without microbubbles. We have also considered the effect of heat convection due to blood flow and perfusion with a machine-perfused liver. Local injections of microbubbles during HIFU can produce targeted, controlled, mild hyperthermia. This technique is well-suited for drug enhancement applications such as chemotherapy for liver cancer which we plan to consider next.
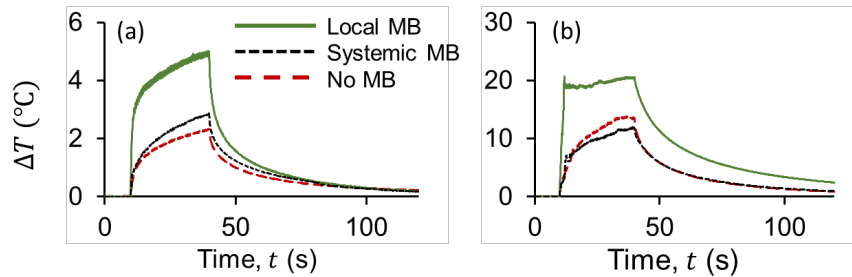
Figure 2. Average measured focal temperature elevation in machine-perfused porcine liver with and without microbubbles for two focal pressures: (a) 1.25 and (b) 2.50 MPa. Two types of microbubble injection were used: local (solid line) and systemic (short dash line). Shaded areas have been removed for clarity and follow the trends set in Fig. 1a.

References

[1]. Izamis M-L, Efstathiades A, Keravnou C, Leen EL, Averkiou MA. Dynamic contrast-enhanced ultrasound of slaughterhouse porcine livers in machine perfusion. Ultrasound in medicine & biology 2014; 40:2217-30.

Spatial and Temporal processing for ultrafast Power Doppler

M. Toulemonde[1], K. Riemer[1], L. Taylor[1], P.D. Weinberg[1], M.X. Tang[1]

[1]*Department of Bioengineering, Imperial College London, London, UK*
Corresponding authors: m.toulemonde@imperial.ac.uk, mengxing.tang@imperial.ac.uk

Introduction

Ultrafast Power Doppler (PD) imaging with microbubble contrast agents is a promising technique to provide microvascular imaging with superior sensitivity than its non-contrast counterpart. However PD method still suffers from the noise background as the ensemble averaging reduces the noise power variance but not the mean of the noise background. Several methods have been proposed to improve PD like the acoustic subaperture imaging (ASAP) method where the received channel signals are split into two subapertures and the beamformed data from each subaperture is temporally correlated to reduce the noise [1]. Furthermore the Frame-Multiply-and-Sum-Based Nonlinear Compounding (FMAS) is another method where each transmission is coupled and multiplied in all possible pairs and then combined to improve the contrast resolution of the PD imaging [2].

In this work, we proposed to combine both ASAP (temporal) and FMAS (spatial) processing methods to reduce the noise and improve the contrast resolution of Power Doppler.

Methods
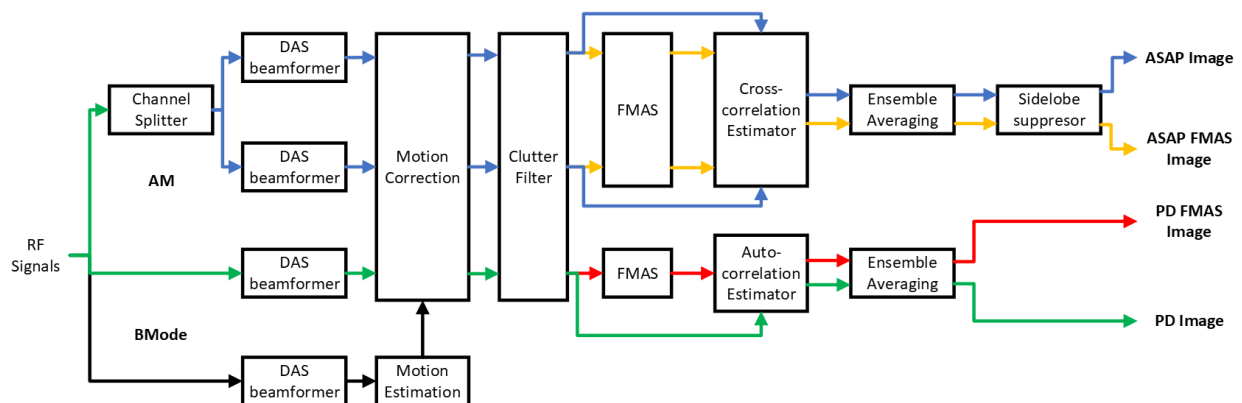
Figure 1. Signal processing methods for PD, PD FMAS, ASAP and ASAP FMAS imaging

In post-processing, ASAP is combined with FMAS (ASAP FMAS), and compared with three other methods PD DAS, PD FMAS and ASAP using data sets generated from the same acquisition. The outline of the signal processing steps of all methods is shown in Figure 1 and it follows the conventional methods of both ASAP and FMAS [1] [2]. In this work, both ASAP and FMAS ASAP methods are generated by splitting the channels into two nonoverlapping subapertures by selecting the odd and even channels while in the original method the apertures are made by alternately placing four consecutive channels in one of the two groups.

The kidney of a male New Zealand White rabbit was investigated using a Verasonics Vantage research ultrasound system with the multiplexed GEL3-12D linear probe. An amplitude modulation (AM) contrast specific acquisition (half, full, half) was performed with two apertures, 10 imaging angles and a frame rate of 100 Hz for a PRF of 1000. The centre frequency was 5 MHz with a single cycle transmission and for a total of 450 frames. All experiments complied with the Animals (Scientific Procedures) Act 1986 and were approved by the Animal Welfare and Ethical Review Body of Imperial College London.

To evaluate the methods, the Contrast-to-Noise Ratio (CNR) and Signal-to-Noise Ratio (SNR) are calculated at several positions.

$$CNR = 10 \log_{10} \left(\frac{|\mu_{signal} - \mu_{background}|}{\sigma_{background}} \right)$$

$$SNR = 10 \log_{10} \left(\frac{\mu_s}{\mu_{background}} \right)$$

where μ_{signal} and $\mu_{background}$ represent the mean blood flow signal and the mean background noise isgnal in each region of interest, respectively, and $\sigma_{background}$ is the standard deviation of the background noise signal.

Results
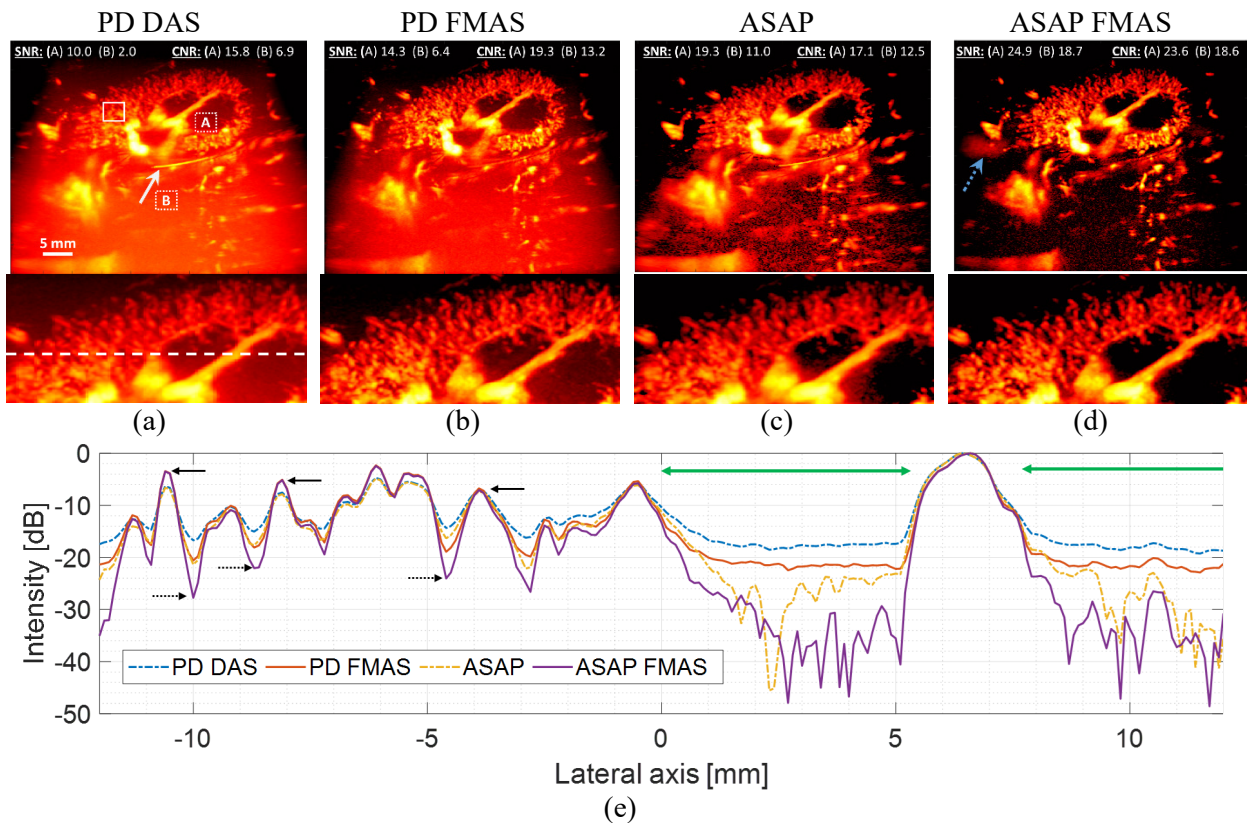
Figure 2. In-vivo acquisition of a rabbit kidney after a bolus injection of ultrasound contrast agent and imaged with an Amplitude Modulation transmission: Power Doppler (PD) DAS (a), PD FMAS (b), ASAP (c) and ASAP FMAS (d) processing and corresponding magnified images, displayed at 40dB of dynamic range. The white solid arrow in (a) shows a tissue boundary artefact and the blue dashed arrow in (d) shows a grating lobe artefact. The intensity profiles (e) are extracted from the white dashed line marked on the PD DAS image. Tissue (full white box) and noise (dashed white boxes) region-of-interests to quantify the SNR and CNR are provided in (a).

Figure 2 (a-d) shows in-vivo images and results for each implemented method. ASAP and ASAP FMAS allow noise background reduction at the deep position, ASAP FMAS has the best SNR and CNR, while PD FMAS and ASAP FMAS improve the contrast resolution at the level of the microvasculature. Figure 2.e highlights the noise reduction and contrast resolution improvement with the intensity profile along the lateral axis. The dark arrows show that ASAP FMAS has a better local contrast resolution where noise between vessels is lower and vessel intensity is higher. The green arrows highlight the noise reduction where no vessels are present for both ASAP and ASAP FMAS.

Another benefit of the FMAS method is artefact reduction. The white arrow in Figure 2.a shows a reflection artefact visible in PD DAS and ASAP but highly reduced in PD FMAS and ASAP FMAS.

However, a limit of the ASAP FMAS method is the generation of some sidelobes or grating lobes shown by the blue arrow in Figure 2.d. They come from the split aperture of ASAP approach and different aperture patterns may provide different sidelobes or grating lobes pattern. They may be reduce by the sidelobe processor step.

Conclusions

The combination of FMAS with ASAP has the benefit of the noise reduction of ASAP at deep positions and the contrast resolution improvement of FMAS. Overall SNR and CNR are improved but with the cost of grating lobes generation where the position of them depends of the subaperture generation. Further analysis needs to be done to optimized the sidelobe suppresor for ASAP FMAS to further reduce the artefacts.

Acknowledgment

References

[1]. A. Stanziola, C.H. Leow, E. Bazigou, P.D. Weinberg, and M.X. Tang, "ASAP: Super-Contrast Vasculature Imaging Using Coherence Analysis and High Frame-Rate Contrast Enhanced Ultrasound", IEEE Trans. On Med. Imaging, vol. 37, no. 8, 2018.

[2]. J. Kang, D. Go, I. Song, and Y. Yoo, "Ultrafast Power Doppler Imaging Using Frame-Multiply-and-Sum-Based Nonlinear Compounding", IEEE Trans. on UFFC, vol. 68, no. 3, 2021.

[3]. J. Hansen-Shearer, M. Lerendegui, M. Toulemonde, and M.X. Tang, "Ultrafast 3-D Ultrasound Imaging Using Row–Column Array-Specific Frame-Multiply-and-Sum Beamforming", IEEE Trans. on UFFC, vol. 69, no. 2, 2022.

The Influence of Cell Rheology on Microbubble Induced Cell-Deformation Measured using Ultra-High Speed Digital Image Correlation

Oliver Pattinson[1], Dario Carugo[2], Fabrice Pierron[1], Nicholas D. Evans[1]

[1]*Department of Engineering, University of Southampton, Southampton, United Kingdom*
[2]*Department of Pharmaceutics, University College London, London, United Kingdom*
Corresponding author: op1g15@soton.ac.uk

Introduction

Ultra-high speed (UHS) imaging, that is imaging greater than 1 million frames per second, provides sufficient resolution to study and resolve microbubble oscillation under ultrasound [1], [2]. UHS-based technologies have driven key findings and developments in the field of therapeutic microbubble treatments by providing a greater understanding of microbubble behaviour upon exposure to ultrasound (US) waves [3]. However, limitations in UHS imaging make it difficult to study the tissue with which microbubbles interact at sufficient spatial resolution while deforming at high frequency. This has resulted in a lack of quantification of the response of tissue, such as cell deformation, membrane strain and pore formation at the high frequencies associated with microbubble therapy. Advances in imaging techniques may address these limitations, providing an opportunity to study tissue at the same high temporal resolutions utilised previously to image microbubbles. Improved image processing techniques, such as digital image correlation (DIC), enables the capture of strain responses at high speeds [4] and has already been tested on biological tissues [5], [6]. DIC however, has not yet been applied to single cell studies. Successful application could resolve microbubble induced cell deformation at therapeutically relevant strain rates, allowing quantification of cell deformation at UHS. The aim of this study was to use UHS and DIC to quantify microbubble induced cell deformation, in order to study the relationship between cell rheology and microbubble therapy.

Methods

A Hypervision HPV-X camera (Shimadzu, Tokyo, Japan), capable of capturing up to 5 million frames per second, was utilised in a custom-designed ultra-high speed imaging apparatus. A high-speed pulsed laser was used to illuminate samples on an inverted microscope connected to the UHS camera (Fig. 1a). A custom-built acoustofluidic device was used to house microbubble-cell interactions, stimulated with a pulsed ultrasound regime (1,000 Hz pulse repetition frequency, 30% duty cycle) from a 1 MHz ultrasound transducer (Precision Acoustics, Dorchester, United Kingdom). Within the acoustofluidic device, distearoylphosphatidylcholine (DSPC) – polyethylene glycol (40) stearate (PEG40s) (Merck, Darmstadt, Germany) microbubbles, were incubated with MG-63 osteosarcoma cells. The device was inverted to induce interactions between the microbubbles and cells before 128-frame UHS videos of ultrasound-induced microbubble oscillation in the presence of cells were captured.

DIC was used to process the image results and analyse the mechanical response of cells through pattern tracking methods. Cell deformation was obtained from the DIC results, as well as quantification of cell strain, across the entire cell membrane. Microbubble oscillation was also captured during the interactions and quantified using edge detection image processing methods.

The UHS experiments, and subsequent DIC analysis, were used to perform a number of experiments demonstrating the different deformation patterns and mechanical response in cells as a result of different microbubble-cell interactions. The structural properties of the cells were altered through paraformaldehyde (PFA) fixation to identify the relationship between cell stiffness [7] and microbubble-induced deformation. Similarly, the properties of the microbubbles were altered through the inclusion of cationic 1,2-distearoyl-

sn-glycero-3-ethylphosphocholine (DSEPC) (Merck, Darmstadt, Germany) to induce electrostatic interaction and study how the contact between cell and microbubble affects the cell response.
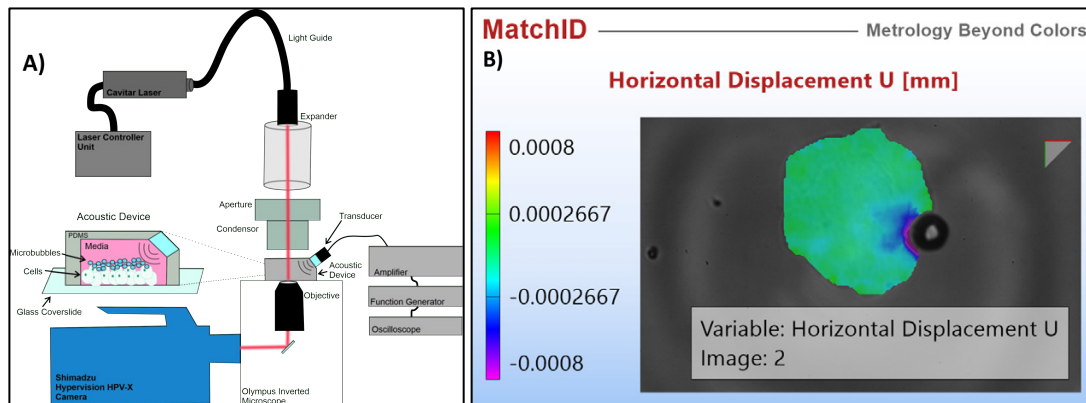
Figure 1. A) Ultra-high speed and acoustofluidic system designed for imaging cell-microbubble interactions at 5 million frames per second. B) DIC results showing spatially resolved deformation in a cell (coloured region of interest) as a result of an oscillating microbubble. Colour bar scale represents horizontal deformation reported in millimeters with a positive deformation defined as moving from left to right.

Results

DIC was successfully applied in a biological study to single cells, as the imaging resolution provided sufficient contrast and clarity. It was shown that DIC can converge when used to measure cells of different sizes and under different loading conditions as inflicted by oscillating microbubbles (Fig. 1b). Deformation values within the range of 50 nm up to almost 3 μm were measured in cells across various UHS images, resulting in strains of up to 10%. Spatial quantification of the deformation pattern was used to reveal the relationship between deformation magnitude and distance from the contact point between the cell and bubble. In all cases deformation decreased as the distance increased and the data set seen in Fig. 1b) fitted a two-phase exponential decay with an R-squared value of 0.92 (Fig. 2a). In experiments comparing the mechanical response of cells with different structural properties, it was found that fixation of the cells and cross-linking of the cell's cytoskeleton, did not have a significant effect on the maximal cell displacement (Fig. 2b).
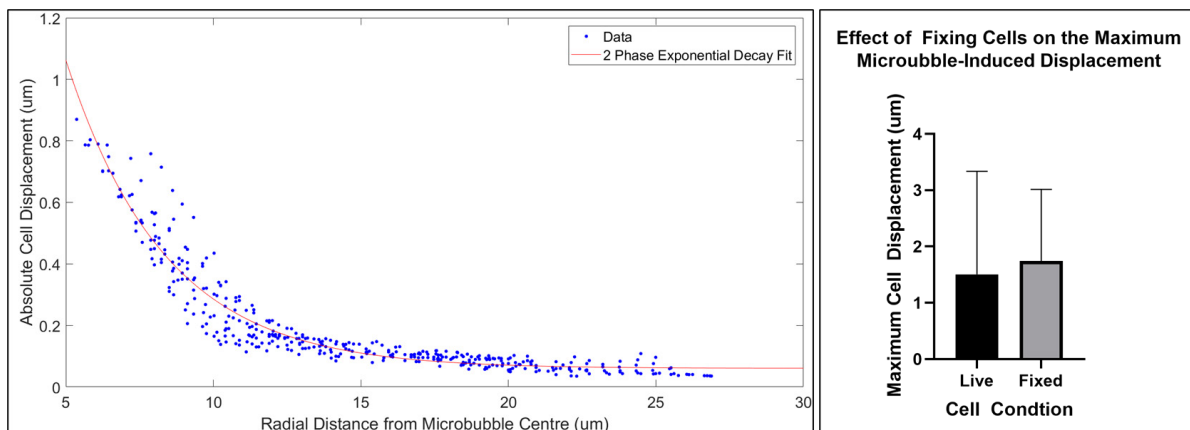
Figure 2. A) Plot showing the decrease in cell displacement measured using DIC as the distance from the microbubble centre increases. The red line corresponds to a two-phase exponential function fitted to the data. B) Bar graph comparing the maximal displacement felt from both live cells and PFA fixed cells following microbubble stimulation (n = 4).

Conclusions

Digital image correlation has been shown to be a suitable and powerful tool for cell analysis during microbubble-mediated ultrasound stimulation, with the capability to resolve cell deformation at time resolutions up to 5 MHz. These findings supported the further analysis of the factors affecting cell deformation, such as the cell's rheology, and revealed the possibility to study how the cell responds during different therapeutic conditions. The future applications of this method and the experiments it can support are vast and represent a large step forward towards finally understanding the unresolved mechanisms that drive the therapeutic interactions between cells and microbubbles.

References

[1] K. Chetty, C. A. Sennoga, J. V. Hajnal, R. J. Eckersley, and E. Stride, "High speed optical observations and simulation results of lipid based microbubbles at low insonation pressures," Proc. - IEEE Ultrason. Symp., vol. 1, no. 6, pp. 1354–1357, 2006.

[2] I. Beekers et al., "Combined Confocal Microscope and Brandaris 128 Ultra-High-Speed Camera," Ultrasound Med. Biol., vol. 45, no. 9, pp. 2575–2582, Sep. 2019.

[3] X. Chen, J. Wang, M. Versluis, N. De Jong, and F. S. Villanueva, "Ultra-fast bright field and fluorescence imaging of the dynamics of micrometer-sized objects," Rev. Sci. Instrum., vol. 84, no. 6, p. 063701, Jun. 2013.

[4] R. Seghir and F. Pierron, "A Novel Image-based Ultrasonic Test to Map Material Mechanical Properties at High Strain-rates," Exp. Mech., vol. 58, no. 2, pp. 183–206, 2018.

[5] D. Zhang and D. D. Arola, "Applications of digital image correlation to biological tissues," J. Biomed. Opt., vol. 9, no. 4, p. 691, 2004.

[6] T. Y. F. Chen et al., "Use of Digital Image Correlation Method to Measure Bio-Tissue Deformation," Coatings 2021, Vol. 11, Page 924, vol. 11, no. 8, p. 924, Aug. 2021.

[7] S. O. Kim, J. Kim, T. Okajima, and N. J. Cho, "Mechanical properties of paraformaldehyde-treated individual cells investigated by atomic force microscopy and scanning ion conductance microscopy," Nano Converg., vol. 4, no. 1, p. 5, Dec. 2017.

A Capillary-sized Microfluidic Phantom:
A Platform for Studying Acoustic Cavitation in Microvessels

Shusei Kawara[1], James Bezer[1], James Choi[1], Sam Au[1]

[1]*Noninvasive Surgery and Biopsy Laboratory/Department of Bioengineering, Imperial College London, London, UK*
Corresponding author: s.kawara19@imperial.ac.uk

Introduction

Microbubbles are used in ultrasound imaging to provide contrast and in ultrasound therapy to produce a therapeutic response. However, while several studies have investigated how bubbles driven by sound (i.e., acoustic cavitation) behaves in free body fluid, or in larger vessels (greater than 10 μm), there is very little understanding of how microbubbles behave in capillary-sized vessels (less than or equal to 10 μm). Several computer simulation studies have predicted that microvascular confinement could significantly alter the behaviour of microbubbles[1], but there has not yet been a microvascular phantom which could confirm these findings. A suitable microvascular phantom must accomodate several traits, which have made their construction difficult: optical transparency, acoustic properties similar to tissue, a small vessel diameter (5-10 μm), and a capacity to accomodate flow. In this study, we describe a hydrogel-based microfluidic phantom that satisfies these requirements. This novel platform could accelerate the experimental analysis of acoustic cavitation in confinement.

Methods

Tapered glass capillaries were used as the inlet and outlet to provide a structural support near such small vessels. The surface of the glass was treated with3-(trimethoxysilyl) propyl methacrylate (TMSPMA) following a previously reported protocol [2]. The hydroxyl groups on the glass formed hydrogen bonds with silane, hence the surface was grafted with the anchors. The functionalized glass capillaries were set within a 3D printed scaffold (Material: VeroClear, Object30 Pro, TRI-TECH 3D Inc., UK) device. A copper wire with the diameter of 10 μm were used as a template for the round channel. To avoid the hydrogel sticking to the wire, the surface of the wire was coated with Parylene C using a vapour deposition system. Polyacrylamide was used as the tissue-mimmicking material due to its optical transparency and the range of Young's moduli it could accomodate [3]. During the polymerization, the methacrylate groups on the TMSPMA grafted on the glass capillary were co-polymerized, creating a tough bond between the capillary and hydrogel. After fully polymerized (>1h), the wire was carefully removed. The dimension of the gel was 10 ×30 ×17 mm. Both sides of the device were open to allow ultrasound to propagate in and out of the hydrogel. The integrity of the channel was then evaluated using a fluorescent probe while its suitability of studying acoustic cavitation was evaluated by administering microbubbles and exposing them to ultrasound.

Results

Channels with diameters between 10 and 100 μm were successfully made with the methods described above. In particular, we were able to create a 10-μm-in-diameter channel, which was intact as shown by the infustion of a FITC-dextran solution (Figure 1). No leakage or cracking were observed during the experiment (> 1h). The capillary surface was smooth due to the chemical resistance of parylene c deposited on the wire. We also confirmed the suitability of this platform for studying acosutic cavitation. A microbubble solution was administered into the capillary. An isolated microbubble was then sonicated at with a pulse (centre frequency: 300 kHz, peak-rarefactional pressure: 300 kPa, pulse length: 10 ms) and its movement was tracked as it was displaced through the primary acoustic radiation force .

Conclusions

A capillary-sized microfluidic phantom were successfully made using methods readily available in most laboratories. This device was optically transparent and used a hydrogel which can be easily manipulated to mimmick the mechanical properties of human tissue. Bubbles were introduced to the channel

without any leakage or cracking in the hydrogel. This device may help the acoustics community to optically and acoustically understand the acoustic cavitation in human capillaries.
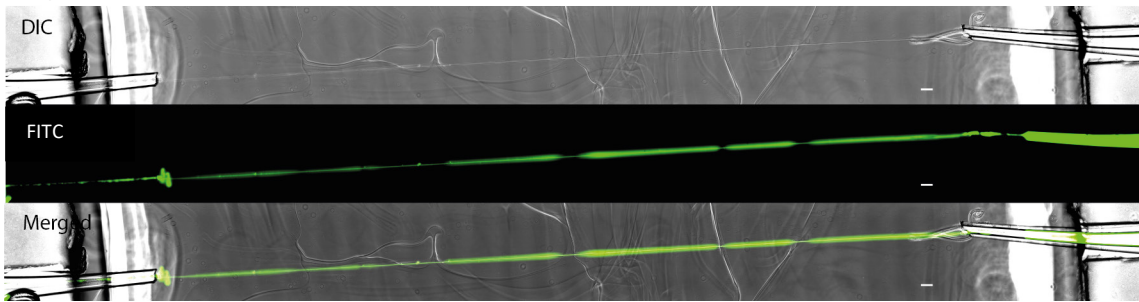
Figure 1. The microfluidic phantom with a diameter of 10 μm. FITC-dextran (2000 kDa, Sigma-Aldrich, UK) was dissolved in deionized water and the solution was infused at 10 nL/s from left to right. The images correspond to differencial interference contrast (DIC), fluorescein isothiocyanate (FITC) and combined respectively.
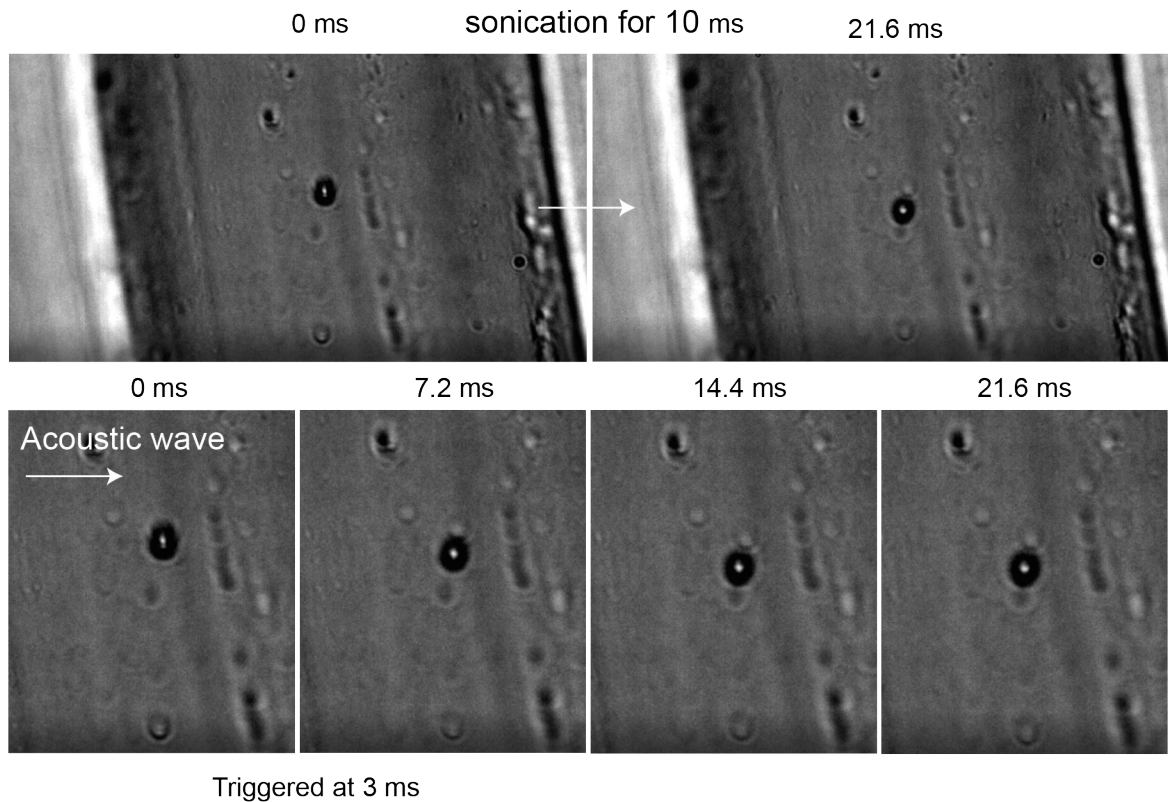
Figure 2. Demosntration of a signle-microbubble sonication. A single bubble was sonicated at the frequency of 300 kHz. The calibrated pressure was at 300 kPa.

References

[1]. P. Marmottant *et al.*, "A model for large amplitude oscillations of coated bubbles accounting for buckling and rupture," *J. Acoust. Soc. Am.*, vol. 118, no. 6, pp. 3499–3505, Dec. 2005, doi: 10.1121/1.2109427.

[2]. H. Yuk, T. Zhang, S. Lin, G. A. Parada, and X. Zhao, "Tough bonding of hydrogels to diverse non-porous surfaces," *Nat. Mater.*, vol. 15, no. 2, pp. 190–196, Feb. 2016, doi: 10.1038/nmat4463.

[3]. J. H. Bezer, H. Koruk, C. J. Rowlands, and J. J. Choi, "Elastic Deformation of Soft Tissue-Mimicking Materials Using a Single Microbubble and Acoustic Radiation Force," *Ultrasound Med. Biol.*, vol. 46, no. 12, pp. 3327–3338, Dec. 2020, doi: 10.1016/j.ultrasmedbio.2020.08.012.

Sonothrombolysis after percutaneous coronary intervention in STEMI patients with increased risk for microvascular obstruction: a multicenter randomized controlled trial

S. El Kadi [1], S. Li [2], E. Spoormans [1], N.W. Verouden [1], F. Xie [2], O. Kamp [1], T.R. Porter [2]

[1]*Amsterdam Cardiovascular Sciences, Amsterdam University Medical Centers - location Vrije Universiteit, Amsterdam, Netherlands*
[2]*Department of Cardiovascular Sciences, University of Nebraska Medical Center, Omaha, Nebraska, United States*
Corresponding author: s.elkadi@amsterdamumc.nl

Introduction

Despite successful recanalization with percutaneous coronary intervention (PCI), approximately 50% of patients with ST-elevation myocardial infarction (STEMI) suffer from ongoing infarction due to microvascular obstruction (MVO) (Nijveldt et al., 2009). Contributors to the complex mechanism of MVO are distal embolization of thrombus particles, increased in situ thrombogenesis, plugging of activated platelets and leukocytes and vasoconstriction (Sezer et al., 2018). The use of intravascular microbubbles with concomittant intermittent high mechanical index (HMI) ultrasound impulses has been shown to dissolve thrombi and augment microvascular perfusion through vasodilative pathways (El Kadi et al., 2022). This technique, also termed sonothrombolysis, could potentially be used in STEMI patients at high risk of developing MVO, to enhance reperfusion and limit infarct size.

Methods

In this ongoing multi-center, prospective, randomized controlled trial, 118 STEMI patients with increased risk for MVO (defined as occlusion of the left anterior descending (LAD) artery [center 1] or incomplete ST-resolution (≤70%) on the electrocardiogram (ECG) after PCI irrespective of culprit artery [center 2]) will be randomized to either sonothrombolysis or control. Sonothrombolysis treatment consists of a 3% infusion of Luminity microspheres with simultaneous delivery of 40-80 intermittent HMI ultrasound pulses (frequency: 1.8/1.8 MHz, MI: 1.2-1.3, 10 flash frames, pulse duration <5µs). Control cases also receive a 3% Luminity microspheres infusion with low mechanical index (LMI) ultrasound and no more than 6 HMI pulses for perfusion imaging purposes. Primary endpoints are infarct size (% of LV mass) and left ventricular ejection fraction (LVEF %) as assessed on cardiac magnetic resonance (CMR) imaging two months after inclusion. Secondary endpoints include change in infarct size and LVEF on CMR (CMR < 1 week versus CMR at 2 months), ST-resolution on serial ECGs, ejection fraction and global longitudinal strain (%) on echocardiography, microvascular perfusion before and after study intervention and clinical outcome measures at six months after inclusion.

Baseline characteristics			
	Sonothrombolysis (n= 51)	**Control (n= 49)**	**P-value**
Age, y	62 (±12)	63 (±12)	0.24
Male sex, n (%)	45 (88)	37 (76)	0.10
Body mass index, kg/m^2	26 (24-30)	27 (24-30)	0.94
SBP, mmHg	133 (112-145)	126 (113-150)	0.90
Medical history, n (%)			
Diabetes mellitus	11 (22)	6 (12)	0.22

Hypertension	16 (31)	22 (46)	0.14
Dyslipidemia	17 (35)	19 (39)	0.62
Smoking	20 (39)	19 (39)	0.96
Previous myocardial infarction	5 (10)	6 (12)	0.70
Previous PCI	4 (8)	6 (12)	0.46
Positive family history	12 (24)	16 (34)	0.25
Drug use before admission			
Aspirin	7 (14)	11 (22)	0.26
Statin	9 (18)	11 (22)	0.69
Beta-blocker	5 (10)	5 (10)	0.95
Calcium-channel blocker	6 (12)	3 (6)	0.32
ACE-i / ARB	7 (14)	11 (22)	0.26
Timing			
Symptom-to-diagnosis time (min)	97 (48 - 174)	105 (55 – 228)	0.29
Diagnosis-to-reperfusion time (min)	45 (36 – 63)	49 (40 – 59)	0.52

Results

To date, 100 patients have been included in the study. Baseline characteristics are provided in Table 1. Mean age of all patients was 62 ($\pm$ 12) and 82 patients (82%) were male. Culprit artery in patients included in center 2 was LAD in 38 patients (72%), right coronary artery in 11 patients (21%) and circumflex artery in 4 patients (7%). Time to first medical contact was 97 (IQR: 48 -174) and 105 (IQR: 55 - 228) minutes and time from diagnosis to PCI was 45 (IQR: 36 - 63) and 49 (IQR: 40 - 59) minutes in the sonothrombolysis group and in the control group respectively. Summed ST-elevation on ECG before and after PCI was not statistically different: 11.5 mm (6.5 – 16.1) and 11.2 mm (5.9 - 16.9) (p= 0.81) before PCI and 8.4 mm (4.3 – 13.0) and 9.7 mm (4.1 - 16.4) (p= 0.39) after PCI, in the sonothrombolysis and control group.

No statistically differences between the groups were observed in medical history and drug use before admission.

Conclusions

STEMI patients with LAD occlusion and patients with incomplete ST-resolution on ECG after PCI are at increased risk of MVO and have worse clinical prognosis (van Kranenburg et al., 2014). This clinical trial aims to assess efficacy of post-PCI sonothrombolysis in this patient population to limit final infarct size and salvage myocardial function. Currently, 100 patients have been included with overall similar baseline characteristics. Inclusion, blinded assessment of primary and secondary endpoints and clinical follow up is expected to be completed in 2023.

A

B
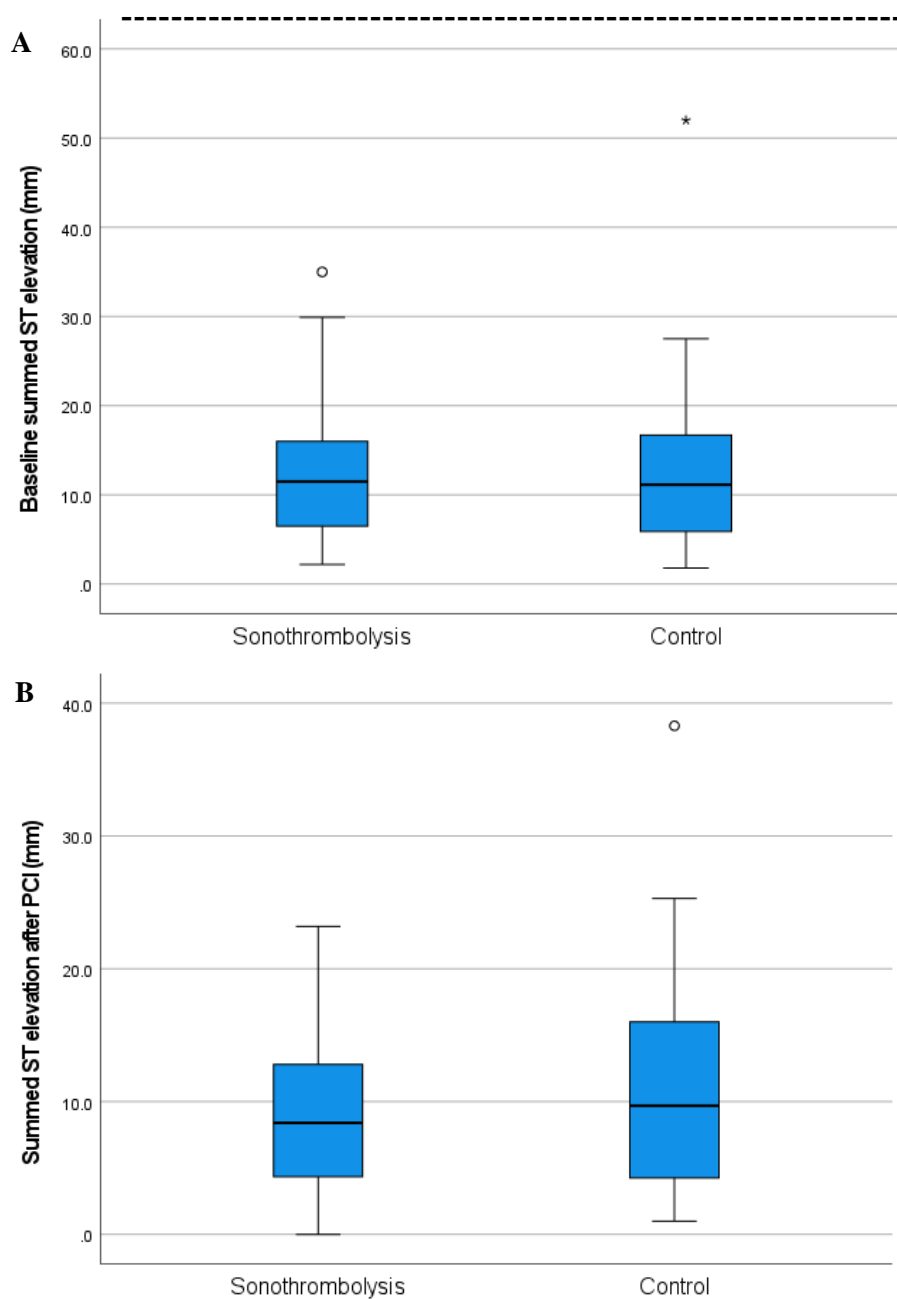
Figure 1: Boxplot of baseline summed ST-elevation in mm before PCI (A) and after PCI (B).

References

[1]. El Kadi, S., Porter, T. R., Verouden, N. J. W., van Rossum, A. C., & Kamp, O. (2022). Contrast Ultrasound, Sonothrombolysis and Sonoperfusion in Cardiovascular Disease: Shifting to Theragnostic Clinical Trials. *JACC Cardiovasc Imaging*, *15*(2), 345-360. https://doi.org/10.1016/j.jcmg.2021.07.028

[2]. Nijveldt, R., Hofman, M. B., Hirsch, A., Beek, A. M., Umans, V. A., Algra, P. R., Piek, J. J., & van Rossum, A. C. (2009). Assessment of microvascular obstruction and prediction of short-term remodeling after acute myocardial infarction: cardiac MR imaging study. *Radiology*, *250*(2), 363-370. https://doi.org/10.1148/radiol.2502080739

[3]. Sezer, M., van Royen, N., Umman, B., Bugra, Z., Bulluck, H., Hausenloy, D. J., & Umman, S. (2018). Coronary Microvascular Injury in Reperfused Acute Myocardial Infarction: A View From an Integrative Perspective. *J Am Heart Assoc*, *7*(21), e009949. https://doi.org/10.1161/JAHA.118.009949

[4]. van Kranenburg, M., Magro, M., Thiele, H., de Waha, S., Eitel, I., Cochet, A., Cottin, Y., Atar, D., Buser, P., Wu, E., Lee, D., Bodi, V., Klug, G., Metzler, B., Delewi, R., Bernhardt, P., Rottbauer, W., Boersma, E., Zijlstra, F., & van Geuns, R. J. (2014). Prognostic value of microvascular obstruction and infarct size, as measured by CMR in STEMI patients. *JACC Cardiovasc Imaging*, *7*(9), 930-939. https://doi.org/10.1016/j.jcmg.2014.05.010

Implementation of Ultrasound Localization Microscopy (ULM) for in Vitro and ex Ovo Experiments

Redouane Ternifi, Maria Costa, Mina Lykakis, Emmanuel Gaud, Isabelle Tardy, Thierry Bettinger
Bracco Suisse SA, 31 route de la Galaise, 1228 Plan-Les-Ouates, Geneva, Switzerland
Corresponding author: redouane.ternifi@bracco.com

Introduction

The microvascular system is profoundly altered by a variety of pathologies. In conjunction with the aging population, these microcirculation dysfunctions and small vessel diseases are likely to become more prevalent. However, medical imaging on this scale is not currently possible due to the limitations of the imaging modalities. A recent development in contrast-enhanced ultrasound, known as super-resolution ultrasound imaging (SRUI), demonstrated that capillary-size blood vessels can be imaged *in vivo*, improving the resolution by more than 10-fold below the diffraction limit [1].

Methods

Based on the ultrasound localization microscopy (ULM) technique [2], which is inspired by optical nanoscopy, SRUI uses point spread functions to localize and track the centroid of ultrasound contrast agents, such as microbubbles (MB). The super-resolved image is created by accumulating the localized and tracked MB events, which allows vessels to be distinguished spatially within a few micrometers. In this research work, we present the results of our efforts to optimize SRUI in *in vitro* and *ex ovo* studies, screen different concentrations of SonoVue microbubbles (MB), and analyze them by ULM processing. In the study, the performance of ULM in terms of total number of detected MB and percentage of the tracked MB was first evaluated *in vitro* using homemade microflow phantoms (channel diameters range from 170 μm to 500 μm), followed by validation in the chicken embryo chorioallantoic membrane (CAM) model. The concentration scenarios included low ($2.8\times10^{+4}$ MB/mL), medium ($1.8\times10^{+5}$ MB/mL), and high ($1\times10^{+6}$ MB/mL) numbers of microbubbles diluted by in saline solution. The Verasonics system was used to acquire plane wave ultrasound images of different MB concentrations at different flow rates using homemade microflow phantoms and *ex ovo* CAM model.

Following the conventional post processing, tissue signal and noise were removed using singular value decomposition (SVD) processing on the complex in-phase and quadrature (IQ) data [3]. After the MB were localized using a weighted average algorithm and tracked over several frames using simpletraker algorithm, final super-resolved image and velocity map were produced. Furthermore, Jerman's Hessian-based tubular (vesselness) enhancement filters [4] were applied in order to smooth the connection of vessel network and enabling estimation of morphological metrics such as density, diameter and tortuosity of the vessels.

Results

In the microflow phantom study, the mean number of detected MB events per 100 frames was roughly 3000, 1800 and 1000 for high, medium and low concentrations, respectively at the same flow rate. Consequently, the percentage of tracked MB decreases with concentration due to the overlapping event, reaching 67% at low, 45% at medium and only 30% at high concentration. In the chicken embryo CAM study, the optical image revealed a vessel density of 8.0% of the reference image, as shown in Figure 1. With only 3 seconds acquisition time, SRUI was able to achieve 5.78% and 4.41% at high and medium concentrations, respectively.

Conclusions

In conclusion, we have implemented a super-resolution ultrasound imaging technique using standard ultrasound localization methods in order to test its performances with different ultrasound contrast agent formulations. To determine the optimal agent, further analyses will be required using an in vitro microflow calibration setup, an ex ovo CAM model with an optical reference, and in vivo studies.
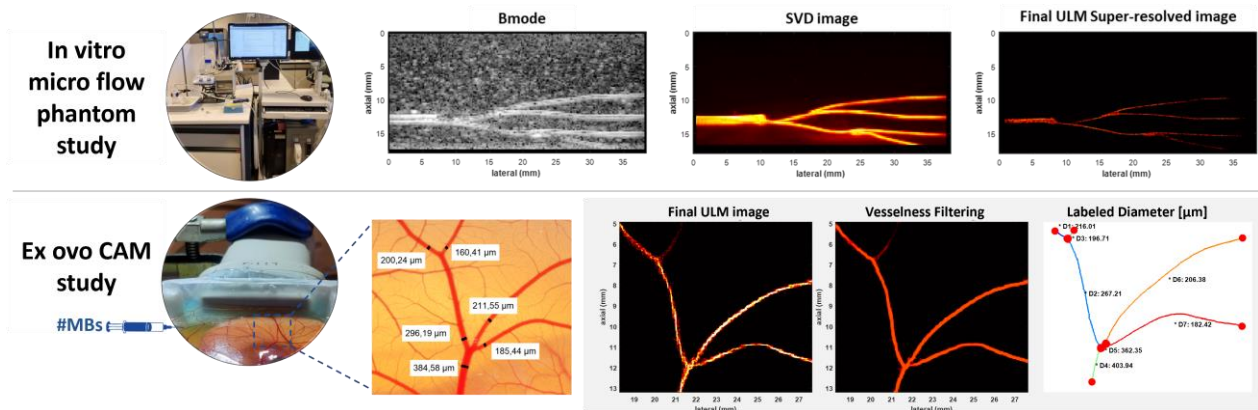
Figure 1. Illustration of *in vitro* microflow phantom study and *ex-ovo* ULM results.

References

[1]. Kirsten Christensen-Jeffries, Olivier Couture, Paul A. Dayton, Yonina C. Eldar, Kullervo Hynynen, Fabian Kiessling, Meaghan O'Reilly, Gianmarco F. Pinton, Georg Schmitz, Meng-Xing Tang, Mickael Tanter, Ruud J.G. van Sloun, Super-resolution Ultrasound Imaging, Ultrasound in Medicine & Biology, Volume 46, Issue 4, 2020, Pages 865-891.

[2]. Heiles, B., Chavignon, A., Hingot, V. et al. Performance benchmarking of microbubble-localization algorithms for ultrasound localization microscopy. Nat. Biomed. Eng 6, 605–616 (2022).

[3]. Desailly, Y., Tissier, A. M., Correas, J. M., Wintzenrieth, F., Tanter, M., & Couture, O. (2016). Contrast enhanced ultrasound by real-time spatiotemporal filtering of ultrafast images. Physics in Medicine & Biology, 62(1), 31.

[4]. T. Jerman, F. Pernuš, B. Likar and Ž. Špiclin, "Enhancement of Vascular Structures in 3D and 2D Angiographic Images," in IEEE Transactions on Medical Imaging, vol. 35, no. 9, pp. 2107-2118, Sept. 2016.

Ultrasound localization microscopy using non-sparse microbubble concentrations

Anton A. Odarenko[1], _Jonah S. Harmon[1]_, _Tobias Prasse[1]_, _Lindsay N. Cates[1]_, _Zin Z. Khaing[1]_,
Charles Tremblay-Darveau[2], _Matthew F. Bruce[3]_

[1]Department of Neurological Surgery, University of Washington, Seattle, USA
[2]Philips Medical Systems, Bothell, USA
[3]Applied Physics Laboratory, University of Washington, Seattle, USA
Corresponding author: mbruce@uw.edu

Introduction

Current ultrasound localization microscopy (ULM) approaches utilize sparse microbubble concentrations to isolate and track non-overlapping point spread functions. However, this requires lengthy acquisition times (> 20 sec to several minutes) to produce a super-resolved vascular map. This is impractical for critical care scenarios (e.g., intraoperative use for spinal cord injury) or cases with substantial tissue motion (e.g., abdomen), limiting the clinical applicability of ULM. Multiple studies have explored methods to alleviate this limitation, including AI/ML-based approaches.[1-2] In this work, we instead apply ULM processing to non-sparse acquisitions to achieve super-resolution with substantially reduced total dwell time.

Methods

An amplitude modulated multiangle plane wave sequence was implemented on a Verasonics research ultrasound platform (Kirkland, WA, USA) using a 18 MHz linear array transducer (Vermon, Tours, France). Imaging was conducted in the rat spinal cord at thoracic level T7-T9 following a laminectomy. Color Doppler and high-concentration ULM images were constructed from a nonlinear Doppler ensemble (4 kHz PRF; 180 msec acquisition duration) acquired at the peak intensity following a bolus injection of Definity (0.1 mL, 0.2 mL saline flush).[3] Sparse ULM was constructed from 25.2 sec total acquisition time initiated 5 mins after the bolus injection. Following motion correction and SVD filtering, localization (cross-correlation) and tracking (Hungarian linker) with differing parameters were applied to construct both sparse and non sparse ULM images.

Results

All three methods captured the largest penetrating ventral arteries and the major ascending veins on the dorsal aspect of the cord (Fig. 1). Full-width at half-maximum (FWHM) measurements of penetrating arteries indicated that sparse and high-concentration ULM produced super-resolved vascular maps compared to color Doppler (135±2.81, 41.7±2.21, and 40.6±2.89 um for color Doppler, sparse ULM, and high-concentration ULM respectively). Overall image resolution measured using the Fourier ring correlation was comparable between both ULM images (24.8 vs 33.8 um for sparse vs high-concentration ULM, respectively).[4] High-concentration ULM did result in loss of information, particularly with respect to the smallest vessels, but was achieved with 140-fold lower total dwell time (180 msec vs 25.2 sec).

Conclusions

Application of ULM processing to densely-populated microbubble acquisitions enables super-resolution imaging with a 100 fold reduction in acquisition times. In addition to rendering ULM more clinically feasible and less susceptible to major tissue motion, this may recover the temporal information that is lost with sparse ULM. For example, whereas sparse ULM produces output averaged over many cardiac cycles, high-concentration ULM may be useful to quantify pulsatility or other shorter-timescale flow dynamics.

Color Doppler | Sparse ULM | High-concentration ULM

180 msec | 25.2 sec | 180 msec
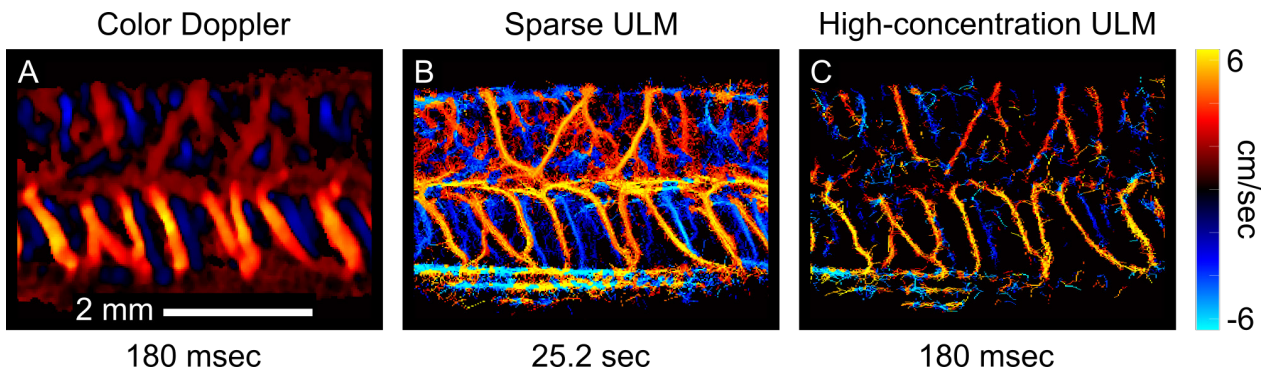
Figure 1. High-concentration ULM enables super-resolution with substantially reduced total dwell time. Representative color Doppler (A), ultrasound localization microscopy (ULM; B), and ULM applied to a densely-concentrated acquisition (C) are shown. High-concentration ULM enabled super-resolution of the vasculature with a 140-fold shorter total acquisition time compared to sparse ULM (180 msec vs 25.2 sec). While high-concentration ULM does not depict the smallest vessels, the largest arteries and veins were visualised. Overall image resolution was comparable between sparse and high-concentration ULM (24.8 vs 33.8 um).

References

[1]. van Sloun, RJG, O Solomon, M. Bruce, Z. Khaing, H Wijkstra, Yonina C. Eldar, and M Mischi. "Super-resolution ultrasound localization microscopy through deep learning." IEEE TMI 40, no. 3 (2020): 829-839.

[2]. Bar-Zion, A, O Solomon, C Tremblay-Darveau, D Adam, and Y Eldar. "SUSHI: Sparsity-based ultrasound super-resolution hemodynamic imaging." IEEE transactions on UFFC 65, no. 12 (2018): 2365-2380.

[3]. Bruce, M, A Hannah, R Hammond, Z Khaing, C Tremblay-Darveau, P Burns, and C Hofstetter. "High-frequency nonlinear doppler contrast-enhanced ultrasound imaging of blood flow." IEEE Transactions on UFFC 67, no. 9 (2020): 1776-1784.

[4]. V Hingot, A Chavignon, B Heiles, and O Couture. "Measuring Image Resolution in Ultrasound Localization Microscopy." IEEE TMI, no. 12 (2021): 3812-3819.

Visualizing the Angiogenesis of Glioblastoma in Mice Using Completely Non-Invasive Volumetric Ultrasound Localization Microscopy

__Jacob R. McCall__[1], Ryan DeRuiter[2], Mark Ross[2], Gianmarco F. Pinton[2], Paul A. Dayton[2]

[1]*Department of Electrical and Computer Engineering, NC State University, Raleigh, NC, USA*
[2]*Joint Department of Biomedical Engineering, UNC Chapel Hill and NC State University, Chapel Hill and Raleigh, NC, USA*
Corresponding author: jmccall4@ncsu.edu

Introduction

Standard initial diagnostic procedures for brain cancer involve MRI or CT evaluation, followed by a biopsy if a tumor is suspected. CT involves radiation, MRI is expensive, and either procedure requires access to primary care imaging centers. With the decreasing cost and increasing portability of ultrasound, a method for ultrasound brain cancer diagnostics would provide increased accessibility. Glioblastoma is an aggressive form of cancer with a prognosis that often can be six months or less. It is known that microvascular angiogenesis is a biomarker of cancer, but traditional ultrasound has been unable to visualize angiogenesis. Ultrasound localization microscopy (ULM) has demonstrated potential as a powerful new capability to resolve microvasculature. In this study, we demonstrate the potential of 3-D super-resolution ultrasound for detection of glioblastoma in the mouse brain through visualization of angiogenic biomarkers.

Methods

The vascular growth of 4 control mice and 8 mice affected by glioblastoma was non-invasively monitored up to three weeks. To do this, we acquired a volumetric scan of the each mouse's brain using volumetric ULM. These scans were acquired using the Verasonics (Verasonics Inc., Kirkland, WA, USA) volumetric imaging system, which consists of four 256-channel Vantage systems coordinated by four controllers. These were used to synchronously operate all channels of a 1024-channel 8 MHz fully-addressed matrix array (Vermon, Tours, France). For each mouse, a fully volumetric, transcranial 200 s contrast-enhanced scan was acquired at a volume rate of 500 vps using a 5-angle plane-wave compounding scheme (-3 to +3 on both axes). A total of 100k coarsely beamformed volumes were processed using singular value decomposition filtering, microbubble localization, and microbubble tracking. The mice were anesthetized using isofluorane carried by oxygen gas. A dilution of 9e7 MB/mL/g was infused intravenously at a rate of 6 μL/min.

Results

The development of the disease was monitored over the lifetime of the mice affected by glioblastoma, and we observed the development of abnormal vascular growth each week. Fig. 1 (a)-(c) shows the maximum intensity projection over the saggital dimension of the same mouse over the course of three weeks to demonstrate the overall change in vasculature. By week 3, the tumor has caused significant disruption to the appearance of the vascular system. Fig. 1 (d)-(e) shows the local angiogenesis of a tortuous vessel at the site of cell implantation in a mouse with glioblastoma observed in just one week. Overall, we observed a significant decrease in vascular presence in the mice affected by glioblastoma at week three.

Conclusions

In this work, we demonstrated the repeatability of a volumetric super-resolution imaging modality for pre-clinical studies that can obtain high-resolution images in mice brains without any surgical procedures beyond the insertion of a tail vein catheter. We observed primarily two characteristics of the vascular growth over three weeks. First, we observed the local growth of angiogenic vessels that correlates with the tumor cell implantation site that can be detected as early as three weeks post-implantation and can be differentiated

between one week of imaging. Second, we observed that mice that survived to four weeks had significantly less vascular appearance than in weeks two and three, which is possibly caused by the slow perfusion of dense vascular networks that may be filtered out when SVD filtering. By comparison, healthy mice maintained similar levels of vascular signal at three weeks.
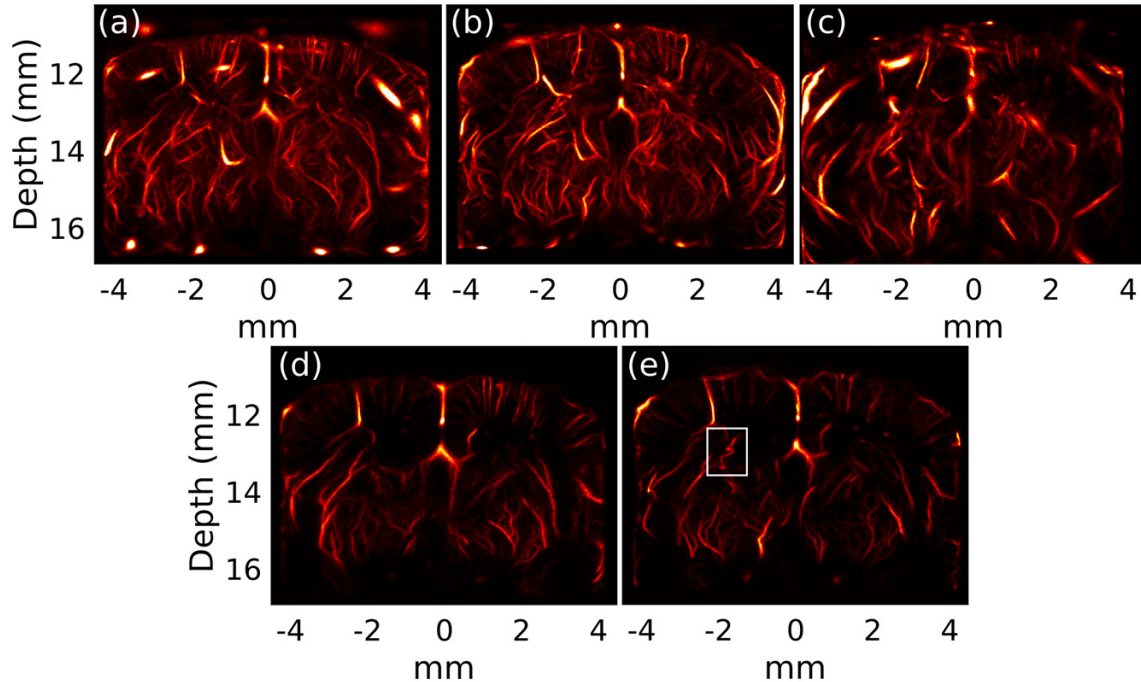
Figure 1. The development of the microvasculature at (a) two weeks, (b) three weeks, and (c) four weeks post-implantation of U87 GBM cells. A small section of the brain for (d) week one and (e) week two are shown. The growth of abnormal vasculature, demonstated in the white box in (e), appears after three weeks of cell growth.

Noninvasive Diagnosis of Chronic Exertional Compartment Syndrome with Subharmonic Aided Pressure Estimation and Shearwave Elastography

Corinne E. Wessner[1], Rachel Blackman[1], Corbin Pomeranz[1], Michael K. Hoy[1], Kristen Bradigan[1], Marc I. Harwood[2], Levon Nazarian[1], Andrej Lyshchik[1], <u>Flemming Forsberg[1]</u>

[1]Department of Radiology, Thomas Jefferson University, Philadelphia, PA, 19107, USA
[2]Non-Operative Sports Medicine Department, Rothman Orthopaedic Institute, Philadelphia, PA, 19107, USA

Introduction

Chronic exertional compartment syndrome (CECS) is an underdiagnosed condition that primarily affects 10-60% of young, active people (mainly athletes) with exercise induced leg pain most commonly in the calf [1]. CECS is caused by exercise-induced pain with increased compartmental pressure in the fascial spaces causing impaired tissue perfusion during physical exercise. Definitive treatment is with fasciotomy, which has a success rate of up to 95% [2]. However, the average delay between diagnosis and subsequent treatment is 2 years, which has been shown to decrease the success rate of both conservative and surgical therapy [1-3].

Currently, the reference standard for diagnosing CECS is invasive compartment pressure testing, which involves inserting a handheld 18G gauge needle with a pressure monitor system (Stryker Instruments, Kalamazoo, MI, USA) into the four calf compartments and measuring the compartment pressure directly (in mmHg). Direct compartment testing is invasive, painful, and carries a complication risk of neurovascular damage and infection. Furthermore, there is significant variability in this technique with some studies finding more than 5 mmHg difference in 40% of compartmental pressure measurements [4, 5].

Recently, other imaging modalities such as magnetic resonance imaging (MRI) and infrared spectroscopy have been studied for this application [5, 6]. Another alternative is shear wave elastography (SWE), which is a noninvasive imaging modality that evaluates tissue stiffness by measuring in real-time the speed of the shear wave propagation in tissues using ultrasound [7]. SWE is primarily used in the liver (to diagnose nonalcoholic fatty liver disease (NAFLD) or liver fibrosis), but its use has also been explored in musculoskeletal applications to diagnose and monitor disease progression [8, 9]. Moreover, subharmonic aided pressure estimation (SHAPE) is a noninvasive method for pressure estimation using ultrasound contrast agents and subharmonic imaging, which has shown encouraging results in clinical trials of portal hypertension and interstitial fluid pressure measurements [10. 11]. The objective of this study was to compare SHAPE and SWE to the invasive, reference standard compartment pressure testing for the diagnosis of CECS.

Materials and Methods

In this ongoing, prospective**,** pilot study, healthy volunteers and subjects diagnosed with CECS provided written informed consent to participate. The study was approved by the University's Institutional Review Board as well as the United States Food and Drug administration (IND no. 112, 241). The full protocol and statistical analysis plan are available at *https://clinicaltrials.gov/ct2/show/NCT05247541* (trial registration number: NCT05247541).

Both study groups (i.e., volunteers and subjects with CECS) underwent ultrasound imaging before and immediately after exercise. A standardized exercise treadmill protocol was used to induce fatigue and/or elicit symptoms: running 5.95 km/h against a 5° slope for 6 minutes or until symptom onset. If symptoms did not occur by 6 minutes of exercise, speed was increased to a maximum of 8.0 km/h and/or the slope was increased to 8° for an additional 6 minutes (or until symptom onset). In the healthy volunteers, the anterior calf compartment was imaged, while the symptomatic compartment was imaged in the CECS subjects. Patients were scanned in a supine position with the ankle in a neutral position using a modified Logiq E10 scanner (GE Healthcare, Waukesha WI, USA) with C1-6 and C2-9 probes. Conventional 2D ultrasound was used to identify the muscle of interest.

First, the probe was positioned perpendicular to the muscle to optimize the SWE imaging. For pre and post exercise acquisitions, real-time SWE color maps were generated at a depth of approximately 3 cm. Twelve regions of interests were drawn offline and the system quantified the median shear wave velocity (m/s), velocity interquartile range (IQR) (m/s), and velocity IQR to velocity median ratio percentage (in m/s) for each examination. For quality assurance purposes, an IQR to median ratio ≤ 15% was considered a reliable SWE examination.

Next, an intravenous infusion of 2 vials of the ultrasound contrast agent Definity (Lantheus Medical Imaging, N Billerica, MA, USA) in 50 mL of saline was administered over 5-10 minutes for SHAPE data acquisitions. Once contrast microbubbles were visualized within the compartment muscle, a power optimization algorithm was run to establish individual acoustic parameters [10-12]. Once the optimal power was determined, three 5 second clips were acquired. After the pre-exercise SHAPE acquisitions, the subject performed an exercise protocol for approximately 6 minutes (or until symptoms were elicited); as described above. Immediately after exercise, the subject returned to the supine position and another three 5 second post-exercise SHAPE clips were acquired. Regions of interests were drawn offline around the symptomatic compartment muscle and an adjacent vessel pre and post SHAPE (Figure 1). Finally, the post exercise SWE acquisitions were performed. SHAPE and SWE results were compared between groups and relative to the compartment pressure testing (in mmHg; the reference standard) using paired and unpaired t-test and linear regression analysis. All tests were performed using Prism 9.3.1 (GraphPad Software, San Diego, CA, USA) with p-values less than 0.05 indicating statistical significance.
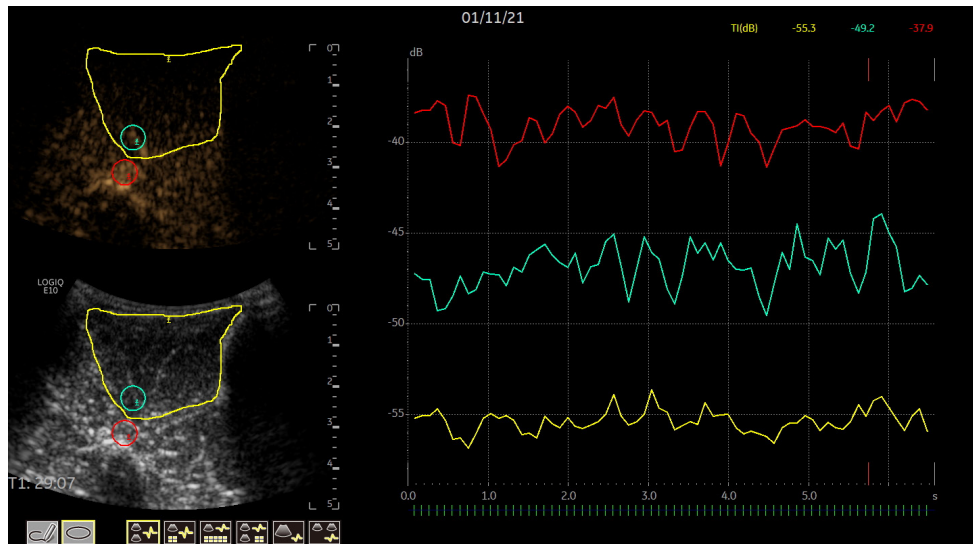
Figure 1: Time intensity analysis of 3 regions of interest (the whole calf muscle - yellow; the maximum signal within the muscle - turquois and the signal in a vessel outside the muscle - red) of a healthy volunteer.

Results

To date, data analysis has been completed in 10 healthy volunteers and 4 CECS patients. Among these subjects, the mean age of the healthy volunteers was 33 ± 16 years, while for the CECS patients it was 27 ± 5 years. The healthy volunteers consisted of 6 males and 4 females and among the CECS patients there was 1 male and 3 females.

When evaluating SWE in the healthy volunteers from pre to post exercise there was a statistically significance difference ($p = 0.01$), which was not seen in the CECS patients ($p = 0.14$). Moreover, comparing healthy volunteers and CECS patients did not identify any difference using SWE ($p = 0.23$). Linear regression analysis was performed to correlate the invasive compartment pressure testing (in mmHg) with the SWE data, but again no statistically significant relationship was observed ($R^2 = 0.50$; $p = 0.29$).

When evaluating the whole muscle with SHAPE pre and post exercise both the healthy volunteers and the CECS subjects demonstrated a decrease in percent difference, which was statistically significant ($p < 0.01$). When comparing healthy volunteers to CECS patients evaluating the whole muscle vs. adjacent vessels with SHAPE there was no difference ($p = 0.57$). Linear regression analysis was statistically

significant when evaluating the correlation between compartment pressure testing results (in mmHg) and SHAPE estimates ($R^2 = 0.96$; p = 0.02). Alternatively, when correlating the percent difference between compartment pressure testing and SHAPE, there was no statistically significant correlation ($R^2 = 0.12$, p = 0.65).

Conclusions

These preliminary data indicate that SHAPE, and to a lesser degree SWE, may be an inexpensive, noninvasive, and better tolerated alternative for evaluating CECS patients, which would be a more tolerable option for patients to consider.

Acknowledgements

References

[1] Tucker AK: Chronic exertional compartment syndrome of the leg. *Curr Rev Musculoskelet Med* 2010; 3(1-4):32-37.
[2] Maher JM, Brook EM, Chiodo C, Smith J, Bluman EM, Matzkin EG: Patient-reported outcomes following fasciotomy for chronic exertional compartment syndrome. *Foot Ankle Spec*. 2018; 11(5):471-477.
[3] Canale ST, Beaty JH, Campbell WC: Campbell's operative orthopaedics. 2013.
[4] Large TM, Agel J, Holtzman DJ, Benirschke SK, Krieg JC: Interobserver variability in the measurement of lower leg compartment pressures. *J Orthop Trauma* 2015; 29(7):316-321.
[5] Ringler MD, Litwiller DV, Felmlee JP, Shahid KR, Finnoff JT, Carter RE, Amrami KK: MRI accurately detects chronic exertional compartment syndrome: a validation study. *Skelet Radiol* 2013; 42(3):385-392.
[6] Goldfarb SJ, Kaeding CC. Bilateral acute-on-chronic exertional lateral compartment syndrome of the leg: a case report and review of the literature. *Clin J Sport Med* 1997; 7(1):59-61.
[7] Tamaki N, Kurosaki M, Huang DQ, Loomba R. Noninvasive assessment of liver fibrosis and its clinical significance in nonalcoholic fatty liver disease. *Hepatol Res*. 2022; 52(6):497-507.
[8] DeWall RJ, Slane LC, Lee KS, Thelen DG: Spatial variations in Achilles tendon shear wave speed. *J Biomech* 2014; 47(11):2685-2692.
[9] Ličen U, Kozinc Ž. Using shear-wave elastography to assess exercise-induced muscle damage: A review. *Sensors (Basel)* 2022; 22(19):7574.
[10] Nam K, Eisenbrey JR, Stanczak M, Sridharan A, Berger AC, Avery T, Palazzo JP, Forsberg F: Monitoring neoadjuvant chemotherapy for breast cancer by using three-dimensional subharmonic aided pressure estimation and imaging with US contrast agents: Preliminary Experience. *Radiology* 2017, 285(1):53-62.
[11] Gupta I, Eisenbrey JR, Machado P, Stanczak M, Wessner CE, Shaw CM, Gummadi S, Fenkel JM, Tan A, Miller C, Parent J, Schultz S, Soulen MC, Sehgal CM, Wallace K, Forsberg F. Diagnosing portal hypertension with noninvasive subharmonic pressure estimates from a US contrast agent. *Radiology*. 2021; 298(1):104-111.
[12] Dave JK, Halldorsdottir VG, Eisenbrey JR, Merton DA, Liu JB, Machado P, Zhao H, Park S, Dianis S, Chalek CL, Thomenius KE, Brown DB, Forsberg F. On the implementation of an automated acoustic output optimization algorithm for subharmonic aided pressure estimation. *Ultrasonics*. 2013; 53(4):880-888.

Unraveling Plasma Protein Corona by Ultrasonic Cavitation Augments Active-Transporting of Liposome in Solid Tumor

Guowei Wang,[1, 2] **Yifan Jiang,**[1] **Junjun Xu,**[1] **Jiaxin Shen,**[1] **Tao Lin,**[1] **Jifan Chen,**[1] **Weidong Fei,**[2] **Yating Qin,**[2] **Zhuxian Zhou,**[2] **Youqing Shen,**[2] **and Pintong Huang**[1]

[1] *Department of Ultrasound in Medicine, The Second Affiliated Hospital of Zhejiang University School of Medicine, Zhejiang University, Hangzhou 310009, China.*
[2] *Key Laboratory of Biomass Chemical Engineering of Ministry of Education and Zhejiang Key Laboratory of Smart Biomaterials, College of Chemical and Biological Engineering, Zhejiang University, Hangzhou 310027, China.*
Corresponding author: wangguowei@zju.edu.cn, and huangpintong@zju.edu.cn

Introduction

Ligand/receptor-mediated targeted drug delivery has been widely recognized as a promising strategy for improving nanomedicines' clinical efficacy but was attenuated by the binding of plasma protein on the surface of nanoparticles to form protein corona. Here, we show that ultrasonic cavitation can be used to unravel surface plasma coronas on liposomal nanoparticles through ultrasound (US)-induced liposomal reassembly. To demonstrate the feasibility and effectiveness of the method, we developed transcytosis-targeting peptide decorated reconfigurable liposomes (LPGL) loaded with gemcitabine (GEM) and perfluoropentane (PFP) for cancer-targeted therapy. In the blood circulation, the targeting peptides were deactivated by plasma corona and lost their targeting capability. Once they reached tumor blood vessels, the US irradiation induced transformation of LPGL from nanodrops into microbubble via liquid-gas phase transition and decorticated surface corona by reassembly of the lipid membrane. The activated liposomes regained the capability to recognize the receptors on tumor neovascularization, initiated ligand/receptor-mediated transcytosis, achieved efficient tumor accumulation and penetration, and led to potent antitumor activity in multiple tumor models of patient-derived tumor xenograft. This study presents an effective strategy to tackle the fluid biological barriers of protein corona and develop transcytosis-targeting liposomes for active tumor transport and efficient cancer therapy.

Methods

Here, we first demonstrate the feasibility and effectiveness of the US-induced liposomal reassembly strategy for unveiling the protein corona and apply the method to develop protein corona-free liposomal drug delivery systems for transcytosis-based active tumor delivery. To demonstrate the concepts, we designed a transcytosis-targeting ligand-modified and perfluoropentane-encapsulated gemcitabine 5'-elaidate-integrated liposomal nanodroplet (LPGL) (**Scheme 1**). We selected cRGD peptide (cyclic sequence of Cys-Arg-Gly-Asp-Lys-Gly-Pro-Asp-Cys, binding to integrin $\alpha v\beta 3$ receptor) and NGR peptide (Gly-Gly-Cys-Asn-Gly-Arg-Cys sequence, binding to aminopeptidase-N CD13 receptor) that are overexpressed during tumor neovascularization as the transcytosis-targeting ligand. LPGL was fabricated using the cRGD or NGR peptide-modified 1, 2-distearoyl-sn-glycero-3-phosphoethanolamine-N-[methoxy (polyethylene glycol)-2000] (DSPE-PEG-cRGD (or NGR)), 1, 2-dipalmitoyl-sn-glycero-3-phosphocholine (DPPC), and a lipophilic fatty acid ester derivative of gemcitabine (CP4126), and loaded with perfluoropentane (PFP) (**Scheme 1A**). Once reaching tumor vasculature, LPGL liposomes change from nanodroplets to microbubbles via the liquid-gas phase transition of PFP irritated by the US. Then the microbubbles burst and reassemble into smaller nano-sized liposomes. The protein corona is decorticated during this process, and the targeting ligands are exposed on the surface. The exposed targeting ligands of LPGL can recognize the receptors and initiate an active transporting process - endocytosis, intracellular transport, exocytosis, and intercellular transport, across tumor vascular endothelial cells, thereby augmenting the tumor accumulation and penetrating deep into tumor parenchyma. Meanwhile, LPGL gradually releases the effective metabolite

of gemcitabine triphosphate (dFdCTP) through the cleavage of CP4126 by intracellular esterase to generate potent antitumor activity (**Scheme 1B**).
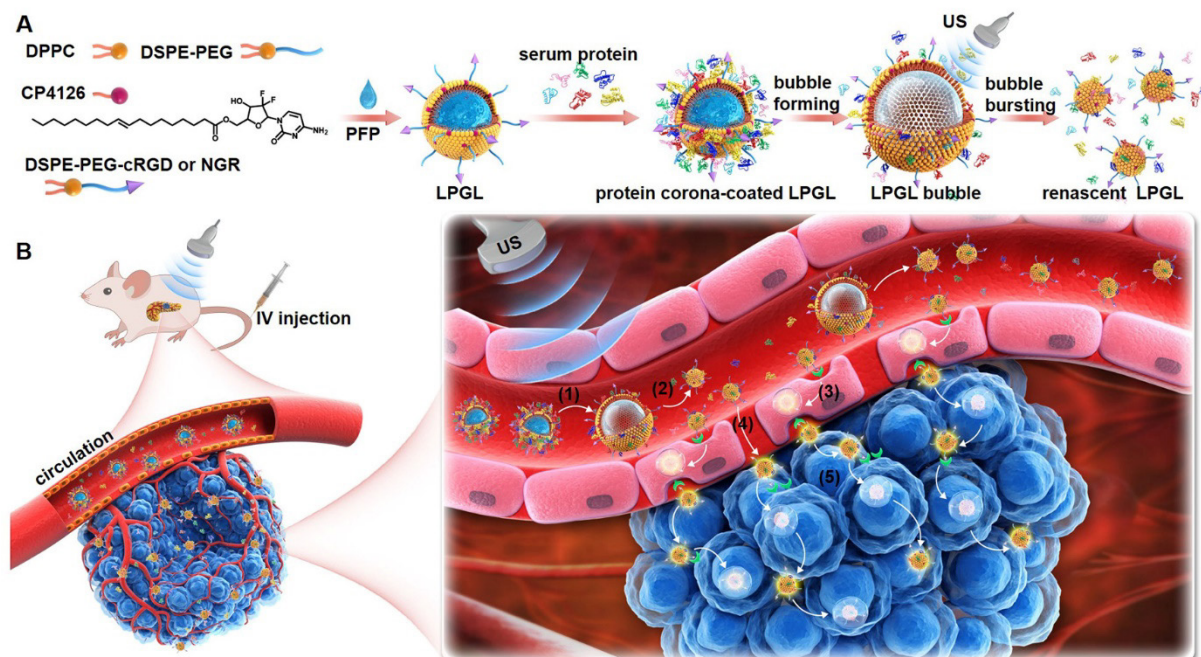
Scheme 1. Schematic representation of LPGL for active tumor targeting via ultrasonic cavitation-assisted protein corona decortication and receptor-mediated transcytosis.

Results

To test this assumption, we prepared a cRGD-peptide targeted reconfigurable liposomal drug delivery system and analyzed the deposition of coronas. LPGL liposomes were prepared by mixing lipids of DSPE-PEG-cRGD, DPPC, DSPE-PEG, and CP4126 at a mass ratio of 1.5 : 1.5 : 1 : 1 and followed by the encapsulation of PFP. Approximately 8.63% of the total lipid molecules in per liposome was the cRGD ligand modified-lipid molecules. CP4126 is a potent anticancer prodrug, a lipophilic fatty acid ester derivative of gemcitabine (GEM) in clinical trials, and can be fully integrated into the liposomes as the component of phospholipid membrane during the size transformation and membrane crack. The encapsulation efficiency of CP4126 in liposomes was nearly 100%, and the GEM content was 10%. The prepared LPGL was in a form of milky emulsion with a particle size of 188.4 ± 14.5 nm (PDI: 0.21) and a zeta potential of -9.1 ± 2.7 mV as measured by dynamic light scattering (DLS). The cryo-transmission electron microscope (cryo-TEM) image showed that LPGL had a uniform unilamellar lipid membrane with a distinct ice-cloud shadow of PFP in the center. The loading content of PFP was about 0.16 ± 0.07 vol.% as measured using the automatic headspace gas chromatographic-mass spectrometric technique. We also prepared three kinds of liposomes as control groups, including the non-targeting and non-size-conversional nanodroplets (GL), the targeting only nanodroplets (LGL), and the PFP-loaded size-conversion only nanodroplets (PGL). The particles sizes of GL, LGL and PGL were 149.4 ± 11.7 nm (PDI: 0.16), 154.1 ± 12.5 nm (PDI: 0.18), 185.7 ± 13.3 nm (PDI: 0.23) respectively, as determined by DLS. The cryo-TEM images showed that GL and LGL were empty capsules, and PGL were capsules with ice-cloud shadows similar to LPGL.

Once incubating with plasma for more than 15 min, all the liposomes would absorb abundant types of proteins (molecular weight from 25 kDa to 180 kDa) with an average total protein content of about 24 µg/mg lipids. After US irritation for 5 min, the total protein content in LPGL and PGL was reduced to less than 20%, while those GL and LGL showed no significant changes. Additionally, the decortication of protein

corona by ultrasonic cavitation could be enhanced with the increase of US intensity as well as a high frequency of 3 MHz , and the protein contents on LPGL and PGL varied with ultrasonic duration.

We evaluated the antitumor activity of the liposomes in BALB/c nude mice bearing patient-derived tumor xenograft of PDA that could reproduce the clinical tumor state and simulate the PDA microenvironment. The mice were intravenously administered with GEM, GL, LGL, PGL, and LPGL (GEM-equivalent dose 10 mg/kg) or blank control of LPL and PBS four times every two days when the tumors reached a size of about 150 mm^3. Mice treated with LPL or PBS showed continuous tumor growth during the treatment, and no significant difference was observed between the two groups. The tumor growth of the GEM, GL, LGL, and PGL group was delayed during the treatment but recovered to grow after the treatment. In contrast, the tumor growth of the LPGL group was substantially inhibited and continued to regress after the treatment. Half of the LPGL-treated mice were tumor-free at the end of the experiment. On day 36, all the mice were sacrificed, and tumors were collected, photographed, and weighted. The tumor inhibition rate of LPGL was 98.3%, which was much higher than those of GEM (34.1%), GL (56.3%), LGL (76.6%), and PGL (75.8%). All the mice treated with the liposomes showed no noticeable side effects in terms of body weight change and white blood cell and blood platelet levels, whereas the mice treated with GEM showed distinct body weight loss and hematological damage as indicated by the sharp decrease of white blood cell and blood platelet.

Conclusions

In summary, we developed an ultrasonic cavitation-based strategy to remove protein corona on targeted drug delivery systems. We demonstrated the feasibility and effectiveness of the strategy for developing transcytosis-based tumor active transporting liposomes for solid tumor treatment. The strategy utilized the ultrasonic cavitation-triggered reassembly of liposomes to decorticate protein corona and reinitiate active ligand/receptor-mediated transcytosis for enhancing the nanomedicine's transendothelial cellular transport and tumor intercellular transport. The designated active transcytosis LPGL liposomes achieved superior tumor accumulation and deep penetration and generated effective antitumor activity in multiple tumor models of patient-derived tumor xenograft of PDA and HCC. The ultrasonic cavitation-based reconfigurable liposomes are practical and efficient carriers for active tumor targeting drug delivery.

References

[1]. Guowei Wang, Yifan Jiang, Junjun Xu, Jiaxin Shen, Tao Lin, Jifan Chen, Weidong Fei, Yating Qin, Zhuxian Zhou, Youqing Shen, and Pintong Huang[*]. Unraveling Plasma Protein Corona by Ultrasonic Cavitation Augments Active-Transporting of Liposome in Solid Tumor. *Advanced Materials*, 2023.

The effect of consecutive pulses on cell sonoporation in vitro

M. Amate[1], T. Gervais[2], F. Yu[1]

[1]_Département de Radiologie, Université de Montréal, Montréal, Québec, Canada_
[2]_Département de Génie Biomédical, École Polytechnique Montréal, Montréal, Québec, Canada_
Corresponding author: marie.amate@montreal.ca

Introduction

Ultrasound (US) induced microbubble (MB) cavitation causes a provascular response that can improve cancer radiotherapy [1]. ATP and eNOS-mediated vasodilation have been shown to be implicated in the signaling pathways leading to the vasodilation response [2][3]. We are interested in deciphering if sonoporation (formation of temporary pores on the cell membrane) or cell death (formation of permanent pores) may induce the activation of vasodilation pathways [3], that can provide a better radiosensibilisation of hypoxic solid tumor [4]. In this study, we propose a microfluidic model to characterize sonoporation under flowing conditions following US+MB treatment.

Methods

HUVEC cells were grown on the ceiling of PDMS microfluidic chips (figure 1A). Cells were seeded (500 cells/mm^2) in chips previously coated with fibronectin (100ug/ml, 1h; room temperature). The chips were flipped upside down and incubated for 28h (37°C; 5% CO2) to allow cell sedimentation and attachment on their ceiling. The US probe (A303S-SU, 1MHz, 0.5 Inch) was positioned 2,7 cm far from the channels with an angle of 60° with the chip (figure 1B). The microscope and the US beam were co-aligned at the same focal spot, taking into account the US refraction angle, using an in-house-designed 3D printed device. Then, MB (10^7 MB/ml) and Propidium Iodide (PI 25 ug/ml – sonoporation and cell death marker) were continuously infused in the chip (100 ul/min). Meanwhile, the chip was exposed to US to observe PI uptake in real-time. Each experiment consisted of a serie of 7 identical US pulses varying pressure (200, 300, 400, 500, 600 kPa) and the number of cycles (10, 100 cycles), applied with a 2 min interval to allow temporary sonopores to heal and MB replenishment between pulses. PI images were taken right before every pulse. After the treatment, calcein-AM (12 ug/ml – viability tracer) was incubated with the cells for 30min (37°C; 5% CO2) and chips were imaged.
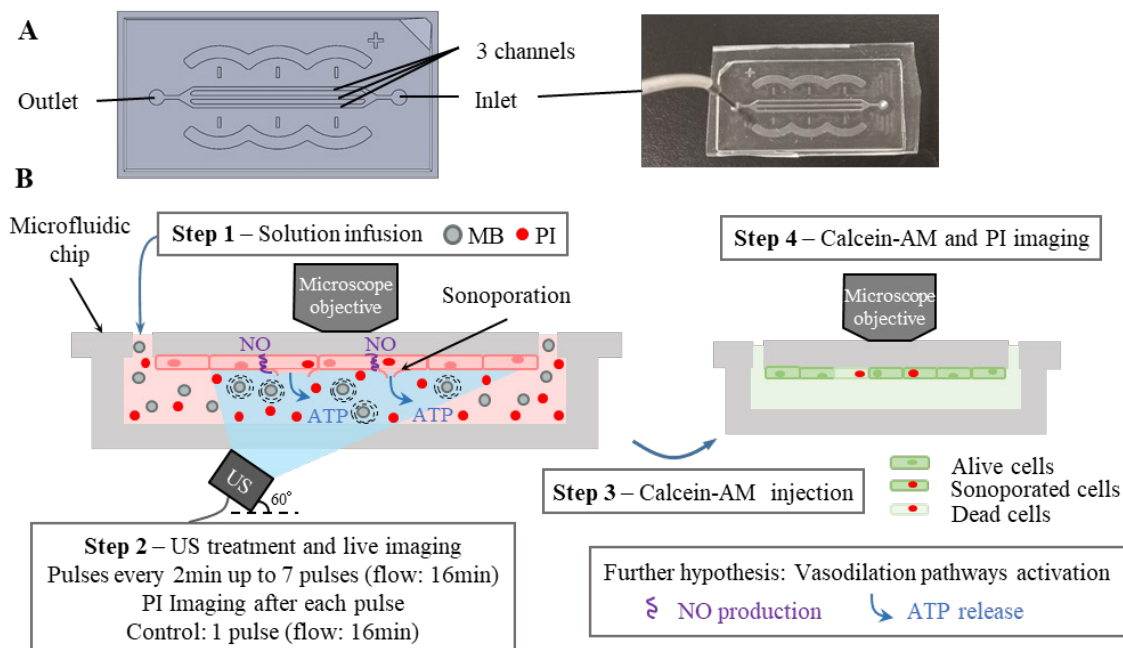
Figure 1. (A) The PDMS microfluidic chip. (B) Experimental design and hypothesis.

PI cineloop and Calcein-AM images were processed with an in-house Matlab program: Each cell was labeled and then classified into "sonoporated cell" vs "dead cell" category based on calcein-AM/PI colocalization and PI intensity (figure 2A).

Data were analyzed with a two-way ANOVA, with Tukey multiple comparison test (Prism 8, GraphPad). $p < 0.05$ was considered significant.

Results

To confirm that time and flow did not impact the sonoporation in our model, the effect of a single pulse ({300kPa ; 100#cyc}, {400kPa ; 100#cyc} or {500kPa ; 100#cyc}) after 2min and 16min exposition to flow were compared (figure 2B). The dead and sonoporated cells proportions after a single pulse were not significantly different after 2min exposition compared to 16min exposition. This support that the flow exposition during and after the US treatment does not have an impact on the sonoporation rate, at least until 16min of flow.

With all pulses, the proportion of dead cells is higher than the proportion of sonoporated at each pulse. The dead cell proportions were significantly higher than the sonoporated cell proportions for some US parameter (figure 2C, purple stars *: $p<0.05$ sonoporated cells vs dead cells for one pulse).

The total PI-positive cell proportions increased with the pressure for the two different pulse lengths tested, as expected (figure 2C). In contrary with what was expected, increasing the pulse length also increased the sonoporation proportion at a pressure of 500kPa after the 6th pulse (sonoporated cell proportion at pulse 6 {500kPa ; 10#cyc} vs. {500kPa ; 100#cyc} p=0,025 and pulse 7 {500kPa ; 10#cyc} vs. {500kPa ; 100#cyc} p=0,0041). Moreover, the proportion of dead cells were higher with short pulses. The increase in the radiation force for longer pulses may explain why longer pulses interestingly induce more sonoporation.

The increase in sonoporated cell proportion is linearly correlated with the number of consecutive pulses for {300kPa; 100#cyc}, {400kPa; 100#cyc} and {500kPa; 100#cyc} (figure 2C, R1, R2, R3). This suggests that these successive pulses cause an equal amount of sonoporation at least until 7 pulses. Moreover, for all of these pulses, the sonoporated proportion is archieving nearly the same rate (around 8%) after 7 pulses for every pressure. Interestingly, the proportion of dead cells proportion is increasing with the pressure. Data with 100#cyc suggest that the pulse {300kPa ; 100#cyc} is the best compromise between sonoporated and dead cells proportion.
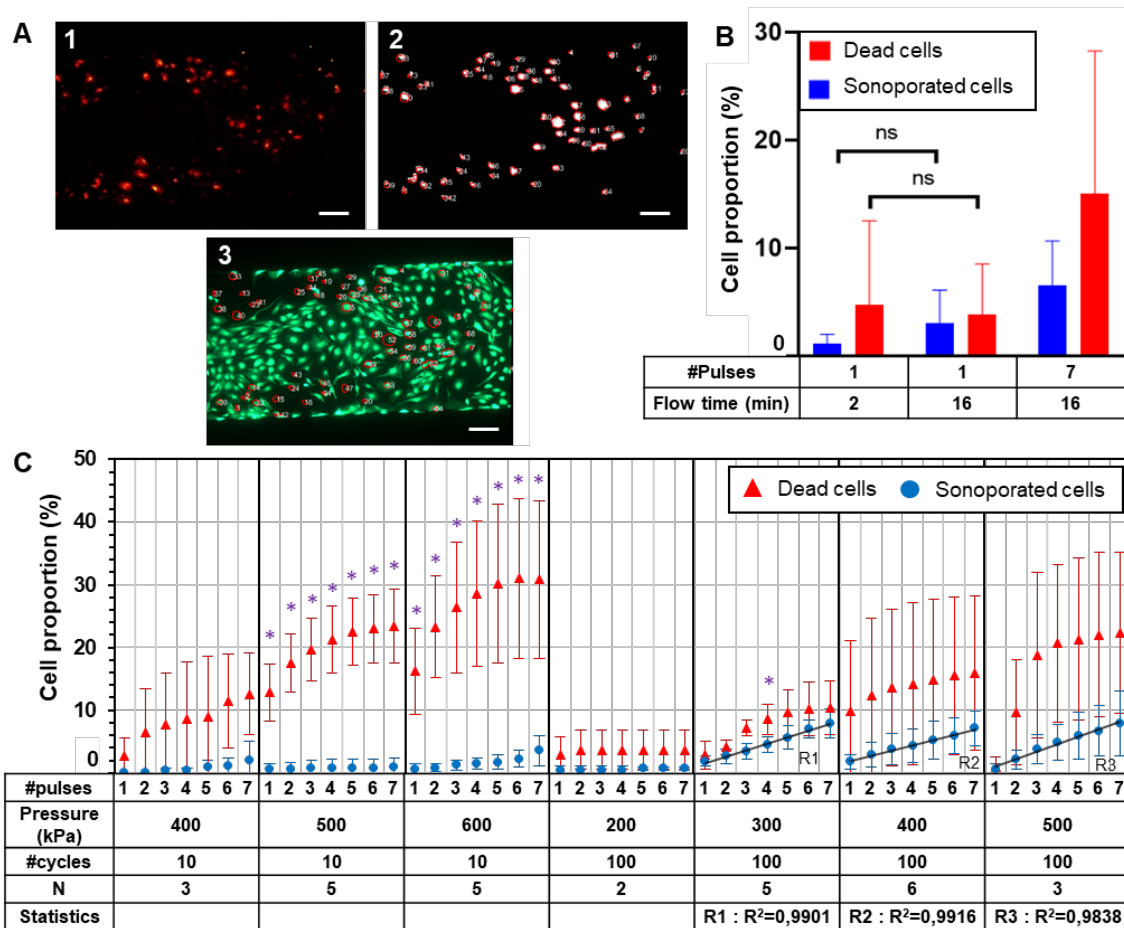
Figure 2. (A1) PI channel image (7 pulses pressure : 400kPa ; 100#cycles, 20x). (A2) Image A1 with the cells segmented and labeled. (A3) Image A2 merged with the calcein-AM image corresponding. Scale bars represent 100um. (B) Impact of flow on treated cells. (C) Proportion of sonoporated and dead cells after each pulse among the total number of cells in the image.

Conclusions

We developed an approach that allowed us to quantify the effect of successive pulses of US on endothelial cell sonoporation based on calcein-AM/PI colocalization and PI intensity. Overall, longer pulses tend to be more efficient and the pulse {300kPa ; 100#cyc} has shown the best efficiency in sonoporation.

We identified US conditions that will allow us to study ATP and nitric oxide release with the objective of finding a compromise between the efficiency and the toxicity of the treatment. We expect this work to provide a greater understanding of sonoporation mechanisms to optimize the treatment *in vivo* and improve the outcome of anti-cancer radiotherapy.

References

[1]. Michon, S., Rodier, F., & Yu, F. T. (2022). Targeted Anti-Cancer Provascular Therapy Using Ultrasound, Microbubbles, and Nitrite to Increase Radiotherapy Efficacy. *Bioconjugate Chemistry*.

[2]. Francois, T. H., Chen, X., Straub, A. C., & Pacella, J. J. (2017). The role of nitric oxide during sonoreperfusion of microvascular obstruction. Theranostics, 7(14), 3527.

[3]. Belcik, J. T., Davidson, B. P., Xie, A., Wu, M. D., Yadava, M., Qi, Y., ... & Lindner, J. R. (2017). Augmentation of muscle blood flow by ultrasound cavitation is mediated by ATP and purinergic signaling. *Circulation*, 135(13), 1240-1252.

[4]. Jordan, B. F., & Sonveaux, P. (2012). Targeting tumor perfusion and oxygenation to improve the outcome of anticancer therapy. *Frontiers in pharmacology*, 3, 94.

Effect of tumor radiosensitization following administration of ultrasound sensitive lonidamine-loaded oxygen microbubbles

Quezia Lacerda MS[1,2], Hebah Falatah MS[1,2,4], Ji-Bin Liu MD[1], Corinne E. Wessner MBA[1,2], Brian Oeffinger MS[2], Dennis B. Leeper PhD[3], Flemming Forsberg PhD[1], Patrick O'Kane MD[1], Margaret A. Wheatley PhD[2], John R. Eisenbrey PhD[1]

[1]*Department of Radiology, Thomas Jefferson University, Philadelphia, PA, 19107, USA*
[2]*School of Biomedical Engineering and Heath Sciences, Drexel University, Philadelphia, PA, 19104, USA*
[3]*Department of Radiation Oncology, Thomas Jefferson University, Philadelphia, PA, 19107, US*
[4]*College of Applied Medical Sciences King Saud Bin Abdulaziz University for Health Sciences, Jeddah, 22384, Saudi Arabia*
[5]*King Abdullah International Medical Research Center, Jeddah, 22384, Saudi Arabia*

Introduction

Several studies have shown that tumor hypoxia is directly associated with a poor prognosis in patients with advanced head and neck squamous cell carcinoma HNSCC [1-3]. Hypoxic and/or anoxic areas have an oxygen partial pressure (pO_2) ranging from 0 to 10 mmHg. A pO_2 <10 mmHg in HNSCC patients is directly linked to poor local tumor control, disease-free and overall survival, irrespective of treatment whether by radiation alone or combined with surgery or systemic chemotherapy [4-6]. Increasing the oxygen tension of HNSCC would significantly improve its sensitivity to radiation, especially as nearly 75% of all HNSCC patients receive radiation therapy [7, 8]. As a means to mitigate tumor hypoxia before radiation, several treatment modifications have been investigated including ultrasound-sensitive microbubbles (MBs) containing oxygen [7, 9-10].

Our group has developed an O_2 MB stabilized by sorbitan monostearate and water-soluble vitamin E (TPGS) (termed SE61O_2) that provides enhancement under ultrasound interrogation *in vitro* for over 10 mins [11-13]. These bubbles are easily imaged within hypoxic tumors and can be noninvasively destroyed within the tumor vasculature. Prior work demonstrated the feasibility of disrupting oxygen bubbles within a murine breast tumor model and a model of metastatic breast cancer in the brain where in both cases oxygenation significantly improved both tumor control and animal survival [14-15]. However, the duration of oxygenation using this platform was limited, lasting only 2-3 minutes *in vivo*. More recently, our group published modifications to the current O_2 MB platform by combining the localized delivery of O_2 with a pharmacological inhibitor of tumor mitochondrial respiration (lonidamine (LND)), which resulted in ultrasound-sensitive MB loaded with O_2 and LND. Animals that had O_2 and LND co-administered via ultrasound-sensitive MBs (SE61O_2/LND) had an intratumoral peak increase of 29.05 ± 8.3 mmHg, and prolonged oxygenation relative to oxygenated MBs alone, with levels remaining elevated for up to 5 min [16]. The objective of the current study was to assess the effect of MBs loaded with O_2 and mitochondrial respiration inhibitors on an *in vivo* HNSCC model treated with different radiation dose rates.

Materials and Methods

Surfactant-shelled oxygen-MBs (SE61O_2) composed of a sonicated solution of water-soluble vitamin E (TPGS) and sorbitan monostearate were fabricated. In the microbubbles loaded with LND, the drug was loaded into the shell by pre-incubation with the TPGS (for 48 hrs.) to form drug-loaded micelles, which were then added to the sorbitan monostearate solution. Oxygen was added after freeze-drying the SE61.

Acoustic enhancement and stability were quantified *in vitro* in a closed-loop flow phantom setup (ATS Laboratories, CIRS, Norfolk, VA, USA). MBs were injected and insonated using a 10L4 transducer and an Acuson Sequoia scanner (Siemens Healthineers, Issaquah, WA, USA). Imaging of the MBs flowing through

153

the embedded vessel was performed in cadence pulse sequencing mode every 30 seconds for 10 minutes (Fig.1.A).

For the *in vivo* experiments, HNSCC tumors were generated in athymic nude mice by injecting 5×10^5 CAL27 cells (ATCC, Manassas, VA, USA) mixed with 100 μL matrigel subcutaneously on the right flank. Additionally, cohorts of animals were placed in a pre-treatment group receiving oral metformin (OM), a drug that displays a 50-60% absolute oral bioavailability, while also inhibiting mitochondrial respiration in tumors. Animals received 0.1 mL injections of $SE61O_2$ with or without LND, and with, or without ultrasound, using a 10L4 transducer and an Acuson Sequoia scanner. Animals receiving ultrasound triggering (mechanical index = 1.4) underwent 75 seconds of flash-destruction replenishment sequences (Fig.1.B). Animals receiving radiation therapy were placed 40 cm from the radiation source and covered with 4 mm lead shielding exposing the right flank and tail. Immediately following ultrasound triggering, animals received 5 Gy using an X-RAD 320 biological irradiator (Precision X-Ray, CT,USA) at 320 kV with two different added filtrations (2 mm aluminum designated as Filter 1 (F1), or 1.5 mm aluminum, 0.25 mm copper and 0.75 mm tin designated as Filter 2 (F2)). These filters corresponded to radiation dose rates of 3.59 and 1.36 Gy/min, respectively. Tumor-bearing animals were assigned to the treatment groups listed in Table 1.

Table 1. Treatment groups

Group	Treatment	Ultrasound	5 Gy	OM
1	none	no	no	no
2	none	yes	yes	no
3	$SE61O_2$	yes	no	no
4	IP Lonidamine	yes	yes	no
5	Oral Metformin	yes	yes	yes
6	$SE61O_2$	yes	yes	no
7	$SE61O_2$ + IP LND	yes	yes	no
8	$SE61O_2$	yes	yes	yes
9	$SE61O_2$/LND	no	yes	yes
10	$SE61O_2$/LND	yes	yes	no
11	$SE61O_2$/LND	yes	yes	yes
12	$SE61N_2$/LND	yes	yes	yes

Results

In the pulsatile flow phantom insonated in a single plane, a strong signal from $SE61O_2$ with or without LND was observed within the lumen remaining stable for over 10 minutes. The ability to noninvasively destroy these MBs with higher intensity ultrasound pulses was confirmed in this setup (Fig.1.A).
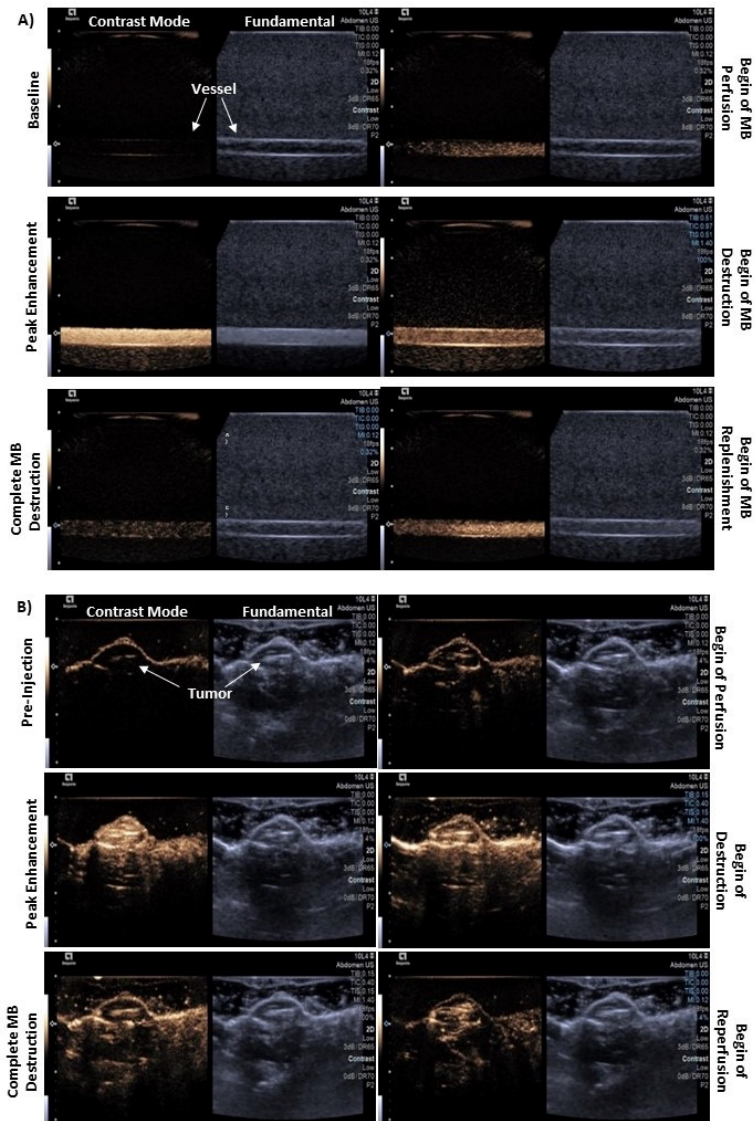
Figure 1. Example of ultrasound images A) of flow phantom showing contrast mode (left) and fundamental (B-mode) (right) of SE61O$_2$/LND and B) in athymic nude mice also in dual B-mode/cadence pulse sequencing mode, imaging subcutaneous CAL27 human squamous cell carcinoma.

For the therapy experiments, the experimental group (Group 11) that received SE61O$_2$/LND triggered with ultrasound followed by 5 Gy with F1 and OM pretreatment showed a median animal survival of 63 days. This was a statistically significant improvement compared to animals that received SE61O$_2$ triggered with ultrasound and 5 Gy (44 days), OM pretreatment with ultrasound and 5 Gy, and group that had ultrasound and 5 Gy administered (42 days) ($p < 0.0001$). Additionally, animals that had SE61O$_2$/LND triggered with ultrasound followed by 5 Gy with F1 showed an improved tumoral growth control and survival, with a median survival of 52 days when compared to animals that received the same treatment with 5 Gy with F2 (21 days; p= 0.0004). However, there was no significant difference in median animal survival for groups treated with SE61O$_2$/LND or SE61O$_2$ triggered with ultrasound followed by 5 Gy with F1 (p= 0.29). This demonstrates that while the platform provides significant improvement in tumor control, a relatively high radiation dose rate is still required given the limited duration of oxygenation.

Conclusions

The co-delivery of O$_2$ and LND via ultrasound-sensitive microbubbles and OM improved radiosensitivity and survival in a HNSCC model. Additionally, this work highlights the importance of dose rate given the currently limited duration of oxygenation currently available with this microbubble platform.

References

[1]. Nordsmark M, Bentzen SM, Rudat V, et al. Prognostic value of tumor oxygenation in 397 head and neck tumors after primary radiation therapy. An international multi-center study. Radiother Oncol. 2005;77(1):18-24. doi:10.1016/j.radonc.2005.06.038

[2]. Rudat V, Stadler P, Becker A, et al. Predictive value of the tumor oxygenation by means of pO2 histography in patients with advanced head and neck cancer. Strahlenther Onkol Organ Dtsch Rontgengesellschaft Al. 2001;177(9):462-468. doi:10.1007/pl00002427

[3]. Brizel DM, Dodge RK, Clough RW, Dewhirst MW. Oxygenation of head and neck cancer: changes during radiotherapy and impact on treatment outcome. Radiother Oncol J Eur Soc Ther Radiol Oncol. 1999;53(2):113-117. doi:10.1016/s0167-8140(99)00102-4

[4]. Bredell MG, Ernst J, El-Kochairi I, Dahlem Y, Ikenberg K, Schumann DM. Current relevance of hypoxia in head and neck cancer. Oncotarget. 2016;7(31):50781-50804. doi:10.18632/oncotarget.9549

[5]. Janssen HL, Haustermans KM, Balm AJ, Begg AC. Hypoxia in head and neck cancer: How much, how important? Head Neck. 2005;27(7):622-638. doi:10.1002/hed.20223

[6]. Marur S, Forastiere AA. Head and Neck Squamous Cell Carcinoma: Update on Epidemiology, Diagnosis, and Treatment. Mayo Clin Proc. 2016;91(3):386-396. doi:10.1016/j.mayocp.2015.12.017

[7]. Rockwell S, Dobrucki IT, Kim EY, Marrison ST, Vu VT. Hypoxia and radiation therapy: past history, ongoing research, and future promise. Curr Mol Med. 2009;9(4):442-458. doi:10.2174/156652409788167087

[8]. Alfouzan AF. Radiation therapy in head and neck cancer. Saudi Med J. 2021;42(3):247-254. doi:10.15537/smj.2021.42.3.20210660

[9]. Hoskin PJ, Rojas AM, Phillips H, Saunders MI. Acute and late morbidity in the treatment of advanced bladder carcinoma with accelerated radiotherapy, carbogen, and nicotinamide. Cancer. 2005;103(11):2287-2297. doi:10.1002/cncr.21048

[10]. Janssens GO, Rademakers SE, Terhaard CH, et al. Accelerated radiotherapy with carbogen and nicotinamide for laryngeal cancer: results of a phase III randomized trial. J Clin Oncol Off J Am Soc Clin Oncol. 2012;30(15):1777-1783. doi:10.1200/JCO.2011.35.9315

[11]. Eisenbrey JR, Albala L, Kramer MR, et al. Development of an ultrasound sensitive oxygen carrier for oxygen delivery to hypoxic tissue. Int J Pharm. 2015;478(1):361-367. doi:10.1016/j.ijpharm.2014.11.023

[12]. Vaidya PB, Oeffinger BE, Patel R, et al. Shaping the synthesis of surfactant-stabilized oxygen microbubbles to accommodate encapsulated drug. Colloids Surf B Biointerfaces. 2021;208:112049. doi:10.1016/j.colsurfb.2021.112049

[13]. Oeffinger BE, Vaidya P, Ayaz I, Shraim R, Eisenbrey JR, Wheatley MA. Preserving the Integrity of Surfactant-Stabilized Microbubble Membranes for Localized Oxygen Delivery. Langmuir ACS J Surf Colloids. 2019;35(31):10068-10078. doi:10.1021/acs.langmuir.8b03725

[14]. Eisenbrey JR, Shraim R, Liu JB, et al. Sensitization of Hypoxic Tumors to Radiation Therapy Using Ultrasound-Sensitive Oxygen Microbubbles. Int J Radiat Oncol Biol Phys. 2018;101(1):88-96. doi:10.1016/j.ijrobp.2018.01.042

[15]. Delaney LJ, Ciraku L, Oeffinger BE, et al. Breast Cancer Brain Metastasis Response to Radiation After Microbubble Oxygen Delivery in a Murine Model. J Ultrasound Med Off J Am Inst Ultrasound Med. 2019;38(12):3221-3228. doi:10.1002/jum.15031

[16]. Lacerda Q, Rochani A, Oeffinger B, et al. Tumoral oxygenation and biodistribution of Lonidamine oxygen microbubbles following localized ultrasound-triggered delivery. Int J Pharm. 2022;625:122072. doi:10.1016/j.ijpharm.2022.122072

Acoustically mediated drug delivery in 3D spheroid model

<u>Marie Roy</u>[1], Corentin Alix[1], Ayache Bouakaz[1], Sophie Serrière[1,2], Jean-Michel Escoffre[1]

[1]UMR 1253, iBrain, Université de Tours, Inserm, Tours, France
[2]Département d'Imagerie Préclinique, Plateforme Scientifique et Technique Analyse des Systèmes Biologiques, Université de Tours, Tours, France
Corresponding author: marie.roy@univ-tours.fr

Introduction

Microbubble-assisted ultrasound (MB-assisted US) is a non-invasive and targeted drug delivery method that enhances the therapeutic efficacy of anti-cancer drugs by increasing their intratumoral biodistribution and reducing their off-target effects [1]. MB-assisted US generates a number of local acoustic events (*e.g*., pulling/pushing process, microstreaming, shock waves, microjet) near the plasma membrane of cells. These events promote a reversible membrane permeabilization allowing their intracellular uptake through the formation of membrane pores and/or the stimulation of endocytotic pathways [2]. Several parameters influence the efficacy of this drug delivery method (*i.e* pharmacological properties of anti-cancer drugs and MBs, the physiology of tumor tissue, US devices and parameters, and treatment schemes). The tumor spheroids are promising 3D *in-vitro* tumor models in order to investigate these processes and to define the optimal acoustic parameters for drug delivery. Indeed, their architectures reflect the 3D organization of tumor, tumoral heterogeneity and microenvironment, resulting in a greater resistance to drugs than that observed in 2D *in-vitro* models [3,4]. In this context, this study aims at investigating the influence of acoustic pressure (peak negative pressure, PNP) on the permeabilization, the growth and the viability of colorectal cancer (CRC) spheroids. Secondly, these spheroids were exploited to study the therapeutic efficacy of acoustically mediated bleomycin delivery.

Methods

PNP influence on the spheroid permeabilization, growth and viability: The CRC spheroids (5 spheroids in 1.5 mL medium) were placed in the plastic cuvette. Then, a fluorescent dye, the propidium iodide (PI; 100 μM), used as a drug model, and Vevo MicroMarker MBs (30 μL; 2.10^9 MB/mL) were added in the cuvette. The center of the cuvette was positionned at the focal distance of the transducer in a deionized water tank at 37°C. The mixture was kept uniform using gentle magnetic stirring during the ultrasound application. Subsequently, the spheroids were exposed to 1 MHz sinusoid ultrasound waves for 30 s with a pulse repetition period of 100 μs, 40 cycles per pulse. The acoustic pressures range from 100 kPa to 400 kPa PNP. Few minutes later, the penetration and the intracellular accumulation of PI into tumor cells were assessed using fluorescence microscopy. The influence of the acoustic pressure on spheroid growth and viability were determined by measuring the spheroid growth for 10 days under optical microscope and by using a trypan blue assay at 13th day, respectively.

Acoustically mediated bleomycin delivery: The spheroids were treated with 0.1 μM or 1 μM of bleomycin on its own or delivered using MB-assisted US as previously described. Ten minutes later, spheroids were transferred into ULA 96-well microplate for their culture. Spheroid growth and viability was evaluated as described above.

Results

Influence of PNP on the permeabilization, the growth and the viability of spheroids: The exposure of spheroids to an acoustic pressure of 100 kPa in presence of MBs significantly induced an increase of the fluorescence intensity into the spheroids compared to PI treatment alone ($p < 0.05$), demonstrating a significant enhancement of the penetration and the accumulation of PI into the spheroids (Figures 1A & 1B). The increase of the acoustic pressure from 200 kPa to 300 kPa resulted in an additional increase of the fluorescence intensity compared with 100 kPa condition ($p < 0.05$). At both 300 and 400 kPa, a similar

fluorescence intensity was detected into spheroids ($p > 0.05$). As displayed in Figure 1B, the increase of the acoustic pressure from 100 to 300 kPa induced a linear increase of the fluorescence intensity before to reach a plateau. Finally, the increase of the acoustic pressure from 100 to 400 kPa did not affect the spheroid growth and viability (Figures 1C & 1D, respectively).
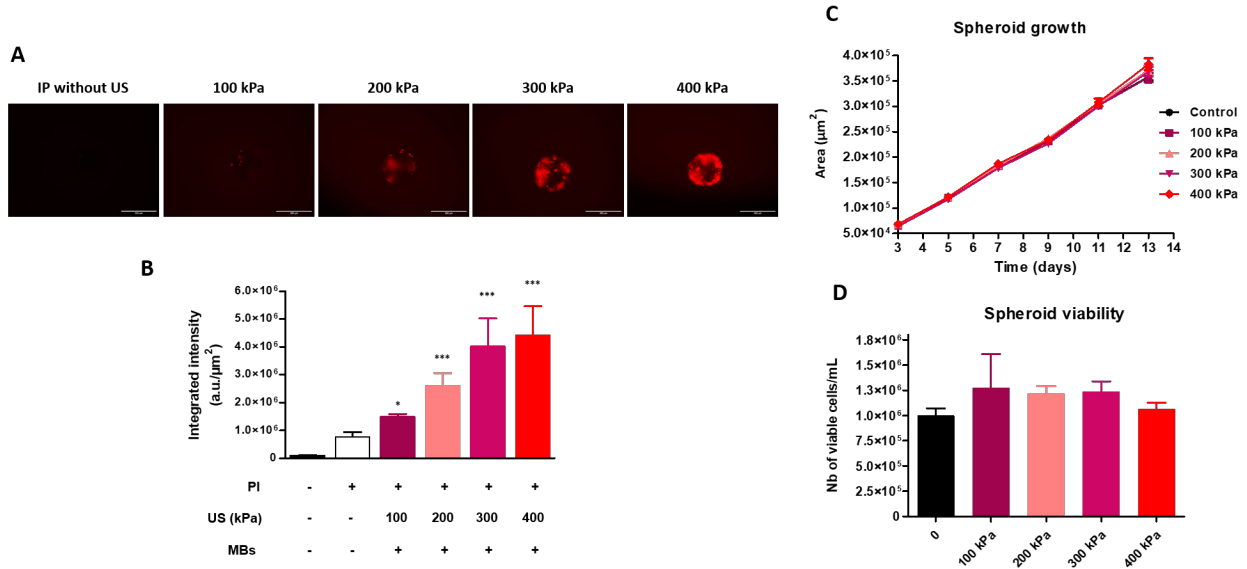
Figure 1. Effect of acoustic pressure on the permeabilization, the growth and the viability of CRC spheroids. (A) Microscopic observations of the acoutically-mediated permeabilization of spheroids to a fluorescent dye, the propidium iodide (PI). (B) Quantitative analysis of spheroid permeabilization. (C) Spheroid growth. (D) Spheroid viability at the 13th day. The Mann Whitney, nonparametric test was used for statistical analysis (*p < 0.05 and *** p < 0.005). Each bar represents the mean ± standard error of the mean (SEM).

Cytotoxic effects of bleomycin delivered by MB-assisted US on CRC spheroid: The treatment with bleomycin alone (0.1 or 1 µM) induced a significant decrease in spheroid growth compared to the control condition (no treatment). This cytotoxic effect on spheroid growth was potentiated when the bleomycin was delivered using MB-assisted US. Indeed, the acoustically mediated delivery of bleomycin at 0.1 µM resulted in a significant reduction of spheroid growth, same as spheroids treated only with a 10-fold higher concentration of bleomycin. In addition, the acoustically mediated delivery of bleomycin at 1 µM completely inhibited spheroid growth from the first post-treatment days (Figure 2). Trypan blue assay confirmed these results at the 13th day. Indeed, the delivery of 0.1 µM bleomycin using MB-assisted US induced 2-fold decrease in the spheroid viability compared to the bleomycin treatment alone. This reduction of spheroid viability was similar to the effect of spheroid treatment with 1 µM bleomycin only. As expected, the acoustically mediated delivery of 1 µM bleomycin significantly decreased the spheroid viability compared to the control condition and the bleomycin treatment alone.
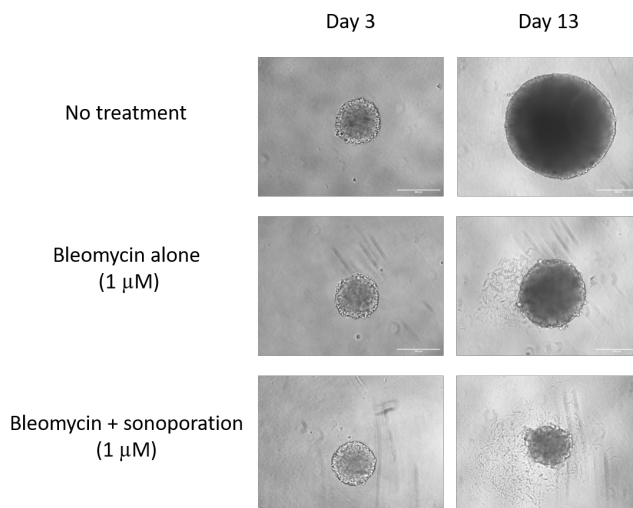
Figure 2. Acoustically mediated bleomycin delivery in CRC spheroids.

Conclusions

In conclusion, MB-assisted US induced an efficient and reversible permeabilization of CRC spheroids to small molecules (< 4 kDa). The increase of the acoustic pressure induced a significant and gradual permeabilization of CRC spheroids without affecting their viability and their growth. The bleomycin delivery using MB-assisted US significantly improved the cytotoxic effect of bleomycin, thus resulting in an inhibition of spheroid growth.

References

[1]. Lammertink, B. H. A. et al. Sonochemotherapy: from bench to bedside. Frontiers in Pharmacology 6, (2015).

[2]. Escoffre, J.-M. & Bouakaz, A. Minireview: Biophysical Mechanisms of Cell Membrane Sonopermeabilization. Knowns and Unknowns. Langmuir 35, 10151–10165 (2019).

[3]. Torisawa, Y.-S., Takagi, A., Shiku, H., Yasukawa, T. & Matsue, T. A multicellular spheroid-based drug sensitivity test by scanning electrochemical microscopy. Oncol Rep 13, 1107–1112 (2005).

[4]. Ward, J. P. & King, J. R. Mathematical modelling of drug transport in tumour multicell spheroids and monolayer cultures. Mathematical Biosciences 181, 177–207 (2003)

Contrast-enhanced ultrasound imaging of displaced humeral fractures: Early results of a pragmatic single-centre study.

D. Cadoux-Hudson[1], M.Thomas[1,] J.Hurst[1], R.Schranz[1], A.Gerrish[1], K.Wallace[3], D.Warwick[1], D.Carugo[4], Stride E[5], S.Tilley[1], N.D.Evans[2]

[1]University Hospitals Southampton, UK; [2]University of Southampton,UK; [3]GE Medical Imaging; [4]University College London, UK; [5]University of Oxford, UK.

Corresponding Authors: D.Cadoux-Hudson@soton.ac.uk; n.d.evans@soton.ac.uk

Introduction

Microbubbles have been commercially available in ultrasonography for the purposes of contrast enhanced imaging for several decades. As the understanding of the properties of microbubbles has improved, so has the scope for their use in a therapeutic setting. Microbubbles have been described in an orthopaedic setting as a method for determining the likely cause of an established non-union in the clinical setting(1). There is, however, little literature describing the behaviour of microbubbles in acute bone fractures, or therefore their potential for therapeutic and diagnostic use in this application. The aim of this study is to determine the ability of microbubbles to perfuse acute fractures in the clinical setting.

Methods

Patients who had sustained a humeral shaft fracture were recruited to undergo ultrasound enhanced contrast imaging of the fracture site within 28 days of injury. They underwent ultrasound imaging and peripheral injection of commercially available SonoVue (Bracco, Italy) microbubbles. B-mode images were captured together with time-intensity curves to assess presence of microbubbles at the fracture site.

Results

Four patients underwent ultrasound enhanced contrast imaging of acute humeral fractures with a mean time to scan of 16 days. The average Peak Intensity (PI) was 1.16×10-6 acoustic units (AU) with an average Area Under the Curve (AuC) of 3.23×10-6 and average Time to Peak (TtP) of 19.8 seconds. There was a noticeable drop in these metrics with increased time from injury, (5 versus 28 days; PI, 42.6%, AuC 55.5% and TtP 25.5%). There was a significant flow of microbubbles confined to within the fracture site and within the callus itself, as shown in Figure 1, which demonstrates microbubble contrast within the fracture site outlined.
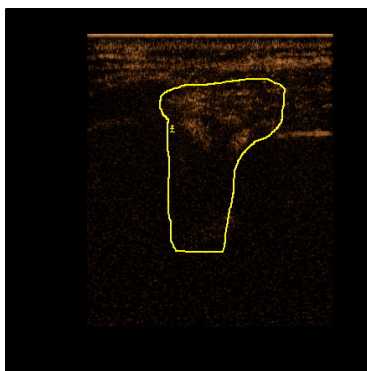
Figure 1: Microbubble contrast in acute humeral fracture

Conclusions

This preliminary human clinical study demonstrates the presence of peripherally injected microbubbles in acute fractures. This demonstrates the viability of using microbubbles for therapeutic purposes and for assessing changes in blood flow through fractures over time from acute injury in clinical settings.

References

[1]. Fischer C, Haug T, Weber MA, Kauczor HU, Bruckner T, Schmidmaier G. Contrast-Enhanced Ultrasound (CEUS) Identifies Perfusion Differences Between Tibial Fracture Unions and Non-Unions. Ultraschall Med - Eur J Ultrasound. 2020 Feb;41(01):44–51.

Fibrin-Targeted Phase Shift Microbubbles Outperformed Fibrin-Targeted Microbubbles in Microvascular Obstruction Treatment

Soheb Anwar Mohammed[1], Muhammad Wahab Amjad[1], Xucai Chen[1], Maria F. Acosta[2], Dillon Hanrahan[2], Evan C. Unger[2], Emmanuelle J. Meuillet[2], John J. Pacella*[1]

[1]Center for Ultrasound Molecular Imaging and Therapeutics, University of Pittsburgh. Pittsburgh, PA, USA

[2]Microvascular Therapeutics, LLC, Tucson, AZ, USA

Corresponding author: pacellajj@upmc.edu

Introduction

Cardiovascular disease is the leading cause of morbidity and mortality in the United States [1]. More than 1 million Americans are estimated to have a new or recurrent acute myocardial infarction (**AMI**) each year [2]. Although the mortality from AMI has decreased in recent years, post-MI congestive heart failure is increasing due to microvascular obstruction (**MVO**), ultimately limiting the myocardial salvage [3]. It has been estimated that up to 60% of all acute ST-elevated myocardial infarction (**STEMI**) patients receiving the percutaneous coronary intervention (**PCI**) develop MVO, with subsequent decreased left ventricular systolic function and major adverse cardiac events, including cardiac death, stroke, myocardial infarction, and heart failure requiring hospitalization [4]. Conventional strategies for treating MVO include the administration of vasodilators, antiplatelet therapy, thrombus aspiration, embolic protection devices, and even hyperoxemic intracoronary reperfusion therapy [5]. Even with the strategies mentioned above, no definitive therapeutic consensus for MVO exists, and many clinical trials have yielded conflicting results [6]. Therefore, we aim to address an urgent unmet need by devising an image-guided therapy, termed sonoreperfusion (**SRP**), that resolves MVO by ultrasound-targeted microbubble cavitation (**UTMC**) [7]. To further improve this therapy, currently, we are evaluating safe and stable lipid-based fibrin-targeted phase shift microbubbles (**FTPSMBs**) (Microvascular Therapeutics, Inc) to treat MVO. We hypothesized that owing to the smaller size and more efficient microthrombi penetration, **FTPSMBs** would improve SRP efficacy, compared to standard fibrin targeted microbubbles (**FTMBs**) ($\sim$200 nm vs. 1-3 µm).

Methods

MVO of the rat (_n_=6) hindlimb was created by directly injecting freshly prepared porcine microthrombi into the left femoral artery under contrast-enhanced ultrasound imaging (**CEUS**) guidance. DEFINITY® MBs (Lantheus Medical Imaging) was infused (2 mL/hr) through the right external jugular vein for CEUS. Following a stable 10 min. of MVO, a therapeutic transducer (1 MHz, 1.5 MPa peak negative pressure, 5 ms pulse duration, 5-sec pulse interval) was positioned vertically above the hindlimb for therapeutic US pulses during concomitant administration of fibrin-targeted MBs/PSMBs (3 mL/hr). CEUS cine loops with burst replenishment were obtained by

Figure 1: Schematic representation of US-targeted MB/PSMB cavitation during sonoreperfusion therapy.

imaging transducer (7 MHz CPS, Imaging MI 0.2, 200 ms frame interval, burst MI 1.9) at baseline (BL), 10 min post-MVO, and after each of the two SRP treatment sessions (TX1, TX2) and analyzed (MATLAB_R2021a).

Results

We successfully created MVO in both groups. After the first treatment, UTMC with FTPSMBs resulted in a more rapid increase in the blood volume (dB) and flow rate (dB/sec) when compared with FTMBs (**Figure 2**). Both blood volume and flow rate returned to baseline after treatment 1 with fibrin-targeted phase shift microbubbles (FTPSMB), which did not occur with fibrin-targeted microbubbles (FTMB).
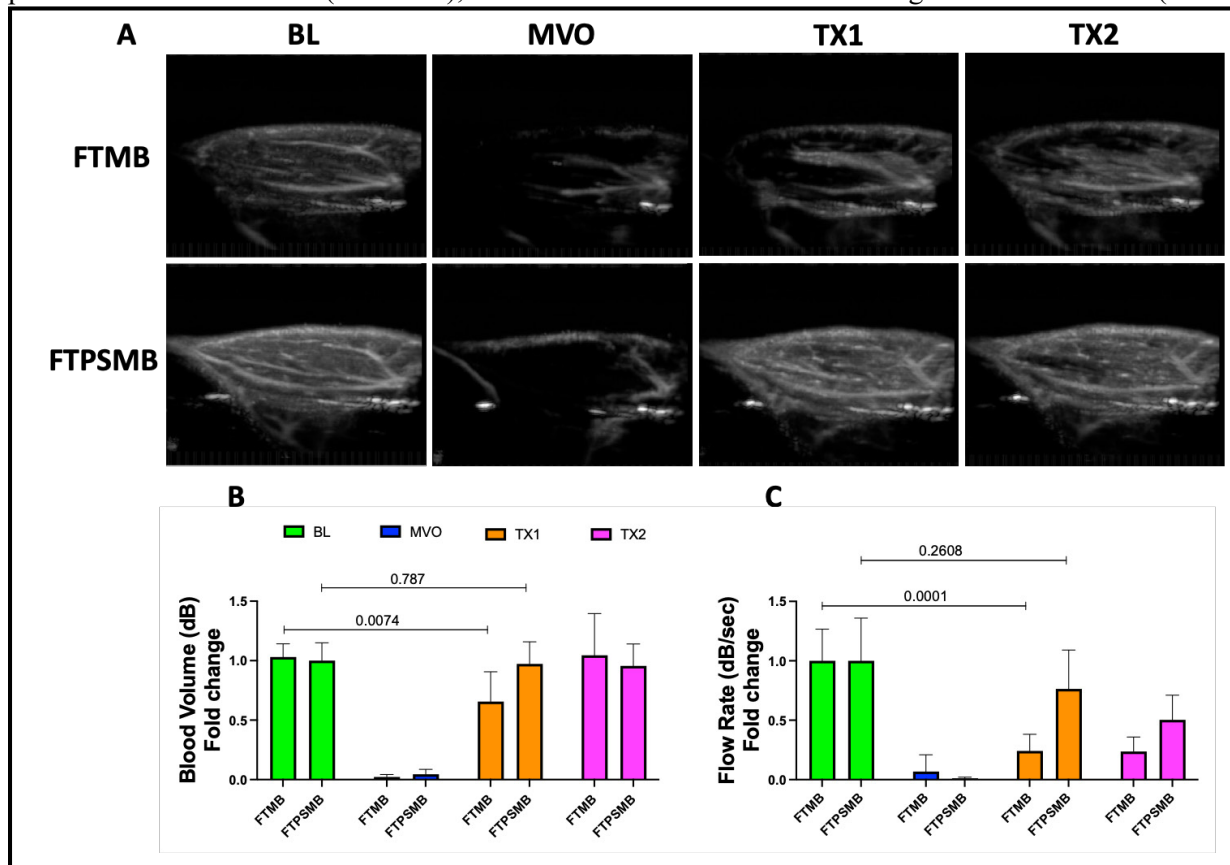
Figure 2: Fibrin-targeted Phase shift microbubbles (FTPSMBs) rescued microvascular obstruction. **[A]** Exapmle contrast-enhanced ultrasound images of rat hindlimb. **[B]** Peak plateau video intensity which reflects vascular cross-sectional area. **[C]** Flow rate. Data expressed as mean ± standard error (*n*=6).

Conclusions

US-guided FTPSMB cavitation causes more rapid and complete reperfusion of rat hindlimb following MVO compared to FTMB, likely owing to their small size and more effective thrombus penetration. Studies to explore the underlying molecular mechanisms associated with sonoreperfusion treatments are underway.

References

[1] S.S. Virani, A. Alonso, H.J. Aparicio, et al, American Heart Association Council on Epidemiology and Prevention Statistics Committee and Stroke Statistics Subcommittee, Heart Disease and Stroke Statistics-2021 Update: A Report From the American Heart Association, Circulation. 143 (2021) e254–e743.
[2] E.J. Benjamin, P. Muntner, A. Alonso, et al, American Heart Association Council on Epidemiology and Prevention Statistics Committee and Stroke Statistics Subcommittee, Heart Disease and Stroke Statistics-2019 Update: A Report From the American Heart Association, Circulation. 139 (2019) e56–e528.
[3] B. Ibáñez, G. Heusch, M. Ovize, F. Van de Werf, Evolving therapies for myocardial ischemia/reperfusion injury, J. Am. Coll. Cardiol. 65 (2015) 1454–1471.
[4] A. Galli, F. Lombardi, Postinfarct Left Ventricular Remodelling: A Prevailing Cause of Heart Failure, Cardiol. Res. Pract. 2016 (2016) 2579832.
[5] S.H. Rezkalla, R.V. Stankowski, J. Hanna, R.A. Kloner, Management of No-Reflow Phenomenon in the Catheterization Laboratory, JACC Cardiovasc. Interv. 10 (2017) 215–223.
[6] J. Mazhar, M. Mashicharan, A. Farshid, Predictors and outcome of no-reflow post primary percutaneous coronary intervention for ST elevation myocardial infarction, Int. J. Cardiol. Heart Vasc. 10 (2016) 8–12.
[7] F.T.H. Yu, X. Chen, A.C. Straub, J.J. Pacella, The Role of Nitric Oxide during Sonoreperfusion of Microvascular Obstruction, Theranostics. 7 (2017) 3527–3538.

Ultrasound targeted microbubble cavitation-induced endothelial hyperpermeability is calcium-dependent

Anurag N. Paranjape, Xucai Chen, Flordeliza S. Villanueva

Center for Ultrasound Molecular Imaging and Therapeutics, University of Pittsburgh, Pittsburgh, PA, USA
Corresponding author: villanuevafs@upmc.edu

Introduction

Ultrasound (US) targeted Microbubble (MB) Cavitation (UTMC) aids in enhancing drug delivery across the endothelial barrier [1]. The molecular mechanisms regulating UTMC-induced hyperpermeability require further investigation for successful clinical application of this technique. Our lab and others have reported Ca^{2+} influx into cells upon UTMC [2,3]. Here we explore if this Ca^{2+} influx is necessary for UTMC-induced hyperpermeability.

Methods

Primary human coronary artery endothelial cells (HCAECs) were seeded abluminally on transwells with 0.4 μm pores and US was delivered using a single element transducer (A302S-SU, 1 inch diameter, Olympus NDT, Waltham, MA, USA) placed in a water tank for 10 s (1 MHz, 250 kPa, 10 cycles, 10 ms interval). Permeability was measured using transendothelial electrical resistance (TEER) and dextran transfer. VE-cadherin immunostaining was performed to quantify inter-endothelial gaps and phalloidin staining for quantifying stress fibers. For live-cell imaging, fibronectin-coated coverslips with confluent HCAECs were placed over the media containing MBs in a 50 mm glass dish. Using an in-house designed cone housing an immersion transducer (A303S-SU, 0.5 inch diameter, Olympus NDT), US was delivered for 10 s (1 MHz, 250 kPa, 10 cycles, 10 ms interval). Fluo4-AM was used to visualize Ca^{2+} and sonoporation was confirmed with propidium iodide [3]. Calcein-AM was used to assess cell viability at the end of the experiments. To assess involvement of Piezo1 channels, the inhibitor GsMTx4 and siRNA pool were used.

Results

Transwell assays showed that UTMC reduces transendothelial electrical resistance (1.7 fold, $p<0.05$) and increases dextran flux across the transwells (2-fold, $p<0.01$ for 70 kDa dextran, 1.6 fold, $p<0.05$ for 10 kDa dextran). UTMC enhanced the permeability by increasing transient inter-endothelial gaps. UTMC caused significant Ca^{2+} influx which was abrogated when Piezo1 channels were inhibited ($n=5$, $p<0.0001$) using GsMTx4. Reduction in Ca^{2+} influx diminished inter-endothelial gaps suggesting Ca^{2+} influx is required, at least partly, for UTMC-induced hyperpermeability. Further, siRNA-mediated downmodulation of Piezo1 channels resulted in significant reduction of UTMC-induced Ca^{2+} influx, confirming the specificity. Immunostaining showed that upon UTMC, VE-cadherin reorganized from mostly linear to interrupted pattern, known to be associated with hyperpermeability [4]. This also correlated with increased stress fiber formation, which was Ca^{2+} influx-dependent, suggesting increased cell contraction leading to gap formation [4].

Conclusions

We show that UTMC causes endothelial barrier hyperpermeability via a Ca^{2+} dependent mechanism, mediated at least partly by mechanosensitive Piezo1 channels. UTMC led to a change in VE-cadherin organization to an interrupted pattern, along with increased stress fiber formation in about half of the cells, suggesting that other pathways downstream of Ca^{2+} influx might also be involved. Further investigation to decipher these pathways will help in clinical translation and optimization of UTMC for delivery of cell-impermeant drugs.

References

[1]. Tsutsui, J. M., Xie, F., & Porter, R. T. (2004). The use of microbubbles to target drug delivery. Cardiovasc Ultrasound, 2, 23.

[2]. Fan, Z., Kumon, R. E., Park, J., & Deng, C. X. (2010). Intracellular delivery and calcium transients generated in sonoporation facilitated by microbubbles. J Control Release, 142(1), 31-39.

[3]. Helfield, B., Chen, X., Watkins, S. C., & Villanueva, F. S. (2020). Transendothelial Perforations and the Sphere of Influence of Single-Site Sonoporation. Ultrasound Med Biol, 46(7), 1686-1697.

[4]. Millan, J., Cain, R. J., Reglero-Real, N., Bigarella, C., Marcos-Ramiro, B., Fernandez-Martin, L., Correas, I., & Ridley, A. J. (2010). Adherens junctions connect stress fibres between adjacent endothelial cells. BMC Biol, 8, 11.

Localisation and tracking of bubbles in a volume using a 1D unfocused linear transducer array and Volumetric Information Projection Super Resolution Ultrasound (VIP-SRUS)

Bingxue Wang[1], Kai Riemer[1], Matthieu Toulemonde[1], Jipeng Yan[1], Meng-Xing Tang[1]

[1]*Department of Bioengineering, Imperial College London, London, UK*
Corresponding author: mengxing.tang@ic.ac.uk

Introduction

Super-Resolution Ultrasound (SRUS) Imaging has been demonstrated to overcome the wave diffraction limit and reveal microvasculature [1] [2]. However, 3D SRUS imaging remains a challenge due to the fabrication and computational complexity of 2D matrix array probes. Inspired by X-ray radiography, which can present volumetric information in a single projection image with much simpler hardware than X-ray CT, this study aims to demonstrate the feasibility of two-dimentional localisation and tracking of contrast agents within a volume using a 1D unfocused linear transducer in Volumetric Information Projection SR (VIPSR) ultrasound imaging.

Methods

For a fair comparison with different imaging methods and to validate the tracking performance of the proposed VIPSR method, a 7.8MHz multiplexed matrix array probe with 32x32 elements (Vermon, France) was used to mimic different types of probes, 1) 1D linear array with a lens for conventional 2D SRUS by taking the central slice image out of the 3D BF image, 2) 1D linear array without a lens for VIP SRUS by summing the RF data along one lateral direction, reducing the number of channels from 32×32 to 32×1, and 3) a full 2D matrix array to do 3D SRUS as a gold-standard reference. The processing flow chart is shown in Figure 1.

A Verasonics 256 system was used to transmit zero-angle plane waves without steering and compounding with four sub-apertures together by multiplexing, and receive echoes with each sub-aperture sequentially. 1000 and 1500 frames were acquired at a frame rate of 500Hz for *in vitro* and *in vivo* experiments using microbubbles, respectively. Normalized cross-orrelation was used for localization. Graph-based tracking algorithm incorporating Kalman Filter in its cost function [4] was used for flow tracking.

Results

Figure 2 and Figure 3 show the velocity amplitude tracking results of the *in vitro* and *in vivo* experiments, respectively. As indicated by the triangles in Figure 2, only a tiny part of the out-of-plane tube can be seen

Figure 2 In vitro velocity amplitude tracking results

Figure 1 Processing Flow Chart

Figure 3 In vivo velocity amplitude tracking results

in 2D SRUS results, whereas the VIPSR method captured a similar structure as the 3D results. A similar phenomenon can also be seen in Figure 3, where branches of vessels stretching out of the central imaging plane that the conventional 2D SRUS cannot even capture can be tracked in the VIPSR method, although the imaging quality of it was deteriorated compared to 3D.

Discussions and conclusions

In conventional 2D SRUS, the existence of a focal lens on the elevational direction reduces the pressure intensity dramatically outside the focal imaging slices. While such focusing improves elevational resolution, it limited the field of view to a thin imag plane. By removing the lens in VIP-SRUS, the pressure intensity profile along the elevational direction is more uniform, and microbubbles that move in any direction in the volume can still be detected and tracked in the projection SR results. The SRUS localisation and tracking can recover and further improve the resolution loss due to the removal of lens.

In summary, this study demonstrates the ability of the VIPSR technique to localise and track microbubbles in a 3D volume with 2D projection position and flow velocity information, using a 1D linear array probe with the fabrication and computational cost similar to that of a traditional 1D array probe, and one order of magnitude less than that of a 2D array probe.

References

[1]. K. Christensen-Jeffries, J. Brown, P. Aljabar, M. Tang, C. Dunsby, and R. J. Eckersley, "In Vivo Acoustic Super-Resolution and Super- Resolved Velocity Mapping Using Microbubbles," IEEE Transactions on Ultrasonics, Ferroelectrics, and Frequency Control, vol. 34, no. 2, pp. 443–440, 2015.

[2]. C. Errico, J. Pierre, S. Pezet, Y. Desailly, Z. Lenkei, O. Couture, and M. Tanter, "Ultrafast ultrasound localization microscopy for deep super- resolution vascular imaging," Nature, vol. 527, no. 7579, pp. 499–502, 2015.

[3]. B. Wang, K. Riemer, M. Toulemonde, J. Broughton-Venner, X. Zhou and M-X. Tang, "Volumetric Super-Resolution Ultrasound with a 1D array probe: a simulation study," 2021 IEEE International Ultrasonics Symposium (IUS), 2021, pp. 1-3, doi: 10.1109/IUS52206.2021.9593553.

[4]. J. Yan, T. Zhang, J. Broughton-Venner, P. Huang, and M. X. Tang, "Super-Resolution Ultrasound Through Sparsity-Based Deconvolution and Multi-Feature Tracking," IEEE Transactions on Medical Imaging, vol. 0062, no. c, pp. 1–10, 2022.

On the Sequence of Motion Correction and SVD in Super-Resolution Ultrasound

Laura Taylor[1], Kai Riemer[1], Jipeng Yan[1], Matthieu Toulemonde[1], Meng-Xing Tang[1]

[1]*Department of Bioengineering, Imperial College London, London, UK*
Corresponding author: mengxing.tang@imperial.ac.uk

Introduction

In super-resolution ultrasound (SRUS), singular value decomposition (SVD) is commonly used to filter out the tissue signal leaving the bubble signal for super-localisation and tracking. As tissue motion will affect the localisations and hence the SR image, motion correction (MoCo) is often also included during post-processing [1]. The order of SVD Filtering and MoCo is of interest as the SVD filter uses the spatio-temporal properties of the microbubbles and tissue – hence the output of the filter may be affected by MoCo [2]. Here we compare the SR images generated when MoCo is applied before and after SVD.

Methods

In this study, a B-Mode acquisition of a rabbit kidney is used to compare post-processing with no MoCo, MoCo applied after SVD filtering, and MoCo applied before SVD filtering. All experiments complied with the Animals (Scientific Procedures) Act of 1986 and were approved by the Animal Welfare and Ethical Review Body of Imperial College London. The acquisition consists of 2000 frames at a frame rate of 1000 Hz after a bolus injection of homemade microbubble contrast agent. Nonrigid motion estimation was computed using the image data after beamforming and using this MoCo was done on either the complex beamformed data or the complex data after SVD filtering. Based on the work in [3], the correlation between the spatial singular vectors (in particular local regions of correlation) was used to decide the cut-off value for the SVD filter for each processing stream [3]. Here, the mean of the correlation between each spatial singular vector and the next 10 vectors is computed and the cut-off value is chosen to be the first vector where this mean reaches a threshold of 0.6 (see Figure 1). Prior to super-localisation, the data is normalized and pixel values below a lower bound of 0.05 are classified as noise and zeroed out. The super-localisation method is based on the cross-correlation between an estimated bubble PSF and the bubble data. The PSF was estimated using a sample of 25 manually selected bubbles and the same PSF and correlation threshold was used for all processing streams.

Results

The selection of the SVD filter cut-offs for the data with and without MoCo applied is shown in Figure 1 *(a)*. The full super-resolution images when using no MoCo, MoCo after SVD, and MoCo before SVD as well as two regions of interest are shown *(b)*. Example pixel intensity curves examining the impact of MoCo and differences between localisations found in the different methods are provided in *(c-d)*.As shown in Figure 1, there are differences between the SL images resulting from applying MoCo before or after SVD, and more microvascular features become present when SVD is done after MoCo. With these in vivo images, however, the ground truth of the vessel structure is not known making it challenging to determine which image better corresponds to true vascular anatomy. Further investigation is needed to understand the relationship between the tissue motion and microbubble flow velocity and how this may impact differences seen in the SR images.

Conclusions

Our initial results suggest that the sequence of MoCo and SVD in the post-processing can significantly alter the SRUS imaging results.
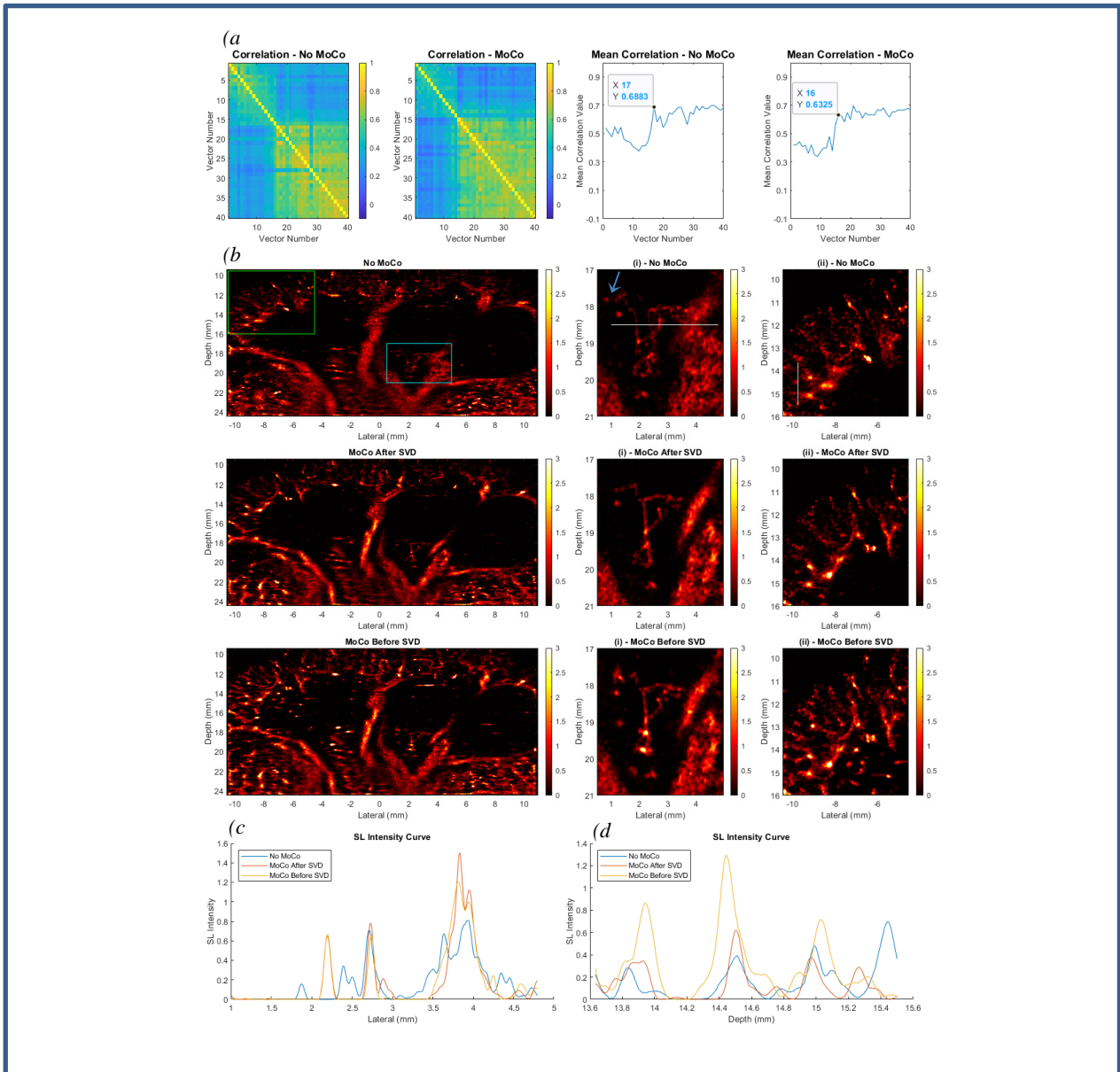
Figure 1. *(a)* Correlation between the spatial singular vectors (left images) and mean correlation between each spatial singular vector and the next 10 vectors (right curves). The selected SVD cutoff values are shown in the curves. *(b)* SR images for all processing streams (left), blue region in the SR images (middle), green region in the SR images (right). The arrow in the middle image highlights another area of difference between the streams. *(c)* Pixel intensity averaged over 10 pixels in the depth dimension around the line shown in (i) – No MoCo *(d)* Pixel intensity averaged over 10 pixels in the lateral dimension around the line shown in (ii) – No Moco.

References

[1] S. Harput *et al.*, "Two-Stage Motion Correction for Super-Resolution Ultrasound Imaging in Human Lower Limb," in *IEEE Transactions on Ultrasonics, Ferroelectrics, and Frequency Control*, vol. 65, no. 5, pp. 803-814, May 2018, doi: 10.1109/TUFFC.2018.2824846.

[2] Zhu J, Lin S, Leow CH, Rowland EM, Riemer K, Harput S, Weinberg PD, Tang MX. High Frame Rate Contrast-Enhanced Ultrasound Imaging for Slow Lymphatic Flow: Influence of Ultrasound Pressure and Flow Rate on Bubble Disruption and Image Persistence. Ultrasound Med Biol. 2019 Sep;45(9):2456-2470. doi: 10.1016/j.ultrasmedbio.2019.05.016. Epub 2019 Jul 3. PMID: 31279503.

[3] J. Baranger, B. Arnal, F. Perren, O. Baud, M. Tanter and C. Demené, "Adaptive Spatiotemporal SVD Clutter Filtering for Ultrafast Doppler Imaging Using Similarity of Spatial Singular Vectors," in *IEEE Transactions on Medical Imaging*, vol. 37, no. 7, pp. 1574-1586, July 2018, doi: 10.1109/TMI.2018.2789499.

Ambient pressure changes can modulate the subharmonic response of individual contrast bubbles

Sander Spiekhout[1], Jason Voorneveld[1], Benjamin van Elburg[2], Tim Segers[3], Michel Versluis[2], Nico de Jong[1,4], Johannes Bosch[1]

[1]*Biomedical Engineering Group, Dept. of Cardiology, Erasmus MC, University Medical Center Rotterdam, Rotterdam, The Netherlands*
[2]*Physics of Fluids Group, Department of Science and Technology, and Technical Medical Center, University of Twente, Enschede, The Netherlands*
[3]*BIOS / Lab on a Chip Group, Max Planck Center for Complex Fluid Dynamics, University of Twente, Enschede, The Netherlands*
[4]*Laboratory of Medical Imaging, Department of Imaging Physics, Delft University of Technology, Delft, The Netherlands*
Corresponding author: s.spiekhout@erasmusmc.nl

Introduction

Ultrasound contrast agents (UCA) have long been hypothesized to be usable for detecting local blood pressure. The reasoning is that the surface tension of their lipid shells can introduce pressure-sensitive nonlinear behavior like subharmonic oscillations. It is known that differences in initial surface tension can entirely change the microbubble's response,[1] so slight pressure changes that change the initial surface tension can, in principle, lead to a measurable effect in bubble response.

The idea of using contrast agents to measure changes in blood pressure has been explored in numerous studies,[2,3] and clinical trials.[4] The common denominator in these works is to relate the subharmonic scattered pressure of a population of microbubbles to that experienced at ambient pressure, allowing the quantification of pressure changes over a single cardiac cycle.[2,3] Although bulk measurements have demonstrated the pressure sensitivity of microbubbles, so far they have not been able to identify the mechanisms responsible for the local pressure sensitivity of their subharmonic response.

In this work we investigate whether changes in subharmonic vibrations as a function of ambient pressure are measurable on individual microbubbles using the 'acoustical camera' principle.[5] We demonstrate that a subset of SonoVue (Bracco, Milan, Italy) microbubbles can act as highly sensitive pressure sensors, and show in simulations that this behaviour may be linked to a low initial surface tension.

Methods (measurements)

The setup shown in Figure 1 was used to measure the dynamics of single microbubbles in response to a 1000-cycle 4-MHz 200-kPa wave (shown in green) transmitted by a low-frequency (LF) transducer (PA275, Precision Acoustics, Dorchester, UK). This setup makes use of the acoustical camera principle, introduced by Renaud et al.[5] Briefly, it measures a single bubble response using an identical pair of perpendicularly-positioned high-frequency (HF) transducers (V324, Olympus Industrial, Essex, UK) with coaligned foci, with HF1 transmitting a 25-MHz 500-kPa wave (shown in blue in Fig. 1), and HF2 receiving the scattered signal of the single bubble located in the focus.

The hydrostatic overpressure due to the water level in the tank was 20 mmHg. To introduce ambient pressure changes similar to those occurring in the cardiovascular system but on a timescale measureable in the acoustical camera, we added an audio frequency immersion transducer (TC1026, Teledyne RESON, Slangerup, Denmark) to the setup. This audio frequency transducer transmitted 5 cycles of a 20-kHz, 20-mmHg (2.7 kPa) amplitude wave (speaker, displayed red in Fig 1), synced to the start of the LF transmission. The HF, LF and 20-kHz signals are received by the bubble in the order as shown in Fig 2A.

The scattered HF amplitude at 25 MHz quasi-linearly follows the normalized vibrational amplitude of the individual microbubble.[5] The height of the tank above the probed volume is sufficient to prevent any reflections during the 250 µs acquisition duration.

The headspace of a SonoVue vial was replaced with C_4F_{10} prior to activation to increase bubble stability, and 2 μL of bubble suspension was diluted into 1.8 L of water left overnight at room temperature and added to the tank. Mild stirring ensures fresh bubbles moving through the focus, where they can be measured for up to 1 ms. The 250 μs excitations are triggered when a bubble is detected by a shorter preceding HF burst. This triggering scheme minimizes the risk of measuring a bubble which has been acoustically excited extensively, which can affect its response to an acoustical pulse.[6] This triggering scheme probably introduces a bias for larger microbubbles to be detected, and we assume bubbles with a radius R < 1.5 μm are unlikely to be detected.[7]

Quantitative results are presented as mean ± standard deviation.

Methods (processing)

A total of 821 individual signals were measured over the course of four experiments each lasting 20 minutes. The bubbles vibrate in response to the combination of the 20-kHz (red in Fig. 2A) and LF wave (green in Fig. 2A). Amplitude demodulation of the scattered 25 MHz probing signal (blue in Fig. 2A) was performed as in ref. 8), to obtain the modulus of the analytic scattered signals. This was compared to the 20 μs HF sections (blue in Fig. 2A) prior and post LF excitation to obtain the bubble's vibrational relative size change (radial strain). An example is given in Fig. 2B, where across the 90-115 μs timeframe an increase in subharmonic vibrations can be observed.

From the 821 measurements, 524 microbubble signals were selected with 1) minimal slow drift in amplitude levels, i.e., a bubble remaining in focus during acquisition, and 2) at least 3 % normalized radial strain to ensure an actual microbubble was measured (as opposed to a dirt particle).

To identify changes in subharmonic vibrations as a function of the 20-kHz wave, Short-time Fourier transforms were performed on the amplitude-demodulated strain signals for blocks of 1500 samples (6 μs) with 1400 samples overlap (0.4 μs steps). This procedure is sketched in Fig. 2C, where the spectrogram of the demodulated time signal (from Fig 2B) is displayed in a surface plot. The 5 cycles of the 20-kHz wave are added to Fig. 2C to highlight the change in the subharmonic response we are trying to identify. The subharmonic at 2 MHz (f/2) was extracted from the spectrogram to analyse its time variance. The ratio of expansion over compression was extracted from the strain signal as in ref. 9).

Methods (simulations)

To compare the observed bubble responses to modeled behavior, the Rayleigh-Plesset equation with the Marmottant[10] assumption was solved numerically for a range of bubble sizes similar to our bubble population in response to the 4 MHz driving pulse as used in the experiments, with an ambient overpressure that is the sum of the static 20 mmHg, and the 20 kHz sinusoidal wave of 5 cycles with a 20 mmHg amplitude. The model was solved for all combinations of the following bubble properties, R_0 = 1.5, 2, 2.5, 3.0, 3.5 μm, and initial surface tension $\sigma(R_0)$ = 0 to 0.03 N/m with 0.002 increments. The shell viscosity was set to 4×10^{-9} kg s^{-1}, shell stiffness to 2.5 N/m, and the viscosity of water was set to 1 mPa·s and doubled to account for thermal damping.

Results

Of the 524 measured bubbles, 82 were substantially subharmonic (radial strain$_{@2MHz}$>0.5 %), and of these 82, 35 subharmonic signals showed a considerable modulation (>0.2 %) at 20 kHz. On average, the 82 subharmonic bubbles had a 0.17% ± 0.12% modulating component in their subharmonic response at 20 kHz, compared to 0.06% ±0.07% for all 524 measured bubbles.

The average ratio of expansion to compression was 0.9 ± 0.21. For the bubbles with a subharmonic response, this ratio decreased to 0.86 ± 0.18. A compression bias is associated with low initial surface tension values.[11]

From the simulations shown in Fig. 4, it was seen that the subharmonic bubble vibrations are sensitive to the 20 kHz wave for a radius R_0 of 2.5 μm if the initial surface tension ranges from 6-14 mN/m, while

for an R_0 of 3 μm this sensitive region is between 6-12 mN/m. Bubbles with R_0 of 2.5 μm showed a peak sensitivity of 1.1 % strain, while for R_0 of 3 μm this is 0.55 %. Interestingly the pressure sensitivity is also present at initial surface tension values close to 0 mN/m for the bubbles with R_0 of 2.5 and 3 μm. The bubbles with R_0 of 1.5, 2.0 and 3.5 showed no subharmonics, so no modulation could be determined.

Conclusions

Here it is demonstrated that ambient pressure changes similar to those encountered in the cardiovascular system can modulate the subharmonic vibrations of a subset of *in vitro* SonoVue microbubbles. This subset of microbubbles shows compression-only behavior, often associated with low initial surface tension values. We showed that for this subset of individual bubbles, the subharmonic time-evolution follows that of a 20 kHz modulation of the ambient pressure with an amplitude of 20 mmHg. This indicates that such bubbles - in principle - can be used to track the pressure changes during a cardiac cycle, assuming a prolonged stability at that timescale (0.5-1 s) and that the haemodynamic conditions do not interfere with the subharmonic response. The effects of a higher ambient pressure, and of physiological blood properties on the bubble responses have not been addressed here, nor have the differences in rate of pressure change been included.

These results can aid the development of specialized monodisperse bubble formulations aimed at intravascular pressure sensing, since it suggests the need for a low initial surface tension. A future study aims at a more complete characterization of the pressure sensitive bubbles encountered here.
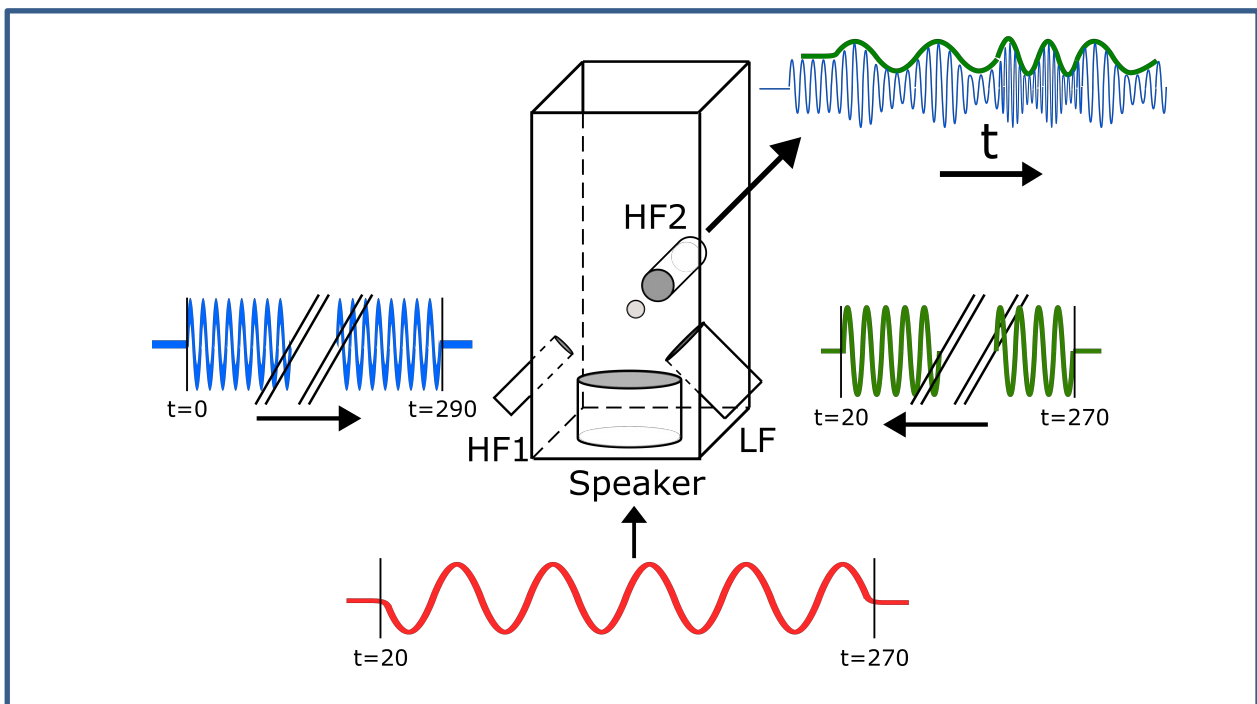
Figure 1. Acoustical camera setup used. The ambient pressure wave displayed in red is a 5-cycle, 20-kHz wave with 20 mmHg amplitude. The LF wave in green is a 200 kPa amplitude, 4 MHz excitation and lasts 1000 cycles. The pair of HF transducers are used to track bubble vibrations. HF1 transmits a 500 kPa, 25 MHz wave that lasts 7250 cycles. The signal received by HF2 is amplitude modulated following the vibrations induced by the LF wave. All displayed numbers are in μs.
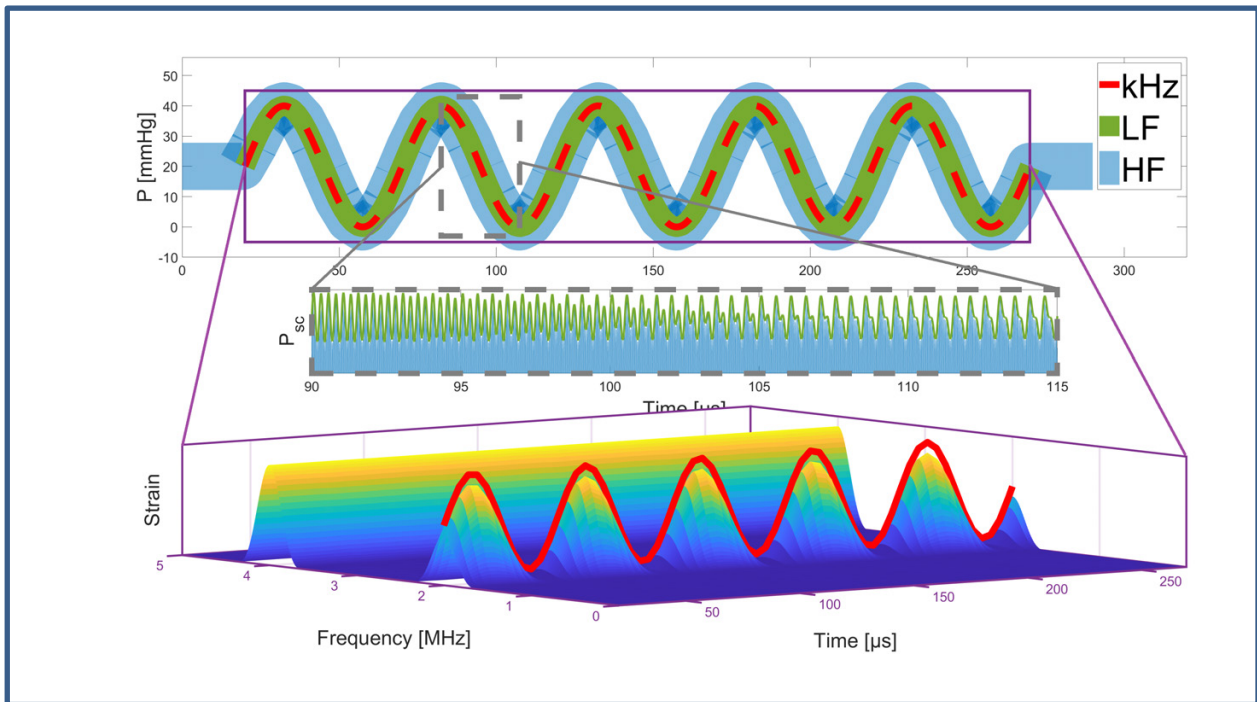
Figure 2. A) Signals transmitted to the individual microbubbles, with the 5 cycles of the 20-kHz wave in red and the LF and HF wave in green and transparent blue respectively. The HF signal is transmitted 20 µs prior to the LF and 20-kHz wave. B) Scattered HF signal from a single vibrating microbubble across the 90-115 µs time interval from 2A. The green envelope marks the amplitude modulation resulting from the bubble vibration. C) Spectrogram of the demodulated scatter signal across the 20-270 µs mark from 2A. The subharmonic response is modulated by the 5 cycles of the 20-kHz wave.
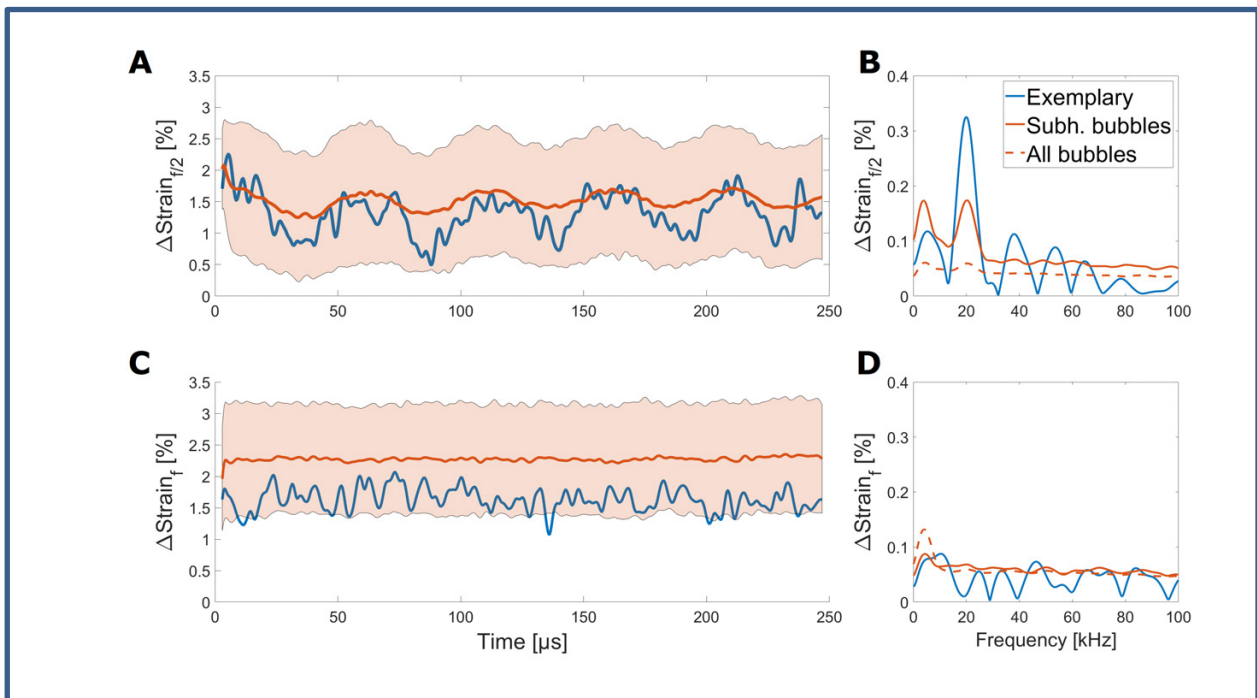
Figure 3. A) Time-evolution of measured subharmonic signals of exemplary (blue) and all 82 (red) subharmonic bubble signals. The transparent red region indicates the standard deviation. B) Frequency spectrum of subharmonic frequency time-evolution in A), with a strong component at 20 kHz. Dashed line indicates all 524 bubbles. C) Time-evolution of fundamental signals, with the blue line extracted from the

same exemplary acquisition of A, and the red line showing all 82 subharmonic bubbles. D) Frequency spectrum of fundamental frequency time-evolution in C).
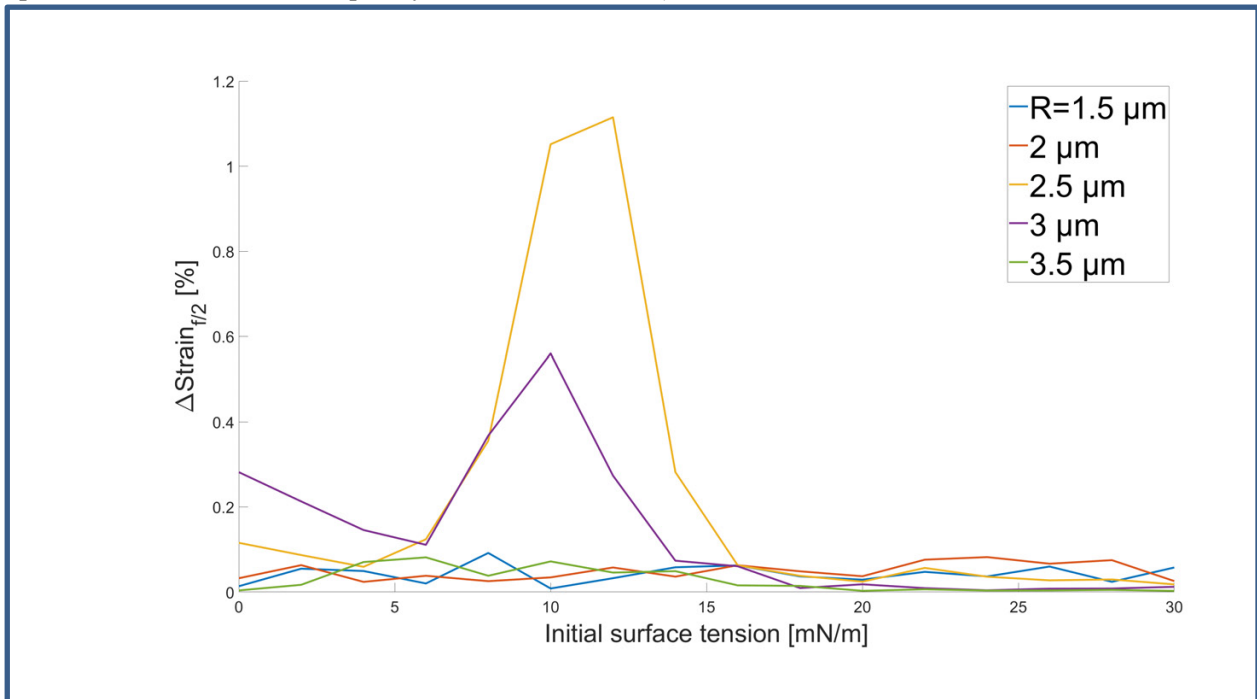
Figure 4. Modulation of subharmonic signal caused by the 20 kHz wave. Simulated magnitudes for different bubble sizes over a range of initial surface tensions. The highest sensitivity is expected for bubbles with R_0 of 2.5 µm and initial surface tension values of 8-14 mN/m.

References

[1]. Overvelde, M., Garbin, V., Sijl, J., Dollet, B., de Jong, N., Lohse, D., & Versluis, M. (2010). Nonlinear shell behavior of phospholipid-coated microbubbles. Ultrasound in medicine & biology, 36(12), 2080–2092.

[2]. Li, F., Li, D., & Yan, F. (2018). Improvement of Detection Sensitivity of Microbubbles as Sensors to Detect Ambient Pressure. Sensors (Basel, Switzerland), 18(12), 4083.

[3]. Forsberg, F., Gupta, I., Machado, P., Shaw, C. M., Fenkel, J. M., Wallace, K., & Eisenbrey, J. R. (2020). Contrast-Enhanced Subharmonic Aided Pressure Estimation (SHAPE) using Ultrasound Imaging with a Focus on Identifying Portal Hypertension. Journal of visualized experiments: JoVE, (166), 10.3791/62050.

[4]. Eisenbrey, J. R., Dave, J. K., Halldorsdottir, V. G., Merton, D. A., Miller, C., Gonzalez, J. M., Machado, P., Park, S., Dianis, S., Chalek, C. L., Kim, C. E., Baliff, J. P., Thomenius, K. E., Brown, D. B., Navarro, V., & Forsberg, F. (2013). Chronic liver disease: noninvasive subharmonic aided pressure estimation of hepatic venous pressure gradient. Radiology, 268(2), 581–588.

[5]. G. Renaud, J. G. Bosch, A. F. W. van der Steen, and N. de Jong (2012). "An "acoustical camera" for in vitro characterization of contrast agent microbubble vibrations", Appl. Phys. Lett. 100, 101911

[6]. Segers, T., de Rond, L., de Jong, N., Borden, M.A., & Versluis, M. (2016). Stability of Monodisperse Phospholipid-Coated Microbubbles Formed by Flow-Focusing at High Production Rates. Langmuir: the ACS journal of surfaces and colloids, 32 16, 3937-44.

[7]. Maresca, D., Emmer, M., van Neer, P. L., Vos, H. J., Versluis, M., Muller, M., de Jong, N., & van der Steen, A. F. (2010). Acoustic sizing of an ultrasound contrast agent. Ultrasound in medicine & biology, 36(10), 1713–1721.

[8]. Sander Spiekhout, Jason Voorneveld, Benjamin van Elburg, Guillaume Renaud, Tim Segers, Guillaume P. R. Lajoinie, Michel Versluis, Martin D. Verweij, Nico de Jong, and Johannes G. Bosch, (2022). "Time-resolved absolute radius estimation of vibrating contrast microbubbles using an acoustical camera", The Journal of the Acoustical Society of America 151, 3993-4003

[9]. Ying Luan, Guillaume Renaud, Jason L. Raymond, Tim Segers, Guillaume Lajoinie, Robert Beurskens, Frits Mastik, Tom J. A. Kokhuis, Antonius F. W. van der Steen, Michel Versluis, and Nico de Jong (2016). "Combined optical sizing and acoustical characterization of single freely-floating microbubbles", Appl. Phys. Lett. 109, 234104.

[10]. P. Marmottant, S. van der Meer, M. Emmer, M. Versluis, N. de Jong, S. Hilgenfeldt and D. Lohse (2005). "A model for large amplitude oscillations of coated bubbles accounting for buckling and rupture", The Journal of the Acoustical Society of America, 118.6: 3499-3505.

[11]. de Jong, N., Emmer, M., Chin, C. T., Bouakaz, A., Mastik, F., Lohse, D., & Versluis, M. (2007). "Compression-only" behavior of phospholipid-coated contrast bubbles. Ultrasound in medicine & biology, 33(4), 653–656.

Radiation-induced nanodroplet vaporization for proton range verification: first *in vivo* proof of concept

Bram Carlier[1,2,3], Gonzalo Collado-Lara[4], Sophie V. Heymans[5,6], Marcus Ingram[6], Yosra Toumia[7], Luigi Musetta[2,3], Gaio Paradossi[7], Hendrik J. Vos[4], Koen Van Den Abeele[5], Jan D'hooge[6], Uwe Himmelreich[2,3], Edmond Sterpin[1,3,8]

[1]*Department of Oncology, KU Leuven, Leuven, Belgium*
[2]*Department of Imaging & Pathology, KU Leuven, Leuven, Belgium*
[3]*Molecular small animal imaging center (MoSAIC), KU Leuven, Leuven, Belgium*
[4]*Department of Biomedical Engineering, Erasmus Medical Center, Rotterdam, The Netherlands*
[5]*Department of Physics, KU Leuven campus Kulak, Kortrijk, Belgium*
[6]*Department of Cardiovascular Sciences, KU Leuven, Leuven, Belgium*
[7]*Department of Chemical Science and Technologies, University of Rome Tor Vergata, Rome, Italy*
[8]*Particle Therapy Interuniversity Center Leuven – PARTICLE, Leuven, Belgium*
Corresponding author: sophie.heymans@kuleuven.be

Introduction

The ability to vaporize superheated nanodroplets by exposure to ionizing radiation was recently demonstrated, opening the door for ultrasound-based radiation dosimetry applications [1]. In particular, the safety and efficacy of proton therapy could be improved by measuring the proton range (*i.e.*, the position at which the proton beam ends) *in vivo*, thereby reducing the large safety margins currently applied to account for the various sources of range uncertainties. Our team showed a strong nanodroplet vaporization response to proton beams in phantoms, which allowed us to retrieve the proton range with sub-millimeter accuracy from ultrasound contrast profiles [2,3]. In this contribution, we present the first *in vivo* demonstration of radiation-induced nanodroplet vaporization in the liver of healthy rats during proton irradiation.

Methods

Superheated nanodroplets with a perfluorobutane (C_4F_{10}, b.p. -2°C) core and polyvinyl alcohol shell were prepared following a previously described protocol [2] and their concentration was quantified using ^{19}F NMR spectroscopy (400 MHz Avance II, Bruker Biospin GmbH, Germany). Healthy female Sprague-Dawley rats were anaesthetized and received a first dose of 200 µmol/kg via tail vein injection. The animals were positioned such that their liver was in the proton beam path (Fig. 1a), and an ultrasound probe (7.5 MHz linear array, L7-Xtech, Vermon, France) connected to an ultrasound research platform (DiPhAs, Fraunhofer IBMT, Germany) was positioned to continuously image the liver during proton irradiation (5 plane waves compounding, frame rate of 10 Hz). The acoustic power was kept sufficiently low to avoid acoustic droplet vaporization. Irradiations were performed with a passively-scattered collimated proton beam at fixed energies (Cyclotron Resources Center, Louvain-la-Neuve, Belgium). The animals received first a dose of 5 Gy (2 Gy/min), using a beam energy of 49.7 MeV, followed by a second 5 Gy irradiation at the higher energy of 62 MeV, to evaluate whether the nanodroplet response depends on the beam energy, and hence, the proton range. Two animals received an additional nanodroplet injection of 350 µmol/kg before being irradiated a third time (5 Gy, 62 MeV). The ultrasound B-mode acquisitions were processed offline using Matlab. Frames acquired before and after irradiation were correlated to identify pairs of frames corresponding to the same phase of the respiratory cycle. Then, an ROI was manually selected and the contrast generation was quantified by measuring the contrast difference in paired frames before and after irradiation. Ultrasound contrast profiles in the direction parallel to the proton beam were obtained by summing contrast values along the axial ultrasound direction.

Results

Previous observations in gel phantoms showed that nanodroplets irradiated by protons at 37°C exhibited a uniform vaporization response proximal to the proton range [2,3] due to vaporization being induced by

heavy secondary particles, and as predicted by the theory of radiation-induced nucleation in superheated liquids. A similar response was observed in the irradiated animals (Fig. 1b), with a uniform increase in contrast in the proton path, compared to pre-irradiation images displaying little contrast. When the energy was increased from 49.7 MeV (~ 2 cm range) to 62 MeV (~3 cm range), the vaporization zone shifted deeper into the animal liver tissue (Fig 1b, bottom). We assessed the energy-dependent shift in contrast both visually, by delineating manually the end of the vaporization region on ultrasound images (Fig. 1b), and quantitatively, by measuring the distance between the 50% drops in contrast profiles (Fig. 1c). Both range shift estimates are reported in Fig. 1d. The visual assessment performed better than the automatic assessment, with a lower standard deviation and a mean value closer to the theoretical range shift in liver tissue, which was estimated to be 10.1 mm. In addition, the total amount of generated contrast was observed to increase with the radiation dose (Fig. 1e).

(d)	**Visual range shift assessment**	**Automatic range shift assessment**
Animal 1	10 mm	5.5 mm
Animal 2	8.5 mm	9.7 mm
Animal 3	11 mm	11.3 mm
Mean ± std	9.8 mm ± 1.3 mm	8.8 mm ± 3 mm
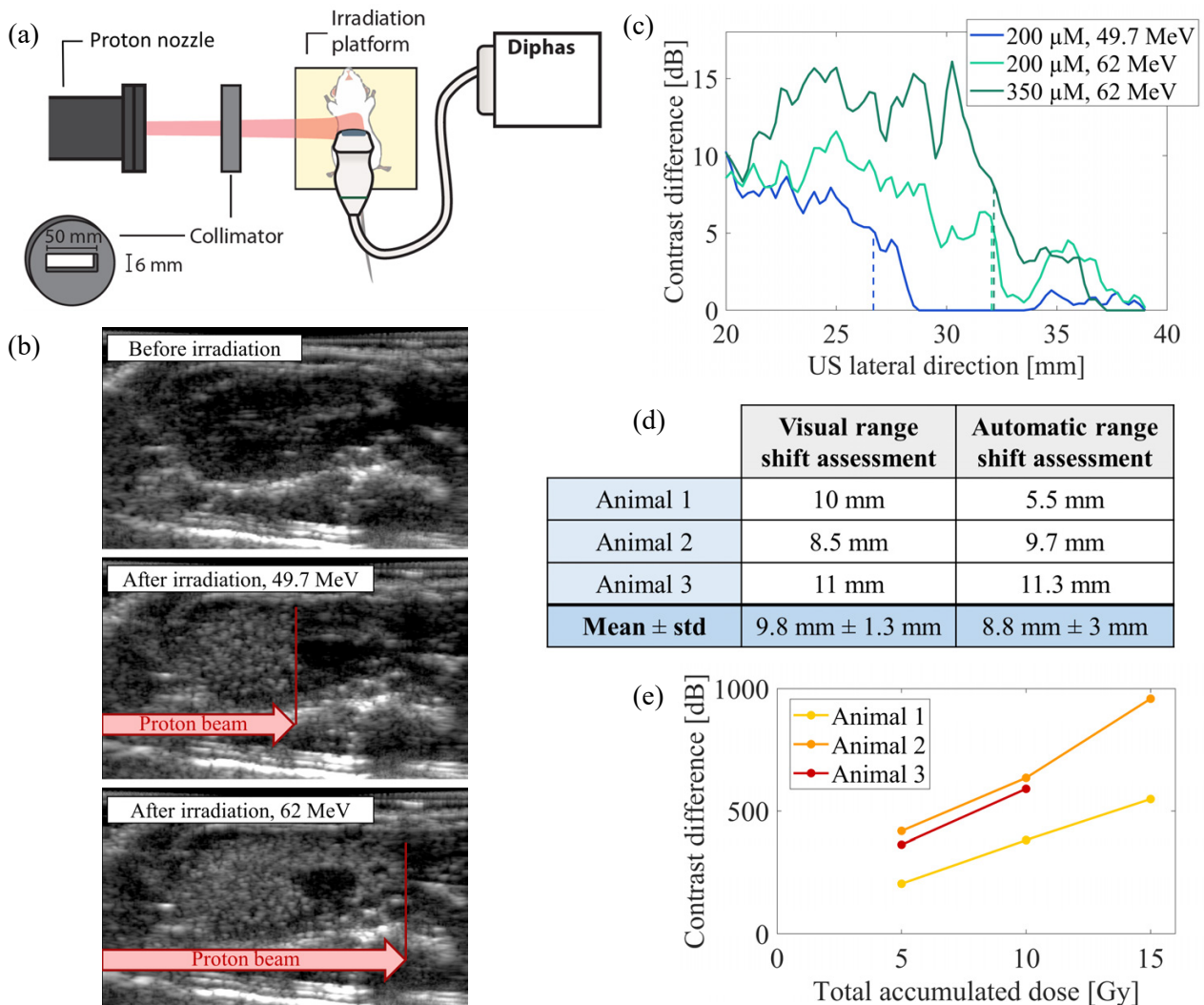
Figure 1. (a) Experimental setup for *in vivo* proton irradiation of the rat liver and simultaneous ultrasound imaging. (b) Ultrasound images of the liver before and after irradiation with two different beam energies. The arrows show the proton beam direction and red vertical lines represent the visual assessment of the end of the vaporization zone. (c) Contrast profiles for one animal and (d) statistics of the range shift measured in three animals. (e) Relationship between contrast generation and cumulative radiation dose (max 3x5 Gy/animal).

Conclusions

These results provide a first *in vivo* demonstration of the energy-dependent radiation response of nanodroplets in a proton beam. The strength of the ultrasound response and its correlation with the shift in proton range is promising and warrants further efforts to bring this technology to the clinic. The ultrasound image acquisition and processing pipeline needs to be optimized to improve the quantitative assessment of

the contrast generation, which is currently limited due to the motion of the target. For instance, active or passive Ultrasound Localization Microscopy could be implemented to quantify individual vaporization events [3,4], together with appropriate motion management strategies. In addition, future studies will focus on providing an absolute assessment of the *in vivo* proton range.

References

[1]. Carlier B, Heymans SV, Nooijens S, et al., Proton range verification with ultrasound imaging using injectable radiation sensitive nanodroplets: a feasibility study, *Physics in Medicine and Biology*, 65: 065013, 2020.

[2]. Heymans SV, Carlier B, Toumia Y, et al., Modulating ultrasound contrast generation from injectable nanodroplets for proton range verification by varying the degree of superheat, *Medical Physics*, 48(4), 2021.

[3]. Collado-Lara G, Heymans SV, Rovituso M et al. Spatiotemporal distribution of nanodroplet vaporization in a proton beam using real-time ultrasound imaging for range verification, *Ultrasound in Medicine and Biology,* 48(1) 2022.

[4]. Heymans SV, Collado-Lara G, Rovituso M et al. Passive Ultrasound Localization Microscopy of Nanodroplet Vaporizations During Proton Irradiation, *IEEE Open Journal of Ultrasonics, Ferroelectrics, and Frequency Control,* 2, 2022.

Comparison of amplitude modulation and cross amplitude modulation pressure fields through a monodisperse microbubble cloud

Agisilaos Matalliotakis[1], Martin D. Verweij[1, 2], David Maresca[1]

[1]*Department of Imaging Physics, Faculty of Applied Sciences, Delft University of Technology, Delft, The Netherlands*
[2]*Department of Biomedical Engineering, Thoraxcenter, Erasmus University Medical Center, Rotterdam, The Netherlands*

Introduction

Contrast-enhanced ultrasound imaging methods rely on the fast detection of ultrasound contrast agents against tissue background. To do so, highly sensitive but also specific methods are desired to prevent mislabelling image artefacts as contrast agents. Cross amplitude modulation (xAM) is one of the most promising pulse sequences to achieve sensitive and specific ultrasound imaging of nonlinear ultrasound contrast agents [1]. Although there has been research on the noncollinear interaction of infinitely long progressive plane waves, the fundamental physical principles behind an in vivo study are still unknown. In this framework, we shed light on the noncollinear interaction of cross-propagating plane waves (or x-waves) in general, and on the significance of local nonlinearities in particular. Our results demonstrate the superior specificity of xAM imaging compared to conventional amplitude modulation imaging (AM).

Methods

We used the Iterative Nonlinear Contrast Source (INCS) method [2] to simulate ultrasound pressure fields transmitted in AM and xAM imaging. Brielfy, INCS solves the Westervelt equation in a 4D spatiotemporal domain by explicitly computing the incident pressure field. The incident pressure field is iteratively updated via nonlinear field corrections calculated by the convolution of each nonlinear contrast source with the Green's function of a "linearized" medium. In this study, INCS was extended by incorporating the d'Alembertian operator of the Lagrangian density as a new contrast source term to account for the local field nonlinearities. We also added an inclusion of ultrasound contrast agents in the propagation medium as an extra contrast source term, where each microbubble is regarded as a contrast point source. In each iteration, the temporal signature of each source was computed by solving the Marmottant model [3]. In physical terms, each iteration adds an order of multiple scattering to the pressure field description. Here we report the transmitted pressure fields of a high frequency linear transducer array driven to transmit cross-propagating plane waves or flat plane waves through a monodispere microbubble cloud.

Results

We simulated a 64-element, 15 MHz linear transducer array to generate incident pressure fields of interest. Each element had a width of 80 μm and an elevation aperture of 1.6 mm. The pitch was 100μm. The elevation focus was set to 8 mm and a tukey apodization was used (cosine fraction of 0.2). The imaging pulse were gaussian windowed pulses transmitted at a pressure at the source surface of P_0= 400 kPa. The computational domain was discretized with a sampling frequency of F_s=105 MHz to capture all the nonlinear phenomena that occur due to the multiple interactions in the microbubble population. The dimensions of this domain were 6.4 mm x 1.6 mm x 10 mm. The microbubble inclusion was a 1mm long cylinder with a radius of 1 mm (Figure 1a). The cloud consisted of monodisperse microbubbles of 1.2 μm diameter.

Total pressure fields generated using flat and 20° cross plane wave transmissions are depicted in Figures 1b-f. These results include a description of linear transmitted field components, cumulative field nonlinearities, local field nonlinearities, and nonlinear ultrasound contrast agent scattering. Figure 1b shows that monodisperse contrast agents attenuate the transmitted pressure field downstream of the inclusion.

However, the cross-propagating plane waves, or x-wave pressure field appeared more robust to attenuation thanks to non-collinear transmissions (Figure 1c).

In Figure 1d, the AM residual pressure field clearly shows that significant nonlinearities accumulate downstream the bubble inclusion. In comparison, the 20° xAM residual pressure field (Figure 1e) minimizes nonlinearities along the centerline and only showed weak accumulation of nonlinearty along the direction
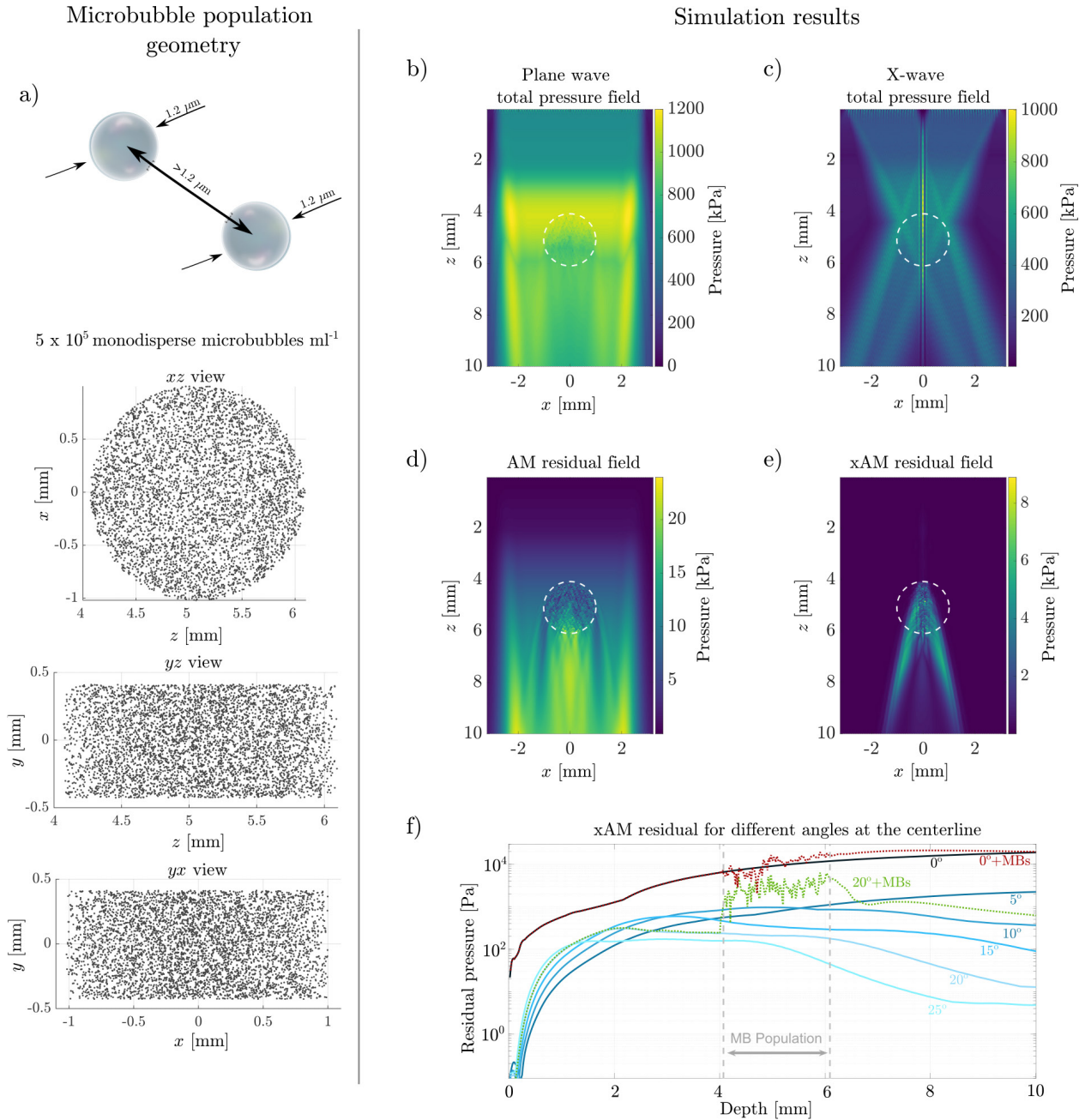
Figure 1. a) Geometry of a microbubble population consisted of 1.2 µm diameter monodisperse point scatterers.
b) Total pressure field of a plane wave transmitted from L22-14xV,
c) Total pressure field generated from the interaction of two cross propagating plane waves transmitted at an angle of 20°.
d) Residual map after applying amplitude modulation,
e) Residual map after applying the xAM (X – Left – Right).
f) Residual pressure at the centerline as a function of depth for different angles of transmission.
The location of the microbubble inclusion is depicted with dotted white lines.

of propagation of each cross propagating plane wave. This result highlights why xAM enables specific imaging void of distal nonlinear imaging artifacts.

Figure 1f displays (x)AM residual pressure fields along the centerline (X=0, Y=0). Here, results are presented for a range of x-wave angles ranging between 0° and 25° with a step of 5°. The black line is the result of AM and the lines with the different shades of blue are the results of xAM. As the angle increases, the peak residual pressure decreases significantly. The residual pressure for 0° is constantly increasing along depth due to cumulative nonlinear effects, whereas for the 20° case, there is an increase at the intersection of the two plane waves and then the residual pressure drops significantly. Results for the 0° and the 20° X-wave case in the presence of microbubbles are included with green and red colored lines, respectively. From the former, it can be deduced that the microbubble population enhances the total residual pressure mainly behind the inclusion, meaning that it is prone to significant downstream nonlinear artifacts. In comparison, for the 20° case, the residual pressure from the microbubble cloud is strong at the location of the inclusion and decreases sharply downstream the agent inclusion, demonstrating the higher specificity of xAM.

Conclusions

To conclude, INCS has been extended to include local nonlinearities due to the noncollinear nonlinear interaction of two cross-propagating plane waves and nonlinear scattering arising from a microbubble inclusion. Our results show that, in the absence of microbubbles, the peak residual pressure of an AM mode increases as the angle of transmission decreases. In other words, residual nonlinearities are minimized for higher x-wave angles. In the presence of microbubbles, flat plane wave transmissions lead to increasing nonlinearities along depth, and these are enhanced downstream of a resonant monodisperse microbubble inclusion. In the 20° x-wave transmission case, nonlinearities are minimized downstream of the microbubble population and increase moderately along the direction of propagation. Our study provides novel physical insights into nonlinear effects occuring in contrast-enhanced ultrasound imaging and can serve as a tool for their optimization.

References

[1]. D. Maresca et. al, "*Nonlinear X-Wave Ultrasound Imaging of Acoustic Biomolecules*", Physical Review X (**8**), 041002, 2018 (Maresca et al. PRX 2018)

[2]. K. Huijssen , and M. D. Verweij, "*An iterative method for the computation of nonlinear, wide-angle, pulsed acoustic fields of medical diagnostic transducers*", J. Acoust. Soc. Am. 127 (**1**), 2010

[3]. P. Marmottant et. al, "*A model for large amplitude oscillations of coated bubbles accounting for buckling and rupture*", J. Acoust. Soc. Am. 118 (**6**), 2005

A physically realistic simulation framework for contrast enhanced ultrasound imaging

A. Kuliesh[1, *], N. Blanken[2, *], B. Heiles[1, *], K. Jain[3], D. Maresca[1], G. Lajoinie[2]
(contributed equally)*

[1]*Department of Imaging Physics, Delft University of Technology, Delft, The Netherlands*
[2]*Physics of Fluids group, Technical Medical (TechMed) Centre, University of Twente, Enschede, The Netherlands*
[3]*Engineering Fluid Dynamics Group, Department of Thermal and Fluid Engineering, University of Twente, Enschede, The Netherlands.*
Corresponding authors: k.jain@utwente.nl, d.maresca@tudelft.nl, g.p.r.lajoinie@utwente.nl

Introduction

Contrast-enhanced ultrasound techniques have already shown a great scientific and clinical potential. Two notable examples are vector flow imaging (i.e. echoPIV) and ultrasound localization microscopy (ULM) [1, 2]. However, it is very difficult to give an objective account of their performance due to the lack of benchmark or ground truth. Furthermore, supervised super-resolution approaches using artificial intelligence rely on the availability of training datasets which cannot be acquired *in vitro* or *in vivo*. To date, only a synthetic approach can provide an objective benchmark and enable exploration of deep learning full potential.

We have identified five criteria for a simulation tool to faithfully emulate contrast-enhanced ultrasound imaging: (i) hemodynamics within a realistic vascular architecture, (ii) nonlinear wave propagation, (iii) nonlinear microbubble dynamics, (iv) microbubble acoustic coupling, and (v) realistic pressure field from the virtual transducer. Here, we present a simulator which accounts for all these criteria. Our toolbox can generate pulse-echo radiofrequency data for clinical transducer arrays in both normal and nonlinear contrast modes. We show its capabilities on ULM reconstruction of the renal arterial tree vasculature. The simulator offers a high accuracy mode as well as a fast mode with minimal accuracy loss. Furthermore, the simulator can handle arbitrary (off-grid) microbubble positions, which is critical for super-resolution techniques. We also incorporated the polydisperse and monodisperse microbubble distributions. To facilitate use of the simulator we wrapped it up in a user-friendly Graphical User Interface (GUI). Upon release, the simulator will be made fully open access and available on GitHub.

Methods

Our simulator has a modular architecture and relies on synchronised communication between its components. In the hemodynamics simulation module, we perform flow computations with MUSUBI solver and estimate blood velocities in the vasculature [3, 4]. The streamlines predicted from this simulation are used to propagate microbubbles through the vasculature for the duration of the imaging sequence. The ultrasound module simulates inhomogeneous, nonlinear wave propagation in 3D using k-Wave toolbox [5]. The vibration module solves the Rayleigh-Plesset equation to compute the nonlinear response of the microbubbles to the driving ultrasound pulse from the transducer and neighbouring bubbles, Fig. 1a.

The simulator features an average simulation time of ~10 min per frame in high accuracy mode on an NVIDIA Quadro RTX 6000 GPU. It is a limiting factor for the simulation of long imaging sequences, e.g., thousands of frames for ULM [1]. Taking benefit from the low amplitude of the waves reemitted by the bubbles, the fast simulation mode exploits the analytical solution to lossy, linear, and isotropic propagation of the bubble echoes. This minor approximation allows a speed-up of two order of magnitude with minimal loss of accuracy.

We have implemented arbitrary (off-grid) bubble positions using the method described in [6]. This method allows to simulate arbitrary shaped source and sensor distributions. So, the bubble positions in the frames can be disentangled from the computational grid and take continuous values. This way upon data processing the reconstructed tracks from circulating contrast agents are free from "staircasing" effect. We also applied this method for transducer elements definition to match the dimensions to probe characteristics.

Currently, only polydisperse microbubbles are clinically approved [7]. These contrast agents have a wide range in size distribution and are not optimised to any specific transducer frequency. In contrast, the use of monodisperse bubbles has become widely spread in research. The simulator can handle arbitrary size distributions and features pre-programed examples for monodisperse and SonoVue microbubble populations [8]. Fig. 1b demonstrates the added value of a monodisperse population.

Results

With the fast mode, we simulated the circulation of 10 microbubbles through a renal arterial system for 5 seconds [9] at a framerate of 500 Hz, resulting in 2500 frames. The microbubbles were insonified with phased array (P4-1, Philips ATL) at 2.5 MHz. We opted for a monodisperse microbubble distribution with mean radius of 2.14 μm Contrast was enhanced with amplitude modulation pulsing scheme. To beat the diffraction limit we utilized the radial symmetry algorithm on the beamformed IQ data within the LOTUS toolbox [10]. The accumulated localizations through all the frames allowed us to (partially) reconstruct the renal tree geometry, see Fig. 1c. We estimated the RMSE to be approximately equal to one third of a wavelength (195 μm), with a Jaccard index of 61.5 %. The trajectories of the circulating bubbles were subsequently predicted using the Hungarian method, which allowed us to measure the in-plane velocities. Reconstructed and ground-truth velocimetry maps are shown in Fig. 1c.
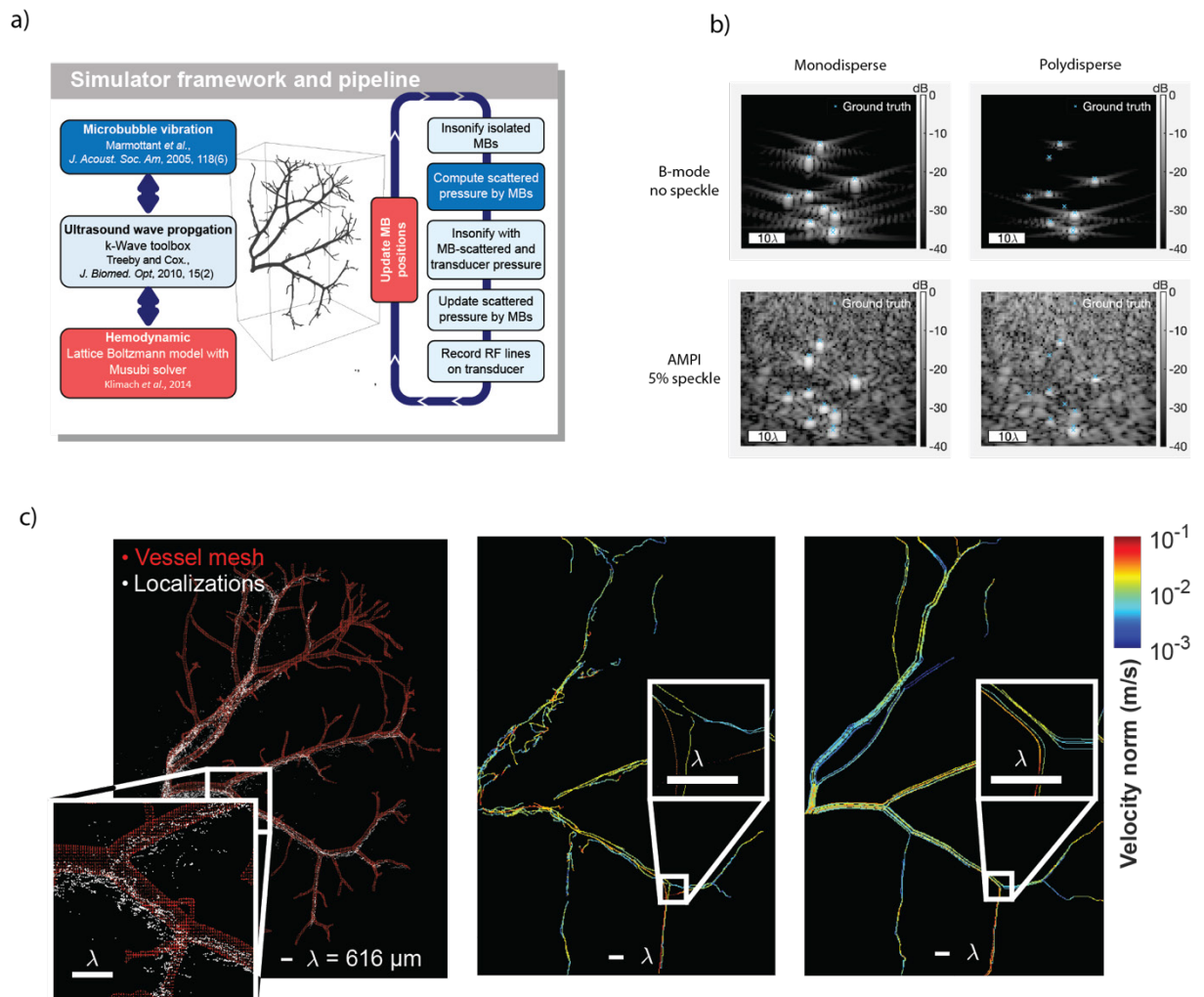
Figure 1. a) Modular architecture of the simulation framework and the simulator pipeline. b) B-mode frames containing 10 microbubbles in water insonified with a P4-1 probe at 2.5 MHz, $\lambda = 616\ \mu m$. On the left the population of contrast agents is monodisperse with a smean radius close to resonance. On the right, the bubble sizes are sampled from the SonoVue distribution. In the bottom row, we substituted water with tissue (5% inhomogeneity). Amplitude modulation pulse inversion pulsing scheme (AMPI) was used to suppress the linear signal from tissue. c) From left to

right: density map with localizations from 2500 frames overlayed with the underlying vessels geometry; output of microbubble tracking algorithm; ground truth velocimetry map predicted by fluid dynamics module.

Conclusions

The proposed simulator represents a significant progress towards a physically realistic simulation framework for CEUS. Our toolbox accounts for hemodynamics, nonlinear wave propagation, nonlinear microbubble dynamics, bubble-bubble interaction, and generates realistic pressure fields from virtual probes. Additionally, semi-analytical mode allows for the fast generation of large datasets necessary for some of the possible applications. The developed GUI significantly improves the end-user experience from the interaction with the framework. Thus we hope that this effort will support the CEUS community in the generation of reliable synthetic data.

References

[1]. Errico, C., et al., Ultrafast ultrasound localization microscopy for deep super-resolution vascular imaging. Nature, 2015. **527**(7579): p. 499-502.

[2]. Engelhard, S., et al. High-frame-rate contrast-enhanced US particle image velocimetry in the abdominal aorta: first human results. *Radiology* 289.1 (2018): 119-125.

[3]. Klimach, H., K. Jain, and S. Roller, End-to-end parallel simulations with apes, in Parallel computing: accelerating computational science and engineering (CSE). 2014, IOS Press. p. 703-711.

[4]. Available from: https://apes.osdn.io.

[5]. Treeby, B.E. and B.T. Cox, k-Wave: MATLAB toolbox for the simulation and reconstruction of photoacoustic wave fields. Journal of biomedical optics, 2010. **15**(2): p. 021314.

[6]. Wise, Elliott S., et al. Representing arbitrary acoustic source and sensor distributions in Fourier collocation methods. *The Journal of the Acoustical Society of America* 146.1 (2019): 278-288.

[7]. Quaia E. Classification and safety of microbubble-based contrast agents. In: Quaia E. (eds), Contrast Media in Ultrasonography. Medical Radiology (Diagnostic Imaging). Berlin, Heidelberg: Springer; 2005:3-14.

[8]. Segers, T., et al. Monodisperse versus polydisperse ultrasound contrast agents: Non-linear response, sensitivity, and deep tissue imaging potential. *Ultrasound in medicine & biology* 44.7 (2018): 1482-1492.

[9]. Nordsletten, D. A., Blackett, S., Bentley, M. D., Ritman, E. L., & Smith, N. P. (2006). Structural morphology of renal vasculature. *American Journal of Physiology-Heart and Circulatory Physiology*, *291*(1), H296-H309.

[10]. Heiles and Chavignon, et al, Performance benchmarking of microbubble-localization algorithms for ultrasound localization microscopy, [in press], Nat. Biomed. Eng., 2021

BUFF: BUbble Flow Field – A tool for simulating ultrasound imaging of vascular flow with microbubbles

Marcelo Lerendegui[1], Kai Riemer[1], Bingxue Wang[1], Christopher Dunsby[2], Meng-Xing Tang[1]

[1]*Department of Bioengineering, Imperial College London, London, United Kingdom*
[2]*Department of Physics, Imperial College London, London, United Kingdom*

Introduction

Ultrasound Localization Microscopy (ULM) can produce sub-wavelength images and velocity maps of vascular structures by localizing isolated microbubbles (MBs) across multiple frames. While impresive results have been achieved, there is still a need of improving the performance of ULM algorithms both in better bubble separation and precision of localizations. Testing and validation with ground truth data is required during development of new algorithms, moreover, large datasets containing tens of thousands of MBs are required for training the models of the increasingly popular deep learning based methods. In this work we present a comprehensive simulation platform BUbble Flow Field (BUFF) that generates contrast enhanced ultrasound images in vascular tree geometries with realistic flow characteristics and validation algorithms for ULM.

Methods

BUFF comprises four modules: (1) Microvascular Structure Generator, (2) Fast Flow Simulator, (3) Acoustic and Bubble Simulator, and (4) Evaluation. The microvascular generator is an automated tool that can be configured to create organic vessel network structures using a recurrent vasculogenesis-sprouting angiogenesis process. The flow simulator uses Hagen–Poiseuille law to quickly compute mean flow and pressures across networks, and can simulate particles moving in constant velocity streamlines, obtaining ground truth tables with accurate particle positions and velocities. The acoustic and bubble simulator integrates linear acoustic simulation1 with non-linear microbubble simulation2. The evaluation module incorporates tools and metrics to automate the assessment and benchmark of algorithms.

Results

Two randomly generated networks of microvascular vessels were created, Microbubbles were seeded through the networks, and two acoustic simulations of the flowing microbubbles were performed: (1) high frequency ultrasound simulation using a L11-4v transducer; (2) low frequency ultrasound simulation using a GE-M5ScD transducer. Thre MBs were localized on the B-Mode images using an Centroid Detection & Kalman Filter approach (Fig 1). Superresolved images were generated using microbuble track densities (Fig 2). The performance of the algorithm was evaluated using six metrics comprising both localization and tracking (Fig 3).

FIGURE 1

FIGURE 2

FIGURE 3

Localization	
Precision	0.48
Recall	0.51
RMSE	$135.79\mu m$
Tracking	
Precision	0.99
Recall	0.43
J_{map}	-0.71

Localization	
Precision	0.74
Recall	0.66
RMSE	$47.34\mu m$
Tracking	
Precision	0.56
Recall	0.44
J_{map}	-0.57
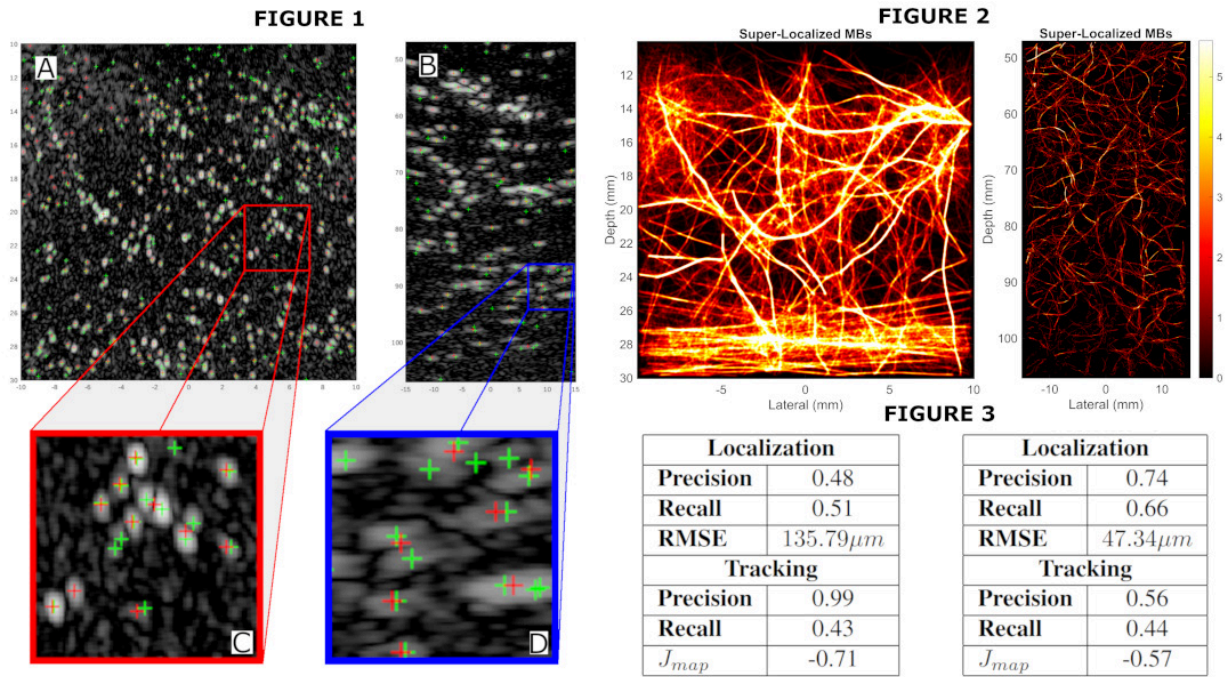
Figure 1: Localization results. (A & C) HF B-MODE frame 149. (B & D) LF B-MODE frame 4.

Figure 2: Superresolution Image, (Left) HF, (Right) LF.

Figure 3: Evaluation Results, (Left) HF, (Right) LF.

Conclusions

This work introduces BUFF, a simulation framework that simplifies the development and assesment of algorithms for ULM. Thanks to its efficient performance on dataset creation, both deep learning models and traditional algorithms can benefit from it. As proof of its capabilities, BUFF was used to evaluate a complete ULM pipeline by generating two datasets and mesuring the pipeline performance.

References

[1]. J. Jensen, "FIELD: A program for simulating ultrasound systems," Medical and Biological Engineering and Computing, vol. 34, pp. 351–352, Jan. 1996.

[2]. P. Marmottant, S. Meer, M. Emmer, et al., "A model for large amplitude oscillations of coated bubbles accounting for buckling and rupture," Journal of The Acoustical Society of America - J ACOUST SOC AMER, vol. 118, pp. 3499–3505, Dec. 2005.

A Method To Characterize 3D Flow in Helical Stents Using 2D Contrast-Enhanced Ultrasound

A. Ghanbarzadeh-Dagheyan[1,2], E. Groot Jebbink[1], M. Reijnen[1,3], M. Versluis[2]

[1]*Multimodality Imaging (M3i) group, University of Twente, Enschede, The Netherlands*
[2]*Physics of Fluids (PoF) group, University of Twente, Enschede, The Netherlands*
[3] *Rijnstate Hospital, Arnhem, The Netherlands*
Corresponding author: a.ghanbarzadeh-dagheyan@utwente.nl

Introduction

In recent years, contrast microbubbles have been utilized within various fields of ultrasound imaging [1], including echo particle image velocimetry (echoPIV), which enables investiging of flow characteristics *in vitro* [2] and *in vivo* [3]. Through high-frame-rate imaging of up to 10,000 frames per second, the movement of microbubbles can be tracked inside a flow, and later, with the help of a correlation-based algorithim, velocity vectors can be deduced by a frame-to-frame analysis [2]. This method has become popular especially for studying blood flow and in the context of cardiovascular disease [4].

Given that two-dimensional (2D) ultrasound imaging is the predominant ultrasound modality within medecine, thus far, most studies have used echoPIV to investigate 2D features of blood flow, such as in-plane vortices [5]. This study, however, aims to apply 2D echoPIV in the search of signatures of a 3D flow, called *swirling flow*, inside some helical stents, which were developed to mimic native swirling flow inside the blood [6].

It was hypothesized that if swirling flow existed, (a) it would leave some signatures in the flow, such as increased vector "complexity" and (b) 2D contrast-enhanced ultrasound (CEUS), alongside with echoPIV, would be able to capture these signatures. Therefore, an in-vitro study was designed to test these hypotheses.

Methods

Three helical stents (Veryan, UK) with three different levels of helicity were CT-scanned with the aim of creating helical lumens replicating the original stent geometries (Fig. 1-(a)). They all had an inner diameter of 7 mm and an straight length of 150 mm, developed for the superficial femoral artery (SFA). These stents were implemented in thin-walled tubes at different compression levels to mimic the compression values that occur in the SFA in various postures of the leg [7]. The recreated geometries were tubulated and 3D-printed using a flexible resin (Flexible-80A, Formlabds, USA). They were then installed in a flow setup consisting of a gylcerol-based blood-mimiking fluid [7], a pulsating pump (Vivitro, Canada),
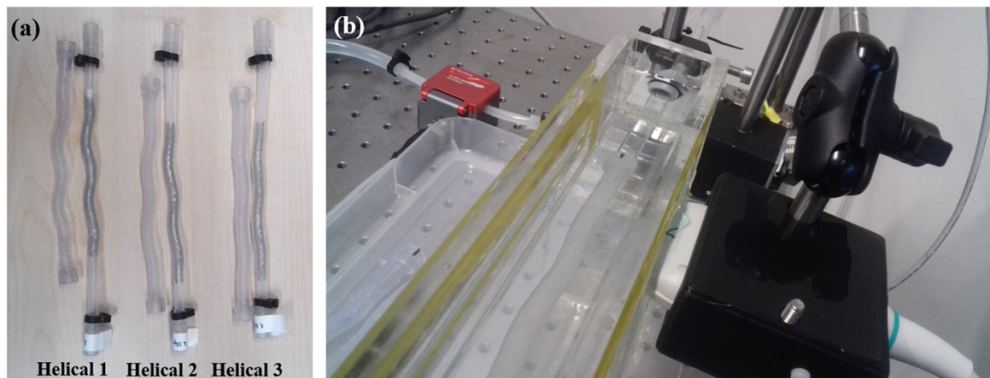

Figure 1. Experimental setup: (a) the helical stent models (right: original stents, left: 3D printed models) with three levels of helicity, from the most helical (Helical 1) to the least helical (Helical 3), (b) Ultrasound imaging of Helical 2 with L12-3 probe. The model was submerged in water.

flow sensors (Sonotec, Germany), and several resistances and a compliance to control the flow rate profile within the fluid circuit. The flow rate was set to mimic the cardiac cycle in the SFA [8].

In-house microbubbles (Physics of Fluid, University of Twente, NL [9]) in a mixture of 6 to 8 micrometers in diameter were injected in the circulating fluid to serve as contrast agents for utrasound imaging. Vatnage-256 system and L12-3 ultrasound probe (both from Verasonics, USA) were used to acquire and record the data at the inlet and outlet of each stent model (8 datasets in total). L12-3 (number of elements: 192, elevation focus: 20 mm, sensetivity: -58.4 dB) was set to work at 7.5 MHz and a maximum voltage of 5 V. The Verasonics code was configured to do planewave imaging—for fast acquisition—and the framerate was set at 2000 fps for a duration of 4 seconds. A probe holder was designed to stably position the probe, align it with the central plane of stent models, and keep the lumens not far from the elevation focus of the probe (Fig. 1-(b)).

The aquired images were processed with the echoPIV algorithm and velocity vector fields for all the frames were extracted. In computing the correlation values, four passes were used and the kernel sizes in each pass were respecitvely P1(64×64), P2(32×32), P3(16×16), and P4(16×16) in pixels. Next, vector complexity was calculated according to the following equation [10]:

$$VC = 1 - \sqrt{\bar{x}^2 + \bar{y}^2}$$

where

$$\bar{x} = \frac{1}{n}\sum_{i=1}^{n}\cos\theta_i \, , \bar{y} = \frac{1}{n}\sum_{i=1}^{n}\sin\theta_i$$
$$\theta_i = \tan^{-1}(v_i, u_i)$$

in which u_i and v_i represent the axial and lateral components of each velocity vector and n is the number of vectors in the field. Finally, the mean value of VC was calcuated for three cardiac cycles and it was utilized as a metric to test the hypothesis.

Results

The vector field output of echoPIV is shown in Fig. 2-(a), averaged for one cardiac cycle and calculated over a region of interest, 1 cm alongside the lumen of the stent model and spanning over its diameter. The
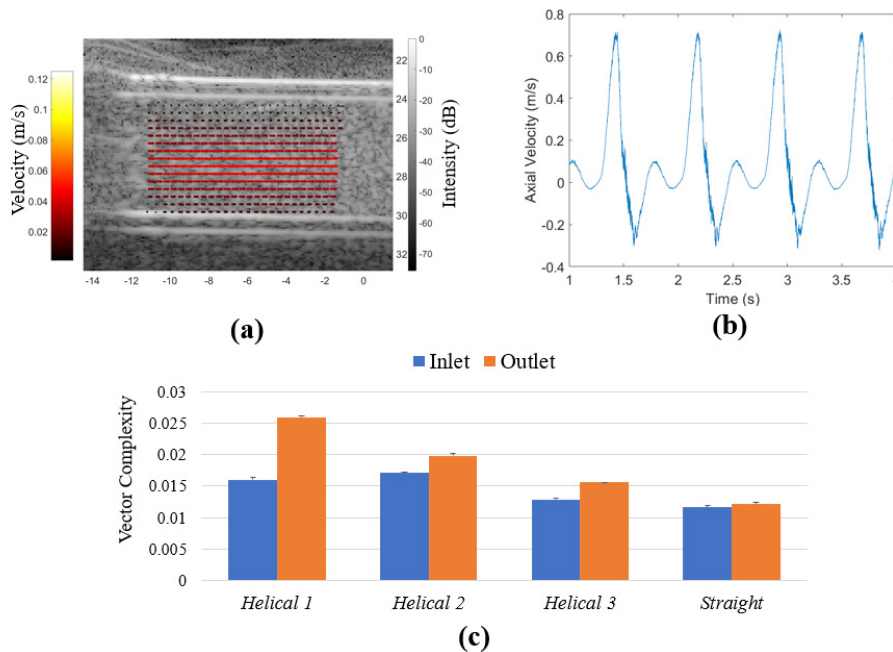

Figure 2. Contrast imaging for flow characterization: (a) Velocity vector field, averaged over one cardiac cycle, the outlet of Helical 1, (b) axial velocity profile over time in the central point of the vector field, (c) vector complexity (VC) calculated for all the inlets and outlets and averaged over three cardiac

The velocity profile in the central point of the vector field in Fig. 2-(a) is shown over time in Fig.2-(b), matching with the profile reported in [8]. Figure 2-(c) shows VC values, averaged over three cardiac cycles, with standard error bars ($\sigma/\sqrt{N}$, with σ denoting standard deviation and $N = 3$, number of cycles). It is clear that in each helical stent model, VC is meaninfully higher in the outlet than in the inlet. This increase is about 62.2%, 15.7%. and 20.9% for Helical 1, 2, and 3 respectively, while the difference between VC in the inlet and outlet of the straight stent is only 4.7%. Also, it is noticeable that in all helical cases, VC is higher than that of the straight, whether in the inlet or the outlet. Higher VC in the inlet of the helical models with respect to that of the straight model may be due to the backflow caused by the higher flow resistance due to the helical shape.

Conclusions

In this study, 2D contrast-enhanced ultrasound (CEUS) was applied to characterize a 3D flow caused by the helical shape of three different stent models. Several observations can be made from the results: (i) using 2D CEUS, one can characterize flow in the inlet and outlet of stent models of diameters as small as 7 mm, (ii) the characterizion and vector field calculation by echoPIV is sensentive to changes in vector complexity (VC), serving as a metric for flow characterization, and (iii) the helical shape of the stents which is expected to generate 3D swirling flow leave signatures such as increased VC in the vector field, measurable by echoPIV. These observations validate the hypothesis of this study. The results also show that CEUS, alognside with echPIV, is a sensetive method for flow characterization in medical stent models.

References

[1]. Yusefi, Hossein, and Brandon Helfield. "Ultrasound Contrast Imaging: Fundamentals and Emerging Technology." Frontiers in Physics (2022): 100.

[2]. Hoving, Astrid M., et al. "In vitro performance of echoPIV for assessment of laminar flow profiles in a carotid artery stent." Journal of medical imaging 8.1 (2021): 017001.

[3]. Walker, Andrew M., et al. "In vitro post-stenotic flow quantification and validation using echo particle image velocimetry (Echo PIV)." Experiments in fluids 55.10 (2014): 1-16.

[4]. Engelhard, Stefan, et al. "High-frame-rate contrast-enhanced US particle image velocimetry in the abdominal aorta: first human results." Radiology 289.1 (2018): 119-125.

[5]. Prinz, Christian, et al. "Can echocardiographic particle image velocimetry correctly detect motion patterns as they occur in blood inside heart chambers? A validation study using moving phantoms." Cardiovascular ultrasound 10.1 (2012): 1-10.

[6]. Sullivan, Timothy M., et al. "Swirling flow and wall shear: evaluating the biomimics 3d helical centerline stent for the femoropopliteal segment." *International Journal of Vascular Medicine* 2018 (2018).

[7]. Poulson, William, et al. "Limb flexion-induced axial compression and bending in human femoropopliteal artery segments." Journal of vascular surgery 67.2 (2018): 607-613.

[8]. Brindise, Melissa C., Margaret M. Busse, and Pavlos P. Vlachos. "Density-and viscosity-matched Newtonian and non-Newtonian blood-analog solutions with PDMS refractive index." Experiments in fluids 59.11 (2018): 1-8.

[9]. Mohajer, Kiyarash, et al. "Superficial femoral artery occlusive disease severity correlates with MR cine phase-contrast flow measurements." *Journal of Magnetic Resonance Imaging: An Official Journal of the International Society for Magnetic Resonance in Medicine* 23.3 (2006): 355-360.

[10]. Segers, Tim, et al. "Stability of monodisperse phospholipid-coated microbubbles formed by flow-focusing at high production rates." Langmuir 32.16 (2016): 3937-3944.

[11]. Saris, Anne ECM, et al. "In vivo blood velocity vector imaging using adaptive velocity compounding in the carotid artery bifurcation." Ultrasound in medicine & biology 45.7 (2019): 1691-1707.

Ambient pressure dependent scattering of shell-tuned monodisperse microbubbles

Benjamin van Elburg[1], Wilmer Schroer[1], Nathan Blanken[1],
Michel Versluis[1], Guillaume Lajoinie[1], and Tim Segers[2]

[1]_Physics of Fluids Group and Technical Medical (TechMed) Center,_
University of Twente, The Netherlands
[2]_BIOS Lab-on-a-Chip group,_
Max-Planck Center Twente for Complex Fluid Dynamics,
MESA+ Institute for Nanotechnology, University of Twente, The Netherlands
Corresponding authors: b.vanelburg@utwente.nl, t.j.segers@utwente.nl

Introduction

Today, local blood pressure measurement in vivo is only possible through the invasive insertion of a pressure sensitive catheter. Pressure measurement deep in the body, e.g. in arteries and the portal vein, is therefore risky as it may induce haemorrhage and infection. Microbubbles bear potential as non-invasive pressure sensors since their nonlinear echo response can be strongly dependent on the ambient pressure, in particular the subharmonic [1]. The pressure-induced change in subharmonic signal originates from the nonlinear dependence of the interfacial tension on surface dilatation [2]. The subharmonic response is then governed by the change in stiffness around the equilibrium interfacial tension [2]. Thus, the non-linear response can be enhanced by increasing shell stiffness. Furthermore, as the bubble echo is strongly dependent on the microbubble size, high precision sensing requires the use of monodisperse microbubbles. [3]. Here, we study the role of microbubble stiffness and concentration on the change in subharmonic response with an increase in ambient pressure.

Methods

Monodisperse C_4F_{10}-filled microbubbles were produced in a flow-focusing device [4] operated at 55°C and using a gas mixture of 15 v% C_4F_{10} in CO_2 [5,6,7] (Fig. 1A). The lipid mixtures comprised DSPC and DPPE-PEG5000 mixed at a 9:1 molar ratio and at a total concentration of 12.5 mg/mL. Palmitic acid (PA) was added at 30 mol% and 45 mol% to tune the dilatational shell stiffness curve. These shell stiffness curves (Fig. 1B) were measured using ambient pressure dependent attenuation measurements [4]. The maximum stiffness for 0 mol% PA was 0.6 N/m and for 30 and 45 mol% PA it was 1.4 N/m and 2.5 N/m, respectively. The acoustic scattering response of the microbubbles was measured inside a custom-made bubble container that can be pressurized (Fig. 1C). Narrowband 16-cycle ultrasound pulses were transmitted and echos were recorded using the Verasonics system and the P4-1 probe transmitting at a frequency of 3.4 MHz. The acoustic pressure amplitude was 75 kPa. The employed mean microbubble size of all bubble suspensions was such that the ensemble resonance frequency was 1.7 MHz, which was exactly half of the driving frequency (3.4 MHz) in order to most efficiently drive a subharmonic response. These frequencies were selected such that both fall within the bandwidth of the ultrasound probe at a similar sensitivity.

Results

Fig. 1D shows the change in subharmonic scattered power for the three microbubble suspensions. The bubbles with a maximum stiffness of 0.6 N/m did not generate subharmonic signals that exceeded the noise level of the imaging system, also not at increased ambient pressures. However, the subharmonic response of the stiffer bubbles exceeded the noise level and did strongly depend on the ambient pressure. The stiffest microbubbles (2.5 N/m) presented an 8-dB increase in subharmonic power over a 100 mmHg increase in ambient pressure.

The change in subharmonic power upon a 200 mmHg increase in ambient pressure with respect to athmospheric pressure, and as function of bubble concentration and depth inside the container, is plotted in

Fig. 1E for the microbubbles with a maximum stiffness of 0.5 N/m. The subharmonic response disappears both with an increase in bubble concentration and with an increase in imaging depth. By contrast, the subharmonic signal of the bubbles with the stiffest shell (2.5 N/m, Fig. 1F) increases with both bubble concentration and imaging depth.
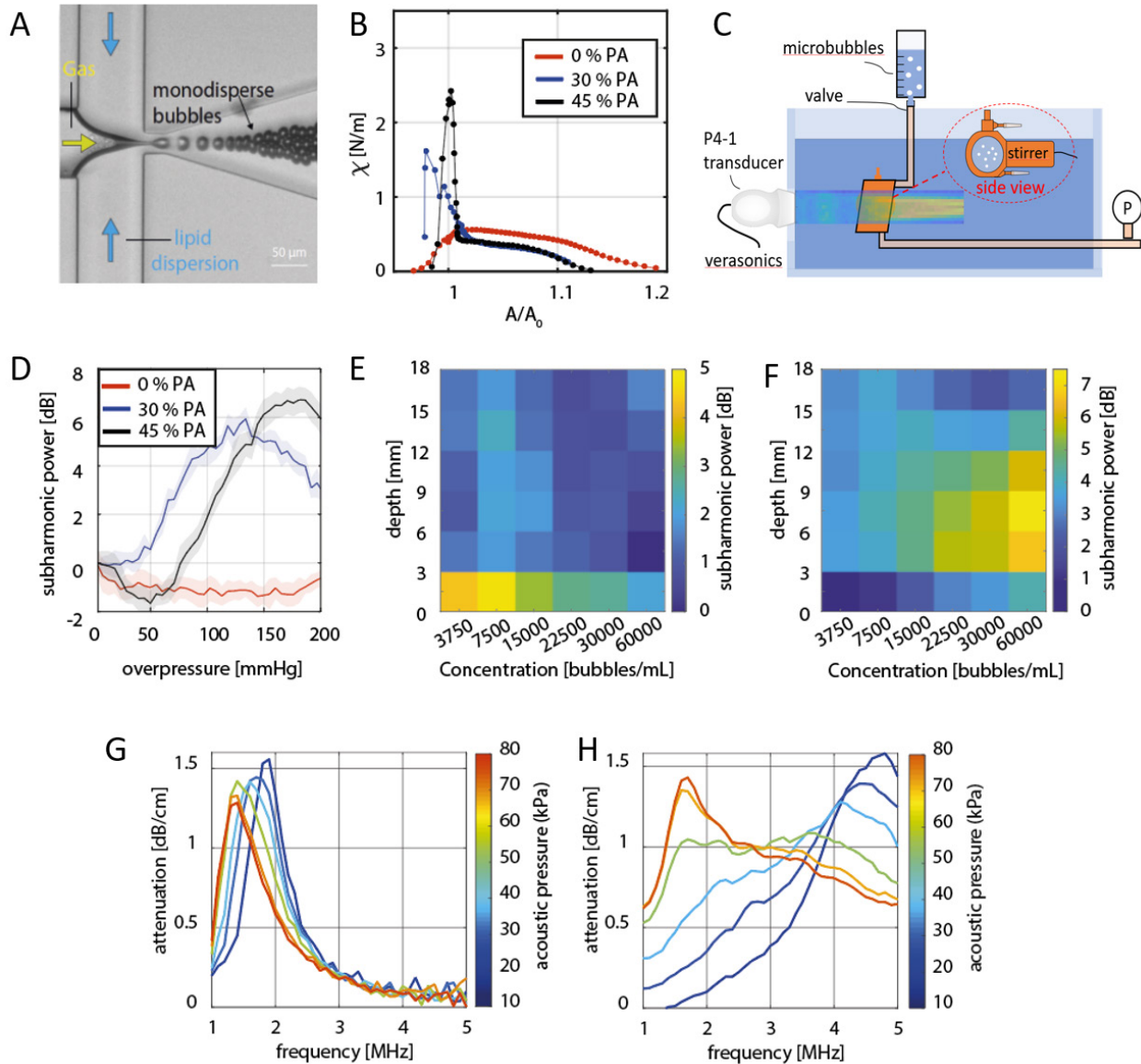
Figure 1. (A) Monodisperse microbubbles were produced in a flow-focusing device. (B) Microbubble stiffness as a function of normalized surface area. Adding palmitic acid (PA) to the shell formulation resulted in a stiffer bubble shell. (C) Schematic of the setup used to measure the microbubble response. The sample holder can be pressurized. (D) Change in subharmonic response versus overpressure. Microbubbles with a stiffer shell show a strong ambient pressure dependency of the subharmonic echo. (E) and (F) The change in subharmonic signal strength for 0% PA and 45% PA bubbles, respectively, between 0 mmHg and 200 mmHg overpressure as a function of bubble concentration and depth inside the bubble container. (G) Attenuation spectra for bubbles with a maximum shell stiffness of 0.6 N/m at acoustic pressures ranging from 10 to 80 kPa in steps of 10 kPa. For these bubbles, the shift in resonance frequency upon an increase in acoustic driving pressure is low as compared to that measured for bubbles with a maximum shell stiffness of 2.5 N/m, as shown in (H).

This remarkably different behavior is explained by the acoustic pressure dependent resonance frequency, which is entirely different for bubbles with a shell stiffness of 0.6 N/m as compared to that of bubbles with a stiffness of 2.5 N/m. The resonance frequency corresponds to the frequency of maximum attenuation in an attenuation spectrum. Figures G and H show the attenuation spectra of the microbubble suspensions with the lowest and the highest stiffness (0.6 N/m versus 2.5 N/m), respectively. The frequency of maximum attenuation decreases when the acoustic pressure in increased. This shift is caused by the decrease in effective shell stiffness as the amplitude of oscillation increases. For the bubbles with the stiffest shell, the shift in resonance frequency is more than 5 times larger than that for the bubbles with the lowest shell stiffness (compare Figs. 1G and H). The frequency of the subharmonic echo generated by both bubble suspensions is 1.7 MHz. For the bubbles with the lowest shell stiffnes, this 1.7 MHz subharmonic echo falls well within the attenuation spectrum of the bubbles driven at low acoustic pressure (dark blue curve in Fig. 1G). Thus, as the pressure waves generated by a bubble are of low amplitude, the subharmonic echo generated by a bubble is strongly attenuated while traveling through the bubble suspension on its way to the imaging probe. However, for the bubbles with the highest shell stiffness, the subharmonic echo at 1.7 MHz does not overlap with their resonance curve at low acoustic pressure. There, the subharmonic echo generated by a stiff bubble is barely attenuated by the other bubbles in the suspension. To conclude, an increase in shell stiffness not only boosts the subharmonic echo response (Fig. 1D), it also allows the subharmonic echo to travel through the bubble cloud at low attenuation thereby potentially allowing deep-tissue subharmonic pressure sensing.

Conclusions

Increasing the shell stiffness of monodisperse microbubbles greatly increases their ambient pressure sensitivity. The stiff microbubbles generate a stronger ambient pressure dependent subharmonic response. Furthermore, the microbubbles with a stiff shell attenuate their own subharmonic echo less than bubbles with a lower shell stiffness potentially allowing non-invasive pressure sensing deep in the body at increased bubble concentrations.

References
[1]. C. Tremblay-Darveau, R. Williams, and P. N. Burns. Measuring absolute blood pressure using microbubbles. Ultrasound in Medicine & Biology 40(4), 775-787 (2014).

[2]. J. Sijl, B. Dollet, M. Overvelde, V. Garbin, R. Rozendal, N. De Jong, D. Lohse, and M. Versluis. Subharmonic behavior of phospholipid-coated ultrasound contrast agent microbubbles. The Journal of the Acoustical Society of America 128(5), 3239-3252 (2010).

[3]. Tim Segers, Pieter Kruizinga, Maarten P. Kok, Guillaume Lajoinie, Nico de Jong, Michel Versluis, Monodisperse Versus Polydisperse Ultrasound Contrast Agents: Non-Linear Response, Sensitity, and Deep Tissue Imaging Potential, Ultrasound in Medicine & Biology, Volume 44, Issue 7, 2018.

[4]. Tim Segers, Emannuel Gaud, Michel Versluis, and Peter Frinking. High-precision acoustic measurements of the nonlinear dilatational elasticity of phospholipid coated monodisperse microbubbles. *Soft matter*, *14*(47), 9550-9561 (2018).

[5]. T. Segers, A. Lassus, P. Bussat, E. Gaud, and P. Frinking, "Improved coalescence stability of monodisperse phospholipid-coated microbubbles formed by flow-focusing at elevated temperatures," Lab on a Chip, 19.1: 158-167, 2019.

[6]. T. Segers, E. Gaud, G. Casqueiro, A. Lassus, M. Versluis, and P. Frinking, "Foam-free monodisperse lipid-coated ultrasound contrast agent synthesis by flow-focusing through multi-gas-component microbubble stabilization", Applied Physics Letters, 116.17: 173701, 2020.

[7]. Benjamin van Elburg, Gonzalo Collado-Lara, Gert-Wim Bruggert, Tim Segers, Michel Versluis, and Guillaume Lajoinie, Feedback-controlled microbubble generator producing one million monodisperse bubbles per second, Review of Scientific Instruments 92, 035110 (2021)

Creating Positively Charged Surfactant Microbubbles for Loading Negatively Charged Therapeutics

Brian E. Oeffinger[1], Meredith Y. Davies[1], Ankit S. Patel [1], John R. Eisenbrey[2], Margaret A. Wheatley[1]

[1]*School of Biomedical Engineering, Science and Health Systems, Drexel University, Philadelphia, USA*
[2]*Department of Radiology, Thomas Jefferson University, Philadelphia, USA*
Corresponding author: maw25@drexel.edu

Introduction

Our group has developed a surfactant-stabilized microbubble platform with a shell composed of sorbitan monostearate (Span 60) and water-soluble vitamin E (α-tocopheryl polyethylene glycol succinate, abbreviated as TPGS), named SE61, which we have used for imaging and targeted theraputic delivery utilizing ultrasound. We have successfully used these microbubbles filled with oxygen to target hypoxic tumors,[1] and have utilized the hydrophobic nature of the surfactant tails of the bubble shell to co-deliver hydrophobic pharmacological agents such as lonidamine and paclitaxel.[2,3] These hydrophobic areas, however, are not condusive to loading hydrophilic or charged agents.

One possible way to load hydrophilic theraputics to SE61 would be to create a charged surface to attach electrostatically. Cationic microbubbles loaded with plasmid DNA in combination with ultrasound have been shown to improve gene transfection, while attachment of siRNA also improves transfection.[4-7] Other hydrophilic molecules, such as the sodium salt of xanthene dye, rose bengal (974 g/mole MW), which has been utilized for ultrasound guided sondynamic therapy [8], have the potential to be loaded in this manner.

This work characterized the zeta potential of SE61, and investigated the insertion of cationic molecules to create a positively charged microbubble for loading of anionic therapeutic agents. The zeta potential of SE61 is likely negative, as mixtures containing Span 60 have been reported to have a zeta potential near -30 mV due to the orientation of water molecules caused by hydrogen bonding with hydroxyl groups.[9] Cationic microbubbles used for plasma DNA loading have had zeta potentials ranging 30-60 mV. [5,6]

Methods

SE61 microbubbles were fabricated using a previously reported method with appropriate modifications.[10] Briefly, standard SE61 microbubbles were created using an 85 mM surfactant mixture comprised of TPGS (20%) and Span 60 (80%) in PBS (phosphate buffered saline) with added sodium chloride (30g/L). Probe sonication at 20kHz while purging with octofloropropane gas created microbubbles, which were then washed and separated by gravity. Collected microbubbles were diluted 1:1 with 10% w/v glucose (cryo/lyoprotectant), frozen using a -20°C bath, lyophilized for 18-20 h, then sealed under vacuum. Prior to testing, the vials were filled with octofloropropane and reconstituted with 0.5x PBS.

The following cationic surfactants and lipids were added to the surfactant mixture at 5%, 15%, and 25% molar ratios: hexadecyltrimethylammonium bromide (CTAB), didodecyldimethylammonium bromide (DDAB), 1,2-dioleoyl-3-trimethylammonium-propane (DOTAP), 1,2-stearoyl-3-trimethyl-ammonium-propane (DSTAP), and 1,2-dimyristoyl-3-trimethylammonium-propane (DMTAP). Total surfactant concentration was kept constant at 85 mM, and TPGS and SPAN 60 reduced, keeping a relative 1:4 ratio. Acoustical dose responses of the microbubbles were conducted using a custom *in vitro* setup that closely mimics *in vivo* conditions,[11] consisting of a pulsed 5 MHz transducer focused in a sample vessel submerged in a water bath (37°C). Bubble size and concentrations were measured using an AccuSizer A7000 (Entegris Inc., Billerica MA, USA). Zeta potentials were determined using a Zetasizer Nano ZS (Malvern Inst., Worcestershire, UK).

Rose bengal and double stranded DNA were added to 15% CTAB microbubbles to evaluate loading potential. Rose bengal (100 mg) was added to approximately 120 mL of microbubbles after the first

wash/seperation step, followed by 3 washes with deionized water, then collected and freeze dried as above. Rose bengal loading was determined by reconstituting microbubbles with ethanol and measuring absorption using a Synergy H1 plate reader (BioTek, Winooski, VT, USA) at 560 nm and comparing to a standard curve. Microscope images were taken using an IX71 flourescent microscope (Olympus, Tokyo, Japan), using a TRITC filter for flourescent imaging.

Double stranded DNA comprised of 21 base pairs (5'–AATGAGCCCTTGCATCTAAGAA-3') was utilized as a model for siRNA. After the wash and seperation steps, a solution of 250 mM dsDNA and a solution of 20% w/v glucose (cryoprotectant for future freezing) was added to collected microbubbles in a 1:1:2 ratio. These bubbles were then tested by adding 5mL deionized water to the loaded microbubbles and allowing dsDNA-loaded microbubbles to seperatedue to gravity. The resulting wash with remaining unattached dsDNA was collected and tested using the Quant-iT PicoGreen dsDNA assay (invitrogen) with the starting amount of dsDNA subtracted to determine loading.

Results

Pre-freeze drying, standard SE61 was found to have a mean size of 2.2 μm, a concentration of 3.2×10^9 bubbles/mL, and a zeta potential of approximately -40 mV. Freeze drying resulted in a loss of microbubbles, reducing the concentration to 1.1×10^9 bubbles/mL, including distruction of a population between 3 and 6 μm, which reduced the mean bubble size to 1.6 μm. The zeta potential was approximately -30 mV, and the maximum acoustic responses for reconstituted freeze dried SE61 was above 15dB.

CTAB was successfully incorporated into the SE61 microbubbles, increasing the zeta potential, shown in Figure 1. Both 15% and 25% CTAB microbubbles were near or above +30 mV when measured pre and post freeze drying. As the amount of CTAB increased, the concentration of bubbles increased, ranging from 2.3 to 7.8×10^9 bubbles/mL pre freeze drying, while the mean bubble size decreased, ranging from 2.5 to 1.6 μm. All CTAB bubbles generated acceptable accustical responses greater than 15dB.

Incorporating DDAB and DOTAP (both of which have double, hydrophobic tails poorly oriented to fit into the SE61 microbubble) was difficult, likely due to steric interferance in the microbubble shell. While addition of DDAB to SE61 did increase the zeta potential to at least +30 mV for 25% DDAB pre and post freeze drying, increasing the amount of DDAB decreased the concentration of bubbles created during sonication, from 3.4×10^9 bubbles/mL for 5% DDAB to 0.73×10^9 bubbles/mL for 25% DDAB, which made the wash steps difficult. Increased amounts of DOTAP prevented SE61 microbubble formation during sonication, and only 5% DOTAP solutions resulted in bubbles sutable for testing. Pre and post freeze drying zeta potentials of 5% DOTAP bubbles were less than +15 mV.
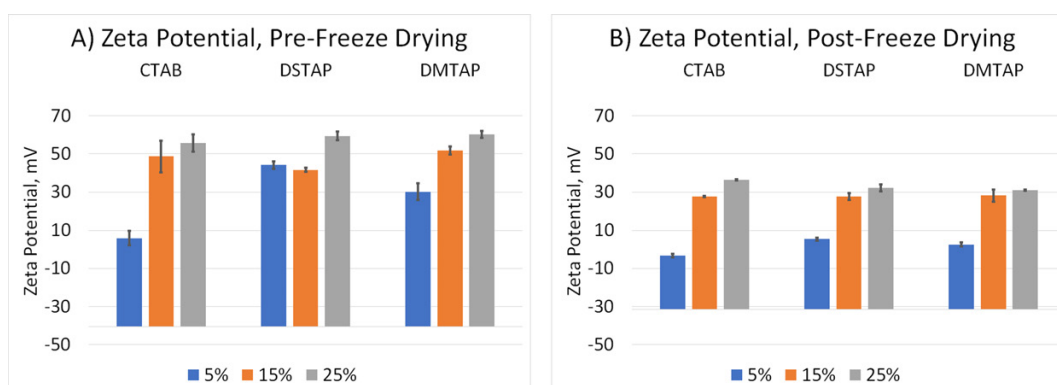
Figure 1. Zeta potentials of 5%, 15% and 25% loaded SE61 microbubbles using CTAB, DSTAP and DMTAP both a) pre-freeze drying and b) post-freeze drying. The values of the bottom of the bars represents the zeta potential for unmodified SE61.

Both DSTAP and DMTAP (with more accomodating double hydrophobic tails) were successfully incorporated into the SE61 microbubble, increasing the zeta potential, as shown in Figure 1. For both DSTAP and DMTAP, 15% and 25% microbubbles were near or above +30 mV when measured pre and

post freeze drying. No major shifts in bubble populations were observed as the amount of DSTAP and DMTAP were increased, with a minimum of 3.4×10^9 bubbles/mL created during sonication. All freeze-dried bubbles had acceptable accustical responses greater than 15dB.

Exploratory studies were conducted using 15% CTAB-loaded SE61 (more available) to determine the feasability of attracting anionic species. Rose bengal was found to be loaded onto 15% CTAB SE61 in a concentration of 23.5 µg/mL of microbubble (4.2% loading) compared to 1.5 µg/mL of microbubble (0.3% loading) unmodfided SE61. Images in Figure 2, taken using a flouresent microscope, clearly show rose bengal loading onto the walls of the 15% CTAB SE61, but not unmodified SE61. Short dsDNA fragments were also able to be loaded onto the surface of 15% CTAB, with 373 µg/mL DNA / mL of microbubble (63.5% loading) attached compaired to essentially undetectable (-1.0% loading) with unmodified SE61.

Figure 2. Rose bengal loaded microbubbles images of unmodified SE61 with a) brightfield and b) flourescence (TRITC filter) and of 15% CTAB SE61 with c) brightfield and d) flourescence. Bars = 20µm.

Conclusions

SE61 microbubbles, which have a negative zeta potential (-30mV), can be modified with the addition of carefully selected cationic molecules such as the surfactant CTAB or the lipids DSTAP and DMTAP to create a positively c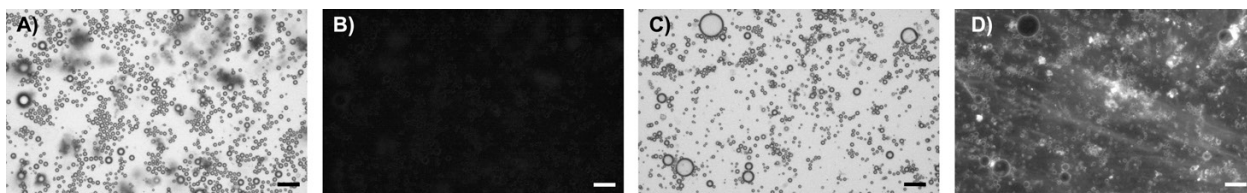harged bubble while still maintaining approraite size and accoustical properties for ultrasound contrast agents. The resulting positively charged microbubbles can be loaded with a variety of negatively charged theraputic agents, such as rose bengal (useful in sonodynamic therapy) and nucleic acids (useful in gene and siRNA delivery), which would be suitable for targeted delivery mediated by ultrasound.

References

[1]. Eisenbrey JR, et al., Sensitization of Hypoxic Tumors to Radiation Therapy Using Ultrasound-Sensitive Oxygen Microbubbles, Int. J. Radiat. Oncol. Biol. Phys., 101:88-96, 2018.

[2]. Patel R, et al., Development of a Dual Drug-Loaded, Surfactant-Stabilized Constrast Agent Containing Oxygen, Polymers, 14:1568, 2022.

[3]. Lacerda Q, et al., Tumoral oxygenation and biodistribution of Lonidamine oxygen microbubbles following localized ultrasound-triggered delivery, Int. J. Pharm, 625, 2022.

[4]. Christiansen JP, et al., Targeted tissue transfection with ultrasound destruction of plasmid-bearing cationic microbubbles, Ultrasound in medicine & biology, 29:1759-1767, 2003.

[5]. Borden MA, et al., DNA and Polylysine Adsorption and Multilayer Construction onto Cationic Lipid-Coated Microbubbles, Langmuir, 23:9401-9408, 2007.

[6]. Nomikou, et al., Studies on neutral, cationic and biotinylated cationic microbubbles in enhancing ultrasound-mediated delivery in vitro and in vivo, Acta biomaterialia, 8:1273-1280, 2012.

[7]. Carson AR, et al., Ultrasound-targeted microbubble desrtruction to deliver siRNA cancer therapy, Cancer research, 72:6191-6199, 2012.

[8]. Hou R, et al., In situ conversion of rose bengal microbubbles into nanoparticles for ultrasound imaging guided sonodynamic therapy with enhanced antitumor efficacy, Biomaterals Science, 8:2526, 2020.

[9]. Hong IK, Kim SI, Lee SB, Effects of HLB value on oil-in-water emulsions: Droplet size, rheological behavior, zeta-potential, and creaming index, Journal of industrial and engineering chemistry, 67:123-131, 2018.

[10]. Oeffinger BE, et al., Preserving the Inegrity of Surfactant-Stabilized Microbubble Membranes for Localized Oxygen Delivery, Langmuir, 35:10068-10078, 2019.

[11]. Wheatley MA, et al., Comparison of in vitro and in vivo acoustic response of a novel 50:50 PLGA contrast agent, Ultrasonics, 44:360-367, 2006.

Optimising the manufacture of lipid-shelled perfluorocarbon nanodroplets through varying sonication parameters

Christopher K. Campbell[1], _Kirsten O'Brien[1], Dariusz Kosk[1], Gareth LuTheryn[2],_
Jonathan P. May[1], Peter Glynne-Jones[1], Jeremy Webb[3], Peter R. Birkin[3], Nicholas D. Evans[1],
Dario Carugo[2]

[1]_School of Engineering, University of Southampton, Southampton, U.K._
[2]_School of Pharmacy, University College London, London, U.K._
[3]_School of Chemistry, University of Southampton, Southampton, U.K._
[4]_National Biofilms Innovation Centre (NBIC), School of Biological Sciences, University of Southampton, Southampton, U.K._
Corresponding author: c.k.campbell@soton.ac.uk

Introduction:

Perfluorocarbon-core nanodroplets (NDs) have emerged as a promising system in the field of antimicrobial interventions, particularly in the treatment of biofilm-associated infections. Nitric oxide (NO) is a potent signalling molecule known to induce biofilm dispersal; however, it has an extremely short half-life, making it difficult to deliver to a biofilm in therapeutically relevant amounts. The liquid perfluorocarbon (PFC) core of NDs is stabilised by a lipid shell, and can be loaded with NO [1]. PFC NDs are responsive to ultrasound waves and can be converted into gas-filled microbubbles through acoustic droplet vapourisation (ADV) [2]. Microbubble cavitation can then be induced, and has the potential to increase temporal control over the release of therapeutic molecules loaded into or on the droplet. These characteristics of NDs make them a promising platform for co-delivery of biofilm dispersal promoters (such as NO) and antibacterial compounds. PFC NDs therefore present a potential improvement in the short-term passive release of NO compared to gas-core NO microbubbles [1]. Use of sonication to manufacture NDs is a highly stochastic process, and control over the resulting ND populations is possible through modification of sonication parameters [3]. Control over the mean diameter and size dispersity of NDs will allow for optimisation of the acoustic response of these droplets: a lower size dispersity will lead to a more uniform reponse [4].

This study aims to elucidate the changes in nanodroplet size when manufactured with varying sonication parameters and to develop a method for controlling the temperature of samples during manufacture.

Methods

To manufacture nanodroplets, a lipid solution and perfluoro-n-pentane (PFP, Strem Chemicals, UK) were emulsified by two-stage sonication, using a Model 120 Sonic Dismembrator (Fisher Scientific, UK). The general protocol for ND manufacture was modified from Ferri _et al._ [3].

Lipids were dispersed in phosphate-buffered saline (PBS) in the first-stage of sonication. 1,2-distearoyl-sn-glycero-3-phosphocholine (DSPC) and polyoxyethylene (40) stearate (PEG40S) were combined in a 9:1 molar ratio as the lipid shell constituents. Prior to second sonication, PFP was added in a 1:10 volumetric ratio and vortexed for 5 s to create precursor droplets. The second sonication stage utilised a pulsed regime to allow the sample to cool between pulses. PFP has a bulk transition temperature of 28 °C, and samples must be kept cool to prevent loss of PFP or vapourisation of the droplets during manufacture.

To assess the efficacy of cooling methods during the second sonication step, a reference sonication protocol of 60% amplitude and 60 s total sonication (on) time was used. Two cooling methods were tested, either a ice-water bath or saturated-saline (~26% w/w) ice bath. Pulsed sonication of either 2 s on - 5 s off (duty cycle: ~28.6%) or 2 s on - 15 s off (duty cycle: ~11.8%) were tested .

A thermocouple data logger was used to measure changes in temperature, with measurements taken every 100 ms throughout the varying sonication protocols. Prior to starting sonication, the sample was allowed to cool to the temperature of the surrounding bath. For each sample, three independent repeats were

measured. After manufacture, each sample was measured by nanoparticle tracking analysis (NTA) using a NanoSight NS300 (Malvern, UK).

To assess the effect of varying sonication intensity and length, pulsed sonication consisted of 2 s on and 15 s off. The total sonication on time were varied between 15 and 120 s, in 15 s increments.

The amplitude (%) was varied between 20% and 100%, in 20% increments. Three samples per condition were prepared and then analysed by NTA.

Table 1. Summary of Cooling Bath and Sonication Pulse patterns

Name	Pulse Pattern	Cooling Bath Composition	Average Cooling Bath Temperature (°C)
2/5-I	2 s on, 5 s off	Water + Ice	1.26±0.18
2/15-I	2s on, 15 s off		
2/5-S	2 s on, 5 s off	Saturated-Saline + Ice	-8.54±0.27

Results

The sample temperature changed during sonication (Figure 1). For the 2s on - 5s off pulsation regime the maximum sample temperature reached for the saline-ice bath (2/5-S) was 16.04 °C with a mean temperature of 14.75±1.15 °C at this time-point (191.1s). The maximum temperature reached for the ice-water bath (2/15-I) was 26.68 °C with a mean temperature of 24.84±2.27 °C at this time-point (156.0s). For the 2 s on - 15 s pulsation regime with ice-water bath (2/15-I) the maximum temperature reached was 15.48 °C with a mean temperature of 14.15±1.72 °C at this time-point (495.3s). NTA was used to analyse the size characteristics of nanodroplet samples manufactured with the different cooling bath-sonication regime pairings. Using a one-way ANOVA, no significant difference ($P<0.05$) was found between the median or standard devation of the three test conditions. 2/5-I, 2/15-I and 2/5-S had median values of 191.8±6.7 nm, 192.3±2.2 nm and 187±9.7 nm, respectively. All errors stated are ±1S.D.

A temperature target of <20 °C was set to reduce the likelihood of PFP loss and unnecessary heating. Of the three conditions tested, both 2/15-I and 2/5-S kept samples under this target, with both maintaining sample temperature under 16 °C. Though significant differences between the three conditions are not apparent when analysed by NTA, significant foaming was observed for 2/5-I, indicating bubble formation and potential loss of PFP. The 2/15-I condition was selected for ongoing optimisation experiments varying the amplitude (%) and total sonication time (s).

Conclusions

Both using a saline-ice bath or a longer off time between sonication pulses allowed the ND sample to remain under 16 °C, which is an improvement over the higher temperatures seen in the 2 s on - 5 s off ice-water bath. The combination of 2 s on - 15 s off pulsation regime and an ice-water bath was selected due to the occasional freezing of the ND samples when cooling with the saline-ice bath. Ongoing work is studying the effect of changing sonication intensity and duration on the size characteristics of perfluorocarbon nanodroplet populations.
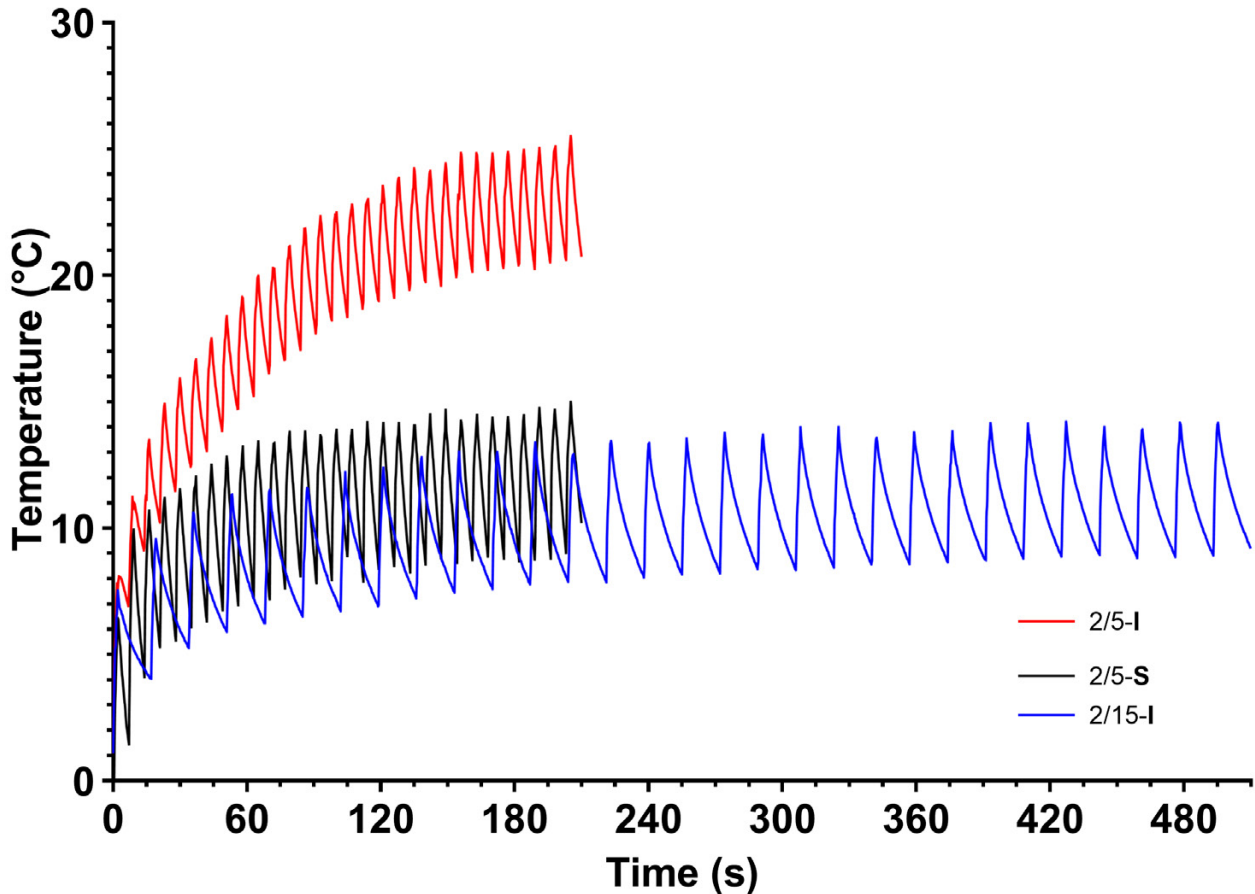
Figure 1. Graph showing changes in temperature over time of three different samples. The water-ice bath cooling method was tested with both 2 s on - 5 s off and 2 s on - 15 s off pulsation regimes (2/5-I, 2/15-I). The saline-ice bath was tested with the 2 s on - 5 s off pulse regime (2/5-S).

References

[1]. Choi, M., Jazani, A.M., Oh, J.K. and Noh, S.M., 2022. Perfluorocarbon Nanodroplets for Dual Delivery with Ultrasound/GSH-Responsive Release of Model Drug and Passive Release of Nitric Oxide. Polymers, 14(11), p.2240.

[2]. Zhou, Y., 2015. Application of acoustic droplet vaporization in ultrasound therapy. Journal of therapeutic ultrasound, 3(1), pp.1-18.

[3]. Ferri, S., Wu, Q., De Grazia, A., Polydorou, A., May, J.P., Stride, E., Evans, N.D. and Carugo, D., 2021. Tailoring the size of ultrasound responsive lipid-shelled nanodroplets by varying production parameters and environmental conditions. Ultrasonics sonochemistry, 73, p.105482.

[4]. Sheeran, P.S. and Dayton, P.A., 2014. Improving the performance of phase-change perfluorocarbon droplets for medical ultrasonography: current progress, challenges, and prospects. Scientifica, 2014.

Carrier-free messenger RNA delivery into cells using albumin-based contrast nanobubbles and a home-made sonoporator

Hiroshi Kida[1], Yutaro Yamasaki[1], Loreto B. Feril[1], Hitomi Endo [1], Katsuro Tachibana[1]

[1]Department of Anatomy, School of Medicine, Fukuoka University, Fukuoka, Japan
Corresponding author: kida_hiroshi@fukuoka-u.ac.jp

Introduction

In recent years, research on the use of messenger RNA (mRNA) as a drug, including vaccines against infectious diseases, has progressed rapidly. Sonoporation, which uses acoustic cavitation of bubble reagents induced by ultrasound (US) irradiation, is the only method that can deliver carrier-free mRNA or plasmid DNA into cells with high efficiency [1]. Albumin-based nanobubbles (A-NBs) stay in the liquid longer than microbubbles and act as cavitation nuclei [2-4]. However, clinical application of carrier-free mRNA delivery into cells by sonoporation for vaccination requires the development of a dedicated device that can be used as easily as a syringe in a clinical setting. Here, we devised an inexpensive, home-made, AA battery powered, hand-held ultrasound device for intracellular delivery of mRNA, which is effective in combination with nanobubbles.

Methods

A portable ultrasound device was fabricated as a sonoporator (acoustic intensity: 0.66 W/cm^2, frequency: 39.5 kHz) (Figure 1). A-NB was generated by dissolving 0.06% albumin in ultrapure water and vibrating it vigorously in a closed container filled with perfluoropropane gas (C3F8). The particle size and concentration of A-NB were measured by nanoparticle tracking analysis (NTA).

Flow phantoms consisting of a square shape container of acrylic resin filled with ultrasound gel pad (Aquaflex ultrasound gel pad; Parker lab, NJ, USA) were custom made for the ultrasound contrast-enhanced imaging experiment setup. The 5 mm diameter cylindrical inner cavity of the phantom was directly perfused with 3x diluted A-NB at 2 mL/min and observed with L8-18i-D probe (4-14 MHz, MI 0.6) on harmonic mode of LOGIQ E9 (GE Healthcare). Ultrasound from a home-made sonoporator was applied from the side during observation to evaluate for acoustic interference.

Ninety-six multi-well plates cultured with HSC2 cells were added opti-MEM containing A-NBs and 500 ng of Gluc mRNA. US was applied from the sonoporator through the polyethylene bottom of the cell culture plate for 15 seconds. After 48 hours of incubation, the luminescence intensity of the supernatant reacted with D-luciferin substrate was measured. Cell viability was measured by MTT assay.

Results

The mean size and concentration of A- NBs were 266.7 ± 17.1 nm and 1.38×10^{10}/ml, respectively (Figure 2).

The increased brightness caused by A-NBs was clearly depicted on ultrasound imaging (Figure 3). The A-NBs were stable and clearly delineated during the 45-second recording time. Furthermore, ultrasound irradiation from the home-made sonoporator did not interfere with the echographic image delineation.

Ultrasound irradiation of A-NBs increased mRNA transfection efficiency by 1.8-fold (Figure 4). Ultrasound irradiation of optiMEM without A-NBs did not increase the efficiency of gene transfer. Cell viavility was decreased to 93.8% when the medium containing A-NBs was irradiated to US. There was no cytotoxicity with US alone.

Conclusions

Our albumin-based nanobubbles was useful both as ultrasound contrast reagents and as drug and gene delivery reagents. Intracellular delivery of carrier-free mRNA was achieved by combining a portable hand-

held sonoporator and albumin-based nanobubbles. It was confirmed that unexpectedly low-intensity and low-frequency ultrasound induced transfection of mRNA. In addition, ultrasound at frequencies as low as 40 KHz would allow simultaneous gene delivery without interfering with diagnostic imaging. The innovative contrast nanobubbles and sonoporator we developed may become the cornerstone of future mRNA drug delivery technology to living organs. Further studies are needed to elucidate the relationship between ultrasound conditions and nanobubble resonance.

Acoustic intensity: 0.66 W/cm^2
Frequency: 39.5kHz
Duration: 15 sec (preset)
AA battery powered
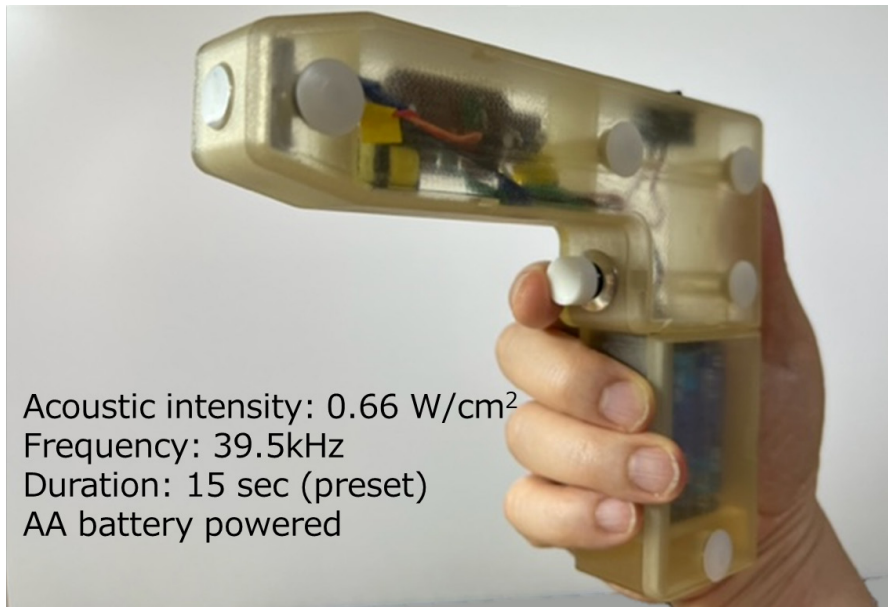
Figure 1. Portable home made sonoporator.

Particle size: 266.7 ± 17.1 nm
Concentration: 1.38×10^{10}/mL
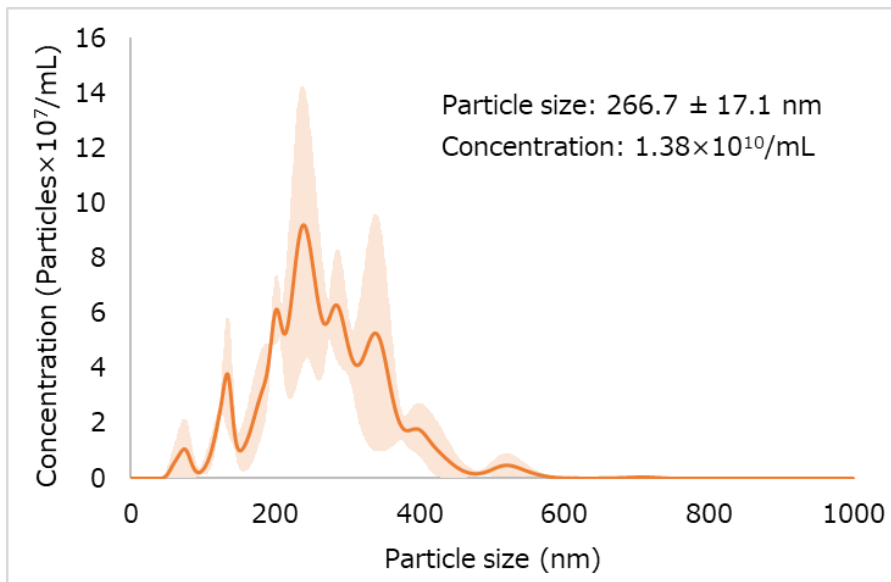
Figure 2. Size distribution and concetration of albumin-based nanobubbles

----
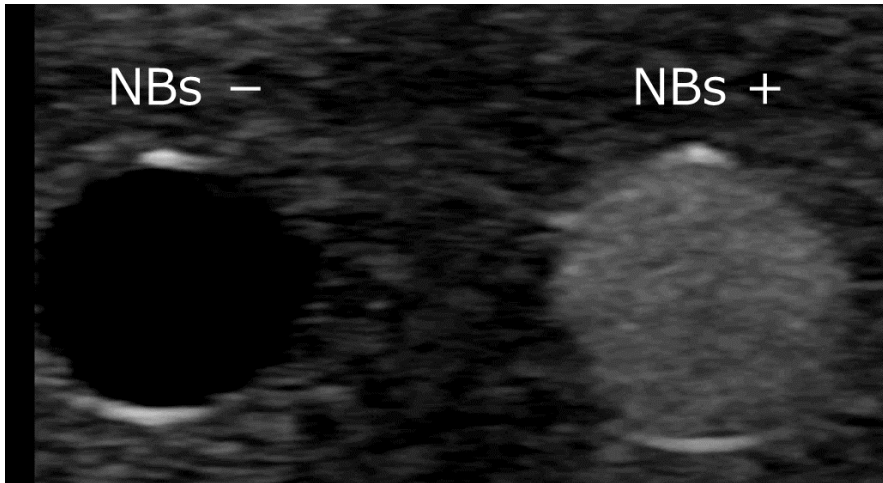
Figure 3. Contrast effect by nanobubbles. NBs: nanobubbles
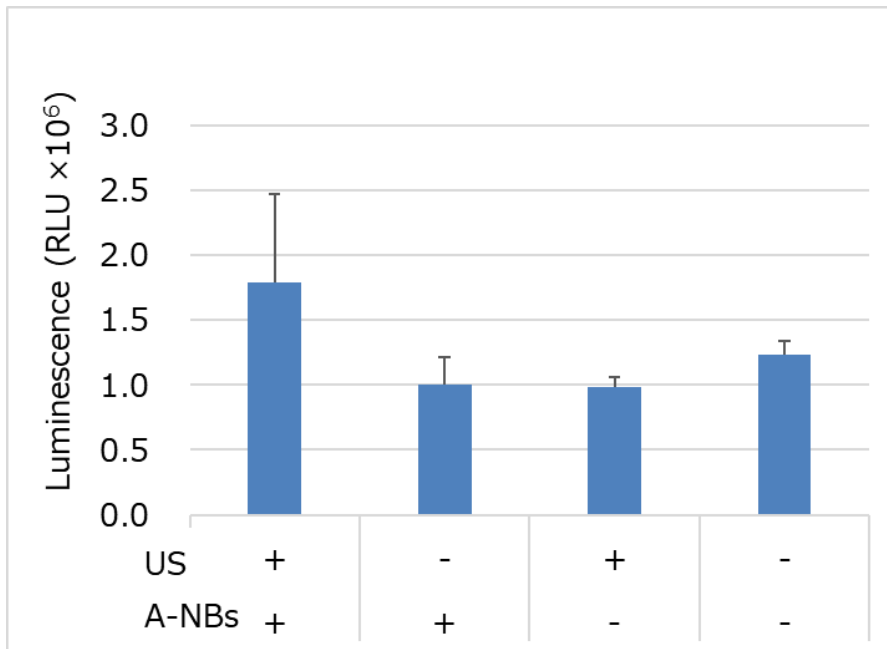
Figure 3. Efficiency of mRNA transfection by combination of ultrasound and nanobubbles.

References

[1]. Kida H, Feril LB, Irie Y, Endo H, Itaka K, Tachibana K. Influence of nanobubble size distribution on ultrasound-mediated plasmid DNA and messenger RNA gene delivery. Frontiers in Pharmacology. 2022;13.

[2]. Lafond M, Watanabe A, Yoshizawa S, Umemura SI, Tachibana K. Cavitation-threshold Determination and Rheological-parameters Estimation of Albumin-stabilized Nanobubbles. Sci Rep. 2018;8(1):7472.

[3]. Watanabe A, Sheng H, Endo H, Feril LB, Irie Y, Ogawa K, et al. Echographic and physical characterization of albumin-stabilized nanobubbles. Heliyon. 2019;5(6):e01907.

[4]. Kida H, Nishimura K, Ogawa K, Watanabe A, Feril LB, Irie Y, et al. Nanobubble mediated gene delivery in conjunction with a hand-held ultrasound scanner. Frontiers in Pharmacology. 2020;11.

Collagenase-Loaded Nanoparticles Enhance Ultrasound Imaging-Guided Sonodynamic Therapy *via* Digesting Stromal Barriers

Jiali Luo [1,2], Tao Zhang [1,2,], and Pintong Huang [1,2,*]*

[1] *Department of Ultrasound in Medicine, The Second Affiliated Hospital of Zhejiang University School of Medicine, No.88 Jiefang Road, Shangcheng District, Hangzhou 310009, P.R. China*
[2] *Research Center of Ultrasound in Medicine and Biomedical Engineering, The Second Affiliated Hospital of Zhejiang University School of Medicine, No.88 Jiefang Road, Zhejiang University, Shangcheng District, Hangzhou 310009, P.R. China.*
Corresponding author: huangpintong@zju.edu.cn

Introduction

Pancreatic cancer has risen to the third-leading cause of death globally in 2022 due to its increasing incidence and mortality rates.[1] Currently, surgical resection is the primary option for curing pancreatic cancer, but 80–85 % of patients have advanced diseases that cannot be resected. Unfortunately, pancreatic cancer responds poorly to the majority of clinical treatments, including chemotherapy and immunotherapy,[1,2] and there is an urgent need for the development of alternative treatment strategies. Sonodynamic therapy (SDT) is an emerging therapeutic tumor treatment tool based on ultrasound, sonosensitizers, and reactive oxygen species (ROS). Briefly, sonosensitizers accumulated in the tumor can generate ROS triggered by ultrasonic exposure and sonoluminescence, which thereby induce cancer cell apoptosis. In addition, due to the negligible tissue attenuation coefficient of ultrasound, SDT can penetrate deep within soft tissues up to a depth of 10 cm and possesses the capability to precisely target the tumor thus avoiding any potential damage to adjacent normal tissues.[3] However, the pancreatic tumor, surrounded by the abundant tumor stroma, is characterized by high interstitial fluid pressures (IFP) and hypoxia tumor microenvironment (TME), which limits the penetration of sonosensitizers into the tumor, causing unsatisfactory SDT efficiency.[4,5] Therefore, overcoming the stromal biological barrier and enhancing ROS generation remain obstacles for efficient SDT treatment of pancreatic cancer.[6]

The barrier to penetration in tumors that limits the delivery of therapeutics is associated with pathophysiological elements comprising the solid tumor microenvironment and the high IFP,[7] which is major in the dense tumor stroma around the tumor.[8] In clinical trials, the strategies for the elimination of the extracellular matrix (ECM) barrier,[9] supplemented with chemotherapeutic treatment have shown advantageous outcomes.[10] Targeting the TME, particularly the ECM barrier, to promote accurate and efficient drug delivery could be a potential technique for treating pancreatic cancer.[11] Hence, several ECM-targeting treatment strategies have been developed to improve therapeutic efficacy in tumor therapy,[12] such as the utilization of hyaluronidase (HAase) and cancer-associated fibroblasts (CAFs).[13] Collagen is the most abundant protein in the ECM of pancreatic cancer.[14] Recent studies have shown that collagen digestion can reduce drug resistance of tumors and improve the efficacy of chemotherapy treatment for pancreatic cancer.[4,15,16] However, encapsulation of proteins into nanoparticles (NPs) must overcome several challenges, including potential protein denaturation during loading and maintenance of a therapeutic release rate at the site of action. Since the half-life of collagenase in circulation declines very rapidly after injection,[15] collagenase-containing therapies require enzyme protection before activation within the target tumor site, the collagenase alone could not cause damage to cancer cells.[4] The ECM barrier and high IFP also restrict the production of ROS. There are numerous strategies to increase ROS production, including increasing the catalytic performance of the sonosensitizer, decorating enzymes, and alleviating the tumor's hypoxic environment.[6,17] Above all, the overall design of efficient sonosensitizers is the essence of effective ROS generation. Therefore, using an efficient sonosensitizer as a carrier and carrying collagenase is a promising strategy to improve SDT efficiency in pancreatic cancer.

An essential requirement in SDT is a sonosensitizer that can achieve a reasonable therapeutic release rate at the site of action under US irradiation. Recently, various sonosensitizers such as organic sonosensitizers and inorganic sonosensitizers have been reported for SDT. [18,19] However, the applications of organic sonosensitizers are restricted by their poor aqueous solubility, chemical instability, and phototoxicity,[20,21] while inorganic sonosensitizers are thought to be great candidates because of their distinctive chemical and

physical features.[21] Inorganic sonosensitizers such as TiO_2 have great potential for SDT,[22] because of their capacity to generate full ROS and excellent chemical stability against ROS.[23,24] However, pure TiO_2 leads to only moderate $^1O_2$ and •OH production due to its quick electron-hole recombination kinetics and narrow-spectrum response to US irradiation restricted by their broad bandgap, thus limiting its clinical application.[25] Numerous approaches, such as generating an oxygen-deficient layer on the surface, have been developed to address this problem.[26] The hollow TiO_2 (H-TiO_2) possesses electron-rich sites, which provide abundant defective species, in particular, oxygen defects which can help to separate electron (e^-) and hole (h^+) produced by US irradiation,[27] so hollow TiO_2 can furnish an increased quantity of ROS (•OH and $^1O_2$) upon US irradiation and be employed as an acoustic sensitizer during SDT to cause oxidative damage of cancer cells.[6, 28] Furthermore, the hollow shell could reach a high drug loading rate.[17]

Herein, a strategy that encapsulated collagenase was developed to alleviate solid stress. The enzyme's activity of collagenase was prolonged and it was protected from early deactivation within plasma via loading into H-TiO_2 (Col-H-TiO_2). This approach can function as a rapid screening test for perfusion-enhancing and stress-reducing drugs. An *in vitro–in vivo* combinatorial phage display method was used in this study to identify novel tumor stroma-targeting NPs that are capable of targeting collagen. Our approach can overcome the stromal biological barrier and enhance the production of ROS to improve the efficacy of SDT in pancreatic cancer. It also accomplished treatment visualization.

Methods

Synthesis of Hollow Titanium Dioxide (H-TiO_2)

First, the Stöber method was used to prepare silica NPs.[29] 2.3 mL tetraethyl orthosilicate (TEOS; Aladdin, China) was added to a mixture comprising 60 mL ethanol, 3 mL ammonia water, and 1mL deionized water. A silica template was produced after 6 h of reaction at 50°C with stirring. Then, the prepared silica was redispersed in a mixed solution of 130 mL of ethanol and 2 mL of deionized water. For the preparation of the NPs coated with titanium dioxide, 1.45 mL of titanium isopropoxide (TTIP; Macklin, China) was added to the previously described solution. The reaction was then stirred for 6 h in an ice bath. The silica-titania dioxide core-shell structured NPs were added to 1.0 M sodium hydroxide for etching to obtain hollow titanium dioxide NPs. The obtained hollow NPs (H-TiO_2) were collected by centrifugation after being washed with deionized water.

Synthesis of Col-H-TiO_2

The free collagenase solution (17018029, Gibco,1 mg/mL, 2 mL) was mixed with 10 mg of the produced H-TiO_2 NPs. The mixture was stirred for 48 hours at 4°C under dark conditions. The precipitate was centrifuged and then washed three times with PBS. The loading amounts were determined using collagenase's typical optical absorbance at 260 nm, and the loading efficiency (LE) was calculated using the equation below.

$$\mathrm{LE}(\%) = \left[\mathrm{m}_{original\ collagenase} - \mathrm{m}_{collagenase\ in\ supernatant} \right] / \left(\mathrm{m}_{H-TiO_2} - \mathrm{m}_{collagenase\ in\ supernatant} \right) \times 100\% \quad [17]$$

Detection of collagenase activity on the surface of enzyme-linked H-TiO_2 (Col-H-TiO_2)

FITC (F8070, Solarbio, China) and collagenase-degradable gelatin (ST1339, Beyotime, China) were mixed to produce a solid yellow gelatin-FITC gel. After it had solidified, the gelatin-FITC was immersed in double distilled water and repeatedly washed until the supernatant of the immersed gelatin-FITC showed no fluorescence when measured using a fluorescence spectrophotometer. The gelatin was then treated with ddH$_2$O, H-TiO_2, Col-H-TiO_2, and collagenase-1. A fluorescence spectrophotometer (Tecan Spark, Tecan, Switzerland) was used to detect the supernatant's fluorescence after 1 h and to compare it to gelatin that had been treated with collagenase.

US-responsive Collagenase Release Profile

The collagenase release of Col-H-TiO_2 was estimated at 37 °C at 100 rpm utilizing dialysis tubes (1000 kDa) in PBS with or without the US. For each H-TiO_2 formulation, three vials were used. The Micro BCA protein assay kit (23235, Thermo Fisher, USA) was employed to determine the concentration of the released protein.

Assessment of Free Radical Generation in Solution

Singlet oxygen ($^1O_2$), hydrogen peroxide (H_2O_2), and hydroxyl radical (•OH) were assessed with a SOSG assay (MA0326, Meilune, China), APF probe (Sigma-Aldrich, USA), and an H_2O_2 assay (S0038, Beyotime, China). Briefly, TiO_2 and $H-TiO_2$ were diluted in ddH_2O solutions with various amounts of oxygen at the same concentration of Ti (25 µg/mL), and the mixtures were then exposed to the US under the same condition (1.0 W/cm^2, duty cycle 50%, 1 MHz), following which their fluorescence was determined using a multiscan spectrum as described previously (Tecan Spark, Tecan, Switzerland).

Assessment of H-TiO$_2$-Mediated CEUS ability

CEUS imaging (ZS3, Mindray, China) and a stereoscopic microscope (S9i, Leica microsystems, Germany) were used to analyze $Col-H-TiO_2$-mediated bubble production at room temperature. $H-TiO_2$ samples were suspended in various concentrations (0, 62.5, 125, 250, 500, and 1000 µg/mL) in ordinary or deoxygenated ddH_2O.

Cell experiment

The BxPC-3 pancreatic cancer cell line was originally obtained from American Type Culture Collection (ATCC) and cultured in RIPA 1640 (Gibco, USA) supplemented with 10% FBS (Gibco, USA), penicillin (100 U/mL), and streptomycin (100 µg/mL; Gibco, USA). All cells were maintained at 37°C in a humidified chamber with 5% CO_2.

Intracellular Assessment of Free Radical Generation

Detection of free radical generation within cells was carried out through DCFH-DA (S0033S, Beyotime, China). Briefly, BxPC-3 cells were grown on cell climbing slices and then exposed to PBS, TiO_2, $Col-H-TiO_2$, $H-TiO_2$ + US, and $Col-H-TiO_2$ + US. $H-TiO_2$ (25 µg/mL in 1640) and $Col-H-TiO_2$ (25 µg/mL in 1640) were added 24 h after plating, and the cells were allowed to incubate for another 24 h. Following 20 minutes of incubation with DCFH-DA for 20 min, the cells were treated with or without US (1.0 W/cm^2, 1 MHz, 50% duty cycle, 1 min). CLSM was employed to detect free radical fluorescence.

In vitro Cytotoxicity of Col-H-TiO$_2$ and therapeutic efficacy evaluation

The cytocompatibility of $Col-H-TiO_2$ was assessed using a Cell Counting Kit-8 (K0301, MCE, USA). BxPC-3 and HUVECs cells were plated overnight in 96-well plates. Then, media comprising appropriate $Col-H-TiO_2$ was added with Ti concentrations of 3.125, 6.25, 12.5, 25, 50, and 100 µg/mL. Following another 24 h of incubation, the medium was removed and a CCK-8 assay was conducted following the conventional protocols to ascertain cell viability.

The synergistic therapeutic effects of $Col-H-TiO_2$ were also studied using Bxpc-3 cells treated with five different experimental treatments: PBS, PBS + US, $Col-H-TiO_2$, $H-TiO_2$ + US, and $Col-H-TiO_2$ + US (25 µg/mL; 1.0 W/cm^2, 1 MHz, 50% duty cycle, 1 min). Then test the cell viability through a CCK-8 assay.

BxPC-3 cells were allowed to culture for 24 h until they reached 80% confluency, then treated for 8 hours with various solutions. The cells were then treated with or without US (1.0 W/cm^2, 1 MHz, 50% duty cycle, 1 min) before being incubated for 16 h. The cells were then rinsed in PBS and digested with trypsin (without EDTA). FITC Annexin V Apoptosis Detection Kit I (556547, BD Pharmingen, USA) and flow cytometric analysis (Beckman CytoFLEX, Beckman Coulter, Inc.) were used to investigate apoptosis.

Live–Dead Cell Staining, BxPC-3 cells cultured for 24 h were washed with PBS and incubated with $Col-H-TiO_2$ (25 $µg/mL^{-1}$) for 8 h. The cells were exposed to US (1.0 W/cm^2, 1 MHz, 50% duty cycle, 1 min), and after 16 h, they were stained using the Calcein-AM/PI Cell Viability/Cytotoxicity Assay Kit (C2015S, Beyotime, China) for 30 min and visualized using fluorescence microscopy (Leica Microsystems, Germany).

Cellular uptake assays

Flow cytometry was utilized to measure $Col-H-TiO_2$ uptake (Beckman CytoFLEX; Beckman Coulter, Inc.). Briefly, BxPC-3 cells were added to 6-well plates for 24 h, after which the media was replaced with media supplemented with FITC-labeled $Col-H-TiO_2$ (25 µg/mL). Cells were collected and analyzed using flow cytometry after being incubated for 4, 8, 12, or 24 h. Similarly, after incubation of 2 h and 12 h, the uptake of $Col-H-TiO_2$ was measured by the CLSM (Leica Microsystems, Germany).

3D MCSs culture

As previously reported, the hanging drop approach was used to establish MCSs.[40] BxPC-3 cells were suspended in a 1.2 % methylcellulose/RPMI 1640 medium suspension containing 10^6 cells per mL. The cell suspension was then carefully placed on the lid of the cell culture plate. After 5 days of culture, the MCSs were transferred to a 96-well plate containing 100 μL of 1% agarose. Ultimately, 100 μL of culture medium was poured into separate wells to culture the MCSs for future investigations. The final testing concentrations of H-TiO$_2$ and Col-H-TiO$_2$ were added to the wells and incubated for 12 h.

Results

Construction and Characterization of Col-H-TiO$_2$

Scheme 1 represents the procedure for the synthesis and the anticancer action of Col-H-TiO$_2$. As depicted by the transmission electron micrographs (TEM), the as-prepared TiO$_2$ NPs had a uniform hollow spherical shape and a mean particle size of around 100 nm (Figure. 1a, b). H-TiO$_2$ and Col-H-TiO$_2$ have respective hydrated particle sizes equivalent to 174.3 nm and 210.4 nm (Figure. 1c). The elemental image obtained via EDS depicts the distribution of Ti and Si, as a result of the etching and redeposition of silicon dioxide, which provides support for the hollow structure (Figure. 1d).[30] The N$_2$ adsorption-desorption isotherms and pore size distributions of H-TiO$_2$ are depicted in Figure 1e. The Brunauer-Emmett-Teller surface area and pore volume of H-TiO$_2$ were 75.89 m^2 g^{-1} and 0.0950 cm^3 g^{-1}. The Barrett-Joyner-Halenda pore size of H-TiO$_2$ was precisely 3.24 nm. The unique mesoporous channel and the large cavity of TiO$_2$ render H-TiO$_2$ a promising choice for loading of drug cargo, delivery, and subsequent release. The ultraviolet−visible absorption (UV−vis) of the collagenase and Col-H-TiO$_2$ showed absorption and emission peaks at ~ 260 nm, indicating the successful loading of collagenase (Figure 1f). Based on the standard curve depicted in Figure S1, the H-TiO$_2$ drug loading rate can be estimated to be 11 %. As displayed in Figure 1g, the US radiation treatment accelerates the release of the drug. The cavitation effect of the US irradiation may destroy the interactions between the H-TiO$_2$ and collagenase molecules, thereby substantially accelerating collagenase release. This result indicated that US irradiation enhanced the destruction of Col-H-TiO$_2$ within tumor cells and stimulated the release of collagenase, with subsequent sonodynamic activity resulting in a profound free collagenase and deep NPs penetration. To evaluate the stability of Col-H-TiO$_2$, the hydrated particle size of Col-H-TiO$_2$ was assessed in saline and cell culture medium (DMEM) containing 10% FBS were assessed. The diameters didn't change much after 7 days (Figure S2). To characterize the ability of Col-H-TiO$_2$ of digesting collagen fibers, a mixture of gelatin and FITC powder was used to assess the enzyme activity. The enzyme activity of Col-H-TiO$_2$ was 35.64 ± 3.24 % of that of free collagenase, whereas H-TiO$_2$ showed almost little activity. (Figure S3) This result indicated that the loading process did not affect the enzyme activity of collagenase.

Assessment of H-TiO$_2$ ROS-generating properties

To quantify the ROS yield of H-TiO$_2$ after ultrasound irradiation, singlet oxygen sensor green (SOSG), aminophenyl fluorescein (APF), and H$_2$O$_2$ assays were carried out for tracking the generated ^{1}O$_2$, •OH, and H$_2$O$_2$. In comparison to PBS and pure TiO$_2$, H-TiO$_2$ possesses a much higher ^{1}O$_2$ generation efficiency (Figure. 2a, b). In addition, H-TiO$_2$ displayed a greater •OH generation efficiency than pure TiO$_2$ under hypoxic conditions (Figure. 2c) and induced a greater H$_2$O$_2$ generation after ultrasound irradiation in both normoxia and hypoxia (Figure. 2d). This data indicated that this H-TiO$_2$ could generate sufficient ROS for the treatment of pancreatic cancer with hypoxic solid tumors, which can primarily be attributed to the fact that the hollow structure of TiO$_2$ can considerably promote the ROS generation and improve the SDT effect.[6] Subsequently, the intracellular ROS generation of Col-H-TiO$_2$ under US irradiation was investigated by using the ROS probe, 2′,7′-dichlorofluorescein diacetate (DCFH-DA). ROS can oxidize the probe, generating 2,7 -dichlorofluorescein (DCF) with green fluorescence. The strongest fluorescence was found In BxPC-3 cells following the combination treatment of Col-H-TiO$_2$ and H-TiO$_2$ after US irradiation, as shown in Figure 2e, indicating that the loading of collagenase maintains the enhanced ROS generation for SDT. These findings indicated that an increase in the specific surface area suggests the involvement of a greater number of active sites in the catalytic process, by which improves the catalytic effect. This, in turn,

would be advantageous in terms of the separation efficacy of h^+ and e^- triggered by US irradiation, subsequently enhancing the generation of ROS.[17, 31]

Assessment of the *in vitro* sonodynamic antitumor efficacy of Col-H-TiO$_2$

The tumor therapeutic efficacy of Col-H-TiO$_2$ was also assessed in light of its ROS production performance. First, the biocompatibility of Col-H-TiO$_2$ was evaluated using a CCK-8 kit. Without US irradiation, no apparent cell toxicity was induced by the NPs in human epithelial cells (HUVECs) and human pancreatic tumor cells (BxPC-3) after incubation with a range of equivalent Ti concentrations (0, 3.125, 6.25, 12.5, 25, 50 and 100 μg/mL) for a period of 24 h (Figure. 2a, b). Similarly, no obvious cytotoxicity was induced by these NPs in human epithelial cells HUVECs. BxPC-3 cell viability was evaluated after following Col-H-TiO$_2$ treatment and US exposure (1.0 W/cm^2, 1 MHz, 50% duty cycle, 1 min). Both H-TiO$_2$ + US and Col-H-TiO$_2$ + US groups showed a significant decline in the cell viability, although US irradiation alone had no detrimental effects on BxPC-3 cell viability over the intensity range examined (Figure. 2c). Flow cytometry was employed to determine whether Col-H-TiO$_2$ induces apoptosis of cells to investigate the cellular mechanism by which Col-H-TiO$_2$ and US kill tumor cells. Following US exposure (1.0 W/cm^2, 1 MHz, 50% duty cycle, 1 min), apoptosis was induced by H-TiO$_2$ (early apoptosis + late apoptosis = 41.27 ± 5.94 %), as well as Col-H-TiO$_2$ (early apoptosis + late apoptosis = 43.34 ± 6.22 %), providing sufficient proof for the ability of sonodynamic to cause the death of tumor cells (Figure 3d, e). These findings were further confirmed by calcein-AM/PI co-staining, which showed a notable increase, in PI-stained cells after the treatment of Col-H-TiO$_2$ and H-TiO$_2$ under US exposure (Figure. 3f). Since the results were consistent with the CCK-8 assay, it is verified that Col-H-TiO$_2$ is suitable for SDT-mediated antitumor therapy.

Assessment of the penetration in tumors of Col-H-TiO$_2$.

Cellular uptake of Col-H-TiO$_2$ was evaluated by culturing BxPC-3 cells with fluorescein isothiocyanate (FITC) labeled NPs for different periods (0, 4, 8, 12, and 24 H) and then collecting cells *via* flow cytometry. The results showed that the cellular uptake of Col-H-TiO$_2$ uptake was maximum within 12 h. (Figure S4). As shown in Figure S5, the green signal of FITC-labelled Col-H-TiO$_2$ visually showed the intracellular uptake. Fluorescence intensity is time-dependent, indicating the Col-H-TiO$_2$ can achieve great cellular uptake ability.

To investigate the penetration of Col-H-TiO$_2$ in tumors, multicellular spheroids (MCSs) were employed. Three-dimensional (3D) culture models, for instance, spheroids,[32] have a better resemblance to the *in vivo* conditions in comparison to 2D models and can mimic tissues for ECM (such as collagen) production and cell-cell connections.[33] BxPC-3 MCSs having a diameter of approximately 300 nm were constructed following the previously reported method.[34] CLSM was employed for observing the penetration behavior, through Z-stack scanning with a 10 μm scanning step.

The H-TiO$_2$ and Col-H-TiO$_2$ NPs were placed n various confocal plates that had been treated with or without the US. As shown in Figure 4, without the US, faint green fluorescence was observed from H-TiO$_2$ NPs at the edge of the MCSs, from 10 to 40 μm depth sections, where the Col-H-TiO$_2$ NPs showed deeper penetrating ability, and at a scanning depth of 40 μm, the green fluorescence was even full in the Col-H-TiO$_2$ + US group. The results indicate that collagenase-free NPs were incapable of penetrating MCSs, however, following US irradiation of Col-H-TiO$_2$, the released collagenase allowed for increased penetration, most likely due to the presence of dense ECM within tumor cells.

Assessment of the US imaging effect and tumor accumulation of Col-H-TiO$_2$.

Col-H-TiO$_2$ performs the same function as contrast-enhanced ultrasound (CEUS) imaging. There was nearly no signal in the PBS group, while the echo signal intensity of NPs was significantly increased as the Ti concentration increased *in vitro* (Figure. 5b). Thus, the accumulation of NPs could be evaluated through CEUS, probably due to its hollow structure's ability to contain gas. CEUS and inductively plasma-mass spectrometry (ICP-OES) were performed on pancreatic ductal adenocarcinoma (PDAC) PDX models to further validate the accumulation and biodistribution of the Col-H-TiO$_2$ (Figure. 5c, 5d). Compared to H-TiO$_2$, the accumulation of Col-H-TiO$_2$ was more sufficient 12 h after the injection, and the retention was significantly greater after 24 h. The tumor ICP-OES data also confirmed this result. These results showed that Col-H-TiO$_2$ could function as an ultrasonic contrast agent for monitoring the treatment, and is capable

of degrading collagen fibers to increase the permeability and retention of the NPs into tissues *in vivo*, thereby effectively enhancing the SDT efficiency.

Conclusions

In conclusion, H-TiO$_2$ adorned with collagenase was successfully synthesized to break through the stromal biological barrier and stimulate ROS production, which can accelerate tumor penetration synergistically and improve sonodynamic therapy of pancreatic cancers. This hollow shell structure not only improves drug loading but also provides more active sites by increasing specific surface area, thereby strengthening the catalytic action following US irradiation, and substantially enhancing SDT-induced ROS production. Furthermore, after US irradiation, the loaded collagenase in the TiO$_2$ cavity may escape and act as a molecular scavenger, digesting collagen fibers. Col-H-TiO$_2$ SDT can increase vascular density and decrease IFP in tumor centers, inducing cell death and necrosis, and exerting a clear therapeutic effect to destroy tumors without being constrained by the tumor ECM biology barrier. It is also a one-of-a-kind sonodynamic nano agent that can simultaneously visualize tumor penetration ability and monitor treatment in situ. As a result, this work provides a promising method for altering TME for the efficient treatment of clinical pancreatic cancer.
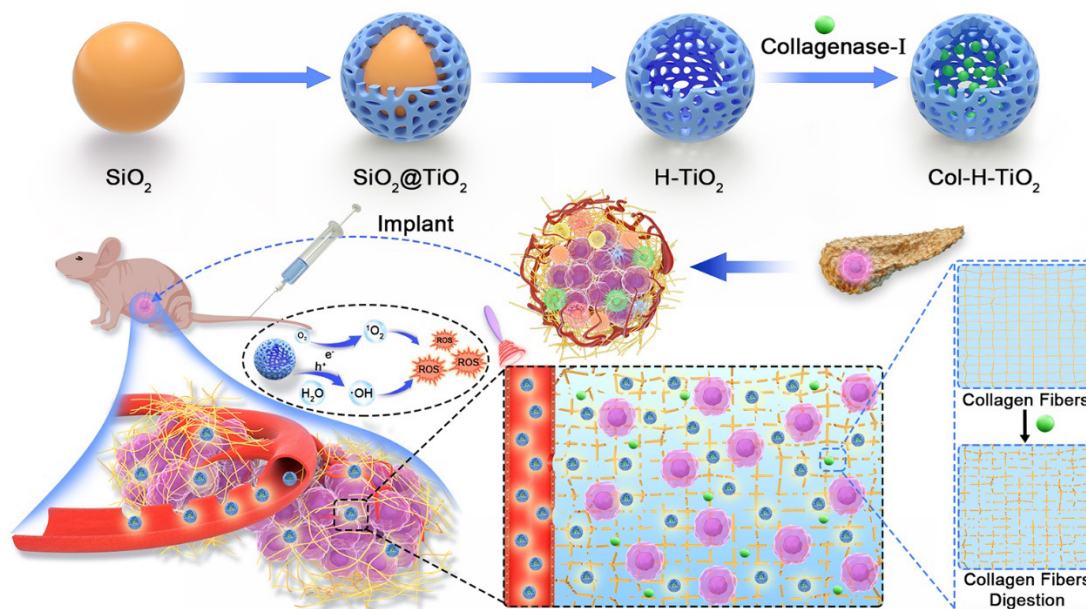
Scheme 1. Schematic illustration mechanism of Col-H-TiO$_2$ mediated SDT.
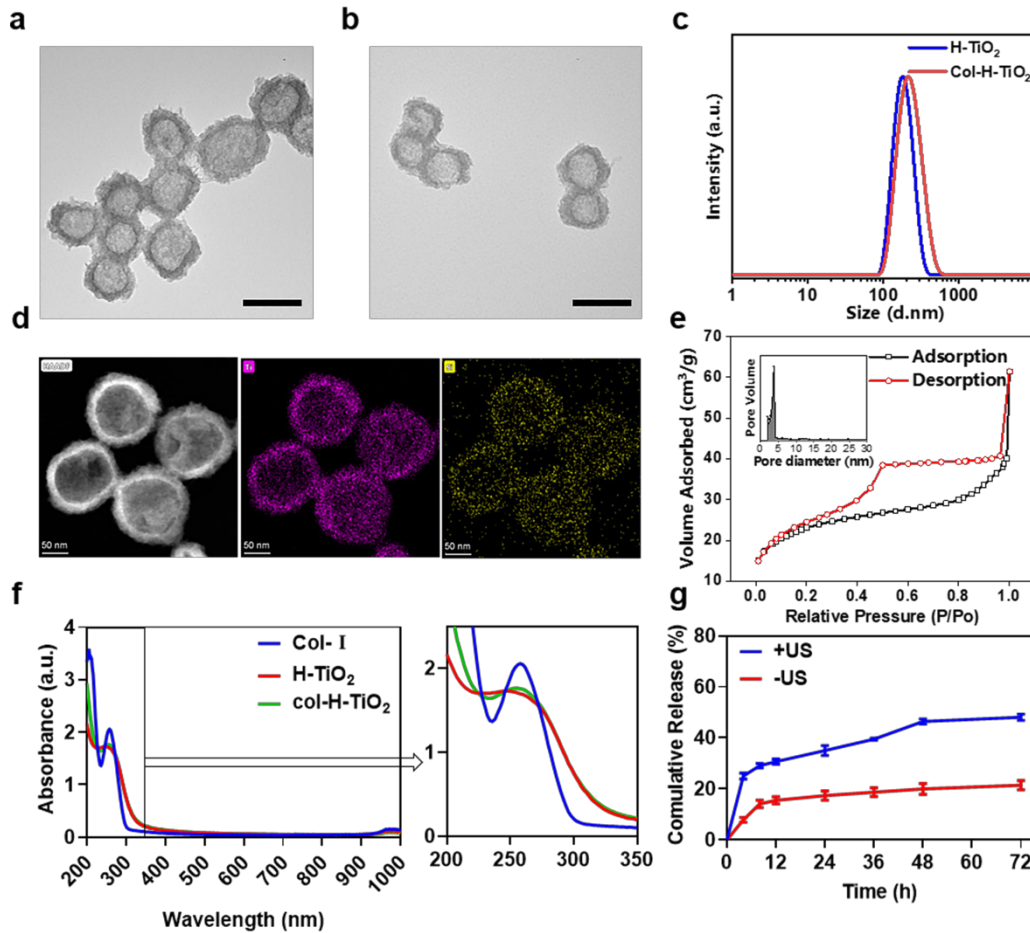
Figure 1. (a, b) TEM micrographs of H-TiO$_2$ and Col-H-TiO$_2$ (scale bar = 100nm); (c) Dynamic Light Scattering (DLS) measurements of H-TiO$_2$ and Col-H-TiO$_2$; (d) The elemental mappings of Ti and Si in H-TiO$_2$; (e) Collagenase standard curve by UV-Vis method as a function of mass concentration; (f) The UV–vis spectra of Collagenase type-I (Col- I), H-TiO$_2$, and Col-H-TiO$_2$; (g) The collagenase release from Col-H-TiO$_2$ triggered by US irradiation (1.0 W/cm^2, 1 MHz, 50% duty cycle, 1 min) in different time points (n = 3).
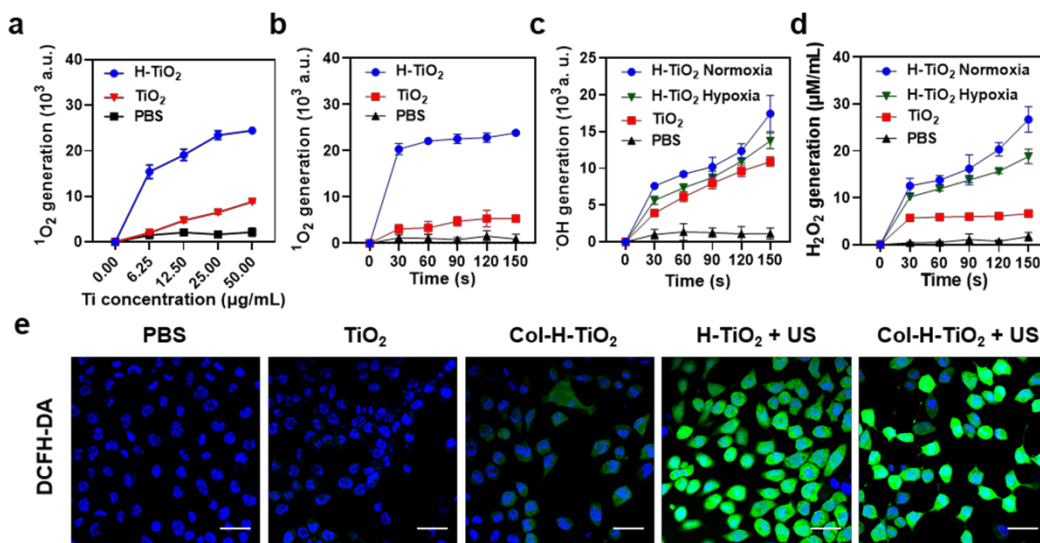
Figure 2. Quantitative measurement of $^1O_2$ (a, b), ^-OH (c), H$_2$O$_2$ (d) generation following TiO$_2$ (12.5 µg/mL) and H-TiO$_2$ (12.5 µg/mL) treatment after US irradiation (1.0 W/cm^2, 1 MHz, 50% duty cycle, 1 min), n = 3 (e) Intracellular ROS levels measured by the DCFH-DA probe. BxPC-3 cells were treated with PBS, TiO$_2$,

Col-H-TiO$_2$, H-TiO$_2$ + US (1.0 MHz, 1 W/cm^2, 1 min, 50% duty cycle), or Col-H-TiO$_2$ + US (scale bar: 30 μm).
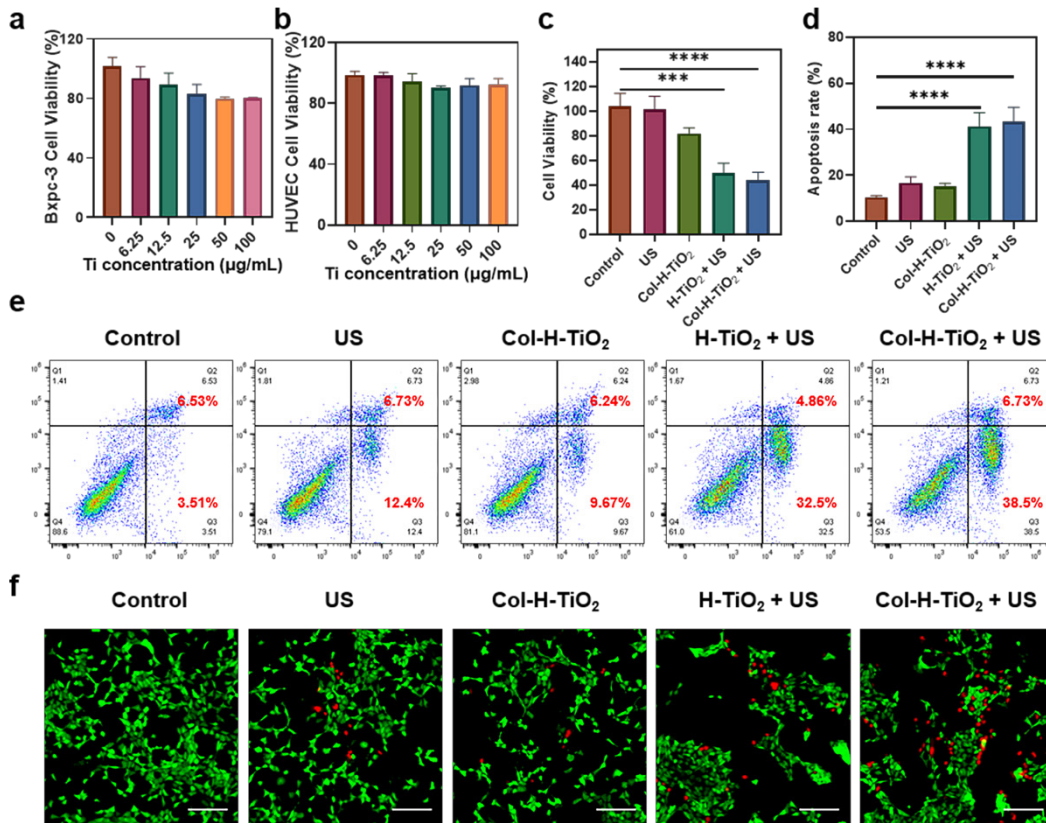

Figure 3. (a) The cell viability of various Ti concentrations of BxPC-3 cells; (b) The cell viability of different Ti concentrations of Huvec cells; (c) The cell viability of BxPC-3 cells after PBS, US, Col-TiO$_2$, H-TiO$_2$ + US, or Col-TiO$_2$ + US treatment; (d, e) Flow cytometric analysis of necrosis and apoptosis of tumor cells following various treatments, n = 3; (f) Calcein-AM/PI staining of BxPC-3 cells following various treatments (Green and red indicate living and dead cells; scale bar = 200 μm).

Figure 4. CLSM images demonstrating the penetration of FITC-labeled H-TiO$_2$ NPs and Col-H-TiO$_2$ NPs *in vitro* in 3D-cultured BxPC-3 MCSs. The MCSs were incubated with H-TiO$_2$ or Col-H-TiO$_2$ with or without the US, measured using CLSM from the top to bottom with 10 μm per section (scale bar: 200μm).
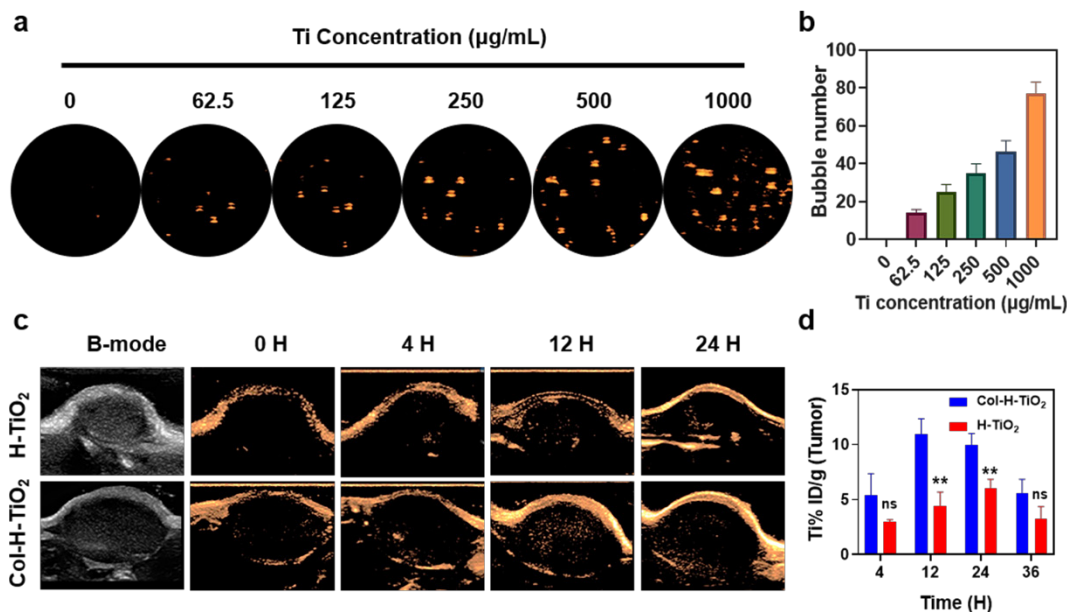

Figure 5. (a, b) Representative US images of various H-TiO$_2$ concentrations and the signal intensity quantification; (c) CEUS imaging of H-TiO$_2$ and Col-H-TiO$_2$ delivery over time; (d) Ti biodistribution in the tumor following intravenous injection with H-TiO$_2$ and Col-TiO$_2$ for 4, 12, 24, and 48 H. Statistical significances were calculated via unpaired t-test (** $p < 0.01$, n = 3).

References

[1]. Siegel, R. L.; Miller, K. D.; Fuchs, H. E.; Jemal, A. Cancer statistics, 2022. CA Cancer J Clin 2022, 72 (1), 7-33.

[2]. Vincent, A.; Herman, J.; Schulick, R.; Hruban, R. H.; Goggins, M. Pancreatic cancer. The Lancet 2011, 378 (9791), 607-620.

[3]. Zhang, Y.; Zhang, X.; Yang, H.; Yu, L.; Xu, Y.; Sharma, A.; Yin, P.; Li, X.; Kim, J. S.; Sun, Y. Advanced biotechnology-assisted precise sonodynamic therapy. Chem Soc Rev 2021, 50 (20), 11227-11248.

[4]. Zinger, A.; Koren, L.; Adir, O.; Poley, M.; Alyan, M.; Yaari, Z.; Noor, N.; Krinsky, N.; Simon, A.; Gibori, H.; et al. Collagenase Nanoparticles Enhance the Penetration of Drugs into Pancreatic Tumors. ACS Nano 2019, 13 (10), 11008-11021.

[5]. Olive, K. P.; Jacobetz, M. A.; Davidson, C. J.; Gopinathan, A.; McIntyre, D.; Honess, D.; Madhu, B.; Goldgraben, M. A.; Caldwell, M. E.; Allard, D.; et al. Inhibition of Hedgehog signaling enhances delivery of chemotherapy in a mouse model of pancreatic cancer. Science 2009, 324 (5933), 1457-1461.

[6]. Tao, N.; Li, H.; Deng, L.; Zhao, S.; Ouyang, J.; Wen, M.; Chen, W.; Zeng, K.; Wei, C.; Liu, Y. N. A Cascade Nanozyme with Amplified Sonodynamic Therapeutic Effects through Comodulation of Hypoxia and Immunosuppression against Cancer. ACS Nano 2022, 16, 485-501.

[7]. Fang, J.; Islam, W.; Maeda, H. Exploiting the dynamics of the EPR effect and strategies to improve the therapeutic effects of nanomedicines by using EPR effect enhancers. Adv Drug Deliv Rev 2020, 157, 142-160.

[8]. Miao, L.; Lin, C. M.; Huang, L. Stromal barriers and strategies for the delivery of nanomedicine to desmoplastic tumors. J Control Release 2015, 219, 192-204.

[9]. Hingorani, S. R.; Zheng, L.; Bullock, A. J.; Seery, T. E.; Harris, W. P.; Sigal, D. S.; Braiteh, F.; Ritch, P. S.; Zalupski, M. M.; Bahary, N.; et al. HALO 202: Randomized Phase II Study of PEGPH20 Plus Nab-Paclitaxel/Gemcitabine Versus Nab-Paclitaxel/Gemcitabine in Patients With Untreated, Metastatic Pancreatic Ductal Adenocarcinoma. Journal of Clinical Oncology 2018, 36 (4), 359-366.

[10]. Murphy, J. E.; Wo, J. Y.; Ryan, D. P.; Clark, J. W.; Jiang, W.; Yeap, B. Y.; Drapek, L. C.; Ly, L.; Baglini, C. V.; Blaszkowsky, L. S.; et al. Total Neoadjuvant Therapy With FOLFIRINOX in Combination With Losartan Followed by Chemoradiotherapy for Locally Advanced Pancreatic Cancer: A Phase 2 Clinical Trial. JAMA Oncol 2019, 5 (7), 1020-1027.

[11]. Wang, J.; Wu, Q.; Wang, Y.; Xiang, L.; Feng, J.; Zhou, Z.; Fu, Q.; Zhang, L. Collagenase-loaded pH-sensitive nanocarriers efficiently remodeled tumor stroma matrixes and improved the enrichment of nanomedicines. Nanoscale 2021, 13 (20), 9402-9414.

[12]. Dai, Y.; Xu, C.; Sun, X.; Chen, X. Nanoparticle design strategies for enhanced anticancer therapy by exploiting the tumour microenvironment. Chemical Society Reviews 2017, 46 (12), 3830-3852.

[13]. Wang, H.; Han, X.; Dong, Z.; Xu, J.; Wang, J.; Liu, Z. Hyaluronidase with pH‑responsive Dextran Modification as an Adjuvant Nanomedicine for Enhanced Photodynamic‑Immunotherapy of Cancer. Advanced Functional Materials 2019, 29 (29), 1902440.

[14]. Neesse, A.; Michl, P.; Frese, K. K.; Feig, C.; Cook, N.; Jacobetz, M. A.; Lolkema, M. P.; Buchholz, M.; Olive, K. P.; Gress, T. M.; et al. Stromal biology and therapy in pancreatic cancer. Gut 2011, 60 (6), 861-868.

[15]. Xu, F.; Huang, X.; Wang, Y.; Zhou, S. A Size-Changeable Collagenase-Modified Nanoscavenger for Increasing Penetration and Retention of Nanomedicine in Deep Tumor Tissue. Adv Mater 2020, 32 (16), e1906745.

[16]. Liu, J.; Tian, L.; Zhang, R.; Dong, Z.; Wang, H.; Liu, Z. Collagenase-Encapsulated pH-Responsive Nanoscale Coordination Polymers for Tumor Microenvironment Modulation and Enhanced Photodynamic Nanomedicine. ACS Appl Mater Interfaces 2018, 10 (50), 43493-43502.

[17]. Liang, S.; Deng, X.; Xu, G.; Xiao, X.; Wang, M.; Guo, X.; Ma, P. a.; Cheng, Z.; Zhang, D.; Lin, J. A Novel Pt‑TiO2 Heterostructure with Oxygen‑Deficient Layer as Bilaterally Enhanced Sonosensitizer for Synergistic ChemoSonodynamic Cancer Therapy. Advanced Functional Materials 2020, 30 (13), 1908598.

[18]. Deprez, J.; Lajoinie, G.; Engelen, Y.; De Smedt, S. C.; Lentacker, I. Opening doors with ultrasound and microbubbles: Beating biological barriers to promote drug delivery. Adv Drug Deliv Rev 2021, 172, 9-36.

[19]. Tan, X.; Huang, J.; Wang, Y.; He, S.; Jia, L.; Zhu, Y.; Pu, K.; Zhang, Y.; Yang, X. Transformable Nanosensitizer with Tumor Microenvironment-Activated Sonodynamic Process and Calcium Release for Enhanced Cancer Immunotherapy. Angew Chem Int Ed Engl 2021, 60 (25), 14051-14059.

[20]. Wang, X.; Zhong, X.; Bai, L.; Xu, J.; Gong, F.; Dong, Z.; Yang, Z.; Zeng, Z.; Liu, Z.; Cheng, L. Ultrafine Titanium Monoxide (TiO1+x) Nanorods for Enhanced Sonodynamic Therapy. J Am Chem Soc 2020, 142 (14), 6527-6537.

[21]. Liang, S.; Xiao, X.; Bai, L.; Liu, B.; Yuan, M.; Ma, P.; Pang, M.; Cheng, Z.; Lin, J. Conferring Ti-Based MOFs with Defects for Enhanced Sonodynamic Cancer Therapy. Adv Mater 2021, 33 (18), e2100333.

[22]. Sun, L.; Wang, P.; Zhang, J.; Sun, Y.; Sun, S.; Xu, M.; Zhang, L.; Wang, S.; Liang, X.; Cui, L. Design and application of inorganic nanoparticles for sonodynamic cancer therapy. Biomater Sci 2021, 9 (6), 1945-1960.

[23]. Bai, S.; Yang, N.; Wang, X.; Gong, F.; Dong, Z.; Gong, Y.; Liu, Z.; Cheng, L. Ultrasmall Iron-Doped Titanium Oxide Nanodots for Enhanced Sonodynamic and Chemodynamic Cancer Therapy. ACS Nano 2020, 14 (11), 15119-15130.

[24]. Geng, B.; Xu, S.; Li, P.; Li, X.; Fang, F.; Pan, D.; Shen, L. Platinum Crosslinked Carbon Dot@TiO2- x p-n Junctions for Relapse-Free Sonodynamic Tumor Eradication via High-Yield ROS and GSH Depletion. Small 2022, 18 (6), e2103528.

[25]. You, D. G.; Deepagan, V. G.; Um, W.; Jeon, S.; Son, S.; Chang, H.; Yoon, H. I.; Cho, Y. W.; Swierczewska, M.; Lee, S.; et al. ROS-generating TiO2 nanoparticles for non-invasive sonodynamic therapy of cancer. Sci Rep 2016, 6, 23200.

[26].   Han, X.; Huang, J.; Jing, X.; Yang, D.; Lin, H.; Wang, Z.; Li, P.; Chen, Y. Oxygen-Deficient Black Titania for Synergistic/Enhanced Sonodynamic and Photoinduced Cancer Therapy at Near Infrared-II Biowindow. ACS Nano 2018, 12 (5), 4545-4555.

[27].   Li, Y.; Teng, X.; Wang, Y.; Yang, C.; Yan, X.; Li, J. Neutrophil Delivered Hollow Titania Covered Persistent Luminescent Nanosensitizer for Ultrosound Augmented Chemo/Immuno Glioblastoma Therapy. Adv Sci (Weinh) 2021, 8 (17), e2004381.

[28].   Shi, J.; Liu, W.; Fu, Y.; Yin, N.; Zhang, H.; Chang, J.; Zhang, Z. "US-detonated nano bombs" facilitate targeting treatment of resistant breast cancer. J Control Release 2018, 274, 9-23.

[29].   Oh, W.-K.; Kim, S.; Choi, M.; Kim, C.; Jeong, Y. S.; Cho, B.-R.; Hahn, J.-S.; Jang, J. Cellular uptake, cytotoxicity, and innate immune response of silica-titania hollow nanoparticles based on size and surface functionality. ACS Nano 2010, 4 (9), 5301-5313.

[30].   Leshuk, T.; Linley, S.; Baxter, G.; Gu, F. Mesoporous hollow sphere titanium dioxide photocatalysts through hydrothermal silica etching. ACS Appl Mater Interfaces 2012, 4 (11), 6062-6070.

[31].   Sun, B.; Bu, J.; Du, Y.; Chen, X.; Li, Z.; Zhou, W. O, S-Dual-Vacancy Defects Mediated Efficient Charge Separation in ZnIn2S4/Black TiO2 Heterojunction Hollow Spheres for Boosting Photocatalytic Hydrogen Production. ACS Appl Mater Interfaces 2021, 13 (31), 37545-37552.

[32].   Lazzari, G.; Couvreur, P.; Mura, S. Multicellular tumor spheroids: a relevant 3D model for the in vitro preclinical investigation of polymer nanomedicines. Polymer Chemistry 2017, 8 (34), 4947-4969.

[33].   Priwitaningrum, D. L.; Blonde, J. G.; Sridhar, A.; van Baarlen, J.; Hennink, W. E.; Storm, G.; Le Gac, S.; Prakash, J. Tumor stroma-containing 3D spheroid arrays: A tool to study nanoparticle penetration. J Control Release 2016, 244 (Pt B), 257-268.

[34].   Goodman, T. T.; Olive, P. L.; Pun, S. H. Increased nanoparticle penetration in collagenase-treated multicellular spheroids. Int J Nanomedicine 2007, 2 (2), 265-274.

[35].   Yoshida, G. J. Applications of patient-derived tumor xenograft models and tumor organoids. J Hematol Oncol 2020, 13 (1), 4.

Tailoring Perfluoropentane Nanodroplet Formulation Parameters for Increased Reproducibility Using Sonication

Kirsten O'Brien[1], Christopher Campbell[1], Dariusz Kosk[1], Jonathan May[1], Robin Rumney[2], Eleanor Stride[3], Peter Birkin[4], Dario Carugo,[5] Nicholas Evans[1]

[1]School of Engineering, University of Southampton, Southampton, UK
[2]School of Pharmacy & Biomedical Sciences, University of Portsmouth, Portsmouth, UK
[3]Institute of Biomedical Engineering, Department of Engineering Sciences, University of Oxford, Oxford, UK
[4]School of Chemistry, University of Southampton, Southampton,UK
[5]School of Pharmacy, University College London, London, UK

Corresponding author: K.E.OBrien@soton.ac.uk

Introduction:

Perfluorocarbons are capable of dissolving very large amounts of oxygen. This makes them a possible candidate for targeted oxygen delivery into hypoxic regions around bone fractures. As perfluorocarbons are insoluble in blood, they must be stabilised by a monolayer of an amphiphatic molecule (such as phospholipids) to form a nanodroplet. Sonication is the most common laboratory process for making nanodroplets with perfluorocarbons heavier than perfluorobutane. However, sonication is a very stochastic process and this can result in reduced repeatability. As the diameter of the nanodroplets will affect many of the nanodroplets' characteristics, from the peak negative pressure required for acoustic droplet vaporisation to their ability to be detected by the immune system, optimising the repeatability of the sonication process is integral. In this work, a new sonicator set up was designed to allow for improved control over the sonication process. The tip height and perfluoropentane (PFP) concentration were then investigated in unison, in terms of their effect on nanodroplet size and size dispersity.

Methods:

To create the nanodroplets, a lipid film was first made. 1,2-distearoyl-sn-glycero-3phosphocholine (DSPC) and polyoxyethylene (40) stearate (PEG(40)s) solutions were made up to 31.6 mM and 4.89 mM concentrations respectively by dissolving the lipids in chloroform.The resulting mixture was left overnight in a fume hood to allow the chloroform to evaporate leaving a dry lipid film. The lipid film was rehydrated using phosphate buffered saline (PBS) to create a final lipid concentration of 4 mg/mL. The resulting solution was then homogenised by sonicating it continuously for 2.5 minutes at the 40% amplitude setting using a Model 120 Sonic Dismembrator with a 3.22 mm diameter sonicator tip.

The concentration of perfluoropentane (PFP) added was investigated by keeping a constant volume of lipid solution (800 µl) with different volumes of PFP (120 µl, 80 µl, 40 µl, 20 µl, 10 µl, 0 µl). Given the PFP is more dense than the lipid solution, the height of the tip and the volume of PFP are variables that will affect each other. As such, each PFP concentration was tested against each tip height condition. This experiment was performed at tip heights of 2 mm, 5mm, 8 mm, 10 mm and 12 mm from the bottom of the Eppendorf tube. The lipid-PFP solution was then sonicated for 60 s total at 60% amplitude using a pulsed regime of 2 s on and 5 s off. This second sonication was performed in an ice-water bath to keep the temperature throughout the whole sonication below the boiling point of PFP (29 ℃) The setup of the sonicator during the second sonication can be seen in Figure 1. These nanodroplets can be loaded with oxygen by placing them in a 100% oxygen atmosphere after sonication.

To assess reproducibility, the nanodroplets were measured using nanoparticle tracking analysis (NTA) to determine the median, standard deviation and concentration of the particle size distribution as well as light microscopy to determine if larger nanodroplets were present.

Results:

Both the tip height and the PFP concentration were found to have a significant contribution using a 2-way ANOVA (P<0.0001). The PFP concentration appears to have a more significant influence on the median and standard deviation of the particle size distribution than the tip height. Below 40 µl of PFP, there is no clear difference between the values of the median or the standard deviation including the 0 µl group. Therefore, below 40 µl, there is no clear evidence of nanodroplets being formed instead of lipid micelles or other supramolecular structures. In general, increasing tip height led to a lower median diameter and standard deviation. The optimum values (median 156.4 nm and standard deviation 91.73 nm) for nanodroplet formulation were found to be 40 µl of PFP at a 12 mm tip height.

Conclusions:

The concentration of PFP has a very significant effect on the nanodroplet median and standard deviation. More PFP led to a larger size dispersity and larger average size of the nanodroplets. The tip height had less of an effect on the nanodroplets but did affect the relationship between the PFP concentration and nanodroplet size. For the purpose of delivering oxygen to bone, 40 µl of PFP and 12 mm tip height were found to be the optimum conditions.
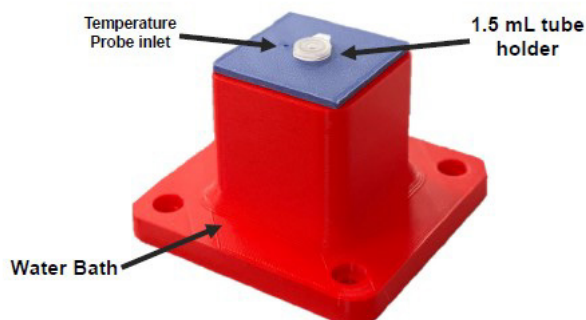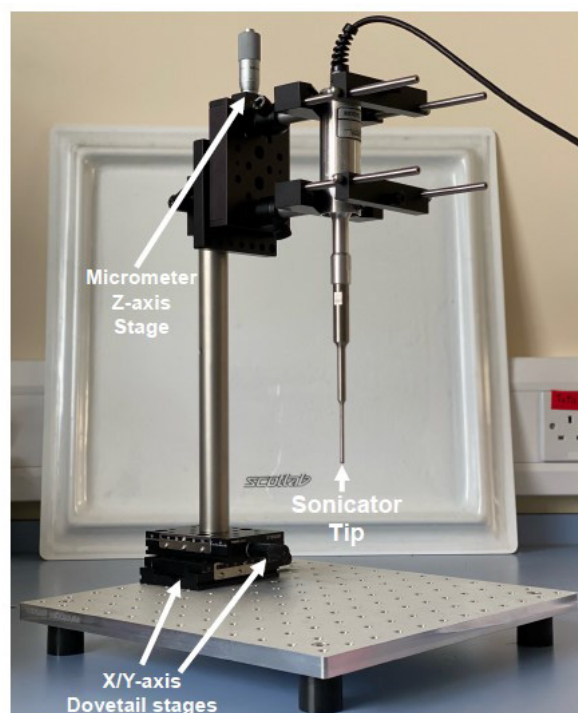

Figure 1. Sonicator setup designed as part of this work. The red water bath contains ice and water during sonication. The water bath is filled with ice and water and screwed down directly underneath the sonicator.

Enhancing acoustic response and drug loading of polymeric microbubbles by tailoring synthesis components

Roman A. Barmin,[1] Anshuman Dasgupta,[1] Céline Bastard,[2,3,4] Laura De Laporte, [2,3,4] Fabian Kiessling,[1] Twan Lammers,[1] and Roger M. Pallares[1]

[1] *Institute for Experimental Molecular Imaging, RWTH Aachen University Hospital, Aachen, 52074, Germany.*
[2] *DWI – Leibniz Institute for Interactive Materials, RWTH Aachen University, Aachen, 52074, Germany*
[3] *Institute for Technical and Macromolecular Chemistry, RWTH Aachen University, Aachen, 52074 Germany*
[4] *Institute of Applied Medical Engineering, Department of Advanced Materials for Biomedicine, RWTH Aachen University, Aachen, 52074 Germany*
Corresponding authors: tlammers@ukaachen.de, rmoltopallar@ukaachen.de

Introduction

Gas-filled microbubbles (MB) are widely used as ultrasound (US) contrast agents. Recent research has also focused on their application as drug delivery formulations based on their US stimuli-responsiveness and established drug loading and bioconjugation routes [1,2]. While lipid-based soft-shelled MB are preferred for US imaging, polymer-based MB can outperform their lipid-based counterparts for drug delivery applications due to the higher drug loading capabilities of the polymeric shell [3]. Among the several poly(alkyl cyanoacrylate) (PACA) polymers used for MB synthesis, poly(butyl cyanoacrylate) (PBCA) is most commonly employed, because of its biocompatibility and clinical application as a surgical glue for wound closure [4,5]. Because MB size, shape uniformity, and shell composition directly affect the drug loading capacity and US response of PACA MB, fine control over their morphology is required for improved diagnostic and therapeutic performance. Thus, a systematic evaluation of the impact of materials involved in PACA MB formation on MB morphology and properties is required.

Surfactants and alkyl cyanoacrylate monomers are essential components for PACA MB synthesis. While surfactants reduce the gas-liquid interfacial tension, monomers participate in the polymerization reaction at the gas-liquid interface, resulting in MB formation [6]. Surfactant colloidal behavior depends on chemical structure, molecular weight (MW), and hydrophilic-lipophilic balance (HLB); however, the impact of these parameters on MB formation and functionality remains elusive. Moreover, while alkyl side chain length of the initial monomer impacts the elasticity of the resulting PACA chain [7], as shown for polymer films [8], its effect on MB synthesis parameters and MB functional properties remains unexplored. Here, we set out to study the effect of key component characteristics (chemical structure, MW, and HLB for surfactants, and alkyl side chain length of monomers) on the formation of PACA-based polymeric MB, as well as on their shell thickness, drug loading, and US responsiveness.

Methods

The effect of three surfactants of the Triton family and three surfactants of the Tween family on the synthesis and properties of PACA MB were evaluated. These surfactants were selected because they enable the formation of PBCA MB while showing opposite MW-HLB trends: HLB values increase and decrease with surfactant MW for Triton and Tween compounds, respectively (**Figure 1a**). PBCA MB were synthesized via anionic polymerization under high-speed stirring, where the number of surfactant and monomer molecules was kept constant for all samples (**Figure 1b**).
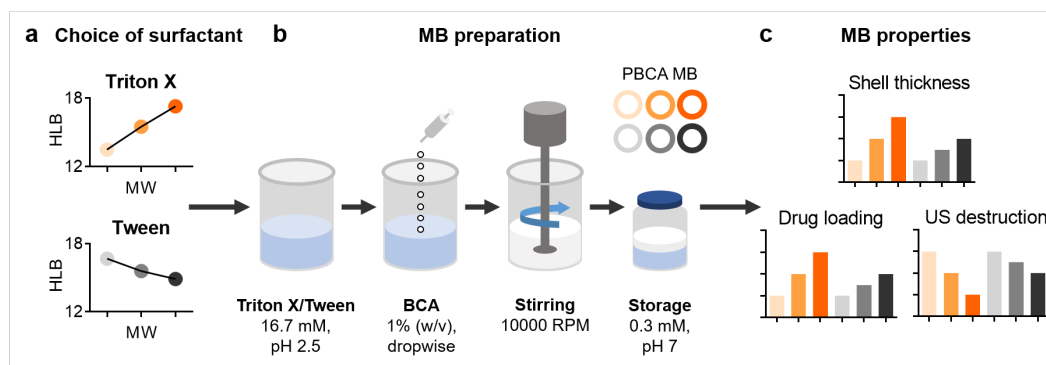
Figure 1. Surfactants to engineer MB properties. (**a**) Surfactants of the Triton and Tween families were used to synthesize PBCA MB to exploit their different MW-HLB trends. (**b**) Each MB sample was prepared with an equal amount of surfactant molecules (16.7 mM) via anionic polymerization of BCA under high-speed stirring. After purification, all samples were stored with the solution of the corresponding surfactant (0.3 mM). (**c**) Shell thickness, acoustic response, and drug loading capacity of the PBCA MB were characterized to investigate the impact of the properties of surfactants during the synthesis.

To study the effect of alkyl side chain length of the monomer in the resulting polymeric MB, three alkyl cyanoacrylate monomers were selected: ECA, BCA and OCA. Those monomers were chosen based on the trend of lower polymer elasticity (referred to as glass transition temperature, T_g) with increasing alkyl side chain length (**Figure 2a**). PACA MB were synthesized by copolymerizing different alkyl cyanoacrylate monomers (*i.e.* ECA and BCA, BCA and BCA, or OCA and BCA) in the presence of Triton X-100, while keeping the total amount of monomers constant (**Figure 2b**). Butyl cyanoacrylate monomer was added to the synthesis of all samples because monopolymerization of ECA and OCA did not produce stable MB.
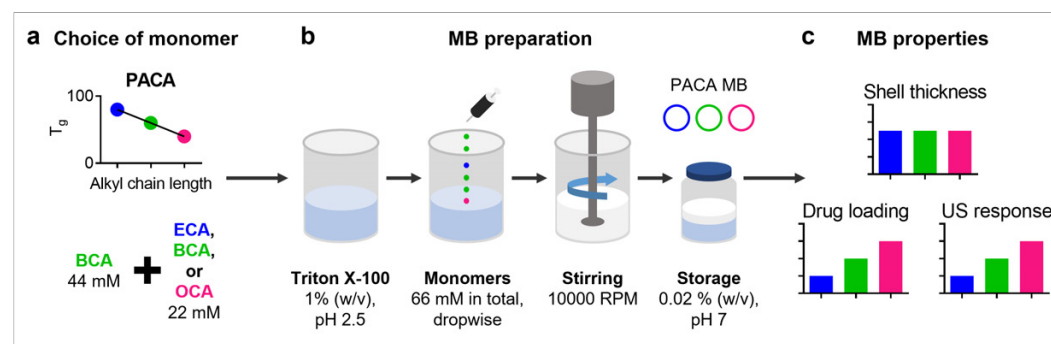

Figure 2. Alkyl cyanoacrylate monomers to engineer MB properties. (**a**) Alkyl cyanoacrylate monomers with different akyl side chain length were used to synthesize PACA MB. During MB synthesis, an equal amount of ethyl, butyl, or octyl cyanoacrylate (ECA, BCA, and OCA, respectively) monomers (22 mM) was mixed with a constant amount of BCA (44 mM) for copolymerization. (**b**) Each MB sample was synthesized with an equal amount of Triton X-100 surfactant via copolymerization of alkyl cyanoacrylate monomers (66 mM in total) under high-speed stirring. (**c**) The impact of monomers was evaluated by characterization of shell thickness, acoustic response, and drug loading capacity of the produced PACA MB.

Results

All produced MB samples displayed similar mean diameters upon flotation purification (between 2 – 3 µm), allowing us to investigate the effect of key component characteristics on MB synthesis and the resulting MB functional properties.

For Triton X and Tween-based agents, we observed that the shell thickness of PBCA MB increased with the MW of the surfactants (**Figure 3a**), while no clear trends were identified between MB properties and surfactant HLB values. MB with up to three-fold thicker shell were synthesized. PBCA MB with thicker

shells were capable to load higher amounts of Coumarin 6 as hydrophobic drug (**Figure 3b**) and reduced acoustic response in non-linear contrast (NLC) mode (**Figure 3d**) combined with showed higher acoustic stability (**Figure 3e**). US images of surfactant-tailored PBCA MB in NLC mode and acoustic power of 4% are presented in **Figure 3c**. The chemical structure of the surfactants also affected the resulting MB properties, since the Triton X-based samples had a larger proportion of smaller polymer chains than the Tween-based MB did, likely resulting in lower polymer entanglement, which may explain the enhanced drug loading and increased US contrast response of Triton X-based MB as compared to Tween-based MB.
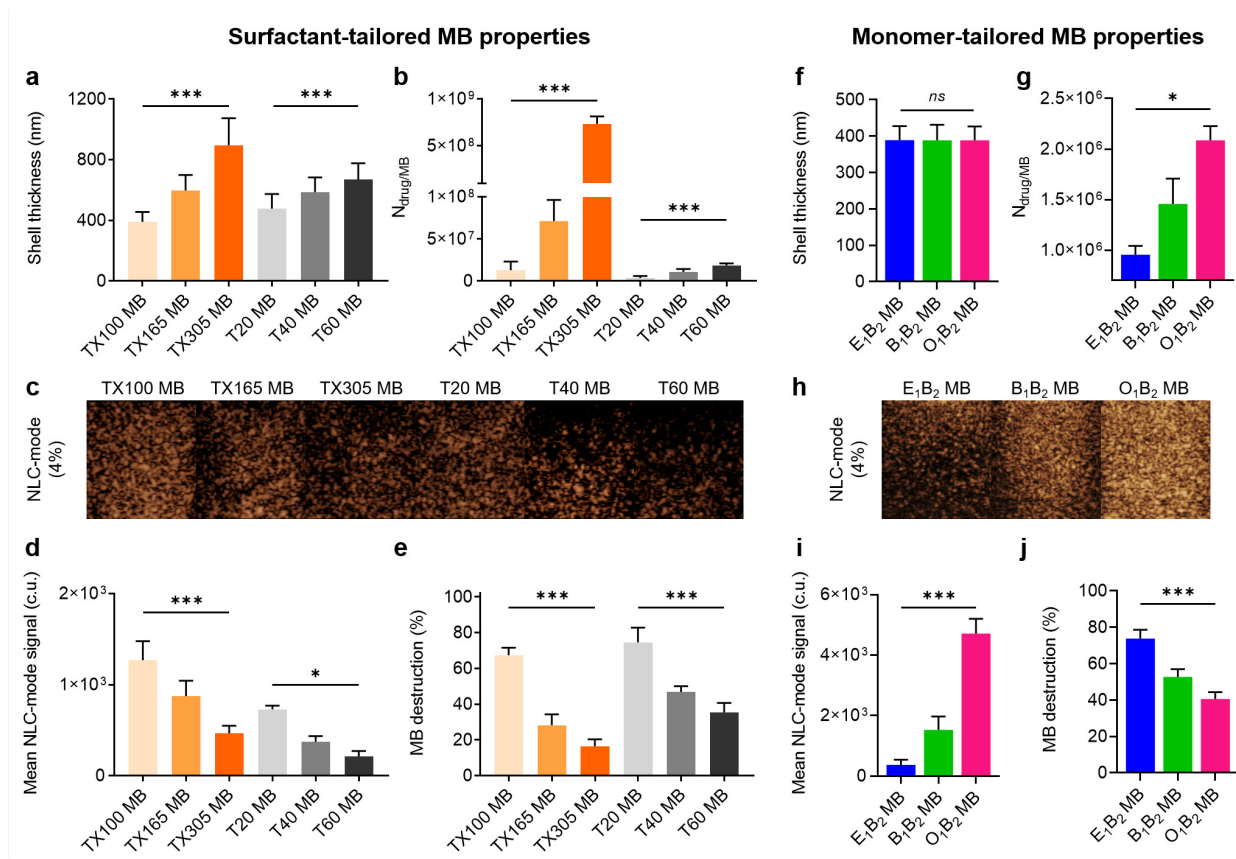

Figure 3. Surfactant- and monomer- tailored PACA MB properties of shell thickness, drug loading, and acoustic response. (**a**) Shell thickness measurements of PBCA MB produced using Triton X and Tween surfactants by CLSM images. (**b**) Numbers of drug molecules loaded into the shell per one MB ($N_{drug/MB}$) of surfactant-tailored PBCA MB. (**c**) Representative NLC mode images for PBCA MB produced with Triton X and Tween surfactants at 4 % acoustic power. (**d**) Mean signal intensities of MB in NLC mode at the acoustic power of 4 % for samples produced with Triton X- and Tween- surfactants. (**e**) PBCA MB destruction at the acoustic power of 10 % for samples produced with Triton X- and Tween- surfactants. (**f**) Shell thickness measurements of PACA MB produced using monomers with different alkyl chain length by CLSM images. (**g**) Numbers of drug molecules loaded into the shell per one MB ($N_{drug/MB}$) of monomer-tailored PACA MB. (**h**) Representative NLC mode images for PACA MB produced with alkyl cyanoacrylate monomers at 4 % acoustic power. (**i**) Mean signal intensities MB in NLC mode at the acoustic power of 4 % for samples produced with alkyl cyanoacrylate monomers. (**j**) PACA MB destruction at the acoustic power of 10 % for samples produced with alkyl cyanoacrylate monomers. Values represent mean ± standard deviation of three different batches of PACA MB, measured in triplicates. (*), and (***) indicate groups that are significantly different with $p < 0.05$, and $p < 0.001$, respectively (one-way ANOVA with post hoc Tukey HSD test).

For MB produced with different alkyl cyanoacrylate monomers, we observed that the shell thickness of PACA MB was the same for all samples (**Figure 3f**), while the increased concentration of MB produced with shortened side-chain monomers could indicate higher reactivity of the monomers. The introduction of extended alkyl side chain monomers resulted in higher drug loading capabilities, acoustic response, and acoustic stability of produced PACA MB, as demonstrated in **Figures 3g, 3i** and **3j**, respectively.

Conclusions

We identified the impact of surfactants and monomers on the formation and properties of PACA MB, including acoustic response, drug loading capablities and US-mediated destruction. These findings enable fine-tuning the properties of PACA MB and provide new opportunities for their applications as US-responsive drug delivery systems and imaging agents.

References

[1]. Stride, E., Segers, T., Lajoinie, G., Cherkaoui, S., Bettinger, T., Versluis, M., & Borden, M. (2020). Microbubble Agents: New Directions. Ultrasound in Medicine & Biology, 46, 6, 1326–1343.

[2]. Rudakovskaya, P.G., Barmin, R.A., Kuzmin, P.S., Fedotkina, E.P., Sencha, A.N., Gorin, D.A. (2022) Microbubbles Stabilized by Protein Shell: From Pioneering Ultrasound Contrast Agents to Advanced Theranostic Systems. Pharmaceutics, 14(6), 1236.

[3]. Sirsi, S. R., & Borden, M. A. (2009). Microbubble compositions, properties and biomedical applications. Bubble Science, Engineering & Technology, 1(1-2), 3–17.

[4]. Couvreur, P. (2021). (Poly-cyanoacrylate) nanomedicines for cancer and beyond: Lessons learned. Journal of Controlled Release, 334, 318–326.

[5]. Koczera, P., Appold, L., Shi, Y., Liu, M., Dasgupta, A., Pathak, V., … Lammers, T. (2017). PBCA-based polymeric microbubbles for molecular imaging and drug delivery. Journal of Controlled Release, 259, 128–135.

[6]. Appold, L., Shi, Y., Rütten, S., Kühne, A., Pich, A., Kiessling, F., & Lammers, T. (2017). Physicochemical Characterization of the Shell Composition of PBCA-Based Polymeric Microbubbles. Macromolecular Bioscience, 17(10), 1700002.

[7]. Duffy, C., Zetterlund, P., & Aldabbagh, F. (2018). Radical Polymerization of Alkyl 2-Cyanoacrylates. Molecules, 23(2), 465.

[8]. Wischke, C., Weigel, J., Neffe, A. T., & Lendlein, A. (2011). Understanding Instability and Rupture of Poly(Alkyl-2-Cyanoacrylate) Capsules. The International Journal of Artificial Organs, 34(2), 243–248.

Ultrasound targeted drug loaded microbubbles for oncolytic virotherapy of breast cancer

Kishan S. Italiya[1,2], Victor Mullins-Dansereau[2,3], Tommy Alain[5], Marie-Claude Bourgeois-Daigneault[2,3] and <u>François T.H. Yu</u>[1,2,4]

[1]*Microbubble Theranostics Laboratory, Centre de recherche du Centre hospitalier de l'Université de Montréal, Montreal, Canada*

[2]*Institut du Cancer de Montréal, Montreal, Canada*

[3]*Département de Microbiologie, Infectiologie et Immunologie, Faculté de Médecine, Université de Montréal, Montreal, Canada*

[4]*Departement de radiologie, radio-oncologie et médecine nucléaire, Université de Montréal, Montreal, Canada*

[5]*Department of Biochemistry, Microbiology and Immunology, Faculty of Medicine, University of Ottawa, Canada*

Corresponding author: francois.yu@umontreal.ca

Introduction

Oncolytic viruses (OVs) are an emerging class of bio-therapeutics which selectively kill cancer [1]. The therapeutic response of intratumorally injected OVs is hampered by heterogeneous distribution. However intravenous delivery is inefficient since most of the viruses are neutralized by the complement and immune system, leading to a limited viral replication in the tumor. Numerous small molecules have been identified as viral sensitizers, they enhance virus replication as much as 1,000-fold in tumor cells. One of these molecules we named virus-sensitizers 1 (VS1) [2,3, unpublished data from our lab]. Furthermore, VS1 has hematological dose limiting toxicities. Thus, new strategies to target VS1 toward solid cancer and to avoid accumulation in platelets may be beneficial. In this work, we developed a targeted delivery approach using VS1 carrying lipid MBs (VS1LPMBs) and demonstrate that it improves OV therapy in vitro.

Methods

VS1-carrying lipid MB (VS1LPMB) were developed using a thin-film hydration mechanical vibration method. In brief, lipids (DPPC:DSPE:Hydro Egg PC; 60:20:20 mol%) and VS1 (2 mg) solubilized in chloroform were dried overnight and resuspended in ultrapure water at a concentration of 7.0 mg/mL. The hydrated solution was then capped with a head space of perfluorobutane and agitated for 45s with a Vialmix. MB count and size, morphology, and drug-loading were determined using electrical zone sensing (Beckman Multisizer 3), microscopy and high performance liquid chromatography (HPLC). We also assessed the stability of MB formulation at 4 ˚C for 6 h. The effect of VS1LPMB on OV replication and cytotoxicity were evaluated on 4T1 cells in 96 well plates (1×10^4 cells per well; N=6). MB destruction was obtained using the burst-mode on a Acuson Sequoia scanner (15L8, CPS7, Burst MI=1.9). US was applied through the cover plate using coupling gel. A total of 45 bursts were given per well and MB destruction was confirmed by imaging. Four hours later, 4T1 cells were infected with fluorescent-OV (VSVd51-YFP) for 24h at 0.1 multiplicity of infection (MOI). After 24 h, OV replication and cell viability were quantified using fluorescence microscopy and Coomassie blue staining, respectively. Statistical analysis was performed using GraphPad Prism 8 (Version 8.0.2) software.

Results

For VS1LPMBs, drug loading was 12-15 µg of VS1 per 1 x 10^8 MB with average size 1.59 ± 0.79 µm. VS1LPMBs were acoustically active and could be burst by US. VS1LPMBs were stable (>85 % MB) at 4°C for at least 6 h,which confirms its storage stability on ice for future *in-vivo* experiments. VS1LPMB

significantly increased OV replication by 2.5 times at 0.5 μM and 1.5 times at 0.2 μM compared to BlankMB. This was corroborated by an increase in viral titers at 0.2 μM and 1 μM. Finally, cell viability decreased in the VS1LPMB group at 5 μM ($p<0.05$) (Figure 1B), which was corroborated by detached and rounded cells at 5 μM in brightfiled microscopy (Figure 2). All this data supports that VS1 can be delivered using MB+US.

Conclusions

In this work, we demonstrate that MB can be used to deliver OV sensitizing drugs to cells in vitro. In vivo, targeted delivery of OV sensitizing drugs is expected to enhance OV replication in sonicated tumors, potentially allowing intravenous administration of OV therapy.
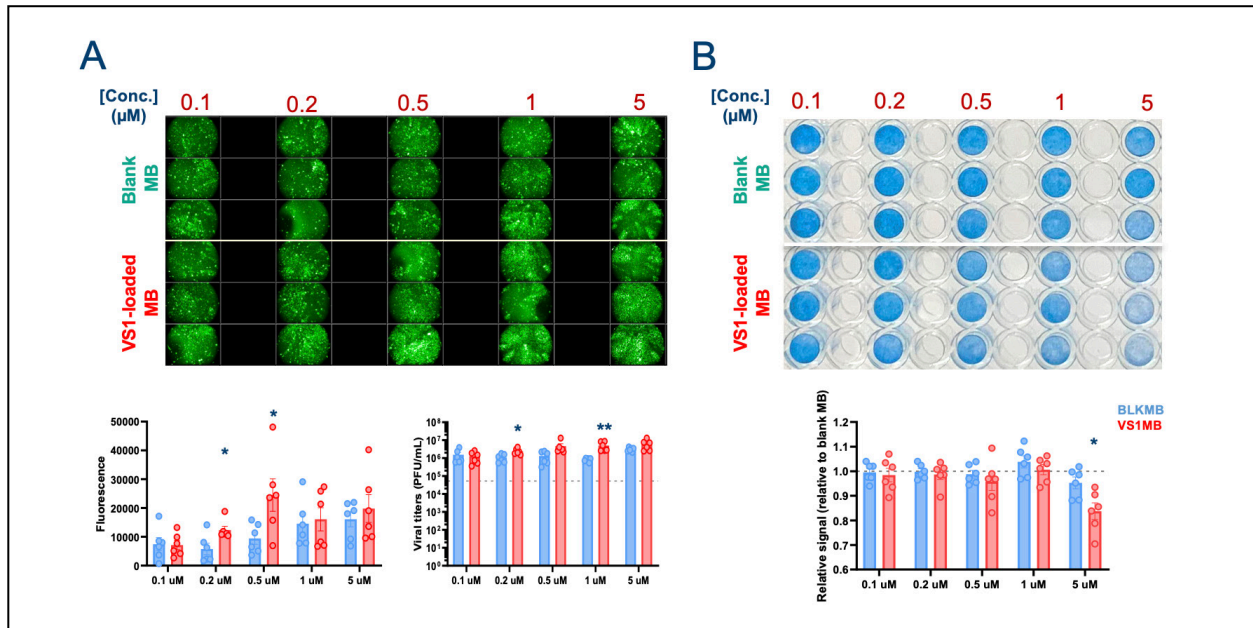

Figure 1. VS1 loaded Microbubbels (VS1LPMB) enhances Vascular stomatitis virus (VSVd51-YFP; MOI: 0.1) replication and cytotoxicity in mouse breast cancer cells (4T1): (A) Virus replication, (B) Cell viability of 4T1 cells using Coomassie blue staining. *$p<0.05$; Statistical analysis was performed using Mann-Whitney test.
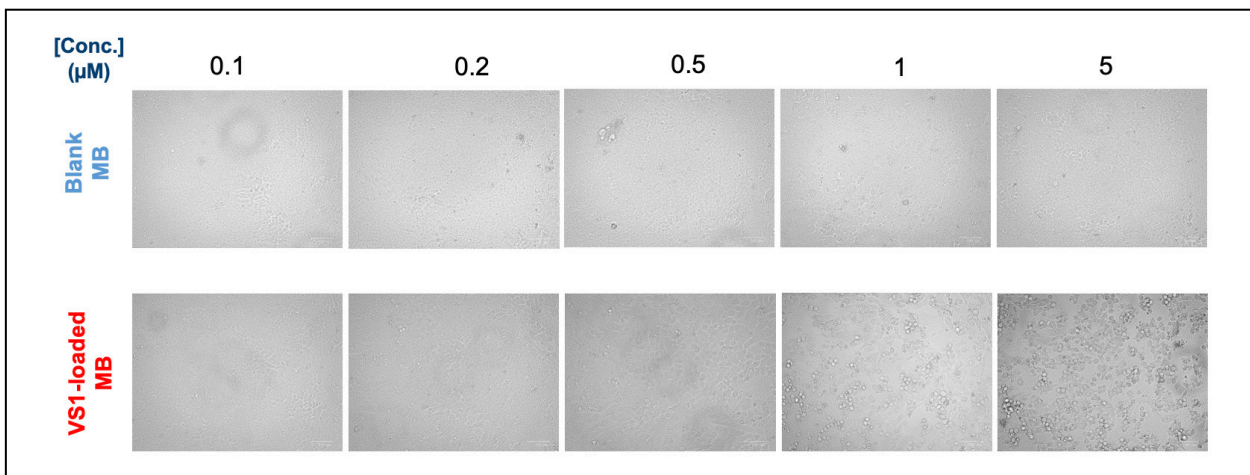

Figure 2. Representative micrographs: Morphologic changes in 4T1 cells treated by VS1LPMB or BlankMB with ultrasound followed by VSV (VSVd51-YFP; MOI: 0.1) at 24 h.

References:

[1] Breitbach, Caroline J., Brian D. Lichty, and John C. Bell. "Oncolytic viruses: therapeutics with an identity crisis." EBioMedicine 9 (2016): 31-36.

[2] Diallo, Jean-Simon, et al. "A high-throughput pharmacoviral approach identifies novel oncolytic virus sensitizers." *Molecular Therapy* 18.6 (2010): 1123-1129.

[3] Spiesschaert, Bart, et al. "Combining Oncolytic Viruses and Small Molecule Therapeutics: Mutual Benefits." *Cancers* 13.14 (2021): 3386.

Reloadable depots and focused ultrasound extend longevity of non-invasively delivered molecules in the brain

Phillip G. Durham[1], Christopher Moody[2], Yevgeny Brudno[2], Paul A. Dayton[2]

[1]Eshelman School of Pharmacy, UNC Chapel Hill, NC, USA
[2]Joint Department of Biomedical Engineering, UNC/NCSU, Chapel Hill NC, USA
Corresponding author: pgdurham@email.unc.edu

Introduction

The combination of focused ultrasound and microbubbles can be used to temporarily and non-invasively alter the permeability of the blood-brain barrier for the purposes of targeted drug delivery. This has tremendous potential for applications in diseases ranging from brain cancer to neurocognitive disorders. While focused ultrasound and microbubbles can help deliver molecules and particles beyond the vascular barrier, the therapeutics must then contend with a variety of clearance mechanisms which reduce therapeutic exposure.

With first-in-human trials demonstrating safe blood-brain barrier disruption, attention has turned to mechanisms for retaining drugs in the brain for sustained delivery. Chemically reactive drug depots which utilize complimentary click chemistry pairs have been evaluated as a system to capture systemically administered compounds and release them locally over time [1]. Evaluations against experimental cancer demonstrate that this can reduce off-target toxicities and improve tumor control. The present study evaluates the use of focused ultrasound to deliver a reactive fluorophore to a depot in the murine brain to extend retention beyond the ability of focused ultrasound alone.

Methods

Animals (n=8) were implanted with a 2 µL injection of STP-Azide into one hemisphere of the brain, and received a complimentary injection of phosphate buffered saline in the contralateral hemisphere. After animals were allowed to heal for 3 weeks, animals received an infusion of Cy5-DBCO and microbubbles, and were treated with 1 MHz focused ultrasound in an alternating grid pattern to temporarily increase the permeability of the blood brain barrier and deliver Cy5-DBCO to both hemispheres. After 1 week, animals were perfused and imaged via ex-vivo fluorescence imaging.

Results

Experiments in healthy animals without STP-Azide depots demonstrated that fluorescence of ex-vivo brain specimens in the Cy5-DBCO channel did not increase significantly from animals receiving no injection, suggesting Cy5-DBCO is unable to cross the blood-brain barrier without focused ultrasound. Significant extravasation and retention of Cy5-DBCO was observed following ultrasound-mediated disruption, but retained fluorescence returned to control levels within 7 days following ultrasound treatment. Combining ultrasound with STP-Azide depots significantly enhanced fluorescence retention at 7 days compared to contralateral hemisphere which received sham depots and ultrasound ($p = 0.0029$).
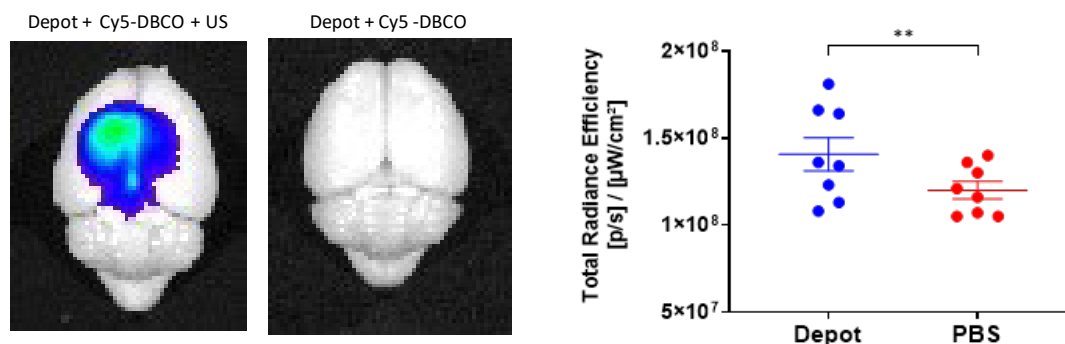

Figure 1. Reactive drug depots in the brain filled non-invasively with focused ultrasound extend the local residence of systemically administered compounds.

Conclusions

We have demonstrated that a model drug fluorophore which does not cross the blood-brain barrier natively can be delivered to, and captured by, intracranial drug reservoirs, which significantly extends the presence of fluorecence in the brain. Focused ultrasound-mediated delivery alone in the contrralateral hemisphere was insufficient to retain fluorescence. In conclusion, the utility of click reactive reloadable drug depots can be extended to the brain with focused ultrasound.

References
[1] Brudno Y, Pezone MJ, Snyder TK, Uzun O, Moody CT, Aizenberg M, Mooney DJ. Replenishable drug depot to combat post-resection cancer recurrence. Biomaterials Elsevier, 2018;178:373–382.

In vitro sonoporation using hard shell PBCA-MB under various US intensities

Julia Blöck, Junlin Chen, Anne Rix, Christopher Hark, Jan-Niklas May, Fabian Kießling

Institute for Experimental Molecular Imaging, Medical Faculty, RWTH Aachen International University, Germany
Corresponding author: jbloeck@ukaachen.de

Introduction

Sonoporation describes the creation of pores in cells by ultrasound (US), often in combination with microbubbles (MB). These pores can occur reversible or irreversible either in the cell membrane of a single cell or in the cell layer by opening cell-cell contacts [1],[2]. Lipid-based soft shell MB are frequently used for this purpose as a strong stable cavitation can be induced at mild US intensities and they burst when exposed to more harsh US intensities. In comparison, hard shell MB show a weaker stable oscillation as the shell is less flexible causing MB bursting at lower US intensities [2],[3]. The bursting causes microjets triggering the sonoporation effect [1],[3]. This study evaluates suitable US parameters for the application of hard shell poly(n-butyl cyanoacrylate) (PBCA) MB to induce opening of cell membranes or cell-cell contacts.

Methods

Epithelial Madin-Darby canine kidney (MDCK) cells were seeded on cell culture transwell inserts from the bottom side. MB ($2x10^7$) were added from below to allow direct contact to the cells. Focused US at 1 MHz (PRF: 2 kHz) was applied for 2 s from below with acoustic pressures between 300 and 4000 kPa (Fig. 1 & 2). Control groups (n=3) were treated equally as the treatment groups (n=3), but without MB. Cell membrane opening was investigated by propidium iodide (PI) uptake, as it can not pass an intact cell membrane [4]. Additionally, the cytoplasm of intact cells was stained with fluorescein diacetate (FDA). To evaluate pore resealing, both dyes (PI and FDA) were added to the cells 15 min after treatment. For both experiments, dye uptake was detected using fluorescence microscopy and quantified via the software Fiji. The presence of FDA and absence of PI confirmed resealed membrane pores. Opening of cell-cell contacts was monitored by transepithelial electrical resistance (TEER) measurements. The TEER was compared before and directly after US exposure in the treatment (US-MB; n=3) and control group (US, no MB; n=3) using an EVOM2 device with a STX2 electrode.

Results

US-MB treated groups showed higher uptake of PI in comparison to the control group (US, no MB) independently of the applied acoustic pressure (Fig 1 A). PI/FDA staining 15 min after treatment (US-MB/ US no MB) could prove the resealing of the cell membrane within this time after treatment (Fig 1 D). Independent of the US intensity, the TEER values decreased after US-MB treatment, pointing to an opening of cell-cell-contacts (Fig. 2). Except the 300 kPa group, no significant decrease of TEER before and after treatment could be proven.

Conclusions

Sonoporation with hard shell PBCA-MB induces temporary pores in the cell membrane and disrupts intercellular contacts indicated by PI/ FDA uptake and TEER, respectively, already at low US intensities. We hypothesized that the maximal effect of sonoporation was already induced at 300 kPa. As a next step, we will evaluate whether similar sonoporation effects can be induced by using soft shell MB with the same US settings. Finally, we will investigate the effects of the most promising sonoporation parameteres on the accumulation of different drug delivery systems in tumors.
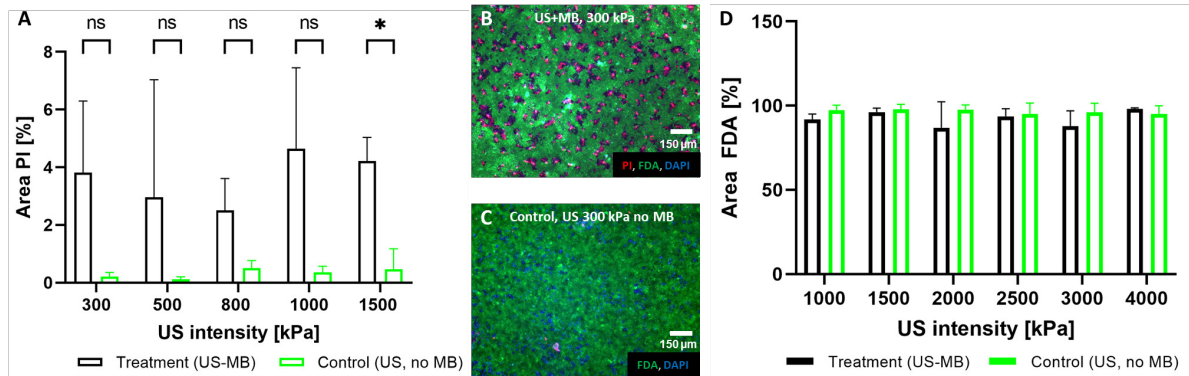
Figure 1: A: Area fraction (mean +SD) of PI uptake into cells of the US-MB treated (n=3) and control groups (US, no MB) (n=3) showing more PI uptake in the treatment group with a significant difference in the 1500 kPa group (p≤ 0.05). B and C: PI and FDA staining of MDCK cells visualizing PI uptake in US-MB treated (B) and PI absence in the control group (US, no MB) (C). D: Cellular uptake of FDA (mean + SD) for US-MB treated (n=3) and control groups (US, no MB) (n=3) proves pore resealing in all groups 15 minutes after exposure to the respective treatment. (* p ≤ 0.05; ns: not signifcant)
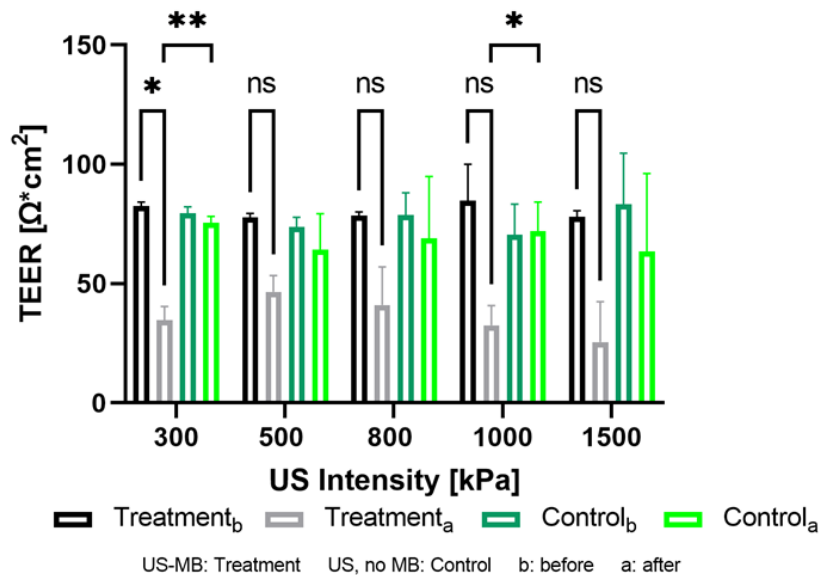

Figure 2: TEER (mean + SD) of the US-MB treated group (n=3) and control group (US, no MB) (n=3) before (b) and after (a) respective treatment showing the reduction of TEER after US-MB treatment significant for the 300 kPa group (p≤ 0.05) demonstrating the opening of cell-cell contacts. For the 300 kPa group and 1000 kPa group also a significant difference between US-MB treated and control group after respective treatment is determined with p≤ 0.01 and p≤ 0.05, respectively. (* p ≤ 0.05; ** p ≤ 0.01; ns: not signifcant)

References

[1]. [1] A. Escoffre, Jean-Michel; Bouakaz, *Therapeutic Ultrasound (Overview)*, vol. 880. 2016. [Online]. Available: http://www.springer.com/series/5584

[2]. [2] P. Frinking, T. Segers, Y. Luan, and F. Tranquart, "Three Decades of Ultrasound Contrast Agents: A Review of the Past, Present and Future Improvements," *Ultrasound Med. Biol.*, vol. 46, no. 4, pp. 892–908, 2020, doi: 10.1016/j.ultrasmedbio.2019.12.008.

[3]. [3] V. Paefgen, D. Doleschel, and F. Kiessling, "Evolution of contrast agents for ultrasound imaging and ultrasound-mediated drug delivery," *Front. Pharmacol.*, vol. 6, no. SEP, pp. 1–16, 2015, doi: 10.3389/fphar.2015.00197.

[4]. [4] Y. Hu, J. M. F. Wan, and A. C. H. Yu, "Membrane Perforation and Recovery Dynamics in Microbubble-Mediated Sonoporation," *Ultrasound Med. Biol.*, vol. 39, no. 12, pp. 2393–2405, 2013, doi: 10.1016/j.ultrasmedbio.2013.08.003.

Direct Electrophysiological Response of Human Brain Endothelial Cell mediated by Ultrasound and Microbubbles

Jifan Chen[1-2], Jean-Michel Escoffre[2], Oliver Romito[3], Christophe Vendier[3], Pintong Huang[1], Ayache Bouakaz[2]

[1] Department of Ultrasound in Medicine, The Second Affiliated Hospital of Zhejiang University, School of Medicine, Zhejiang University, Zhejiang, China.

[2] Inserm UMR 1253, iBrain, Université de Tours, Inserm, Tours, France.

[3] Inserm UMR 1069 Nutrition, Croissance et Cancer, Faculté de Médecine, Université de Tours F-37032, France, Réseau Molécules Marines, Métabolisme et Cancer and Réseau CASTOR Ganceropole Grand Ouest, France.

Corresponding author: ayache.bouakaz@univ-tours.fr, huangpintong@zju.edu.cn

Introduction

The bubble-cell mechanical iteraction will cause physiological endothelial cell response directly [1]. The pore formation on the cell plasma membrane caused by US+MBs can be ascribed to a mechanical interaction from microbubble stable cavitation which push and pull the cell membrane directly. Thanks to the transient pore formation, intra- and extra-cellular ions can exchange based on the concentration gradient, which can be a reasonable hypothesis to explain US+MBs induced blood-brain barrier opening.

Methods

Patch-clamp technique was used to monitor the modification of the cell potential properties as induced by ultrasound-activated microbubbles. A custom device [2] was established for performing the patch-clamp experiment. Our study used the patch-clamp in the whole-cell configuration. An inverted microscope was used on an antivibration table. Human brain endothelial cells were placed into 35-mm culture dishes for electrophysiological analyses at 1500 cells/cm^2. The standard bath solution and pipette solutions were prepared.

Results

An ultrasound and patch-clamp combination device was applied to stimulate human brain endothelial cells using US+MBs in a whole-cell configuration. The electrical signals were recorded and then post-processed to remove the background noises. (Figure 1A, B&C) As shown in Figure 1D, with the presence of MBs, the whole cell hyperpolarization (outflow of whole-cell current) appeared with US irradiation and the cellular potentials recovered to baseline when US was turned off.

Conclusions

Using in-vitro BBB model, the study showed that US and MBs induce a cascade of electrophysiolocal events where the cell membrane first undergoes hyperpolarization and then ion exchange beteen the medium and the cell.
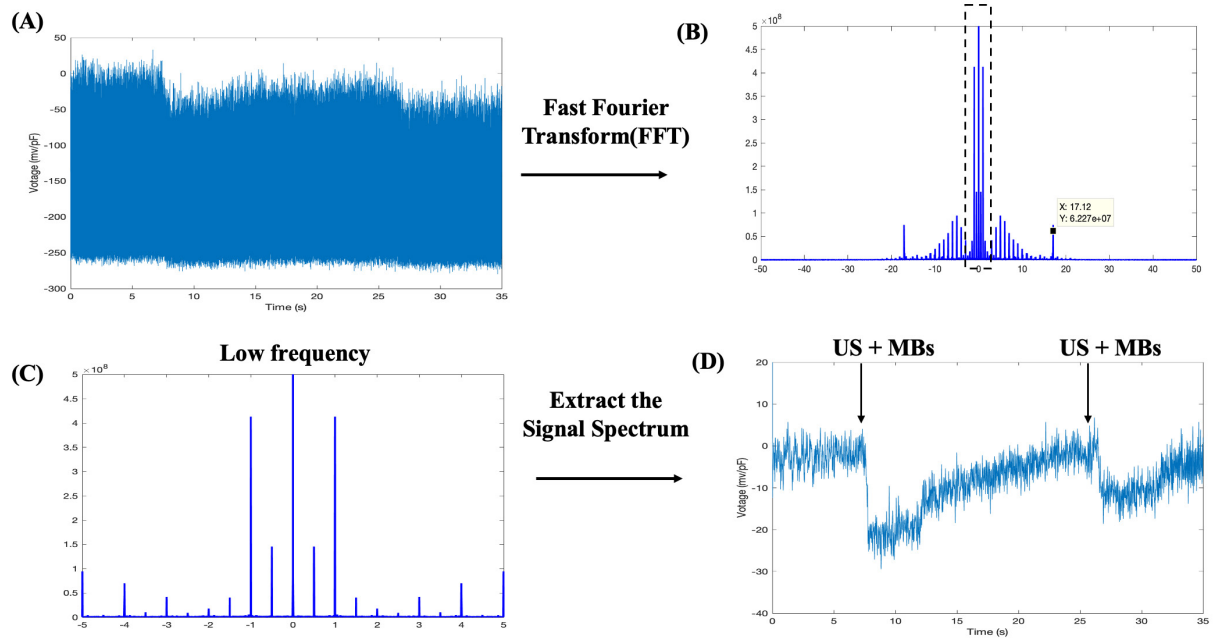
Figure 1. The patch-clamp signal and data-postprocess. (A) Original Electrical Signal (B) Frequency spectrum from -50 to 50Hz (C) Frequency spectrum from -5 to 5 Hz (D) The actual signal extract after removing the background noise.

References

[1]. Song Y, Chen J, Zhang C, Xin L, Li Q, Liu Y, Zhang C, Li S, Huang P. Mechanosensitive channel Piezo1 induces cell apoptosis in pancreatic cancer by ultrasound with microbubbles iScience. 2022 Jan 7;25(2):103733. doi: 10.1016/j.isci.2022.103733

[2]. Truong A T, Jean YLG, Philippe B, Franc T, and Ayache B. Characterization of cell membrane response to ultrasound activated microbubbles IEEE Trans Ultrason Ferroelectr Freq Control. 2008 Jan;55(1):43-9. doi: 10.1109/TUFFC.2008.615.

Polymeric microbubble-based mRNA delivery mediated by focused ultrasound in cancer: comparing Co-formulation and Co-administration

__Junlin Chen [1]__, Anne Rix[1], Yuchen Wang[1], Bi Wang[1], Harald Radermacher[1], Jinwei Qi[1], Jeffrey Momoh[1], Yang Shi[1], Fabian Kiessling[1]

[1]*Institute for Experimental Molecular Imaging, RWTH Aachen University, Aachen 52074, Germany*
Corresponding author: fkiessling@ukaachen.de

Introduction

The cell membrane is a major barrier to intracellular mRNA delivery [1]. Sonotransfection using microbubbles (MB) provides a promising platform capable of inducing pore formation on cell membranes to enable the passage of payload [2]. Enormous efforts have been made to optimize the potential of ultrasound-mediated gene delivery using various types of MB in cell culture and in vivo studies [3]. Unfortunately, defining the most appropriate acoustic parameters is challenging because of the wide range of possible variations and the need to closely match the MB's physicochemical properties. Furthermore, whether the mRNA-containing carrier needs to be applied separately to the MB (co-administration) or higher efficiency can be achieved by attaching the carrier to the MB (co-formulation) is incompletely understood. Herein, we hypothesized that we could improve the mRNA delivery efficacy by sonotransfection using poly (n-butyl cyanoacrylate) (PBCA) MB. Both, synergistic effects of MB and mRNA-loaded lipoplexes (co-formulation and co-administration approach) in sonotransfection were systematically evaluated in breast cancer cells.

Methods

Murine breast cancer cells (4T1) were cultured on the basolateral membrane of transwell cell inserts (Fig. 1A). They were exposed to focused ultrasound (fUS) at a frequency of 1 MHz and a pulse repetition frequency of 20 kHz. The mCherry mRNA (mDsRed) was used as a reporter gene. Firstly, we evaluated the lipofectamine™3000 mediated mRNA transfection efficiency at different acoustic pressures (100, 200, 300, 400 kPa) and exposure times (1, 5, 10, 30, 60 seconds) by measuring the expression of DsRed using fluorescence microscopy. The number of transfected cells was counted by the CellProfiler™ software. Secondly, we compared the transfection efficiency of the co-administration and co-formulation approaches using mRNA-loaded DOTAP/DOPE liposomes (lipoplexes) and PBCA MB (Fig. 1 C, D). To achieve this, 4T1 cells were treated with lipoplexes only, co-administration, or co-formulation approach with or without fUS at 400 kPa for 1 s. DsRed expression was again quantified via fluorescence microscpy.

Results

At 200, 300, and 400 kPa fUS, PBCA MB enhanced the mRNA transfection significantly compared to fUS only. The highest transfection efficiency without significantly decreasing cell viability was achieved at 400 kPa for 1s (Fig. 1B). Therefore, this setting was applied for all following experiments. The mRNA delivery efficacy was significantly enhanced by both approaches, co-administration, and co-formulation in presence of fUS. In this regard, the co-formulation approach showed a higher dependency of the transfection on the application of fUS, whereas the co-administration approach presented with the highest transfection efficiency (Fig. 1E, F).

Conclusions

PBCA MB can be used as a potential enhancer of transfection efficacy. Compared to liposomal transfection, co-administration in combination with fUS can significantly improve mRNA delivery. Furthermore, our in vitro results indicate that a more fUS dependent transfection can be achieved in a co-formulation approach, which higher efficacy can be achieved by co-administration. This can be

therapeutically important as for some therapeutic genes off site transfection needs to be strongly avoided while for others maximizing the degree of transfection is decive for the therapeutic outcome. However, whether these findings also hold true in vivo still needs to be evaluated.
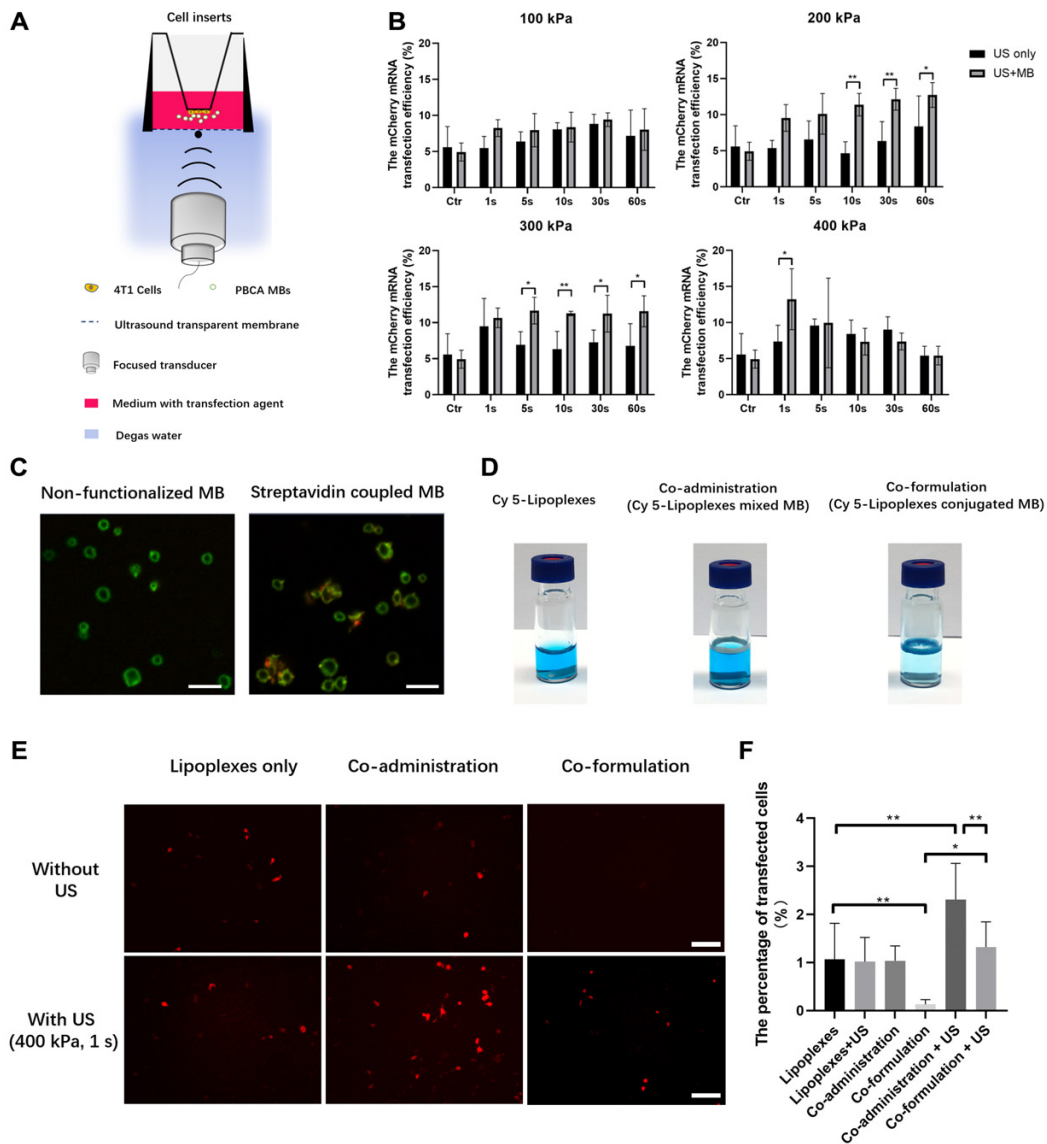

Figure 1. (A) Illustration of the in vitro setting for sonotransfection. (B) Transfection efficiency of mCherry mRNA using Lipofectamine^{TM}3000 under different negative acoustic pressures and sonication times. Data are represented as mean $\pm$ SD. *$p<0.05$, **$p<0.01$. (C) Fluorescent images of MB and lipoplex-conjugated MB (600×, scale bar = 5 μm). MB were pre-dyed with rhodamine (in green), while the lipoplexes were loaded with Cyanine 5 (Cy5, in red). (D) Formulations of Cy5 lipoplexes only (left), Cy5-lipoplexes mixed with MB (flowted to the top, middle), and Cy5 lipoplexes coupled to MB (right). (E) Representative fluorescence microscopy images of 4T1 cells transfected with mCherry mRNA using lipoplexes only (DOTAP/DOPE), co-administration of lipoplexes and MB, and the co-formulation approach with and without fUS (100×, scale bar = 5 μm). (F) Quantification of the transfection efficiency of 4T1 cells using the previously mentioned settings. The best transfection specificity could be detected for the co-formulation approach, whereas the co-administration approach with fUS presents the highest efficiency. *$p<0.05$, **$p<0.01$.

References

[1]. Hou X, Zaks T, Langer R. et al. Lipid nanoparticles for mRNA delivery. Nat Rev Mater 6: 1078–1094, 2021.

[2]. Fabian K, Stanley F, Patrick K, Wiltrud L, Twan L. Journal of Nuclear Medicine. Mar 53 (3) 345-348, 2012.

[3]. Zhou, Y, Ultrasound-mediated drug/gene delivery in solid tumor treatment. J Healthc Eng, 4 (2): 223-54, 2013.

Sonoporation of the round window membrane on a sheep model: A safety study

Sandrine Kerneis[1], Jean-Michel Escoffre[2], John J. Galvin III[3,5], Ayache Bouakaz[2], Antoine Presset[2], Corentin Alix[2], Edward Oujagir[2], Antoine Lefèvre[2], Hélène Blasco[2,3,4], David Bakhos[1, 2, 3, 5]

[1]_ENT and Cervico-Facial Surgery Department, University Hospital Center of Tours, 2 Boulevard Tonnellé, 37044 Tours, France_
[2]_UMR 1253, iBrain, Inserm, Université de Tours, 10 Boulevard Tonnellé, 37044 Tours, France_
[3]_Faculty of Medicine, Université de Tours, 10 Boulevard Tonnellé, 37000 Tours, France_
[4]_Department of Biochemistry and Molecular Biology, University Hospital Center of Tours, 2 Boulevard Tonnellé, 37044 Tours, France_
[5]_House Institute Foundation, 2100 W 3rd Street, Suite 111, Los Angeles, CA 90057, USA_
Corresponding author: sandrine.kerneis@gmail.com; Tel.: +33-247-474-785; Fax: +33-247-473-600

Introduction

Microbubble-assisted ultrasound (also termed sonoporation) increases the permeability of biological barriers (_e.g.,_ plasma membrane, blood-tumor barriers, blood-brain barrier, _etc._) to therapeutic molecules [1]. The permeabilization of the round window membrane (RWM) using this drug delivery method could increase the intracochlear bioavailability of corticoids or antibiotics in order to treat hearing diseases (_e.g.,_ infection, inflammation, _etc._). The present study aims to assess the safety of a sonoporation protocol to permeabilize the RWM [2] in a sheep model. To achieve this objective, we assessed auditory function, cochlear heating and analyzed metabolomics profiles of perilymph and plasma.

Methods

Six normal-hearing ewes were recruited, with one sonoporation and one control ear for each ewe. Mastoidectomy was performed on both ears. On the sonoporation side, Vevo MicroMarker® microbubbbles at a concentration of $2x10^8$ MB/mL were locally injected into the middle ear, and exposed to 1.1 MHz sinusoidal ultrasonic waves, at 0.3 MPa negative peak pressure with 40% duty cycle and 100 μs interpulse period for 1 min, repeated thrice with a time interval of 1 min. Then, we assessed 1) the auditory function by measuring auditory brainstem responses, with a stimulation via B71W bone transducer and responses recorded via subcutaneous needle electrodes; 2) the cochlear heating using a thermal probe which was placed in contact with the promontory; and 3) metabolomics profiles of perilymph and plasma using Liquid Chromatography – High Resolution Mass Spectrometry (LC-HRMS). The auditory function and cochlear heating were measured before and after sonoporation and compared to the control ear for each ewe. Metabolomics analysis [3] of plasma was performed on samples collected before and after sonoporation while those of perilymph were made on samples collected of sonoporated and control ears at the end of the sonoporation procedure.

Results

The sonoporation protocol did not induce any hearing impairment (Fig. 1) or toxic overheating compared to the control condition. The metabolomic analysis did not reveal any significant metabolomic difference between perilymph samples of sonoporation and control conditions. However, this analysis showed stress and energy consumption pathways in plasma, which can be attributed to the surgery and general anesthesia.
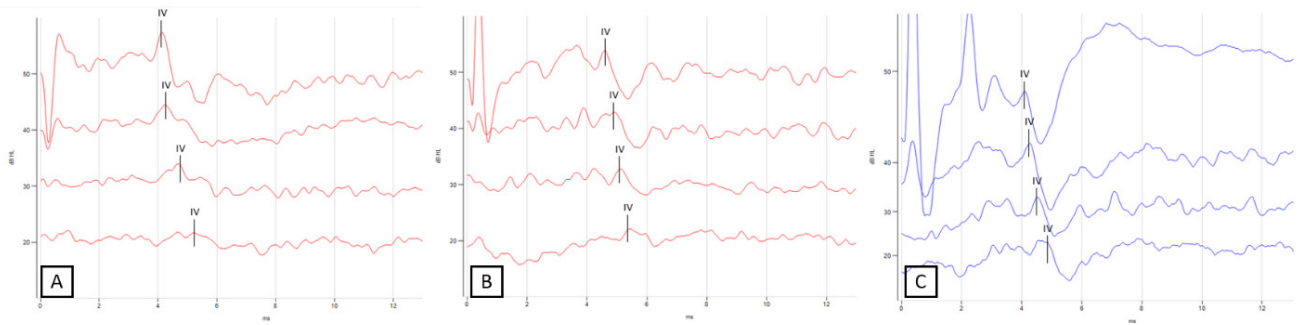
Figure 1. Representative measurement of bone conduction ABR with sonoporation side (right) before sonoporation (A), after sonoporation (B) and control side (left) (C). Waves IV are clearly distinguishable and not modified by sonoporation.

Conclusions

In conclusion, our sonoporation protocol of the RWM is applicable to a sheep model without inducing damage to the inner ear.

Grants

References

[1]. Escoffre JM, Bouakaz A. Minireview: Biophysical Mechanisms of Cell Membrane Sonopermeabilization. Knowns and Unknowns. Langmuir. 2019;35(31):10151-10165. doi:10.1021/acs.langmuir.8b03538

[2]. Lin YC, Chen HC, Chen HK, et al. Ultrastructural Changes Associated With the Enhanced Permeability of the Round Window Membrane Mediated by Ultrasound Microbubbles. Front Pharmacol. 2020;10:1580. doi:10.3389/fphar.2019.01580

[3]. Mavel S, Lefèvre A, Bakhos D, et al. Validation of metabolomics analysis of human perilymph fluid using liquid chromatography-mass spectroscopy. Hear Res. 2018;367:129-136. doi:10.1016/j.heares.2018.05.016

Real-time Monitoring of Cellular Response to Ultrasound and Microbubbles in an *in vitro* Brain Microvascular Endothelial Model

L. Hu [1], O. Jung[1,2], Q. Wu[1], L. Bau[1], M. Gray[1], M. Ferrer[2], J. L. Ruan [1,3], K. Petersson[3], E. Stride[1]

[1]*BUBBL group, Department of Biomedical Engineering, University of Oxford, Oxford, United Kingdom,*
[2]*3D Tissue Bioprinting Lab, Division of Preclinical Innovation, National Center for Advancing Translational Sciences, National Institutes of Health, Rockville, MD, USA,* [3]*CRUK-MRC Oxford Institute for Radiation Oncology, University of Oxford*
Corresponding author: luna.hu@eng.ox.ax.uk

Introduction

Drug delivery to the brain is severely limited by the blood brain barrier (BBB) [1]. The combination of focused ultrasound (FUS) and microbubbles (MBs) has been shown to non-invasively and reversibly open the BBB by reducing vascular integrity both transcellularly and paracellularly [2, 3, 4]. However, the detailed mechanisms of permeabilization are not yet fully understood and concerns have been raised about adverse bioeffects. The aim of this study was to investigate, in real time, the effect of MB distribution and dynamics on cell-cell contacts in a primary brain endothelial model in response to FUS exposure; and to compare these effects to the cells' response to non-mechanical stimuli which induce BBB opening.

Methods

MBs were produced by probe sonication, using the same constituents as Definity (not currently commercially available in the UK). 1,2-dipalm itoyl-sn-glycero-3-phosphocholine (DPPC, 25 mg/mL in chloroform), 1,2-dipalmitoyl-sn-glycero-3-phosphate (DPPA, 25 mg/mL in chloroform) and 1,2-distearoyl-snglycero-3-phosphoethanolamine-N-[methoxy(polyethylene glycol)-5000] (DSPE-PEG5K, powder form) were combined at a molar ratio of 8:1:1 to form MB films, then resuspended and sonicated in a perfluorocarbon atmosphere to form MBs. Brain microvasculature endothelial cells (BMVECs) were used between passages 3-5. To visualise real time changes in cell-cell contact, which is responsible for maintaining BBB membrane integrity, adherens junction protein VE-Cadherin were tagged with green fluorescence protein (GFP).

In a custom-built ultrasound exposure tank (Fig. 1, 2a), the BMVEC coated coverslip was placed with the cells facing down immersed in phosphate buffered saline (PBS) at 37 degrees, and at the centre of the optical and acoustic focal regions. MBs were injected under the cells and allowed to rise so that they were in contact with cells and could be detected optically and acoustically. An iCCD camera (Teledyne Princeton Instruments PI-MAX 4) was used to capture fluorescent images of the cells 30 seconds before ultrasound exposure, during, and then again after exposure for 10 minutes to enable any cell responses to be observed. Images were also captured for cells exposed to US only, MBs only and D-mannitol, which is a hyperosmotic agent used for BBB opening. The changes in cell-cell contact were quantified as shown in Fig. 3a. For treatment group frames, an additional mask for microbubble tracking was applied to monitor changes in microbubble concentration and distribution over time, which was then overlaid on the change of gap area to assess causative/correlative effects on cell-cell contacts. US exposure conditions were chosen based on existing literature for BBB opening using FUS + MBs: 0.5 MHz centre frequency, 0.17 MPa pp, 25 Hz pulse repetition frequency, 10 US cycles per pulse, for 2 minutes. A 3.5 MHz single element transducer was also used to capture acoustic emissions during treatment (Panametrics V301, 40mm focus).

Results

As shown in Fig.3b there was a ~190% increase in the relative change in intercellular area over time during exposure to FUS in the presence of MBs, compared to the pre-treatment images. This was substantially larger than in both negative controls (MB only: 2%, US only: 7%); and the positive control, D-mannitol: 32%. Furthermore, the relative change appears to be correlated with the total number of MBs in the field of view over time (Fig 3c). Qualitatively, the regions of maximum cell-cell opening appear to coincide with MB locations. Further analysis is needed to determine whether the duration of MB exposure is correlated to the degree of cell-cell opening and whether the type of microbubble dynamics affects the process. Repeating the experiment in a 3-dimensional cell model is also critical to determine whether the same degree of cell-cell opening is observed. PCD data confirms non-linear oscillations of MBs without broadband noise.

Conclusions

Exposure of BMVECs to FUS and MB was seen to promote an increase in paracellular changes, specifically cell-cell contacts, as observed by GFP signals tagged to VE-Cadherin. This change was substantially different from that seen in unexposed cells, or cells exposed to FUS or MB alone. Increase in the time MBs spent in proximity of cells during US exposure increased the change in intracellular area which suggested cell-cell opening was initiated by close contact with oscillating MB. These results imply that paracellular transport is an important component of BBB permeabilization. Further work is needed to understand whether there are any long-term effects of these cellular responses.
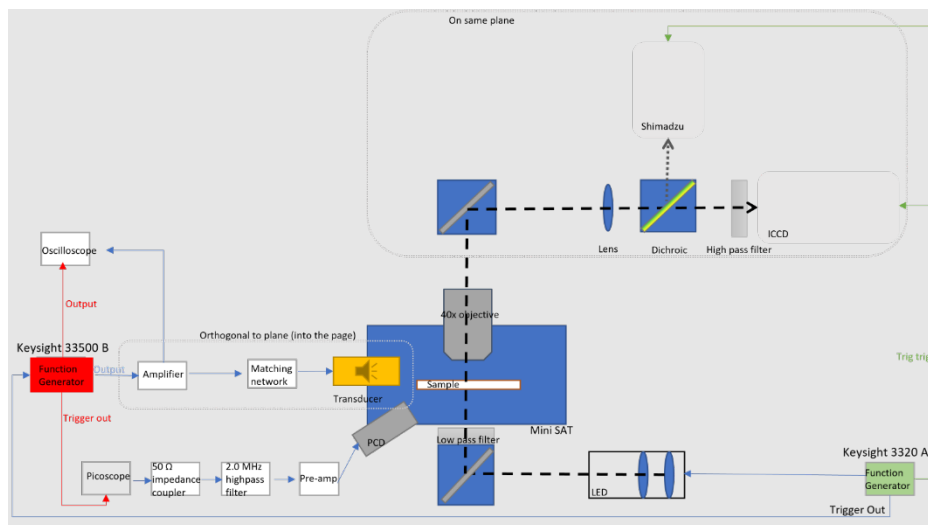

Figure 1. Ultrasound exposure tank and cameras setup. Light source, cameras and ultrasound components are synchronized to minimise phototoxicity, photobleaching, and to ensure all real time changes of MB dynamics and cell-cell contacts are captured.

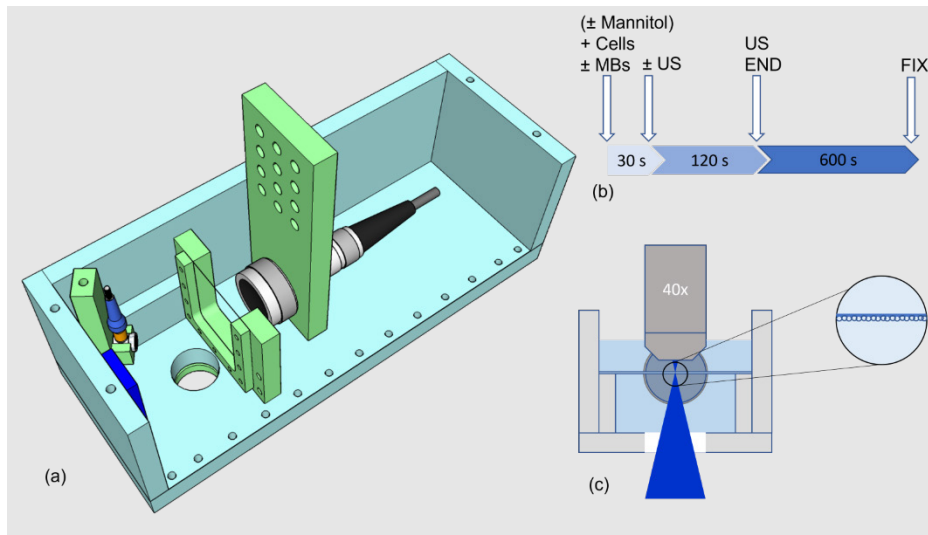--

Figure 2. Schematics of the ultrasound exposure tank and experimental timeline. (a) 3D rendering of the US exposure tank showing relative positioning of transducer mounted to backing plate, PCD in the corner, and illumination window directly below US focus. (b) Timeline showing reagent addition and ultrasound onset. (c) Frontal view of US exposure tank showing position of cells on an inverted glass slide and MBs resting on the same plane.
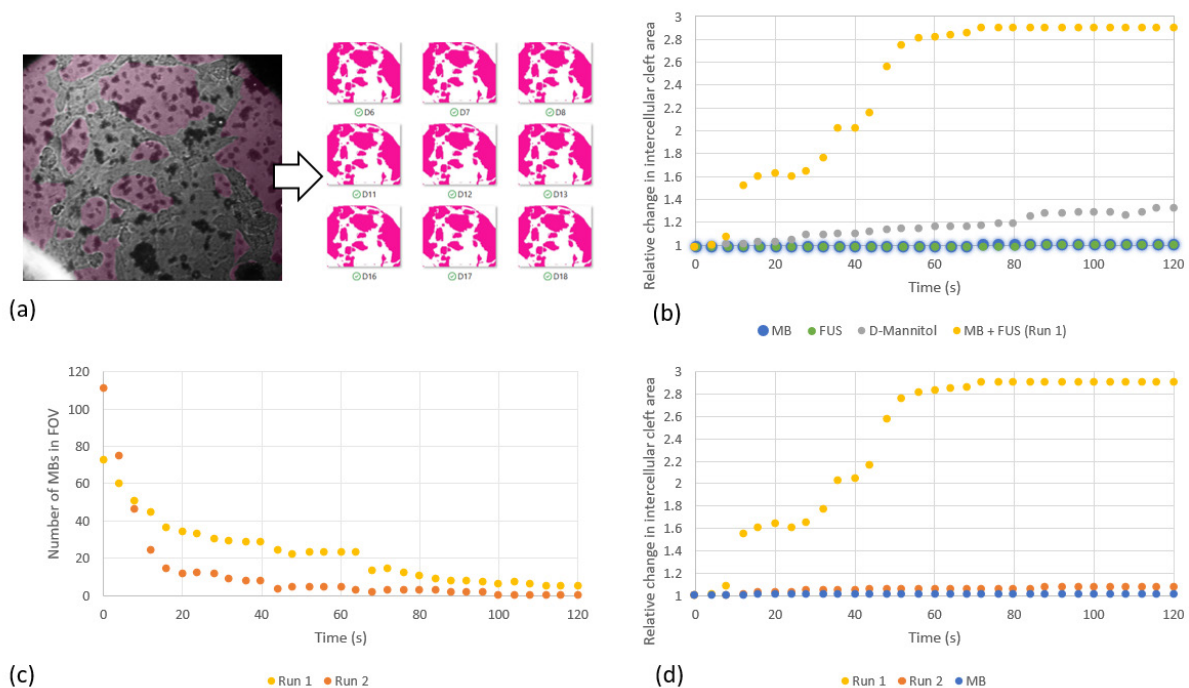

Figure 3. Data analysis and results. (a) Representative iCCD image (left), with visible intercellular cleft masked in pink, which is extracted for every frame (right, selective frames shown due to limited space). (b) Relative change in intercellular cleft area normalized to initial frame per group, over 120 second treatment period +/- US. (b) Number of MBs in FOV over 120 second treatment period, for 2 runs with MB + FUS, and (c) the corresponding relative change in intercellular cleft area, with MB only control group shown as a reference.

References

[1]. W. M. Pardridge, "The blood-brain barrier: Bottleneck in brain drug development," NeuroRX, vol. 2, no. 1, pp. 3-14, 2005/01/01 2005, doi: 10.1602/neurorx.2.1.3.

[2]. S. Roovers et al., "The Role of Ultrasound-Driven Microbubble Dynamics in Drug Delivery: From Microbubble Fundamentals to Clinical Translation," Langmuir, vol. 35, no. 31, pp. 10173-10191, 2019/08/06 2019, doi: 10.1021/acs.langmuir.8b03779.

[3]. Y. Taniyama et al., "Local Delivery of Plasmid DNA Into Rat Carotid Artery Using Ultrasound," Circulation, vol. 105, no. 10, pp. 1233-1239, 2002, doi: doi:10.1161/hc1002.105228.

[4]. K. Hynynen, N. McDannold, N. A. Sheikov, F. A. Jolesz, and N. Vykhodtseva, "Local and reversible blood-brain barrier disruption by noninvasive focused ultrasound at frequencies suitable for trans-skull sonications," (in eng), Neuroimage, vol. 24, no. 1, pp. 12-20, Jan 1 2005, doi: 10.1016/j.neuroimage.2004.06.046.

Understanding the Mechanisms of Ultrasound-Targeted Microbubble Cavitation-Mediated Blood Brain Barrier Opening

Grace E. Conway[1], Anurag N. Paranjape[1], Xucai Chen[1], Flordeliza S. Villanueva[1]

[1]*Center for Ultrasound Molecular Imaging and Therapeutics, University of Pittsburgh, Pittsburgh, PA, USA*
Corresponding author: villanuevafs@upmc.edu

Introduction

The blood brain barrier (**BBB**) poses a significant challenge for deliverying drugs to the brain. Ultrasound-targeted microbubble cavitation (**UTMC**) is being explored as a technique to transiently open the BBB, and pre-clinical studies have shown that UTMC-mediated BBB opening increases drug delivery to the brain. Phase I and II clinical trials for UTMC-mediated BBB opening in patients are ongoing, yet the underlying mechanisms are incompletely understood. We previously developed a contact co-culture transwell model of the BBB to study the mechanisms underlying BBB hyperpermeability after UTMC and determined that the hyperpermeability is mediated through an influx of calcium. Activation of RhoA is calcium dependent, can lead to actin cytoskeletal reorganization, and ultimately to heightened paracellular permeability. Thus, we sought to test the hypothesis that UTMC activation of RhoA leads to BBB hyperpermeability.

Methods

We utilized a transwell model with murine brain endothelial cells (bEnd.3) on the abluminal and murine C8-D1A astrocytes on luminal side of a 1.0 μm transwell support membrance. In-house lipid microbubbles (**MB**; mean size 3.0 μm) were added at a 3:1 MB to endothelial cell ratio before applying pulsed ultrasound (1 MHz, 250 kPa, 10 μs pulse duration, 10 ms pulse interval) for 20 s. Prior to the UTMC treatment, cells were incubated with Rho inhibitor II (Y16; 50 μM) or vehicle (water) for one hour at 37°C. Cells were stained with Hoechst 33342 (nucleus), propidium iodide (sonoporation), and calcein-AM (viability). Endothelial barrier function was assessed using two metrics: transendothelial electrical resistance (**TEER**) and permeability using 10 kDa Texas Red dextran as a model drug. Differences between vehicle and Y16 treament groups were compared using unpaired 2-tailed *t*-test. For multiple group comparison, one way ANOVA with correction of mutliple comparison post-hoc *t*-testing was performed. Significance was defined as $p<0.05$.

Results

After incubation with Y16, there was no difference in endothelial cell death or viably sonoporated endothelial cells compared to vehicle. Compared to no UTMC, UTMC increased dextran flux across the endothelial barrier from 15 to 60 minutes in the vehicle treatment. Without UTMC, there was no difference in dextran flux between Y16 and vehicle. After UTMC, there was less dextran flux at 30 and 60 minutes in the Y16 treatment compared to vehicle (**Figure 1A**). In the vehicle treatment, there was a decrease in TEER two minutes after UTMC that remained decreased for at least 60 minutes (**Figure 1B**). In the Y16 treatment group, TEER did not change after UTMC (**Figure 1B**).

Conclusions

We developed a contact co-culture model of the BBB that simulates hyperpermeability after UTMC. RhoA inhibition decreased UTMC-induced endothelial hyperpermeability. Future studies will explore how the downstream signaling of RhoA leads to changes in BBB hyperpermeability after UTMC. Understanding the mechanims mediating BBB hyperpermeability after UTMC should facilitate the development of UTMC as a drug delivery strategy for the treatment of neurologic diseases.
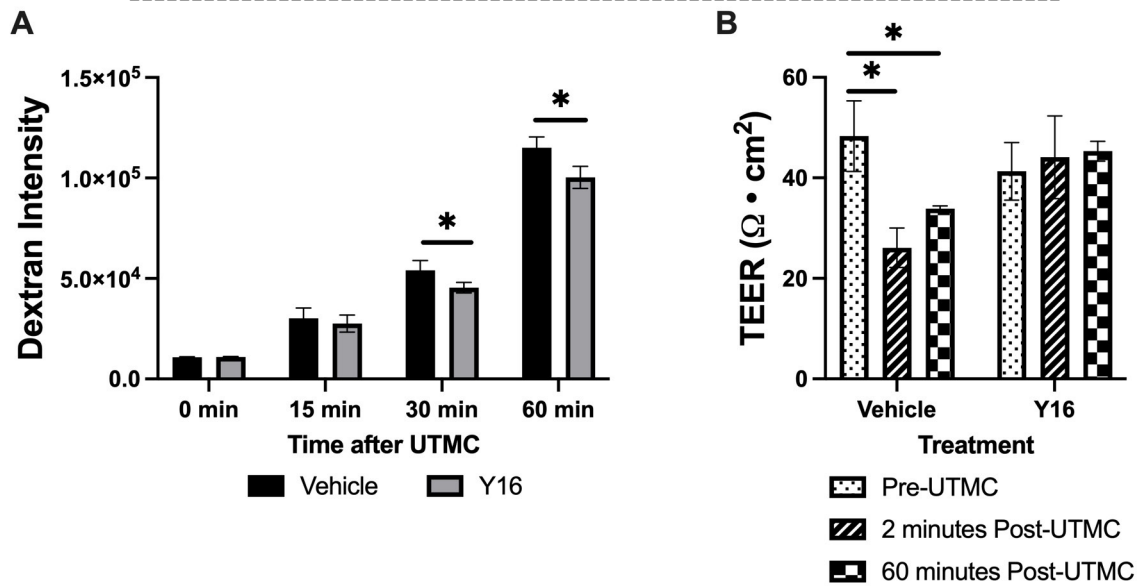
Figure 1. Inhibiting RhoA decreased UTMC mediated BBB hypermeability. Data represents mean ± SD (*n*=3-6). * $p<0.05$. **(A)** There was a decrease in 10 kDa Texas Red dextran flux across the endothelial barrier at 30 and 60 minutes in the Y16 treatment compared to vehicle after UTMC. **(B)** After UTMC, there was a decrease in TEER two minutes after UTMC that remained decreased for at least 60 minutes in the vehicle. In the Y16 treatment group, the change in TEER after UTMC was attenuated.

Microbubble-mediated induced vascular leakage in a vessel-on-a-chip model

Bram Meijlink[1], Inés Beekers[1,2], Simone A.G. Langeveld[1], Kristina Bishard[3], Antonius F.W. van der Steen[1,4], Nico de Jong[1,4], Sebastiaan J. Trietsch[3], Klazina Kooiman[1]

[1]*Department of Biomedical Engineering, Erasmus MC, Rotterdam, the Netherlands*
[2]*Department of Health, ORTEC B.V., Zoetermeer, the Netherlands*
[3]*Mimetas B.V., Leiden, the Netherlands*
[4]*Acoustical Wavefield Imaging, Delft University of Technology, Delft, the Netherlands*
Corresponding author: k.meijlink@erasmusmc.nl

Introduction

The delivery of drugs to diseased tissue is often hindered by the vessel wall. Local vascular permeability enhancement to improve drug delivery can be induced using microbubbles (MBs) which oscillate upon ultrasound (US) insonification [1]. However, more insight into the mechanism and the most efficient US pulsing scheme is needed to optimize microbubble-mediated drug delivery. A vessel-on-a-chip model, which can be grown in the OrganoPlate® 3-lane 40 (Mimetas B.V., Leiden, NL), provides the possibility to grow an advanced membrane-free model in which transcellular drug delivery can be investigated. Previously, we have reported a proof-of-concept, using this vessel-on-a-chip model to investigate the relationship between vascular permeability increase and treatment with MBs and US pressures with different pressures and cycle lengths. US pressure of 350 kPa Peak Negative Pressure (PNP) at 10×1000 cycles and 480 kPa PNP at 10×10 or 10×1000 cycle length pulses showed significant increases in permeability compared to control conditions within ~45 min after US treatment. Furthermore, at 350 and 480 kPa PNP, we showed a significant increase in sonoporation in the 10×1000 cycles groups whereas this was not seen in the 10×10 cycles group [2]. In the present study, the aim was to investigate the leakage pattern within the first 5 min upon US treatment in more detail. Furthermore, we investigated whether the MB and US treatment affected the cell viability within the vessels.

Methods

A confluent 3D microvascular tube ($300\times220\times2200$ µm) with perfusable lumen was grown by loading collagen I matrix gel in the OrganoPlate® 3-lane 40. The inside of the tube was coated using fibronectin after which Human Microvascular Endothelial Cells (HMEC) were seeded and cultured for four days under flow. DSPC-based MBs with a C_4F_{10} gas core were produced by probe sonication and targeted towards the angiogenic marker $\alpha_v\beta_3$ as previously described [3]. The microvessels were treated with MBs and 2 MHz US pulses of 10×10 or 10×1000 cycles and pressures ranging from 55-480 kPa (PNP). Control microvessels were either non-treated (sham), treated with MBs only, or treated with US only (2 MHz, 480 kPa PNP and 10×10 or 10×1000 cycles). The 10 ultrasound pulses were delivered every 3 s over a time period of 30 s. The leakage through the vessel wall was assessed with a Barrier Integrity (BI) assay using a 150 kDa FITC-dextran green fluorescent dye [2]. Initial state leakage was assessed for 45 min using fluorescence microscopy imaging (4× air objective, DS-Fi3 colour camera, Nikon Instruments). After the initial state, US treatment was performed directly followed by time-lapse imaging (12 frames/min) for 5 min. After time-lapse imaging, the vessels were imaged for another ~45 min with a frame interval of ~10 min. Leakage curves were made by dividing the intensity outside the vessel by the intensity inside the vessel using MATLAB. Furthermore, to assess the pattern of the leakage, a spatial leakage distribution was made by combining the FITC-dextran signal increase per frame of the time-lapse imaging. Finally, cell viability was assessed using a WST-8 chromatography assay. Cell free tubes and vessels with dead cells were included as a negative and positive control.

Results

Figure 1A and B represent the BI leakage data of four representative conditions. The time-lapse imaging during the first 5 min after US treatment (Fig. 1A, B) shows a clear increase in leakage directly upon treatment for the 350 and 480 kPa 10×1000 cycles groups, albeit that the increase was larger in the 480 kPa than 350 kPa group. For the 480 kPa 10×10 cycles group, hardly any leakage increase could be observed during the first 5 min after US treatment (Fig. 1A, B) while a clear increase can be seen ~25 min after US treatment (Fig. 1A). The plateau of the 10×1000 cycles with MBs groups approached 100% whereas the 480 kPa 10×10 cycles vessel plateaued at ~70%, indicating that the barrier loss was less with the short cycles treatment. Sham (Fig. 1A, B) vessels did not show a clear increase in leakage. The spatial leakage distribution of the vessels from figure 1A&B show that the leakage increase was unevenly distributed over the vessel with higher leakage into some regions compared with others (Fig. 1C). This suggests that some parts of the vessel were more affected by the treatment than others. Further analysis of the sonoporation and MB movement profiles could potentially explain the observed differences. Finally, cell viability was assessed to see whether this could explain the observed differences in leakage (Fig. 1D). There were no significant differences between the MB- and US-treated vessels and the sham condition, while all vessels showed significantly higher viability compared to the positive and negative control.

Conclusion

The 350-480 kPa and 10×1000 cycles US treatment induced an earlier onset and more vascular leakage compared with the 10×10 cycles group. Furthermore, the vessel seemed to be only partially affected as the leakage only occurred in certain regions. These findings illustrate that the vessel responded differently depending on the US settings. Finally, the US- and MB-treatment did not affect the cell viability within the vessels. These results underline the importance of determining the correct US pulsing scheme for future microbubble-mediated drug delivery treatments.
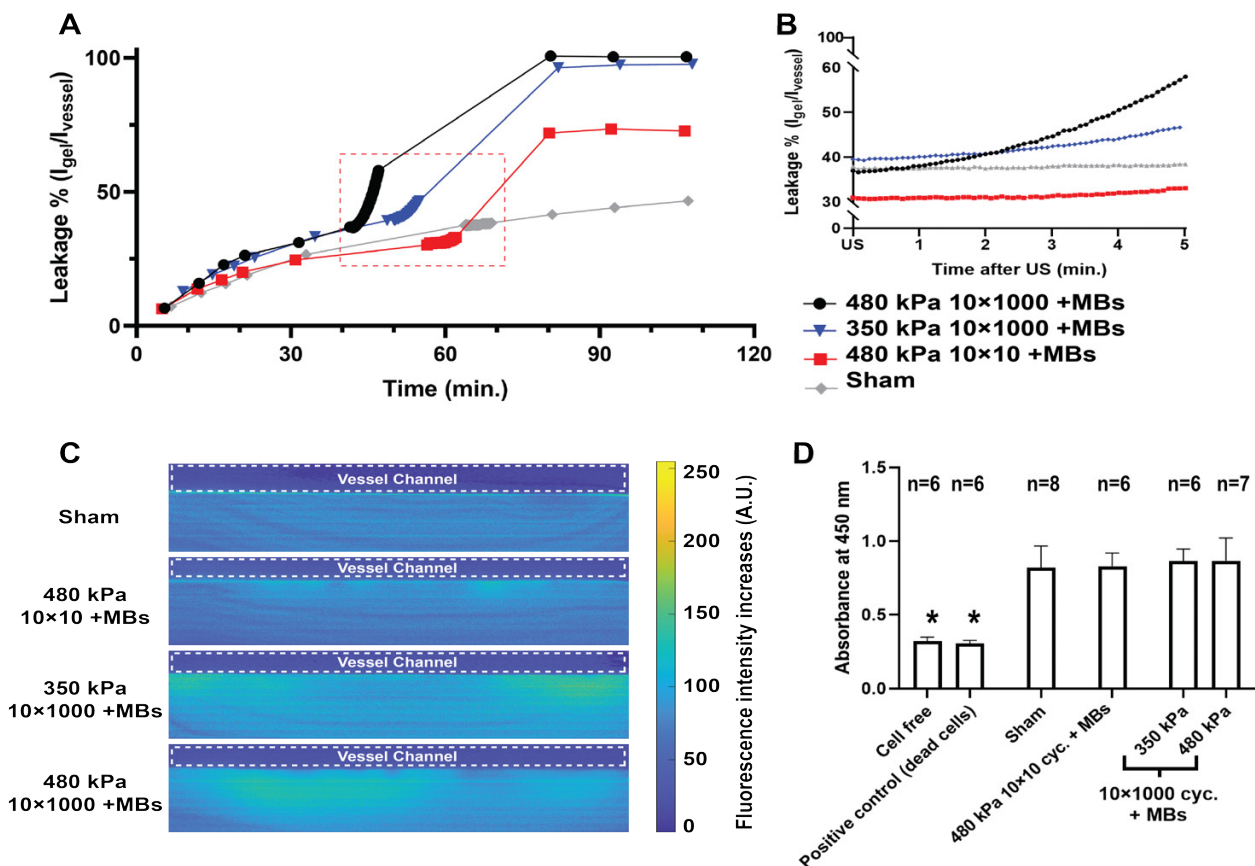

Figure 1: A) Quantification of the leakage during the BI assay with the 5-min time-lapse imaging shown in the red dashed rectangle. **B)** Zoom-in on the leakage quantification during the 5-min time-lapse imaging directly after the last US pulse treatment. **C)** Spatial leakage distribution during the 5-min. time-lapse imaging of the same vessels as in figure A & B. Part of the vessel channel is outlined with white dotted lines. **D)** Cell viability quantification in which higher absorbance indicates more viable cells. Significance shown with *p< 0.05. Bar graph showing standard deviation with whiskers.

References

[1]. Kooiman K, Roovers S, Langeveld SAG, Kleven RT, Dewitte H, O'Reilly MA, Escoffre JM, Bouakaz A, Verweij MD, Hynynen K, Lentacker I, Stride E, Holland CK, Ultrasound-Responsive Cavitation Nuclei for Therapy and Drug Delivery. Ultrasound Med Biol., VOL. 46, NO. 6, JUN 2020.

[2]. Meijlink B, Beekers I, Langeveld SAG, Bishard K, van der Steen AFW, de Jong N, Trietsch SJ, Kooiman K, The OrganoPlate® as vessel-on-a-chip model to investigate microbubble-mediated drug delivery mechanisms, 27th European symposium on Ultrasound Contrast Imaging, JAN 2021

[3]. Langeveld SAG, Beekers I, Collado-Lara G, van der Steen AFW, de Jong N, Kooiman K, The Impact of Lipid Handling and Phase Distribution on the Acoustic Behavior of Microbubbles, Pharmaceutics, VOL. 13, NO. 1, JAN 2021.

Molecular Size Threshold of Drug Delivery to the Brain using a Rapid Short-Pulse Ultrasound Sequence

William Lim Kee Chang[1,2], Sophie V. Morse[1], Federica Raguseo[2],
Nicholas J. Long[2], James J. Choi[1]

[1]*Department of Bioengineering, Imperial College London, United Kingdom*
[2]*Department of Chemistry, Imperial College London, United Kingdom*
Corresponding author: j.choi@imperial.ac.uk

Introduction

The application of rapid short-pulses of ultrasound has been shown to deliver a 3 kDa model drug (dextran) across the blood-brain barrier [1]. Compared with standard long pulses traditionally used for ultrasound-mediated delivery, rapid short-pulses can deliver drugs with an improved delivery and safety profile. 3 kDa dextran has been delivered to brain tissues with a uniform distribution, with no compromise on the dose delivered. Deliveries with this sequence have been achieved without detectable red blood cell leakage or tissue damage; and blood-brain barrier integrity has been found to be restored within 10 minutes. However, many drugs have far higher molecular weight than 3 kDa, such as protein-based (e.g. antibody fragments) and nucleotide-based therapies (e.g. antisense oligonucleotides). Here, we evaluate whether model agents of larger molecular weights can be delivered using the rapid short-pulse sequence.

Methods

Ten wild-type C57BL/6 mice were intravenously administered with *SonoVue* microbubbles (8 μL/g, 100 μL) along with Texas Red-conjugated 10 kDa or 70 kDa dextran. The hydrodynamic diameters of 3 kDa, 10 kDa and 70 kDa non-fluorescent biotinylated dextrans (0.1 mg/mL, PBS) were measured by dynamic light scattering. Focused ultrasound was applied to the left hippocampus in a rapid short-pulse sequence (1 MHz; 5-cycle pulses; peak negative pressure 0.35 MPa; 1.25 kHz pulse repetition frequency; 0.5 MHz burst frequency). Mice were sacrificed immediately following the treatment, perfused and fixed. 30-μm-thick horizontal brain slices were imaged by fluorescence microscopy (10x magnification, λ_{ex} = 562/40 nm, λ_{ex} = 624/40 nm).

Results

Fluorescent signals were detected in the left hippocampus from both 10 kDa and 70 kDa dextrans, but not in the right hippocampus, which was not exposed to ultrasound and served as a control. Appreciable delivery of 10 kDa dextran was observed, albeit with an uneven, less diffuse delivery distribution within the ultrasound beam than observed with 3 kDa dextran. Doses of 70 kDa dextran delivered were more variable and discrete areas of concentrated fluorescence were observed, resulting in a heterogeneous, speckled delivery pattern. The hydrodynamic diameters of the 3 kDa, 10 kDa and 70 kDa dextran analogues were determined to be 3.47 ± 0.65 nm, 5.39 ± 0.90 nm and 8.02 ± 1.60 nm respectively.

Conclusions

10 kDa and 70 kDa fluorescent dextran tracers can be delivered to the brain parenchyma using a rapid short-pulse ultrasound sequence, which at 0.35 MPa, has demonstrated an improved safety profile over long pulses [1]. This signifies its potential for wider application to the safe delivery of larger therapeutic drugs or imaging agents of comparable sizes, such as antibody fragments, siRNA and small nanoparticles. These findings, coupled with our previous findings [1,2], indicate that the size threshold for the delivery of compounds using rapid short-pulse ultrasound at 0.35 MPa is between 70 kDa and 150 kDa. In terms of hydrodnyamic diameter, this threshold is between 8 nm and approximately 11 nm.
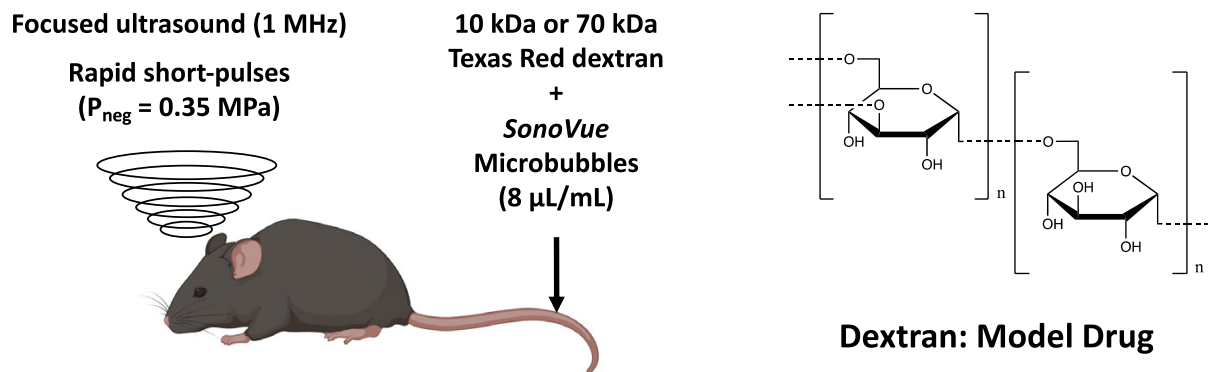
Figure 1. Dextran delivered to the murine brain using the rapid short-pulse sequence.
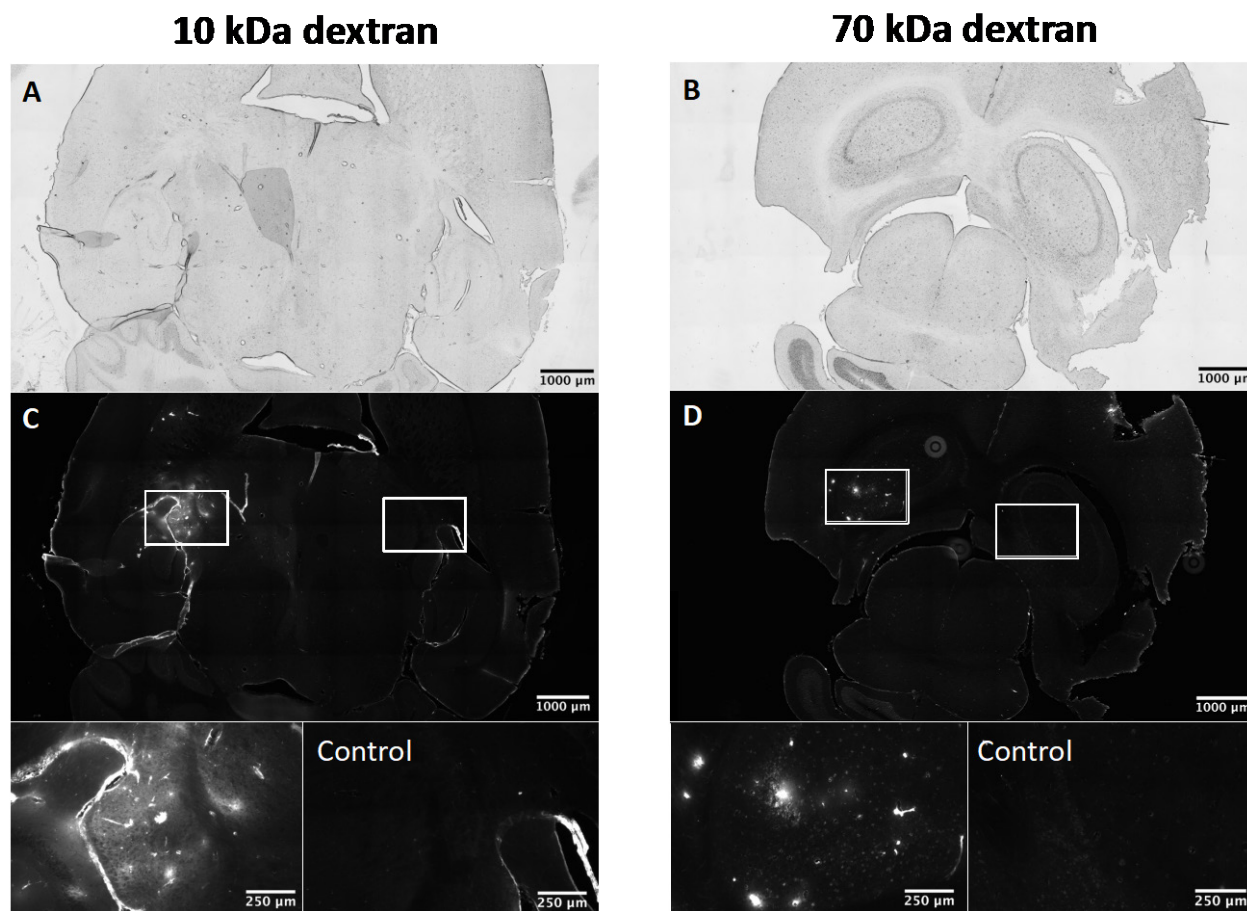

Figure 2. Rapid short-pulse ultrasound delivery of 10 kDa and 70 kDa fluorescent dextrans to the brain. A) and B) Brightfield images of mice brain slices. Fluorescence microscopy images show successful delivery of **C)** 10 kDa and **D)** 70 kDa fluorescent dextrans to the targeted left hippocampus.

References

[1]. Morse SV, Pouliopoulos AN, Chan TG, Copping MJ, Lin J, Long NJ, Choi JJ, Rapid short-pulse ultrasound delivers drugs uniformly across the murine blood-brain barrier with negligible disruption, Radiology, 291: 459-466, 2019.

[2]. Morse SV, Mishra A, Chan TG, de Rosales RTM, Choi JJ, Liposome delivery to the brain with rapid short-pulses of focused ultrasound and microbubbles, Journal of Controlled Release, 341: 605-615, 2022.

The 28th European Symposium on Ultrasound Contrast Imaging Rotterdam is sponsored by:

Bracco Suisse SA

Marco Graf, Senior
Communication Events Manager
Cadempino, Switzerland

Mindray Medical Germany GmbH

Hongbo Zhu
Marketing Ultrasound Europe
Darmstadt, Germany

Erasmus University MC - Thorax Center

Prof.dr. Felix Zijlstra,
Head of the department
Rotterdam
The Netherlands

Siemens Healthineers

Helen Cleminson
SHS US IN ADGI
United Kingdom

GE Healthcare

Christopher (Scott) Lee
Product Leader – Optison
Missouri USA

Samsung Medison

Luc van Dalen, account
manager HME of the
Samsung Electronics Benelux

Solstice Pharmaceutic Managing directorals

Wim van Hoeve, Sales Manager
Enschede, the Netherlands

Verasonics, Inc

Sara Shager
Marketing and Sales Associate
Kirkland, WA

Oldelft Ultrasound

Stefan Roggeveen
Commercial Manager
Delft, the Netherlands

Fujifilm VisualSonics

Adrie Gubbels, Sales Manager
Visualsonics
Amsterdam, the Netherlands

FIRST ANNOUNCEMENT 2024

29th EUROPEAN SYMPOSIUM ON ULTRASOUND CONTRAST IMAGING

18-19 JANUARY 2024

ROTTERDAM, THE NETHERLANDS

Information on the 29th **EUROPEAN SYMPOSIUM ON ULTRASOUND CONTRAST IMAGING**: Sharon Sewell, info@echocontrast.nl

sponsors:

Silver sponsor

Erasmus MC

THORAX CENTRUM

mindray
healthcare within reach

GE Healthcare

BRACCO
LIFE FROM INSIDE

SILVER

SIEMENS
Healthineers

Bronze sponsor

Hartstichting

SAMSUNG

BRONZE

Solstice
pharmaceuticals

FUJIFILM
VISUAL SONICS

Oldelft
Ultrasound

Verasonics
The leader in Research Ultrasound™

The 28th European Symposium on Ultrasound Contrast Imaging, Rotterdam is sponsored by: